NSEL Report Series
Report No. NSEL-039
June 2015

Development of a Long-term, Multimetric Structural Health Monitoring System for a Historic Steel Truss Swing Bridge

Ryan K. Giles

and

Billie F. Spencer, Jr.

Department of Civil and Environmental Engineering
University of Illinois at Urbana-Champaign

UILU-ENG-2015-1805

ISSN: 1940-9826

The Newmark Structural Engineering Laboratory (NSEL) of the Department of Civil and Environmental Engineering at the University of Illinois at Urbana-Champaign has a long history of excellence in research and education that has contributed greatly to the state-of-the-art in civil engineering. Completed in 1967 and extended in 1971, the structural testing area of the laboratory has a versatile strong-floor/wall and a three-story clear height that can be used to carry out a wide range of tests of building materials, models, and structural systems. The laboratory is named for Dr. Nathan M. Newmark, an internationally known educator and engineer, who was the Head of the Department of Civil Engineering at the University of Illinois [1956-73] and the Chair of the Digital Computing Laboratory [1947-57]. He developed simple, yet powerful and widely used, methods for analyzing complex structures and assemblages subjected to a variety of static, dynamic, blast, and earthquake loadings. Dr. Newmark received numerous honors and awards for his achievements, including the prestigious National Medal of Science awarded in 1968 by President Lyndon B. Johnson. He was also one of the founding members of the National Academy of Engineering.

Contact:
Prof. B.F. Spencer, Jr.
Director, Newmark Structural Engineering Laboratory
2213 NCEL, MC-250
205 North Mathews Ave.
Urbana, IL 61801
Telephone (217) 333-8630
E-mail: bfs@illinois.edu

This technical report is based on the first author's doctoral dissertation of the same title, which was completed in December 2013. The second author served as the dissertation advisor for this work.

Financial support for this research was provided in part by the Army Corps of Engineers Construction Engineering Research Laboratory (CERL) through a subcontract with Mandaree Enterprise Corporation. In addition, we would like to thank the numerous collaborators on this work, including Carol K. Shield, Steven C. Sweeney, Steve Olson, Lawrence Bergman, Soojin Cho, Robin Kim, Reginald Askew, Christopher Hsiao, Christian Hawkinson, Mike Dunne, Hongki Jo, and Kirill Mechitov.

The cover photographs are used with permission. The Trans-Alaska Pipeline photograph was provided by Terra Galleria Photography (http://www.terragalleria.com/).

ABSTRACT

The bridge stock across the United States is ageing, with many bridges approaching the end of their design life. The situation is so dire that the American Society of Civil Engineers gave the nation's bridges a grade of "C+" in the 2013 edition of their *Report Card on America's Infrastructure*. In fact, at the end of 2011, nearly a quarter of all bridges in the United States were classified as either structurally deficient or functionally obsolete. Thus, the nation's bridges are in desperate need of rehabilitation and maintenance. However, limited funds are available for the repair of bridges. Management of the nation's bridge infrastructure requires an efficient and effective use of available funds to direct the maintenance and repair efforts. Structural health monitoring has the potential to supplement the current routine of scheduled bridge inspections by providing an objective and detailed source of information about the status of the bridge.

This research develops a framework for the long-term monitoring of bridges that leverages multimetric data to provide value to the bridge manager. The framework is applied to the Rock Island Arsenal Government Bridge. This bridge is a historic, steel truss, swing bridge that spans the Mississippi River between Rock Island, IL and Davenport, IA. The bridge is owned and operated by the US Army Corps of Engineers (USACE) and is a vital link for vehicular, train, and barge traffic. The USACE had a system of fiber optic strain gages installed on the bridge. As part of this research, this system was supplemented with a wireless sensor network that measured accelerations on the bridge. The multimetric data from the sensor systems was collected using a program developed in the course of this research. The data was then analyzed and metrics were developed that could be used to determine the health of the structure and the sensor networks themselves. Statistical process control methods were established to detect anomalous behavior in the short and long term time scales. Methods to locate and quantify the damage that has occurred in the structure once an anomaly has been detected were demonstrated. One of the methods developed as part of this research was a first order flexibility method.

The SHM system this research develops has the desirable characteristics of being continuous temporally, multimetric, scalable, robust, autonomous, and informative. By necessity, some aspects of the developed SHM framework are unique and customized exclusively for the Rock Island Government Bridge. However, the principles developed in the framework are applicable to the development of an SHM system for any other bridge. Application of the SHM framework this research develops to other bridges has the potential to increase objectivity in the evaluation of bridges and focus maintenance efforts and funds on the bridges that are most critical to the public safety.

TABLE OF CONTENTS

CHAPTER 1 INTRODUCTION 1

CHAPTER 2 BRIDGE INSPECTION PRACTICES AND CONCERNS 5
2.1 Bridge Inspections 5
2.2 Corrosion 12
2.3 Bridge Deficiency Statistics 14
2.4 Bridge Collapse Statistics 17

CHAPTER 3 REVIEW OF STRUCTURAL HEALTH MONITORING 20
3.1 Desirable Characteristics of an SHM System 23
3.2 SHM Installations 28
3.3 Structural Behavior 29
3.4 Sensor Selection and Data Acquisition 32

CHAPTER 4 THE ROCK ISLAND ARSENAL GOVERNMENT BRIDGE 41
4.1 Steel Bridges 41
4.2 Rock Island Arsenal Government Bridge 46

CHAPTER 5 ANALYSIS OF THE FIBER OPTIC SENSOR SYSTEM ON THE ROCK ISLAND ARSENAL GOVERNMENT BRIDGE 65
5.1 Fiber Optic Sensors 65
5.2 Structural Health Monitoring System Installed on the Rock Island Bridge . 73
5.3 Analysis of the FO Installation 87
5.4 Acceleration 88
5.5 Strain 94
5.6 Temperature 102
5.7 Tilt 111
5.8 Summary 116

CHAPTER 6 FINITE ELEMENT MODELING OF THE ROCK ISLAND ARSENAL GOVERNMENT BRIDGE 117
6.1 Rock Island FE Model 117
6.2 Model Updating 122
6.3 Mode Shapes 135
6.4 Load Distribution and Strain Patterns 161
6.5 Summary 163

CHAPTER 7 SUPPLEMENTAL SENSOR SYSTEMS INSTALLED ON THE ROCK ISLAND ARSENAL GOVERNMENT BRIDGE 164
7.1 Wireless Smart Sensor Network 164
7.2 Digital USB Compass 187
7.3 Summary 190

CHAPTER 8 INTEGRATED SHM DATA COLLECTION PROGRAM 191
8.1 Event Detection Algorithm 191
8.2 Integrated SHM Data Collection Program 198
8.3 Summary 207

CHAPTER 9 ANOMALY DETECTION FOR COLLECTED DATA 209
9.1 Statistical Process Control 211
9.2 Data Collection and Feature Selection 218
9.3 Coefficient of Thermal Expansion 220
9.4 Change in Strain at Swing Events ($\Delta\epsilon$) 226
9.5 Mechanical Strain 260
9.6 Summary 266

CHAPTER 10 DATA INTERPRETATION AND DAMAGE DETECTION 267
10.1 Damage Locating Vector Method 268
10.2 First Order Flexibility Strain Damage Detection 273
10.3 Summary 310

CHAPTER 11 CONCLUSIONS AND FUTURE WORK 313
11.1 Future Work 314
11.2 Discussion 315

REFERENCES 317

Chapter 1

INTRODUCTION

The Rock Island Arsenal Government Bridge,[1] shown in Figure 1.1, was built in 1896. The bridge is built on the same location as two previous bridges. The first, built in 1856, was thrown off its piers in 1868 in a wind storm. The second, built in 1872, was quickly deemed functionally obsolete amid fears that it would collapse as so many other bridges at the time had under increasing train loads. In building the current bridge in 1896, it was designed and built to last to avoid having to build another in just a few years.

For 116 years the bridge has remained in continuous operation. Repairs and maintenance to the bridge have kept the eight spans of the steel truss, double-decked bridge operating just as originally designed carrying both vehicular and rail traffic and swinging to allow navigation on the river. The second span is a draw span (see Figure 1.2) that swings just as it first did on May 21, 1896. Computers and video cameras in the operator's house now assist in ensuring that the bridge swings safely, but the same four levers are used to operate the bridge, and it still takes about ninety seconds for the bridge to turn ninety degrees for a barge to pass. A more in depth history and description of the bridge is presented in Chapter 4.

However, the Rock Island Bridge has been classified as functionally obsolete because, even though it is still in relatively good condition, some trucks are unable to drive on the lower deck due to low clearance. Unlike the Rock Island Bridge, other bridges across the country are not in good condition and have been classified as deficient. At the end of 2011, 23.7% of the national bridge inventory had been deemed either deficient or functionally obsolete, leading the American Society of Civil Engineers to give the nation's bridges a grade of "C+" in the latest edition of their *Report Card on America's Infrastructure* in 2013 [1]. Even though the root cause was a design flaw, the tragic I-35 Mississippi River bridge collapse on August 1, 2007, further raised awareness of the importance of understanding the as-built condition and health of the nation's bridges.

The collapse of the Silver Bridge over the Ohio River in 1967 led to the introduc-

[1]The bridge is variably referred to as the Government Bridge, the Arsenal Bridge, or the Rock Island Bridge.

Figure 1.1: Rock Island Government Bridge looking downstream with Rock Island, IL on the left and Davenport, IA on the right.

Figure 1.2: Span II (swing span) with barges entering lock.

tion of federal requirements for routine inspections. The Federal Highway Administration (FHWA) and the American Association of State Highway and Transportation Officials (AASHTO) developed rating systems to assess the condition of bridges during visual inspections. The ratings systems have been revised numerous times to improve their effectiveness in managing the bridge inventory. Chapter 2 contains further discussion of current bridge inspection practices. However, visual inspections are often not enough to find problems in bridges. As a result, non-destructive evaluation (NDE) techniques for examining bridges in more objective detail were developed.

Structural health monitoring (SHM) of bridges has been an outgrowth of NDE. A structural health monitoring system can be defined as a continuous and reliable set of sensors and computers that acquires, processes, manages, and interprets structural data to supplement bridge inspections and allow bridge owners to make better decisions as to the performance and maintenance of their bridges. SHM deployments have been made using a number of sensor technologies. Traditional, wired sensors based on changes to electrical properties (e.g., resistance or capacitance) were the first technology to be employed. In recent years, fiber optic sensor systems based on changes to optical properties and wireless sensor networks have become common. Each sensor technology has its own benefits and drawbacks. Bridges across the globe have been instrumented with SHM systems of various sizes and complexities that vary in the quality of information they provide. Chapter 3 will discuss SHM in greater depth.

However, many factors impede an even broader adoption of SHM as a system wide tool. The cost of the SHM system is often cited as one of the major impediments. Yet, for bridge managers, the question is not gross cost of the SHM system but the cost-benefit of the SHM system [2]. The information provided by the SHM system has to be of value to the bridge manager to warrant the expenditures of installing the system. An SHM system improves its value to a bridge manager by doing more than just taking data. The system needs to process the collected data and present it in a form that the bridge manager can use and quickly understand.

The US Army Corps of Engineers (USACE) owns and manages the Rock Island Government Bridge. To help maintain and preserve the bridge, the USACE through their Engi-

neering Research and Development Center (ERDC) decided to install an SHM system on the swing span of the bridge. The installed SHM system consisted of a multimetric fiber optic sensor system, a wireless corrosion sensor system, and an acoustic emission sensor system. The various components had limited success after installation. The fiber optic system has proved the most useful and the analysis of the system as installed is presented in Chapter 5.

The objective of this research was to develop a framework for the long-term monitoring of bridges that leverages multimetric data to provide value to the bridge manager by using a diagnostic finite element model and statistical anomaly detection methods to evaluate the bridge condition. Figure 1.3 provides a flowchart of the SHM framework that has been developed during the course of this research. Each chapter in this dissertation discusses a different aspect of the developed framework. Chapter 5 evaluates the fiber optic strain system installed previously by the USACE and how it can be used in the proposed long-term monitoring framework. Chapter 6 presents the development and updating of a finite element model of the bridge. The model was used to choose locations for the wireless smart sensors that were installed on the bridge and are discussed in Chapter 7. The data from the fiber optic and wireless sensors systems as well as a USB digital compass are all collected and processed by the Integrated SHM Data Collection Program developed during this research and presented in Chapter 8. The Integrated SHM Data Collection Program includes an event detection algorithm that uses pattern recognition to determine when the bridge is swinging or trains are crossing. Chapter 9 describes the initial steps in the process of data interpretation and anomaly detection by identifying appropriate data features and applying statistical process control methods to them. Chapter 10 presents methods for locating members that are likely damaged and warrant further attention by the bridge inspector as well as a method quantifying the severity of damage at those locations. Finally, Chapter 11 presents the conclusions of this work, provides a discussion of lessons learned that are applicable to other bridges, and points the direction for future studies.

The long term SHM framework developed in this research is designed to have the following desirable characteristics: temporally continuous, multimetric, scalable, robust, autonomous, informative, and intuitive. By necessity, some of the features of the developed framework are very specific to the Rock Island Bridge. Each bridge is unique and so some customization is needed for the system to provide useful information. However, the general methodologies employed in this research, such as pattern recognition, statistical process control, and damage detection algorithms are applicable to all bridges. Even more relevant to any structural health monitoring installation is the concept of ensuring data quality and that the data collected is measuring what is intended to be measured. Applying the concepts employed in the developed for the SHM framework for the Rock Island Bridge to other installations will make SHM a more viable tool for the management of individual bridges and bridge networks.

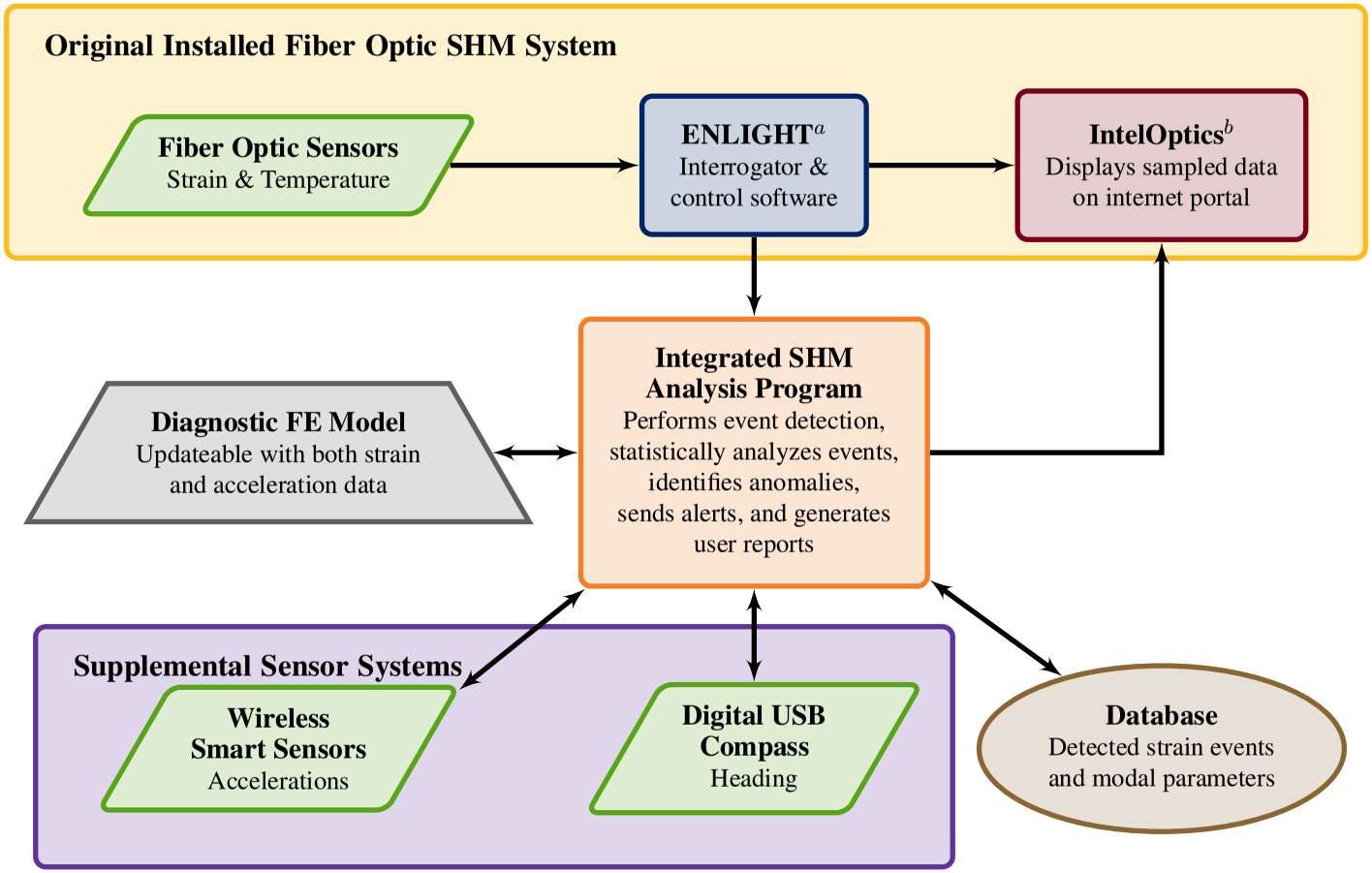

[a] ENLIGHT is a software program provided by the sensor manufacturer MicronOptics to interface with the fiber optic interrogator and can provide an interface for data collection.
[b] IntelOptics is a software program created by Chandler Monitoring Systems that can display data online and store it periodically in a database.

Figure 1.3: Flowchart of the Integrated SHM System for the Rock Island Bridge.

Chapter 2

BRIDGE INSPECTION PRACTICES AND CONCERNS

Structural health monitoring is intended to supplement – not replace – visual bridge inspection by trained inspectors. To better appreciate the role SHM can play in bridge inspection and management, understanding the history and methods of the current bridge inspection practices is important and will be reviewed in this chapter. The dominant causes of bridge failures, including corrosion, will also be discussed to provide a basis for designing an SHM system that can best prevent such failures.

2.1 Bridge Inspections

On December 15, 1967 the Silver Bridge over the Ohio River collapsed sending thirty-one automobiles into the river below [3]. Forty-six people died and another nine were seriously injured. Investigations into why the aluminum painted steel truss bridge built in 1928 collapsed led to a minute crack that was formed during the fabrication of one of the bridge's many eye-bars. Over its forty-nine year existence, the tiny undetectable[1] cracks grew under the little understood phenomenon of stress corrosion cracking and fatigue cracking until the eye-bar failed causing a chain reaction that brought the whole bridge down.

The Silver Bridge was not the first bridge to collapse (see Section 4.1.1), and it unfortunately was not the last (see Section 2.4). However, with television news crews rushing to the scene, the nation as a whole was deeply affected by the catastrophe. Bridges of similar designs were shut down, and Lyndon B. Johnson ordered an investigation into the safety of the national bridge stock. The concern was that even in 1967, more than 1,800 bridges were over forty years old, and 1,100 of those highway bridges had been designed for traffic loads corresponding to the Ford Model-T, which was nearly three times lighter than the average vehicle in 1967 [3].

2.1.1 National Bridge Inspection Standards

As a more permanent reaction to the Silver Bridge collapse, the U.S. Congress passed the Federal-Aid Highway Act of 1968[2] that included a provision (U.S. Code, Title 23, Chapter

[1] Technology at the time of the collapse was unable to detect such cracks let alone the technology available during construction.

[2] Federal-Aid Highway Acts were passed regularly to provide funding for the sates to build the highway system. The most recent Federal-Aid Highway Act prior to that passed in 1968 was in 1966. The Federal-Aid Highway Act of 1956 established the Eisenhower Interstate system.

1, §151) that called for the establishment of National Bridge Inspection Standards (NBIS). The law called for the creation of standards that would, to quote the legislation:

1. specify, in detail, the method by which such inspections shall be carried out by the States;
2. establish the maximum time period between inspections;
3. establish the qualifications for those charged with carrying out the inspections;
4. require each State to maintain and make available ... written reports on the results of highway bridge inspections ... and current inventory data...;
5. establish a procedure for national certification of highway bridge inspectors.

To be clear, bridge inspections did not begin in 1968. State departments of transportation and railroad owners had been inspecting their bridges for years as part of their regular maintenance programs. However, the 1968 legislation mandated the creation of national standards, made funds available for compliance, and made funds for construction and repair contingent on following the national standards.

In March of 1968, the FHWA issued a memo that asked the states to inspect all bridges by January 1970, required that all bridges subsequently be inspected once every five years or every two years for important structures, and recommended the 1964 AASHO[3] *Information Guide for Maintenance Personnel* as a guide for instructing bridge inspectors. By 1970, not only had the states performed their mandated inspections, fixed many issues that they encountered, and provided data on their bridge stock to the federal government, but AASHO compiled the first edition of their *Manual for Maintenance Inspection of Bridges* and the FHWA released their *Bridge Inspector's Training Manual 70*. These founding documents of bridge inspection were codified in 1971 as the National Bridge Inspection Standards that had been mandated in 1968.

In 1971, the NBIS required that all bridges be inspected every two years, and the first cycle had to be completed by July 1973. Detailed reporting formats were established and guidelines and criteria for appraisal ratings and sufficiency ratings were laid out. A licensed engineer was required in each state department of transportation. It also established the five types of inspections that are still standard today [4]. The five inspection types are[4]:

Inventory Inspection: the first inspection of a bridge as it becomes a part of the bridge's database file to provide all Structure Inventory and Appraisal (SI&A) data and other relevant data and to determine baseline structural conditions. The Inventory Inspection is also known as an Initial Inspection.

Routine Inspection: a regularly scheduled inspection consisting of observations and measurements needed to determine the physical and functional condition of the bridge, to identify any changes from initial or previously recorded conditions, and to ensure that the structure continues to satisfy present service requirements.

[3]Now known as AASHTO, AASHO was founded in 1914. The "T" standing for transportation was not added to make it AASHTO until 1973.

[4]The descriptions of the inspection types are quoted from the most recent update (2004) to the National Bridge Inspection Standards in the Code of Federal Regulations [4].

Damage Inspection: an unscheduled inspection to assess structural damage resulting from environmental factors or human actions.

In-Depth Inspection: a close-up inspection of one or more members above or below the water level to identify any deficiencies not readily detectable using routine inspection procedures; hands-on inspection may be necessary at some locations. In-Depth Inspections include Fracture Critical Member Inspections as a subset.

Interim Inspection: an inspection scheduled at the discretion of the individual responsible for bridge inspection activities, used to monitor a particular known or suspected deficiency. Interim Inspections are also known as a Special Inspections.

The NBIS standards have been updated periodically in the intervening decades since their establishment in 1971. The qualifications for bridge inspectors have also changed over the years. As concerns over certain aspects of bridge safety (e.g., fracture critical members or scour) have arisen, the standards have been altered to single out these factors and improve the ability of the mandated inspections to prevent associated disasters. The AASHTO *Manual for Maintenance Inspection of Bridges* and the FHWA *Bridge Inspector's Training Manual* have seen numerous revisions and additional manuals with more specific applicability have been published. The most recent revision to the NBIS was done in 2004 though it was updated to include the 2008 publication of the *Manual for Bridge Evaluation*[5] by AASHTO as the guide for highway bridge inspection procedures.

The railroad industry and its bridges are not covered under the mandates of the NBIS. However, AREMA (American Railway Engineering and Maintenance-of-Way Association) has prepared their own guidelines and procedures for the routine inspection of railroad bridges. The latest guide was published in 2008 as the *AREMA Bridge Inspection Handbook* [5]. The copyright page of the manual explicitly states that "Actual [inspection] policies and practices are the prerogative of individual railroads." Nevertheless, the *AREMA Bridge Inspection Handbook* is very similar to the AASHTO and FHWA guides, and the critiques of highway bridge inspection are equally valid for the inspection of railroad bridges.

Part of the evolution of the NBIS has been to take advantage of the improvements in computing that have paralleled that of bridge inspection. In 1975, Texas was the first state to use a punch-card reporting scheme accepted by the FWHA; the punch-card scheme was later required of all states [6]. Bridge inspection reports were later cataloged and entered onto personal computers. Over the decaodes, the computational and data management capabilities of modern computers has continued to grow. However, the amount of data collected in bridge inspections has not increased since the days of the punch cards. The limited amounts of data required by the NBIS are outdated with respect to the data management and processing capability of modern computers.

The primary problem with the NBIS was that the bridge rating and inspection process just did not provide enough detail. Each bridge was given a condition rating on only its four principal parts: superstructure, substructure, deck, and culverts. And each of these parts was rated on a scale from 0 to 9 defined as follows: [7]

[5]AASHTO released a second edition of the *Manual for Bridge Evaluation* in 2011 that includes interim revisions but this new edition has not yet been codified in to the federal standards.

9 Excellent Condition

8 Very Good Condition – no problems noted.

7 Good Condition – some minor problems.

6 Satisfactory Condition – structural elements show minor deterioration.

5 Fair Condition – all primary structural elements are sound but may have minor section loss, cracking, spalling, or scour.

4 Poor Condition – advanced section loss, deterioration, spalling, or scour.

3 Serious Condition – loss of section, deterioration, spalling, or scour have seriously affected primary structural components. Local failures are possible. Fatigue cracks in steel or shear cracks in concrete may be present.

2 Critical Condition – advanced deterioration of primary structural elements. Fatigue cracks in steel or shear cracks in concrete may be present or scour may have removed substructure support. Unless closely monitored it may be necessary to close the bridge until corrective action is taken.

1 "Imminent" Failure Condition – major deterioration or section loss present in critical structural components, or obvious vertical or horizontal movement affecting structure stability. Bridge is closed to traffic but corrective action may put bridge back in light service.

0 Failed Condition – out of service; beyond corrective action.

These ratings do not give a very clear understanding of the complex condition state of the nation's bridges.

In addition, the NBIS rating system is highly subjective. The designated bridge rating for a bridge can vary from one inspector to another or even for the same inspector from day to day (see Section 2.1.3). The rating system did nothing to identify the process or extent of the deterioration and could hide severe local deterioration in an individual member because the majority of the bridge was in a better condition [8]. Because federal funds were given based on the sufficiency rating derived from the condition ratings, they were not always allocated effectively. A new data management system that had the detail required to better manage the monies allocated for maintenance, repair, and rehabilitation (MR&R) was needed.

2.1.2 Bridge Management Systems and CoRe Elements

In 1991, as part of the Intermodal Surface Transportation Act, each state was required to produce and use a bridge management system (BMS) by 1998. The mandated BMS approach would improve the type, quantity, and quality of data collected during bridge inspections and, more significantly, how it was used and analyzed. Using the data collected

from inspections, the BMS could assess current MR&R needs and set priorities for fund allocations. Bridge managers also wanted the BMS to make reliable predictions about the future needs of the state department of transportation based on the analysis of the data collected. Using BMS, allocated funds could be used effectively and efficiently, and the effects of future funding levels on the bridge stock could be predicted to help secure needed funding levels. Pontis [8], a BMS program developed for the FHWA with the help of the California Department of Transportation (Caltrans), was given as an example. Over the years, Pontis has been improved and integrated into AASHTOware [9] suite of software products as "AASHTOware Bridge: Management." In 2012, forty-three states, Puerto Rico, the District of Columbia, and Italy had licenses to use the Pontis/AASHTOware based software [10].

At the heart of the BMS mandate and the Pontis software is the idea that the bridge inspection process needs to break the bridge down into more than just four constituent parts. The *AASHTO Guide for Commonly Recognized (CoRe) Structural Elements* [11] has identified elements that are commonly used in highway bridge construction and easily identifiable during bridge inspections. A CoRe element is a component (or group of components) that are: made of the same material and therefore subject to the same deterioration processes, expected to deteriorate at the same rate under normal service conditions, and can be inventoried with units (e.g., length or area) that are easily recorded by the inspector. The first version of Pontis contained a menu of 160 available CoRe elements of which each bridge would be expected to have on average ten elements [8]. Through discussions amongst the state department of transportation, the number of CoRe elements was finally codified as just 108 standard elements.

CoRe elements are varied and include designations for piers, bearings, decks, trusses, and railings, amongst others. The *AASHTO Guide for Commonly Recognized (CoRe) Structural Elements* contains a description of each element as well as a description of the condition states that each element can have. Each element typically has three to five condition states that can be selected during the inspection process and each state represents a more severe state of deterioration. "Smart flags" can be used to identify unique situations that are not addressed by the standard condition states for a CoRe element. However, as the smart flags are not standardized, their usefulness in the overall BMS system is minimized.

In the NBIS, the truss of the Rock Island Government bridge would be considered the superstructure and have just a single rating. However, the Government Bridge truss would have the following CoRe elements:

- 121 Through Truss (Bottom Chord) – Painted Steel
- 126 Through Truss (Excluding Bottom Chord) – Painted Steel
- 113 Stringer – Painted Steel
- 152 Floor beam – Painted Steel

Each of these CoRe elements is associated with the five condition states for painted steel elements:

- Condition State 1: The paint system is sound and functioning as intended to protect the steel surface.

- Condition State 2: The paint system may be chalking, peeling, curling or showing other early evidence of paint system distress but there is no exposure of steel. There is little or no corrosion. Surface or freckled rust has formed or is forming.
- Condition State 3: The paint system is no longer functioning as intended. Surface or freckled rust is prevalent. There may be exposed steel but there is no corrosion which is causing loss of section.
- Condition State 4: Corrosion is present but any section loss due to corrosion does not yet warrant structural analysis of either the element or the bridge.
- Condition State 5: Corrosion has caused section loss and is sufficient to warrant structural analysis to ascertain the impact on the ultimate strength and/or serviceability of either the element or the bridge.

A single condition level is not assigned for each element. Instead, each CoRe elements is assigned a length and each condition level is assigned a portion of the total length. For example, the swing span of the Rock Island Government Bridge is about 365 feet long, thus for CoRe element "121 Through Truss (Bottom Chord) – Painted Steel" the total unit length would be 730 feet to account for both bottom chords on the truss. After inspecting the bridge and realizing that the paint is still in relatively good shape except for chipped paint found in a few locations where rust had begun to appear, the condition assessment may be assigned as follows[6]:

- Condition State 1: 670 feet
- Condition State 2: 40 feet
- Condition State 3: 10 feet
- Condition State 4: 10 feet
- Condition State 5: 0 feet

A bridge manager who sees this inspection report has a much clearer understanding of the condition of the bottom chord of the bridge. Using this information, he could assign a crew to patch the paint in the twenty feet identified as in Condition States 2 and 3, while not having to incur the costs of painting the entire truss. An elemental condition assessment portrays the condition of the bridge better than assigning a single number to the entire superstructure.

2.1.3 Reliability of Visual Inspections

The use of BMS and CoRe elements has improved the ability of the states to manage their infrastructure assets. However, the concern that the quality and accuracy of inspections can

[6]The condition assessment presented here is theoretical and for demonstration purposes only.

still vary from inspector to inspector has not been fully addressed. In 2001, the FHWA released a study [7] it commissioned to investigate the reliability of visual inspection of highway bridges. The study focused on routine and in-depth inspections and followed the standard NBIS criteria and procedures (e.g., CoRe elements were not used). Forty-nine practicing bridge inspectors from twenty-five states[7] from all regions of the country were asked to perform visual inspections of the Non-Destructive Evaluation Validation Center (NDEVC) test bridges located in northern Virginia and southern Pennsylvania.

One task the participants were asked to do was to perform a routine inspection of a decommissioned single span simply supported steel girder bridge. The participants assigned a condition rating (0–9) for the deck, substructure, and superstructure of the bridge as per NBIS standards. Figure 2.1 shows a plot of the condition ratings assigned by the bridge inspectors. The bridge inspectors assigned condition ratings that varied about ± 2 ratings from the average rating. The bridge had previously been assigned a reference ratings by the experts at the NDEVC to determine the "accuracy" of the bridge inspectors. Table 2.1 shows the statistics for the sample of inspectors that rated the bridge.

In the FHWA study, analyses determined that, in most cases, the average inspector rating was statistically different from the reference condition rating. Even if there is an error allowance in the determination of the reference condition, a majority of inspections are still statistically different from the actual condition of the bridge. The study concluded that 95% of NBIS primary element Condition Ratings for individual bridges will vary within two rating points of the average. These results suggest that a bridge that should actually be rated a 6 could be rated an 8 during one inspection and rated a 4 just two years later, even

[7]Each state chosen to participate was asked to provide two bridge inspectors. One inspector was to be more experienced than the other.

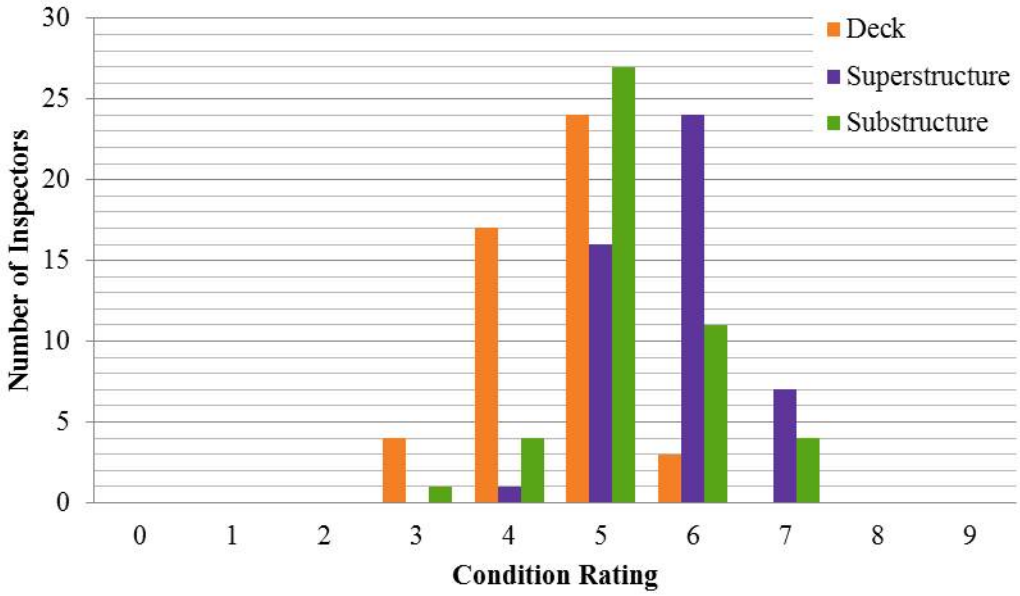

Figure 2.1: Inspector condition ratings from a routine inspection in a FHWA study of visual inspection reliability.

Table 2.1: Statistics from a routine bridge inspection in a FHWA study of visual inspection reliability.

	Primary Element		
	Deck	Superstructure	Substructure
Reference Rating	4	6	6
Mean	4.5	5.8	5.3
Standard Deviation	0.74	0.72	0.83
COV	0.16	0.13	0.16
Minimum	3	4	3
Maximum	6	7	7
Mode	5	6	5
N	48	48	47

though the bridge condition did not change in the interim. More significantly, the FHWA study determined that inspectors performing in-depth inspections "are not likely to detect and identify the specific types of defects for which this inspection is sometimes prescribed," and "a significant proportion of the in-depth inspections will not reveal deficiencies beyond those that could be noted during a routine inspection" [7, p. 478].

The subjective nature of visual inspections, and the fact that they do not always catch the bridge deficiencies they are designed to detect, leaves room for improvement. Structural health monitoring, therefore, has the potential to become a tool that the departments of transportation in the United States can use to provide objective, continuous, and reliable data on the condition of their bridge stock. SHM will not completely replace visual inspection, but rather SHM will serve as a compliment to visual inspection that can increase the efficiency and accuracy of the process.

2.2 Corrosion

A primary concern in the inspection of steel bridges is the detection and tracking of corrosion of the bridge material. The presence of corrosion is usually indicated by discoloration due to the presence of rust. The rust, or hydrated iron(III) oxide to be chemically correct, is the result of two simple oxidation-reduction (or redox) reactions that takes place in the presence of water and oxygen. In the first redox equation, iron in its solid elemental state at the anode reacts with oxygen and hydronium ions in water to form iron(II) ions as shown in the following equation.

$$\mathrm{Fe}_{(s)} + \frac{1}{2}\mathrm{O}_{2(g)} + 2\mathrm{H}_3\mathrm{O}^+_{(aq)} \rightarrow \mathrm{Fe}^{2+}_{(aq)} + 3\mathrm{H}_2\mathrm{O}_{(\ell)} \tag{2.1}$$

The iron(II) ions migrate to the cathode where they are oxidized again in the presence of oxygen to form rust ($\mathrm{Fe_2O_3 \cdot }x\mathrm{H_2O}$) according to the following equation.

$$2\mathrm{Fe}^{2+}_{(aq)} + \frac{1}{2}\mathrm{O}_{2(g)} + (6+x)\mathrm{H_2O}_{(\ell)} \rightarrow \mathrm{Fe_2O_3 \cdot }x\mathrm{H_2O}_{(\ell)} + 4\mathrm{H_3O}^{+}_{(aq)} \tag{2.2}$$

Notice that the hydronium ions that are produced as a result of the formation of rust in Equation (2.2) are what are needed to start the corrosion process in Equation (2.1). Therefore, the corrosion cycle can continue as long as oxygen is supplied [12].

The corrosion rate in steel is influenced by a number of factors. The presence of an electrolyte, for example from dissolved salts used to deice the roads, can facilitate the flow of the charged ions through the water. The more acidic the aqueous solution is, the more hydronium ions are present to start the corrosion process. The acidity of the water can be increased by dissolved carbon dioxide and many elements of air pollution. The presence of another metal with a different electrical potential that is electrically connected to the steel can decrease or increase the corrosion rate of the steel. If the metal is easier to oxidize than iron (i.e., magnesium) than the second metal will become a sacrificial anode and the steel will not corrode in a process called cathodic protection. However, if the second metal is harder to oxidize then the potential differential between the metals will accelerate the corrosion of the steel. The accelerated corrosion is called bimetallic corrosion and can occur for a variety of different metals in conjunction with iron or steel [13].

Bimetallic corrosion is of concern for the Rock Island Bridge because stainless steel is more electropositive than carbon steel. Whereas the original material is all the same mild steel, the casings of the fiber optic sensors installed as part of the structural health monitoring system are made of stainless steel. The spot welding process brings the two metals of different electrical potentials in direct contact completing the electrical circuit necessary for bimetallic corrosion to occur.

The simple electrochemical reactions that describe corrosion hide the devastation that it can cause. Steel structures are typically protected by a layer of paint that prevents the water and oxygen from starting the redox reactions. However, when the paint weathers and chips, the steel exposed to the water and oxygen in the atmosphere acts as the cathode where the rust forms. The anode where the iron molecules are first oxidized develops under the paint where oxygen is not readily available. Pitting occurs at the anode, under the paint, when metal is lost due to the oxidized iron(II) ions migrating to the cathode to become rust. In severe cases, the pitting can cause section loss in the member leading to a loss of capacity and eventually failure.

Though it begins at a molecular level, corrosion and the effects of corrosion are very costly on a national scale. In a study released in 2002 by the Federal Highway Administration [14], the total annual direct cost of corrosion across all industries in 1998 was estimated to be \$276 billion (3.1% of the U.S. GDP). In narrowing the cost of corrosion to just highway bridges,[8] the FHWA report determined that the annual total direct cost of cor-

[8]The direct costs of corrosion on railroad infrastructure could not be determined because the maintenance of the track and bridges is primarily done by the private railroad companies. Nevertheless, corrosion is estimated to cost the railroads \$500 million in the maintenance and replacement of just the railroad cars and

rosion for highway bridges was $8.3 billion. As shown in Figure 2.2, the maintenance and repair of reinforced concrete bridge elements (decks and substructures) due to corrosion of the reinforcing steel accounted for nearly half of the total direct costs of corrosion for highway bridges. Only half a billion dollars was spent maintaining steel bridges. A total of $3.8 billion was spent to replace bridges where corrosion had caused them to become structurally deficient. The age of our nation's infrastructure is likely to only cause these direct costs to increase.

2.3 Bridge Deficiency Statistics

According to the Federal Highway Administration (FHWA) [15], the National Bridge Inventory contained 605,098 bridges as of December 2011 (see Table 2.2). 143,889 of the nation's bridges, or 23.7% of the entire inventory, are either structurally deficient or functionally obsolete. A structurally deficient bridge is defined as one that, during its inspection, has received either:

1. a condition rating of 4 or less for its deck, superstructure, or substructure
2. an appraisal rating of 2 or less for its structural condition or waterway adequacy

Likewise a functionally obsolete bridge is defined as one that has received either:

1. an appraisal rating of 3 or less for its deck geometry, underclearances, or approach roadway alignment

engines.

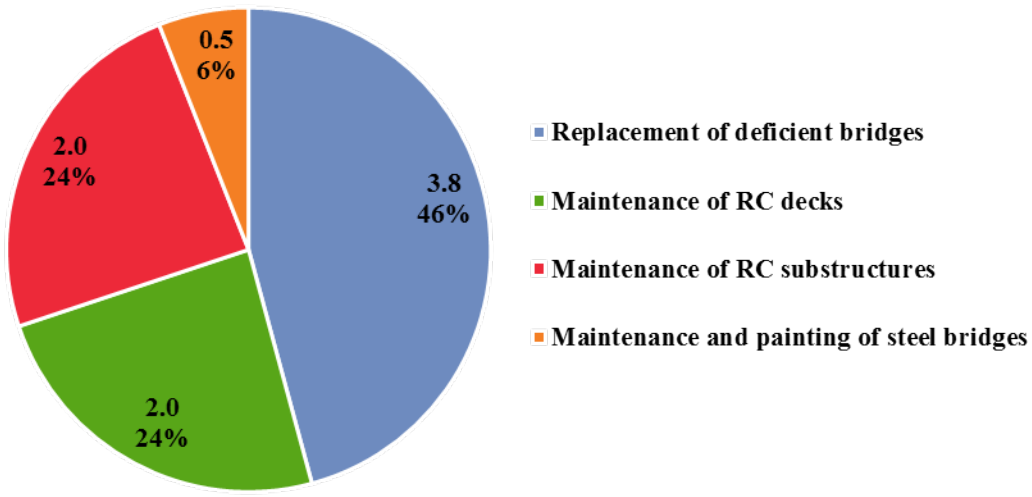

Figure 2.2: Annual direct cost of corrosion for highway bridges in US$ (billions).

Table 2.2: National Bridge Inventory by material and condition.

Material[a]	Condition			Total (Bridges)
	Serviceable	Structurally Deficient	Functionally Obsolete[b]	
Concrete[c]	327,057	26,724	40,337	394,118
Steel	116,235	34,934	32,530	183,699
Wood	11,723	8,886	2,852	23,461
Other[d]	2,519	656	645	3820
Total	461,209	67,525	76,364	605,098

[a]From FHWA data published in Dec. 2011.
[b]Any bridge classified as structurally deficient is excluded from the functionally obsolete category.
[c]Includes pre-stressed concrete bridges
[d]Includes bridges made of masonry, aluminum, iron, and other materials.

2. an appraisal rating of 3 or less for its structural condition or waterway adequacy

In general, functionally obsolete bridges tend to be older and designed for loads or clearances that are not sufficient for modern conditions.

The fact that 23.7% of the bridge inventory is either deficient or obsolete has led the American Society of Civil Engineers to give the nation's bridges a grade of "C+" in the latest edition of their *Report Card on America's Infrastructure* in 2013 [1]. ASCE further estimates that it will cost a total of $850 billion over the next fifty years (or $17 billion annually) to eliminate all existing bridge deficiencies that are currently known and those that are sure to arise in the interim. A minimum of $650 billion would be required just to keep the number of deficient bridges from growing. As seen in Figure 2.3, the nation built a large portion (50.9%) of its highway infrastructure over forty years ago [16]. These bridges are past or approaching their design life of fifty years. As the nation's infrastructure ages, natural deterioration takes it course and more bridges will continue to become deficient unless preventative measures are taken now.

The deficient surface transportation infrastructure is not just expensive in direct maintenance and replacement costs. ASCE estimates result in annual indirect costs of $32 billion due to travel delays and another $97 billion in increased vehicle operating costs. If the investments to repair and maintain the infrastructure are not made in the next ten years, ASCE estimates fixing the nation's transportation infrastructure would require an additional $430 billion, household income would fall by $7,000, and U.S. exports would decrease by $28 billion [17]. ASCE recommends implementing "an asset-management approach to maintaining bridges to achieve an appropriate balance between correcting immediate problems, conducting preventive maintenance, rehabilitating deficient bridges, and periodically replacing older bridges," [18]. Structural health monitoring can be a vital part of implementing such an asset-management approach because it can help determine what needs to be repaired.

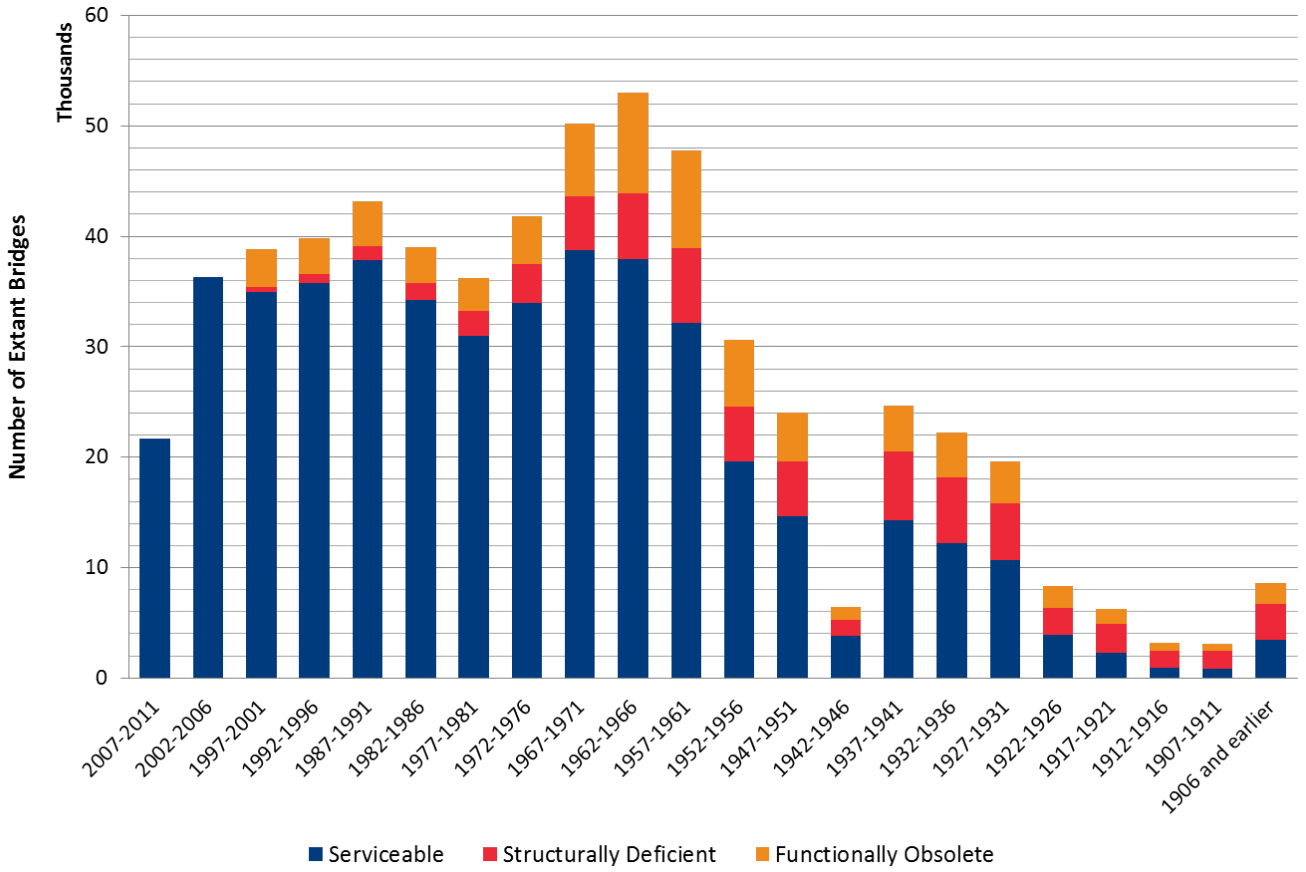

Note: Bridges that are less than 10 years old are never classified as structurally deficient or obsolete. Any bridge classified as structurally deficient is excluded from the functionally obsolete category. From FHWA data as of Dec. 2011 [16].

Figure 2.3: Bridges and their condition by year built.

The previous figures and costs are for all bridges in the National Bridge Inventory. Narrowing the focus, steel bridges account for only 30.4% of the total inventory, but steel bridges account for 46.9% of the structurally deficient or functionally obsolete bridges. Separating the two levels of inadequacy, 19.01% of steel bridges are structurally deficient, which accounts for 51.7% of all structurally deficient bridges with corrosion being the most likely cause of the deficiency. If the category is narrowed even further, to steel bridges that have been in service for over one hundred years, the percentages increase even further. Bridges that were built before 1912 make up only 1.94% (11,730 bridges) of the bridge inventory[9] (see Figure 2.3). Although the FHWA does not provide condition statistics by both age and construction material, it is safe to assume that a majority of the century old bridges are made of steel. Some non-steel bridges are over a century old, but most stone arch bridges have been removed from service, reinforced concrete was just beginning to gain widespread use as a bridge material in 1912,[10] and timber bridges have a shorter lifespan and would have needed to be replaced or rebuilt in the last century. Figure 2.4 gives the percentage of the century old bridges that are structurally deficient and functionally obsolete. The percent of century old bridges that are structurally deficient is 41%, which is a much higher percentage than bridges for all ages (11%).

The goal of any asset management plan is to use funds and existing infrastructure as wisely as possible. Even though the bridges that are over one hundred years old have high levels of structural deficiency, they can still be repaired and brought back to serviceability. Structural health monitoring provides a way to manage the historic bridges more effectively. The goal is to identify problems (e.g., corrosion or fatigue) before they lead to serious degradation of the bridge's capacity or even collapse.

2.4 Bridge Collapse Statistics

In 1990, Harik et al. [19] published one of the first statistical studies of bridge collapses. This study was unique in that it was not concerned about deducing the cause and then applying the lessons learned for an individual collapse, but rather looking in a general sense at what the common concerns in bridge design and maintenance were at the time. Harik et al. collected articles from 1951 through 1988 about bridge collapses from the *Engineering News Record*, the *New York Times*, and the *Courier Journal* from Louisville, Kentucky. In Kentucky, there were thirty-five reported bridge collapses, of which only one was reported nationally. Nationally, seventy-nine[11] bridge failures were reported. These statistics, there-

[9]The percentage of each state's bridge inventory built before 1912 varies greatly. However, the states in the Northeast and Midwest that industrialized first, unsurprisingly, have the greatest percentage of bridges built in 1911 or before. The top six states for century old bridges by percent are: Massachusetts (10.39%), Rhode Island (7.32% but only 55 bridges), Ohio (7.17% with 1,964 century old bridges which is the largest number of any state), New Jersey (6.39%), Pennsylvania (5.93%), and Iowa (4.74%). Illinois is eighth on the list with 1,176 of its 26,436 bridges (4.45%) being built in 1911 or before.

[10]The Alvord Lake Bridge, built in 1889 in San Francisco's Golden Gate Park, is the oldest reinforced concrete bridge in the United States. However, for comparison the oldest concrete bridge in Pennsylvania dates from 1902, the oldest in Minnesota to 1905, and the oldest in Arkansas to 1912.

[11]This figure does not include the one Kentucky bridge failure that was reported nationally

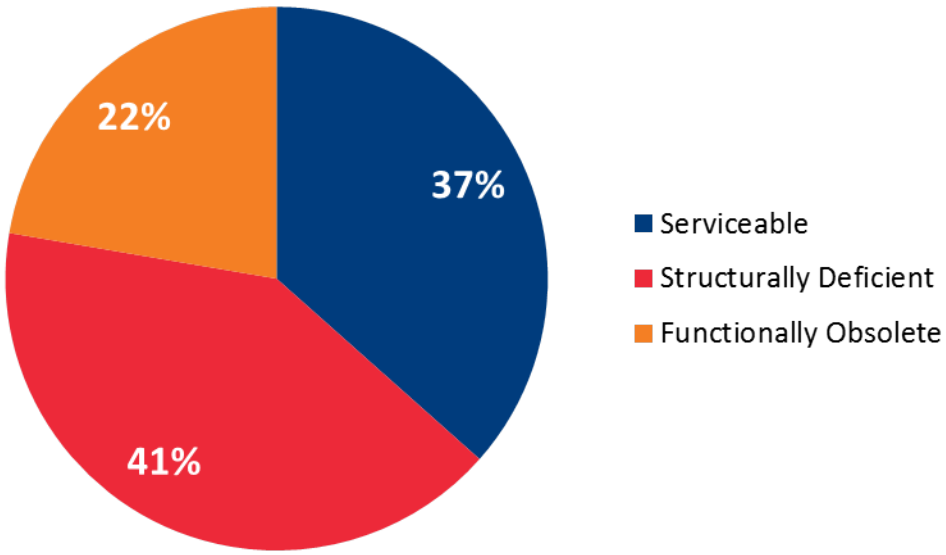

Note: any bridge classified as structurally deficient is excluded from the functionally obsolete category. From FHWA data as of Dec. 2011.

Figure 2.4: Condition of bridges over 100 years in service.

fore, are not conclusive and is indicative of the fact that not all bridge collapses make national headlines. Of the 114 total bridge failures included in the study, only six were reported as being due to fatigue and only one bridge failed as a direct result of corrosion. The majority of bridge failures were due to accidents, extreme natural events, and vehicles exceeding the legal weight limit. Harik et al. concluded that the occurrence of corrosion induced bridge collapse was low because corrosion problems were being identified during inspections and rectified in subsequent repairs. Harik et al. further recommended that the FHWA or NTSB create a database to track bridge failures and their causes.

At the time, the recommendation for a truly national database of bridge failures went unheeded. However, after the collapse of the Thruway Bridge over Schoharie Creek in 1987,[12] the New York Department of Transportation (NYDOT) formed the Bridge Safety Assurance Unit in 1990 that was tasked with collecting information on bridge collapses throughout the United States [21]. As part of their work they created a database that contained information on a large number of bridge collapses from across the nation. This database is sometimes referred to as the National Bridge Failure Database [22], even though it was created by the NYDOT.

In 2003, Wardhana and Hadipirono [21] continued the work of Harik et al. using NYDOT's National Bridge Failure Database and their own investigations on the FHWA and

[12]The Schoharie Creek Bridge was a five-span, simply supported, steel girder bridge built in 1954. It collapsed during a severe spring flood event on April 5, 1987 killing ten people. Investigations indicated that the cause of the collapse was scour under the third pier [20].

state department of transportation websites to compile statistics on bridge failures. For the twelve year period from 1989–2000, they found that there were 503 bridge collapses in the United States. This number is larger than the previous study, not necessarily because bridges are failing in greater numbers, but because the ability to search records and other data mining technology has improved. The relevant statistics for bridges similar to the Rock Island Arsenal Bridge is that 107 (or 21.27%) of those failures were steel truss bridges. Twenty (or 3.98%) of the 503 collapses were attributed to either general steel deterioration or steel corrosion specifically, and another five bridges (or 0.99%) failed due to steel fatigue. As with Harik et al., Wardhana and Hadipirono found that floods[13] (165 failures), general scour (78 failures), collisions (59 failures), and overloads (44 failures) were the most common causes of bridge failure.

Researchers have conducted two additional studies on bridge failure statistics on a more international level. The first looked at 350 steel bridge failures over the last two hundred years [23]. The conclusion was that only 5% of these historic failures were caused by poor maintenance. This conclusion is of less significance because it does not focus on bridges that have been subject to federally mandated inspections. The other study focused on bridge failures in Colombia [24]. Sixty-three Colombian bridges failed between 1986 and 2001. Unique to the political situation in Colombia, terrorist attacks accounted for twenty of the failures while flooding[14] and scour accounted for fifteen failures each. Only one Colombian bridge collapsed due to either a lack of maintenance or corrosion.

Corrosion and lack of maintenance is not the leading cause of bridge collapse in any of the studies. However, collapse due to corrosion is one of the most preventable forms of bridge collapse. A coordinated inspection and maintenance program can detect corrosion and make the necessary repairs before the bridge collapses. Structural health monitoring can help in the process by providing an objective analysis and help focus the trained eyes of the inspector on potentially critical issues.

[13]The Great Flood of 1993 along the Mississippi and Missouri Rivers caused a large spike in the number of bridge failures.

[14]A single flood event in June of 1994 accounted for thirteen of the fifteen bridges that failed due to flooding

Chapter 3

REVIEW OF STRUCTURAL HEALTH MONITORING

Structural health monitoring (SHM) in its most elementary definition can be defined as a system that observes a metric or parameter of a structure continuously, extracts features from the metric, and uses the features to assess the current state of the structure. In the context of SHM, "continuously" does not mean "constantly" but implies that the observations occur uninterrupted over a long period of time. Periodic observations are still continuous observations if they take place for a length of time that is significantly greater than the period of the observation. The period of measurement should also be smaller than the processes involved. For example, if the system takes measurements twice a day, every day, for years then that can be considered continuous monitoring if the process being measured is unlikely to change more than once a week. The output of an SHM system is periodic information about the ability of the structure to continue to perform its designated function as the structure ages. The key features of SHM are long-term continuous monitoring and data processing to determine the condition of the bridge.

SHM is often associated with other closely related terms and processes [25]. Understanding what these related disciplines are and how they differ from SHM will help to clarify what the goals of SHM are. Each of these related disciplines will be explored briefly.

Condition Monitoring (CM) Condition monitoring is typically associated with machinery used in manufacturing or power generation. Sensors, particularly accelerometers, are used to detect changes in the operation of the machinery that indicates when maintenance and repairs are needed. The recorded vibration data is processed to identify the modal parameters of machinery. Changes to these parameters indicated the condition of the machinery has changed. One of the principal differences between CM and SHM is the scope of structures involved.

Non-destructive Evaluation (NDE) Non-destructive evaluation is typically the use of sensors to identify the severity and characterization of damage at a specific time. For bridges and other civil infrastructure, NDE can be performed immediately after construction (e.g., the ultrasonic inspection of welds) as a means of quality control. Or, a bridge manager might request an in-depth inspection that includes NDE techniques after a bridge inspector or an SHM system indicates the possibility of damage. Therefore a primary difference between NDE and SHM is that NDE typically is not performed continuously; it is performed only when needed.

Statistical Process Control (SPC) Statistical process control, like CM, is typically associated with manufacturing. However, unlike CM which is monitoring the manufacturing equipment, SPC monitors the product to determine – using statistical methods – whether the process is producing a product that conforms to determined standards. The end result of SPC is to optimize the production process to produce the desired

product with as little waste as possible. The analogy to SHM is that the performance of the structure is the product and damage or other changes to the health of the structure will produce a performance that is statistically different from the desired performance. Thus SPC analysis techniques can be used in an SHM system to interpret the data to assess the state of the structure but SPC has different output than SHM.

Damage Prognosis (DP) Damage prognosis extends SHM by attempting to predict the performance of the structure. The data acquired in SHM is analyzed, future loadings and the effects of continued deterioration is estimated, and using simulation and past experience the remaining useful life of the structure is calculated [26]. Thus the difference between DP and SHM is that SHM returns an assessment of the current condition while DP attempts to estimate the future condition based on gathered data.

SHM builds on and combines many of these disciplines into a multidisciplinary process of its own. An SHM system performs continuous system identification like CM and observes the identified parameters with respect to time. Multiple sensor systems can be combined in a single SHM system to, like NDE, evaluate the presence, location, and quantity of damage. The principles of SPC are typically employed in SHM systems after a baseline condition is established to determine when the output parameters do not conform to the statistical predictions made for each parameter. Once it has been established that the system has likely changed, the ideal SHM system should make a prediction using DP principles to provide the bridge owner an idea of the severity and immediacy of the situation [27].

Structural health monitoring has the ability to be a transformative technology. As discussed in Section 2.1 most current bridge inspection and maintenance is done on a time-base schedule. The continuous monitoring inherent to an SHM system has the ability to initiate a condition-based maintenance paradigm. Condition-based maintenance relies on SHM to monitor the infrastructure and notify the owner with enough warning time that corrective action before the condition of the bridge degrades to a more serious state. SHM allows the condition to be monitored in time and maintenance funds allocated to those bridges whose condition is most severe or will likely become the most sever if left uncorrected. The benefits of SHM are offset by the requirement that more complex sensor systems and more sophisticated data analysis methods are required [25].

A structural health monitoring system requires a combination of knowledge in many different fields to produce a functional and meaningful system [28]. Figure 3.1 shows the branches of knowledge that are required to create an SHM system. Knowledge of structural behavior rooted in sound structural mechanics is necessary for knowing the forces present in the various members and where to place sensors to glean the best information from the structure. Understanding the types of sensors available, their measurement limits, and how to process the data stream appropriately is necessary to achieve good data. Once the data is collected, knowledge of information management and handling is important to process the data into a form that is accessible to and useful for the responsible parties. The cycle is circular in that once the data is collected, the knowledge of structural behavior is once again used to interpret the results and decide an appropriate course of action.

The multidisciplinary nature of the structural health monitoring makes establishing an effective system difficult. The best structural analysis will not be able to determine the

Figure 3.1: Concept map of the multidisciplinary nature of SHM.

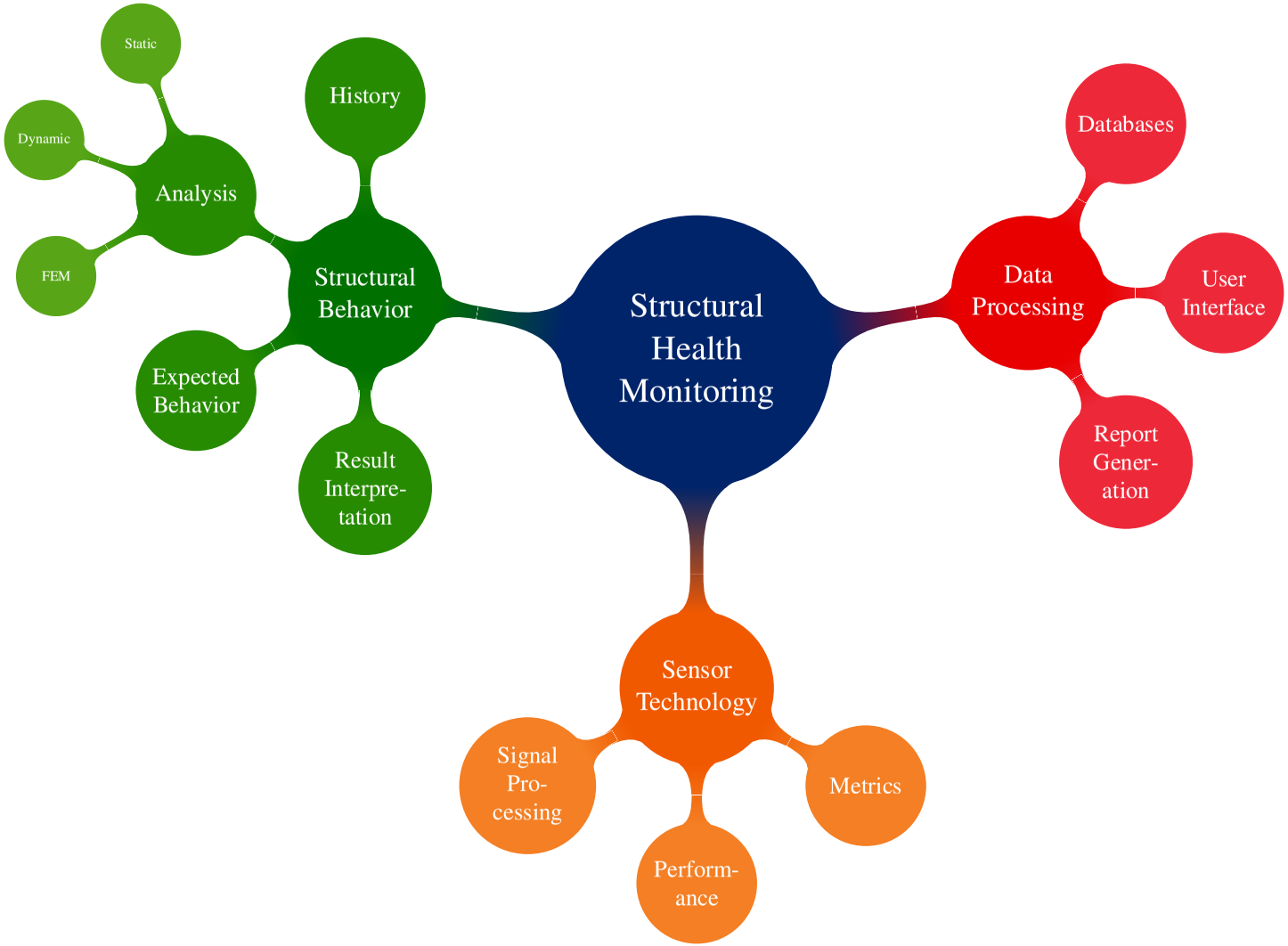

accuracy of the analysis without appropriate sensor technology. The best sensors will not provide good results if they are placed in locations that are limited in their ability to determine the important structural responses. Without proper data processing and management the recorded data will not be useful.

3.1 Desirable Characteristics of an SHM System

The primary goal of any SHM system is to provide a reasonable return on the owner's investment in the system. Calculating the returns is not always straight forward but the following represent some of the most common ways of measuring returns on SHM technology: [29]

- Safe extension of asset life span, lowering life cycle cost of ownership
- Safe deferral of asset maintenance or repair programs
- Safe deferral of asset replacement programs
- Improved prioritization of limited funds
- Removal of unnecessary load restrictions to support commercial traffic and reduce detours, congestion and air pollution
- Identification of dangerous assets that must be replaced or repaired immediately, thereby lowering liability exposure and increasing safety

If the installed SHM system can supply any of the above at a reasonable expense, then it can be considered a success. However, not all SHM systems will provide the desired returns and "reasonable expense" can be defined differently for the many interested parties. The bridge owner must evaluate the available technologies and select a system that is most likely to return the desired results within their definition of a reasonable expense.

When choosing a whether to use SHM technology and what available technologies to use, the FHWA's *Bridge Inspector's Reference Manual* [29] recommends asking the following questions.[1]

1. Is the SHM technology capturing the "right" information to aid decision making without capturing a lot of extraneous information?
2. Can the SHM solution be expanded easily and cost effectively if it is later decided to capture more data?

[1]The questions presented here have been edited for content and clarity from the source material. Primarily, SHM has been substituted for "advanced bridge evaluation" to maintain consistency with the phrasing of this dissertation. See Section 15.4 "Advanced Bridge Evaluation" of the FHWA's *Bridge Inspector's Reference Manual* [29, pg. 15.4.7] for the original wording and context.

3. Should a solution provider be used? Is the provider capable of system configuration and installation? Does the provider provide both the hardware and software? Is the hardware all compatible (i.e., all FBG fiber optic sensors) or does the provider need to integrate sensor systems with software?

4. Should the captured information be able to integrate with the existing information system?

5. How long is the technology expected to be deployed and what is the reliability and durability of the hardware and software?

6. Who has the responsibility for conversion of the structural data into useful information and subsequent analysis of that information?

In answering these questions, the characteristics of an ideal structural health monitoring system become apparent. An SHM system should be continuous, multimetric, scalable, robust, autonomous, informative, and intuitive. Each of these characteristics will be discussed in more detail in the subsequent sections.

3.1.1 Continuous

One of the issues with the current bridge inspections standards are that the two year inspection cycle is not frequent enough to adequately detect some problems; yet resources are insufficient to increase the manual inspection rate. While deterioration is a slow process that takes place on a large time scale, as noted in Section 2.4, other factors, such as collisions or overloads, will occur at random intervals and can change the capacity of the bridge or accelerate fatigue or corrosion. Being able to assess the performance of a bridge at intervals between the visual inspections would be a benefit for the bridge owner. An SHM system operating continuously can provide this function.

In the context of SHM, continuous does not necessarily mean constantly. Most of the data that a system that constantly takes and records is redundant. The key, as stated in Question 1 above, is to get the right data. An SHM system based on accelerations can periodically take data during the day (e.g., four times a day) at a higher sample rate and process the data to determine the natural frequencies of the bridge. Even though the system is not constantly taking data, it is continuously monitoring the structure and the recording the right data in a reasonable quantity. Making the distinction between continuous and constant is possible because, once temperature is properly considered, the natural frequencies of the bridge are not expected to change significantly from day to day without a change to the structure occurring.

The example of periodically taking acceleration data four times a day still represents a scheduled approach to bridge inspection – instead of every two years the bridge is inspected every six hours. Alternatively, data can be buffered constantly but only recorded when important events (as defined by thresholding or other algorithms) take place. In this manner data is taken when it is of most importance. This latter method of continuous monitoring is a form of triggered data collection.

3.1.2 Multimetric

No single metric can completely determine the health and condition of a bridge. Each metric is best suited for determining certain characteristics on different scales. The most commonly used metrics in structural health monitoring have been acceleration and strain. Acceleration measurements are used to determine global characteristics such as natural frequencies and estimates of the stiffness matrix. They are often positioned so as to minimize the effect of local vibrations in individual members to enhance their ability to detect the global parameters. Strain gages on the other hand are more local in nature. Though multiple strain gages spread over a structure can be used to inform global load ratings, strain gages are best at measuring local behavior. Strain gages can be placed close to each other on a single member to isolate defects.

Using both strain and acceleration in a multimetric approach to SHM can provide a more general understanding of the bridge [30]. However, even more metrics than strain and acceleration are either required or useful in an SHM system. Sensors of all types are typically temperature dependent, so accurate temperature measurements are essential to properly correct for thermal effects. Other metrics such as tilt, displacement, corrosion potential,[2] or humidity are all basic metrics that can be useful in SHM applications. Using all the metrics together seamlessly is part of the challenge of developing a structural health monitoring system.

However, the economics of the situation impose limits on the number of metrics and the number of sensors for each metric in an SHM deployment. Each metric and sensor needs to have the value that it can provide weighed against the cost of installation and maintenance of the sensor. The limited resources require a broader understanding of the structural behavior so as to place sensors at locations that will give the most useful information.

3.1.3 Scalable

The scalability of a structural health monitoring system can have two meanings. Scalability can mean the ability to take a system that functions on a small structure and have it also work on a larger structure. In this sense, scalability refers to the scale of the structure, but not necessarily to the scale of the system. The other definition can mean being able to scale the system by adding or removing sensors and having the system still be able to provide meaningful data. In this sense, the system is scalable in its size, but the structure does not change.

The value for the department of transportation in having a scalable SHM solution is that it helps efficiently use the limited resources available for monitoring bridges. A scalable system can be installed in a minimal form and then later easily expanded. The expansion could be because more funds become available or the analysis of the minimum installation indicates that a more thorough investigation is necessary. Having a system that allows itself to be seamlessly expanded (or contracted if the bridge manager needs sensors on another bridge) makes the system as a whole more attractive as a monitoring solution.

[2]The measurement of corrosion potential can directly inform the total amount of corrosion taking place and the corrosion rate.

3.1.4 Robust

Bridges are designed to have at least a fifty-year life span and a structural health monitoring system needs to be able to last just as long. Inevitably, a sensor or two may fail, but ideally the SHM system should be self-aware and alert the bridge manager so the sensor can be repaired or replaced.[3] In the interim, the quality of the data collected by the system should not be greatly affected. Therefore the robustness of the system can be complicated by the number of points of failure that exist in a sensor system.

One of the stated benefits of fiber optic systems is that they can be multiplexed to reduce the amount of fiber cable used in the system. However, the multiplexing also reduces the number of failure points and increases the cost of one of those points failing. Whereas in a traditional wired sensor system, if one wire breaks, then one sensor is lost. However, in a multiplexed system, if one fiber cable breaks then all sensors multiplexed on that cable will fail. Wireless sensors can be programmed to communicate in groups but also reform the network if the group leader were to fail. With proper programming, smart wireless sensor networks can be very robust. Nevertheless, all sensor networks are prone to failure in their primary base station and measures should be taken to allow the systems to restart automatically when the system restarts.

In addition, in a truly robust system, when the sensor is replaced after a failure, the history and ability to continue to track changes in the member or node should not be lost. For acceleration and temperature measurements, this aspect of robustness is natural, because these measurements are set to zero against a universal value – no acceleration or the freezing point of water – and can be calibrated prior to installation. However, strain measurements are dependent on the time and temperature of installation and are not set to universal value. Therefore, to make a strain system robust, the primary strain measurement needs to be converted to a secondary strain measurement through calibration or derivation that is correlated with the zero strain in the member. However, in practice, this correction is rarely done because the complete dead load strain is difficult to determine. In concrete structures, the situation is exacerbated by the presence of creep and shrinkage.

The algorithms that are used to evaluate the data collected by the SHM system should also be robust and fault tolerant. The loss of a sensor or senors should not inhibit the ability of the analysis software to identify structural changes. Programming algorithms to be robust to "Null" input values for any given number of sensors improves the robustness and fault tolerance of the SHM algorithm.

3.1.5 Autonomous

There are often thousands of bridges in a manager's inventory. If an SHM system were installed on every bridge in the inventory, physically observing all of the monitoring systems would be a difficult task. Therefore, the ideal SHM system should be autonomous and have a "start it and leave" mode of operation. The SHM should be able to acquire, process, and interpret data on its own after initial set-up by the user. However, the system does not need

[3] Replacing sensors may be much easier on steel structures where the sensors have to be surface mounted than on concrete structures where the sensors are typically embedded in the concrete during construction.

to be a single switch program that does not allow user manipulation while the program is in operation. Altering parameters, running analyses, and producing reports on demand are an important feature.

Part of the autonomous nature of the system should be able to detect potential issues and alert the bridge manager that closer attention is needed. Some of the issues that the system should be able to determine include: whether a sensor has stopped working, whether there a significant sudden change has occurred in the bridge condition, or whether the system had to restart and resume monitoring. However, the SHM system should be judicious in sending alerts; because, if the system sends too many alerts, like the boy who cried wolf, the bridge manager is likely to ignore them.

3.1.6 Informative

Questions 1, 4 and 6 at the start of Section 3.1 all address the important fact that a structural health monitoring system should be informative. Just because you get data does not mean that it is good data or that it is useful data. It is important to have an SHM system that is collecting data that is useful in and of itself, or can be processed and distilled into meaningful information. Each bridge manager will be responsible for hundreds or thousands of bridges. The manager will not be familiar enough with the individual characteristics of each bridge to be able to look at a graph of either a strain time history or a frequency spectrum and quickly discern if a problems exist. The SHM system needs to be programed to take the data and turn it into a simple yet illuminating form. A complex report will not be thoroughly read when a thousand bridges are sending a thousand reports every week.

The reporting process and what information should be included needs to be developed in cooperation with the bridge owner before the sensors are selected and installed. The information provided by an SHM system is most useful when it supplements or corroborates information already collected during normal inspections. SHM systems should work within the current framework of bridge inspection and provide information that the decision makers can understand. Bridge inspections under the CoRe element paradigm give ratings that can be turned into percentages – a number that is readily understood. Health indices and damage indices can be tailored to provide a similar easily understood processed metric.

3.1.7 Intuitive

The person who programs a piece of software is always the best user as they know all the features and how to access them. However, the programmer of the SHM system will not likely be the end user. In addition, over the course of the lifetime of the system, the end user will likely change many times. Creating a program that is simple, and intuitive will increase the likely hood that the program is used effectively.

Modern computer users have expectations about how to interact with a program. Most end users have become familiar with, and have expectations for, point and click graphical user interfaces. User interfaces that require a list of memorized command lines are less

efficient and less user friendly. Creating a system that is both autonomous and informative necessitates taking a lot of the processing and decision making behind the interface and reducing the complexity of user input. The program should be able to easily give the user what is needed in a manner that reduces the learning curve of the system.

3.2 SHM Installations

SHM systems have been installed around the world with varying levels of complexity. Some systems are designed to fully monitor and analyze the structure in long-term installations. Other deployments have been short-term installations to determine structural properties as one point in time or to test sensors for suitability in long-term deployments. Damns, pipelines, and buildings have all been instrumented [27] as well, but the examples presented below will focus on the monitoring of bridges with various sensor systems. These SHM installations represent a broad range of complexity and purposes.

3.2.1 Tsing Ma Bridge

The Tsing Ma Bridge is a 1,377 meter long suspension bridge that carries rail and vehicular traffic between Tsing Yi and Ma Wan islands in Hong Kong. The Hong Kong Highways Department installed a comprehensive SHM system called the Wind and Structural Health Monitoring System (WASHMS) on the bridge in 1997. At the time, this installation was one of the most comprehensive and functional SHM systems to date. WASHMS consisted of the sensor array, a data acquisition system, a data processing system, and a structural health evaluation algorithm [31]. A total of 285 sensors were installed monitoring many different metrics including acceleration, strain, displacement, temperature, inclination, wind speed, and traffic count. The combination of physical and environmental metrics provides a comprehensive understanding of the bridge behavior during the endless combinations of environmental and loading conditions. Abnormalities in the data trigger alerts that warn of possible overloading. The WASHMS has been in continuous operation since installation and has continued to provide data. The sensors installed were all wired electromagnetic sensors because fiber optics were not commercially available at the time. In 2003 a field test to compare the electromagnetic sensors to a fiber optic system were performed [32]. The fiber optic system and the electromagnetic sensors had excellent agreement.

3.2.2 Bill Emerson Memorial Bridge

The Bill Emerson Memorial Bridge is a 1205.8 meter (main span of 350.6 m) long cable-stayed bridge over the Mississippi River near Cape Girardeau, Missouri. Located in the New Madrid seismic zone, the bridge was instrumented with eighty-four channels of acceleration [33]. The purpose of the long-term deployment was to provide seismic response

data, perform model validation, and evaluate the design in order to improve the design of future cable-stayed bridges. The system does not include any autonomous condition assessment algorithms. Real-time data was to be made available over the internet and accessible for use by the responsible departments of transportation and to other interested parties for off-line processing. Other parties have used the collected data for a variety of purposes including modal analysis and as a test case for damage detection algorithms [34]. The monitoring system is still functional.

3.2.3 Second Jindo Bridge

The Second Jindo Bridge is a 484 meter (main span 344 m) long cable-stayed bridge connecting Jindo Island to the South Korean mainland. The bridge has been instrumented with seventy wireless smart sensors using the Imote2 sensors system equipped primarily with accelerometers but also included temperature, strain, and wind speed sensors [35]. The installation was intended as a test bed for wireless sensors technology. Acceleration data is periodically collected by the sensors and saved in text files for later use. Off-line modal analysis and model updating and verification have been performed. A system to monitor the historic data and perform condition assessment has not been implemented.

3.2.4 Infante Dom Henrique Bridge

The Infante Dom Henrique Bridge is a 371 meter long concrete box girder arch bridge over the River Douro in Oporto, Portugal. The bridge has been instrumented with twelve force balance accelerometers installed in the box girder as well as a number of strain and temperature sensors that were embedded in the concrete during construction [36]. The SHM system's acceleration sensors were programmed to take data every thirty minutes, process it using different system identification techniques, post-process the data to eliminate environmental factors, and store the data to a database. The results of the autonomous operational modal analysis were linked to a graphical user interface that could display the results. For over two years the system has been collecting data. Analytical studies show that should damage occur the change in natural frequencies should be detected by the system.

3.3 Structural Behavior

Understanding structural behavior is accomplished through analysis using the methods now common to most civil engineers. Finite element models are useful tools that, when created and used appropriately, can provide significant insight into the behavior of the structure. Finite element programs can perform static and dynamic analyses that can help guide the selection of sensors and their locations. In turn, the models can help interpret the results. However, the structure as it exists may behave different from the model and so calibrating

the model is important. A common way of calibrating models, and more importantly also determining the safety of a bridge, is by performing load tests.

3.3.1 Load Determination & Event Detection

The ultimate goal of bridge inspections and structural health monitoring is to provide a method of determining whether the bridge is still safe for operation. Determining where damage has occurred and its severity is typically just an intermediate step in determining the damage's effect on the ability of the bridge to safely carry loads and determining appropriate repair and retrofit strategies. A bridge manager will feel a greater immediacy if told his bridge can no longer safely carry a semi-truck than if told that a beam has seen a certain amount of strain increase or a shift in natural frequencies. Getting from the metric to the rating can be a challenge.

Strain gages can only measure the changes in strain that occur after the gage itself has been installed. However, to determine the load capacity of the bridge, the structural response to the dead loads that have already been applied must be known. The response of the bridge to a known live load can be observed and the structural response calculated. This process is generally referred to as a load test of which there are two types [37]. The first type of load test is a diagnostic test. In this test, a vehicle or vehicles of known weight are driven on a defined course so the load and application points are known. The load level is designed to be below the elastic load limit. Strain and deflection sensors record data at strategic locations. The data is used to determine the load distribution and stiffness characteristics of the bridge usually in conjunction with a FE model. The other type of load test is a more direct method in determining the load capacity of the bridge and is called a proof test. In this test, the loads in the truck are increased until either the target load that the manager wants the bridge to be rated at is reached, or the sensors start to observe nonlinear behavior indicating the elastic limit has been reached.

Diagnostic load tests have become a common tool in evaluating structures and validating finite element models [38–40]. However, they can be costly and obtrusive as they involve closing the road to traffic so that only the known loads are acting on the structure.

In a structural health monitoring context, which can be considered as continuous diagnostic testing, the loads that cause sensor response are not typically known. Therefore in the diagnostic algorithms of the monitoring system, when the newly acquired response is compared to historical responses it may not be discernible if the response represents a change in load or a change in the structure. Various methods have been proposed to determine the loads that are causing the measured responses in a strain monitoring system. In a system called Restricted Input Network Activation Scheme (RINAS), Su [41] proposed using a camera placed on the bridge and image processing techniques to determine what type of vehicles were crossing the bridge. Environmental data can also be collected so that the ideal events – the passage of an isolated semi-tractor at night – are the only ones used as input to diagnostic algorithms. Su further proposed, but did not implement, using RFID tags and data collected at state DOT weigh stations to further supplement the knowledge as to the loads of the vehicle.

Another, more direct way of determining the loads is by installing a weigh-in-motion

(WIM) system at the bridge site. [42] WIM systems can take advantage of a number of sensor technologies and could therefore be easily integrated into an already existing structural health monitoring system. The principle behind the scales and embeddable mats that make up a WIM is the same as for a diagnostic test on the bridge. The WIM is calibrated with a known load and then it can use its response to future events to determine the load. The WIM needs regular repair and maintenance and has to be replaced every few years.

An alternative to trying to determine loads for a structural health monitoring application was reported by Whelan et al. [43] Their proposal used a multimetric wireless sensor system that was capable of measuring both strain and acceleration. After installation, a diagnostic load test was performed with a loaded truck to establish an initial structural assessment. Recognizing that the loads would not be known between the initial and any future load testing, the sensors would operate as a vibration monitoring system that would perform anomaly detection continuously. If an anomaly were detected the sensors would alert the bridge manager to schedule an inspection and load rating using the extant wireless strain sensors. In this way, the load ratings which are easily incorporated into the current National Bridge Inventory databases are performed as the bridge inspection community learns to accept vibration based analyses.

3.3.2 Steel Bridges

When developing an SHM system for a bridge, the material and structural system used are important considerations. As shown in Table 2.2, thirty percent of the nation's bridges are considered to have steel as their primary construction material. These steel bridges come in a number of shapes and sizes. Steel truss bridges may be the most easily recognized for the typical motorist but steel box girder bridges and many suspension or cable stayed bridges can be classified as steel bridges.

Each of the different types of steel bridges will present a different set of concerns for the bridge manager. The concerns for each bridge will require a different approach to structural health monitoring and dictate which sensors should be used and where they should be placed. Monitoring the corrosion of individual wire strands in the suspension cables of a bridge requires different sensors and methods than would be used for corrosion monitoring of a steel box girder. The SHM approach needed is determined by the structural system and the likely failure mechanisms of the bridge. Therefore, understanding the design of each bridge so as to identify its potential weaknesses is essential to creating a useful SHM system. An understanding of the engineering practices and knowledge (or lack thereof) of the era in which the bridge was designed is also important in identifying the best SHM system for a specific bridge. A brief history of steel bridge construction will be given in Section 4.1.1 with emphasis on the engineering material and knowledge advancements that contributed to the design of the Rock Island Bridge.

3.4 Sensor Selection and Data Acquisition

When designing an SHM system, after the structural behavior, desired results, and expected performance levels have been determined, selecting the sensor and data acquisition system is the next step. Selecting sensors that measure the correct metric at the appropriate level with acceptable accuracy is not a trivial task. The epigram, "Just because you get data does not mean it is good data," is particularly applicable. The quality of a structural health monitoring system depends on the quality of the sensors that feed data into the system. The selection of sensors for an SHM system requires a multifaceted understanding of the available sensor technology, the expected response of the structure, and the limitations the individual structure imposes on sensor functionality.

The available sensor technology is typically divided into two main families: electromagnetic and optical.[4] Electromagnetic sensors measure changes to the electromagnetic properties (such as resistance, capacitance, magnetic field, etc.) caused in the sensor by the external metric. Typical electric wires are used to connect the sensors to the data acquisition system that converts the signal to a digital format for use by the computer. Microelectromechanical systems (MEMS) that are used in wireless sensor systems are just small-scale electromagnetic sensors on a circuit board. Optical sensors measure changes to the optical properties (refraction, diffusion, reflection, etc.) caused in the sensor by the external metric. The signal is carried by fiber optic cables to the data acquisition system that uses an electromagnetic sensor that has photoelectric properties to convert the signal to the necessary electronic and then digital format.

3.4.1 Metrics

There are a wide range of sensors available that can be used to measure an equally large number of quantities. Each metric has its own nuances that must be fully understood and taken into account to obtain quality data and to properly interpret the results. Each of the principle metrics – strain, temperature, acceleration, tilt, and heading – used on the Rock Island Bridge will be discussed.

Strain

In its simplest engineering form, strain in a single dimensional member can be defined by the equation:

$$\epsilon = \frac{\ell - L}{L} \tag{3.1}$$

where ϵ is the strain, ℓ is the deformed length, and L is the original length of the member. However, this simple equation is true for the total deformation but fails to account for all the possible sources of the deformation or the three dimensional nature of the object itself. Strain in a structural member can be caused by any number of sources: axial loads, bending,

[4]This can be a little confusing because light is part of the "electromagnetic spectrum;" the distinction is that optical sensors act on a stream of light not on a current of electricity.

thermal changes, or residual strains from construction. For a steel truss member, the total strain (ϵ) is:

$$\epsilon = \epsilon_E + \epsilon_P + \epsilon_T + \epsilon_{other} \tag{3.2}$$

where ϵ_E is the elastic strain, ϵ_P is the plastic strain, ϵ_T is the thermal strain.

Together, ϵ_E and ϵ_P can be called the mechanical strain in the member. These strains are generated by the loads (dead loads and live loads) acting on a structure. The structure, under typical service loads, should remain in the elastic deformation region and therefore no plastic strains should develop. When plastic strain is not present, Equation (3.2) can be simplified such that (considering the strains represented by ϵ_{other} to be practically negligible):

$$\epsilon = \epsilon_E + \epsilon_T \tag{3.3}$$

However, once strains exceed the yield strain (ϵ_y) of the material, the plastic strains must be included.

The thermal strain in Equation (3.3) is a function of the change in temperature (ΔT) and the coefficient of thermal expansion (α) of the material.

$$\epsilon_T = \alpha \cdot \ \Delta T \tag{3.4}$$

The coefficient of thermal expansion (CTE) is a material property that is often itself dependent on temperature. The temperature dependence can be a simple linear relationship or a more complex function. For example the CTE for steel, in units of $\mu\epsilon/^{\circ}C$, as a function of temperature is:

$$\alpha_{steel} = 12 + 0.008 \cdot T \tag{3.5}$$

where T is the temperature in degrees Celsius. This is a simple linear equation valid for temperatures below 750°C. Likewise, the CTE of a typical[5] single mode optical fiber, in $\mu\epsilon/^{\circ}C$, can be given as:

$$\alpha_{fiber} = 9.42\times10^{-11}\cdot T^4 - 7.20\times10^{-8}\cdot T^3 + 1.26\times10^{-5}\cdot T^2 + 1.85\times10^{-3}\cdot T - 6.15\times10^{-2} \tag{3.6}$$

where T is the temperature in degrees Kelvin [44]. However, for limited temperature ranges the CTE of a given material can be assumed to be constant. Table 3.1 gives the linear coefficients of thermal expansion at ambient temperatures for common materials that were used in the construction of the Rock Island Government Bridge or its sensor systems. If an accurate temperature measurement can be achieved, then the thermal strain in the member can be calculated and subtracted from the total measured strain to determine the mechanical strain component. The thermal strain can be converted into mechanical strain if the expansion of the material due to thermal changes is restricted.

Temperature

Simply defined, temperature is a measure of the average kinetic energy in a body or quantity of matter. As a metric, temperature is important particularly because a number of other

[5] SPECTRAN photosil type C

Table 3.1: Linear coefficient of thermal expansion for common materials.

Material	$\mu\epsilon/^{\circ}C$
Steel	11-13
Concrete[a]	7.4-13
Sandstone	11-12
Limestone	6
Fiber optic cable	0.45-0.7

[a]CTE of concrete is dependent on the aggregate used.

physical properties and metrics are dependent on the temperature of the object. As just discussed, measuring an accurate temperature is necessary to differentiate thermal strain from mechanical strain because the material expands and contracts based on the temperature. Temperature is measured using electromagnetic sensors that experience changes in conductivity (thermocouple), resistance (thermistor), or expansion (thermometer or bimetallic strips).

When measuring temperature there are a few principles that need to be understood. First, every object or quantity of matter has a distinct temperature at any given point in time. This means that if a measure of the temperature in one object is desired, care must be taken to ensure that the sensor is not measuring the temperature of any of the other objects or quantities of gases or fluids that it is in contact with. Second, two bodies that are in contact with each other that have different temperatures will transfer energy to each other until an equilibrium temperature is achieved. This phenomenon is the guiding principle behind the ability to measure temperature; the temperature of the sensor will reach equilibrium with the temperature of the object being measured. Third, the temperature of an object, including the temperature sensor, will increase if energy is added to the system and decrease if energy is removed thereby maintaining the conservation of energy. If the energy inflow or outflow to the temperature sensor is from a source other than the object being measured then the temperature recorded will not be the true temperature of the desired object. Materials have varying abilities to absorb and retain thermal energy so they will also have varying rates of reaching thermal equilibrium. Therefore, the temperature of two objects made of different materials will reach different temperatures if exposed to the same amount of energy. These material properties control the lag of the temperature sensor and how well the temperature measured by the sensor and the true temperature in the object match when both are exposed to external energy sources.

Therefore, when measuring temperature care has to be taken to make sure that you are measuring the intended temperature and the influence of external heat and energy are blocked. For surface mounted sensors exposed to solar radiation, having the sensor properly shielded is good practice. The ideal shield should totally reflect solar radiation but any shield will absorb some solar radiation. Any solar energy absorbed has to be dissipated through convection or thermal radiation otherwise it will cause the temperature in the sensor to increase.

Table 3.2: Radiative characteristics and temperature excesses for coatings exposed to solar radiation.

Surface	$T - T_a$in$^\circ C$	a_s	a_t	$\frac{a_s}{a_t}$
Glass, silver rear-surfaced mirror	9.9	0.07	0.91	0.08
Aluminized Mylar	27.8	0.22	0.91	0.24
Alkyd gloss white (paint)	29.9	0.24	0.91	0.26
Alkyd satin white (paint)	31.5	0.26	0.91	0.29
Clear polyurethane isocyanate on aluminum foil	32.8	0.27	0.91	0.30
Clear acrylic on aluminum foil, spray can	36.8	0.31	0.91	0.34
Glass, black rear-surfaced	85.9	0.93	0.91	1.02
Chrome plating	78.3	0.28	0.12	2.33
Polished aluminum foil (uncoated)	42.0	0.13	0.05	2.60

August 7, 1964, $R_s = 900\ \frac{\mathrm{W}}{m^2}$, $R_t = 480\ \frac{\mathrm{W}}{m^2}$, air temperature $T_a = 29.6^\circ C$

Fuchs and Tanner [45] conducted a study to determine the best coating for thermometer shields. To this end, the applied the coatings to aluminum shields and measured the temperature of the air and the temperature of the shields using thermocouples. The heat balance equation for an opaque shield surface is:

$$a_s R_s + a_t R_t = a_t \sigma T^4 + L \tag{3.7}$$

where R_s and R_t are the flux densities of solar and thermal radiation incident to the surface, a_s and a_t are the solar and thermal absorptivities, $\sigma T^4$is the black body radiant heat flux density for a temperature T in °K at the shield surface, and L is the convective heat loss per unit area. The lower the ratio of a_s/a_t the lower the surface temperature of the shield and the less error in the temperature measurement in the shielded sensor. Table 3.2 presents the results of the study in order from best to worst. Covering a sensor with a glass mirror is impractical so aluminized Mylar[6] was determined the best followed by white paints and then clear coatings on polished aluminum foil.

Acceleration

Acceleration is the measure of the change of velocity with respect to time. It has proved a useful metric in many engineering disciplines. For example, earthquake engineers have used accelerometers to measure the acceleration of the ground during an earthquake. For earthquake engineers, acceleration is a more useful metric than displacement, as the design forces acting on the structure are equal to the mass of the structure multiplied by its acceleration. Accelerometers need to be tailored to fit the application. Accelerometers exist that can measure many times the force of gravity down to a few hundred thousandths of the force of gravity.

[6] Aluminized Mylar is the material used in space blankets.

All accelerometers contain a seismic mass that moves within the sensor to cause a detectable change in an electrical or optical property to measure acceleration. The size of the seismic mass influences not only the sensitivity of the mechanism but the usable range of accelerations and the fragility of the sensor. As such, the size of the seismic mass and its support need to be tuned to the appropriate sizes for the desired application. Accelerometers for geological monitoring tend to be larger (greater than one cubic inch) to detect the small vibrations of small seismic events but also have sufficient range to record any major earthquake. Smaller, less delicate accelerometers are better suited for laboratory or field applications and still provide sufficient sensitivity and range. Microelectromechanical systems (MEMS) accelerometers have been developed that are also suitable for most structural dynamic applications and yet are small enough to fit on a circuit board. Fiber optic sensors are larger due to the limitations of fiber size.

The type of transducer used to convert the movement of the seismic mass also affects the measuring capabilities of the accelerometer. There are three main types of accelerometers based on the type of electronic transducer used: resistive, capacitive, force-balance, and piezoelectric. A restive accelerometer uses resistors placed on the small beam attached to the seismic mass to measure the flexure in the beam. The resistors, essentially strain gages, will experience a differential resistance change due to the movement of the seismic mass that can be calibrated to correspond to the measured acceleration. Fiber optic accelerometers are based on the same concept as the resistive accelerometer but the resistors are replaced with fiber optic strain gages.

Similarly, the second class of accelerometers called capacitive accelerometers, use capacitors placed on the mass and an insulated casing wall to detect the movement of the seismic mass. The capacitance of the capacitors changes when the distance between the wall and the seismic mass changes and the differential change in capacitance corresponds to the measured acceleration. In their capabilities, resistive and capacitive accelerometers are very similar. They can both be used to measure the gravitational force at 0 Hz, known as DC capability. However, they also often have a limited dynamic range, frequency range ($<$10 kHz), and a damped frequency response. Functionally, resistive and capacitive accelerometers tend to be very fragile and need multi-conductor cables containing at least three wires.

The third class of accelerometer is piezoelectric. This type of accelerometer relies on piezoelectric materials that generate an electrical current when subjected to mechanical stress. Examples of naturally occurring piezoelectric materials are quartz and Rochelle salt. However, synthetic artificially polarized ceramics such as lead zirconate titanate (PZT) are now commonly used. Piezoelectric sensors come in three types, compressive, flexural, and shear, but the shear mechanism has the best overall performance and is the most commonly used type of piezoelectric accelerometer. The seismic mass in a shear type piezoelectric accelerometer is mounted such that its movement causes a shearing force in the piezoelectric material. The shear force causes the material to generate an electric current that is measured to determine the acceleration.

The performance of piezoelectric accelerometers is different than resistive and capacitive accelerometers. The electrical current produced by the piezoelectric material diminishes with time and therefore cannot be used to measure the constant effect of gravity or other low frequency events. Piezoelectric accelerometers are suitable only for dynamic events

typically greater than at least 0.2 Hz. However, piezoelectric accelerometers have a large dynamic range and wide frequency bandwidth (exceeding 10 kHz) that make them suitable for large numbers of applications. The piezoelectric accelerometers also tend to be less fragile than resistive or capacitive accelerometers and, because they generate their own electrical signal, they do not need to be powered.

In applications where accelerometers have DC capability and are measuring the gravitational force, the data is detrended to remove the gravitational contribution. The detrending turns the data into a relative acceleration that is most useful in determining excitation levels in the structure. In theory changes to the tilt of the accelerometer will cause changes to the detrended data because the component of gravity in the direction of the sensor axis is no longer equal to the amount removed in the detrending process. However, the contribution of tilt in a structural health monitoring context is typically small compared to the amplitude of excitation and can be safely ignored.

Tilt

Tilt, or inclination, is a measure of the relative angular displacement from an established axis. There are two primary types of sensors that can measure tilt: electrolytic and gravitational.

Electrolytic sensors use two electrodes partially immersed in an electrically conductive fluid contained in a closed system. The conductivity between the two electrodes is dependent on the length of the electrode that immersed in the fluid. When the sensor is tilted, the fluid level remains at the global horizontal due to gravity and the proportion of the electrodes immersed in the fluid changes. The sensor's angle range is a function of the volume of fluid, electrode spacing, and electrode height. In a dynamic environment the fluid may slosh around so in that case the measurement does not always indicate the sensor's static inclination. Increasing the viscosity of the fluid can eliminate some of the higher frequency dynamic effects but low frequency accelerations will still be interpreted as tilt changes.

Gravitational tiltmeters use a mass-pendulum system to measure the degree of change in the pendulum from the gravitational axis. Essentially this means that gravitational tilt meter is an accelerometer that has DC capability so it can detect the presence of gravity. Tiltmeters, like accelerometers, can be resistive, capacitive, or optical. The pendulum and mass in inclinometers are typically larger so as improve the sensitivity of the system to slight changes in angle. Figure 3.2(a) shows the desired functionality of a tiltmeter designed to measure the angle of inclination from the horizontal.

The change in angle in radians (θ) causes the accelerometer/tiltmeter to detect the component (T) of the gravitational acceleration (g) that is in the direction of the measurement axis. The magnitude of T is:

$$T = g \sin \theta \tag{3.8}$$

Therefore, the measured component of the gravitational acceleration can be converted to a measurement of angle by solving Equation (3.8) for θ to get:

$$\theta = \sin^{-1} \frac{T}{g} \tag{3.9}$$

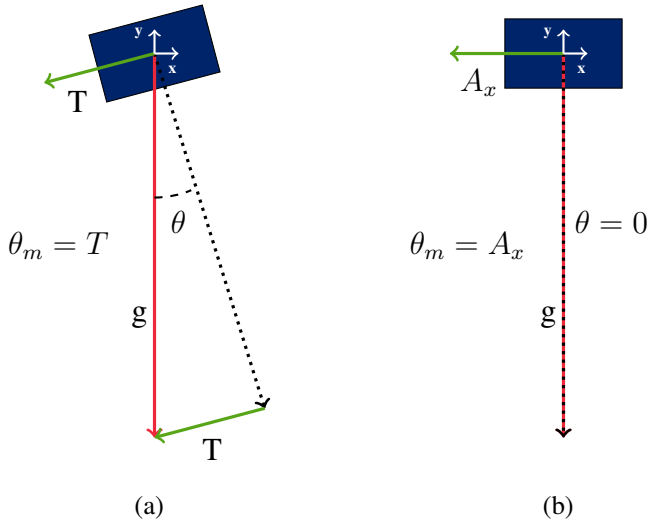

Figure 3.2: Functionality of a gravitational tiltmeter: (a) only gravitational acceleration (b) horizontal acceleration.

For small angles measured in radians, $\sin\theta = \theta$ and the equation can be further simplified to $\theta = T/g$. If the acceleration is given in the units of 'g' then $\theta = T$ and an acceleration of 1 mg is equivalent to a tilt of 1 milli-radian.

In a dynamic environment, accelerations that act in the axis of the tiltmeter's accelerometer will be misinterpreted as a change in tilt. Figure 3.2(b) illustrates this principle in that even though the angle of tilt is zero, the accelerometer has detected a horizontal acceleration (A_x) that will be interpreted as if it were a change in the inclination of the meter. The implication is that Equation (3.9) is valid only when the magnitudes of the acceleration in the axis of the tiltmeter are significantly less than the magnitude of the desired accuracy in the inclination measurement. Otherwise, the measured inclination (θ_m) is determined by the equation:

$$\theta_m = \sin^{-1}\frac{T + A_x\cos\theta + A_y\sin\theta}{g} \tag{3.10}$$

In this equation, T is the component of the gravitational acceleration (g) in the axis of measurement, A_x and A_y are the non-gravitational accelerations in the global coordinates, and θ is the actual inclination of the tiltmeter. Using a low-pass filter can eliminate the influence of acceleration frequencies above the desired data rate but accelerations at or below the filter cutoff will always be present in the measured angle.

Heading

A heading, or more properly the azimuth, is the angle along a horizontal plane between the measurement vector and a predefined reference vector. The azimuth is essentially the

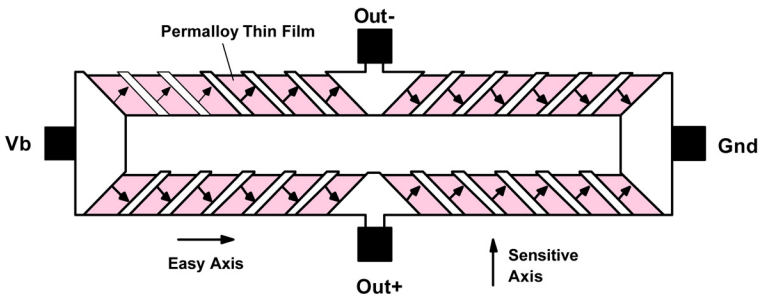

(Honeywell [46])

Figure 3.3: Anisotropic magneto-resistive Wheatstone bridge element.

angle of rotation about the out–of–plane axis[7] of a given object. In practical matters, the predefined reference vector is due north of the observer and therefore the heading is the degree difference from north that the observer is facing. North is defined as 0° and the convention is that heading increases going clockwise such that east is 90°, south is 180° and west is 270°. Heading is measured using a compass with respect to magnetic north which can vary over time and differs from true north.

MEMS compasses are based on magneto-resistive materials that will change their electrical resistance in the presence of a magnetic field. Of particular use are anisotropic magneto-resistive (AMR) materials whose resistance changes not only with presence of a magnetic field but the orientation of the field as well. MEMS AMR sensors are made of a nickel-iron (Permalloy) thin-film deposited on a silicon wafer aligned in strips inclined at a 45° angle to form a resistive strip element that is often termed a 'barber pole' due to its appearance. This structure forces the current not to flow along the "easy axis" of thin film, but at an angle of 45°. Four of the barber poles are arranged in a Wheatstone bridge in the same manner as resistance based foil strain gages as shown in Figure 3.3. Through the Wheatstone bridge, the sensors convert any change in the magnetic field in the sensitive axis to a differential voltage output that can be processed like any other electromagnetic sensor. Three of the AMR sensors can be used in a triaxial combination to determine the heading relative to magnetic north.

There are magneto-optic effects that are being explored as a way to create an optical compass [47]. Just as magneto-resistivity is the basis for MEMS compasses, electromagnetically induced transparency (EIT) is the basis for proposed optical compasses. EIT is where the absorption of a narrow range in an optical spectrum can be triggered by the presence of a magnetic field.

A magnetic compass of any type measures the direction of the earth's magnetic field to find magnetic north. However, as with the other metrics discussed, the sensor will detect any magnetic field and so care must be taken when mounting and calibrating the compass. Local magnetic fields or distortions are classified as either hard or soft iron effects. Hard iron effects come from permanent magnets that supply a constant magnetic field near the compass. Soft iron effects arise from un-magnetized steel, iron, batteries, or wires with a

[7] In the principle flight axes the heading is referred to as the yaw of the aircraft. This is in contrast to the pitch which is rotation about the transverse axis and the roll which is rotation about the longitudinal axis. Tiltmeters or gyroscopes are used to determine pitch and roll and a compass is used to determine heading.

moving current that may be near the compass. Selecting a good location from the sensor away from any of these sources is the best way to achieve good measurement quality. However, calibration can cancel some of the hard-iron effects by rotating the sensor through the magnetic field as long as the source of the distortion is fixed and constant. Techniques to correct for the soft iron effects exist but eliminating the sources of distortion is better. Because the strength of a magnetic field decreases with the square of the distance, even moving the compass a few feet from the soft iron will significantly reduce the distortion.

Chapter 4

THE ROCK ISLAND ARSENAL GOVERNMENT BRIDGE

The Government Bridge at the Rock Island Arsenal is one of over two hundred bridges owned and operated by the United States Army Corps of Engineers (USACE). Originally built in 1896, the current Government Bridge is both an heir to a rich history of bridge building and a vital part of the past, current, and future military operations of the Rock Island Arsenal. In order to help maintain this vital historic and strategic asset, the US Army Engineering and Research Development Center (ERDC) had a structural health monitoring system installed on the bridge. This chapter will review the history of steel bridges and the Government Bridge in particular, and discuss the details of the operation of the bridge and detail the SHM system the ERDC installed on the bridge.

4.1 Steel Bridges

An important part of understanding structural behavior is being aware of the type of structure being analyzed and why it was designed the way it was. Steel bridges account for a significant portion of the bridges in the United States. According to the Federal Highway Administration (FHWA) [15], the National Bridge Inventory contained 605,098 bridges as of December 2011 as shown in Table 2.2. Thirty percent of all those bridges, or 183,699 total bridges, are steel bridges. The large number of steel bridges exhibits great variety of in structural forms ranging from girder bridges to truss bridges. The bridges are also made of a range of steel quality. The structural form and materials used in the construction of a bridge are not independent of the era in which it was designed and built. The engineering knowledge (or often more important the lack thereof) and materials used in the design and construction of a bridge will influence which members are critical and prone to failure. Therefore, to understand the structural behavior of a bridge and create an effective SHM system, the history of the era in which it was designed and built is important knowledge.

4.1.1 History of Steel Bridges

Metal bridges played an important role in – and were influenced by – the industrialization of the United States and Europe. In 2011, the United States had 8,621 bridges still in use that were built before 1906 [16]. Though the FHWA does not differentiate the material used in these century old bridges, the fact that reinforced concrete did not gain favor as an engineering material until later in the twentieth century would make it a safe assumption that a majority of these bridges over 105 years old are steel or iron. Each historic bridge reflects the state of the art in bridge engineering at the time it was designed as well as

the public sentiments and perceptions about material and design safety. Understanding both the progress in the development of engineering skill and materials in the nineteenth century helps set the stage for the Rock Island Bridge. Bridge failures were a driving force behind engineering innovation that also contributed to a public demand for improved safety and rigor in subsequent bridges. A review of the history of metal bridges will contribute to the understanding of the materials and design of the Rock Island Bridge.

The first bridge made entirely of metal - the aptly named Iron Bridge - was built in 1779 in Coalbrookedale, England over the Severn River. [48, 49] The Iron Bridge was a one hundred foot arch bridge made entirely of cast iron that represented a significant first step in modern bridge building. Prior to the Iron Bridge at Coalbrookedale, bridges had been made of natural materials such as stone and timber. Ralph Modjeski, the Chief Engineer of the Rock Island Arsenal Government Bridge once quipped [50], "The first bridge built by man no doubt was of the kind easiest to build - possibly a tree thrown across a stream or ravine. Thus, unwittingly, the man invented the girder." From that first bridge, mankind refined their use of stone and wood to create more permanent structures that could carry heavier loads more efficiently. The entire lexicon of modern bridge building – arch, girder, and suspension – was expressed prior to the building of the first metal bridge. Ancient stone lintel bridges were the precursors to the modern girder bridges. The Romans perfected the stone arch in their many bridges and aqueducts that can be seen across Europe today. Many civilizations built simple rope and wood suspension bridges over creeks and ravines. What changed in 1779, therefore, was not mankind's ability to bridge a river, but the use of a material engineered by man.

The use of cast iron as a building material coincided with, and was a result of, the beginning of the industrial revolution. Though cast iron was discovered in ancient China, it achieved limited use as a construction material because it could not be made in sufficient quantities due to limited mining production and inefficient furnace technology. By the 1750s, the nascent industrial revolution provided advances in mining and furnace technology that allowed manufacturers to produce cast iron inexpensively and in mass quantities [51]. Cast iron, like stone, has immense compressive strength and limited tensile strength. Unlike stone, cast iron could be poured into any shape and the molds could be reused to manufacture identical pieces. Due to cast iron's compressive strength, at first it was used in arches just as stone and masonry had been for centuries.[1] However, engineers soon began to push cast iron beyond the traditional arch form. They began building plate girder[2] and trestle[3] bridges that pushed the boundaries of engineering knowledge and the mechanical limits of cast iron.

Pushing the boundaries of engineering knowledge and the mechanical limits of materials

[1] In 1795 a large spring flood filled the Severn River under the Iron Bridge and caused damage to many of the stone bridges over the river. However, the Iron Bridge survived unharmed because the cast iron work was more open and did not dam up the water like the stone arches did. Thus, the failures of stone bridges where a cast iron one survived helped increase the use of cast iron as an engineering material just as failures of other cast iron structures would eventually lead to its demise [48].

[2] For example the 47 ft. trough girder at Merthyr Tydfil in Wales was built in 1793. It remains the oldest cast iron railway bridge in existence [49].

[3] An example being the Gaunless River Bridge built in 1823 by George Stephenson. This trestle bridge had four 12.5 foot lenticular spans over the Gaunless River in West Auckland, England. This was the first iron railway bridge for use by the general public on a chartered railroad – the Stockton to Darlington Railway [49].

leads to both innovation and economy of materials. However, when designs encounter unknown engineering effects and the limits of a material are exceeded, the results are often disastrous. The limits of cast iron were exposed by the Dee Bridge in May of 1847. Built less than a year before its collapse, the Dee Bridge was designed to be the cast iron girder bridge with the longest span up to that point. Cast iron spans are typically limited by the maximum casting length for the individual pieces which is usually less than twelve meters. The Dee Bridge was 99.6 meters long with three simply supported spans consisting of four parallel girders that were each 33.2 meters each. Each girder consisted of three pieces spliced together with wrought iron tension bars serving as reinforcement.

Various explanations for the collapse of the bridge have been presented over the years that focus on any one of the engineering considerations that were little understood at the time such as eccentric loading, lateral torsional buckling, fatigue, or even ovalization of the bolt holes. At the time of the collapse, investigations blamed both the reinforced girder system and the choice of cast iron as the primary structural material. Regardless of the actual cause, the collapse killed five people, seriously injured approximately thirty more passengers, and effectively ended the use of cast iron as a primary structural element[4] [48]. Further collapses of cast iron railroad bridges – particularly an Erie Railroad bridge in 1850 – caused some American railroads to take even more drastic measures and they dismantled many iron bridges and replaced them with wood trusses [49].

The improved strength and ductility of wrought iron compared to cast iron had been recognized by engineers for years prior to the Dee Bridge collapse. Wrought iron found its first uses as tension members in patent trusses beginning in the early 1840s. The trusses patented in this time period typically shared many traits: they bore the name of their inventor,[5] they used wrought iron tension members and wither wood or cast iron compression members, and they were statically indeterminate. Because the proprietary trusses were statically indeterminate, most were designed without the benefit of structural analysis [49]. Member sizes were based on previous experience and general rules of thumb because the analysis methods[6] that modern civil engineers take for granted had not been invented.

Structural analysis, and consequently the importance of having a formal education in

[4]European engineers had effectively stopped using cast iron for any purpose by 1867. American engineers continued to use cast iron as compression members in bridges for about a decade longer [49].

[5]William Howe patented his namesake truss in 1840 and Thomas and Caleb Pratt patented their namesake truss four years later in 1844 [49].

[6]A modern structural engineer would use the "stiffness" method that sets up a series of simultaneous equations to solve for the forces in an indeterminate truss.

civil engineering,[7] took a large step forward in 1847. In that year, Squire Whipple[8] published a treatise entitled *A Work on Bridge Building: Consisting of Two Essays, the One Elementary and General, the Other Giving Original Plans and Practical Details for Iron and Wooden Bridges*. In this treatise, Whipple introduced a method for analyzing the forces in each member of a truss that today is known as the "method of joints" for truss analysis. To prove the effectiveness of his method for truss analysis, Whipple analyzed a typical Howe truss whose members where sized according to traditional methods. After calculating the forces in the members of the Howe truss, Whipple resized the members accordingly. Using structural analysis, Whipple reduced the amount of material needed to resist compression by half and reduced the amount of material needed to resist tension by one quarter [56].

Combined wrought and cast iron bridges dominated railway bridge construction during the 1840s and 1850s. Wrought iron enabled bridges to take on many different forms: arch bridges, tube bridges, girder bridges, suspension bridges, and truss bridges. The first bridge constructed completely out of wrought iron in the United States was completed in 1859 by the New York Central Railroad. Thousands of bridges of all forms and sizes were built as the railroads expanded across the eastern United States, over the Mississippi River, and eventually completing the first transcontinental route in 1869. This period saw the development of many features and forms that would be used in the construction of the current Rock Island Arsenal Government Bridge in 1896. The Lehigh Valley Railroad built the first pin-connected truss in 1859 but it was not until forged eye-bars were invented by the Pennsylvania Railroad in 1861 that pin-connected trusses became prominent in the United States.[9] In 1863 the Pennsylvania Railroad built a 320 foot iron Whipple truss bridge

[7]The first civil engineering school, École Nationale des Ponts et Chaussées (National School of Bridges and Roads), was founded in Paris in 1747. However, in England and America, civil engineers still learned the "trade" through apprenticeships and on the job training. Large public works projects such as the Erie Canal and later commercial enterprises such as the railroads were the first "schools of engineering." In 1802, the United States Military Academy became the first formal engineering school in the Americas but it took a few decades for its curriculum to develop and focus. The first degrees in "civil engineering" were awarded by Rensselaer Institute to four students in 1835 [52]. Even after schools began granting degrees, the engineering profession took many more years to recognize the importance of an engineering education in addition to experience in the field. On February 3, 1897 (two weeks before the meeting Ralph Modjeski presented his paper on the construction of the Rock Island Bridge [53]), the Western Society of Engineers held a discussion on "Technical Education" [54] due to a visit by the president of the Rensselaer Polytechnic Institute to Chicago. Professor Ira O. Baker, then chair of what is now the Civil and Environmental Engineering Department at the University of Illinois at Urbana-Champaign, made the following comments: "... engineering is truly a learned profession. Fifteen to twenty years ago it was a common thing to hear practicing engineers refer with scant respect ... to the young engineering graduate. This was a result of a misapprehension which has passed away, for now when engineers want assistants they almost universally ask for technical graduates. Of course, the recent graduate is not an experienced nor a competent engineer; but it is reasonably certain that he is well grounded in fundamental principles, and is so equipped as to rapidly acquire valuable personal engineering experience. ... We [professors] cannot make men who are ripe with experience; we can only put them upon the ladder and ... hope that after twenty years they can climb a little higher than you [practicing engineers]. They ought to, ... they started from your shoulders." [54, p. 248]

[8]Squire Whipple, often called the "father of iron bridges", was a civil engineer who had already patented a few truss designs before the release of his essays on bridge construction. In 1841 he patented an all iron bowstring truss and in 1846 patented a trapezoidal truss that had a system of double intersecting diagonals [55]. The latter truss is the type typically referred to as a Whipple Truss.

[9]Pin-connected trusses were popular because they were easily assembled in the remote locations of the

over the Ohio River and sparked greater use of iron trusses to carry heavy freight railroad loads over longer spans. By the 1870s, the Pratt truss (and its derivatives the subdivided Baltimore truss and the camel-back subdivided Petit truss) became popular for short and medium span railway bridges. Pratt trusses were statically determinate so material use could be optimized according to the methods that Whipple had proposed [49].

However, the age of wrought iron construction ended almost as soon as it began. The iron bridges built after 1840 began to fail in large numbers under train loads that were heavier and occurred with greater frequency than for which the bridges were originally designed. Between 1875 and 1888, estimates claim that about one quarter of all bridges in the American railroad inventory were failing annually [49]. In 1867 a Howe truss bridge collapsed under a train in Tariffville, Connecticut. In late December 1876, a Howe deck truss span collapsed under a train load in Ashtabula, Ohio, just eleven years after the original wooden truss bridge had been replaced to accommodate larger loads. Ninety-two passengers died when the train fell into the ravine below the bridge and was consumed by fire [48]. Further collapses in 1877 of a truss bridge in Chattsworth, Illinois and also in 1879 of the Tay Railway Bridge in Scotland continued to fuel a lack of confidence in the engineering profession.

Investigations into the cause of the many collapses in the 1860s and 1870s pointed to a lack of understanding of the principles of fatigue and underestimation of wind loads. In 1864, William Fairbairn published a paper entitled *Experiments to Determine the Effect of Impact, Vibratory Action, and Long-Continued Changes of Load on Wrought-Iron Girders* [57] that is considered the first work in English[10] on the subject of fatigue. In this work, Fairbairn described how wrought iron beams would fracture under cyclical loading at levels far beneath the static fracture level. He also identified that there was a load limit below which the number of cycles required to fracture the beam was far more than the expected life of a bridge. Incorporating the principles of fatigue into the design of bridges took many years after the publication of Fairbairn's article.

Likewise, the effect of lateral loads – and wind loading in particular – was still not fully understood or accounted for in the design of structures. In his treatise that introduced truss analysis [56] in 1847, Squire Whipple made only brief mention of lateral loads. Later publications by Whipple provided recommended dimensions for sway bars and lateral braces but these were not based on analysis but "experience and observation" alone [55]. The failures of the 1860s and 1870s and the investigations that followed led the engineering community to understand that provisions for wind loading needed to be addressed but there was not much agreement on how to do it. In 1881 many railroad companies and bridge builders had developed their own design loads. The American Society of Civil Engineers Committee on Means of Averting Bridge Accidents recommended applying 30 psf though the area of the bridge to be loaded with that force was not specified in the code. The Chicago, Rock Island, and Pacific Railway also used the 30 psf[11] loading but required an additional 10,000 psi in wind bracing members.

In 1867, the invention of open-hearth steel manufacturing enabled steel – which is

American frontier. In Europe where population density was greater, riveted connections were used more often.

[10]The first known fatigue testing began in Germany and was published by Wilhelm Albert in 1837 [58].

[11]The actual requirement was 300 plf (pounds per linear foot) which was 30 psf x 10 ft vertical projection.

stronger and lighter than wrought iron – to be produced more economically and in greater quantities. The first railroad bridge to use any steel was the cast steel arch Eads Bridge over the Mississippi River in St Louis, but it also used masonry and other materials. The first all steel railroad bridge was built in 1879 by the Chicago and Alton Railroad in Glasgow, Missouri [49]. The use of steel for bridges increased greatly after the dramatic failures of wrought and cast iron structures. In 1880, Theodore Cooper, who had worked on the Eads Bridge, published a paper entitled "The use of steel for railway bridges" and soon almost all railway bridges were built of steel. By 1895, the year that construction on the Rock Island Bridge started, nearly all bridges built in the United States were made of steel. Steel dominated bridge building until well after the turn of the century when concrete began to reduce steel's market share.

4.2 Rock Island Arsenal Government Bridge

The Rock Island Bridge, as it currently stands, is not the first bridge to be built on or near the present location. The bridge site has a rich history that encompasses three separate bridges built within forty years of each other. Each bridge reflects the history of the period it was built and the best of engineering knowledge at the time. The historic nature of the bridge makes the installation of a viable structural health monitoring system of greater importance. The National Park Service has regulations that limit the ability to replace, or even fundamentally change the appearance or functionality, of historic structures. Thus, the SHM system will help preserve and protect the bridge and the cultural significance that it embodies. Understanding the design principles and historical context of the current bridge provides valuable insight that is useful in creating models of the structure and evaluating the engineering limits that determine its condition and suitability for continued use.

4.2.1 Historical Legacy of the Rock Island Bridge

The Mississippi River, in a general sense, runs from its headwaters in Minnesota to its delta in Louisiana and runs through or forms the border of ten states. After the Louisiana Purchase in 1803, settlers from the eastern parts of the United States began to move west and settle the area drained by the Mississippi and its tributaries. The rivers were highly navigable and steamships began commercial service from Pittsburgh to St. Louis on the Ohio and then down the Mississippi to New Orleans in 1811 [59]. As the population, agricultural, and industrial output of the region increased, so did the number of steamships. With the Appalachian Mountains forming a barrier to overland transport, the new areas of the United States depended on the river for supplies and contact with the eastern seaboard.

The Upper Mississippi[12] developed slightly later than the Ohio River and the Lower Mississippi River due to impediments to navigation. Two stretches of rapids, along with a reputation for shifting sandbars and shallow water of only about four inches depth for

[12]The Upper Mississippi is defined as being north of St Louis.

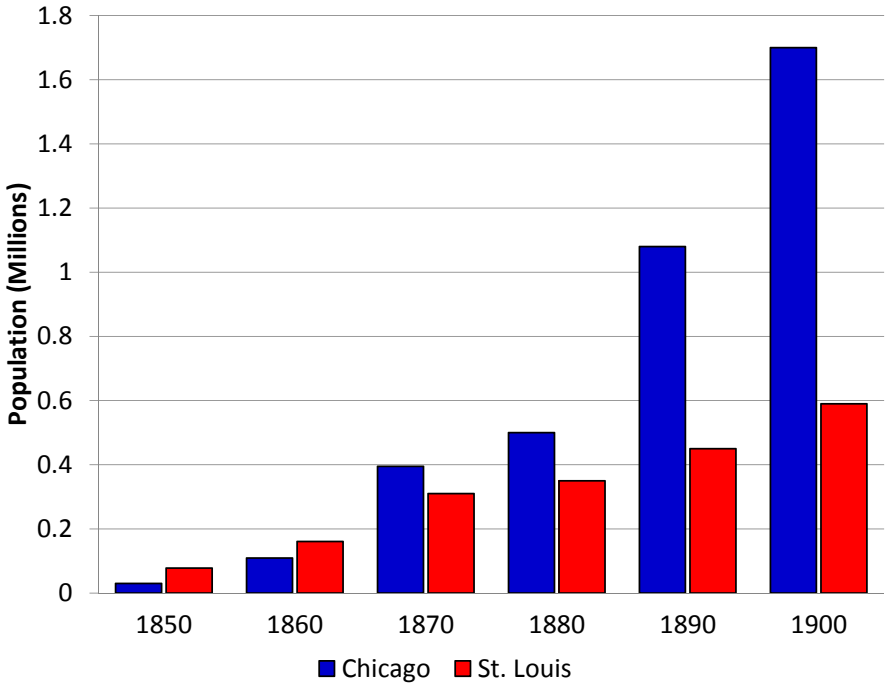

Figure 4.1: Population (in Millions) of St. Louis and Chicago from 1850-1900.

about four months of the year, proved difficult for early ship captains to navigate. One stretch of rapids ran upstream over eleven miles from the confluence of the Des Moines River near Keokuk, Iowa. The other stretch of rapids started at the foot of the Arsenal Island and extended nearly to LeClaire, Iowa. These two obstacles prevented any steamboat from successfully sailing north from St. Louis until 1823 when a small steamboat named *Virginia* took military supplies up to Fort Snelling in Minnesota. The *Virginia* traveled slowly[13] up the river trying to navigate the difficult river. Just above Fort Armstrong on Arsenal Island[14] *Virginia* became stuck in the Rock Island Rapids for two days before a sudden rise in the water level freed it and allowed the ship to continue upstream. The *Virginia*'s round trip took two months but it led to a slow and steady increase in traffic along the Upper Mississippi. Five years after the first voyage on the Upper Mississippi in 1828, the port of Galena, Illinois received 99 steamboats and 74 keelboats. Thirty years later, in 1857, Davenport, Iowa alone received 1,587 steamboats and Rock Island, Illinois across the river received about 1,040 more [59].

The river traffic made St. Louis into a regional power that controlled much of the commerce in the American west. As seen in Figure 4.1 the population of St. Louis was nearly double that of Chicago in 1850. But the invention and expansion of the railroads as the nation industrialized were setting up a conflict that would be played out at Rock Island. As seen in Figure 4.2, by 1854 Chicago had begun to establish itself as a regional hub for a

[13]It is claimed that the tourists that were also on the ship were able to disembark, walk along the shore, and wait to rejoin the ship upstream [59].

[14]The current Rock Island Government Bridge is a good approximation of where this occurred since the ruins of the fort are located just south of the Rock Island entrance to the bridge.

Figure 4.2: Extent of early railroads in the Middle States in 1854 [60]

rail network that ran from the Atlantic Ocean to the Mississippi River. In 1854 no bridges crossed the Mississippi River. The reason no bridges corssed the Mississippi was not because engineers could not build structures long enough to span great rivers, as evidenced by the fact that the Ohio River had already been crossed in 1851. Part of the reason was that prior to the arrival of the railroad at the banks of the river, no need existed. More importantly, unlike the Ohio River where West Virginia and Kentucky own the whole river, the boundary between the states that border the Mississippi runs down the center of the river.

The shared boundary presented a legal problem because the Chicago & Rock Island Railroad in Illinois and the Mississippi & Missouri Railroad in Iowa did not have charters that would allow them to build a bridge over the border. The Illinois legislature passed a special act in 1853 that created a special corporation called the Railroad Bridge Company. The Railroad Bridge Company received the power to "build, maintain, and use a railroad bridge over the Mississippi River ... in such a manner as shall not materially obstruct or interfere with the free navigation of said river [61]." With this act, the Illinois legislature cleared the way for the first bridge over the Mississippi River to finally be built.

4.2.2 First Rock Island Bridge (1856-1868)

Construction of the First Rock Island Bridge began with the excavation of the first pier in Davenport on July 16, 1853. On a pomp filled afternoon in September of 1854, the cornerstone was laid while bands played and politicians gave speeches [62]. The bridge built was 1,581 feet long and made of six wooden through truss spans that carried a single railroad track. The third span (counting from Illinois) was a swing span that was built over the channel the steamboats typically used for navigation when the water levels allowed it [61]. The bridge was officially opened of April 22, 1856 when three locomotives with two tenders and eight passenger cars crossed the Mississippi River for the first time [62].

Effie Alton Case

Not everyone joined in the celebration opening the new bridge. The steamboat interests and the leaders of St. Louis recognized the competition that the railroads would bring to their livelihood. In this context, on May 6, 1856 just a few weeks after the bridge opened, the steamboat *Effie Alton* was headed up river and had just passed the bridge when engine problems caused the boat to veer right and strike the span next to the draw span. The impact caused damage to both the bridge and the boat, but when a stove in one of the boat's cabins tipped over, the bridge eventually caught fire and one 250 foot wooden span was completely destroyed. The span was rebuilt in just four months and by September 8, rail traffic across the river could resume [61].

However, the *Effie Alton's* "accident" resulted in a lawsuit when the steamboat's owner, Captain John Hurd, filed a complaint in the U.S. District Court at Chicago. He claimed the bridge impeded navigation and was the cause of the destruction of his vessel and therefore demanded the Railroad Bridge Company be held liable for the loss of his ship and cargo. The Railroad Bridge Company hired Abraham Lincoln to be their defense attorney. The trial began on September 8, 1857 in the U.S. Circuit Court in Chicago [61]. On September 22, 1857, after nearly two weeks of trial, Lincoln got up to give his closing arguments – they lasted two days. Lincoln argued that the "plaintiffs have to establish that the bridge is a material obstruction, and that they managed their boat with reasonable care and skill"[15] [63], which he claimed they did not. But in the two days of argument he made grander statements about what the railroad was and what it represented. On the first day of his arguments Lincoln said:

> "St. Louis as a commercial place, may desire that this bridge should not stand, as it is adverse to her commerce diverting a portion of it from the river.... But there is a travel from East to West, whose demands are not less important than that of the river.... If the river had not the advantage in priority and legislation, we could enter into free competition with it and we would surpass it." [63]

[15]The actual court proceedings were destroyed in the Great Chicago Fire. The records of what Lincoln said at the trial come from the coverage of the case by Robert Hitt who was reporting for Chicago's *Daily Democratic Press* [63]. The *Daily Democratic Press* had daily coverage of the trial because it was high profile case where most people understood the greater issue of River v Railroad and St. Louis v Chicago.

This statement is very much at the heart of engineering practice: taking what nature has given mankind and improving on it and making things better.

A majority of the jury agreed with Lincoln but they were unable to agree on a verdict (nine for the bridge, three against) so the trial resulted in a hung jury [63]. As a result, the river interests lost the first battle in a legal war, and Chicago, fueled by its railroads, began to grow. By 1870 the population of Chicago overtook that of St. Louis and by 1890 Chicago was double the size of St. Louis, even though the latter had also grown substantially as America moved west.

Further Litigation

Though the Effie Alton Case ended in a hung jury, other cases were brought against either the Rock Island Bridge Company or either of the two railroads it connected. Two of these cases eventually made their way to the United States Supreme Court. The first case brought to the Supreme Court involving the Rock Island Bridge was *Mississippi and Missouri Railroad Company (M&MRC) v. Ward* [64]. James Ward was the owner of three steamboats, and captain of one of them, that regularly sailed between St. Louis, Missouri and St. Paul, Minnesota. His lawyers argued that due to the presence of the Rock Island Bridge, his steamboats suffered undue delay and injury. He sued asking that the bridge be torn down so as not to impinge on his right to the free and unobstructed navigation of the river – in all parts of it.

The circuit judge in Iowa ruled that the part of the bridge in Iowa (where there was no swing span) did obstruct the navigation of the Mississippi River in Iowa. Therefore, he ordered the part of the bridge in Iowa that was within his jurisdiction to be torn down. The M&MRC appealed the decision to the U.S. Supreme Court. After hearing arguments, the court ruled in January 1863 in a 6-3 decision to dismiss the case on the grounds that because the bridge was not fully within the jurisdiction of the circuit court in Iowa and therefore, he had no legal right to issue a verdict.

Because the suit was dismissed on a jurisdictional issue, the majority opinion did not address Ward's primary complaint. However, Justice Samuel Nelson wrote a dissenting opinion that did address what he considered to be the main issue of the case: whether or not the bridge obstructs the free navigation of the Mississippi River. In a similar complaint brought against the Wheeling Bridge over the Ohio River (which is entirely in the state of West Virginia), the Supreme Court had ruled that "if there still existed a free and unobstructed navigation of the river, the bridge would not be considered a nuisance [64]." Justice Nelson argued that the same principle applied in this case even though the bridge exists in two separate states. Though the bridge may indeed obstruct navigation in Iowa, if the draw span in Illinois over the deepest channel did not obstruct navigation then the bridge as whole did not obstruct navigation.

The second Supreme Court case involving the Rock Island Bridge was *The Galena, Dubuque, Dunleith, and Minnesota Packet Co. v. The Rock Island Bridge* [65]. Once again the complaint was that the bridge had caused damage to two steamboats. U.S. District Court for the Northern District of Illinois ruled in favor of the steamboat interests and put a maritime lien on the bridge. The lien was dismissed upon appeal and the Supreme Court

was asked to rule as to correctness of the dismissal. The Supreme Court ruled in December 1867 in favor of the Rock Island Bridge and established the principle that a maritime lien cannot exist on anything that is fixed and immovable like a wharf, a bridge, or real estate of any kind.

Demise of the First Rock Island Bridge

The legal wrangling over the Rock Island Bridge came to an end with the second Supreme Court ruling. However, the bridge itself was destroyed not long after. In March 1868 an ice flow pushed the first pier on the Iowa side about twenty-five feet downstream. Later, in April, a severe wind storm lifted the draw span off the supporting pier and overturned it so that it came to rest upstream of, but resting against, the central pier with both ends up in the air [66].

4.2.3 Second Rock Island Bridge (1872-1896)

The destruction of the First Rock Island Bridge came after the US Congress had already passed two acts, one in 1866 and the other in 1867 authorizing the construction of a new bridge. The acts stipulated that the new bridge be built at a new location downstream from the location of the First Rock Island Bridge[16] and that the piers of that bridge be removed from the river.

The new (Second) Rock Island Bridge was designed to be a double-deck bridge to be used by both the private railroads and the U.S. government. The joint use of the bridge is what has given rise to the nickname "Government Bridge." The US Army Corps of Engineers was to supervise the construction of the new bridge to ensure that the new bridge was not a nuisance to navigation. The Second Rock Island Bridge was finished in 1872 with C. Shaler Smith serving as the chief engineer and the Phoenix Bridge Company building the truss superstructure. The Second Rock Island Bridge was a wrought iron truss bridge consisting of eight spans, the second of which was a swing span. The top deck was originally made of wood (replaced with iron in 1891) and carried a single rail line [66]. The bottom deck was designed for wagon traffic. The designers decided to have the railroad on the top deck because they were afraid the sparks and smoke from the engines would spook the horses if they were on top and it was also easier to interface the wagon road with the streets in Davenport if it was on the bottom [67].

After the completion of the Second Rock Island Bridge, the demands of the railroad continued to grow in both the quantity of trains and the loads that they carried. The single track

[16] Ironically, even though all the lawsuits that tried to get the Rock Island Bridge declared a nuisance and impediment to navigation failed, in 1858 the Committee on Commerce of the U.S. House of Representatives declared the bridge to be a hazard because of the length of the pier, the angle of the bridge, and the swift current under the bridge [61]. When the army decided in 1866 to turn the whole of Rock Island into an arsenal (the northern half had been used as a prisoner of war camp for Confederate soldiers) they stipulated the bridge be moved to improve navigation and also not to bisect the island and interfere with the operations of the new Arsenal [67].

on the upper deck was soon deemed insufficient to handle the increased traffic the railroad required. The majority of the Chicago & Rock Island Railroad line was double-tracked and so the single-track bridge was creating a bottleneck in the flow of traffic. [67] The desire to build a replacement for the bridge was also influenced by the facts that the weight of trains had also increased rapidly and, as described in Section 4.1.1, a large number of high profile failures of wrought iron bridges occurred in the 1870s and 1880s.

4.2.4 Third Rock Island Bridge (1896-Present)

The design and construction of the Third (and current) Rock Island Bridge was very much a product of the history of the bridge site and of bridge engineering in broader sense. This was the third bridge to be built at the same location in less than fifty years. The Second Rock Island Bridge became functionally obsolete within only a few years of the significant financial outlay to have it built. In addition the fact that wrought iron bridges were collapsing at an alarming rate was raising the fears in the general populace about the safety of bridges and distrust of the traditional methods of design. With all this context, Congress authorized not more than $\$490,000$ to be spent by the Department of War on a new bridge at Rock Island with the stipulation that the demands for durability and safety were going to be high. The Rock Island Railroad shared in the cost of the bridge construction.

Colonel A. R.[17] Buffington, the commander of the Rock Island Arsenal was placed in charge of the bridge project for the government. The United States government stipulated that they wanted "A bridge of the highest order, built of steel of a very high elastic limit. The loading to be the heaviest used in the modern practice. [67]" The request that the bridge be made of steel and designed to the heaviest loads reflect the worries that existed about the safety of the wrought iron Second Bridge. To build the new bridge the government selected Ralph Modjeski, who, at the time, was an unknown engineer getting his first major commission.

Ralph Modjeski

The selection of Modjeski as the chief engineer of the Government Bridge seems to be somewhat contradictory. The Government wanted a bridge that would be well designed and last for at least fifty years, but they hired an engineer receiving his very first contract to build any bridge. Eventually Modjeski would become one of the most prolific bridge engineers in the country, and the bridge still exists over one hundred years later; so in hindsight, the decision was well founded. A look into Modjeski's personal history can shed some light on why this decision was made.

Ralph Modjeski was born Rudolph Modrzejewski in Poland on January 27, 1861. His mother was a famous actress and he moved around Europe and later the United States with her as a child. After an unsuccessful first application to the prestigious École Nationale des Ponts et Chaussées (National School of Bridges and Roads), Modjeski took the exam-

[17] Adelbert Rinaldo

ination a second time, passed as the fourth best student, and began his formal engineering studies in 1878.[18] He graduated first in his class with the degree of Civil Engineer in 1885. His thesis had been to design a steel bridge across an American river. Modjeski had become a naturalized American citizen in 1883 so he returned to the U.S. and began to work for George S. Morison [69] – the man who is now called "The Father of American Bridge Building."

Between 1885 and 1893 Modjeski worked for Morison in various positions. He was an assistant engineer during the construction of the Union Pacific's Omaha Bridge. He worked as a quality control inspector of the bridge pieces produced for Morison's company in the bridge building shops. He was Chief Draftsman for Morison's Chicago office during which time he helped Morison design the Memphis Bridge (now known as the Frisco Bridge) over the Mississippi that is considered Morison's masterpiece [69].

After working for Morison for seven years, Modjeski started his own firm in 1893. Initially, the new firm met with little success due to the economic troubles caused by the Panic of 1893. He performed a few small jobs, but the contract to design and supervise the construction of the Rock Island Bridge was his first significant job in his own firm. Modjeski was only thirty-four years old.

In looking at this history, two factors stand out as to why Ralph Modjeski might have been hired to design and build the Third Rock Island Bridge. The first is his technical education that he received at the École Nationale des Ponts et Chaussées. As mentioned in Section 4.1.1, structural analysis as civil engineers now know it did not begin until the middle of the 1800s. The use of structural analysis began slowly start, but after the bridge collapses of the 1870s and 1880s, bridge owners began to favor engineers whose design practices were founded in structural analysis and theory and not just experience. Modjeski's education was one of the best available at the time[19] as it was founded in the scientific principles of modern engineering. The second factor that likely led to his hiring was his relationship with Morison. Morison was the leading bridge engineer in his day and in 1895, the year the Rock Island Bridge contract was let, he was President of the American Society of Civil Engineers. It is not known if Morison had any active role in recommending Modjeski for the job, but the association might have helped allay any fears the Government might have had about hiring a first time chief engineer.

[18]Ralph Modjeski described the experience of failing his entrance exam as follows [68]: "I always wanted to become an engineer, and when I thought that I was sufficiently prepared I was sent to the great engineering school in Paris, Ponts et Chaussées (Bridges and Roads). My first entrance examination was a failure. There were one hundred applicants to take the examination and only twenty-five openings... I passed twenty-seventh in the list, and was rejected with great chagrin and discouragement. Thereupon I decided to abandon the prospect of becoming an engineer and to devote my attention to becoming a professional pianist... eight months [later] I decided to take the examination again at the engineering college. This I did and succeeded in passing fourth in the list. Notwithstanding the application required by such an exacting science as engineering, I have always found time to keep up my music . . . "

[19]Modjeski added to his list of prestigious degrees when he received an honorary Doctorate of Engineering from the University of Illinois in 1911.

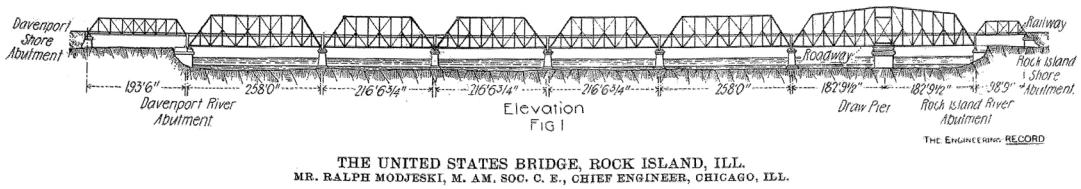

(Ralph Modjeski/Engineering Record 1897 [66])

Figure 4.3: Elevation of the Rock Island Bridge.

Design of the Third Rock Island Bridge

After being selected as chief engineer, Modjeski quickly designed the bridge and by June 1895 had submitted the designs to Col. Buffington. The Phoenix Bridge Company was selected to be the manufacturer in September 1895 [67]. The design of the Third Rock Island Bridge was limited in part by the Second Rock Island Bridge. The Third Bridge was required to use the piers of the Second Bridge and maintain rail operation throughout construction. These restrictions meant the span lengths and elevations for the Third Bridge would have to match those of the Second Bridge. As shown in Figure 4.3, the bridge had a total of eight trusses. By convention the trusses are labeled I–VIII starting in Illinois and proceeding to Iowa so that the swing span is Span II. Spans I and VIII only carry rail traffic and are best described as Pratt trusses. Spans III–VII are Baltimore trusses which can also be classified as subdivided Pratt trusses. The swing span (Span II) is more difficult to classify because of the truss is centrally supported. However, because the principle diagonals are in tension, the central span can perhaps best be described as a Parker 'camelback' truss which is also a Pratt truss in the most general sense.

The trusses were designed with both pin-connected and riveted connections. The pin-connections were more economical and allowed for faster construction though the riveted connections were considered superior. The pin-connections allowed the use of eye-bars in tension members. Unlike many contemporary bridges of similar length and design, Modjeski restricted the use of eye-bars to just the main tension diagonals. As an example, the Burlington Rail Bridge that was built in 1893 to replace a bridge that was built in 1868 and also has a swing span used eye-bars along the bottom chord as well as its diagonals. But Modjeski designed the bottom chord of the swing span of the Government Bridge to be a solid member with rigid splices at the joints. Some of the other spans do have eye-bars along their bottom chords in their center panels. Because pin-connected Pratt truss construction featuring eye-bars was so prevalent in the 1890s to 1920s and today the eye-bars tend to be fracture critical members and responsible for significant cause of concern, the *AREMA Bridge Inspection Handbook* has a separate section in the chapter on steel bridges exclusively dedicated to them [5, Chapter 9, Section 10]. Likewise Topic 8.7 of the *Bridge Inspector's Reference Manual* [29] is entitled "Steel Eye-bars" and even then they get mentioned numerous times in other topics on fatigue and pin assemblies. For the swing span of the Government Bridge, only the L4-U6 eye-bar diagonals are considered fracture critical, because they consist of only two parallel eye-bars. The L6-U8 eye-bar diagonals and the eye-bars in the top chord at U8-U8' consist of four parallel eye-bars and are therefore considered internally redundant.

As requested by the government, the bridge was completely made of steel except for the cast iron bearings and the machinery that operates the swing span. For most of the members, mild steel was specified and material properties and testing/verification requirements were part of the specifications that Modjeski provided to the Phoenix Bridge Company. The specifications indicated that the minimum elastic limit (i.e., yield strength) be 38,000 psi, which is greater than that of modern A36 steel citeBuffington1895. This limit was strictly adhered to.

During construction in October of 1895, Central Iron Works of Harrisburg, PA, a subcontracted steel manufacturer for the Phoenix Bridge Company, tried to get the Modjeski to accept steel whose elastic limit was only 33,000 psi and its ultimate strength between 60,000 and 68,000 psi. This grade of steel was cheaper for them to produce. Modjeski was confident enough that he had over designed the swing span that this lower strength steel would be sufficient. However, Col. Buffington refused to accept any steel that was below the strength indicated in the government's specifications. After two months of Modjeski trying to appease both sides, Col. Buffington wrote directly to the Phoenix Bridge Company in December, 1895 and said:

> "I desire to respectfully say to you, once and for all time, that the requirements of the specifications for workmanship and finished material shall be rigidly adhered to and that material which leaves your work without having passed the required inspection and bearing the marks testifying to it will be rejected – [it] will not be allowed to go into the bridge" [70]

Buffington's insistence on the higher strength material has a direct impact on the capacity and fatigue strength of the members – both are probably higher than expected. The additional capacity provided by the 38,000 psi yield strength has contributed to the bridge being able to withstand loads that have increased significantly since Modjeski designed the bridge.

The dead load was calculated from the weight of the steel that was ordered. The draw span weighed 2,466,271 lbs [66]. For the live loads, the bridge was designed, as requested by the government, to the heaviest loads of the time. In 1890, Theodore Cooper published a revised and updated edition of his *General Specifications for Iron and Steel Railroad Bridges and Viaducts* [71]. In the revised specifications, the heaviest train load was the Lehigh Heavy Grade Engine, which Modjeski used as the design load for the bridge [72]. Figure 4.4(a) shows the axle spacings and loads for the design train. In total, the live load was 11,360 lb/ft of the bridge; of this total, 8,000 lbs/ft was applied on the railroad deck and 3,360 lbs/ft was applied at the highway deck. Modjeski used design loads for wind of 200 lbs/ft at the top chord, 300 lbs/ft at the bottom chord, and 650 lbs/ft at the railroad floor [67]. These wind loads were slightly different than the loads recommended by Cooper which were: 450 lbs/ft on the top chord, 150 lbs/ft on the bottom chord, and 650 lbs/ft at the level of the tracks.

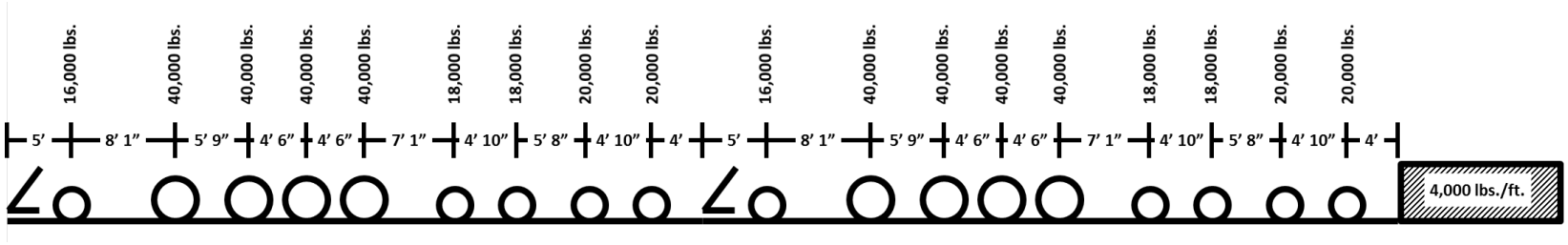

(a) Design train used by Modjeski as the applied live load for the Rock Island Bridge.

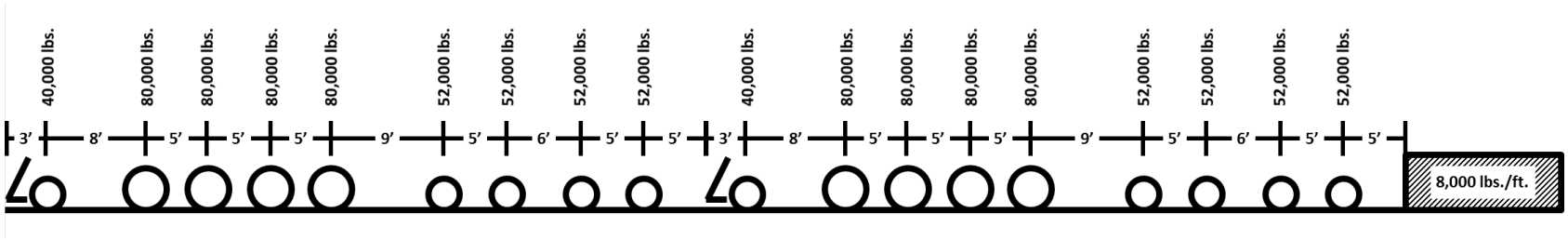

(b) Cooper E80 design train used in the current AREMA code.

Figure 4.4: Axle spacings and weights for design trains used by Modjeski and the modern code.

Erection of the Bridge

Shipment of the steel members began soon after the Phoenix Bridge Company was awarded the contract on September 21, 1895. The members were stored at the Arsenal until they were needed for construction. W. A. Aiken served as the site engineer though Modjeski would make frequent and prolonged trips to Rock Island to oversee much of the construction personally.

Construction, which began in earnest on November 7, 1895, started with expansion of the Second Bridge's piers that were to be reused in the erection of the Third Rock Island Bridge. The dual track nature of the new bridge required that the piers be expanded to accommodate its increased width. To accomplish this task, the coping and part of the old pier were removed and replaced with new masonry and stone. The piers had originally been built with Joliet limestone, but the expansion of the piers used Kettle River sandstone[20] for the facing and coping [72].

The lower deck was closed to wagon and pedestrian traffic on December 10, 1895, and was not reopened again until December 1, 1896. As per the government and railroad company requirements, train traffic was to remain open, and with minimal delays, throughout construction. Boat traffic was also to be as uninterrupted as possible.

To avoid interfering with the river traffic, the swing span was the first span scheduled to be constructed during the winter when the river was frozen. The original construction schedule called for all pieces of the draw span to be on site for construction to begin on December 1, 1895 and be completed by January 1, 1896. However, because of the dispute about material quality mentioned previously, the fabrication was delayed and the members that met the stringent strength requirements did not arrive until February 1896. Construction started as soon as possible.

The span was built using a wooden trestle that supported the rail track during construction. The construction of the swing span was expedited as much as possible. The engineers were concerned that if the ice pack on the river began to break up, it would destroy the wooden trestle and the steel span still under construction. The temperatures were watched carefully and for most of the month it stayed below freezing. However, toward the end of the month a slight warming occurred and the fears of Modjeski and his crewmen increased, but construction continued. A worker was stationed upstream of the bridge site to monitor the ice pack and alert the construction crew if conditions started to change.

On February 25, with just a few days of construction left on the swing span, the temperature again rose and the ice began to shift. The worker tasked with observing the ice alerted the crew and the bridge was evacuated. Not long after the last worker left the span, the ice crushed the wooden trestle and sent a snarl of steel and wood into the river. No one was killed or injured [53]. However, rail traffic was interrupted for five days while the crews worked night and day to rebuild the wooden trestle.

With the thaw of the ice, river traffic would begin soon and with the wooden trestle blocking the navigable channel of swing span, a temporary solution was needed. The

[20] Visitors to the campus of the University of Illinois at Urbana-Champaign should be familiar with Kettle River sandstone. The oldest sections of Altgeld Hall that were built in 1897 – including its bell tower – are also made from Kettle River sandstone [73]. Originally pink in color, the stone has weathered to a brownish-gray in both the bridge and the building.

Rock Island Railroad had a steel truss bridge nearby that could be configured for use as a temporary lift span. Modjeski quickly designed the towers and lift mechanisms and construction began immediately. Two-story towers were built, one on the first pier of Span III and the second adjacent to the pivot pier. A pulley system was installed in the towers to lift the bridge. By March 26, just one month after the accident, the river had been cleared of debris, the temporary lift span installed, and the wooden trestle removed. The first boat of the season passed under the lifted span on March 27.

The construction of the lift span not only delayed the construction of the new bridge, it forced Modjeski to come up with a new construction method. The swing span would now have to be built perpendicular to the railroad track over the pivot pier. The time that it took to construct the temporary lift span enabled new steel members to be fabricated and shipped to the site. The swing span was complete and ready to be swung into place on May 21, 1896. The Rock Island Railroad allowed Modjeski to halt traffic for ten hours to finish the necessary work. After the morning train had passed, the crews began to perform all the necessary tasks. The lift span was lowered onto barges and carried away on the west side while the wooden trestle was removed on the east side. In the center, the center section of track was being removed and turned 90° so that it now ran along the axis of the bridge and not perpendicular to it. Once the lift span was removed and its towers torn down, the channel was reopened to navigation. In the early evening, with some time to spare, the swing span was noiselessly swung and locked in place for the very first time.

The construction of the remaining spans continued without incident.

4.2.5 Inspection, Maintenance, and Repair of the Rock Island Government Bridge

Over the course of its lifetime, the Rock Island Government Bridge has been routinely inspected and repaired. Hsiao [74] compiled the following comprehensive list of the significant events, repairs, and modifications to the bridge that have taken place since its construction in 1896 to 2004.

1909 Casting of roadway floor. Expansion joint casting.

1916 Towers for power lines across Government Bridge rebuilt.

1921 Proposed reinforcement of bridge piers.

1922–1923 All masonry piers, dating back to 1872, encased in concrete. Ice-breaking nose plates installed.

1931 Repair of diagonals.

1931–1933 Construction of Lock and Dam No. 15 completed. This raised the average level of the Mississippi river by approximately 16 feet. The goal was to help river traffic during dry seasons and eliminate the Rock Island rapids. This roller dam is the longest of its kind in the world. The lock is located on either side of the Government Bridge swing span.

1933 Revised end lift arrangement. Installation of equalizing gear for machinery.

1934 Vertical shafts coupled.

1940 Operator's house floor reconstruction.

1941 Proposal of several highway deck road surfaces: solid floor or solid metal floor. Proposal of railway floor reconstruction.

1943 Encased south abutment in concrete.

1946 Repair to lift rollers.

1953 Lower chords reinforced. Reinforcement of posts in swing span. Pier and abutment repair.

1955 Rehabilitation of superstructure. General repair and reinforcement to most members. Filled grate deck of highway deck with concrete. Sidewalk replacement completed.

1956 Repair to span on Rock Island side of the bridge.

1957 Bridge strengthened to carry updated double-track railroad loading (F. K. Ketler Company). Repair, replacement, or reinforcement of almost every type of member. Deck stringers and girders reinforced. Major truss and miscellaneous repairs. Curb plates added. All modifications used welding or high strength bolts. Original erection drawings exist. The design loading was two AASHTO HS-20 trucks (Highway Deck) and a single C.R.I.&P. Railroad Class 5100 steam locomotive (Railroad Deck)

1961 Bridge lighting modifications. Underwater pier repair.

1962 Loose barge incident; repairs to swing span and adjacent span.

1965 Modification of floor plates under rail locks.

1966 Swing span drive chain repair.

1967 Repair and painting of bridge

1968 Stringer replacement. Installation of safety ladder. Secure motor frame to main frame of operator's house

1970 Bottom chords reinforced. Rehabilitation of entire bridge

1972 Repair damage; change bearing for shaft of equalizing gear

1973 General repairs to bridge.

1975 Repair cracked gear.

1976 Installation of automatic gates, repair of curbs and web of posts. General bridge repairs, installation of grating for platforms.

1977 Lighting replacement. Electrical service modifications. Rehabilitation and painting of bridge.

1978 General rehabilitation and painting of the bridge. Repair of barge damage.

1980 Installation of air compressor, guard over gearing for 1st and 2nd shaft

1981 Rehabilitation of operating mechanism for turntable.

1982 Rehabilitation of operating mechanism for turntable

1984 Extensive repairs to all sections of bridge. Debris removal.

1985 Rehabilitation of control house, repair of wing span machinery, truss repairs, trimming strut repairs (turntable section)

1986 Rehabilitation of control house. Deck repairs. Pier repairs. Brake repairs.

1987 Swing span repairs

1988 Swing span repairs. Pier repairs.

1990 Painting of the swing span. Structural repairs as needed; pier repairs; barge accident repair on two spans adjacent to swing span

1991 Miscellaneous truss repairs. Bridge shaft replacement.

1992 Structural repairs to all bridge spans;

1993 The Mississippi flood overtopped the piers. Repairs to all spans. Davenport river abutment repair.

1995 Painting and repair of Government Bridge

1996 Painting and significant repairs to all spans. Repair of center pivot mechanism (turntable section).

1997 Rehabilitation of entire bridge. Repair of center pivot mechanism. Replacement of pivot anchors.

1998 Repair and painting of Bridge

1999 Painting and repair of bridge, concentrating on three spans. Electrical towers and wiring repaired and new fixtures installed. Transformers replaced.

2000 Third and fourth phase of painting and repair of bridge.

2001 Replacement and upgrade of lighting. Lifting system repairs. Repair of barrier arm gates.

2002 Significant repair/replacement of members within center pivot of swing span.

2002 Repair floodwall protection cover (IJO Project)

2003 Repair of center pin assembly. Existing machinery removal. Modified center pivot base Replacement of previous cast iron base. New pony wheels. Revision of swing span drive system and emergency brake.

2004 Upper tread rehabilitation. Incidental structural repairs. Bearing casting modifications. Miscellaneous repairs of structural system and connections. Replacement of end lifts for swing span.

4.2.6 Current Bridge Operation and Condition

The Rock Island Bridge continues to serve as a multimodal transportation connection. In 2007, 3.8 million cars and 1,881 trains passed over the bridge and 2,884 boats pushing 18,568 barges crossed under it. The number of trains and total tonnage that crosses the bridge has been increasing even more. Today, the Iowa Interstate Railroad (IAIS) leases the trackage rights over the bridge from the federal government. In the past few years, the national emphasis on alternative energy and fuel sources has led to an increase in the production of bio-fuels along the IAIS system. Most of this new production ends up passing over the Government Bridge on its way from Iowa to IAIS storage facilities in Rock Island [75].

Despite the continued daily use, the bridge has officially been declared functionally obsolete[21] because of low appraisal ratings in its deck geometry and underclearances. The minimum vertical clearance of the bridge, only 3.75 m (12 ft) for the highway deck, is the principal reason for the low appraisal ratings. This low clearance can be problematic when vehicles that are larger than anything Modjeski could have imagined try to cross the bridge. Figure 4.5 shows the result of a large truck ignoring the low clearance warning and trying to cross the bridge – the bridge wins. These collisions are not uncommon and typically occur at the Davenport approach to the bridge. Even if a collision were to occur on the Rock Island approach, it would be an impact on Span I and not the swing span (Span II). The bridge operators have become concerned about two trains using the bridge simultaneously because the modern E80 Design Train is essentially twice the weight of the train the bridge was originally designed to carry, as shown in Figure 4.4. As such, train traffic has been restricted to just one, therefore trains always run on the upstream track. The swing span itself will experience the train on both sides because it can lock with either of its two tracks in the upstream position.

Even though the bridge is functionally obsolete, the bridge should not be replaced. Granted the bridge cannot carry large trucks due to the low clearance; but the detour is only 3 km (1.9 mi) resulting in a minimal impact on these vehicles and their travel time. In addition, the bridge is not structurally deficient because the continuous regimen of inspection, maintenance, and repair has kept the condition ratings high. The bridge also has intangible historic value that should preclude its replacement. As long as the inspection and maintenance continues, the bridge will be able to continue to serve.

[21] See Section 2.3 for the definition of functionally obsolete.

(John Schultz/Quad Cities Times) [76]

Figure 4.5: Truck stuck at Iowa entrance to the Government Bridge after ignoring clearance warning sign on August 19, 2011.

Bridge Swing Statistics

The Army Corps of Engineers maintain a wide range of information about the locks and dams of the Mississippi River system on their websites.[22] Water heights and other conditions are updated daily at its RiverGages.com website [77] and information about which vessels have passed through the locks is available through its Corps Locks website [78]. The Corps Locks website currently provides the name of the vessel, when it arrived at the locks, when it started the locking process, and when it completed the locking process. Previously, the site also provided information on what type of vessel it was, which lock it used, and the number of cuts it took to pass the vessel through the locks. This data is typically only available for the previous day and the current day at the time of access to the site.

To better understand how often and when the bridge swings, a program was written in C♯ that would access the USACE website, download the lockage information, and store it in a comma delimited file that served as a database. Additional scripts were written in MATLAB to read and process this information. Between the time the program was completed on July 17, 2011 and the time the US Army Corps of Engineers changed their website on May 1, 2012, the program recorded 2,016 lockages through Lock and Dam 15. As seen in Table 4.1, 1,173 of those lockages were for towboats or tugboats with barges

[22]The US Army Corps of Engineers changed their websites and how to access the information about the locks and dams in 2012. The data presented here was acquired before the websites changed. Though the information for the current websites are provided in the Bibliography [77, 78], all past data is not necessarily available.

Table 4.1: Type of vessels locking through Lock and Dam 15: July 17, 2011 - May 1, 2012.

Vessel Type	Count	Percent
Towboats or Tugboats	1173	58.2%
Recreational Vessels	673	33.4%
Lightboats (tug or tow w/o barges)	100	4.9%
Federal Government Vessels	44	2.2%
Passenger Boats & Ferries	26	1.3%
Total	2016	100%

attached and another 100 lockages for towboats without barges. Combined with the federal vessels and ferries, these 1,343 lockages are the most likely to cause the bridge to swing. The bridge will swing only if needed[23] and the larger, non-recreational vessels will always need at least one swing to occur. If the water level is low and the barges are full, then the first cut of a barge will sometimes be able to pass under the bridge without requiring a swing. Of the full towboats, 664 (56.6%) of them required two cuts to pass through the locks. Therefore, the data leads to the estimate that over the course of a year, the bridge will swing approximately 2,000 times.

However, as will be shown in Section 5.6, not all those 2,000 swings will provide viable data that can be used in the structural health monitoring system. Figure 4.6 shows that the tugs and tows pass through the locks at all hours of the day in an approximately even distribution. During the shift changes at the Arsenal plants, the bridge operators usually do not swing the bridge to allow for the free flow of the vehicular traffic so these hours have fewer lockage completions. However, the fact that summer days, when the locks are operating, are longer than winter days, when the locks are closed, has a greater effect on the number of viable data points the system can be expected to gather in a year. Of the recorded lockages, only about 27.8% of the tug and tow lockages took place at night when the bridge can reach a uniform temperature and provide viable data. Therefore, it would be expected that approximately 556 of the annual swings would take place at night. Section 5.6 will show that these swings will provide the most useful information on the bridge health.

Bridge Position Terminology

The swing capabilities of the bridge necessitate a discussion on the nomenclature that will be used to designate the bridge position. The bridge status can be either "locked" to allow vehicular and train traffic or "open" to allow barge traffic. The "open" position is alternatively referred to as the "swung" position. In the "locked" status, there are two distinct

[23]The bridge operators say that many times the recreational boats will come through and request the bridge to swing but unless the river level is very high, the bridge operators will refuse. The recreational boats are required to lower their antennae which often disappoints the boat owners who are trying to impress their passengers.

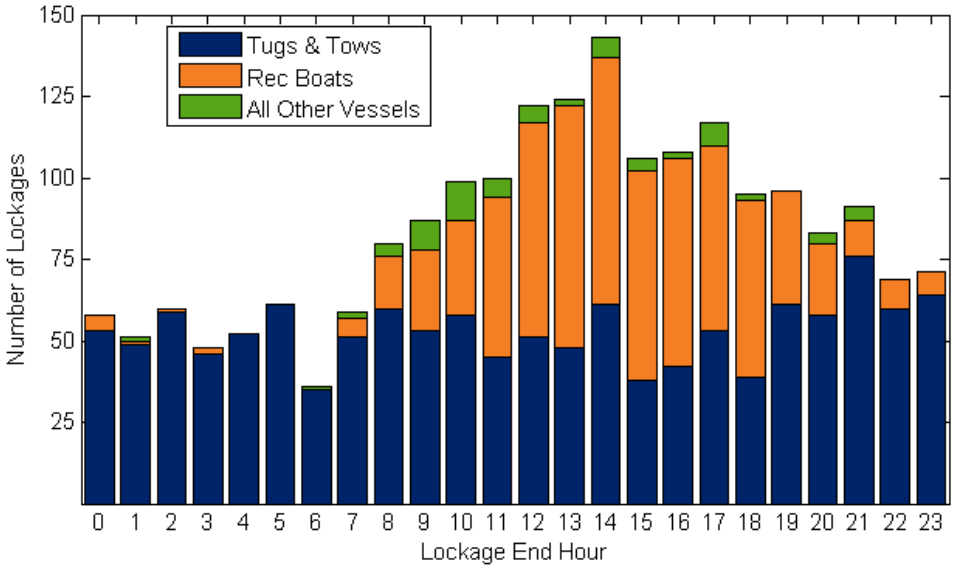

Figure 4.6: Number of lockages by recorded end hour.

alignments that can be defined. The symmetry of the bridge is such that the only distinguishing feature is the stairway that leads up to the operator's house. These stairs can be aligned such that they are on the "upstream" or "downstream" side of the bridge when the bridge is "locked". Thus there are two positions the bridge can be in when "locked" - "locked-upstream" and "locked-downstream." These positions are generally referred to as just "upstream" or "downstream" and the locked position is inferred. Due to slight differences in the interaction of the abutment and bridge locking mechanisms, the locked positions all have slightly different boundary conditions. The differences in the boundary conditions will be explained in further detail in Section 5.5.

Chapter 5

ANALYSIS OF THE FIBER OPTIC SENSOR SYSTEM ON THE ROCK ISLAND ARSENAL GOVERNMENT BRIDGE

As part of a USACE project to deal with corrosion of steel bridges, ERDC-CERL contracted the installation of a fiber-optic structural health monitoring system on the Rock Island Government Bridge. In addition to some sacrificial corrosion sensors and an acoustic emission sensor system, a fiber optic system that consisted of acceleration, strain, temperature, and tilt sensors was installed on the bridge. The sensors were all based on fiber Bragg grating technology. After an introduction to fiber optic sensors, the Government Bridge's fiber optic installation and an analysis of its functionality will be discussed in this chapter.

5.1 Fiber Optic Sensors

Compared with electromagnetic sensors, fiber optic sensors are a relatively new technology. The first optical fibers that were considered suitable for long distance telecommunication applications were not manufactured until the late 1960s [79]. A fiber optic (FO) cable consists of a very thin glass fiber that is surrounded by a series of polymer or sometimes metal layers that serve to protect the fiber. The glass fiber itself is usually made of fused silica (SiO_2). The glass fiber serves as a waveguide that keeps light passing through the core inside due to the principle of total internal reflection.

The development of fiber optic sensors followed soon after the introduction of fiber optic cables in the late 1970s and 1980s as the optical properties of the fibers were investigated. Sensors developed around many different optical properties including refraction, reflection, and scattering effects within the fibers. The principal types of sensors that are now commercially available are presented in Table 5.1. Each sensor can be used for different metrics and each has its own characteristics that make it more suitable than others for specific tasks.

Just as there are many types of FO sensors, there are many types of FO interrogators. In its simplest form, an interrogator consists of a light source that sends light down the cable and a photodetector that measures the quantity of light that comes back. The source or light is typically a swept laser or a broadband source. Both light sources provide light composed of various wavelengths with a determined range at periodic intervals. Photodiode arrays are typically used as the photodetectors that determine the wavelengths and intensity of light that returns to the interrogators. Between the light source and the photodetector, a number of methods to improve the measurement quality have been introduced. Edge filters, tunable filters,[1] and interferometric scanning all have different characteristics that balance the tradeoff between sensitivity and measurement range [81].

[1]The tunable filter is a FBG wrapped around a piezoelectric cylinder that deforms the FBG when a potential is applied.

Table 5.1: Comparison of fiber optic sensing types and performance [80]

		Fiber Bragg Gratings	Fabry-Perot Interferometric	SOFO[a] Interferometric	Raman Scattering	Brillouin Scattering
Classification		Point	Point	Long-gage	Distributed	Distributed
Multiplexing		In-line Parallel	Parallel	Parallel	Distributed	Distributed
Points per Cable		10-50	1	1	10,000	30,000
Typical Accuracy by Metric	Strain ($\mu\epsilon$)	1	1	1	—	20
	Deformation (μm)	1	100	1	—	—
	Temperature ($\circ C$)	0.1	0.1	—	0.1	0.2
Fiber Type		Single Mode	Multi-mode	Single Mode	Multi-mode	Single Mode

[a] **S***urveillance d'***o***uvrages par* **f***ibres* **o***ptiques*

Proponents of FO sensors list several advantages that they have over traditional electromagnetic sensor systems [80]. The glass fibers, unlike metal wires, are chemically inert, even at high temperatures, making FO sensors suitable for highly corrosive and harsh environments. The oil and gas industry has made extensive use of FO sensors in down-hole applications where temperature and pressures are extreme. Another advantage is that optical fibers are immune to electromagnetic interference that can cause noise and distortion in traditional wired sensing systems. FO sensors are also well suited for gas pipelines or other areas of explosion risk, because there is no electricity in the fiber optic cable that can escape and cause a spark. FO cables are also designed to convey data over tens of kilometers.

The previous benefits of fiber optic sensors are universal to all types of FO sensors, other benefits or advantages are specific to the type of FO sensor used. For example, Brillouin scattering sensors have the advantage of being a distributed sensor meaning they can take measurements anywhere along the lengths so a single fiber optic cable can contain a large number of measurement points. On the other hand, Fabry-Perot interferometric sensors are restricted to a single point sensor. The Rock Island Bridge system contains only FO sensors based on fiber Bragg gratings so these sensors will be discussed in more detail

5.1.1 Fiber Bragg Grating Sensors

In 1978, Ken O. Hill discovered that FO fibers that were doped with germanium are photosensitive [79]. Exposure to ultraviolet light will permanently change the refractive index of the fiber at the point of exposure. Bragg gratings are a series of parallel etchings made in the fiber at a tunable distance from each other. The first commercially available FBG sensors were produced in 1995.

A typical FBG consists of evenly spaced etchings though other configurations exist. When light traveling along the length of the fiber reaches the first etching, a portion of that light at all frequencies is reflected back along the fiber. At each successive etching in the FBG another small portion of the light is reflected. The spacing of the etchings causes the reflected light from each etching to have a different phase for most light wavelengths. The reflected light at different phases experiences destructive interference and essentially the individual reflections cancel each other out. However, for light that has a wavelength that is a harmonic of the etching spacing, the light is reflected back in phase and experiences constructive interference increasing the amplitude of the reflected light. The effect of the interference means that the reflected spectrum will essentially only contain one reflected wavelength. The useful spectrum of a low reflective FBG is a sinc function[2] centered at the FBG wavelength [79]. The reflected spectrum of high reflective FBG is broader and has

[2]The sinc function is defined as:

$$\operatorname{sinc}(x) = \begin{cases} \dfrac{\sin(x)}{x} & \text{if } x \neq 0 \\ 1 & \text{if } x = 0 \end{cases}$$

For low reflective FBG the x value in the sinc function is:

$$x = \frac{\pi \cdot N \cdot \Delta\lambda_i}{\lambda_0}$$

fewer side lobes. Figure 5.1(a) shows a simplified example of the reflected and transmitted spectrum caused by an FBG on an optical fiber.

FBGs are typically created with wavelengths specified in the range of 1550 nm, because silica has minimal absorption at this wavelength. The wavelength of light reflected by the FBG is controlled by the spacing of the refractive etchings in the fiber. Wavelengths for FBGs are specified in terms of light in a vacuum. However, the reflected wavelength will be shorter, because the light is traveling through glass and has to pass through the fiber twice. The grating spacing (Λ) to achieve a specified wavelength (λ_0) reflection is determined using the equation:

$$\Lambda = \frac{\lambda_0}{2n} \tag{5.1}$$

where n is the refraction index of the fiber. The relationship between the grid spacing and the wavelength is what makes FBG sensors possible. A change in the spacing between the gratings will causes a change in the reflected wavelength that can be measured using a photodetector. The cause of the change in grid spacing can be either thermal or mechanical strain.

Figure 5.1(b) shows an example of a strained FBG sensor. If Figure 5.1(a) is considered the original strain state of the fiber, then the strain in the Figure 5.1(b) fiber has increased by some $\delta\epsilon$ which has caused an increase in the wavelength reflected back toward the interrogator. A number of strain sensors have been invented to measure strain that vary in their casings and they are attached to the structure. Whether the sensors are intended to be embedded in concrete [82] or welded to a steel structure [83] the fundamental principles remain the same. An FBG that is not mechanically attached to an object but free to expand and contract can serve as a temperature sensor. FBG strain sensors can be used to make other sensors such as accelerometers (see Section 5.2.1).

To measure strain with an FBG strain sensor, the interrogator measures the wavelength being reflected (λ_i) and determines the difference from the base wavelength (λ_0) recorded at the time of installation.

$$\Delta\lambda = \lambda_0 - \lambda_i \tag{5.2}$$

Because the wavelength and grating spacing are proportional as per Equation (5.1), dividing the wavelength shift ($\Delta\lambda$) by the base wavelength (λ_0) is analogous to Equation (3.1) and is the measure of the strain in the substrate/sensor system and leads to the equation:

$$\frac{\Delta\lambda}{\lambda_0} = k \cdot \epsilon + \alpha_\delta \cdot \Delta T \tag{5.3}$$

where k is the gage factor, ϵ is the strain of the substrate, α_δ change in the refractive index of the sensor due to temperature, and ΔT is the change in temperature between the base reading and the current sample. This equation represents the total strain measured by the FBG strain sensor and indicated by the normalized wavelength shift. Using Equations 3.3 and 3.4 for the total and thermal strains respectively to expand ϵ in the previous equation

where N is the number of etched grids and $\Delta\lambda_i$ is the difference between the FBG wavelength λ_0 and a given wavelength λ_i.

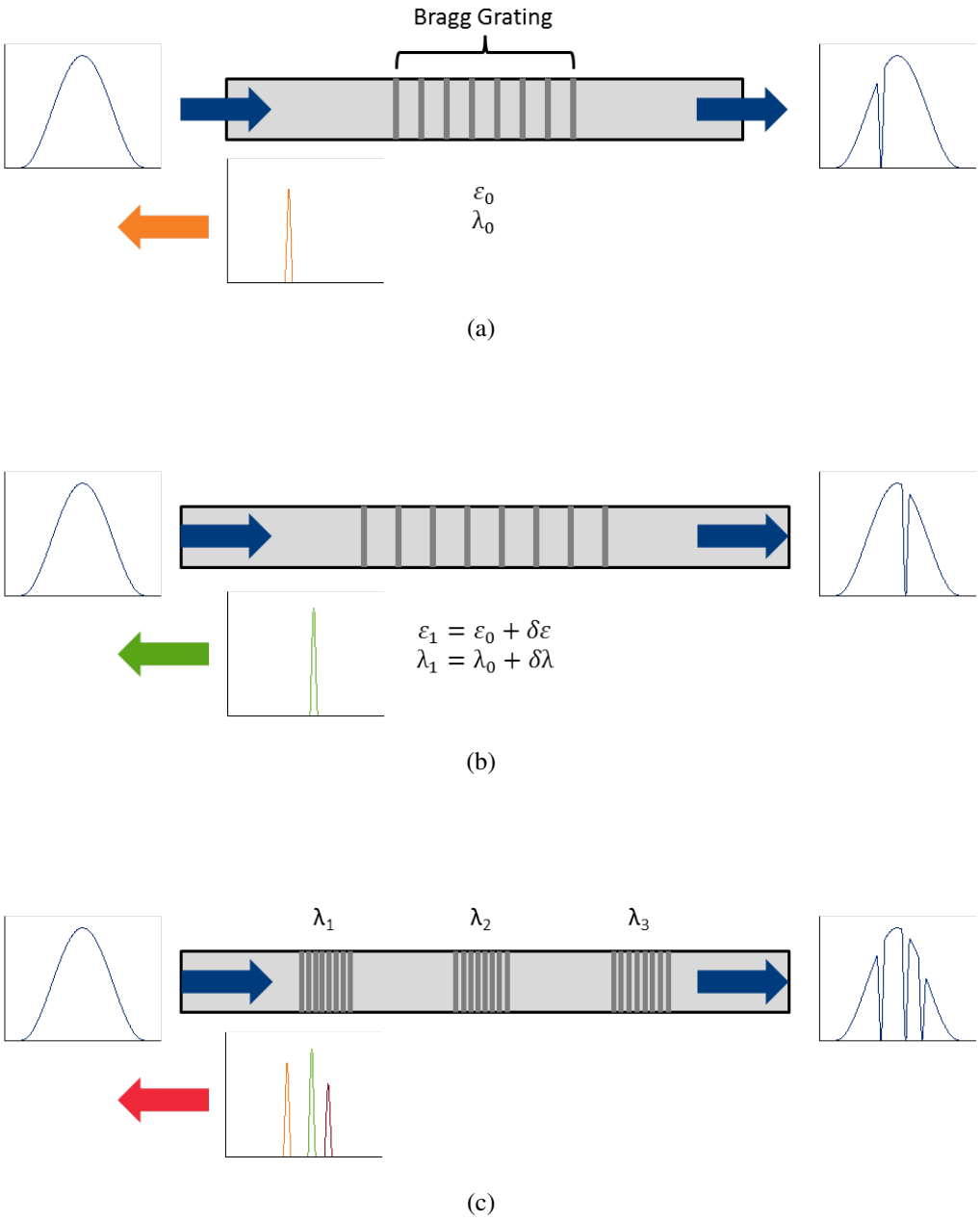

Figure 5.1: Functionality of Fiber Bragg-Grating sensors: (a) the FBG selectively reflecting a specified wavelength of light; (b) the change in reflected wavelength due to a change in strain in the fiber; and (c) a series of three multiplexed Bragg-gratings on the same fiber.

yields

$$\frac{\Delta\lambda}{\lambda_0} = k \cdot (\epsilon_E + \alpha_{eff} \cdot \Delta T) + \alpha_\delta \cdot \Delta T \tag{5.4}$$

where ϵ_E is the elastic mechanical strain and α_{eff} is the effective coefficient of thermal expansion of the specimen/sensor system which is:

$$\alpha_{eff} = \alpha_s - \alpha_g \tag{5.5}$$

where α_s is the CTE of the specimen and α_g is the CTE of the glass fiber sensor.

Substituting Equation (5.5) into Equation (5.4) and solving for the elastic strain yields the following:

$$\epsilon_E = \frac{1}{k}\frac{\Delta\lambda}{\lambda_0} - \left(\alpha_s - \alpha_g + \frac{\alpha_\delta}{k}\right) \cdot \Delta T \tag{5.6}$$

This equation represents the temperature compensated mechanical strain as derived from the FBG and an external temperature sensor [79]. If temperature is held constant then the relationship between the mechanical strain and the measured change in wavelengths is as follows:

$$\lim_{\Delta T \to 0} \epsilon_m = \frac{1}{k}\frac{\Delta\lambda}{\lambda_0} \tag{5.7}$$

The previous equation can apply over short periods of time where the temperature change is minimal even if in the larger context the temperature is free to vary.

Fiber Bragg grating (FBG) sensors are popular because, though they are not distributed, multiple sensors can be combined on a single fiber optic cable in a technique known as wavelength division multiplexing[3] (WDM) [81]. In WDM, FBG with different characteristic wavelengths can be spliced onto the same fiber. As long as the wavelengths are far enough apart, the interrogator can be programed to look for a peak in each range and associate the peak with the correct sensor. Figure 5.1(c) shows a schematic of three FBGs that have been multiplexed with different wavelengths and the reflected spectrum seen back at the interrogator. WDM is touted as a benefit[4] of fiber optic sensors because fewer FO cables are needed for the same number of sensors than when using electrical wires since each electromagnetic sensor requires its own wire. Whereas WDM is a feature that in the upfront cost and installation is very beneficial, multiplexing of fiber optic sensors can lead to larger problems in sensor system reliability. In an electromagnetic sensor system, if one wire is chewed through by a mouse or corroded, then only one sensor in the system will stop providing data. In a FO system with WDM, if the same mouse chews through one FO cable, depending on the relative location of the sensors and the mouse, multiple sensors in the system will no longer provide any data.

Time division multiplexing[5] (TDM) is another form of multiplexing that is common in FO sensor systems [81]. TDM takes place not in the individual FO cables, but in the interrogator. Using delay lengths and high speed switches, the pulsed wavelength bands provided by the light source are assigned a time slot. Each time slot is then passed to

[3] In Table 5.1, WDM is referred to as "in-line" multiplexing

[4] Nearly every paper on FBG sensors, or the use of FBG sensors in any context, has a sentence (often the same sentence) that lists multiplexing as one of the benefits of FBG sensors.

[5] In Table 5.1, TDM is referred to as "parallel" multiplexing

the photodetector in what is essentially a sample and hold scheme. If TDM were not performed, each fiber optic cable would require its own photodetector. However, this process effectively samples the sensors at the light source which leads to aliasing in the system.

In the signal processing sense, aliasing occurs when a signal is sampled that has not been filtered to limit the bandwidth of the signal to the Nyquist frequency. The Nyquist frequency is equal to half the sampling rate. If the signal is not band limited to the Nyquist frequency prior to sampling, any part of the signal greater than the Nyquist frequency will appear to be (hence the term "aliasing") a different frequency in the sampled signal. The frequency that it aliases as is determined by "folding" the signal at the Nyquist frequency. This can be described mathematically by the following formula:

$$f_{aliased} = \left| f - N\frac{f_s}{2} \right| \quad \text{where} \quad 0 \leq f_{aliased} \leq \frac{f_s}{2}, \text{ and } N \in \mathbb{N} \tag{5.8}$$

$f_{aliased}$ is the aliased frequency, f is the un-aliased frequency, N is an integer indicating the number of "folds", and f_s is the sampling frequency. For example, if a signal that contains a 10 Hz and 30 Hz component is sampled at 50 Hz (which means the Nyquist frequency is 25 Hz), the frequency content of the sampled signal will appear to be 10 Hz and 20 Hz. In this example, the 30 Hz component is aliasing as a 20 Hz signal ($|30\text{Hz} - 1 \cdot 50\text{Hz}| = 20\text{Hz}$). Once a signal has been sampled and aliasing has occurred, it cannot be removed from the signal.

Aptly named anti-aliasing filters prevent aliasing from occurring in electrical sensing systems. Anti-aliasing filters are analog low-pass[6] filters that have their cutoff frequency set to the appropriate Nyquist frequency for the given sampling rate. Optical filters analogous to electronic anti-aliasing filters do not exist.

There have been attempts to minimize the effects of aliasing in the FBG interrogators. Van Damme et al. [84] noticed that aliasing could be reduced by varying the ratio between the integration time of the photodetector and the sample rate. As the integration time approached the sampling rate, aliasing decreased which is to be expected as the signal is also approaching an analog state. Bentell et al. [85][7] used oversampling at 250 kHz and then using digital signal processing methods to filter and downsample to seven programmable rates between 128 Hz and 8196 Hz. Any frequency content above 125 kHz is essentially still aliased but the authors assumed that the contribution of these higher frequencies is negligible. Buck et al. [86] tried to use a correlation factor for expected and measured intensity spectra from the photodetector to identify and suppress aliased frequencies. They limited their study to only sinusoidal input.

5.1.2 Fiber Optic Sensors Installed on Civil Structures

Fiber optic sensors have attained widespread use across the world in many SHM applications [87]. The installations have great variety in their sensor technology, metrics, mount-

[6] A low-pass filter is one that allows all frequencies lower than the given cutoff frequency to pass through while eliminating all frequencies above the cutoff.

[7] Two of Bentell et al. are also included in Van Damme et al. including Bentell

ing techniques, and structure types [88]. For FBG strain sensors, a common application has been strain monitoring of reinforced concrete using embedded sensors. Embedded fiber optic sensors have even found their way into steel truss structures, but only to monitor their concrete decks and not the steel truss members [89]. There have been fewer applications presented in the literature of fiber optic sensors, FBG or otherwise, for steel structures where the strain gages have been surface mounted presented in the literature.

In May 1997, Lee et al. [90] instrumented a three span steel truss railroad bridge in Waco, Texas with twelve fiber optic strain gages of the Fabry-Perot interferometer type. The fiber optic sensors were first mounted on stainless steel mounting plates before being spot welded to the steel truss members. Foil strain gages were mounted next to the fiber optic gages for comparison during train events. The data presented indicated that over a timespan a few seconds, the fiber optic sensors produced comparable results to the traditional foil strain gages. No long term monitoring results were presented other than to note that the sensors had survived a full calendar year installed on the bridge and were still producing data. Lee et al. also observed that the diurnal temperature changes were evident in their strain records. However, they insisted that they could still determine the dynamic strains caused by the passage of trains because the time scale of the temperature changes was significantly greater than the time scale of the train events.[8]

In 1998, Vohra et al. [91] placed a wavelength division multiplexed fiber Bragg grating system on a steel box girder bridge that was under construction. Data was collected only for short periods at two points during construction. The strain and temperature FBG sensors were placed inside the box girders. The location inside the girder means the sensors were not exposed to direct solar radiation. The sensors were able to detect construction activities that induced strain changes in the box girder. The sensors also picked up on some local buckling on the lower web of the girder that indicated a curved sliding shoe on the pier cap during the push phase of the girder construction.

More recently, fiber Bragg gratings have been installed on steel rails to monitor railway traffic. Tam et al. [92] installed FBG strain sensors on the tracks of the Kowloon-Canton Railway Corporation's East Rail in 2002. From the strain records, they were able to effectively count the number of axles that passed. Radio-frequency identification (RFID) systems recorded which wagons were passing over the track. Comparing the RFID information to the strain record the number of axles counted using the FBG sensors were never wrong and performed better than traditional magnetic sensors. The FBG sensors were placed on both rails of the track and imbalances were used to assess the risk of derailment.

Filograno et al. [93] similarly instrumented rails of the Madrid-Barcelona High-Speed Line. They took the concept of axle counting one step further and were able to: identify the train types based on the axle configurations, determine the speed of the trains, and detect wheel imperfections. The FBG strain system used is operated on a trigger basis so data is only recorded when a train triggers the system. This eliminates many temperature influences since the train passes over the strain sensors in less than thirteen seconds.

[8]The train event shown in the paper by Lee et al. [90] lasted approximately 10 seconds. This train event is an order of magnitude less than what is observed on the Rock Island Bridge (see Figure 8.2).

Figure 5.2: Flow chart of fiber optic SHM system installed by Chandler Monitoring Systems.

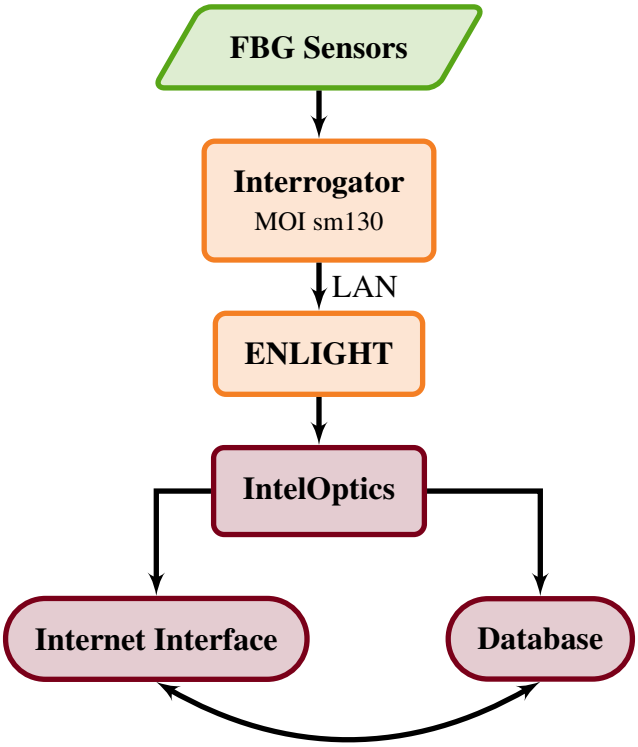

5.2 Structural Health Monitoring System Installed on the Rock Island Bridge

To help maintain and preserve the historic Government Bridge at the Rock Island Arsenal, the US Army Engineering Research and Development Center (ERDC) contracted to install an SHM system on the swing span. A multimetric SHM system was installed that intended to leverage the capabilities of many sensor types to provide the desired functionality. The system was designed to provide real time information that can be viewed on a web-based interface. A fiber-optic sensor system was installed along with an acoustic emissions system and a wireless corrosion monitoring system. Only the fiber optic system will be used as the others have proved unreliable.

5.2.1 Fiber Optic Sensor System

Chandler Monitoring Systems (CMS) installed a multimetric, multiplexed fiber optic sensor system on the Arsenal Bridge in November 2009. Figure 5.2 shows a flow chart of the system from the FBG sensors installed by CMS. The "Internet Interface" and "Database" in the figure are components of IntelOptics (i.e., the proprietary software produced by CMS). At the core of the system is the fiber optic interrogator. CMS chose the sm130-500 op-

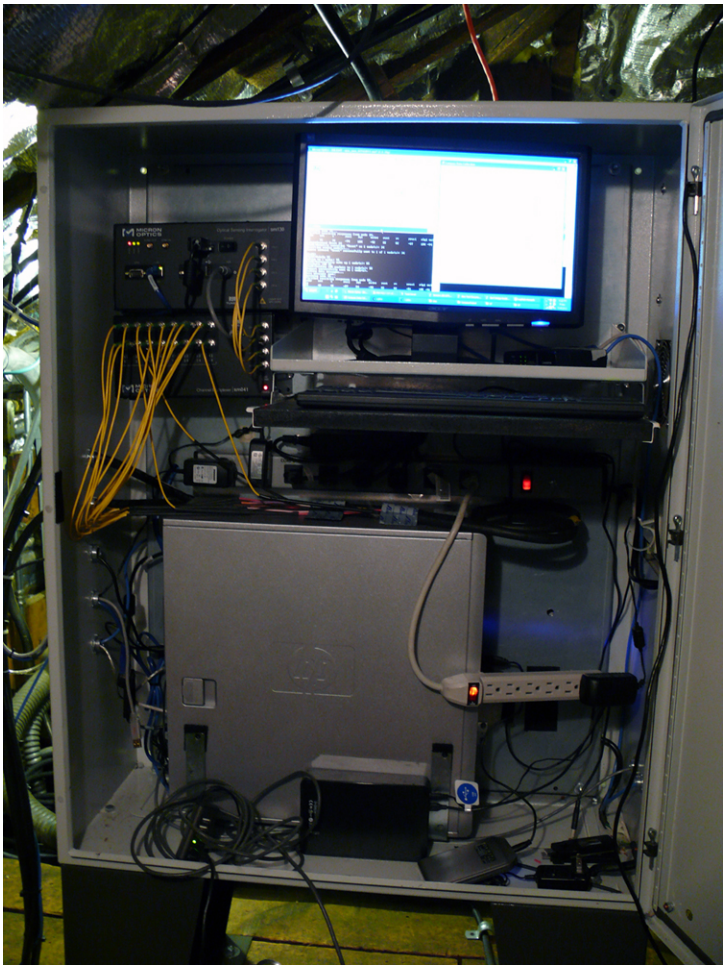

Figure 5.3: Base station computer and fiber optic interrogator in the operator's house attic of the Rock Island Bridge.

tical sensing interrogator by Micron Optics. This interrogator features a swept laser that scans the wavelengths from 1460 to 1620 nm at 500 Hz. The wavelength stability of the interrogator is 2 pm and the wavelength repeatability is 1 pm. The interrogator has four optical channels natively but has been combined with the Micron Optics' sm041 sensor multiplexer to expand the number of channels to sixteen. The increase in the number of optical channels from four to sixteen effectively decreases the scan frequency from 500 Hz to 125 Hz. Thus the maximum sampling frequency of the system as installed is 125 Hz. Both the interrogator and multiplexer can be seen in the upper left of the base station cabinet shown in Figure 5.3.

Each of the sixteen optical channels available has been multiplexed further for a total of eighty-eight channels of sensor data. The sensors used are all based on fiber Bragg-grating technology and measure strain, temperature, acceleration, and tilt. Because the sensors all use FBG technology, the multiplexing of the sensors on the sixteen optical channels was done geographically for convenience. After processing in the interrogator, the data is sent via an Ethernet LAN connection to the base station computer. Micron Optics supplies an interface program entitled ENLIGHT Sensing Analysis Software that is used to process

(Micron Optics [94])

Figure 5.4: Micron Optics os3110 weldable FBG strain gage.

the data sent by the interrogator. ENLIGHT allows the user to create "virtual sensors" that perform calculations on the wavelength measurements to provide output values that are in the desired units. ENLIGHT can store the constants and coefficients necessary to calculate a temperature compensated strain output – as from Equation (5.6) – using two separate FBG readings i.e. one from a strain gage and one from a temperature sensor.

ENLIGHT can also be used to control the wavelength ranges that define each FBG sensor on the fiber and the intensity threshold that is used to detect the wavelength reflected by the sensor. Both these parameters are important as they determine the effectiveness of the interrogator in differentiating the multiplexed FBG sensors from one another. Each sensor has a specified reflectivity at the specified FBG wavelength. Ideally, all sensors multiplexed on a single fiber optic channel would have the same reflectivity so that the range of the intensity of reflected light can be tuned to detect all the sensors equally well. If the intensity range is set too low, a sensor that has a high intensity reflection can exceed the upper limit. When the upper limit is exceeded, the center of the detected wavelength can overflow causing two peaks to appear in the designated wavelength range which causes an erroneous reading. In addition to the thresholds set in ENLGIHT, CMS installed physical attenuators to try to ensure that the threshold limits — both upper and lower — were suitable for all sensors multiplexed on a channel.

Strain

The primary focus of the installed fiber optic system is to measure the strain. CMS chose to install the Micron Optics os3110 weldable strain gage [94]. The gage consists of a stainless steel carrier that holds the fiber optic cable as shown in Figure 5.4. The os3110 are marketed as being equally sensitive and accurate as traditional foil gages but having a greater strain range ($\pm 2500\ \mu\epsilon$) and multiplexing capability. The gages can be ordered with FBG wavelengths ranging from 1460 nm to 1620 nm in 4 nm intervals to allow for multiplexing along a single fiber. The os3110 models are designed to be spot welded to the substrate to make installation easier and epoxy free.

There are a total of thirty-four os3110 strain sensors installed on a variety of members in locations that are doubly symmetric. Figure 5.5 shows the locations and name of the strain gages on both sides of the truss. The sensors marked with 'L' are on the left truss which is the truss with the stairs and those marked with 'R' are on the right truss and the side without the stairs. When the stairs (left truss) are downstream and an observer is standing upstream then the numbering is left to right as shown in Figure 5.5. Note that the numbering system consisting of beam numbers along the bottom and 'U' (Upper), 'M' (Middle) and 'L' (Lower) is consistent with the numbering system used in bridge inspections. The numbers and letters are used to refer to joint locations and beam names.

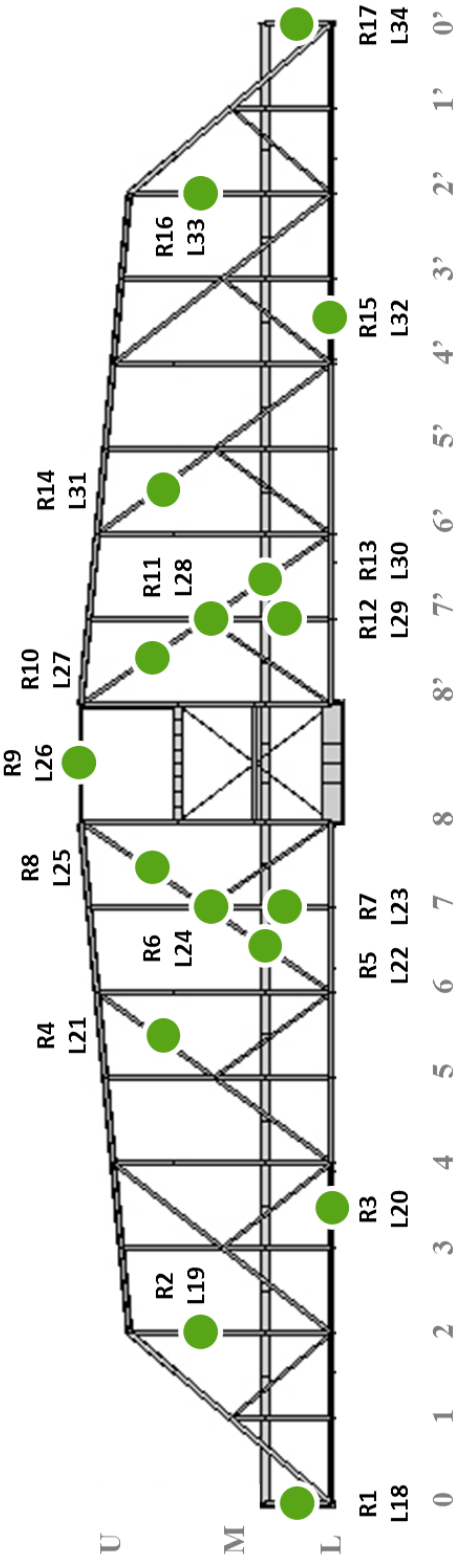

Figure 5.5: Location of installed fiber optic strain gages.

For example, sensor Strain R4 is installed on member M5–U6. This numbering convention will be used on all diagrams showing sensor locations.

The placement of the strain gages on the member cross sections are shown in Figure 5.6. The general rule is that the sensors were placed in the middle of the member on the face that is closest to centerline of the bridge. There was no deviation from this rule in the placement of the sensors on the eye-bars so all the innermost eye-bars have been instrumented.

The installed os3110 strain sensors do not self-correct for temperature. The temperature compensation for the os3110 sensors can be calculated using Equation (5.6). By substituting in the known values for the os3110 sensors installed on the Rock Island Bridge (gage factor $k = 0.89$, CTE of steel $\alpha_{sp} = 12\frac{\mu\epsilon}{^\circ C}$, CTE of glass $\alpha_g = 0.7\frac{\mu\epsilon}{^\circ C}$, and the change in refraction index due to temperature change $\alpha_\delta = 6.23\frac{\mu\epsilon}{^\circ C}$[9]) the following equation is produced.

$$\begin{aligned}
\epsilon_m &= \frac{1}{k}\frac{\Delta\lambda}{\lambda_0} - \left(\alpha_{sp} - \alpha_g + \frac{\alpha_\delta}{k}\right)\cdot\Delta T \\
\epsilon_m &= \frac{1}{0.89}\frac{\Delta\lambda}{\lambda_0} - \left(12 - 0.7 + \frac{6.23}{.89}\right)\cdot\Delta T \\
\epsilon_m &= \frac{1}{0.89}\frac{\Delta\lambda}{\lambda_0} - (18.3)\cdot\Delta T
\end{aligned} \tag{5.9}$$

This equation is of the form $y = mx + b$ where the slope of the line (i.e. the temperature dependence of the mounted sensor or net coefficient of thermal expansion) is 18.3 $\mu\epsilon/^\circ C$.

Temperature

To perform temperature compensation presented in Equation (5.9), CMS installed twenty-three temperature sensors on the Rock Island Bridge. The locations of the installed sensors are shown in Figure 5.8 Note that even though the temperature sensors were designed to provide compensation for the strain sensors, a one-to-one relationship between the strain and temperature sensors does not exist. CMS intended for one temperature sensor to provide compensation for a number of nearby sensors. For example, sensor Temperature R5 is used by CMS to compensate Strain R8 (with which it is collocated) as well as Strain R5, Strain R6, and Strain R7. The effectiveness of this type of temperature compensation will be discussed in Section 5.3

For the temperature sensors, CMS selected and installed the Micron Optics os4350 [95] armored cable flange mounted temperature sensors shown in Figure 5.7. The body of the sensor is a sealed alumina ceramic tube that contains an FBG which in turn is cased in anodized aluminum that has the flanges for easy mounting. The flange has screw holes but an epoxy was used on the Rock Island Government Bridge. The os4350 are marketed as being able to measurement the absolute temperature on a structure's surface for use in the compensation of strain measurements. They are said to feature a faster response time, a wide operating range, and no calibration needed. They are calibrated by MicronOptics

[9]The refraction index, like strain, is a ratio and therefore dimensionless. The units of microstrain have been included here for convenience.

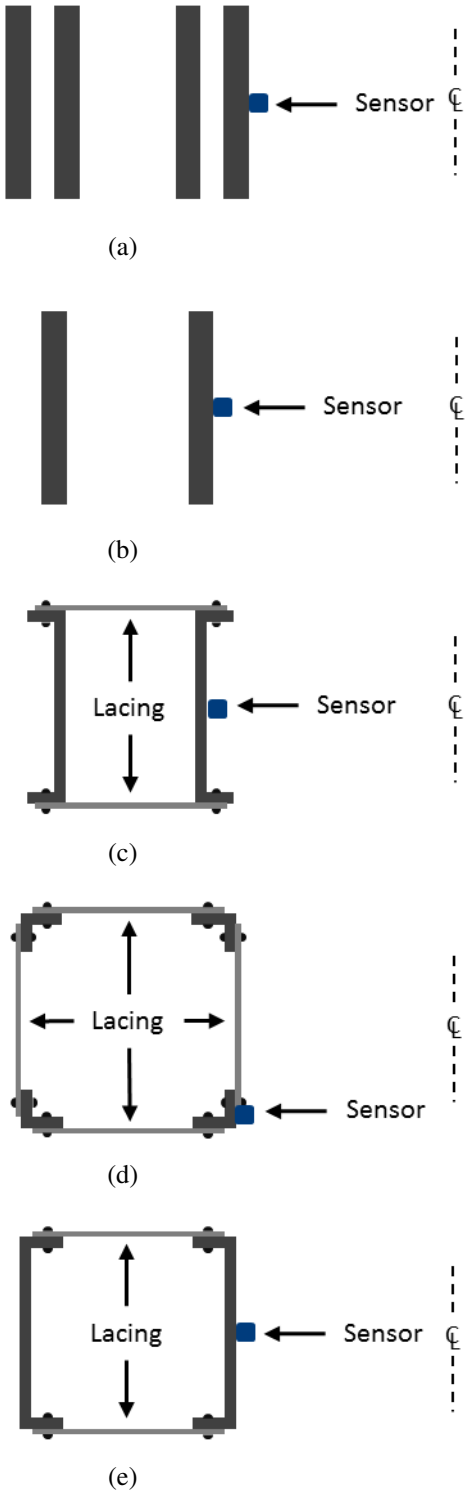

Figure 5.6: Fiber optic sensor placement on member cross sections: (a) sensors located on the diagonals L6-U8 (b) sensors located on the diagonals L4-U6 and members U8-U8' (c) sensors on vertical posts L2-U2 and L0-M0 (d) sensors located on the bottom chord (e) sensors located on vertical posts L7-M7.

(Micron Optics [95])

Figure 5.7: Micron Optics flange mount os4350 FBG temperature sensor.

before shipment and the standard calibration level is 1.0°C long-term and 0.6°C short-term. The response time of the os4350 is said to be 4.2 seconds.

Acceleration

To measure the vibrations and accelerations on the bridge, CMS installed ten triaxial accelerometers on the bridge. CMS chose to install Micron Optics os7100 [96] series accelerometers as they are the only accelerometer available from Micron Optics and based on FBG technology and would therefore function with the rest of the multiplexed system. Each os7100 sensor can measure a single axis of acceleration so to measure three axes of acceleration, a mounting block is used as shown in Figure 5.9. The FBG wavelength can be tailored for each axis to allow the three axes to be multiplexed on a single optical fiber. The optical sensor is encased in a rugged metal casing and the lead fibers are also armored to increase its suitability for long-term outdoor deployments.

The os7100 series is marketed by Micron Optics as being able to measure accelerations from DC (0 Hz) up to a few hundred Hertz. The resonant frequency of the sensor is near 725 Hz and the maximum of the linear response is about 325 Hz as shown in Figure 5.10. The data sheet for the sensor includes a footnote that states "Aliasing can occur for frequencies > 0.5 the sampling frequency." [96] This statement signifies that optical filters are not present to prevent aliasing in either the sensors themselves or the interrogator. The sensitivity of the sensor is 16.7 pm/g so for a typical FBG bandwidth of 250 pm the accelerometer can be rated as being approximately ± 7.5 g. The resolution of the accelerometer is dependent on the sensitivity of the interrogator to changes in wavelength.

The ten triaxial accelerometers were installed underneath the decks of the bridge to capture the vibrations induced by vehicular traffic and trains. Eight of the sensors were installed along the edges of the highway deck and two of them were installed in the on the center of the railroad deck. The positions of the sensors are shown in Figure 5.11. The sensors, are numbered according to the convention established by CMS for the strain and temperature sensors and will be always be preceded by either "Acceleration" or "ACCEL" to avoid confusion with the other similarly labeled sensors. Note that the number designation does not indicate a set position as Acceleration R2 is not in the same location as Strain R2.

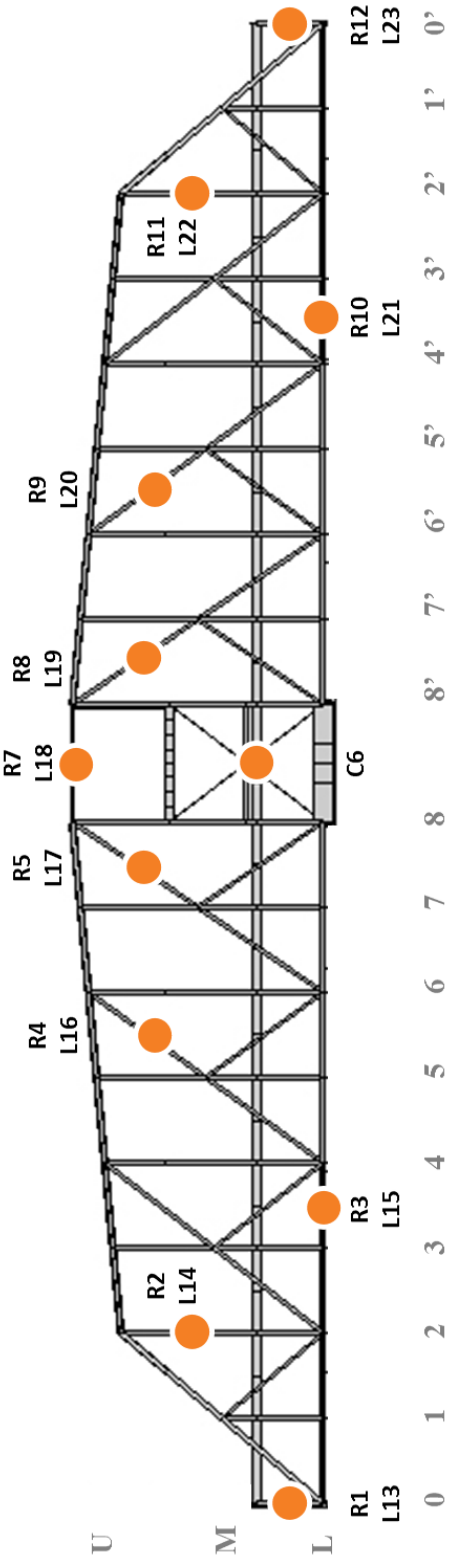

Figure 5.8: Location of installed fiber optic temperature sensors.

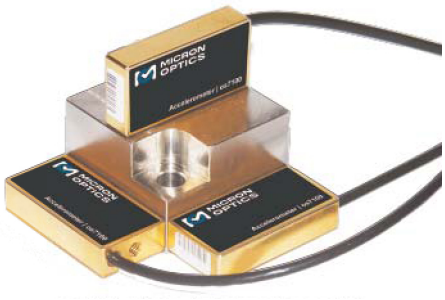

(Micron Optics [96])

Figure 5.9: Micron Optics os7100 triaxial accelerometer.

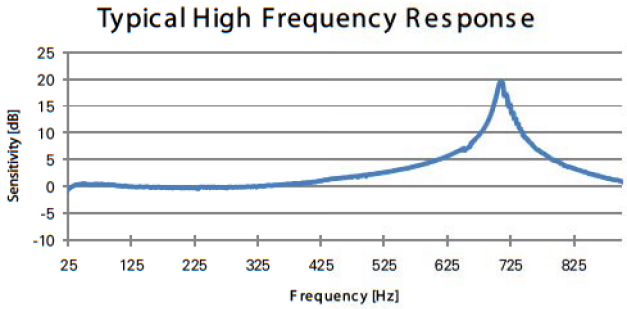

(Micron Optics [96])

Figure 5.10: Frequency response of the Micron Optics os7100.

Tilt

One mono-axial tilt meter has been installed on the Rock Island Bridge. Micron Optics does not manufacture a tiltmeter so CMS installed a Smartec SDS 12.1030 mono-axial tiltmeter [97]. Shown in Figure 5.12, the SDS 12.1030 uses two FBGs installed in a push-pull mechanism on a pendulum mass inside a stainless steel casing. When the sensor tilts, the pendulum moves, causing a corresponding change in the strain of the attached FBG sensors. Having the two sensors measuring the same motion in a push-pull manner is intended to be self-compensating for temperature. The measurements from the two FBG are subtracted from one another effectively canceling out the thermal strain. The pendulum in the tiltmeter signifies that the measurement mechanism is essentially an accelerometer as well. However, the data sheet for the sensor makes no claim as to its suitability for dynamic environments.

The tiltmeter is attached to the bridge using a bi-axial mounting base that is supplied by Smartec. The mounting base consists of two aluminum plates 210mm$\times$270mm$\times$8mm joined together by brackets at a right angle. The mounting bracket is necessary to orient the tiltmeter's single axis with the longitudinal axis of the bridge. The tiltmeter is located in the center of the underside of the highway deck on the floorbeam L1 as shown in Figure 5.11.

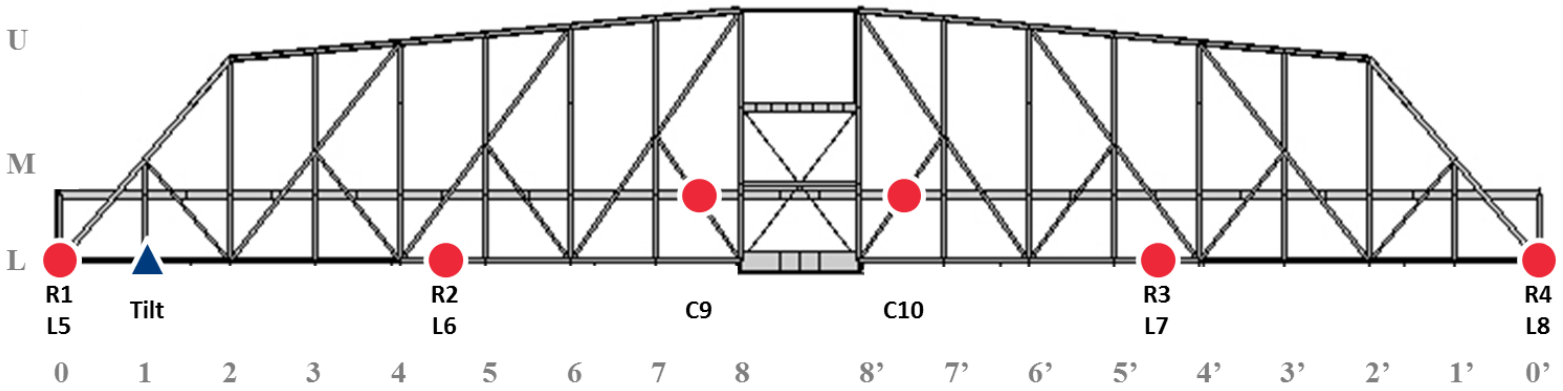

Figure 5.11: Location of installed fiber optic accelerometers and tiltmeter.

Figure 5.12: Smartec SDS 12.1030 MUST mono-axial tiltmeter.

(Smartec [97])

5.2.2 IntelOptics

IntelOptics is a proprietary, trademarked, and customized program developed by Chandler Monitoring that serves as the interface for the currently installed SHM system. IntelOptics interfaces with Micron Optics' ENLIGHT program to access the fiber optic data. The calibration of the sensors and the interrogator sample rate are all controlled by ENLIGHT. A timer with in the IntelOptics controls the sample rate for data storage. For example ENLIGHT, can have its sample rate set to 125 Hz, and the IntelOptics rate storage rate set to 1 Hz. In this scenario, IntelOptics will wait for its timer to fire, read in all samples collected by ENLIGHT since the last time IntelOptics requested data and just record the last sample provided by ENLIGHT. No filtering is performed during this 'downsampling' to the desired rate. As with the acceleration sensors, this approach can result in significant aliasing of the strain signals.

IntelOptics is marketed as featuring continuous 'Green-Yellow-Red' status display on the home screen of the program. The status is determined by simple thresholding based on values set by the user. Exceeding the warning limit set by the user will cause a 'yellow' alert to be sent and the warning lights to be changed from green to yellow. Likewise, a maximum threshold can be set to trigger a red alert. The alerts will appear on screen and also be mailed to the responsible user.

IntelOptics provides comprehensive reporting capabilities. Real-time status (limited by the sampling rate of the system) is made available online. The interface screen shown in Figure 5.13 contains plots of the current value of all the sensors in a zone on the bridge. Note that the displays are fixed and if a new sensor is added or a sensor is removed, the whole interface and all the database procedures and queries need to be hard coded by hand to make the changes. The maximum threshold for each sensor is also displayed and the scale of the graph adjusted to show the value as a percentage of the limits. In addition to the real time internet display, the internet interface can be used to create reports for a selected date range that provide the recorded data for user selected sensors. IntelOptics collects

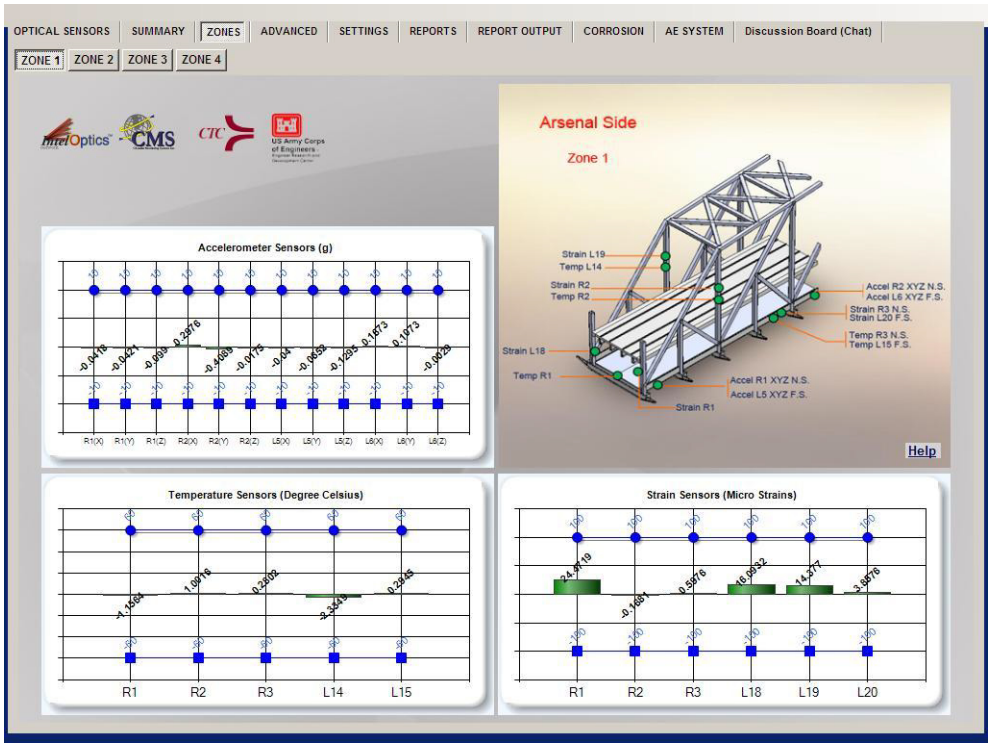

Figure 5.13: Screenshot of the IntelOptics interface.

data, but, other than the simple thresholding, it performs no data processing to distill and track metrics that can indicate bridge health. All data analysis is the responsibility of the user and must be done manually.

5.2.3 Threshold Determination

To establish threshold values for use in the IntelOptics System, O'Donnell Consulting Engineers, Inc. (OCEI) was contracted to provide structural analysis of the Government Bridge [98, 99]. The intent of the analysis was to determine critical bridge members for monitoring and deduce appropriate threshold limits to be used in IntelOptics' 'Green-Yellow-Red' system. OCEI prepared a FE model in ANSYS that consisted of approximately 132,000 elements and 140,000 nodes. The chords, posts, diagonals, beams, and stringers were all modeled using elastic beam elements. The railroad and highway decks were modeled using shell elements. Pinned connections were modeled by releasing the rotational degree of freedom about the pin axis.

Once the model was complete, the following analyses were performed:

- Dead Load: both conditions when the bridge is locked and when it is swung were considered
- Live Load: both static and transient dynamic analyses were performed for an a

Table 5.2: OCEI recommended sensor locations.

Member	Metric	Location
L0-M0	Strain	Midspan of member
L2-U2	Strain	Midspan of Railroad Deck and U2
L3-L4	Strain	Midspan of member
M5-U6	Strain	Midspan of member
L8-M7	Strain	Midspan of member
L6-M7	Strain	Midspan of member
M7 Pin	Strain	Middle of pin length
M7-U8	Strain	Midspan of member
U8-U8'	Strain	Midspan of member
FBL7	Strain	Midspan of member at Railroad Deck
L0	Acceleration	Near support
L4-L5	Acceleration	Midspan of member
L7-U7	Acceleration	Near or on Railroad Deck

CooperE80 train loading and an HS20 truck[10] placed at the midspan of the two sides of the bridge in addition to a 0.64 k/ft lane loading.

OCEI found that the live loading condition created the largest strains and stresses in the bridge members, and the first natural frequency was 4.6 Hz. Based on the analysis, OCEI recommended that sensors be placed on the members indicated in Table 5.2 These sensor locations were predetermined by CMS because OCEI recommended that for the M7 Pin location that CMS "Replace the strain sensors with acoustic emission sensors." OCEI predicted that the stresses in the pins would be mainly due to shear which a strain gage mounted on the surface cannot measure. An acoustic emission sensor could help detect crack initiation and propagation that are the primary concern for these members. However, this recommendation by OCEI was not followed by CMS.

In their analysis, OCEI made the assumption that damage induces changes to the stresses in the members that reduce the safety margin between the undamaged member and a stress approaching yield. Therefore, an estimation of the load capacity of the member would provide a strain value that could indicate when the yield stresses were reached. They determined the threshold values using the general Load and Resistance Factor Rating (LRFR) load rating equation:

$$RF = \frac{C - \gamma_{DC} DC - \gamma_{DW} \pm \gamma_P P}{\gamma_L LL\,(1 + IM)} \tag{5.10}$$

[10]A HS20 truck cannot actually drive on the bridge because the bridge has only 11 ft of vertical clearance. See Figure 4.5 for visual evidence to support this statement.

Where

RF = Rating factor
C = Capacity
γ_{DC} = LRFD load factor for structural components and attachments
DC = Dead load effect due to structural components and attachments
γ_{DW} = LRFD load factor for wearing surfaces and utilities
DW = Dead load effect due to wearing surfaces and utilities
γ_P = LRFD load factor for permanent loads other than dead loads
P = Dead load effect due to permanent loads other than dead loads
γ_L = Evaluation live load factor
LL = Live load effect
IM = Dynamic load allowance

OCEI used the limit states and load factors for the operating design load as found in the *Manual for Condition Evaluation and Load Rating of Highway Bridges Using Load and Resistance Factor Philosophy* [100]. A member with a RF of less than 1.0 does not have sufficient remaining capacity to support live loads with the desired factor of safety. OCEI assumed that the strain gages could not measure the dead load and that DW and P where zero to determine the threshold levels.

Table 5.3 provides the recommended threshold levels based of the rating factor analysis. Note that different levels are given for the locked and swung positions. OCEI remarked that if a threshold were set for the compression in a member in the locked position, it would be

Table 5.3: OCEI recommended stress thresholds (ksi).

	Locked Position				Swung Position			
	Compression		Tension		Compression		Tension	
Member	Red	Yellow	Red	Yellow	Red	Yellow	Red	Yellow
L0-M0	-27	-20	2	5	-26	-18	2	5
L2-U2	-5	-2	18	26	-26	-19	2	5
L3-L4	-5	-2	18	25	-26	-19	2	5
M5-U6	-5	-2	18	25	-4	-1	13	20
L8-M7	-5	-2	18	26	-5	-2	20	27
L6-M7	-5	-2	18	25	-4	-2	15	22
M7 Pin	—	—	—	—	—	—	—	—
M7-U8	-5	-2	18	25	-4	-2	15	22
U8-U8’	-5	-2	20	27	-4	-2	15	22
FBL7	-3	-2	19	27	-3	-2	19	27

Note: A dashed line (—) indicates that OCEI did not provide a recommended stress threshold.

exceeded when the bridge swung open sending a false alarm. Their recommendation was that a sensor somehow detect the bridge opening and switch the thresholds accordingly to avoid the false alarms. CMS never implemented this recommendation and set the limits for the maximum in either condition.

As for acceleration, OCEI recommended thresholds for the magnitude of $\pm$0.05g for a yellow warning and $\pm$0.1g for a red warning. Notice that these threshold values aresignificantly less than the $\pm$7.5g range of the installed sensors as noted in Section 5.2.1.As will be discussed in Section 5.4, the recommended yellow warning limit is less than the noise floor of the sensors and the red warning is much less than the typical excitation caused by vehicles let alone trains. OCEI noted that the magnitude alone can perhaps detect an impact or strong wind but that it was the frequency content, and shifts in the natural frequencies of the structure, that would indicate structural damage. They recommended a change of 5% in any natural frequency as a yellow threshold and a change in 7% as the red warning. Chandler implemented neither of these recommendations in the IntelOptics installation on the Rock Island Government Bridge.

The report by OCEI were not supportive of using their FE model for model updating. They recognized that an "extremely large number of analyses would be required" and it would "require knowing not only quantitative information on event loading but also other loading conditions such as live loads, thermal conditions and wind, making such analyses very difficult and most likely impractical [98, p.3]." These statements are to some extent true if the model updating were to be done by hand and the loading of the bridge was unknown. That is why the research reported herein developed an autonomous model updating procedure for a model that is reduced in complexity but still accurately models the bridge behavior and uses loading information from known loads (i.e., the opening of the closing of the bridge) as input.

5.3 Analysis of the FO Installation

Prior to the creation of the Integrated SHM Data Collection Program that is described in Section 8.2, Chandler Monitoring Systems and the Army Corps of Engineers granted access to the as installed fiber optic strain sensor system. At first, access was provided to the IntelOptics online interface. Initially, IntelOptics recorded data at $0.3\overline{3}$ Hz (one sample every three seconds). However, due to limitations on the cellular modems that were in use at the time and the fact that data was not being stored locally, the data rate was changed to $0.0005\overline{5}$ Hz (one sample every thirty minutes). This sampling rate was not sufficient for a thorough analysis of the system.

To get a better sampling rate for the data, CMS granted direct access to the ENLIGHT program. ENLIGHT has the ability to output data to text files at a given sample rate. This method was used to output data at the system's maximum rate of 125 Hz at periodic intervals during the evaluation period. The poor internet accessibility provided by the cellular modems still limited the amount of data collected, because collecting a day's worth of data could take a week to download from the system. Thus the larger data sets used in analyz-

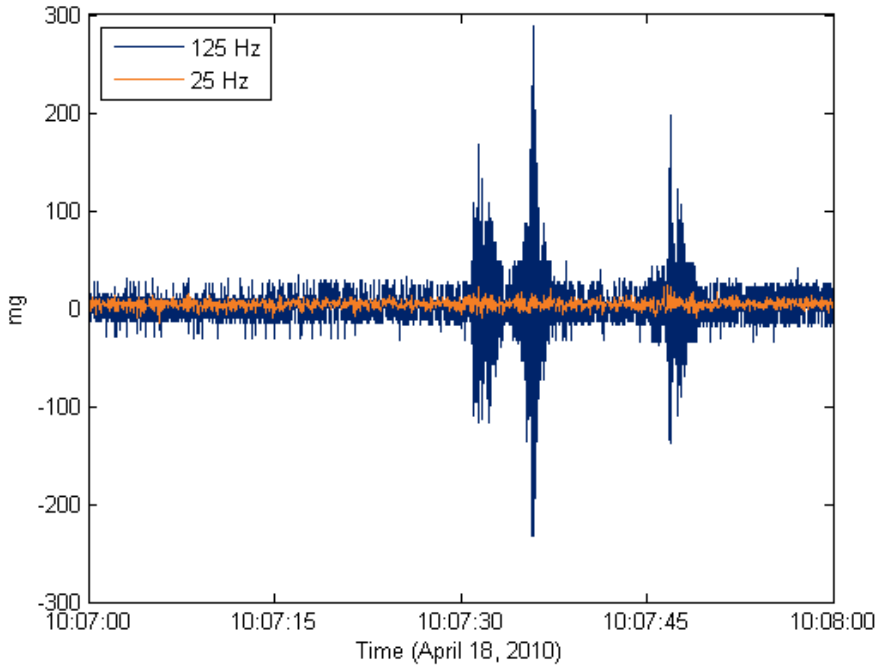

Figure 5.14: Typical acceleration record for FO accelerometer due to vehicular traffic (AccelR2Y).

ing the system were acquired during physical visits to the bridge when the data could be downloaded to a removable drive.

The text files that constitute a dataset were read into Matlab and either used at the native 125 Hz or filtered and downsampled using a 30 order FIR (finite impulse response) filter to either 25 Hz, 5 Hz, or 1 Hz; the filter was employed to eliminate aliasing. Unless otherwise noted below, the 125 Hz data was used in dynamic analysis while the filtered and downsampled 1 Hz data was typically used in static and long term analysis.

5.4 Acceleration

In evaluating the performance of the installed fiber optic sensors, data from April 18, 2010 will serve as an example. Data was recorded for just an hour at 125 Hz and the excitation included both normal vehicular traffic and a train event. Figure 5.14 shows one minute of data from 10:07 to 10:08 that shows the typical ambient response and three peaks that likely represent the passage of three vehicles over the sensor location. The sensor whose response is shown in Figure 5.14 is accelerometer R2Y which is located on the highway deck of the bridge. The vehicles produced a response that had a range of $\pm$300 mg of acceleration for the biggest of the three peaks when sampled at 125 Hz, but much smaller when downsampled to 25 Hz. For vibration induced by a train as shown in Figure 5.15, the response nearly doubles to about $\pm$600mg.

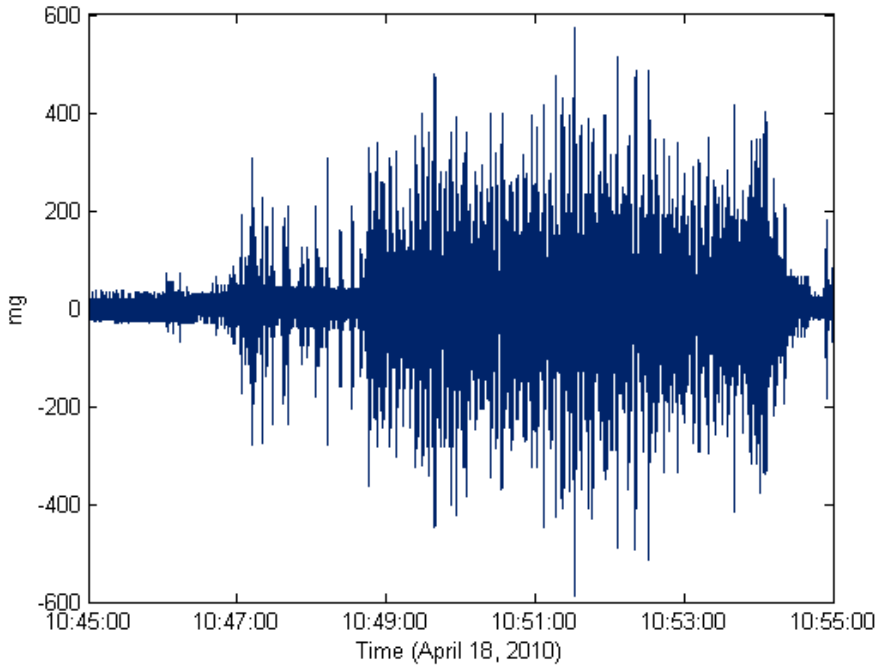

Figure 5.15: Typical acceleration record for FO accelerometer during a train event (AccelR2Y).

Though at first glance, the time history of accelerations shown in Figures 5.14 – 5.15 would indicate that the sensors are performing adequately, a closer examination illustrates some problems. Other than the passage of the three vehicles, the accelerometers should be measuring the ambient vibrations on the bridge. However, the solid band that is about $\pm$20 mg wide is actually the noise floor of the accelerometer. Figure 5.16 is a zoomed in view of the first second of Figure 5.14. In Figure 5.16, the maximum and minimum of the noise floor of the sensor at 20 mg and -20 mg respectively are clearly visible. The quantization of the fiber optic acceleration is also apparent in Figure 5.16. The distinct data levels in the measured acceleration at approximately 4 mg intervals indicate the resolution of the fiber optic accelerometer. An accelerometer with only 4 mg of resolution is not suitable for most ambient vibration applications.

The purpose of the acceleration records is to determine the modal parameters – natural frequencies and mode shapes – of the structure. Taking the auto spectral density of the 125 Hz acceleration record used to produce Figure 5.14 produces the spectrum shown in Figure 5.17. The dominant feature of the spectrum is the large peak at 37.5 Hz and the secondary peak at 23 Hz. These peaks do not represent the natural frequencies of the structure. Recall from Figure 5.10 that the resonant frequency of the os7100 accelerometer is approximately 725 Hz. Because anti-aliasing filters are not present in the entire CMS installed fiber optic system, the 725 Hz resonant frequency of the sensor is "aliasing" as 37.5 Hz[11] in the power spectrum of the acceleration record. The secondary peak is an

[11]The 725 Hz frequency will be "folded over" the 62.5 Hz range 11.6 times. Multiplying 0.6 by 62.5 yields

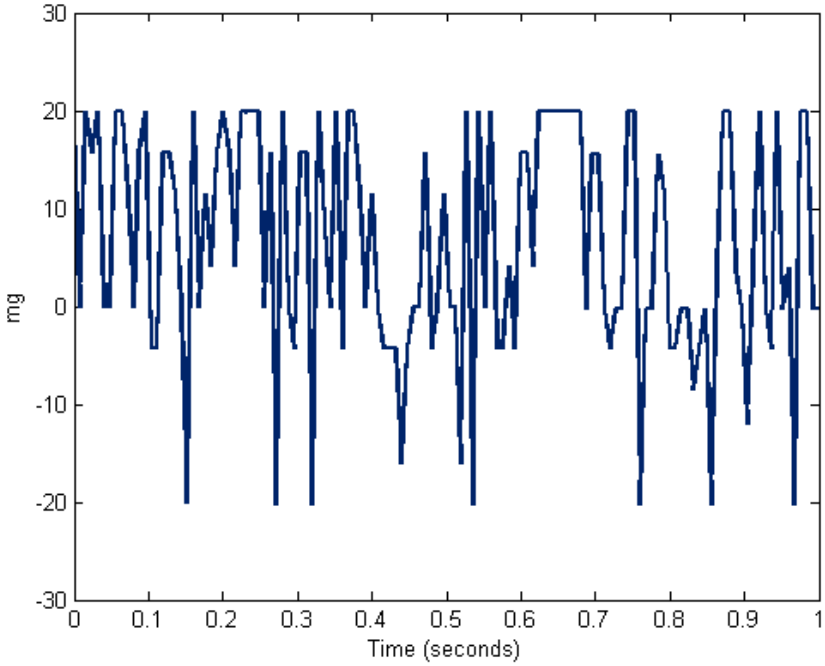

Figure 5.16: FO accelerometer noise floor and quantization (AccelR2Y).

aliased harmonic of the 725 Hz frequency. No peaks are visible in the 0–10 Hz range where the first natural frequencies are expected.

If the data is filtered down to a 25 Hz signal to try and eliminate the aliased resonant frequency of the accelerometer, the magnitude of the acceleration falls to levels that are within the noise floor of the fiber optic system. Figure 5.14 shows the contrast between the unfiltered 125 Hz signal and the 25 Hz filtered signal. The vehicles are indiscernible in the 25 Hz filtered signal due to the effects of the quantization and noise floor. The magnitude of the accelerations caused by the vibrations of the bridge are not as important as the spectrum that can be derived from the acceleration record. The high noise floor, large quantization, and aliasing of the resonant frequency make the acceleration data unusable for the levels of acceleration the bridge experiences. Because they are unsuitable, the installed fiber optic accelerometers were excluded from consideration in the long-term monitoring strategy of the bridge.

5.4.1 Validation of Acceleration Measurements

To validate the functionality — or in this case the unsuitability — of the fiber optic accelerometers, a series of tests using iMote2 wireless sensors fitted with the SHM-A sensor board were performed. The SHM-A contains a triaxial accelerometer with a noise floor of 0.3 mg (66 times better than the fiber optic accelerometer) and resolution of 0.14 mg

the “aliased” frequency of 37.5 Hz signal.

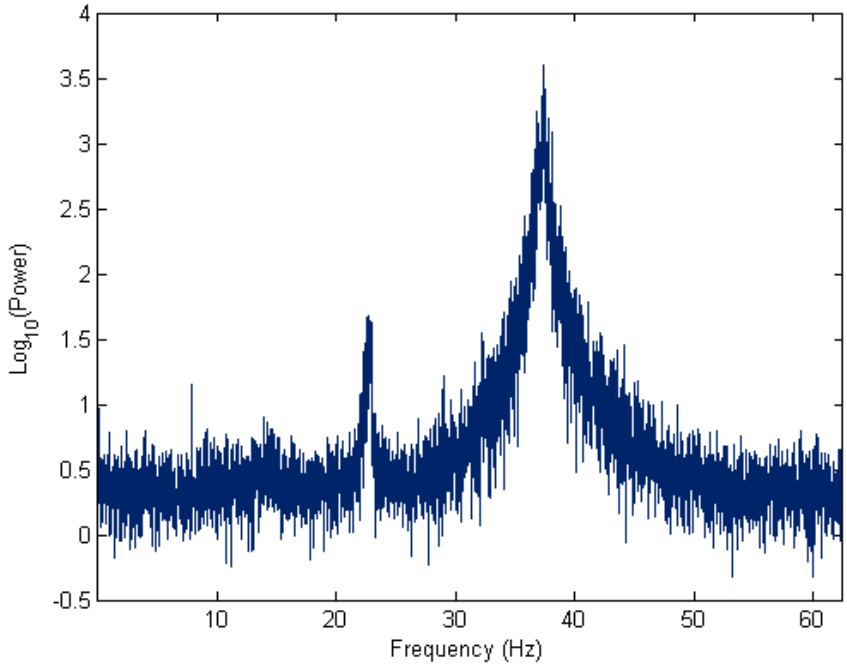

Figure 5.17: Power spectral density of typical FO accelerometer (AccelR2Y).

(29 times better than the fiber optic accelerometer). A total of nine sensor nodes were installed along the bottom chord of the truss on both sides of the bridge near the pedestrian walkways (see Figure 5.18).

Data was collected at 50 Hz and then filtered and downsampled to 25 Hz as done with the fiber optic accelerations. The response from the sensor that was placed at joint L4 on the right truss is shown in Figure 5.19. This sensor was the closest to sensor AccelR2 that was used as the typical example in the previous section. The magnitude of the accelerations caused by the vehicular traffic at this location was less than ± 20 mg which would be under the noise floor of the fiber optic sensor. The ambient vibration is on the order of 1 mg which cannot be resolved by the fiber optic system.

The SHM-A sensor board has a built in analog anti-aliasing filter that eliminate the possibility of aliasing in the signal. As a result of the excitation levels in the lower frequencies being well above the noise floor and proper anti-aliasing the spectrum of the data collected with Imote2, as seen in Figure 5.20, shows vertical natural frequencies near 4, 8 and 11 Hz. Figure 5.20 therefore also demonstrates that when accelerometers with appropriate characteristics are used, system identification is possible. For SHM purposes, accelerometers need to have low noise floors and high resolution due to the low levels of ambient vibration and traffic induced vibration in the frequency range of the first few natural frequencies of the structure. The SHM-A sensor board on the Imote2 platform provides a suitable accelerometer for system identification and long-term monitoring of the Rock Island Government Bridge.

(Chris Hsiao)

Figure 5.18: Installation of iMote2 sensor during the FO accelerometer validation tests.

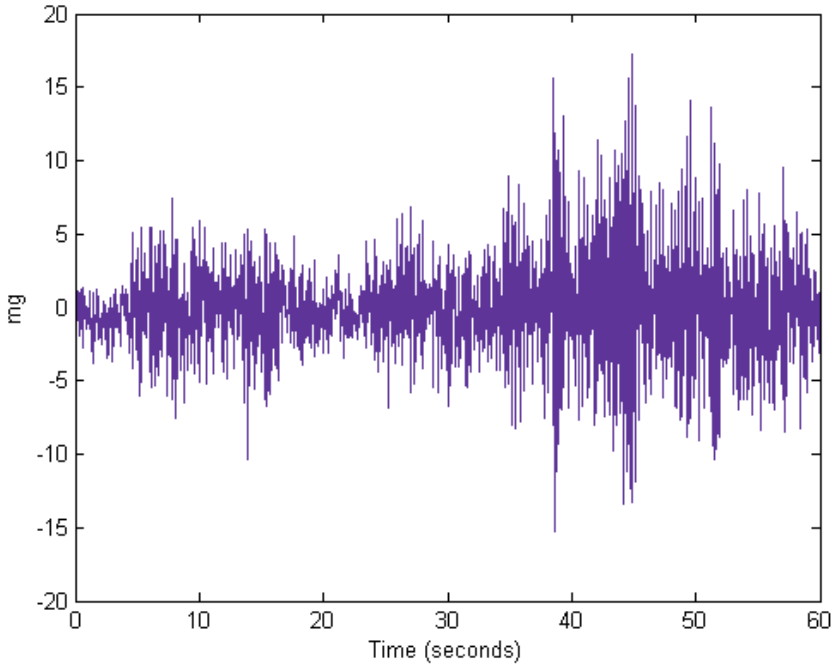

Figure 5.19: Vertical acceleration from iMote2 installed at joint L4.

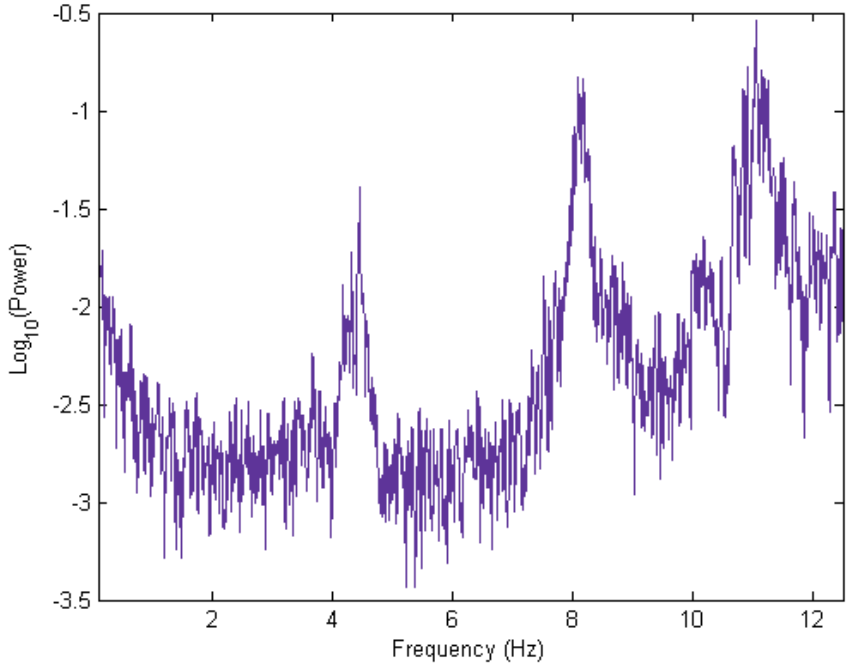

Figure 5.20: Power spectral density of 25 Hz acceleration data collected using an Imote2 and an SHM-A sensor board.

5.4.2 Conclusions

The Micron Optics os7100 accelerometer is not a suitable sensor for use in a structural monitoring system on the Rock Island Government Bridge. When selecting an accelerometer for an SHM application, care must be taken to choose one that is suitable for the expected responses. Though in society it is often assumed that "bigger is better," in the case of the acceleration range the axiom does not hold true. The os7100 optical accelerometer has a range of at least ± 7.5 g while the SHM-A MEMS accelerometer only has a range of ± 2 g. The collected data reveal that the measured responses of the structure do not approach ± 2 g even under the extreme vibrations caused by passing trains. Having the capability to measure accelerations greater than those expected is not a benefit as it decreases the resolution of the instrument as seen in the quantization in the os7100 data at low excitation levels.

Anti-aliasing filters are essential in achieving meaningful acceleration records. Once aliasing has occurred, there is no way to remove its effects. The aliasing occurs at the moment of digitization which in an electrical circuit happens after the analog acceleration from the sensing device has passed through the analog anti-aliasing filters and entered the analog to digital converter. For the fiber optic system, the digitization occurs at the moment the laser sends the pulse down the fiber to take a measurement. Thus, the reflected signal from the FBG sensor will always contain aliased data. As shown in the os7100 data, the resonant frequency of the sensor will dominate and mask any response to the frequency characteristics of the bridge itself. It is not just the os7100 fiber optic sensor that is unsuitable for dynamic measurements, but any fiber optic accelerometer.

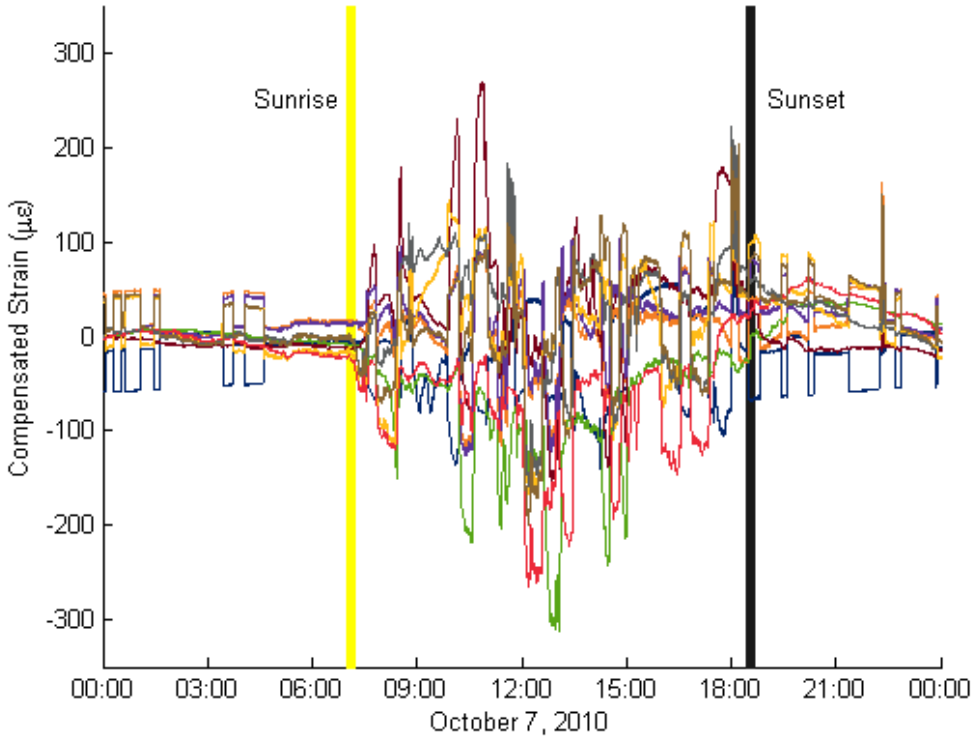

Figure 5.21: Typical temperature compensated CMS strain measurements.

Because the data collected from the os7100 sensors was deemed unsuitable, SHM-A MEMS accelerometers that use the Imote2 platform were installed to provide acceleration measurements of the bridge. This system will be discussed in Section 7.1. The SHM-A is suitable for use in an SHM application on the Rock Island Government Bridge. Its acceleration range, resolution, noise floor, anti-aliasing capability all combine to produce data that provide insight into the structural characteristics of the bridge.

5.5 Strain

The evaluation of the functionality of the installed fiber optic strain gages took place over many months. The high temperature sensitivity of the fiber Bragg grating strain sensors means that both strain and temperature must be evaluated together. The first data sets obtained contained records for the installed temperature and strain sensors where the strain had already had temperature compensation performed within the ENLIGHT program according to equations programmed by Chandler Monitoring Systems. Figure 5.21 shows seven of the thirty-four compensated strain measurements over the course of a single day. The strain measurements appear reasonable until sunrise and then the order found previously disappears. To fully understand what was being measured and how – or if – the

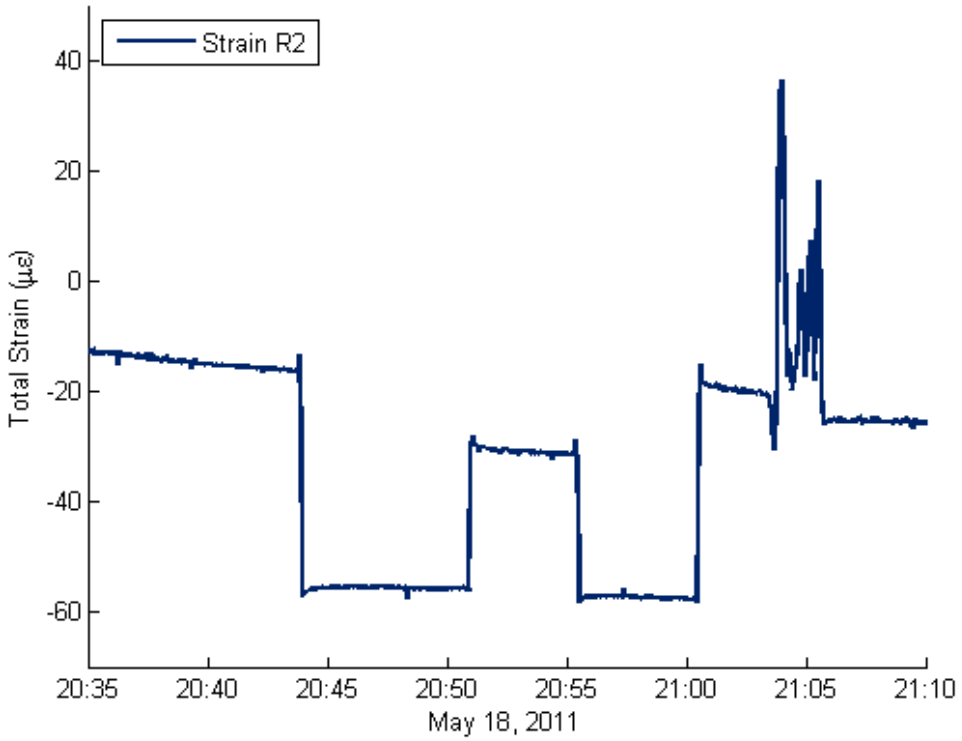

Figure 5.22: Typical strain response (Strain R2) for two swings and a train event.

temperature compensation was working properly, an analysis of the total strain (uncompensated strain) and the temperature separate from each other was necessary.

In this document, the uncompensated strain will be referred to as the total strain, as from Equation (3.3), and the sensors measuring total strain will be referred to solely as Strain (e.g., Strain R2 or Strain L25). The compensated strain will be referred to as the compensated or CMS strain (i.e. the strain measurement provided by Chandler Monitoring Systems) and the sensors measuring the compensated strain will be preceded by "CMS" (e.g., CMS Strain R2 and CMS Strain L25). The total strain will be discussed here, and temperature will be discussed in Section 5.6.

The total strain data should exhibit behavior influenced by both the mechanical strain (induced by vehicles, trains, and swing events) and the thermal strain present in the structure. Figure 5.22 shows the strain record for a single sensor (Strain R2) that is located on a vertical post. The data shown was recorded just after the sun set at 20:17 and takes place before nautical dusk.

The most obvious characteristics of Figure 5.22 are that the measurement experiences two large, sudden, and sustained strain changes followed by one large but varied strain change. Observations of the bridge and correlation of the strain record to the observed occurrences confirmed that the two large, sudden, and sustained strain changes that start at approximately 20:44 and 20:55 respectively are caused by the bridge opening to allow a barge to pass. Each of the strain events is a separate swing event. The large change in

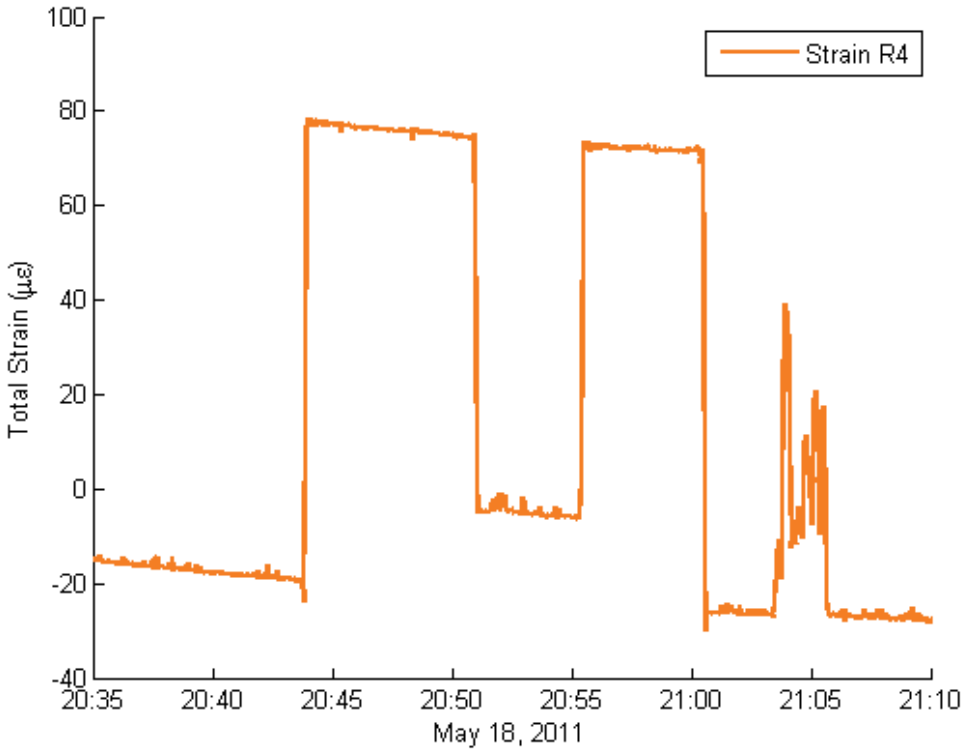

Figure 5.23: Strain response for Strain R4 for swings and train.

strain in the member is expected because when the bridge opens to allow a boat to pass, the weight of the bridge that is supported by the abutment and pier at the ends of the span has to be transferred to the center supports. The load transfer causes the members to undergo a change in member force and therefore also a change in strain. For post L2U2 on which Strain R2 is mounted, the process of changing from the locked to the swung position causes compression to develop and therefore a decrease in strain. When the process reverses itself, the strain in the member again increases.

Each member will have a different change in member force caused by the transition from locked to swung positions. Figure 5.23 shows the strain record for sensor Strain R4 mounted on one of the diagonal eye-bars between M5 and U6. The plot shows the same time period and events as shown in Figure 5.22. Whereas Strain R2 shows a decrease when the bridge unlocks, Strain R4 shows an increase. Considering eye-bars are tension only members, the fact that the change in boundary conditions causes increased tension is expected. However, the fact that some Strain sensors increase and others decrease due to swing events is an important element of the event detection algorithm as presented in later in Section 8.1.

Another important observation about the swing events is that there are two distinct locked positions: one with the stairs facing upstream and one with the stairs facing downstream. In Figures 5.22 and 5.23, the bridge starts out at 20:35 with the stairs locked in the upstream position. When the bridge unlocks to swing at 20:44, sensor Strain R2 undergoes a change

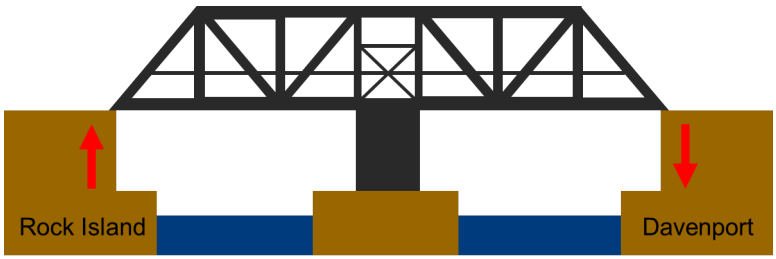

(a)

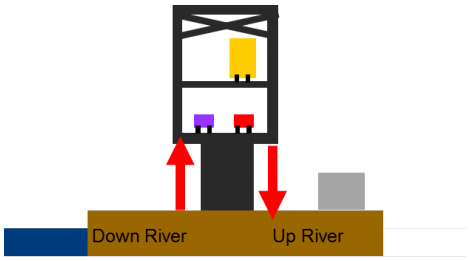

(b)

Figure 5.24: Illustration of possible differential settlements of (a) the end supports of the swing span, and (b) the center pier of the Rock Island Government Bridge.

of nearly -40 microstrain. When the bridge closes again seven minutes later after having rotated a full 180° such that the stairs are now in the downstream position, the change in strain is only about +30 microstrain. In the second swing event, the bridge again swings a full 180° locking in the stairs upstream position and the changes in strain reverse themselves so that it changes -30 microstrain when it opens and +40 microstrain when it closes. Therefore, after making two swings of 180° each, the bridge has returned to its starting position and the total strain level has returned to essentially the same level.

The bridge was designed as a symmetric structure and yet the presence of the two distinct locked positions would indicate that an asymmetry has developed over time. Any probable cause of the behavior would have to be dependent on the position of the bridge. Damage to a member would be expected to be the same in either position and is therefore not the likely cause. The only part of the bridge that changes from one locked position to the other is contact between the bearings and the locking mechanism on each end of the bridge. It was speculated that differential settlement (or imperfect original construction) induced some twist to the ends of the span when locked in place. Figure 5.24 illustrates the two possible types of differential settlement that can cause the effects seen in the bridge.

An end-to-end differential settlement (like that in Figure 5.24(a)) would cause members in identical positions on both the left and right trusses to experience the same change in strain. However, if a side-to-side differential settlement (like that in Figure 5.24(b)) were to develop then strains in members in identical positions on the left and right truss would be different. The data collected from like members on the truss indicate that there is a combination of both end-to-end and side-to-side differential in the structure. Using the finite element model developed for the bridge (as discussed in Section 6) the effects of support displacements can be modeled and confirmed as the likely source of the two distinct

closed positions. One possible cause for any recent differential settlement may be that the trains are only run on the upstream track[12] to prevent two trains from being on the bridge at the same time. The downstream track is unused because the current trains are essentially twice as heavy as those the bridge was designed for in 1896 (see Figure 4.4). Thus making changes to the operation of the bridge to prevent potential overloads may have caused unwanted (but not necessarily dangerous) differential settlement.

As mentioned previously, the strain level of the sensors returns to "essentially" the same level after completing the two 180° swings. The slight difference is due to the change in the thermal strain. As noted, the data displayed in Figure 5.22 was taken just after sunset and the bridge is cooling down and reaching equilibrium with the night air. Between the start of the data and the start of the first swing, the data is linearly decreasing as the temperature of the steel cools at a relatively constant rate. If a line were extended from the start of the first swing, the line would eventually connect with the strain after the end of the second swing. Therefore, in the total strain, the temperature still has an influence on the strain in the two locked positions. Thus the strain itself is not a good indicator of the bridge position, because the strain in a member can have the same value in both locked positions – albeit for different temperatures.

After the two swing events, and when the bridge is once again in the locked with the stairs in the upstream position, a train passes over the bridge at about 21:04. The strain response to the train passage in Figures 5.22 and 5.23 is typical of trains. Strain R2 sees a slight decrease in strain as the train enters the span on the opposite side of the structure and causes an unbalanced load. As the train continues across the bridge, the strain in R2 increases as it takes on some the train's load more directly. Typically, the engine is one of the heaviest parts of the train, and therefore the greatest strain typically occurs at the beginning of the train response. The cars that follow the engines can be of variable weight, so the strain value can increase and decrease accordingly for the remainder of the train. The response of Strain R4 to the train is very similar to that of R2. Unlike the swing events where Strain R2 went into compression and R4 went into tension at the start, during a train event, both sensors go into tension. This fact is used to distinguish between swing events and train events in the event detection algorithm.

In addition to the swing events and train events seen in Figure 5.22, equally important is what is not so obvious. The bridge, while in the locked positions was open to vehicular traffic. Nevertheless, the vehicular loads cause no visible change in the strain levels. By zooming in on the strain levels just before a swing event, as in Figure 5.25, and understanding the process of swinging the bridge, the vehicle induced strain becomes apparent. Before the bridge is swung open, the bridge operator rings a whistle and turns on the warning lights alerting drivers that the bridge will be closed to traffic shortly to allow the bridge to swing. After a minute of warning, gates are swung out to stop traffic. Then, the cameras are checked one last time to make sure the bridge is clear before the railroad tracks are disengaged and then the bridge's end bearings are released. Between the time the gates

[12]The trains will run on either track on the swing span based on the orientation on the bridge and therefore both sets must be maintained. However, on the approaches and other spans, only the upstream track is used and maintained

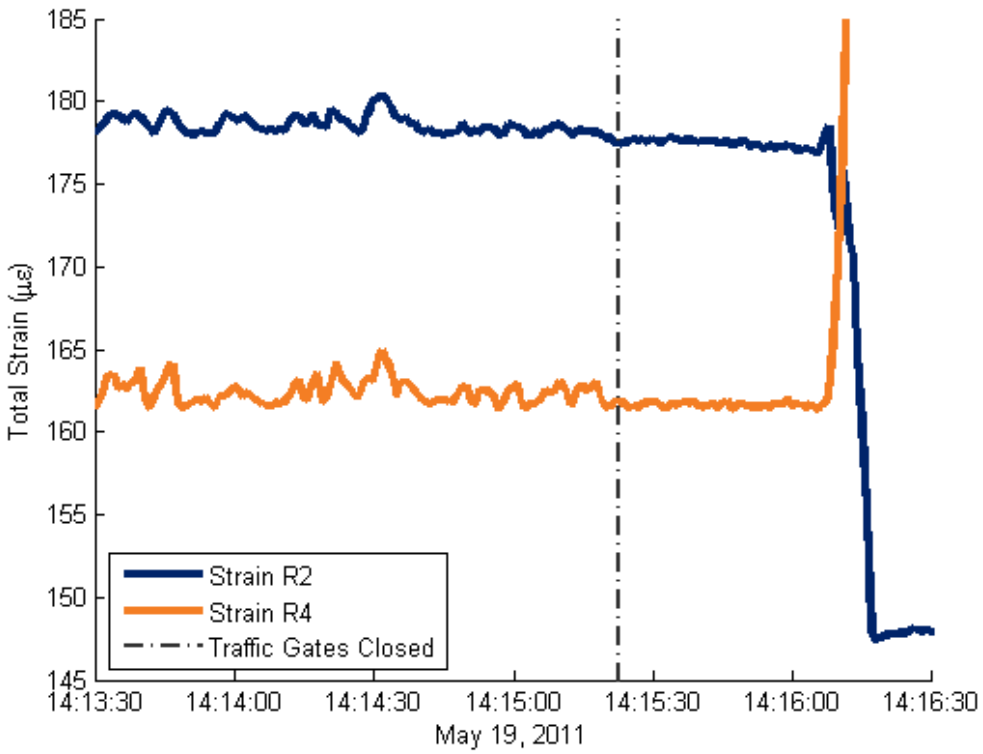

Figure 5.25: Comparison of strains induced by vehicular traffic and a swing event.

are closed and the bridge bearings are released, the bridge is in a locked position free from traffic for a total of about thirty seconds.

In Figure 5.25, the time the traffic gates were closed has been demarcated with a dashed line. Between the dashed line and the start of the swing event at about 14:16:10, the strain in both Strain R2 and Strain R4 has little disturbance. This period represents the time when there is no traffic on the swing span. However, before the gates are closed, both R2 and R4 exhibit somewhat correlated peaks and valleys on the order of 3 and 5 microstrain, respectively. These small changes in strain represent the strain induced by vehicles traversing the bridge. The swing event for Strain R2 is shown for comparison to the vehicular traffic. The swing induces a strain that is ten times greater than any vehicle. Thus, from an engineering perspective, traffic loads are not of high concern because the swing and train events are an order of magnitude greater.

5.5.1 Validation

To validate the CMS strain measurements, fourteen foil strain gages were temporarily installed on the bridge. For labeling purposes, the gages in this installation are called the Illini gages. The Illini gages were typically installed just above the railroad deck on the "Left" truss of the swing span. Some of the sensor locations were chosen to correspond

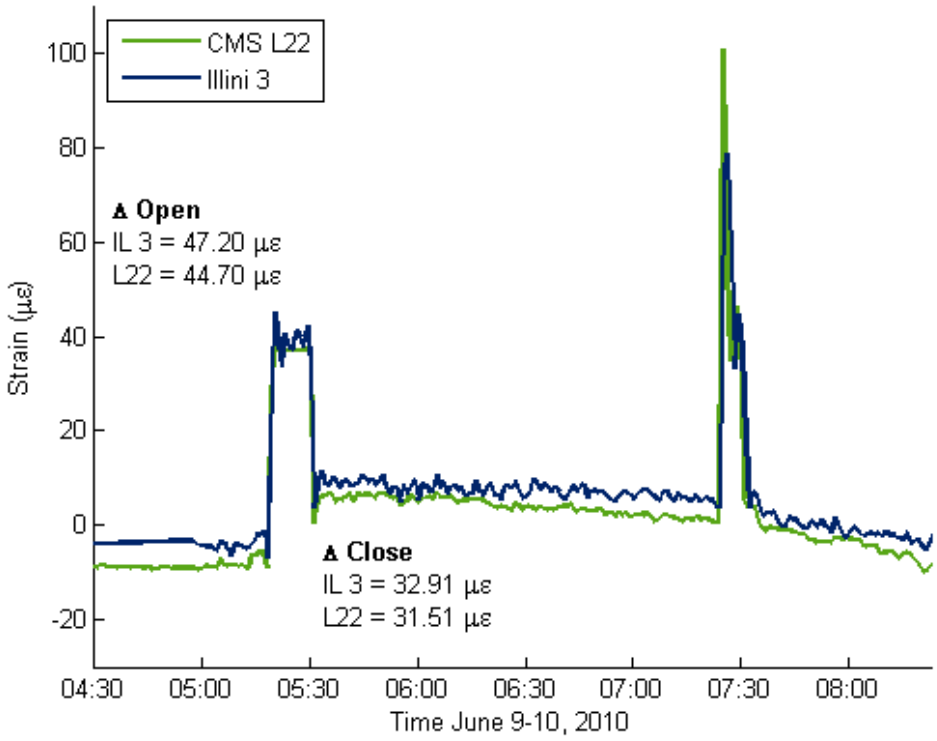

Figure 5.26: Comparison of Illini 3 and CMS L22 during strain validation testing.

with some of the CMS FBG strain gages; other locations were chosen to provide additional information about the bridge's behavior using members that are not currently measured. An example of the latter was that two of the four eye-bars in the L6-M7 positions were instrumented to check the weight distribution among the eye-bars. A full listing of the locations of the Illini gages is given in Table 5.4. Data was collected over night and many swings were captured. Of particular interest was a swing event that occurred during the twilight hours at about 05:20. Data was also collected for the CMS system for the same time period.

Figure 5.26 shows a comparison between CMS L22 and Illini 3 which are both mounted on the L6-M7 eye-bar diagonal that is closest to the centerline of the bridge. The foil gages were installed as close to the fiber optic sensors as possible. Both the optical and resistive strain measurements show the same general trends as far as the temperature effects and response to the swing and train load.

Taking a closer look at the swing event and the change in strain experienced when the bridge is unlocked and then locked again shows an even closer correlation. To make the comparison between the sets of data, the average strain values immediately before, during, and after the swing event were calculated. The computed values for the change is strain ($\Delta\epsilon$) are shown in Figure 5.26 and also in Table 5.4. For Illini 3 and CMS L22, the $\Delta\epsilon$ are essentially identical given the noise and other errors inherent in the systems. These results would indicate the CMS sensors are performing well.

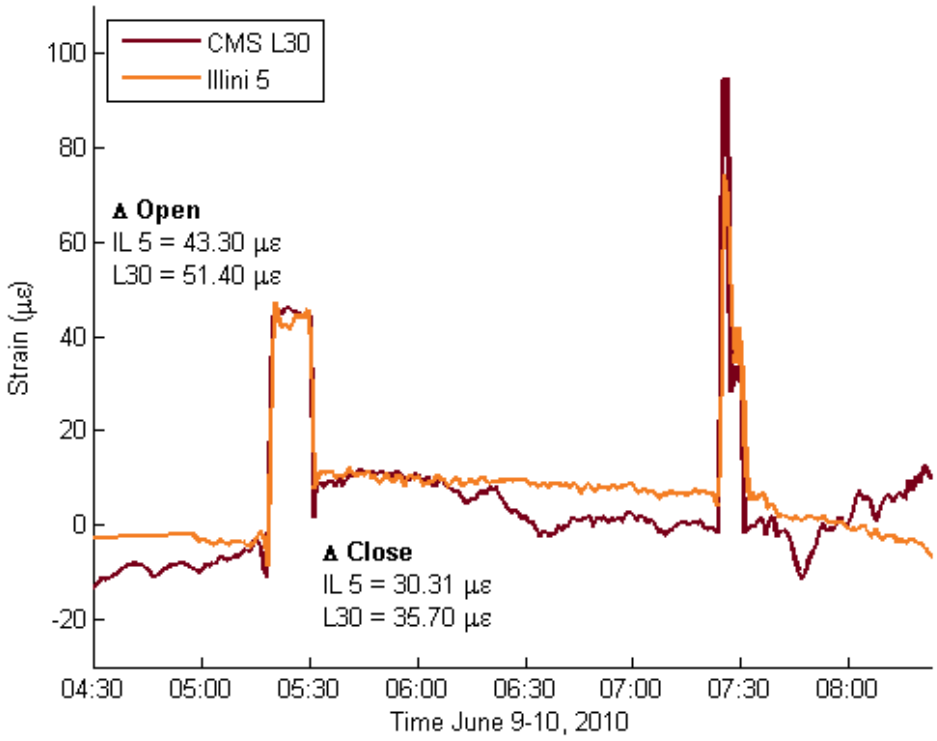

Figure 5.27: Comparison of Illini 5 and CMS L30 during strain validation testing.

However, looking at another set of data in the same way reveals an underlying problem. Figure 5.27 compares the set of sensors (Illini 5 and CMS L30) that are on the L6'-M7' eye-bars. Because these sensors are on an equivalent member as Illini 3 and CMS 22 from the previous example, the responses should generally look the same. Like the previous example, the large strain events (i.e., the swing and the train) for Illini 5 and CMS L30 are well correlated in terms of shape and magnitude. However, the general shape of the strain records between the two large events is quite different for the two sensors. The Illini 5 strain record is generally smooth and shows the same general temperature effects in the curve of the line as seen in both Illini 3 and CMS L22 in Figure 5.26. The CMS 30 fiber optic gage, however, has a significant decrease in strain before the train event and a series of significant peaks and valleys that occur after the train event. Because the gages are mounted on the same member only inches apart, the source of the differences in CMS 30 cannot be from actual changes in strain in the member. Instead it is a result of the temperature compensation using a temperature sensor that is not accurately measuring the temperature of the steel at the location of the strain gage. This issue of temperature compensation will be addressed further in Section 5.6.

For completeness, Table 5.4 contains the results of the analysis of the change in strain for the pre-dawn swing event are shown for all CMS ("Left" truss only) and Illini sensors. The CMS sensors mounted on L3-L4 members were not placed so that they were measuring the principle axis of the member. Therefore, when comparing CMS L32 and Illini 2, they do

not appear very similar because they are not measuring the same value. Many of the other discrepancies are due to similar differences in mounting directions. Of worth noting is that Illini 3 and Illini 4 which are mounted on parallel eye-bars indicate similar changes in strain for both the opening and closing of the bridge. This result means that the eye-bars are likely sharing the load equally among the four eye-bars as designed. Uneven distribution of the load would be problematic, particularly from a fatigue standpoint.

5.5.2 Conclusions

In general, the fiber optic sensors were determined to be accurate as long as the temperature compensation was accurate. However, the strain validation experiments cast doubt on whether or not the temperature sensors were actually measuring the temperature on the steel substrate. The change in strain caused by swing events was similar for both the fiber optic and foil gages mounted on the same members and in the same directions.

Strain analysis also confirmed some of the unintended limitations of the system. CMS installed sensors on the ends of the M7 pins in attempt to measure the shear strain in the pin. However, this demonstrates a poor understanding of what is trying to be measured and how it can be measured. Instead, the end pins are essentially temperature sensors measuring the temperature of the steel. One of these pin sensors was also mislabeled in ENLIGHT. As shown in Figure 5.5, Strain R6 and Strain R7 appear out of order according to the number convention seen on the sensors at similar locations in the other quadrants of the bridge. However, the labeling on this figure is correct as the analysis of the data, and comparisons of R6 to the other M7 pins, confirmed the locations. The correction was carried out in the remainder of the analysis though CMS did not make changes to the numbering in the ENLIGHT system.

The boundary conditions of the bridge are slightly different when it is locked with its stairs upstream than when they are locked downstream. The strain records clearly show two distinct levels when the bridge is locked – one for each of the two positions. The strain record also has a distinct level for the swung position. The strain measurements alone are not sufficient to identify the position of the bridge. However, knowing the position of the bridge is important when identifying events so that measurements from the two locked positions are not compared to each other. A supplemental metric – heading – is required to know the position of the bridge at all times. The digital compass that was installed to supplement the system is discussed in Section 7.2

5.6 Temperature

The analysis of the fiber optic strain gages began by looking at Figure 5.21 and noting that up until sunrise and then after sunset there appeared to reasonable behavior in the compensated strain sensors. However, during the daylight hours, it was difficult to distinguish what was occurring. Compare Figure 5.21 showing the compensated strain to Figure 5.28 that shows the temperature for seven different fiber optic temperature sensors. As in the

Table 5.4: Change in strain for swing event measured by fiber optic CMS strain gages and foil strain gages during validation testing.

			$\Delta\epsilon$			
	Channel		Swing Start		Swing End	
Location	CMS	Illini	CMS	Illini	CMS	Illini
L0-M0	L18	—	29.48	—	96.94	—
L0-M1	—	7	—	69.61	—	55.94
L2-U2	L19	13	44.66	105.56	36.02	59.24
L3-L4	L20	—	12.89	—	6.48	—
M5-U6	L21	—	75.77	—	54.28	—
L6-M7(1)	L22	3	44.70	47.20	31.51	32.91
L6-M7(3)	—	4	—	52.74	—	35.44
L7-M7	L23	—	18.36	—	0.39	—
Pin M7	L24	—	3.42	—	0.36	—
M7-L8	—	9	—	10.83	—	1.88
L8-M8	—	11	—	42.40	—	42.72
M7-U8	L25	—	36.42	—	25.67	—
U8-U8’	L26	—	44.08	—	31.77	—
M7’-U8’	L27	—	42.89	—	31.41	—
L8’-M8’	—	12	—	35.07	—	39.76
M7’-L8’	—	10	—	12.02	—	4.48
Pin M7’	L28	—	3.56	—	0.99	—
L7’-M7’	L29	—	5.38	—	3.31	—
L6’-M7’(1)	L30	5	51.40	43.30	35.70	30.31
L6’-M7’(2)	—	6	—	48.70	—	33.95
M5’-U6’	L31	—	92.71	—	68.69	—
L3’-L4’	L32	2	8.47	54.39	8.40	36.29
L2’-U2’	L33	8	117.21	112.20	90.27	81.13
L0’-M1’	—	14	—	90.09	—	66.56
L0’-M0’	L34	—	9.40	—	79.11	—

Note: A dashed line (—) indicates that a sensor was not present at the given location.

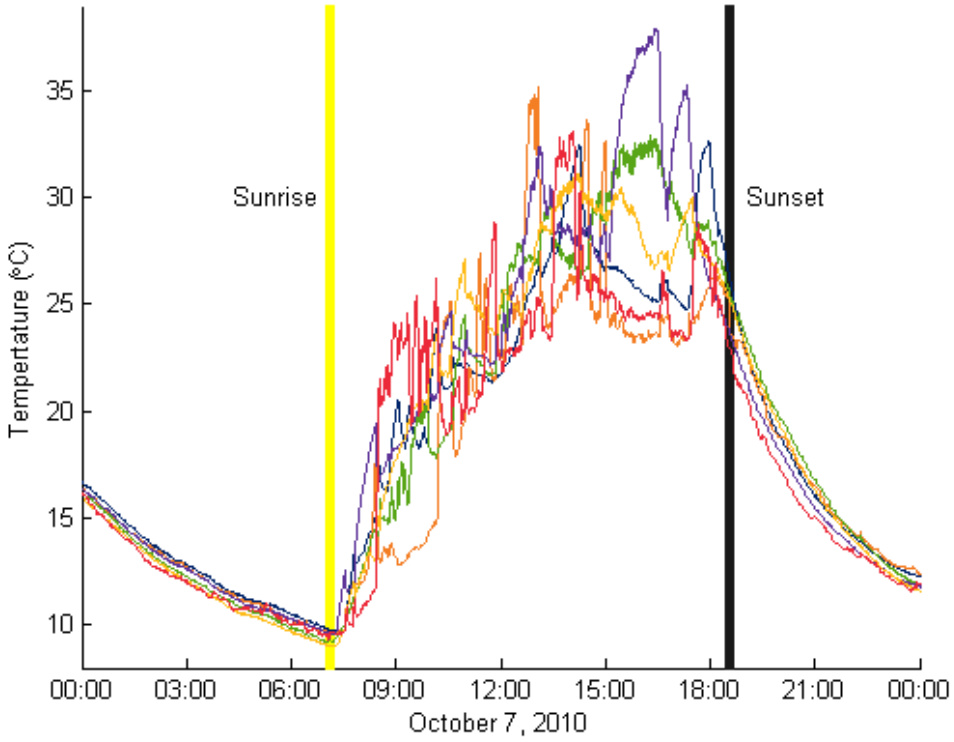

Figure 5.28: Fiber optic temperature measurements on October 7, 2010.

compensated strain plot, before sunrise and after sunset, the temperature as measured by all sensors is much more uniform than during the daylight hours. During the night, the plots exhibit an exponentially decaying trend and the difference in the measured temperatures is minimal. The exponential decay of the temperature matches the typical decay seen in the air temperature after the sunsets and the temperature begins to drop. Thus, Figure 5.28 would indicate that after the sunsets, the bridge reaches an equilibrium temperature with the surrounding night air.

To investigate whether the temperatures measured were reaching equilibrium with the environment after the sunset, the collected temperature data was compared to the reported air temperature. Table 5.5 shows the measured temperature for each sensor at three times during the night (civil dusk, midnight, and civil dawn) for a dataset from April 2010. The minimum, maximum, and mean measured temperature have also been computed for each time. Table 5.5 also provides the air temperature as measured by the official weather station of Lock and Dam 15 at the Rock Island Bridge site. The installed fiber optic temperature sensors, on average, report the same temperature as the air temperature within the short-term accuracy ($\pm 1^{\circ}$C) of the os4350 sensors. Sensor Temperature R9 does not follow the general trends of the other sensors and differs from the air temperatures not in just an offset, but the rate of decrease is accelerated.

As noted in Section 5.1.1, FBG strain sensors are highly temperature dependent on temperature. Therefore, the total strain as measured by the fiber optic strain gages can be

Table 5.5: Temperature (°C) as measured by the temperature sensors on April 18-19, 2010.

Sensor	**Civil Dusk** 20:14	**Midnight** 00:00	**Civil Dawn** 05:47
Minimum	11.10	5.47	0.47
Maximum	17.25	14.55	9.62
Mean	16.22	11.36	6.77
Air Temperature	16.66	11.11	6.66
Temperature R1	17.03	14.55	9.62
Temperature R2	16.13	10.98	6.13
Temperature R3	17.01	12.69	8.00
Temperature R4	16.72	11.25	6.63
Temperature R5	15.63	10.52	6.06
Temperature C6	16.05	11.09	6.36
Temperature R7	16.05	11.09	6.36
Temperature R8	16.32	11.51	7.46
Temperature R9	11.10	5.47	0.47
Temperature R10	16.42	11.79	7.80
Temperature R11	15.80	10.93	6.51
Temperature R12	16.57	12.13	8.38
Temperature L13	—	—	—
Temperature L14	16.04	10.83	5.97
Temperature L15	16.87	12.49	7.85
Temperature L16	17.25	11.64	6.52
Temperature L17	16.64	11.32	6.29
Temperature L18	16.32	11.51	7.46
Temperature L19	16.90	11.51	6.39
Temperature L20	16.83	12.37	8.37
Temperature L21	16.68	11.61	6.79
Temperature L22	—	—	—
Temperature L23	—	—	—

Note: Air temperatures are from the weatherunderground.com historical data-base for weather station MRCKI2 located at Lock and Dam 15. The station records the temperature in °F to the nearest degree. The air temperatures in this table are the temperatures recorded closest to the given event and are therefore approximate.

Note: A dashed line (—) indicates that the given temperature sensor was not functioning when the data was collected.

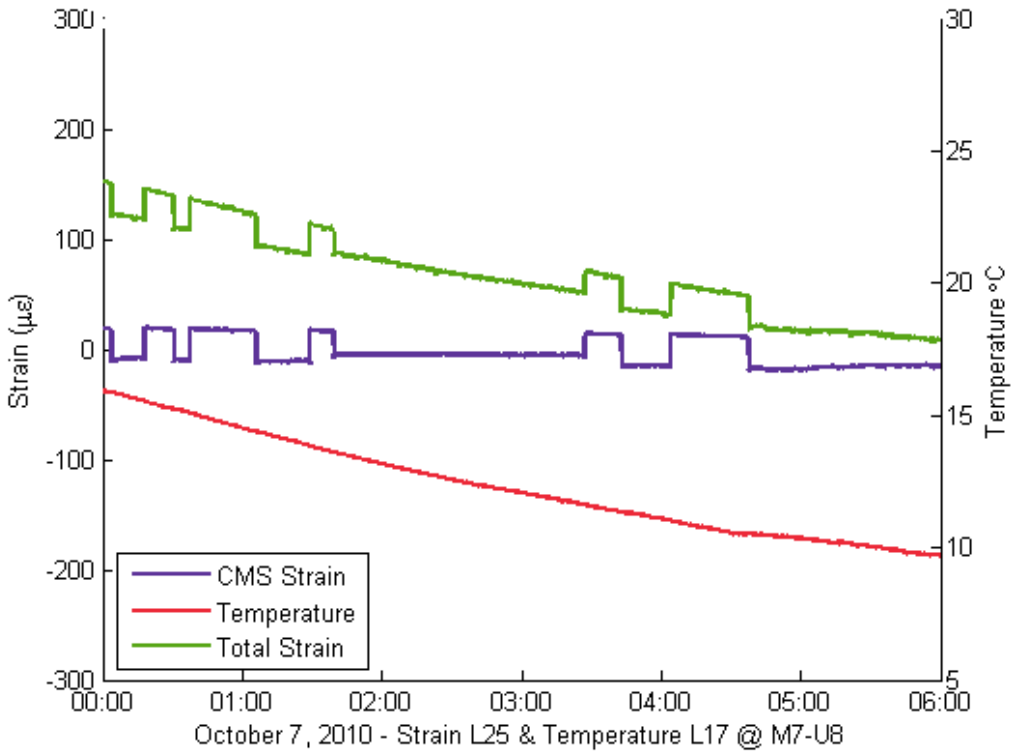

Figure 5.29: Total strain, temperature, and compensated CMS strain from midnight to dawn.

informative about the behavior of the temperature sensors. In Section 5.5 it was determined that the trains and swings are the only significant source of mechanical strain so any changes in the total strain as measured by the strain gages is due to changes in the thermal strain. Therefore, the changes in the temperature should be mimicked by the change in the total strain if the temperature is measuring the temperature of the steel.

Figure 5.29 shows an example of the temperature compensated CMS strain and the total strain and temperature that were used to compute the CMS strain in ENLIGHT during the course of a night. The temperature shows the exponential decay that has been previously discussed as the temperature dropped about five degrees over the course of the night. The total stain shows both the changes in mechanical strain caused by the swing events[13] that occurred during the night and the change in strain due to the change in temperature. At midnight, the bridge is in the open position and then soon closes so that the stairs on the upstream side of the bridge. At 06:00, the bridge, after making a series of swings, is once again locked with the stairs on the upstream side. When the bridge is in the same position, the contributions to the total strain from the mechanical strain should be the same and any change in strain is caused by the thermal strains. Equation (5.9) predicts that for a five degree change in temperature, the thermal strain should change about 91.5 $\mu\epsilon$. The strain change seen in the total strain in Figure 5.29 conforms to this estimate. Therefore,

[13]No trains crossed the bridge for the six hours shown in the figure.

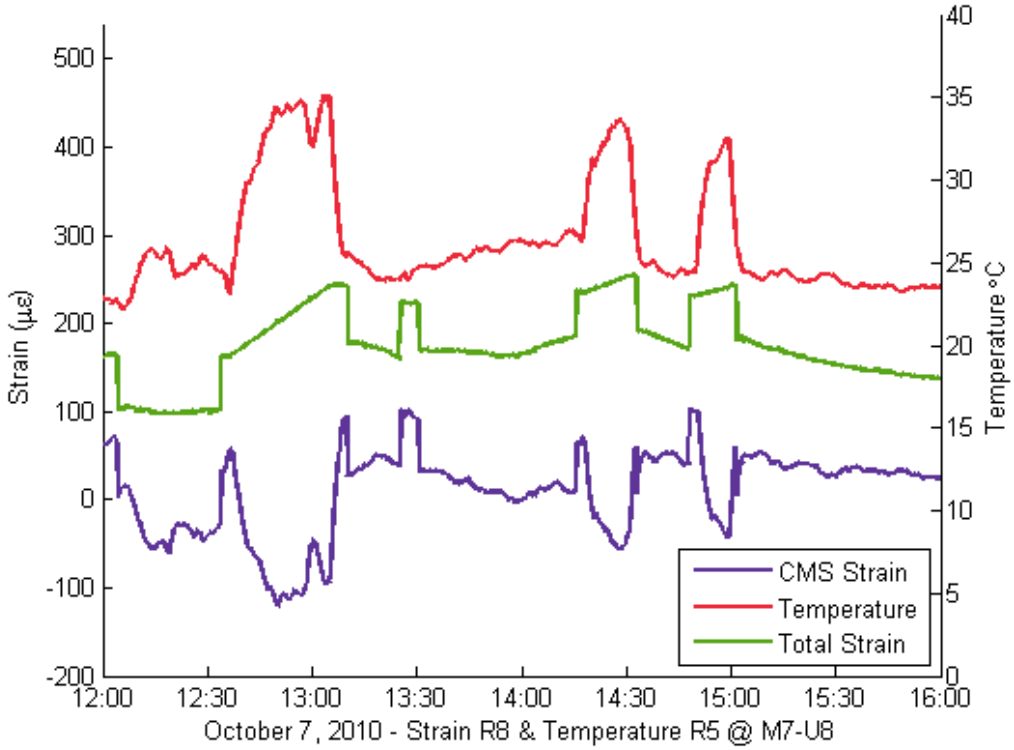

Figure 5.30: Total strain, temperature, and compensated CMS strain during afternoon with swing events.

when the temperature compensation is performed, the result is a straight line broken by the swing events. This shows that at night the temperature measurements are likely properly measuring the temperature of the steel.

However, during the day, the influence of the sun can cause the temperature sensors to measure a temperature that does not wholly represent the temperature in the steel. For example, Figure 5.30 shows an example the temperature compensated CMS strain and the total strain and temperature that were used to compute the CMS strain in ENLIGHT during an afternoon. The total strain in the figure shows that the bridge is in the open position at noon, closes soon after, opens for nearly forty minutes for a swing, then a train crosses the bridge at 13:30, and then two more swings occur later in the afternoon. The strain transitions between the events are generally straight, smooth lines that can increase and decrease at times over the course of the afternoon. This strain pattern indicates that the temperature in the steel changed gradually over the course afternoon. However, the temperature record for the same period shows three distinct peaks and a wide amount of variation between those peaks.

The third peak in temperature that ends at about 15:00 in Figure 5.30 has been isolated in Figure 5.31.[14] This isolated swing event shows a change of about eight degrees between

[14]The total strain has been offset by -100 microstrain from the total strain in Figure 5.30 and the scales have been changed for clarity.

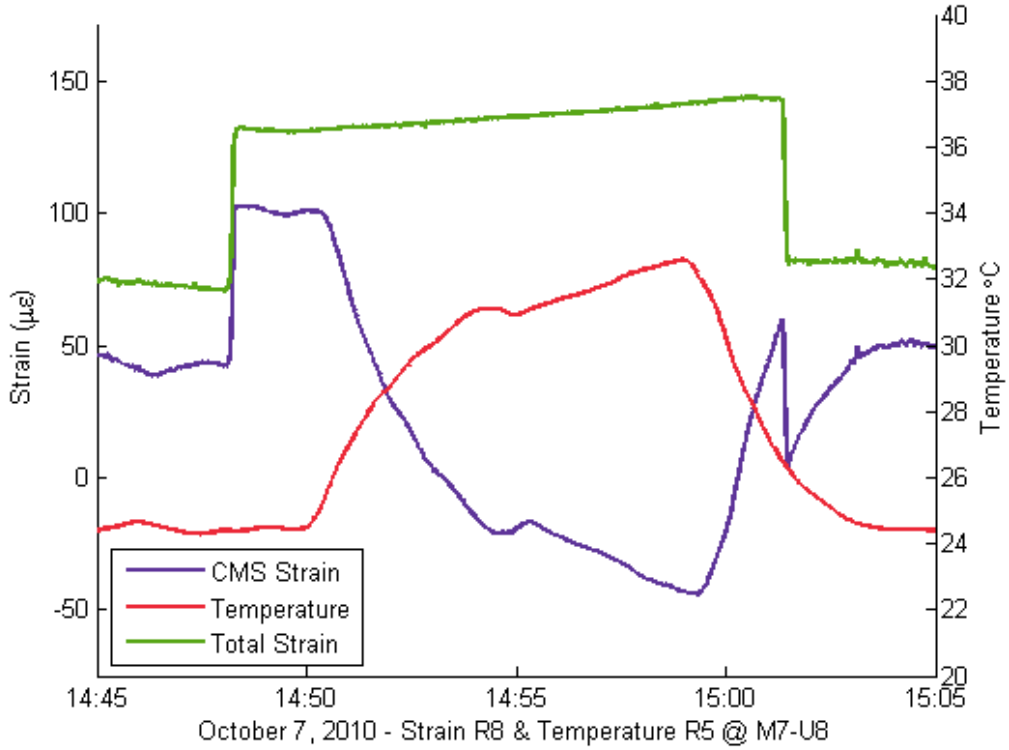

Figure 5.31: Total strain, temperature, and compensated CMS strain during an afternoon swing event.

its maximum temperature and the minimum temperature. Again using Equation (5.9), the change in temperature should correspond to a change in strain of 146.4 $\mu\epsilon$. The total strain does not exhibit this expected response.

What the total strain does show is that just before the start of the third temperature spike, the bridge unlocked and began to swing. The swing does cause the temperature of the steel to increase as seen in the rise in strain while in the open position but the amount and rate of change does not match that indicated by the temperature sensor. As a result, the compensated CMS strain shows the initial strain increase due to the bridge unlocking but once the measured temperature and the steel temperature are mismatched, there is a large decrease in the compensated strain because the formula is over compensating with the measured temperature.

This peak demonstrates that during the day it is possible that the temperature sensor is no longer measuring the temperature of just the steel. A clue as to what is happening is that the bridge is rotating and the sun at this period in the afternoon is highly directional. When the bridge opens and begins to swing, the sensors and the steel eye-bar they are attached to moves from a position of shadow to one of direct sunlight exposure. The solar radiation causes the temperature of the black painted steel to rise increasing the total strain but it also affects the temperature sensor. As noted in Section 5.2.1, the os4350 sensors are enclosed in an anodized aluminum casing. The specific heat of aluminum is 0.91 kJ/(kg·C)

at ambient temperatures while that of steel is 0.49 kJ/(kg·C). When the sensors and member are swung into the sun they are exposed to an amount of solar radiation which has units of W/m^2 which is equivalent to J/(s·m^2) for the same amount of time. The ratio of exposure area to mass for the aluminum clad sensor is 0.0315 m^2/kg while that for the eye-bar the strain sensor is attached to is 0.0027 m^2/kg. Thus for the same solar input, the aluminum would be expected to experience a rise in temperature about 6.28 times greater than that of the steel.

Given that the steel saw a thermal induced strain increase of 13 $\mu\epsilon$, according to Equation (5.9), the steel experienced only a 0.71°C rise in temperature. However, the temperature sensor recorded a rise in temperature of 8.13°C which is 6.28 times greater than the temperature rise in the steel. The difference could be attributed to a combination of the different absorption levels of the radiation and the ability of the steel to radiate heat to the air while the temperature sensor is restricted due to its protective covering. The protective coating may also account for the slight delay in the start of the rise in temperature seen in the measured temperature record.

When the bridge turns back to its original position, the measured temperature begins an exponential decay as it approaches equilibrium with the temperature of the steel as seen between 15:00 and 15:05 in Figure 5.31. Thus undoing the effects of direct solar radiation exposure to the temperature sensor and the steel member. The process of solar heating caused the temperature sensor to record a temperature other than the temperature of the steel in the other swing events shown in Figure 5.30. Note that during the brief train event at 13:30, the strain record shows no significant temperature differential because the bridge has not changed position.

Also note that the dip in temperature at about 13:00 during the first swing event could be caused by the shadows of a cloud. The aluminum also has a thermal conductivity that is greater than that of steel (205 and 36 W/(m·C) respectively). This means that it takes steel longer to heat up or cool down then aluminum. Thus, reductions in the degree of solar exposure or temperature in general will affect the aluminum more than it will the steel. During the night when the steel temperature is above the ambient temperature, the sensitivity of the aluminum allows the temperature sensor to track the steel temperature well, because the steel will lag the temperature. However, when the ambient temperature is greater than the temperature of the steel or solar exposure is present, the aluminum (and therefore the measured temperature) will lead the steel temperature causing the compensation problems.

Figure 5.32 shows the effect of the leading versus lagging effect in the temperature measurement and as a result the temperature compensation. In the pre-dawn hours, the temperature and total strain are well matched and the compensation is adequate. However, after sunrise, the same total strain and temperature that were previously well matched are not any longer. The measured temperature increases faster and greater than the temperature of the steel during the swing events causing problems in the compensation. At 09:00 a spike occurs in the measured temperature that does not appear in the total strain record. This spike of unknown origin is not evidence of a sensor misbehaving (it is doing what it is supposed to do – measure the temperature of the aluminum casing), because no evidence of such behavior exists in the same sensor during the night.

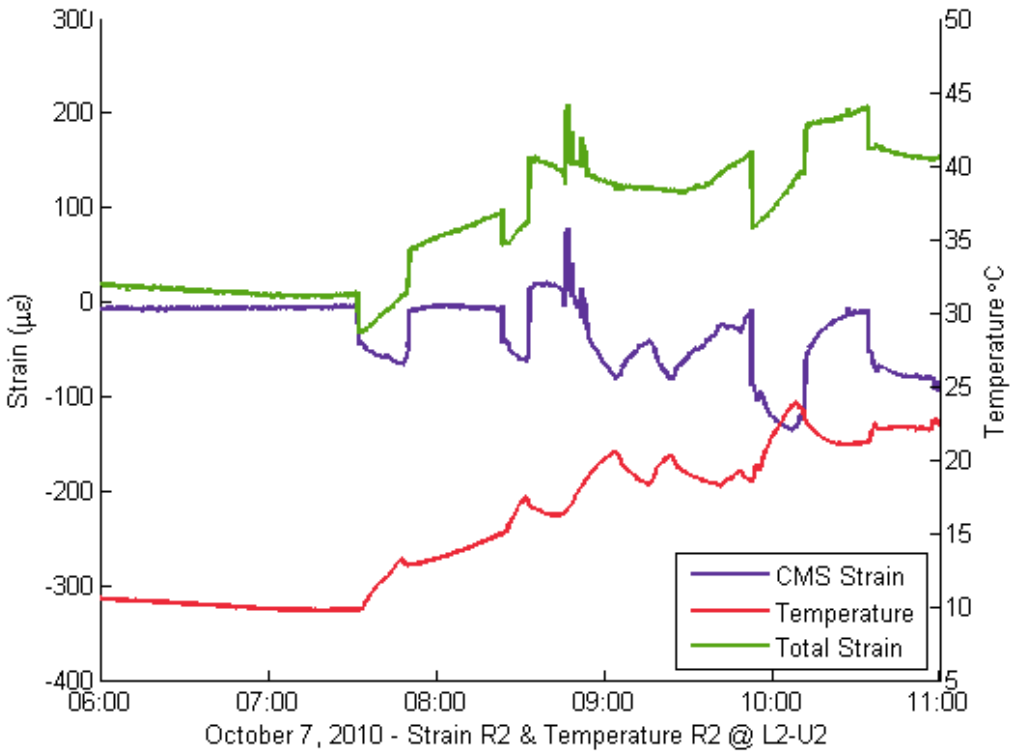

Figure 5.32: Total strain, temperature, and compensated CMS strain from dawn to early morning.

5.6.1 Conclusions

The analysis of the temperature sensors concludes that during the night hours, when the temperature of the steel lags the ambient temperature, the aluminum encased fiber optic sensors can adequately record the temperature of the steel. However, during the daylight hours where the sensors can be exposed to solar radiation that adds heat to the equation of thermal equilibrium at different rates due to the mismatched specific heat values of the steel and aluminum, the os4350 temperature sensors are not measuring the temperature of the steel.

As a result of this analysis, the uncompensated strain measurements are used in the integrated SHM program. This choice is acceptable because the event detection algorithm that lies at the heart of the integrated program is looking for changes in strain that occur over a short period of time. As the period of time decreases the change in temperature approaches zero and therefore so does the thermal strain component of the total strain measured. In addition, the statistics used to determine the bridge condition will be conservatively restricted to those events that fall between nautical dusk an nautical dawn when solar radiation is less likely to affect the sensors.

Researchers in other fields have also noticed the effects of direct solar radiation on fiber optic sensors. Neilson et al. [101] performed studies that submersed fiber optic temperature sensors in water that impedes the penetration of the solar radiation. The fiber optic sensors

exhibited measurable differences in heating due to solar radiation as a function of the depth of the sensor in the water column. The net effects of the radiation seen in the Neilson study were small because the sensors were placed in a moving stream whose flow cooled the sensors. They also determined that close to the stream beds, the heat conduction of the concrete stream bed could dominate the thermodynamics contributing to the temperature measured by the fiber optic sensors. The thermodynamic principles are the same for the stream bed as they are for the Rock Island Bridge. Placing the Rock Island temperature sensors on black painted steel and not allowing cooling other than conduction to the steel substrate exacerbates the radiative effects on the bridge sensors.

Even if ventilated shielding were installed on the Rock Island Bridge temperature sensors, all the radiative effects might not be eliminated. Nakamura and Mahrt [102] developed a model to correct for the observed radiative error in temperature measurements that were shielded with naturally ventilated shields that ideally are supposed to prevent shortwave radiation penetration. However, the correction method depends on the measurement of the wind speed and the net radiation. On the Rock Island Bridge by properly shielding the fiber optic temperature sensors, the error effects might be minimal enough that the heat conduction from the steel would be the dominant influence on the sensors.

5.7 Tilt

Tilt or inclination is usually reported in either units of angle (degrees, radians, arcseconds, etc.) or a ratio of lengths (inches/foot or mm/m). However, in ENLIGHT, the installed CMS tilt sensor has been given the designation of a.u. standing for (arbitrary units). Though arbitrary units are useful in making comparisons, without a physical value they are not as useful in matching recorded results with a model or insight. To exacerbate the situation, though only one tilt sensor is installed on the Rock Island Bridge, ENLIGHT contains four virtual tilt sensors that use the same wavelength readings to compute different values all with arbitrary units. The equations used for the four sensors are as follows:

$$Tilt_1 = \frac{(\lambda_{K2} - \lambda_{K1}) \cdot 1000}{330} - 8.9 \tag{5.11}$$

$$Tilt_2 = (\lambda_{K2} - \lambda_{K1}) \cdot 0.925 - 2.748 \tag{5.12}$$

$$Tilt_3 = \frac{(\lambda_{K2} - \lambda_{K1}) \cdot 1000}{330} - 8.96 \tag{5.13}$$

$$Tilt_4 = \frac{(\lambda_{K2} - \lambda_{K1_0}) \cdot 0.925}{226} \tag{5.14}$$

Equations 5.11–5.14 are all slightly different as far as the constants used and the operations performed. The subtraction of the two wavelengths (λ_{K1} and λ_{K1}) is the method for temperature correction but in the data that was collected, λ_{K2} was always zero.

To begin the analysis, expectations were that the tiltmeter would register a change in angle when the bridge unlocked to be swung open. Figure 5.33 shows the recorded tilt values and the strain response for Strain R2 at the start of a swing event. The change in

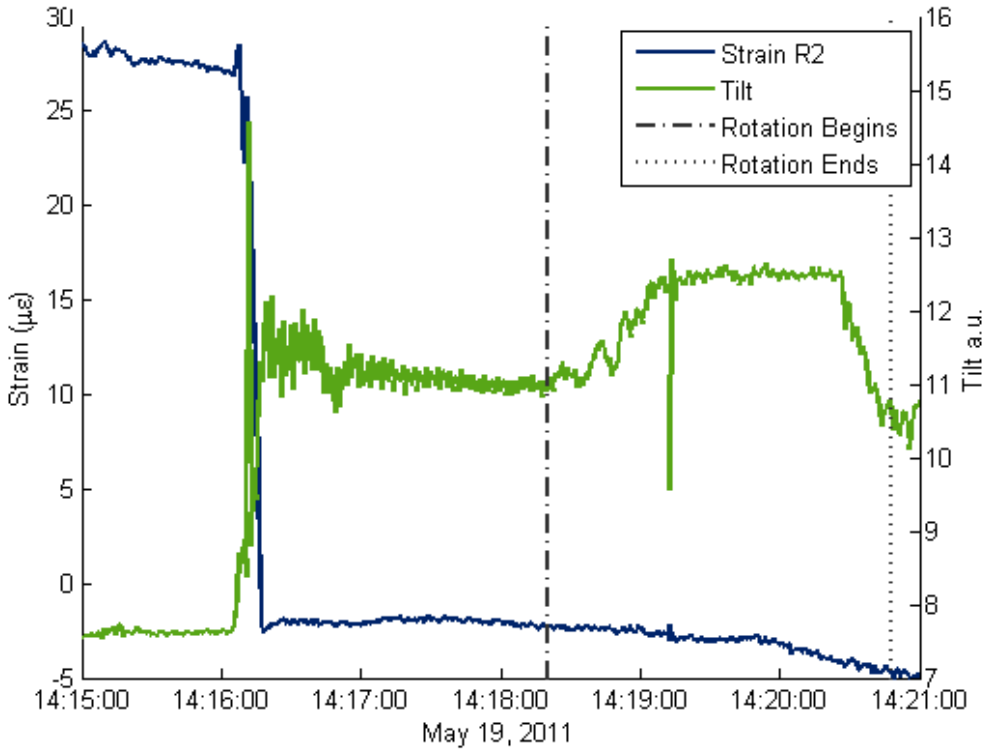

Figure 5.33: Tilt and strain during the start of a swing event showing tilt affected by actual rotation of the bridge.

angle in the tilt record takes place simultaneously with the change in strain. After opening, the bridge 'bounces' according to the tilt record but the vibration is eventually damped out. Once the bridge has unlocked, the bridge operator makes a final check of the cameras to make sure that the bridge has unlocked properly and there are no impediments to rotation. This final check lasts about 30–90 seconds on average before the lever to begin to rotate the bridge is pulled. In Figure 5.33, the time the bridge begins to move is marked by the dashed-dot line. As the rotation begins, the tiltmeter records an increase in tilt that continues as the bridge picks up momentum. When the bridge reaches its turning speed, the tilt plateaus before descending quickly when the break lever is pulled and the bridge comes to rest above the median. This pattern occurs regardless of which end the bridge is turning from or the direction it is turning so it is not likely due to a dip or differential settlement.

Just like the anomalies in the temperature sensors occurred when they were not measuring the temperature of the steel, these paired bumps (one exists at the beginning and end of every swing as seen in Figure 5.35) are a result of the sensor measuring something other than the tilt of the bridge. As mentioned in Section 5.2.1, the underlying functionality of the tilt meter is a mass and pendulum (i.e., an accelerometer). The accelerometer inside the tilt meter is very sensitive and can pick up the 'bouncing' vibrations after the bridge opens better than the fiber optic os7100 accelerometers installed on the bridge. When the bridge

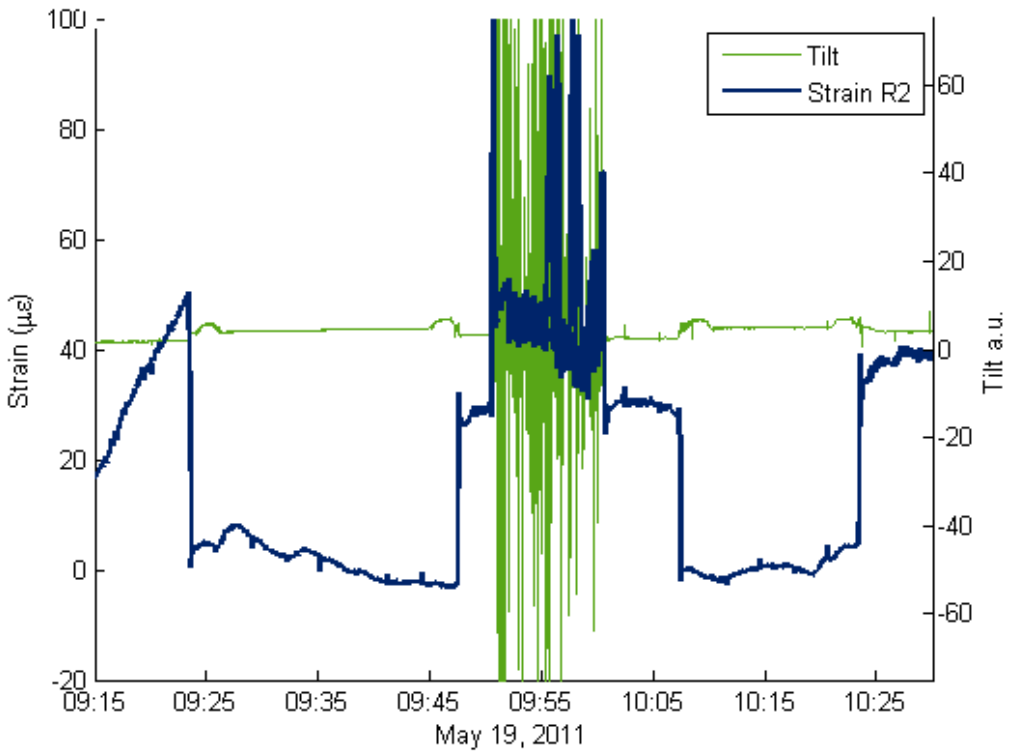

Figure 5.34: Tilt and strain during two swing events and a train crossing.

rotates, it creates a centripetal acceleration (a) that is dependent on the angular velocity (ω) and the radius (r) of the circle traced by the tiltmeter according the equation:

$$a = \omega^2 r \tag{5.15}$$

For the tiltmeter installed on the Rock Island Bridge, given an average angular velocity of the bridge is 0.0131 rad/s (90° in 2 minutes) and the radius is 49.3 m, the centripetal acceleration is 0.0084 m/s^2. The centripetal acceleration acts in the axis of the tiltmeter and therefore gets interpreted as a change in the inclination of the member.

Overall, the centripetal acceleration is of a very small magnitude but it does affect the tiltmeter's performance. The greatest accelerations on the bridge are those caused by trains. If the small centripetal accelerations are detected by the tiltmeter, the large accelerations from the train event are sure to be recorded. Figure 5.34 shows a train event bookended by two swing events as confirmed by the strain record. In the tilt record, the magnitude of the change in angle due to the unlocking of the bridge is very small compared to the magnitude of the recorded values during the passage of the train. The static loading of the bridge with a train would produce some change in angle in the tiltmeter. However, the magnitude of the static train load would be less than that caused by the bridge unlocking to swing which induces a deflection of about 4.5 cm over the 49.3 m long arm. Therefore, the major contribution to the measured tilt during a train event is not the tilt of the bridge but the accelerations acting in the longitudinal direction.

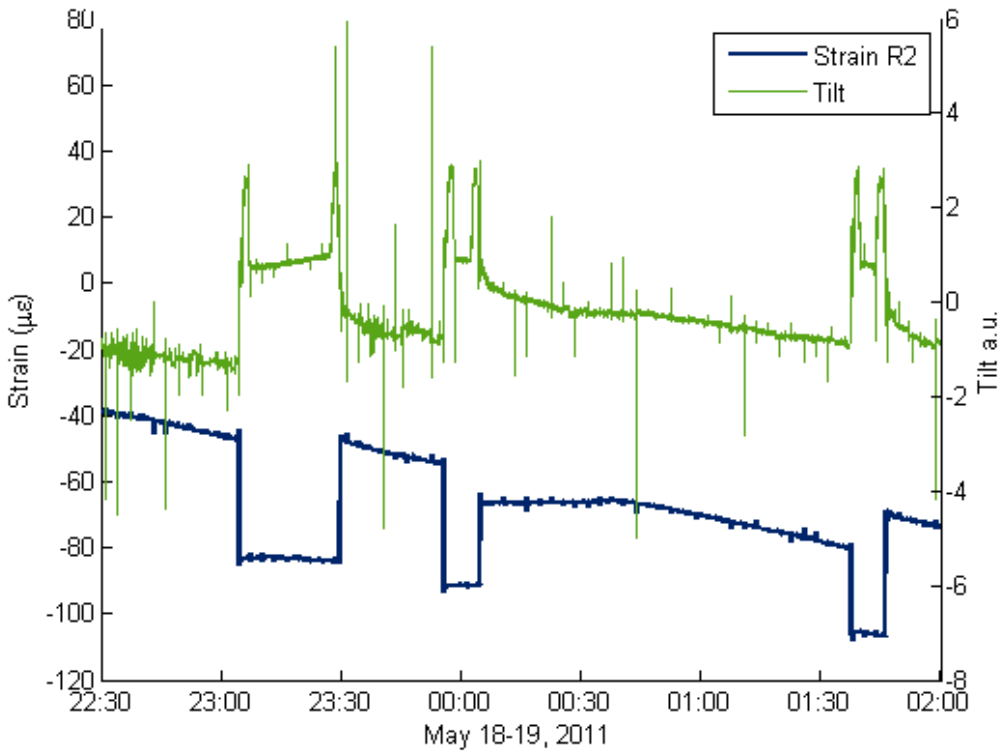

Figure 5.35: Tilt and strain over multiple swing events showing that tilt does not return to previous levels.

Figures 5.33 and 5.34 demonstrate that fundamentally the tiltmeter is exhibiting behavior that is explainable and within the expectations of its function. Figure 5.35, on the other hand points to some of the inconsistencies in the sensor's performance. Both the strain and tilt plotted in Figure 5.35 show three distinct periods of prolonged change starting at approximately 23:00, 00:00, and 01:30. As has been noted before, these represent swing events. The tilt shows two 'bunny ears' that happen during the swing due to the centripetal acceleration as previously discussed. The strain record shows that the bridge is initially in the upstream position, swings open, closes again in the upstream position, swings open, closes again in the downstream position, swings open, and ends up back in the upstream position. This bridge behavior can be deduced because, if the effects of temperature were removed, the closed positions demonstrate distinct and repeatable levels for the two closed positions. Though the tilt record shows significant changes on the swing events, the tilt levels in the closed position are not uniform even if the temperature effects are removed from the tilt record.

The ability of the tiltmeter to be used in event detection is also diminished by it performance under ordinary conditions. Figure 5.36 shows Strain R2 and the tilt measurement over a time period when there are no swing events and no train passages. At 05:20 the inclinometer records a sudden decrease in the measured angle and then gradually increases back to near the original level. Nothing in the strain record at the sudden change in tilt

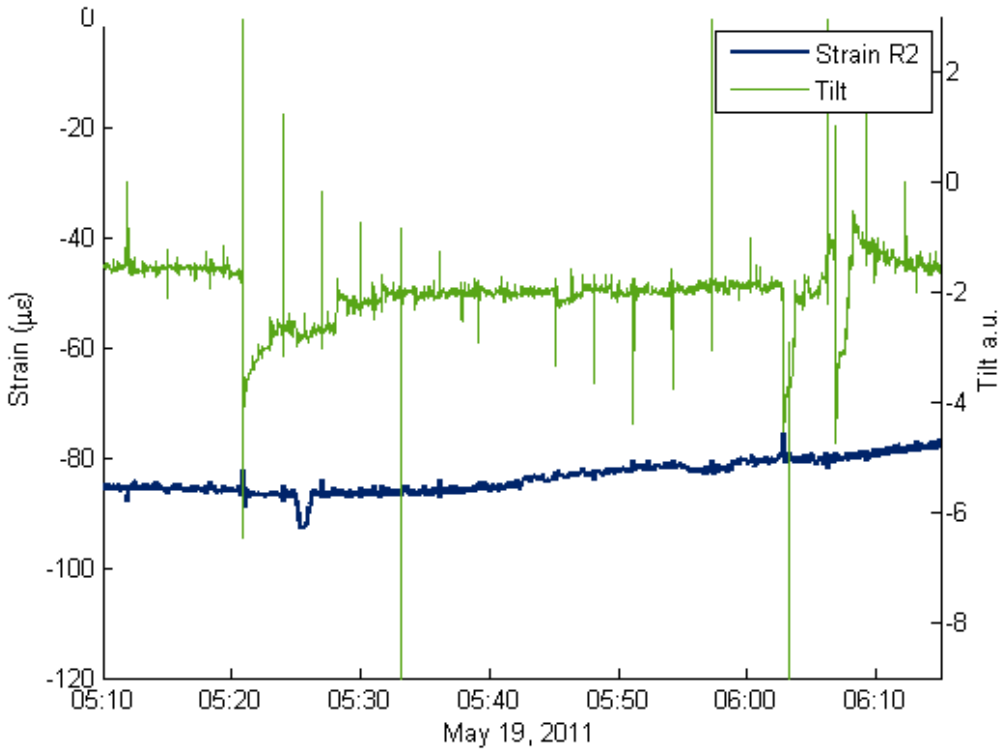

Figure 5.36: Tilt and strain under vehicular loading.

indicates a cause. Because the event occurs before dawn, a sudden temperature change is also not a likely cause. Two additional unexplained jumps in tilt occur between 6:00 and 06:10. The magnitude of these unexplained changes in tilt is the same as those caused by swing events as seen in Figure 5.35.

5.7.1 Conclusions

As currently installed and operated, the tiltmeter provides little useful information that cannot already be gleaned from other sources. The equation in ENLIGHT that converts the wavelength values to conventional units is unclear. The observed data records show that the swing events do cause a change in tilt but the response is neither consistent nor repeatable and the record is prone to unexplained changes that could be falsely identified as swings. The tiltmeter is a sensitive accelerometer and can detect when the bridge is in motion due to the centripetal accelerations generated at its location near the end of the swinging span. However, the digital compass that has been installed to supplement the system can also perform this task.

5.8 Summary

Chandler Monitoring Services installed a multimetric fiber optic sensor system based on FBG technology on the Rock Island Bridge. Analysis of the sensors showed that in many respects, the installed system was inadequate for structural health monitoring purposes. The fiber optic acceleration senors were hampered by aliasing, quantization, and noise floor issues. The temperature sensors were not necessarily measuring the temperature of the structure during daylight hours. The temperature correction of the strain sensors was therefore problematic. The tilt sensors also were inadequate for use in consistently determining if the bridge was open or closed. Nevertheless, at night, the strain and temperature data can be used as part of a SHM system if supplemented with additional sensors.

Chapter 6

FINITE ELEMENT MODELING OF THE ROCK ISLAND ARSENAL GOVERNMENT BRIDGE

To understand the behavior of the Rock Island Government Bridge, a finite element (FE) model was created. FE models can serve as tools in the development of SHM systems as they provide information on the expected behavior of the structure. As data is collected from the bridge, the FE model can be altered and updated so the modeled behavior better matches the available data. As such, the development of an appropriate FE model is an iterative process. This chapter will present the FE model developed for the Rock Island Government Bridge in its final iteration. Notes will be made about where the model was altered from its original form to better match the observed behavior. The reasons for the alterations will be presented. Some references will be made in passing to subject matter, such as the system identification of the bridge, which will be explained in further detail in subsequent chapters. However, because the model will be used to illustrate the observed behavior in the swing span, the creation of the model will be presented first. This chapter will also address the multimetric updating that was carried out on the model and present a comparison of the FE model with the measured responses.

6.1 Rock Island FE Model

Even before any data was collected or analyzed, a finite element model of the Rock Island Arsenal Bridge was created to better understand the expected behavior of the structure [74]. The initial model was created based on the original 1896 drawings and subsequent maintenance and rehabilitation plans provided by the US Army Corps of Engineers. After undergoing many revisions as more was learned about the behavior of the bridge, the current finite element model of the bridge consists of 692 nodes connected by 1764 beam elements composed of 63 different cross-sections. In accordance with the information found in original letters from Col. Buffington [70] and articles published by Modjeski [72], a mild steel (F_y = 38 ksi, F_u = 58 ksi, E = 29,000 ksi) was used as the material properties for all steel members. The cantilevered sidewalks were not modeled physically though their mass was included. Figure 6.1 shows the FE model where the size of the members are representative of the relative capacity of the member and not the actual element cross-section shape.

The model was created using all beam elements; the joints were all frame joints. Having just a single type of element and a single joint type simplified the programming and avoided having to deal with element interfaces. Being that the model was intended for use in model updating, having a model that exhibits the behavior of the real structure while being relatively simple achieves the best balance between complexity and computational power. During the model development, observations indicated that the bridge joints exhibited behavior closer to frame joints than pinned joints in that they transfer bending moments. Even

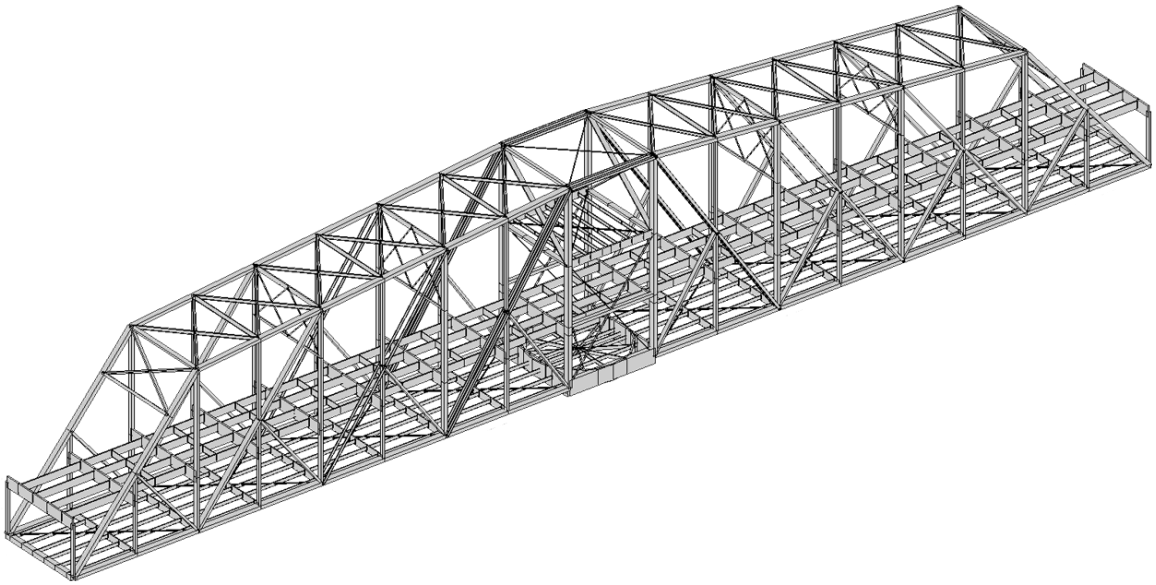

Figure 6.1: Finite element model of the Rock Island Government Bridge.

the typical pinned joint, such as the one along the bottom chord at an L6 position that can be seen in Figure 6.2, exhibited primarily frame like behavior. In the illustrated L6 joint, the vertical post, eye-bars and built-up diagonals are all pinned at the joint. The bottom chord however, is continuous across the node and dictates frame behavior. Thus, modeling both pins and frame nodes added complexity to the model that, given that even the pin joints are not truly pinned, was deemed unwarranted. Not using pinned joints in the model is also a result of the model needing to achieve greater stiffness to match the experimentally obtained results from the bridge.

The cross sections for the beam elements were derived from the original plans and updated, where needed, based on repairs or maintenance that had been performed over the life of the bridge. Many of the bridge elements are made of built-up, riveted, laced sections as can be seen in Figure 6.2 for the vertical post, built up diagonal, and the bottom chord (underneath the grating the lacing can be seen). The majority of the lacing is serpentine (as seen on the vertical post in Figure 6.2) but there is some cross lacing (as seen on the built-up diagonal in Figure 6.2). The lacing runs the entire length of the members except on the ends before it joins another member. Before the bridge joints, the lacing ends and a plate of the same thickness is riveted to the member (as seen in the built-up diagonal in Figure 6.2). In determining the cross-sectional area and moments of inertia for the model members, the lacing was ignored. However, in determining the torsional properties, it was assumed that the lacing allowed the sections to behave as tubes though the lacings themselves did not contribute area to the calculations.

The model has three sets of boundary conditions that have been considered: one for the swung open position, one for the locked position with the stairs upstream, and one for the locked position with the stairs downstream. The boundary conditions at the rim of turntable (shown in Figure 6.3) have been modeled using vertical, lateral, and longitudinal springs and the values of theses springs do not change from position to position. The boundary

(Chris Hsiao)

Figure 6.2: L6 joint on Rock Island Bridge showing eye-bars, laced members, and concrete deck.

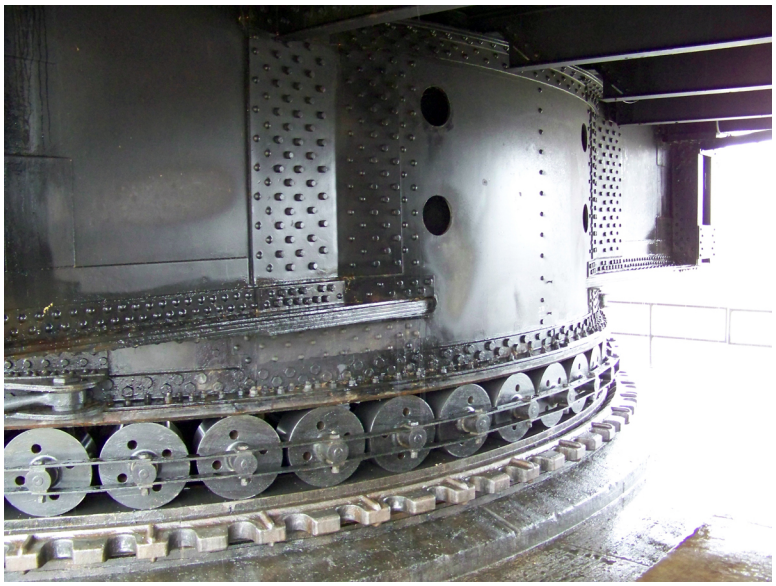

(Chris Hsiao)

Figure 6.3: Turntable of the Rock Island Bridge.

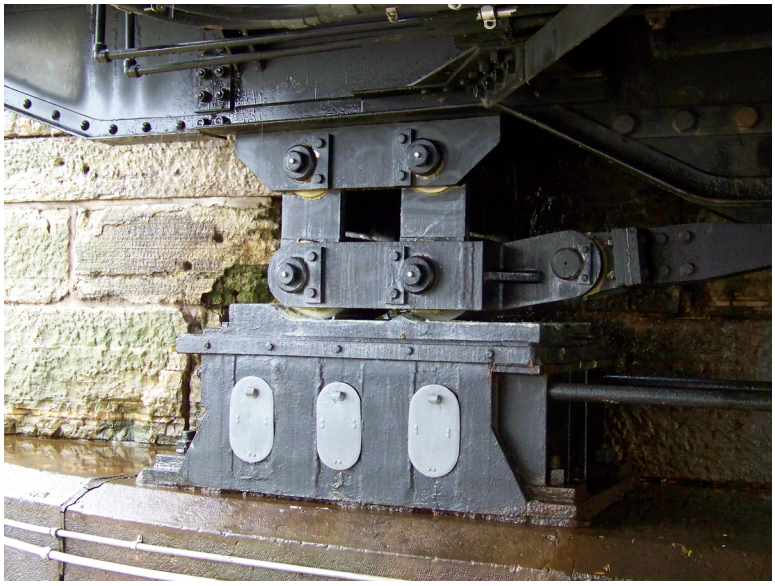

(Chris Hsiao)

Figure 6.4: One half of the Rock Island Bridge locking mechanism at the abutment in the locked position.

conditions on the ends of the bridge were modeled using vertical and lateral springs to capture the behavior of the locking mechanism and its bearings at the abutment and pier (see Figure 6.4). One set of springs was used to represent each of the two closed positions of the bridge: locked upstream and locked downstream. The ends in both positions are free to move in the longitudinal direction. The ends of the bridge were also programmed to have an initial displacement and slope to best model the strains observed in the different closed positions.

As seen in the background of Figure 6.2, the deck of the bridge consists of a concrete filled steel grating.[1] Concrete decks are typically modeled with shell elements to account for the composite and diaphragm action that can develop. To only use beam elements, while still modeling the additional contributions of the composite and diaphragm action to the stiffness of the structure, the effective cross-section and moments of inertia of the stringers were increased. The effective width was calculated as seen in Figure 6.5. The diaphragm action was included by adding diagonals that connect the vertices of the rectangles formed by the stringers and floor beams. These diagonals model the slab as rigid diaphragms [103] and have the thickness and stiffness of the concrete deck. The effective width of the rigid diaphragm is a parameter that can be updated to best match the actual properties of the slab without adding duplicate stiffness to stringers and floor beams. An initial value for the effective width of the rigid diaphragm was calculated using the equations used to calculate the effective width for the composite action in a beam. 5,000 psi concrete was assuemd to model the additional strength from the composite and diaphragm action in the bridge deck.

[1] All the other spans of the bridge have open steel grating decks. The deck of the swing span has been filled with concrete to prevent debris and fluids from entering the turntable and interfering with the operation of the bridge. It also prevents debris from falling into boats that can pass under the bridge without needing the bridge to swing as many recreational boats do.

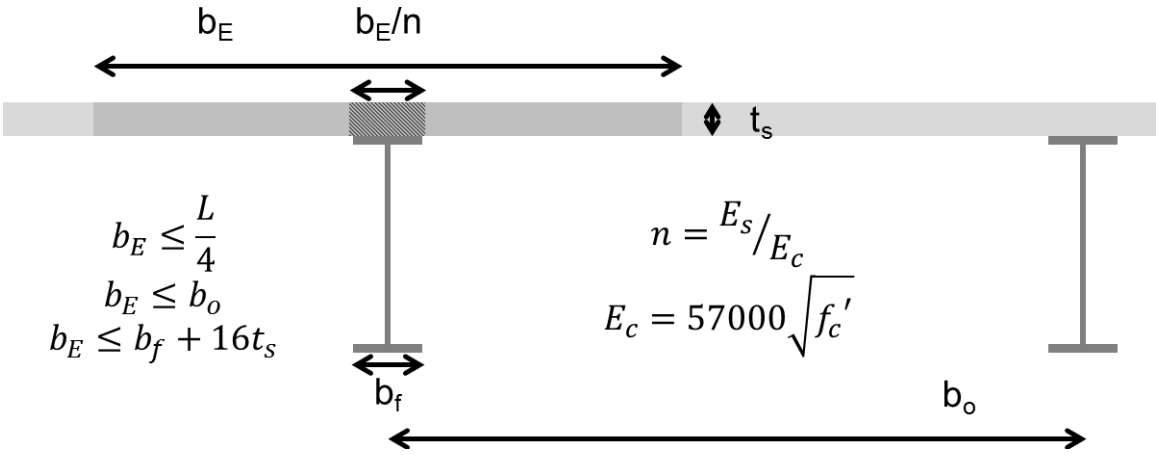

Figure 6.5: Calculation of effective width (b_E) for use in composite action calculations.

Figure 6.6: Close up view of the built-up corrugated railroad deck.

The railroad deck was handled similarly to that of the highway deck. However, as seen in Figure 6.6, the railroad deck is made of steel and has built-up corrugation using riveted channel sections. The composite action between the steel plate decking and the floorbeams as well as the diaphragm diagonals were modeled using an equivalent steel plate. The operator's house was also modeled with additional elements added to account for the stiffness provided by the deck and the operator's house itself.

The mass matrix was calculated using a lumped mass model. The mass of the concrete deck and corrugated railroad deck is added to the nodes using a contributory area approach. The modifications to the stringers account for the composite action and the rigid diaphragm diagonals were massless so as not to double count their mass contributions. Additional mass was added at the operator house level to account for the house and the equipment it holds. A 'bolt factor,' as is used to account for the mass of the bolts in determining dead loads, was also included to add mass to the nodes to account for rivets, lacing, and cover

plates.

6.2 Model Updating

The purpose of model updating is to improve the correlation between the mathematical model and observed results. The differences between the observed and predicted results can be caused by errors in either the measurements or the model. For the Rock Island Bridge, the collection of the measured results and the possible errors will be discussed in Section 7.1.3. On the modeling side, three possible sources of error exist [104]:

1. *Model Structure Errors*: This type of error derives from the fundamental equations that govern the physical properties being modeled. In the case of a structural finite element model, these errors could be associated with the constitutive relationship of the material properties such as linearity assumptions or the finite element formulation itself.

2. *Model Parameter Errors*: This type of error comes from inaccurate assumptions in the parameters used in the model. These parameters can be material properties, geometric dimensions, or assumptions about the boundary conditions of the structure. Often the parameter values are not known exactly but typical values are used and the values can be updated when more information becomes available.

3. *Model Order Errors*: This type of error results from the discretization of complex systems into smaller component parts. One of the challenges of any finite element model is to achieve a mesh size and shape that effectively models the structure. This type of error is sometimes considered a part of model structure errors.

In creating a model, the structure and order are selected and the problem of model updating becomes seeking to adjust the parameters so as to minimize the error between the predicted and measured response metrics. In the case of the FE model created for the Rock Island Government Bridge, the model structure (i.e., beam elements with frame joints) and the model order (i.e., one beam per member between joints) were chosen to simplify the FE model while still modeling the desired behavior of the structure. Over the course of model updating, changes to the model (e.g., the inclusiong of composite action or boundary condition adjustments) were made when the model behavior did not reflect the behavior of the real structure. However, after the changes to the model structure, the updating procedure reduced to a parameter based optimization. Thus, three steps are inherent to model updating: 1) formulate a satisfactory objective function; 2) select appropriate parameters; and 3) perform optimization using a minimization algorithm. The following sections will discuss these three steps and how they were performed for the Government Bridge.

6.2.1 Objective Function Formulation

The objective function provides a measure of the adequacy of the model that is minimized during the optimization process. Ideally, the objective function returns a real, positive value that approaches zero as the model improves. The chosen objective function minimizes two sources of error: 1) error in the natural frequency and 2) error in the mode shape. A good objective function balances these two errors and the formulation of the objective function is almost equal parts science and art. The objective function, $f(\mathbf{P})$, for a given set of parameters, $\mathbf{P}$, for model updating using dynamic properties can be written as:

$$f(\mathbf{P}) = \sum_{i=1}^{n} \left[f(\omega_i) + f(\phi_i) \right] \tag{6.1}$$

where $f(\omega_i)$ is a function of the natural frequencies and $f(\phi_i)$ is a function of the mode shapes.

To create the part of the objective function, $f(\omega_i)$, that accounts for the error in the natural frequency, simply take a percent error between the identified and FE frequencies. To ensure a positive value, either an absolute value or a squared difference can be used.

To account for the error in the mode shapes in the objective function, $f(\phi_i)$, the use of the Modal Assurance Criterion (MAC), or a similarly derived criterion [105] is common. The MAC [106] provides an objective measure of the linearity between two modal vectors or mode shapes. The formulation of the MAC is similar to the formulation for the coherence calculation and goes to unity when the two modal vectors being compared are the same. For model updating purposes, where a FE mode and an identified mode are being compared, the formulation of the MAC is as follows:

$$MAC_{i,j} = \frac{\left(\Phi_{fe,i}, \Phi_{id,j}\right)^2}{\left(\Phi_{fe,i}, \Phi_{fe,i}\right)\left(\Phi_{id,j}, \Phi_{id,j}\right)} \tag{6.2}$$

where $\Phi_{fe,i}$ is the i^{th} mode shape identified from the measured response of the structure and $\Phi_{id,j}$ is the j^{th} mode shape from the FE model that corresponds to the identified mode. The closer the $MAC_{i,j}$ is to one, the more similar the modal vectors are to one another.

The simplest formulation of an objective function using the MAC would be $f(\phi_i) = 1 - MAC_i$ which satisfies the requirement that $f(\phi_i)$ approaches zero as the error is reduced and be strictly positive. However, such a simple objective function is limited to the range of 0 to 1 and may not properly influence the complete objective function to achieve the desired optimization. A number of MAC based objective functions have been included in the literature. Möller and Friberg [107] proposed using squares in the function as follows:

$$f(\phi_i) = f(MAC_i) = \frac{\left(1 - \sqrt{MAC_i}\right)^2}{MAC_i} \tag{6.3}$$

Likewise, Jang et al. [108] used an objective function based on using the MAC as an ex-

pression of the angle between the two vectors being compared.

$$f\left(\phi_i\right) = f\left(MAC_i\right) = \frac{\cos^{-1}\left(MAC_i\right)}{{}^{\pi}/_{2}} \tag{6.4}$$

Askew et al. [109] created a formulation similar to that of Möller and Friberg as follows:

$$f\left(\phi_i\right) = f\left(MAC_i\right) = \frac{1 - \sqrt{MAC_i}}{\sqrt{MAC_i}} \tag{6.5}$$

Each of these formulations of an objective function satisfies the basic requirements of an objective function, but each has its own features.

Figure 6.7 shows a plot of the residual value of each of the three MAC–based objective formulations above. The possible MAC values range from zero to one. The Möller and Friberg formulation, Equation (6.3), is asymptotic to zero as the MAC value approaches one. Therefore, the residual becomes increasingly smaller as the match between the modes increases, but the amount this formulation contributes to the overall objective function, $f\left(\mathbf{P}\right)$ in Equation (6.1), is very small. Essentially, once the mode shapes reach a MAC value of 0.5, the Möller and Friberg formulation places very little weight on matching the mode shape, and the objective function seeks to minimize the error in the natural frequency.

Figure 6.8 shows the derivatives of the MAC based objective function formulations. The derivative of the Möller and Friberg formulation approaches zero as the MAC approaches unity such that the difference in the residual for a given improvement in the MAC value is always decreasing. The Jang et al. formulation, Equation (6.4), is designed to have a greater residual value as the MAC approaches one so that during the optimization, improvements in the mode shape continue to influence the overall objective function. As seen in Figure 6.8, at MAC values very close to one, the derivative of the Jang et al. method approaches negative infinity.[2] The Askew formulation, Equation (6.5), has a value between the other two formulations for MAC values greater than 0.4. The advantage of the Askew formulation is that it has a much larger value than the Jang et al. formulation for MAC values less than 0.4 so that initial grievous mismatches in the mode shapes will have a greater influence on the overall optimization.

Due to its advantages in both the low and high MAC value ranges, the Askew et al. formulation was used to create the overall objective function for the optimization routines. The selected objective function, for the dynamic metrics for a single model, was as follows:

$$f\left(\mathbf{P}\right) = \sum_{i=1}^{n}\left[\alpha_i\left(\frac{\omega_{\mathrm{id},i} - \omega_{\mathrm{fe},i}\left(\mathbf{P}\right)}{\omega_{\mathrm{id},i}}\right)^2 + \beta_i\frac{1 - \sqrt{MAC_i\left(\mathbf{P}\right)}}{\sqrt{MAC_i\left(\mathbf{P}\right)}}\right] \tag{6.6}$$

[2]The derivative of the Jang et al. objective function formulation with respect to the MAC is:

$$f'\left(MAC_i\right) = -\frac{1}{\frac{\pi}{2}\sqrt{1 - {MAC_i}^2}}$$

and

$$\lim_{MAC_i \to 1} -\frac{1}{\frac{\pi}{2}\sqrt{1 - {MAC_i}^2}} = -\infty$$

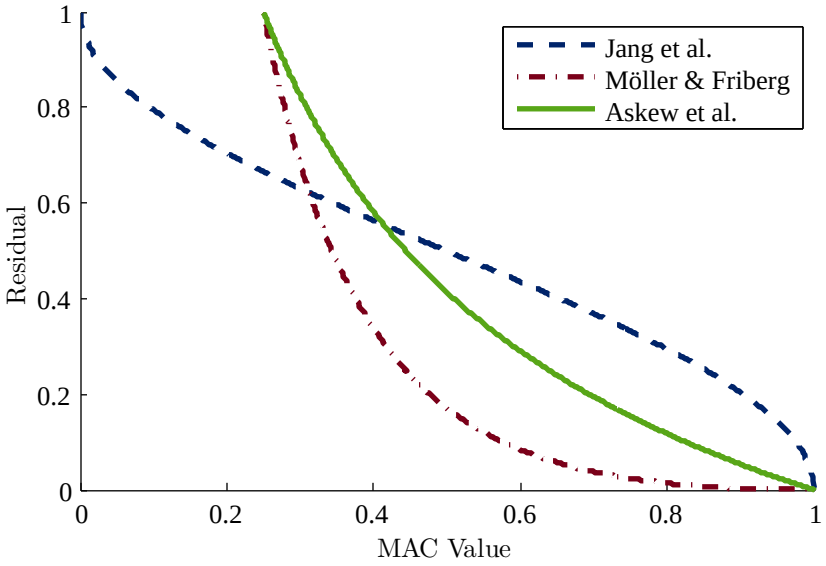

Figure 6.7: Comparison of MAC based residuals for objective function.

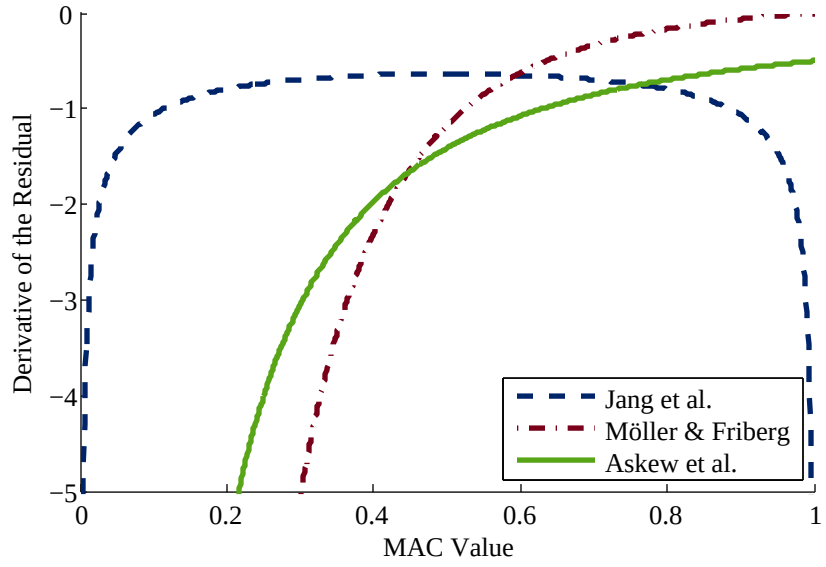

Figure 6.8: Derivative of MAC based residuals for objective function.

In this formulation, $\mathbf{P}$ is the vector of parameters being updated, $\omega_{\mathrm{id},i}$ is the i^{th} identified natural frequency, $\omega_{\mathrm{fe},i}$ is the i^{th} natural frequency for the finite element model and MAC_i is the MAC value computed for the associated modal vectors. Weighting factors α_i and β_i were also included that can be adjusted to weight modes of greater importance or confidence in the measurements. The weights were adjusted so that the β_i factor was double the α_i weight. The weights for the torsional modes were less than for the vertical and lateral modes based on preliminary updating trials.

The objective function in Equation (6.6) was expanded further to account for the three FE models – one for each of the bridge positions – and the multimetric measurements taken. The complete formulation below includes an additional error term, of the same form as that used for the natural frequencies, for the difference between the measured change in strain at the swing events, $\Delta\epsilon_{\mathrm{id},j}$, and changed in strain derived from the finite element model, $\Delta\epsilon_{\mathrm{fe},j}$, that is a function of the updating parameters $\mathbf{P}$. Thus the complete multi-model, mulitmetric objective function is:

$$f(\mathbf{P}) = \sum_{i=1}^{n} \left[\alpha_i \left(\frac{\omega_{\mathrm{id},i} - \omega_{\mathrm{fe},i}(\mathbf{P})}{\omega_{\mathrm{id},i}} \right)^2 + \beta_i \frac{1 - \sqrt{MAC_i(\mathbf{P})}}{\sqrt{MAC_i(\mathbf{P})}} \right] + \sum_{j=1}^{m} \left[\gamma_j \left(\frac{\Delta\epsilon_{\mathrm{id},j} - \Delta\epsilon_{\mathrm{fe},j}(\mathbf{P})}{\Delta\epsilon_{\mathrm{id},j}} \right)^2 \right] \tag{6.7}$$

where n is the number of measured modes from all three bridge positions, and m is the number of measured $\Delta\epsilon$ included in the analysis. Using the objective function in Equation (6.7), ensures that all three models are updated simultaneously.

6.2.2 Parameter Selection

Choosing the parameters for updating is an important part of the updating procedure. Parameters need to be selected that meet two conditions. First, the parameters need to have an effect on the measured response of the structure. Second, the parameters still need to have a basis in reality and a reason for being altered. The reason can be likely sources of damage, boundary conditions that are not ideal, or uncertainty in a measurement or value. The parameters selected for updating in the Rock Island Bridge were chosen for all three reasons. Limits for the parameters were established to make sure they stayed in a range that was physically possible.

Table 6.1 lists the twenty-eight parameters that were updated in the Rock Island Bridge model. The parameters are listed in the table according to which model they affect. The first twelve parameters are used in all the model of the bridge in each of its three positions. Parameters 13–20 describe the boundary conditions of the bridge in the upstream position and parameters 21–28 are the corresponding parameters in the downstream position. The terms left and right are used to differentiate the two ends of the bridge. Whether the left and right term corresponds to the Rock Island abutment of the first river pier switches when the model being considered is in the upstream locked or downstream locked positions. This nomenclature allows the sensor locations and corresponding model members to remain constant.

Most of the parameters were selected because a high degree of uncertainty can be at-

Table 6.1: Parameters used in updating procedures.

Universal		Position Specific			
Open, Upstream, & Downstream		Upstream		Downstream	
Parameter	Units	Parameter	Units	Parameter	Units
1) Concrete Deck Thickness	in.	Left Boundary Conditions		Left Boundary Conditions	
2) Railroad Deck Thickness	in.	13) Lateral Spring	k/in	21) Lateral Spring	k/in
3) Operator's House Deck Thickness	in.	14) Vertical Spring	k/in	22) Vertical Spring	k/in
4) Bolt Allowance	%	15) Slope	in/in	23) Slope	in/in
5) Young's Modulus – Steel	ksi	16) Vertical Deflection	in.	24) Vertical Deflection	in.
Turn Table Boundary Conditions		Right Boundary Conditions		Right Boundary Conditions	
6) Horizontal Spring	k/in	17) Lateral Spring	k/in	25) Lateral Spring	k/in
7) Lateral Spring	k/in	18) Vertical Spring	k/in	26) Vertical Spring	k/in
8) Vertical Spring	k/in	19) Slope	in/in	27) Slope	in/in
9) Railroad Floor Beams I_y	in^4	20) Vertical Deflection	in.	28) Vertical Deflection	in.
10) Inclined End Posts (L0-U2) – I_z	in^4				
11) Operators House Mass Factor	%				
12) Railroad Deck Mass Factor	%				

tributed to their values. For example, all the spring parameters for the ends and the turntable were initially unknown quantities as they represent the boundary conditions of the structure. The boundaries for these parameters was initially very broad to represent the full range of possible values. Other parameters had less uncertainty and had narrow boundaries set. The concrete deck thickness was known to be between 1.75 and 2.5 inches in thickness and limits were set accordingly. Sensitivity analyses were used to help set the parameter limits used in the optimization process.

Figure 6.9 shows the sensitivity analysis for the railroad deck thickness. The railroad deck is comprised of a composite corrugated section as seen previously in the photo in Figure 6.6. The corrugation was represented in the model by using as a steel plate of unknown thickness[3] to calculate the composite action effects on the floorbeams in the FE model. The sensitivity analysis showed that the railroad deck thickness parameter affected the natural frequencies to different degrees and in different ranges. The most obvious feature in the graph is that the parameter can alter the order of the natural frequencies. Between two and three inches, the torsional mode switches from being the third to being the fourth mode. Spatial aliasing (as discussed further in Section 7.1.2) of modes with similar frequencies can cause the switching of mode order to be problematic when performing model updating. Limits were chosen, after the creation of Figures 6.9-6.10, to keep the modes in the desired order.

Whereas the railroad deck thickness and parameters like the bolt allowance and Young's modulus have near universal effects on the all the modes to some degree, other parameters affect only certain modes. The vertical end spring parameters, as would be expected, greatly influence the vertical bending modes of the model but have little influence on the lateral modes. Figure 6.10 illustrates this principle. Modes 5 and 6 change significantly as the vertical end springs become stiffer. As the zoomed in chart in Figure 6.10(b) better illustrates, mode 5, the vertical symmetric mode, begins as the third natural frequency in the

[3]The mass contribution of the corrugated deck and rails was controlled by the separate railroad deck mass factor.

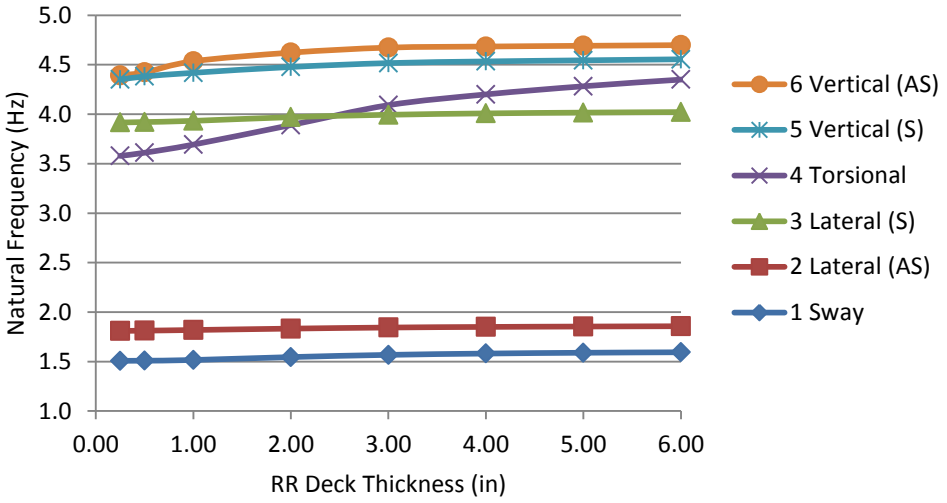

Figure 6.9: Sensitivity analysis for the rail road deck thickness.

ranking before stiffening and becoming the fifth smallest. Also notice how as the stiffness increases, the increase in the natural frequencies of vertical modes continues to diminish. In fact, as the stiffness increases to infinity, the natural frequencies asymptotically approach a maximum limit.

The sensitivity analyses for the selected parameters indicated that some of the modes were coupled together. However, the original model indicated that one of the pair was too stiff and the other not stiff enough. With the modes being coupled in all the parameters, a solution that met both requirements was impossible to obtain. Parameters designed to decouple the modes were therefore chosen. To select these modes, the strain energy was calculated for each of the members using the mode shape as the deflection for the structure. The total amount of strain energy between two modes was normalized and members that exhibited high strain energy in one mode of the coupled pair but not the other were selected. Figure 6.11 shows graphically those members that had low strain energy in the second mode but high strain energy in the fourth mode. The members highlighted in red were the inclined end posts. Further investigation into these candidate members as to what property should be changed indicated that the moment of inertia about the z-axis, controlling the lateral bending of the member, had the greatest effect. Similar analysis were used to decouple the other modal pairs.

6.2.3 Optimization

Once the objective function is determined and the parameters selected, a number of methods can be used to achieve optimization. A tradeoff always exists between speed, accuracy, and completeness among the various algorithms. This study utilizes a stochastic, global, search technique called a genetic algorithm (GA) to achieve optimization of the objective function.

Genetic algorithms [110] were inspired by the biological phenomenon of natural evolution. As such, the development of the genetic algorithm adopted many of the terms typically associated with evolution. The GA begins with a randomly generated set of "individuals" whose "genotype" is described by the set of parameters being optimized. This initial set of individuals is the first "generation" in an iterative process that creates successive generations of individuals according to given criteria.

To create a generation, those individuals that best meet the optimization or fitness criteria are selected to be the seed for the next generation. The individuals' genotypes of parameters are stochastically combined using "crossover" and "mutation" that are controlled by user defined proportions and likelihoods. Crossover is where some of the exact parameters of one individual are combined with the remaining parameters of another individual to create a new whole genotype. Mutation is where the parameters are altered, often severely, to create a new individual. For each new "child" in the next generation, two "parents" are selected from among the best fits, and crossover and mutation is performed.

The genetic algorithm continues to run until one of a number of predefined termination conditions are met. For example, the number of generations can be fixed; a time limit can be imposed; a solution that meets minimal criteria can be reached; or changes to the optimization parameters can reach a tolerance level. Upon termination, the best child in

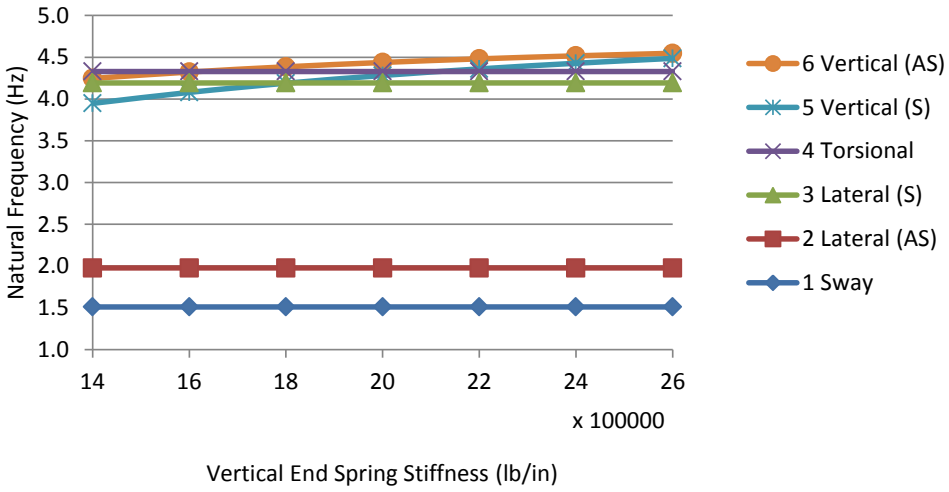

(a) All identified natural frequencies.

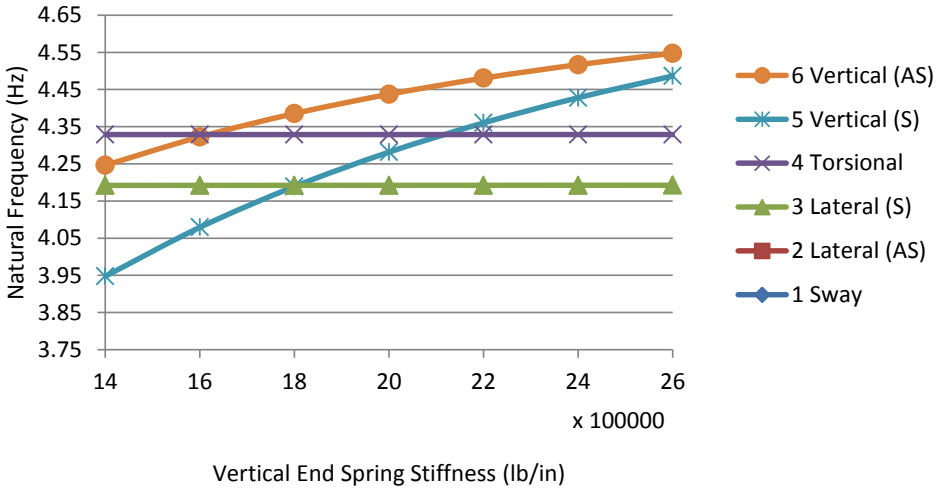

(b) Identified natural frequencies 3–6 only.

Figure 6.10: Sensitivity analysis for the vertical end spring stiffness.

the last generation is selected as the optimal solution. The presence of randomness in the seeding of the initial generation, and also in the production of the children for each successive generation, means that executing the algorithm multiple times will likely result in different optimization results each time. Achieving different results from multiple runs of the algorithm is the tradeoff that exists for the relative speed of the genetic algorithm. The objective function for solving for the eigenvalues and eigenvectors of a structural model can be prohibitively costly in regards to time and computations. Thus, the speed of the heuristic GA trumps its accuracy for this problem.

The use of genetic algorithms for optimization is widespread in a number of fields: bioinformatics, phylogenetics, computer science, engineering, economics, chemistry, manufacturing, mathematics, and physics. Other civil engineering researchers have previously used genetic algorithms to perform model updating of a bridge model. Deng et al. [111] initially used genetic algorithm updating on the model of a concrete beam and then expanded its use to an ANSYS model of a concrete girder bridge. The bridge model represented a structure over the Cypress Bayou in Louisiana. Multimetric data was collected at seven locations on one of the spans of the multispan bridge for a series of static and dynamic load tests. The first three natural frequencies (vertical only) of the bridge were determined and used in the model updating. Seven changes in strain values as the response to the static load tests were also used in the updating process. The researchers used the genetic algorithm to update a total of five parameters (three Young's modulus parameters for the concrete bridge deck, the concrete girders, and the concrete diaphragms, one parameter for the density of the bridge deck, and the final parameter was the stiffness of the rubber bearings). The genetic algorithm gave satisfactory results. The model updating of the Rock Island Bridge model is a more complicated problem than that of the bridge Deng et al. used because of the three

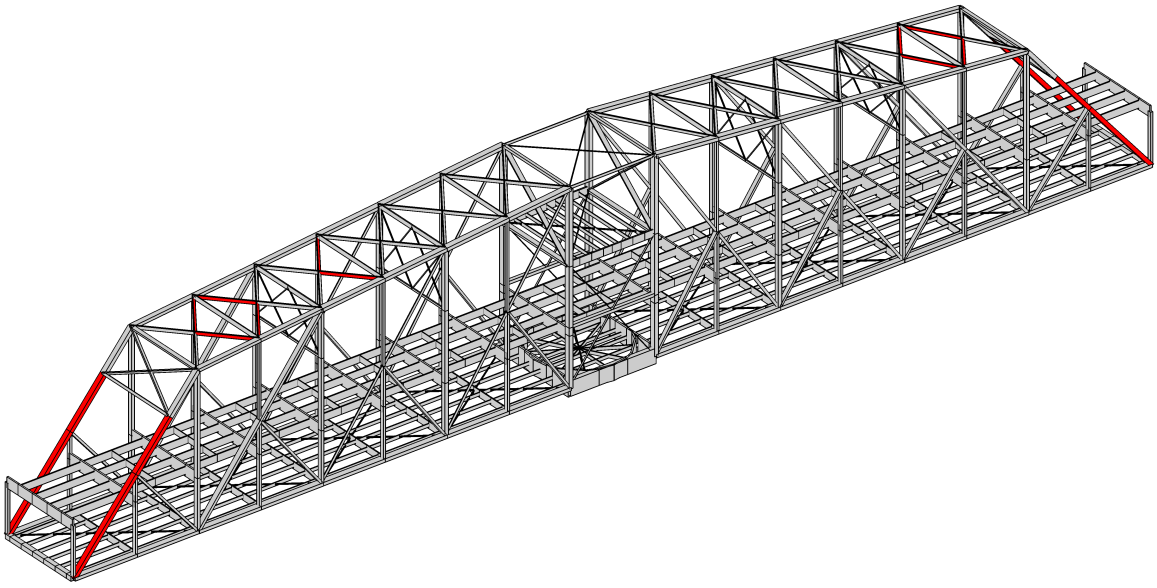

Figure 6.11: Strain energy comparison where Mode 2 has low strain energy and Mode 4 has high strain energy.

Table 6.2: Optimized parameter values: non-model specific.

Parameter	Value	Unit
Concrete Deck Thickness	1.92	in.
Railroad Deck Thickness	0.88	in.
Operator's House Deck Thickness	5.33	in.
Bolt Allowance	124.06	%
Young's Modulus – Steel	29158	ksi
Turn Table Longitudinal Spring	6363	k/in
Turn Table Lateral Spring	1685	k/in
Turn Table Vertical Spring	54394	k/in
Railroad Floor Beams I_y	892	in^4
Inclined End Posts (L0-U2) – I_z	5464	in^4
Operators House Mass Factor	30.86	%
Railroad Deck Mass Factor	4.00	%

dimensional mode shapes and the three different model configurations are being updated simultaneously. Nevertheless, the genetic algorithm is a suitable option for such large scale model updating.

The implementation of the genetic algorithm found in the MATLAB Optimization Toolbox was used to perform the optimization. The population size was 250 individuals, and a limit of 600 generations was used. The optimization used the default setting for the crossover percentage, which was 80%. Settings for the tolerance levels for the termination criteria was set at 10^{-6} for both the residual of the objective function and the average change in the parameters. To speed up the computation, eight processor cores of a Unix workstation were used in parallel to calculate the objective function residual for each individual. The `eigs` command implements a restarted Arnoldi Iteration method to calculate only the specified number of modes of the model. Twenty modes were calculated to ensure that all candidate modes in the model below 5 Hz were computed. Even with the time savings from using the `eigs` command and the multi-core UNIX workstation, each generation of the algorithm took a couple of hours. After five days of running, the genetic algorithm terminated when the average change in the parameters was less than the tolerance. In total, the algorithm calculated 402 generations and created 100,750 individuals.

The optimized parameters are shown in Tables 6.2 and 6.3. The parameters were within the expected boundaries as established by sensitivity studies and physical understanding. The operator's house deck was thicker than the measurements would indicate but the additional stiffness provided by the actual house structure was not previously accounted for so the larger value is not unexpected.

The updated values for the vertical end springs listed in Table 6.3 provide insight into the interaction of the locking mechanism with the abutment and pier. The left and right vertical end springs in the downstream position are nearly exactly the right and left upstream values. This result indicates that the pier and the abutment that are the main source of the asymmetry in the boundary conditions. One of the locking mechanisms does seem to be slightly stiffer than the other but any future changes to the updated vertical end spring

Table 6.3: Optimized parameter values: model specific.

Parameter	Value		Unit
	Upstream	Downstream	
Lateral End Spring			
Left	4939	2853	k/in
Right	5361	3965	k/in
Vertical End Spring			
Left	29248	53060	k/in
Right	51794	26329	k/in
Vertical End Displacement			
Left	4.83	4.81	in.
Right	-3.09	4.22	in.
End Deflection Slope			
Left	0.0049	0.0046	in/in
Right	0.0018	0.0082	in/in

Table 6.4: Model updating results: swung open natural frequencies.

Mode	Description	Natural Frequencies (Hz)		Error
		Measured	FEM	
1	Lateral Anti-Symmetric	0.24	0.24	0.3%
2	Vertical Anti-Symmetric	0.39	0.38	-3.6%
3	Sway	1.07	1.03	-3.8%
4	Lateral Symmetric	1.83	2.42	31.9%
5	Vertical Symmetric	2.08	2.46	18.3%
6	Torsional	2.91	3.29	13.2%

stiffness would more likely indicate changes to the supports and not the mechanism.

Though the updated parameters reflect some of the expected behavior of the structure by themselves, the primary focus of the updating was to match the natural frequencies, mode shapes, and $\Delta\epsilon$ values recorded with the SHM system. Tables 6.4, 6.5, and 6.6 show the results of the dynamic portion of the model updating for the swung, upstream locked, and downstream locked models, respectively. Some of the modes were able to be matched better than others. During the updating process, the torsional and lateral symmetric modes in all three of the models were the most difficult for the model to match properly. These modes were eventually given less weight in the objective function to allow the other modes to have reduced errors.

Tables 6.7 and 6.8 show the $\Delta\epsilon$ values for the upstream and downstream locked positions respectively. For the most part, the strain values of the FE model are more than the recorded values. This result would indicate that the model under estimates the mass of the structure to a certain degree. Additional mass will counteract the inherent stiffness of

Table 6.5: Model updating results: stairs upstream natural frequencies.

		Natural Frequencies (Hz)		
Mode	Description	Measured	FEM	Error
1	Sway	1.68	1.38	-18.1%
2	Lateral Anti-Symmetric	1.98	2.02	2.3%
3	Lateral Symmetric	3.08	3.71	20.7%
4	Vertical Symmetric	4.27	4.08	-4.6%
5	Vertical Anti-Symmetric	4.54	4.41	-3.0%
6	Torsional	3.61	5.00	38.3%

Table 6.6: Model updating results: stairs downstream natural frequencies.

		Natural Frequencies (Hz)		
Mode	Description	Measured	FEM	Error
1	Sway	1.64	1.37	-16.1%
2	Lateral Anti-Symmetric	1.93	1.85	-4.3%
3	Lateral Symmetric	3.10	3.51	13.2%
4	Torsional	3.56	3.99	11.9%
5	Vertical Symmetric	4.08	4.05	-0.7%
6	Vertical Anti-Symmetric	4.32	4.39	1.7%

Table 6.7: Model updating results: stairs upstream $\Delta\epsilon$.

		Delta Strain ($\mu\epsilon$)		
Sensor	Location	Measured	FEM	Error
R2	L2-U2	36.26	43.58	20.2%
R4	L4-U4	87.56	91.39	4.4%
R5	L6-M7	44.65	47.05	5.4%
R8	M7-U8	45.55	54.35	19.3%
L19	L2-U2	39.91	43.37	8.7%
L22	L6-M7	36.22	46.92	29.5%
L31	L4-U4	74.60	90.63	21.5%
L33	L2-U2	23.87	43.00	80.2%

Table 6.8: Model updating results: stairs downstream $\Delta\epsilon$.

		Delta Strain ($\mu\epsilon$)		
Sensor	Location	Measured	FEM	Error
R2	L2-U2	24.53	38.44	56.7%
R4	L4-U4	70.03	81.24	16.0%
R5	L6-M7	36.87	41.78	13.3%
R8	M7-U8	37.86	48.13	27.1%
L19	L2-U2	54.82	38.23	-30.3%
L22	L6-M7	48.77	41.65	-14.6%
L31	L4-U4	98.17	79.72	-18.8%
L33	L2-U2	34.48	38.35	11.2%

the model and, as seen in Table 6.2, the optimized bolt allowance is on the higher end of the amount usually included in estimating the dead load of the structure in the design process. Nevertheless, the observed strain patterns were consistent with the observed values in regard to which position showed greater $\Delta\epsilon$ values for each sensor between the two positions.

6.3 Mode Shapes

The tables of natural frequencies presented in the previous section include a description of the mode shapes of the structure. These descriptions were obtained by looking at the mode shapes produced by the model that represent how the structure actually moves when it is vibrating. The modes are principally classified based on the direction of their dominant motion and whether the two wings of the bridge are moving in the same or opposite directions.

Under this convention the first vertical symmetric mode in a closed position would have one "hump" on each side of the bridge moving up and down in the same direction together. A second vertical anti-symmetric mode would therefore have two vertical sine waves per side but moving in such a way that while the outer wave on the left was up, the outer wave on the right was moving down. A lateral mode is one in which both the top and bottom of the bridge are moving in the same direction. A sway mode is one in which the bottom of the bridge is essentially stationary and the top is moving laterally. A torsional mode is one in which the top and bottom are moving in opposite directions and the two sides are also typically moving in opposite directions creating a twisting motion along the longitudinal axis.

Ideally, animations would help illustrate the modes, but the limitations of the present medium requires static illustrations. To help clarify the illustrations that will be presented, colors were used to help distinguish the quadrants and ends of the bridge. Blue was used for the members on one truss and red was used for the members on the other truss. To provide further clarification, a lighter shade of red and blue were used on one wing of the

truss while darker shades were used on the other. This color scheme helps clarify what the motion is when, as in Figure 6.13(a), the view is down the longitudinal axis and one end of the truss is moving in the opposite direction of the other.

Two types of mode shape illustrations are presented in this chapter. The first shows the motion of all the nodes and members in the FE model. In the second illustration, the modes shapes are only displayed for the nodes where the wireless sensors are located. This type of illustration or formulation of the mode shape will be termed the "abridged" model. The nodes in the abridged model have been connected by fictional elements just to provide some clarity in the motion. The full undeformed shape has been plotted in gray dotted lines in both illustrations to help clarify the motion of the structure.

6.3.1 Identified Modes

The FE code is able to produce graphics that illustrate two types of modes: those that can be identified by the wireless smart sensor system, and those that due to sensor placement and the resultant spatial aliasing the smart sensors are unable to identify. This section will present the modes that are identifiable by the smart sensor network. These modes correspond to the modes that were used in the updating of the FE model and were presented in Tables 6.4, 6.5, and 6.6. The modes are those that can most be considered "global" modes. Some modes are more "local" in nature and a few of these modes will be discussed in the next section.

The mode shapes for the two closed positions are very similar to one another. The difference between the two models is primarily the order of the torsion and vertical modes. Therefore, the downstream modes (Figures 6.12–6.17) and the upstream modes (Figures 6.18–6.23) have similar shapes. One of the features of these modes that stands out is the modal amplitude of the middle pins that connect to the eye-bar diagonal sets. For example, even in downstream mode 5 shown in Figure 6.16(a), which represents a vertical mode, the pins have significant outward lateral amplitude. On trips to the bridge, more vibration was observed in the eye-bars when they were in the closed positions than when the bridge had swung open. The FE model supports this observation. Because of the large activity in these pins, they were purposefully not instrumented so that their motion would not dominate the measured responses.

The mode shapes of the bridge in the swung position (Figures 6.24–6.29) are markedly different from the closed positions, as expected. The first (Figure 6.24) and second (Figure 6.25) mode are modes that are dominated by twisting and rocking of the turntable springs. Other than the twisting and rocking motion, the structure is moving almost purely as a rigid body. These modes are particularly prominent as they were measured while the structure was actually moving.

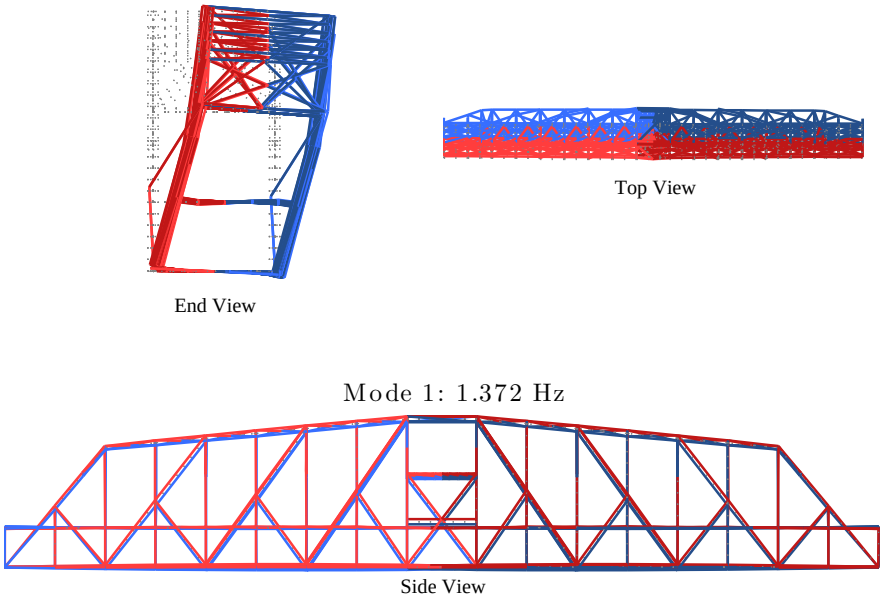

(a)

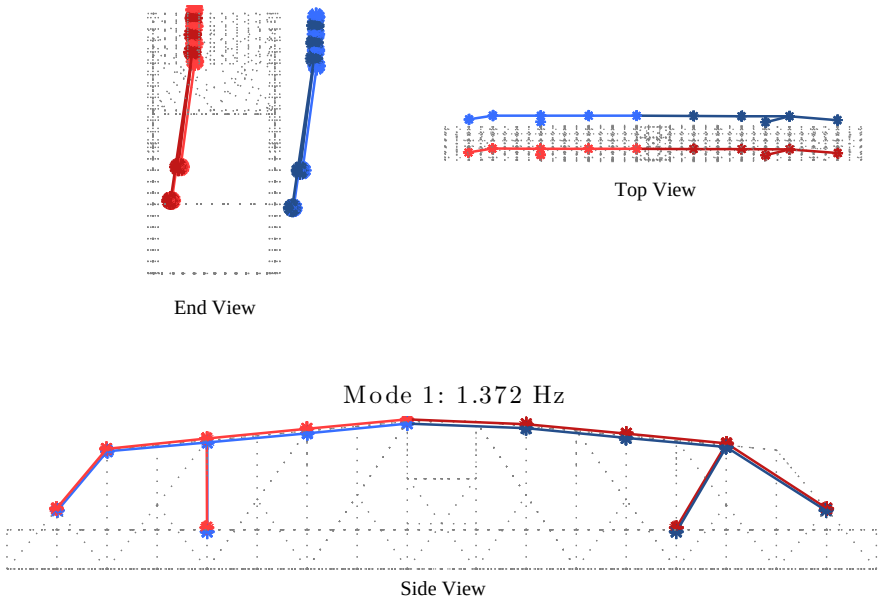

(b)

Figure 6.12: FEM Downstream Locked Mode 1 – Sway: (a) all nodes, (b) abridged to measured nodes.

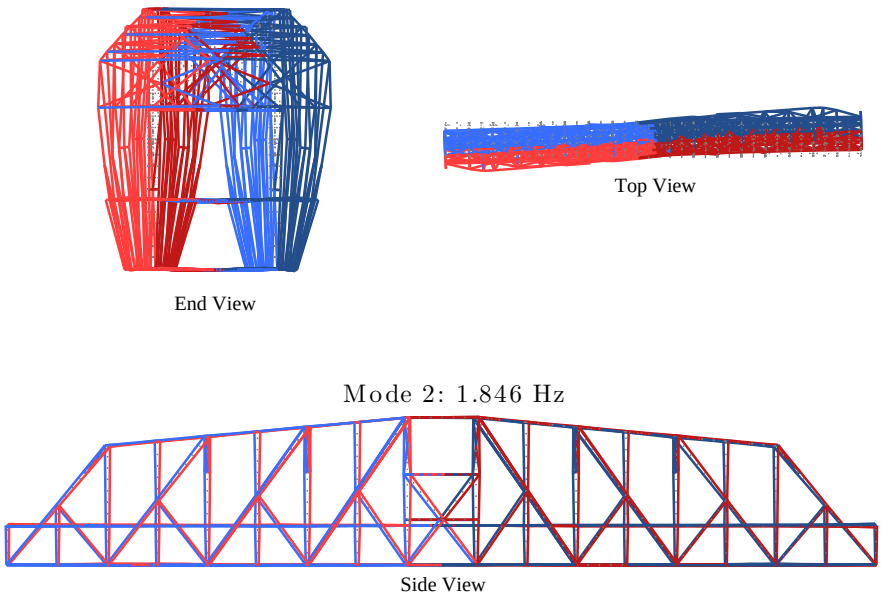

(a)

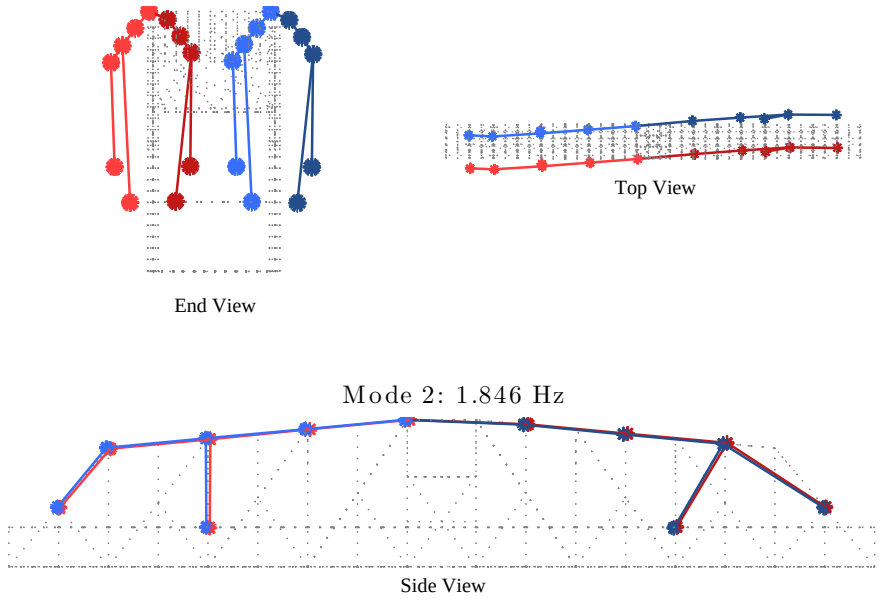

(b)

Figure 6.13: FEM Downstream Locked Mode 2 – Lateral Anti-Symmetric: (a) all nodes, (b) abridged to measured nodes.

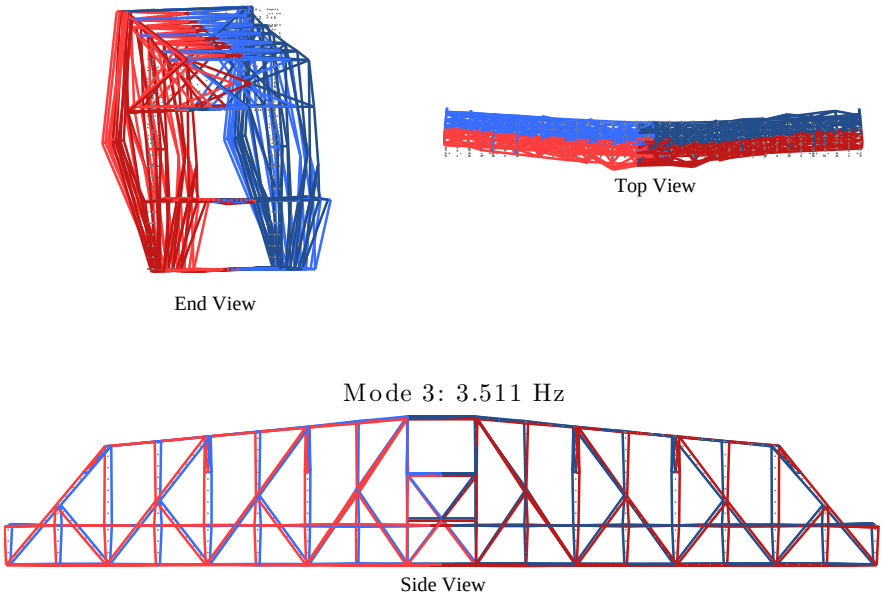

(a)

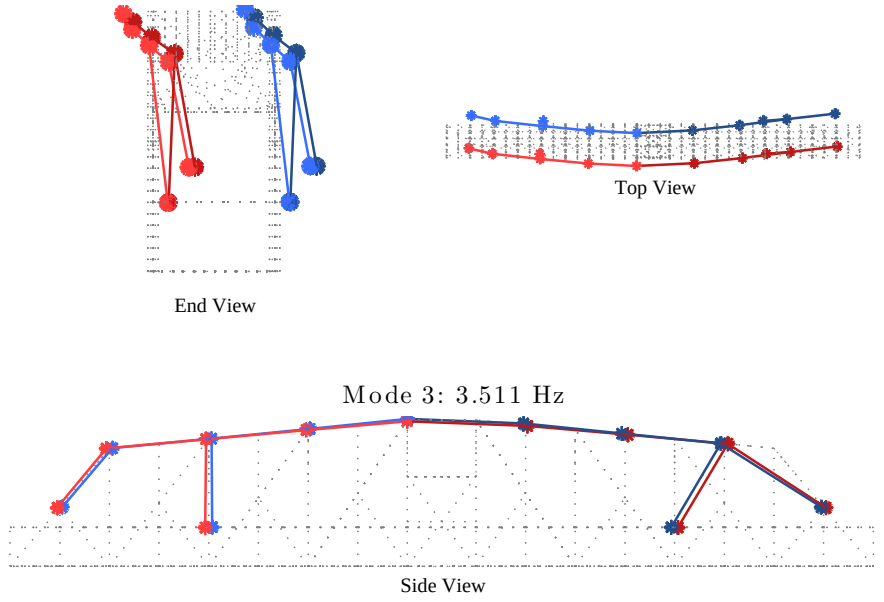

(b)

Figure 6.14: FEM Downstream Locked Mode 3 – Lateral Symmetric: (a) all nodes, (b) abridged to measured nodes.

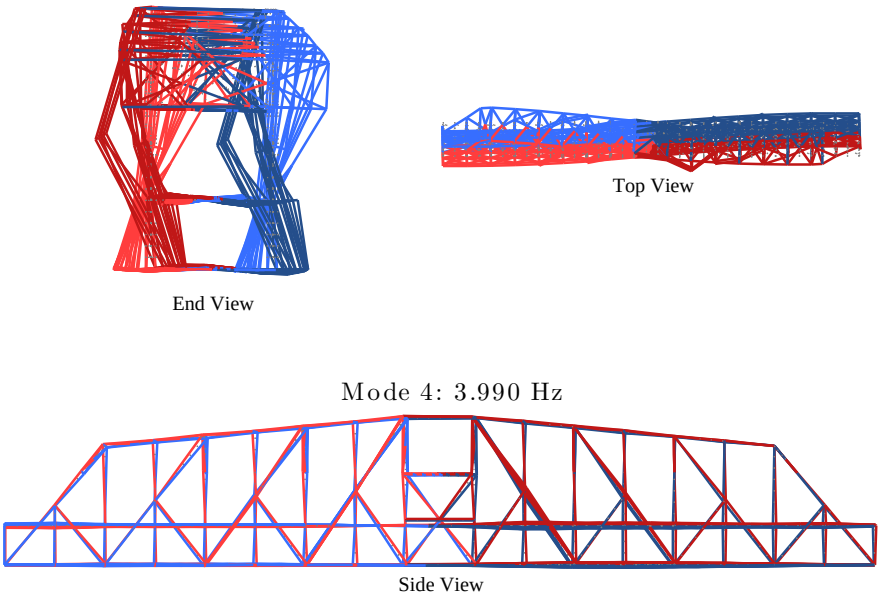

(a)

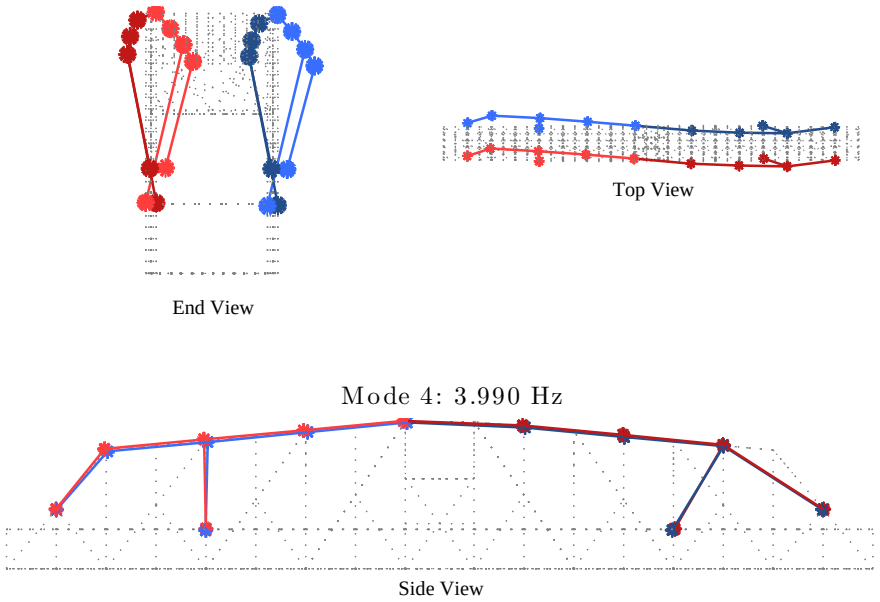

(b)

Figure 6.15: FEM Downstream Locked Mode 4 – Torsional: (a) all nodes, (b) abridged to measured nodes.

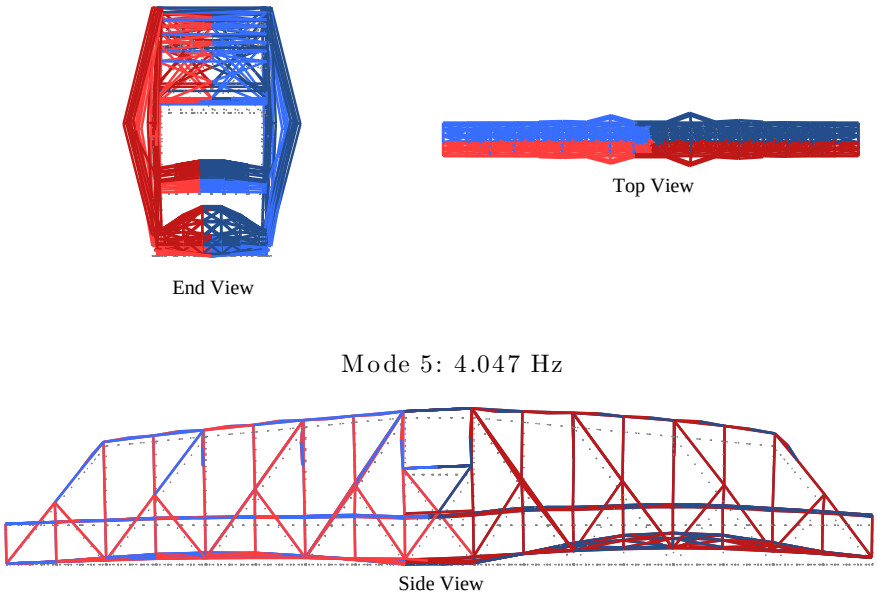

(a)

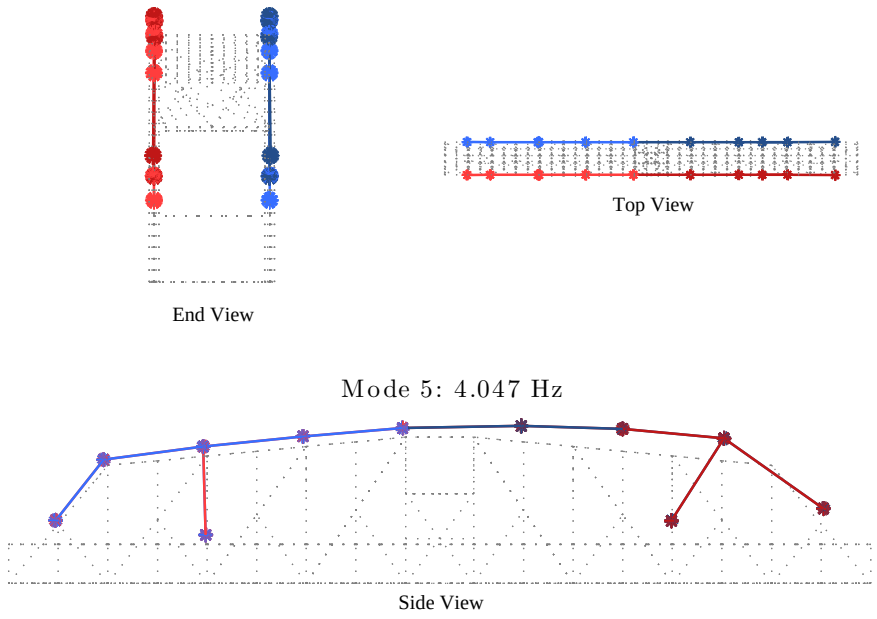

(b)

Figure 6.16: FEM Downstream Locked Mode 5 – Vertical Symmetric: (a) all nodes, (b) abridged to measured nodes.

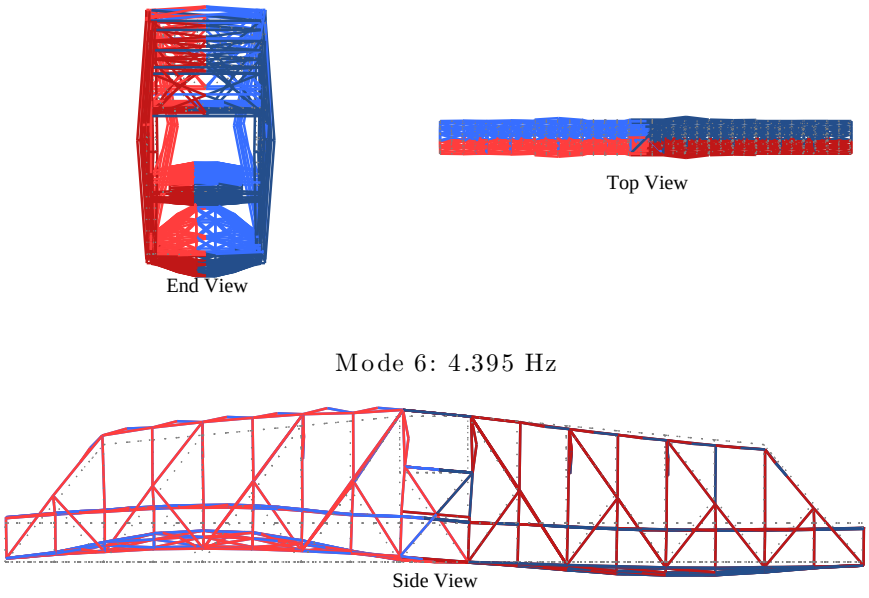

(a)

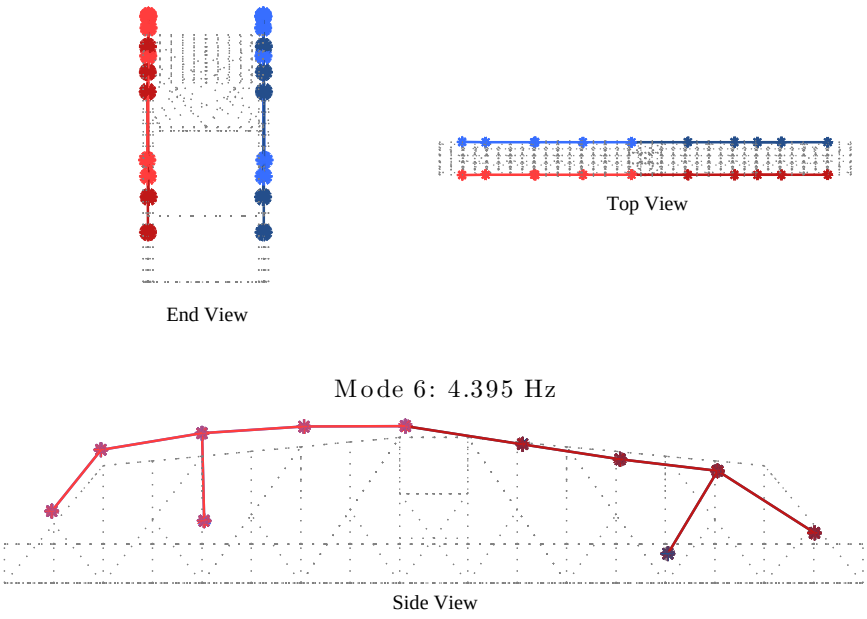

(b)

Figure 6.17: FEM Downstream Locked Mode 6 – Vertical Anti-Symmetric: (a) all nodes, (b) abridged to measured nodes.

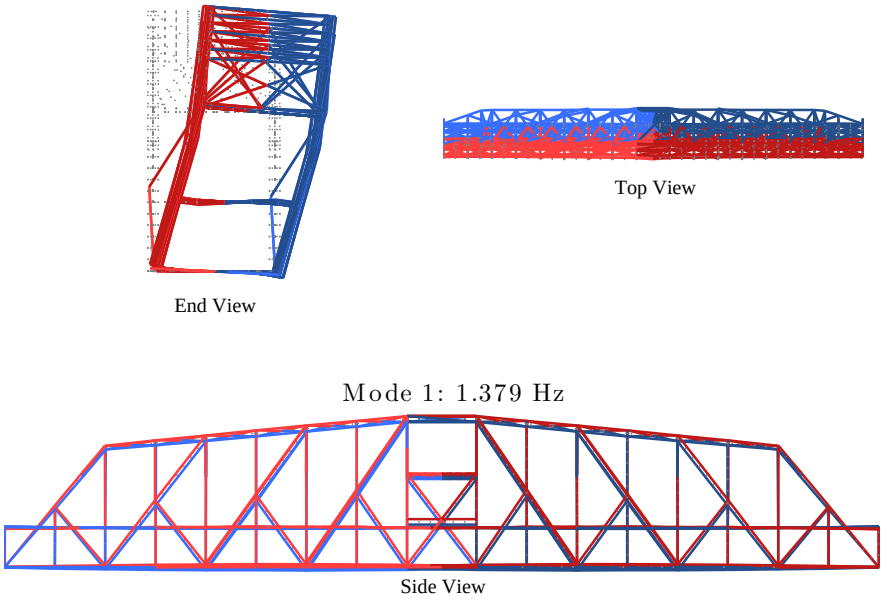

(a)

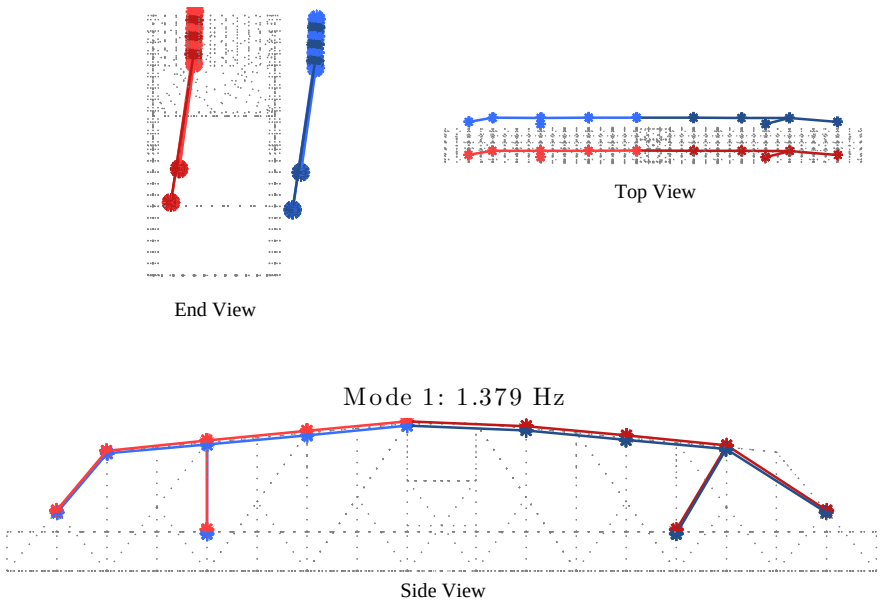

(b)

Figure 6.18: FEM Upstream Locked Mode 1 – Sway: (a) all nodes, (b) abridged to measured nodes.

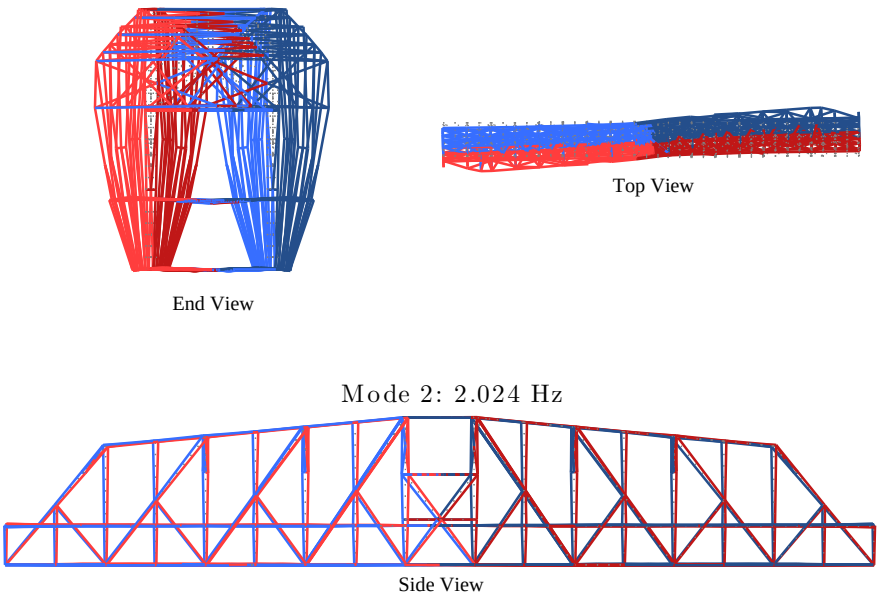

(a)

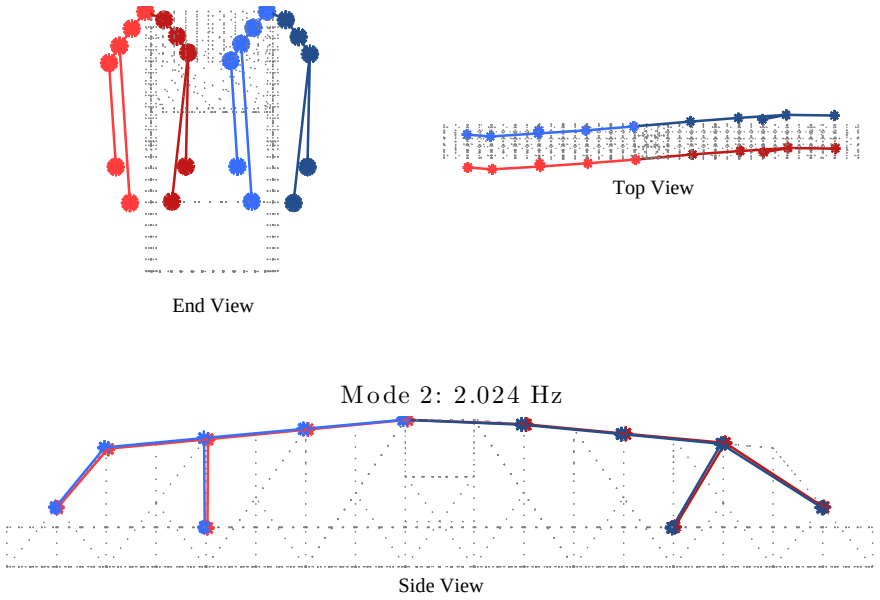

(b)

Figure 6.19: FEM Upstream Locked Mode 2 – Lateral Anti-Symmetric: (a) all nodes, (b) abridged to measured nodes.

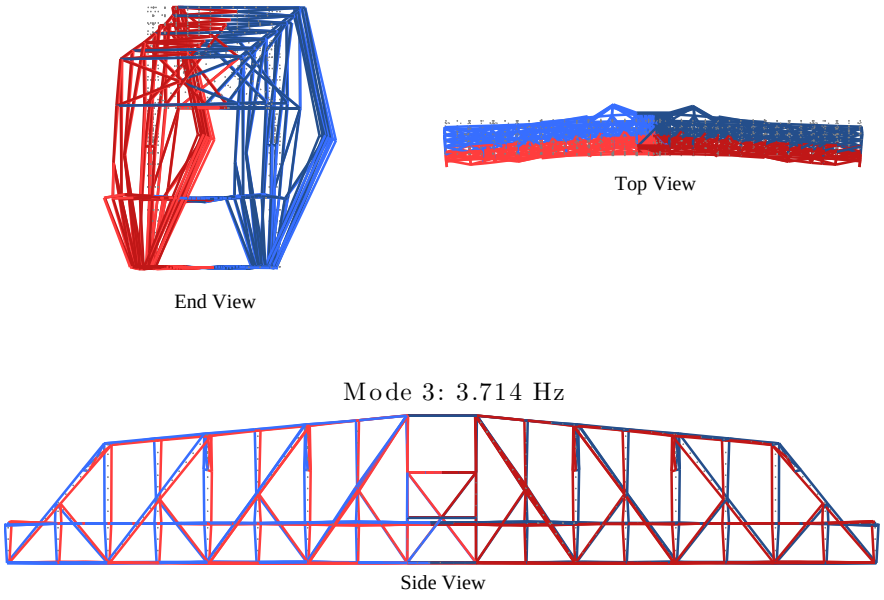

(a)

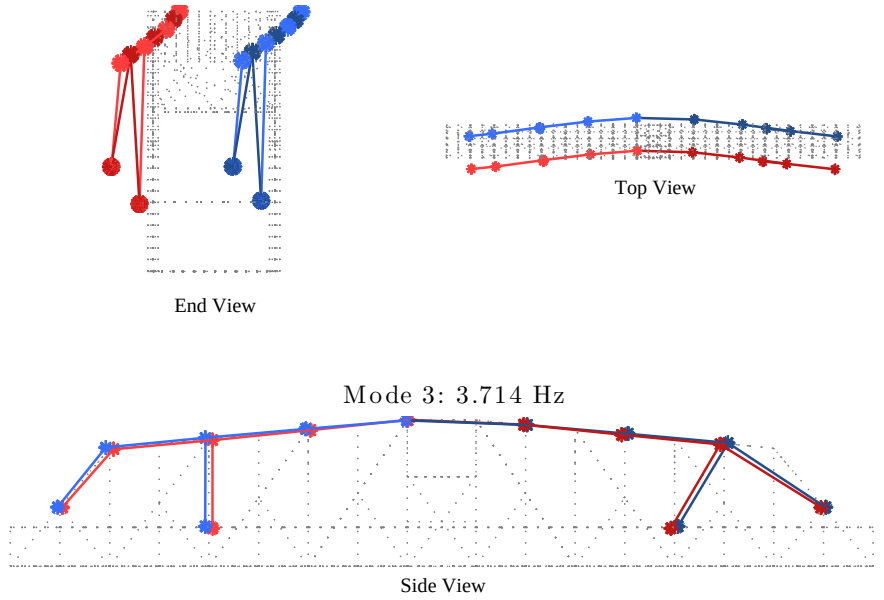

(b)

Figure 6.20: FEM Upstream Locked Mode 3 – Lateral Symmetric: (a) all nodes, (b) abridged to measured nodes.

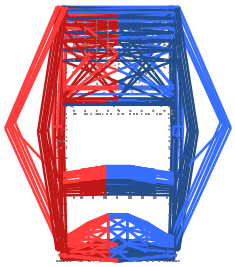

End View

Top View

Mode 4: 4.076 Hz

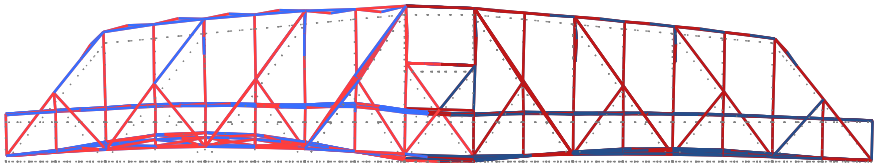

Side View

(a)

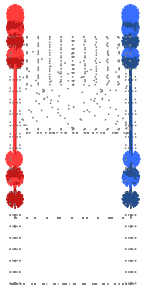

End View

Top View

Mode 4: 4.076 Hz

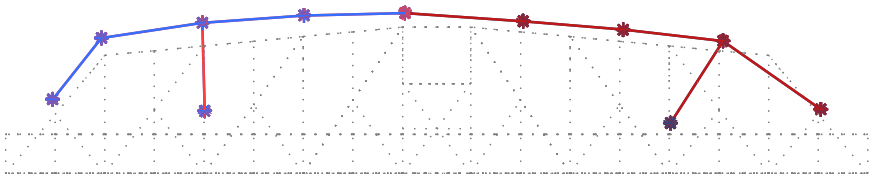

Side View

(b)

Figure 6.21: FEM Upstream Locked Mode 4 – Vertical Symmetric: (a) all nodes, (b) abridged to measured nodes.

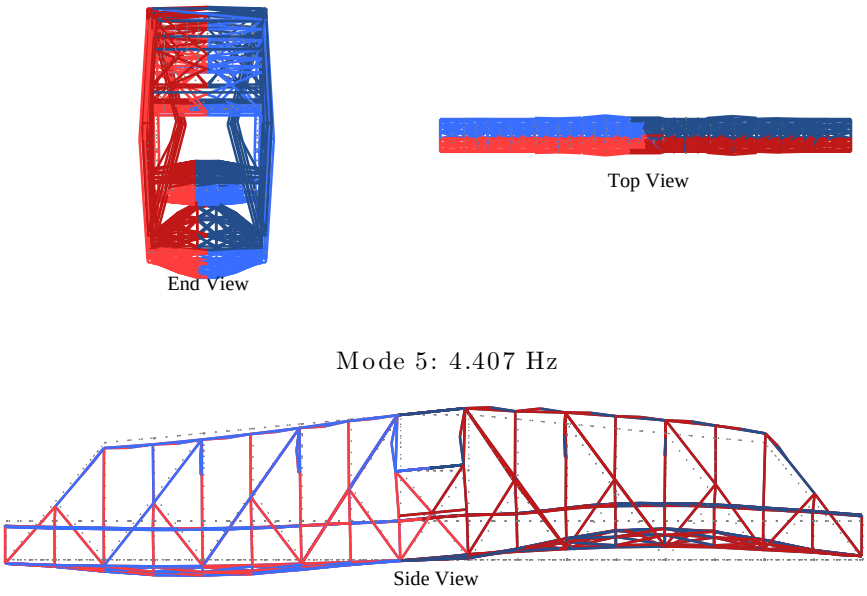

(a)

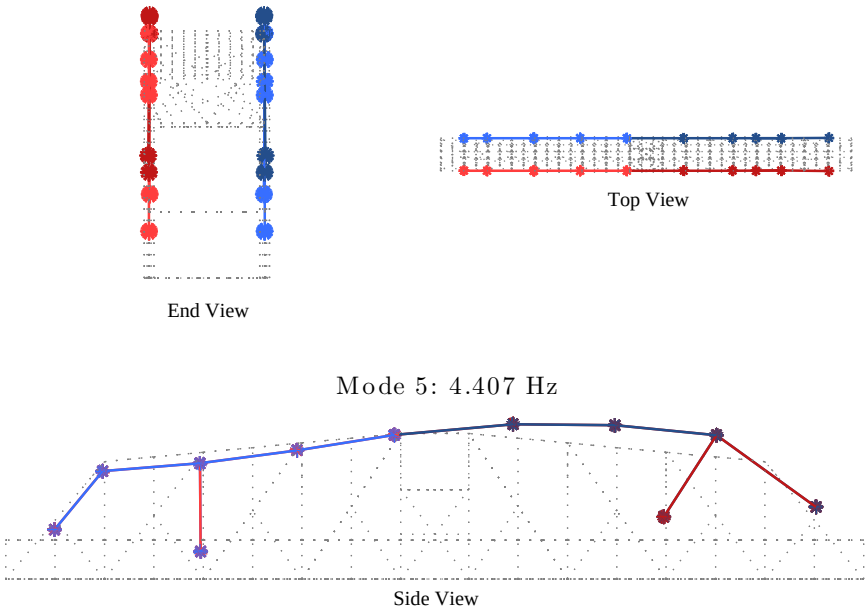

(b)

Figure 6.22: FEM Upstream Locked Mode 5 – Vertical Anti-Symmetric: (a) all nodes, (b) abridged to measured nodes.

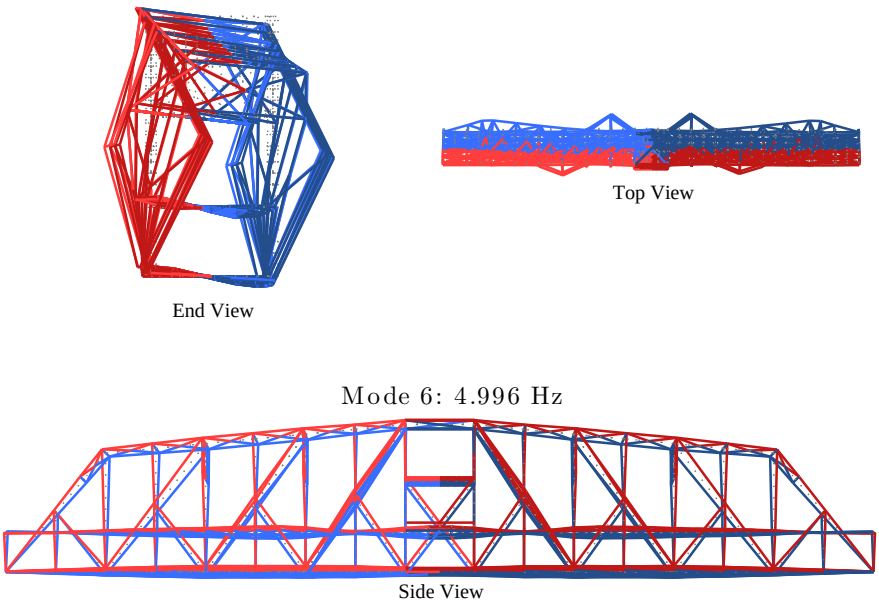

(a)

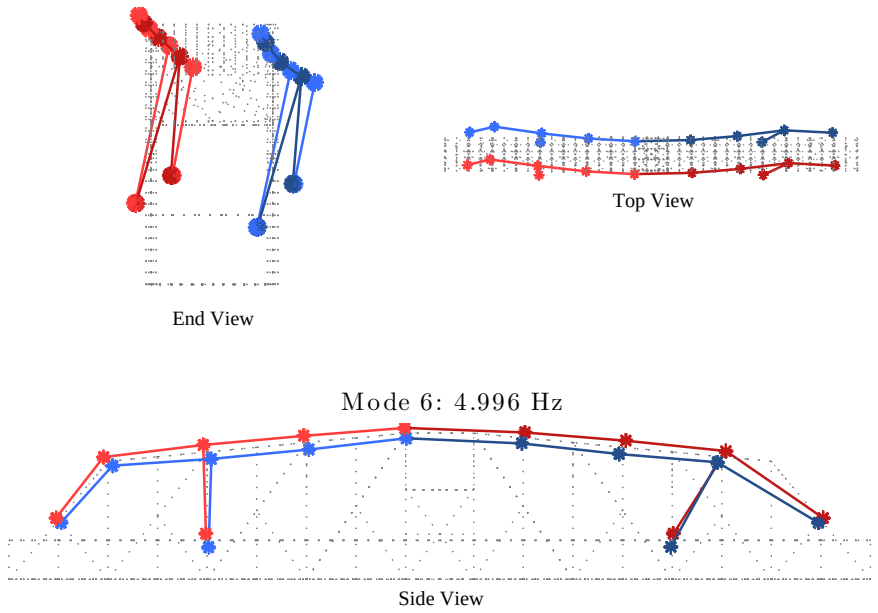

(b)

Figure 6.23: FEM Upstream Locked Mode 6 – Torsional: (a) all nodes, (b) abridged to measured nodes.

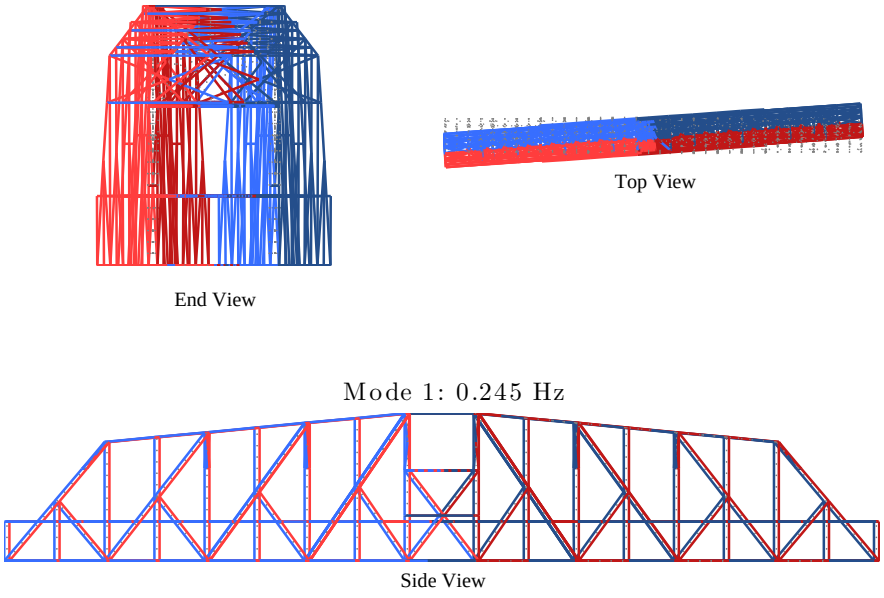

(a)

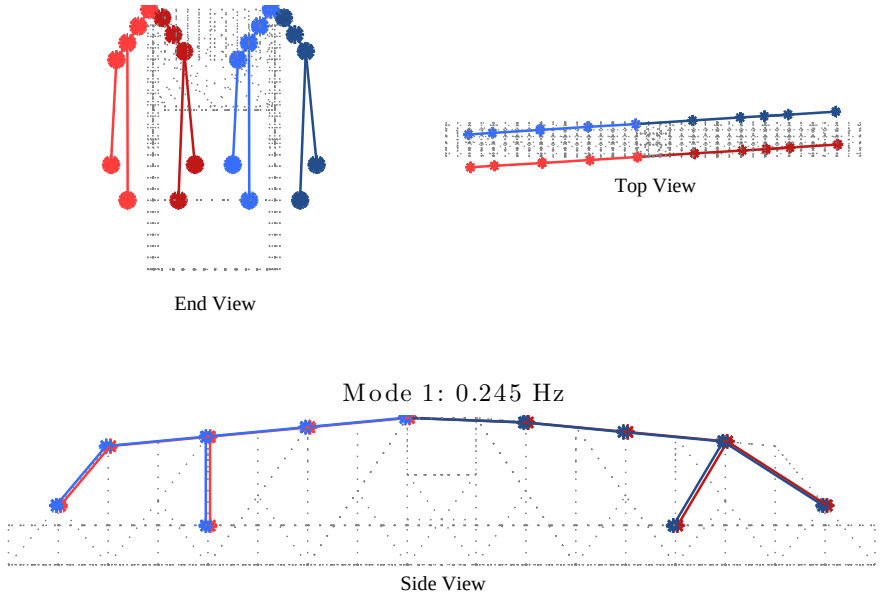

(b)

Figure 6.24: FEM Swung Open Mode 1 – Lateral Anti-Symmetric: (a) all nodes, (b) abridged to measured nodes.

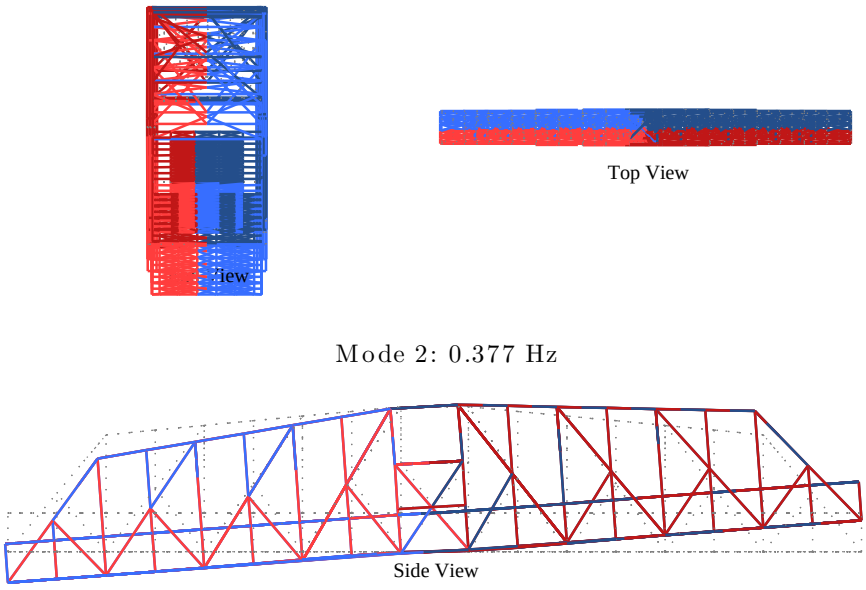

(a)

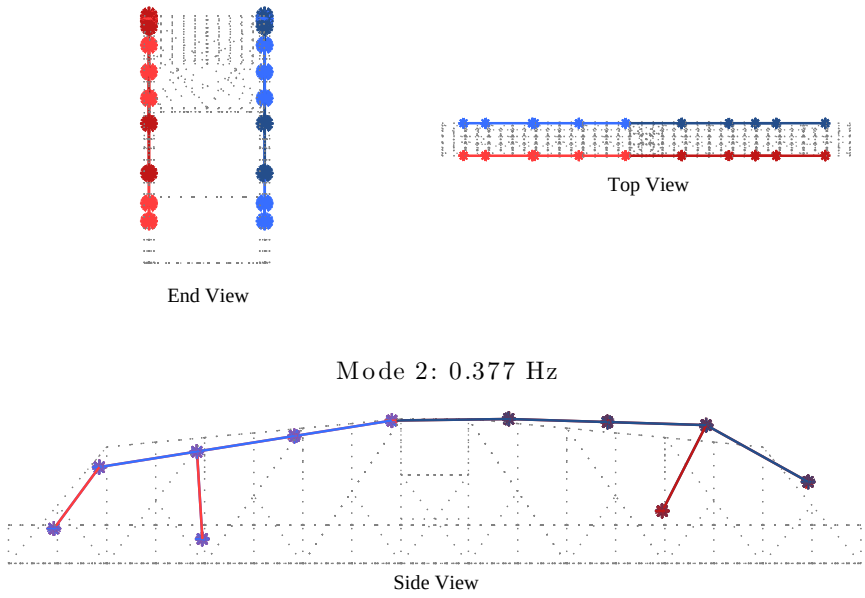

(b)

Figure 6.25: FEM Swung Open Mode 2 – Vertical Anti-Symmetric: (a) all nodes, (b) abridged to measured nodes.

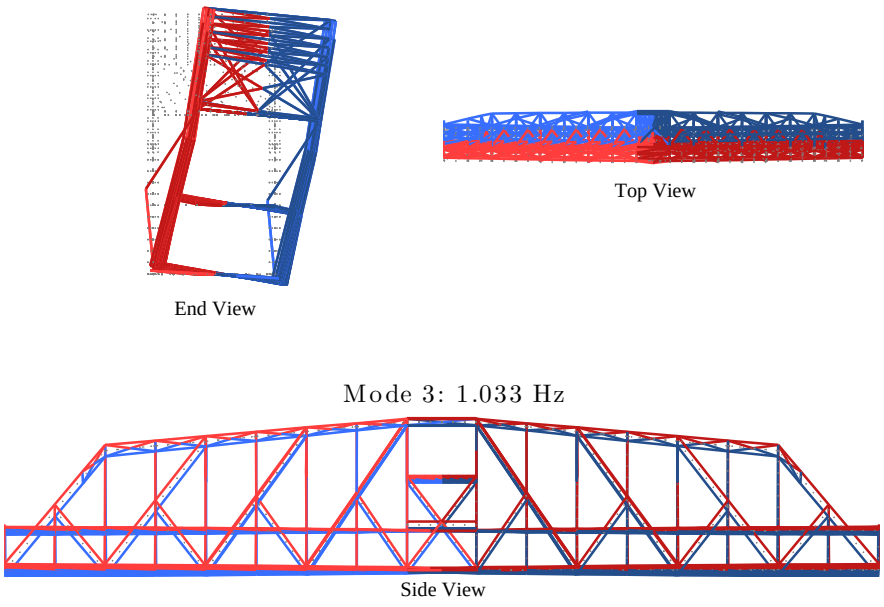

(a)

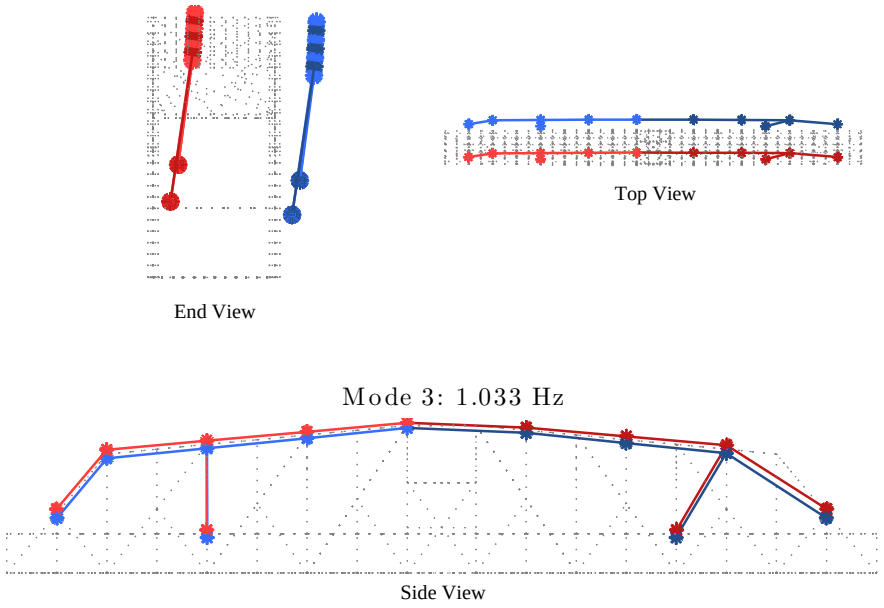

(b)

Figure 6.26: FEM Swung Open Mode 3 – Sway: (a) all nodes, (b) abridged to measured nodes.

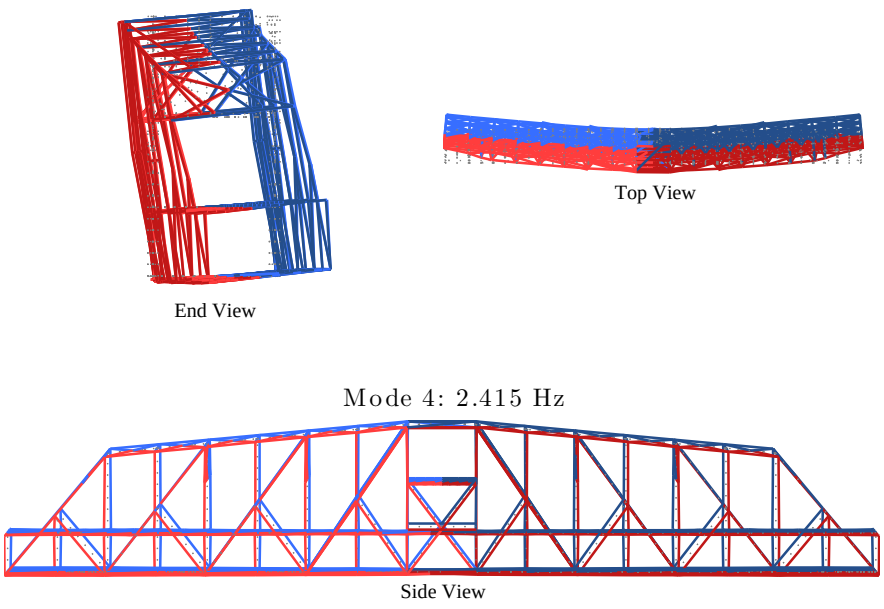

(a)

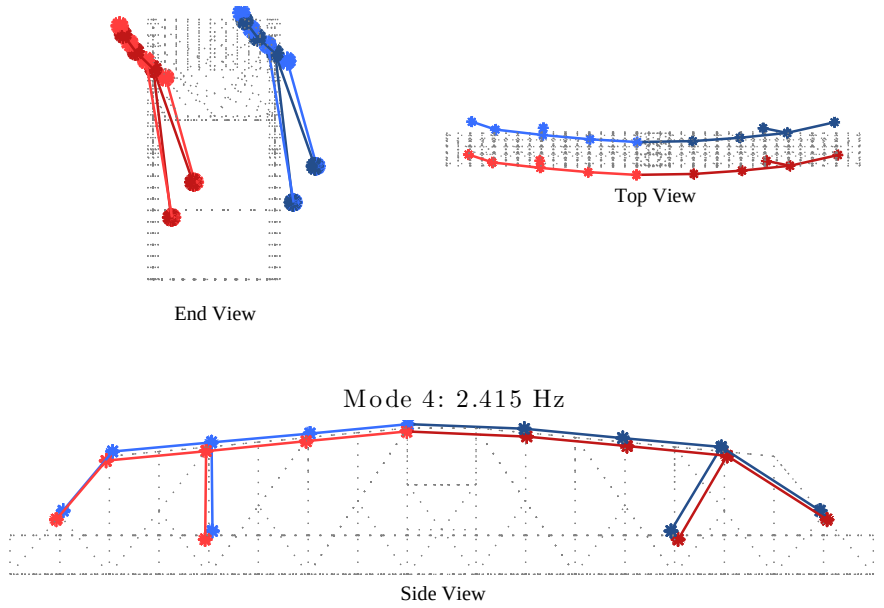

(b)

Figure 6.27: FEM Swung Open Mode 4 – Lateral Symmetric: (a) all nodes, (b) abridged to measured nodes.

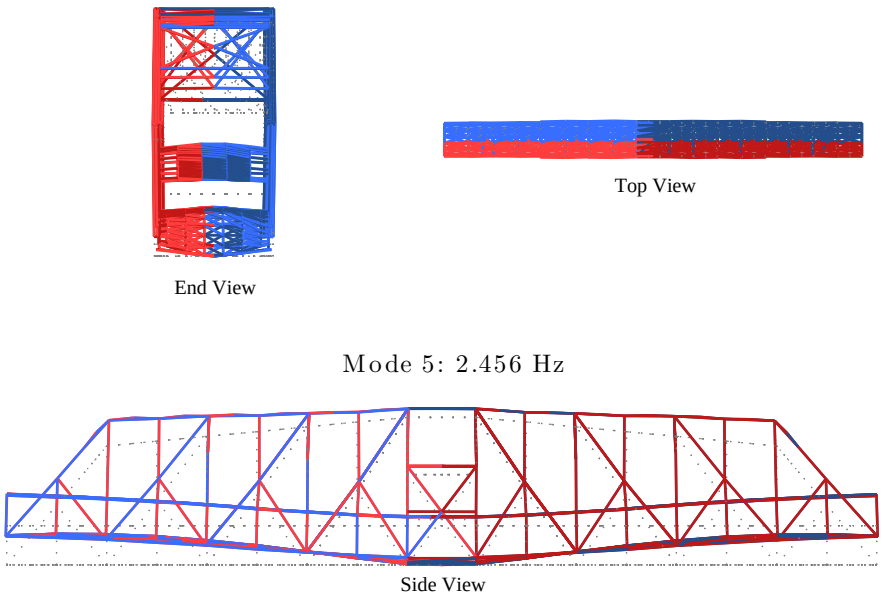

(a)

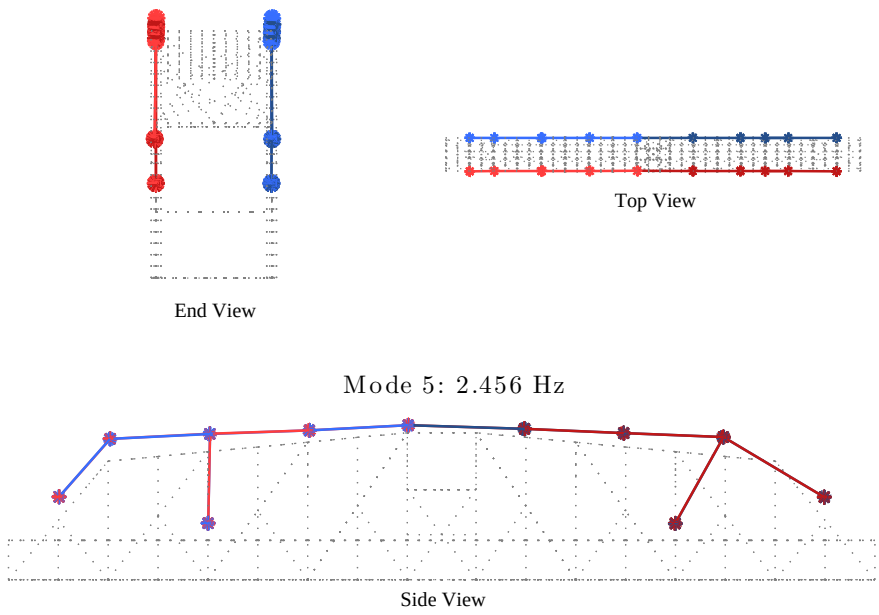

(b)

Figure 6.28: FEM Swung Open Mode 5 – Vertical Symmetric: (a) all nodes, (b) abridged to measured nodes.

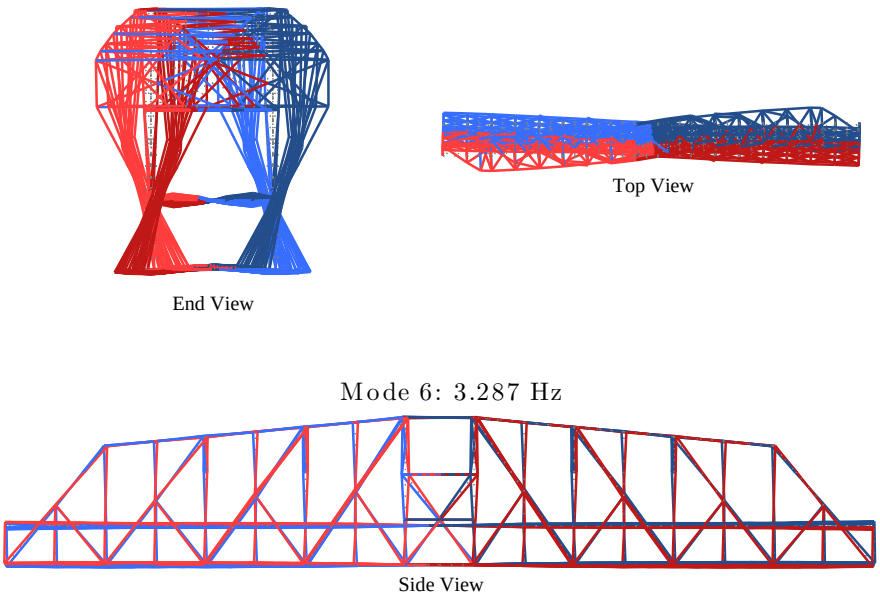

(a)

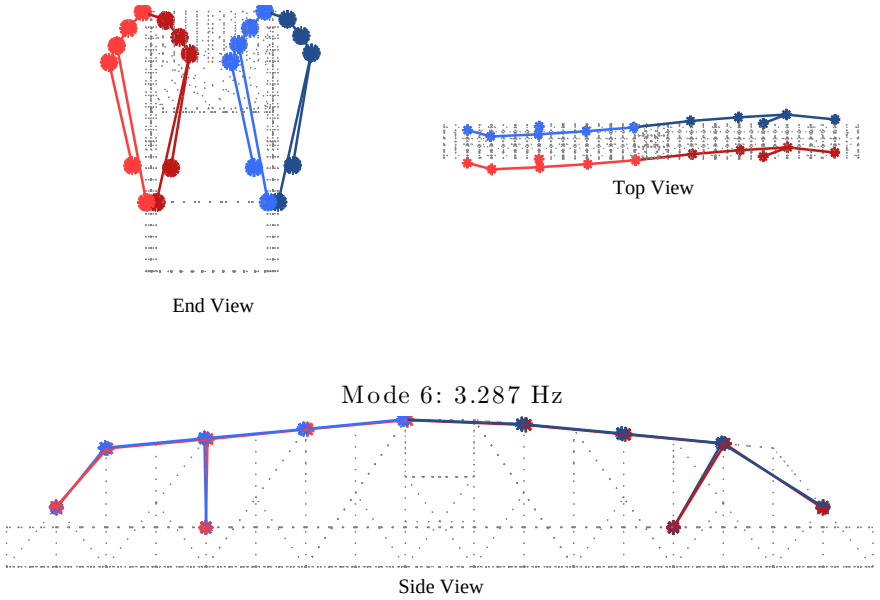

(b)

Figure 6.29: FEM Swung Open Mode 6 – Torsional: (a) all nodes, (b) abridged to measured nodes.

6.3.2 Spatially Aliased Modes

In addition to the identified modes, a number of modes theorized in the FE model could not be identified from the measured data, due to the limited sensor placements. A number of the theorized modes can alias as identifiable modes when they are abridged and normalized with respect to the measured degrees of freedom.

Similar to temporal aliasing as described in Section 5.1.1, spatial is when there are not enough measurement locations to properly identify a mode [112]. Thus a higher mode may "alias" as a lower mode because there are not enough sensors to describe its shape. For a beam, spatial aliasing occurs "when the wave number (k) of one mode exceeds the number (n) of sensors regularly spaced in that direction, the sensor output appears as generated by a mode with a lower wave number ($2n - k$) [113]." This statement assumes that the ends of the beam have no displacement and are included in the "regularly spaced" requirement and is thus similar to Equation (5.8).

To demonstrate the spatial aliasing potential in the model updating process, AutoMAC values were computed for the FE modes. The AutoMAC uses Equation (6.2) but uses just the FE modes in comparison against themselves. The matrix of AutoMAC values should have ones along its diagonal if the modes are all distinct from one another and zeros everywhere else. An off diagonal, non-zero term indicates that there are similarities between the two FE modes themselves.

Figures 6.30-6.32 show the computed AutoMAC values for the FE model visually where the color gradient is darkest at unity and white at zero. The (a) graph of the figures was computed using the modal data from all the displacement degrees of freedom for all nodes. As expected, the only MAC value of significance for each mode is the MAC value computed with itself which is unity by definition[4]. The (b) graphs of the figures were calculated only with those degrees of freedom measured using the wireless sensors mounted on the bridge. These MAC values show significant off diagonal terms indicating that spatial aliasing is possible for certain modes in the current wireless sensor layout. The MAC values in the figures were calculated without any added noise; added noise would increase the likelihood of spatial aliasing.

The two closed position have modes that are nearly identical in the abridged form. For example, in Figure 6.31(b) of the MAC values for the stairs locked downstream model, FE mode 7 and FE mode 10 are shown to have a high MAC value of 0.946. Therefore, these two modes in the finite element model, when the mode shape is abridged, are nearly identical. FE mode 7 is the identified Downstream Locked Mode 5 that was shown in Figure 6.16 and represents the first symmetric vertical bending mode. FE mode 10 is shown in Figure 6.33 for comparison. Notice that when all the nodes are plotted, the two modes look almost nothing alike. Identified Downstream Locked Mode 5 in Figure 6.16(a) has distinct displacement in both the truss and the deck in the expected vertical bending mode direction. Note that a secondary feature of the mode is the middle pinned joint of the sets of eye-bars are also involved in the mode, but the distinguishing feature is still the

[4]The upstream and downstream models have two MAC values that register off the diagonal. Modes 18 and 20 of both models are local modes for the cross bracing of the truss portals. They differ only in the symmetric and asymmetric movement of the center nodes and therefore have a high MAC value because only 2 out of the over 2000 degrees of freedom differ from each other.

vertical bending in the truss and deck. However, FE mode 10, when all nodes are plotted as in Figure 6.33(a), shows very little movement in the deck or truss and the primary feature of the mode is the amplitude of the middle joints of the eye-bar sets. Visually, the two modes are very different and only have a MAC value of 0.018 when all nodes are included. Regardless of these marked differences in the full nodal set, when the mode shapes are abridged to the measured nodes, Figures 6.16(a) and 6.33(a) are indistinguishable from one another.

Spatial aliasing, as illustrated here, can cause difficulty in performing model updating

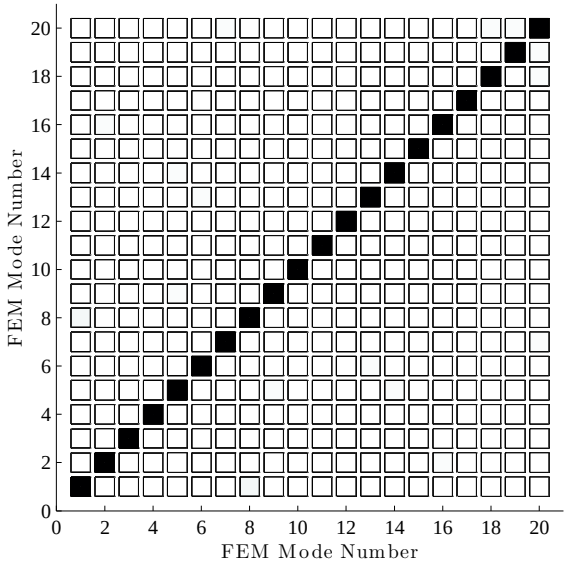

(a) AutoMAC that includes all FE nodes.

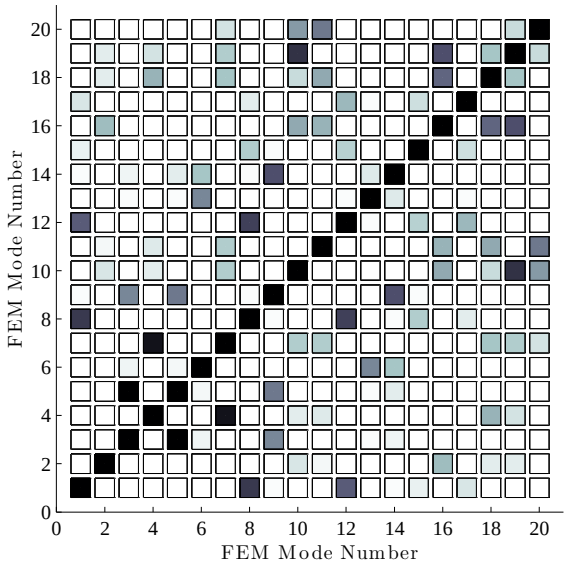

(b) AutoMAC simulating in the FE model only those nodes measured on the Rock Island Bridge.

Figure 6.30: AutoMAC for FE model in the swung open position.

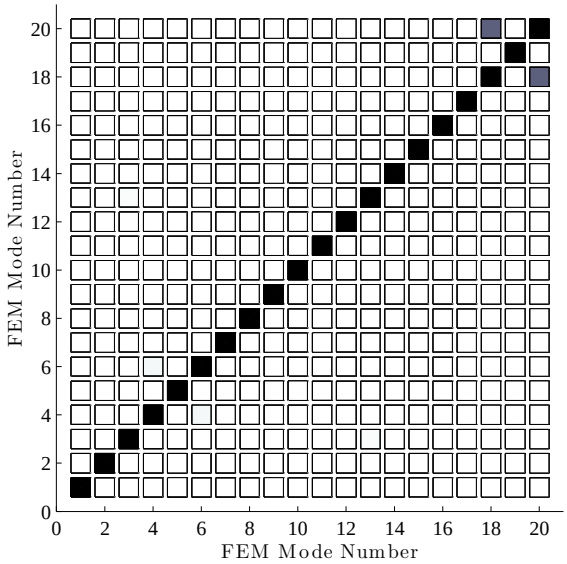

(a) AutoMAC that includes all FE nodes.

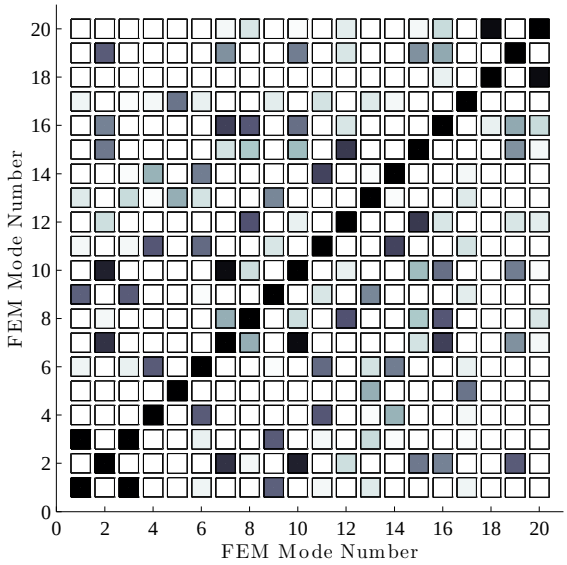

(b) AutoMAC simulating in the FE model only those nodes measured on the Rock Island Bridge.

Figure 6.31: AutoMAC for FE model in the stairs downstream locked position.

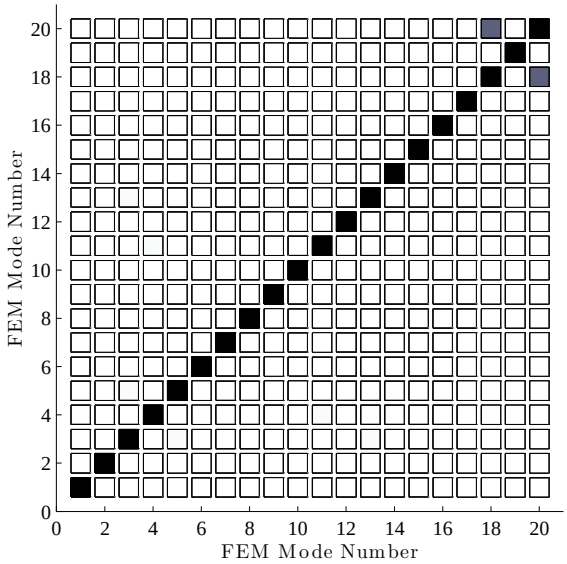

(a) AutoMAC that includes all FE nodes.

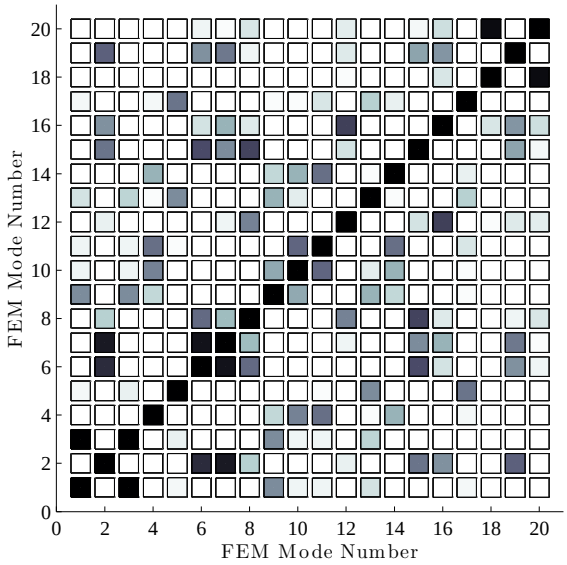

(b) AutoMAC simulating in the FE model only those nodes measured on the Rock Island Bridge.

Figure 6.32: AutoMAC for FE model in the stairs upstream locked position.

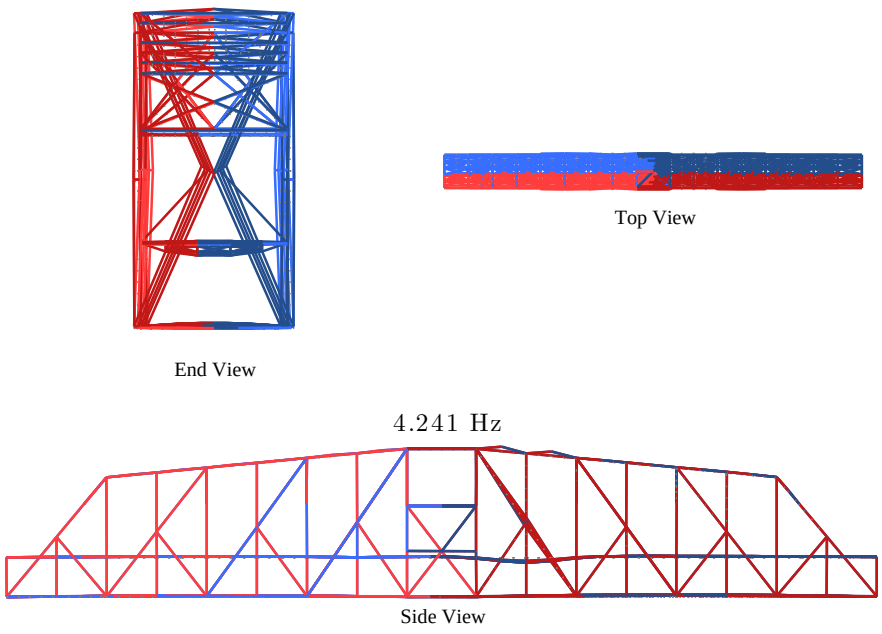

(a)

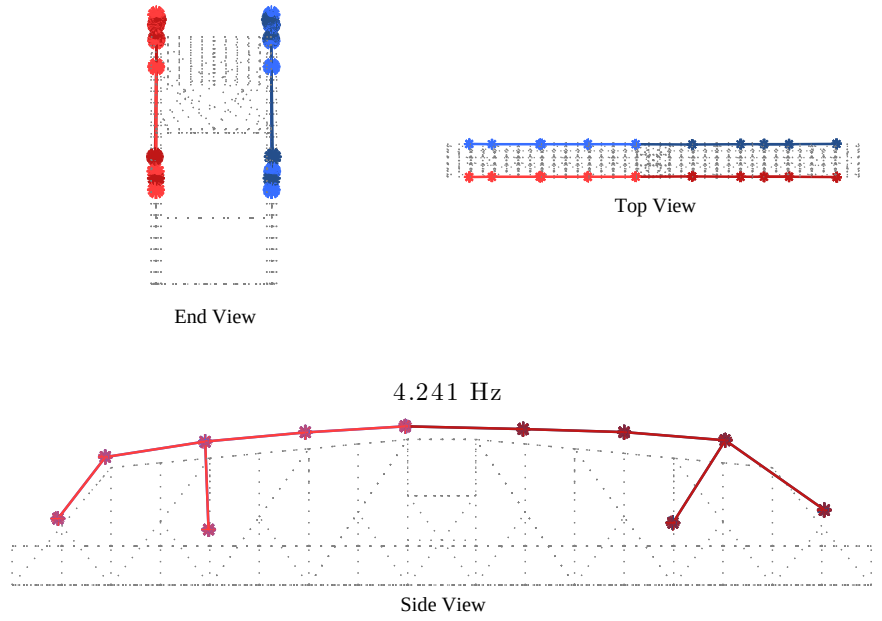

(b)

Figure 6.33: FEM mode shape that spatially aliases as Downstream Locked Mode 5 (a) all nodes, (b) abridged to measured nodes.

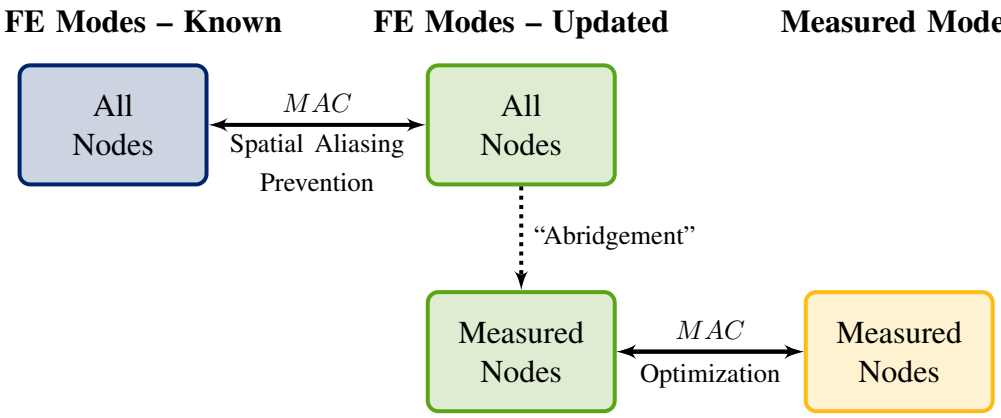

Figure 6.34: Flowchart showing the MAC value calculations used to prevent spatial aliasing and for use in the optimization objective function.

when the natural frequencies of the two modes that are aliased are close together. For downstream identified Mode 5 and downstream FE mode 10, the natural frequencies are 4.047 Hz and 4.241 Hz respectively. The upstream model's corresponding modes, FE modes 6 and 7 in Figure 6.32(b), have even closer natural frequencies. The first vertical bending mode of the upstream model has a natural frequency of 4.076 Hz while the that natural frequency of the mode that it aliases is 4.183 Hz. These modes are closer in the upstream position due to the slightly different parameters between the two FE models. Automatic optimization algorithms can encounter difficulty if the highest MAC of the measured and FE modes is the near mode that aliases. Assurances had to be made in the optimization routine that the program was optimizing the measured mode to the correct FE mode.

To allow for automatic optimization, an extra step was added to the routine to guarantee that spatial aliasing was not an issue. Spatial aliasing has to be dealt with prior to "downsampling" the FE mode shape at the measured locations for comparison to the measured mode shapes. Figure 6.34 contains a flow chart that shows how the model for each new parameter set is used to eliminate the problems caused by spatial aliasing. A set of known or desired mode shapes that uses all FE nodes is determined from the FE model prior to running the optimization routine. Then in the optimization routine, the mode shapes that correspond to the new parameter set are compared to the known mode shapes using the MAC value. Even if the natural frequencies of the modes change and they switch their order, the MAC value will identify the new FE mode that most closely represents the desired non-spatially aliased mode. Though the updated mode may differ slightly from the known mode, even when using all the FE nodes, the MAC values are close to unity and distinct from the close aliased modes. After identifying the modes to compare to the measured modes, the FE model can be abridged and the MAC value for use in the optimization routine calculated.

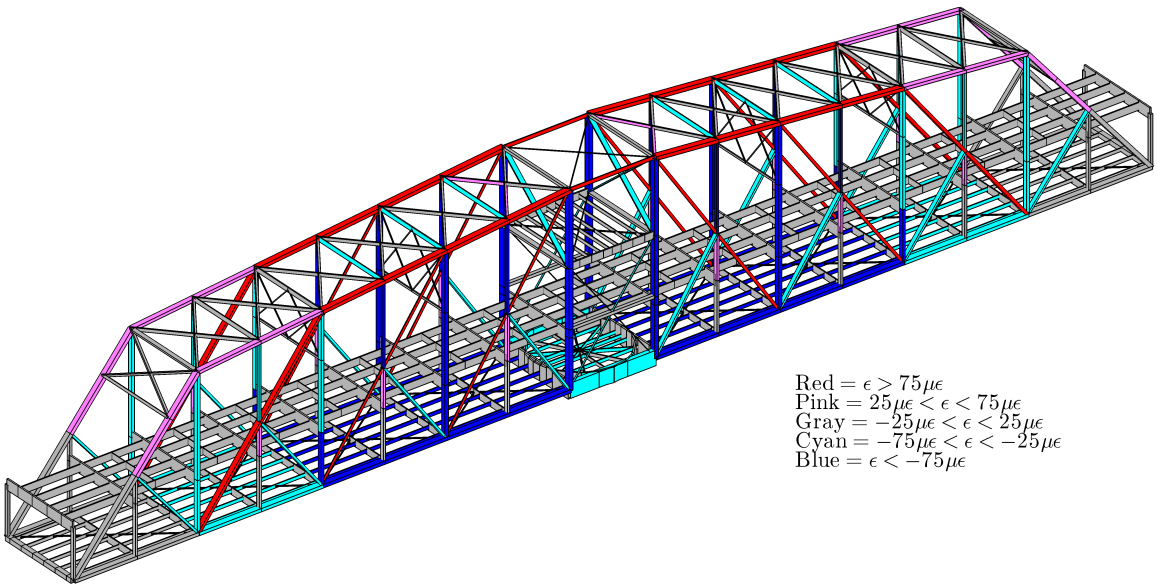

Figure 6.35: Strains in the swung open position.

6.4 Load Distribution and Strain Patterns

The finite element model can also be used to better understand the load distribution and expected strains in the physical structure. The axial strains for the gravity load conditions were computed for the swung open and closed[5] positions. The strains are presented graphically in Figure 6.35 for the swung position and Figure 6.36 for the closed position. The strains in the members have been color coded. The red members are those that have the highest tensile strains and those colored blue have the highest compressive strains. The gray members are those that have a low overall strain level and can be in either tension or compression.

In the swung position of Figure 6.35, tensile forces are greatest in the top chord and compression greatest in the bottom chord. The bridge exhibits a strain pattern that is typical of a cantilever beam. The load from the mass of the deck and truss is passed to the top chord through all the full width diagonals. The vertical post members are all in compression. Large numbers of both red members and blue members in Figure 6.35 indicate that the swung loading condition is the greatest load that these members typically experience.

In contrast, the closed position Figure 6.36 has very few dark red and blue members indicating a lower overall strain level. The addition of the two end boundary conditions allows the dead load of the bridge to be distributed among the three supports and not all carried back to the center turntable. The bridge exhibits a strain pattern typical of beams with the ends locked in place. In the closed position, the top chord is in compression and the bottom chord is now in tension. The L4-U6 and L6-U8 diagonals made of eye-bars remain in tension but the L0-U2 and L2-U4 diagonals have become compression members. The

[5]To simplify the model and discussion, a generic symmetric "closed" position is used here. The model uses an average of the upstream and downstream parameters.

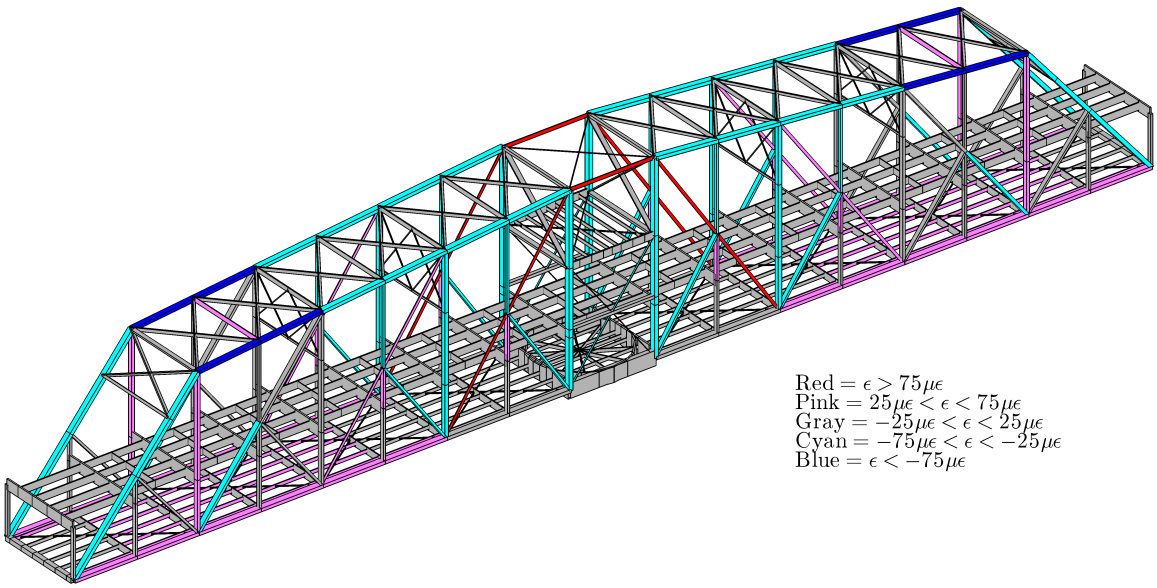

Figure 6.36: Strains in the downstream locked position.

fact that the L2-U4 diagonals have to carry tension in the swung position and compression in the locked positions accounts for these members not being made of eye-bars like the other two interior diagonals.

Though the strain patterns in the bridge positions are informative, they cannot be measured directly using any strain gage. Therefore, what is of interest is the change in strain ($\Delta\epsilon$) observed when the bridge transitions from one state to the next. Figure 6.37 shows a similar plot where the members have been colored according to the change in strain experience as the bridge transitions from the locked to swung state. Here, red represents those members that experienced the greatest positive change (i.e., an increase in tension or a transition from compression to tension) and the blue members are those that had the greatest negative change (i.e., an increase in compression or a transition from tension to compression). The entire upper chord and all the diagonals except the innermost set of eye-bars all experience increases in strain greater than 75 $\mu\epsilon$. The bottom chord from L4-L8 and the vertical post from L5-U5 experience the greatest decrease in strain in the transition from the locked to the swung position.

The plot of the $\Delta\epsilon$ values in Figure 6.37 reveals the locations that would yield large measurable changes in strain levels. Locations with larger measurable strain changes are better suited for measurement and monitoring. A small change to a member or the structure is more detectable in a member that has a large expected change in strain. Unfortunately, of the fiber optic strain sensor locations chosen by Chandler Monitoring Systems, the only instrumented members in the red or blue category are those mounted on the L4-M5 diagonal. The chosen sensor locations demonstrate that the monitoring of the swing events did not factor into the location selection process. Instead, the sensor locations were chosen to represent a geographic distribution on the structure, with a slight focus on the eye-bar diagonals.

Understanding the role of the members in the distribution of loads will be important in

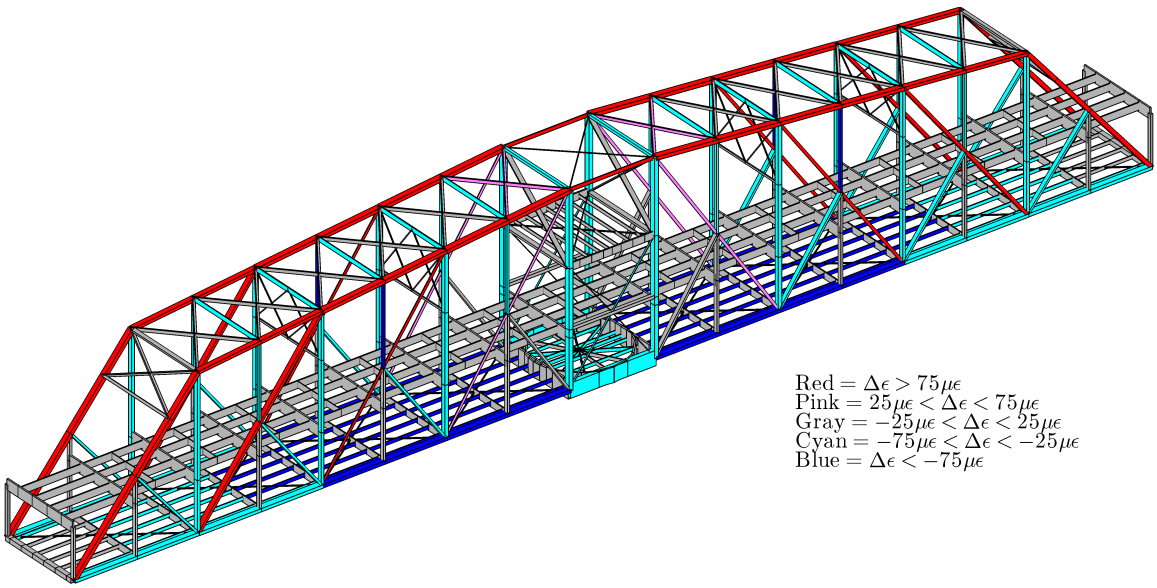

Figure 6.37: Change in strains due to the bridge unlocking at a swing event.

Section 10.2 where a method for determining the damage based on changes in the strain measurement will be developed. Plots similar to those presented here will be used to describe the effects of damage on the affected member and the rest of the structure.

6.5 Summary

A finite element model of the Rock Island Bridge, in all three of its positions, has been developed. The model was changed to account for new insights into the bridge's behavior as data was collected on the bridge. The effects of the deck on the stiffness of the floorbeams was accounted for and model updating performed using a genetic algorithm approach. An innovative method for accounting for spatial aliasing during the updating process was developed. Updating was performed on the model accounting for all three positions using both strain measurements and dynamic properties derived from acceleration measurements.

Chapter 7

SUPPLEMENTAL SENSOR SYSTEMS INSTALLED ON THE ROCK ISLAND ARSENAL GOVERNMENT BRIDGE

After the analysis of the fiber optic sensor systems discussed in Section 5.3, two additional sensor systems were installed to gain a more complete understanding of the operation and health of the Rock Island Arsenal Government Bridge. The first was a wireless smart acceleration monitoring system and the second was a USB digital compass.

7.1 Wireless Smart Sensor Network

Because the fiber optic accelerometers on the bridge were not sufficiently sensitive (see Section 5.4), a wireless smart sensor network (WSSN) was installed. The hardware, software, and sensor locations were chosen carefully as will be described in this section. After installation, data was collected and system identification performed to determine the dynamic properties of the bridge in each of its three positions.

7.1.1 WSSN Hardware and Software

A smart sensor node is an independent sensor platform that is self-powered[1] and contains its own microprocessor, memory, and radio for wireless communication. Wireless sensors have shown potential in some short term SHM applications [114–116] and the long term Jindo Bridge deployment [35, 117]. Researchers have produced many wireless sensor nodes [118] that have been designed for structural health monitoring and other purposes. These wireless systems do not require the large amounts of cabling needed for traditional sensor systems and are often easier to install. However, wireless sensor networks have their own set of challenges, such as synchronization and data loss [119], that have necessitated significant research to develop hardware and software solutions that are suitable for large scale SHM deployments.

The Rock Island Government Bridge WSSN deployment consists of twenty-two Imote2 sensor leaf nodes, an Imote2 gateway node, and a base station computer. Figure 7.1 shows two of the leaf sensors nodes in enclosures as they were installed on the Government Bridge. The interior of a senor node is shown in Figure 7.2. Figure 7.3 shows the gateway node and its enclosure as installed on the government bridge. Note that the gateway node has been equipped with a large, sensitive antenna to improve its communication abilities.

The Imote2 was developed by Intel to be a used in data intensive applications. To perform the complex calculations and store the data necessary for SHM applications, the Imote2 has

[1] Self-powered refers to not having to be plugged in and thus running on batteries. These batteries do not necessarily have to be recharged from solar or other sources to be considered self-powered

(a)

(b)

Figure 7.1: Two examples of the installation locations of the wireless sensors: (a) Node RT11 (b) Node LT02.

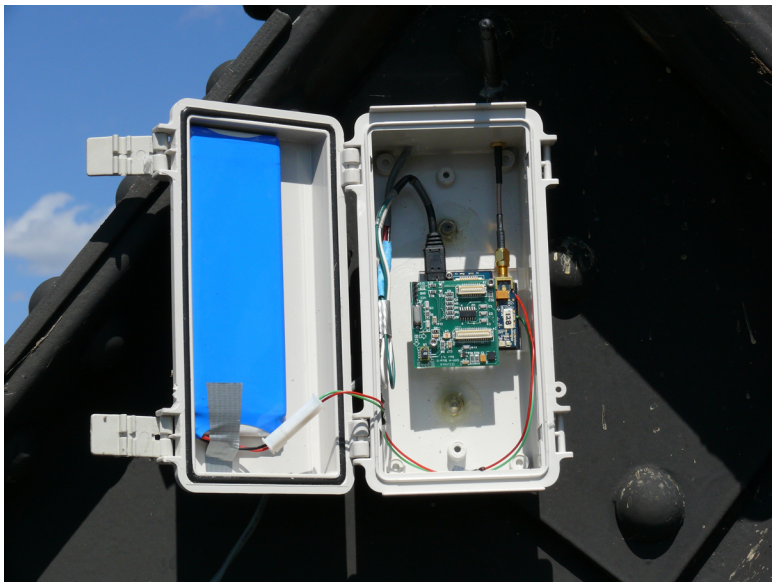

Figure 7.2: Inside the environmental closure of the installed Imote2 sensor nodes.

Figure 7.3: The gateway node installed outside the operator's house on the Government Bridge.

a high-performance processor, 256K SRAM, 32MB SDRAM, and 32MB FLASH. As seen in the evaluation of the fiber optic sensors in Section 5.4, the excitation level on the bridge in "ambient vibration" conditions is low and requires proper anti-aliasing filters. To achieve the necessary data quality, the Imote2s used in the Rock Island Government Bridge WSSN used a sensor board that measures triaxial acceleration (± 2 g) that was designed specifically for civil infrastructure monitoring projects [120]. The SHM-A sensor board has a 16–bit, four channel, analog–to–digital converter that provides anti-aliasing, selectable sampling rates, and customizable digital filters. The SHM-A sensor board can be seen stacked on top of the Imote2 in Figure 7.2.

The sensors are programmed with version 3.1 of the ISHMP (Illinois Structural Health Monitoring Project) Services Toolsuite. The ISHMP Services Toolsuite contains a number of services that can be used to create SHM applications for the Imote2 sensors [120]. The code provides the numerical methods necessary to perform system identification or other data processing functions. The ISHMP Services Toolsuite contains a continuous monitoring routine called `AutoMonitor` that runs autonomously once started. Within this autonomous monitoring framework, synchronized data is taken when predetermined acceleration thresholds are exceeded. The battery voltage and charging status of the sensors is also monitored so that the health of the WSSN is known.

The locations of the installed WSSN nodes are shown in Figure 7.4. The gateway node is located just outside the operator's house on the bridge and is connected to the base station computer via a USB cable that powers it as well as serving as its input/output port. The numbering system and the designation of left and right truss are the same as for the fiber optic sensors with the exception that the sensors on both trusses start with 01 and proceed upward instead of being sequentially numbered. Thus, while Strain R2 and Strain L19 are located across the railroad deck from each other and should therefore exhibit similar behavior, the numbering system does not make this fact immediately apparent. For the wireless sensors, RT02 and LT02 (where T stands for 'Truss' and helps differentiate them from the fiber optic sensors when referenced) are also across the rail deck from each other and the '02' in each designation helps clarify this fact without having to reference the location chart.

The sensor nodes are housed in plastic environmental enclosures and are powered with a rechargeable lithium polymer battery that is located in the lid of the sensor enclosures (see Figure 7.2). The battery is recharged with a solar panel that is external to the node and can be placed in a location that affords it the most light each day. The solar panel location for sensor RT11 can be seen in Figure 7.1(a). The sensors installed on the upper chords had their panels placed on top of the upper chord. The cable attaching sensor LT02 to its solar panel can be seen in Figure 7.1(b). The sensors are attached to the bridge using two strong magnets mounted underneath the enclosure and tied with steel cable around the bridge in the unlikely event that the magnets should become detached from the structure.

7.1.2 Sensor Location Selection

The selection of the sensor locations for the Rock Island Government Bridge, shown in Figure 7.4, was a result of several factors. The number of sensors available for permanent

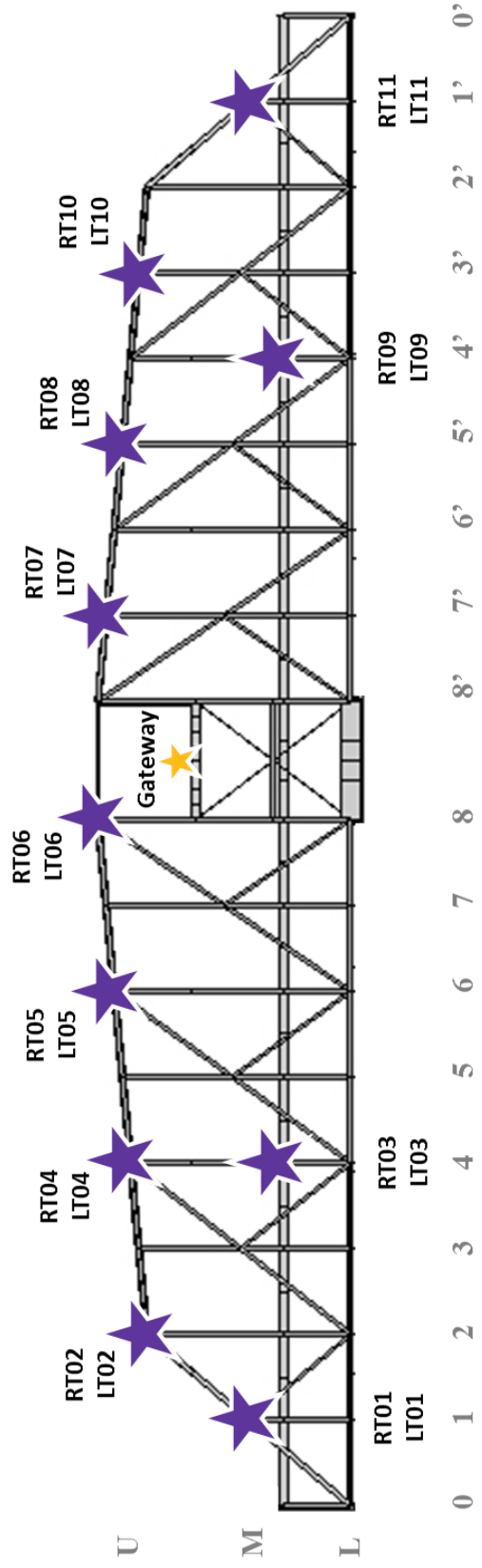

Figure 7.4: Location of the installed wireless acceleration nodes.

installation on the bridge was limited to the twenty-three that were used. There was also concern that pedestrians crossing the bridge might tamper with or be frightened by the presence of the sensor enclosure if the sensors were placed on the lower chords. This limited the placement of the sensors to the railroad deck and above. The upper chords were favored as it was considered the least vulnerable to damage from trains, critters, or birds[2].

The goal of installing this supplementary WSSN was to provide a way to determine the natural frequencies and mode shapes bridge. With a limited number of sensors, spatial aliasing becomes a concern. Spatial aliasing has been an issue in the system identification of many floor and deck structures that exhibit more of a two dimensional mode shape [121–125].

However, the Rock Island Bridge exhibits complex three dimensional mode shapes. Therefore, the location of the sensors was determined to ensure that spatial aliasing for the lowest modes was avoided. The finite element model of the bridge and the preliminary validation of the model (see Section 6.2), indicated that many of the first modes of the structure had both symmetric and anti-symmetric shapes. To differentiate these mode shapes, sensors were required on all four quadrants of the structure. Though the upper chords were favored as stated above, it was also necessary to install sensors at the railroad deck level. The sensors at the lower levels helped determine if the top and bottom of the bridge were moving symmetrically or anti-symmetrically. The model showed that these sensor locations would be sufficient to avoid spatial aliasing for the first lateral and vertical modes in both the symmetrical and anti-symmetrical forms.

7.1.3 System Identification

After installation, data was collected to determine the effectiveness of the system. Figure 7.5 shows the triaxial acceleration for a typical node (RT01) on the Government Bridge. The data in Figure 7.5 was sampled at 50 Hz for ten minutes while the bridge was closed in the downstream position and subjected to only vehicular traffic. The noise floor in the data collected from the WSSN is sufficiently small to see the accelerations caused by vehicles as they cross the bridges. The data also does not display any obvious quantization nor have any aliasing issues.

After confirming that the WSSN could collect data of sufficient quality for SHM purposes, a series of data was collected with the express purpose of performing a system identification of the bridge. For five days, the WSSN, the fiber optic strain system, and the digital compass that will be discussed in Section 7.2, recorded data simultaneously. The wireless accelerometers were programmed to take data no more than ten times daily when it detected more than 20 mg of acceleration present. The sample rate was set to 100 Hz and a low pass, anti-aliasing filter was used at 40 Hz. After collecting the data, the strain and compass records were used to determine the bridge position and loading (train or no train) for all the acceleration records. The acceleration records were segmented [126] according

[2]Seagulls, pelicans, cranes, and other waterfowl are common sights at the bridge, but they do not spend much time perched on the bridge itself. Eagles nest near the bridge that deter most birds from staying too long. The regular passage of trains on the bridge and the vibrations they cause also discourage nesting.

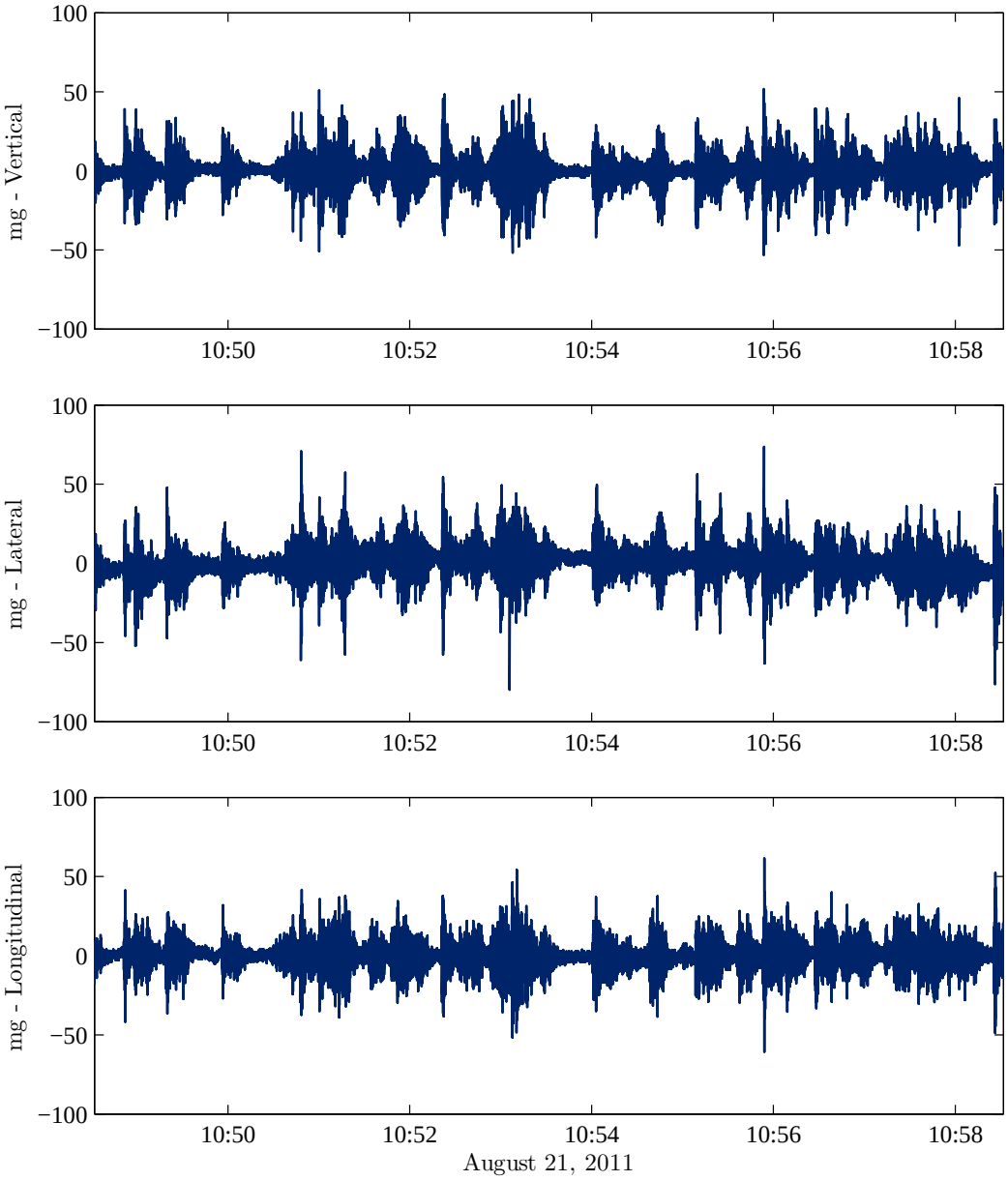

Figure 7.5: Triaxial acceleration recorded for sensor RT01.

to the bridge position and whether a train passed during the record. Segments with train loadings were excluded from the system identification because the mass of the train was significant enough to alter the identified modal parameters. Likewise, when the bridge was in the fully open position and not actually rotating, not enough excitation existed to identify the modal parameters of the structure. While the bridge was actually moving, the rotation mechanism of the chains and wheels caused sufficient excitation.

Orientation Correction

To improve the quality of data, the data was processed to correct for any misalignment present in the sensors [126]. As seen in Figure 7.1(b), despite best efforts, some sensors were not perfectly aligned with the intended member axes. Though these misalignments are small, any improvement in the accuracy of the measurements is helpful in the system identification of the bridge. As mentioned in Section 3.4.1, tilt measurements in MEMS applications are determined using triaxial accelerations that can detect the constant presence of gravity. Therefore, the tilt of the installed wireless sensors was determined using the on board accelerometers and any needed corrections were made.

The process of corrections is essentially a three dimensional change of axis transformation of the current sensor axis into the global bridge axes [127]. To do this transformation, the orientation of the sensor in the bridge/gravitational axes system needs to be determined. The "attitude"[3] of the objects is typically described in terms of the Euler angles: pitch (θ), roll (ϕ), and yaw (ψ). In terms of the Euler angles, the transformation matrix (R_{xyz}) from the bridge coordinate system to the sensor coordinate system can be determined to be:

$$R_{xyz}\left(\psi,\phi,\theta\right) = \begin{pmatrix} \cos\psi\cos\theta + \sin\theta\sin\phi\sin\psi & \cos\phi\sin\psi & \cos\theta\sin\phi\sin\psi - \sin\theta\cos\psi \\ -\cos\theta\sin\psi + \cos\psi\sin\theta\sin\phi & \cos\phi\cos\psi & \cos\psi\cos\theta\sin\phi + \sin\theta\sin\psi \\ \cos\phi\sin\theta & -\sin\phi & \cos\theta\cos\phi \end{pmatrix} \tag{7.1}$$

Using the above transformation matrix, the measured gravitational acceleration in each of the three accelerometers can be determined. Using α, β, and γ to represent the direction of gravity in each of the sensors principal axes and given that, in the bridge coordinate system, gravity can be represented by the vector $[0,0,-1]^{\mathrm{T}}$ g, the measured gravity in each axis is:

$$\begin{pmatrix} \alpha \\ \beta \\ \gamma \end{pmatrix} = R_{xyz}\left(\psi,\phi,\theta\right)\begin{pmatrix} 0 \\ -1 \\ 0 \end{pmatrix} = \begin{pmatrix} -\cos\phi\sin\psi \\ -\cos\phi\cos\psi \\ \sin\phi \end{pmatrix} \tag{7.2}$$

In this formulation, α, β, and γ are determined from the acceleration measurements and the Euler angles that are unknown. Solving the system of equations in Equation7.2 can

[3] In aerospace applications, attitude is the term used to describe a vehicle's orientation in space [127]. In this context, the attitude is describing the individual sensor as the assumption is that the bridge is aligned to the gravitational reference axes used in determining attitude.

determine two of the three Euler angles – roll (ϕ) and yaw (ψ) – as shown below.

$$\psi = \tan^{-1}\left(\frac{\alpha}{\beta}\right) \qquad -\pi < \psi < \pi \tag{7.3}$$

$$\phi = \tan^{-1}\left(\frac{\gamma}{\sqrt{\alpha^2+\beta^2}}\right) \qquad -\frac{\pi}{2} < \phi < \frac{\pi}{2} \tag{7.4}$$

To solve for the third Euler angle – pitch (θ) – additional information in the form of the relationship between the sensor and the member on which it is mounted. A vector normal to the surface of the member should coincide with the z–axis of the sensor node. Therefore, considering vector $[a, b, c]^{\mathrm{T}}$ to be a vector normal to the member surface and $[0, 0, 1]^{\mathrm{T}}$ to be the z–axis of the sensor, the relationship between the two is:

$$\begin{pmatrix} 0 \\ 0 \\ 1 \end{pmatrix} = R_{xyz}\left(\psi, \phi, \theta\right) \begin{pmatrix} a \\ b \\ c \end{pmatrix} \tag{7.5}$$

To solve Equation (7.5) for a, b, and c, it is necessary to multiply by R_{xyz}^{-1}. Because R_{xyz} is orthonormal, its inverse is equal to its transpose and Equation (7.5) can therefore be rewritten as follows.

$$\begin{pmatrix} a \\ b \\ c \end{pmatrix} = R_{xyz}^{-1}\left(\psi, \phi, \theta\right) \begin{pmatrix} 0 \\ 0 \\ 1 \end{pmatrix} = \begin{pmatrix} \cos\phi \sin\theta \\ -\sin\phi \\ \cos\theta\cos\phi \end{pmatrix} \tag{7.6}$$

Solving the above system of equations for θ yields an equation for determining the pitch of the sensors.

$$\theta = \tan^{-1}\left(\frac{a}{c}\right) \qquad -\pi < \theta < \pi \tag{7.7}$$

Therefore, using the knowledge of the sensor's installation location, the measured gravitational response from the triaxial accelerometers, and Equations 7.3, 7.4, and 7.7, the complete attitude of the sensor can be determined. These values can then be substituted into Equation (7.1) to create the transformation matrix that will transform the attitude of the sensors to be in the bridge coordinate system.

Using collected acceleration data, the attitude of all the sensors was determined. As seen in Table 7.1, the attitudes were never more than 6.2° off from the expected attitude and typically the error was significantly less. Transforming the measured accelerations into the global bridge coordinate system improved the correlation of the identified modal parameters and those predicted by the FE model [126].

Frequency Domain Decomposition

The system identification of the Government Bridge was carried out using the frequency domain decomposition (FDD) method [128]. The FDD method is an output-only system identification method that assumes the structural excitation to be broad-band. Figure 7.6,

Table 7.1: Expected attitude and actual attitude for wireless smart sensors.

	Roll (ϕ) (deg.)		Pitch (θ) (deg.)		Yaw (ψ) (deg.)	
Sensor	Expected	Actual	Expected	Actual	Expected	Actual
LT01	0.00	-2.34	0.00	0.00	-90.00	-92.88
LT02	-5.43	-3.15	125.95	125.95	0.00	0.40
LT03	0.00	—	0.00	—	-90.00	—
LT04	-5.43	-5.95	90.00	90.00	0.00	4.11
LT05	-5.43	-8.33	90.00	90.00	0.00	1.83
LT06	-5.43	-7.60	54.05	54.05	0.00	7.01
LT07	-5.43	-4.43	-90.00	-90.00	-180.00	-179.81
LT08	-5.43	-5.50	-90.00	-90.00	-180.00	-177.28
LT09	0.00	-3.10	0.00	0.00	-90.00	-88.53
LT10	-5.43	-6.13	-90.00	-90.00	-180.00	-175.40
LT11	0.00	-5.27	0.00	0.00	-90.00	-87.95
RT01	0.00	-6.11	180.00	180.00	-90.00	-85.32
RT02	-5.43	-7.95	54.05	54.05	-180.00	-177.20
RT03	0.00	-6.88	180.00	180.00	-90.00	-89.28
RT04	-5.43	-6.36	90.00	90.00	-180.00	-178.18
RT05	-5.43	-4.01	90.00	90.00	-180.00	-176.51
RT06	-5.43	-6.81	125.95	125.95	-180.00	-177.60
RT07	-5.43	-4.04	-90.00	-90.00	0.00	0.00
RT08	-5.43	-5.62	-90.00	-90.00	0.00	4.86
RT09	0.00	-2.66	180.00	180.00	-90.00	-90.94
RT10	-5.43	-10.89	-90.00	-90.00	0.00	6.89
RT11	0.00	1.47	180.00	180.00	-90.00	-91.52

Sensor LT03 was not responsive during data collection [126].

Table 7.2: Identified natural frequencies: locked stairs downstream position.

Mode	Description	Nat. Freq. (Hz)	Std. Dev.
1	Sway	1.649	0.017
2	Lateral – anti-symmetric	1.930	0.020
3	Lateral – symmetric	3.110	0.026
4	Torsional	3.547	0.036
5	Vertical – anti-symmetric	4.061	0.029
6	Vertical – symmetric	4.305	0.024

shows the singular values of the bridge as computed during the FDD method. The first singular value of the cross-spectral density matrix represents the energy content of the dominant motions; therefore, the peaks of the first singular values estimate the natural frequencies. The left singular vector of the first singular value at the peak frequencies corresponds to the mode shape. The first singular values can contain peaks that represent either genuine modal peaks or noise peaks.

The second singular value can be used to help distinguish actual modes from noise modes. If, at a peak, the magnitude of the first and second singular values are similar, then the peak contains closely-spaced modes that are difficult to identify separately. In Figures 7.6(a) and 7.6(b), the fifth peaks have first and second singular values that are similar in magnitude indicating closely-spaced modes at that frequency. However, the FE model indicates that the fifth peak is actually a noise mode.

In looking at the singular values plotted in Figure 7.6, the peaks show expected behavior. The two closed positions are very similar in the location, size and number of peaks. Note that both have a set of "twin" peaks below 2 Hz that represent a symmetric and anti-symmetric pair. A similar feature is observed above 4 Hz. The singular value peaks in the swung open position (Figure 7.6(c)) have lower frequencies and the twin peaks are no longer present. This change is expected due to the changes in boundary conditions that occurs when the bridge swings open.

The FDD method identified six natural frequencies and the associated modes from collected data for each of the three bridge positions: locked downstream, locked upstream, and swung open [126]. The modes derived from each of the data segments were averaged together for each bridge position. There was not enough data to determine any environmental effects on the natural frequencies and mode shapes of the bridge. Tables 7.2, 7.3, and 7.4 contain the identified natural frequencies and the standard deviations for each position.

In looking at the natural frequencies in Tables 7.2 and 7.3 representing the downstream and upstream locked positions respectively, the first four modes are generally the same. Figure 7.7 shows the ratio between the two positions. The 95% confidence level has also been computed and plotted for these ratios based on the standard deviations associated with the natural frequencies. The first four modes are statistically the same to the 95% confidence level as the bounds encompass the singular value. However, the last two modes (the vertical modes) of the bridge are statistically different. The difference in the natural frequencies of the two vertical modes indicates that the locking mechanisms provide more stiffness in the vertical direction when the bridge is locked upstream than they do when the

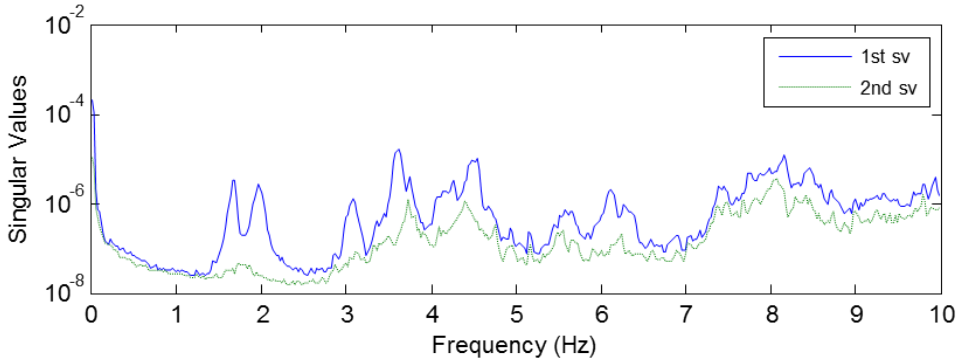

(a)

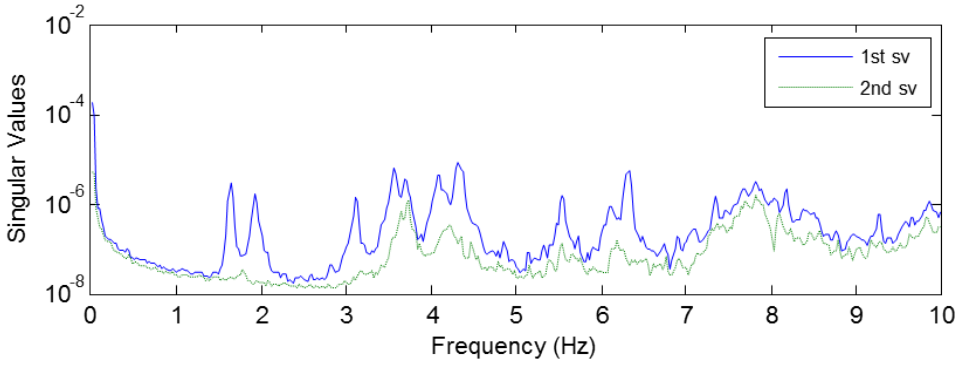

(b)

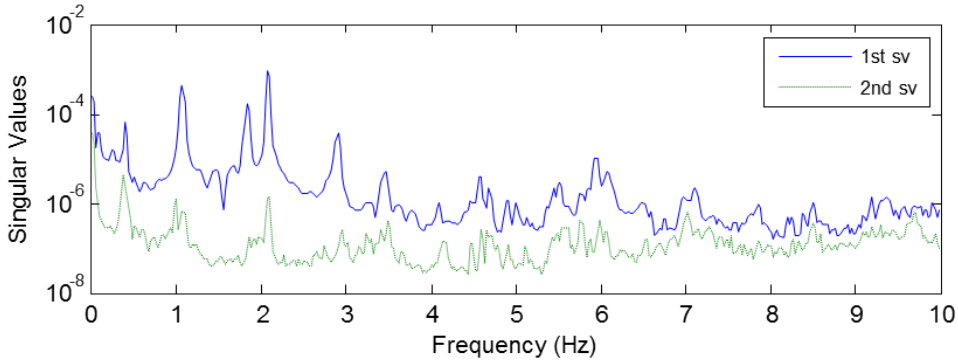

(c)

Figure 7.6: Singular value decomposition for the (a) locked stairs upstream, (b) locked stairs downstream, and (c) swung open positions.

Table 7.3: Identified natural frequencies: locked stairs upstream position.

Mode	Description	Nat. Freq. (Hz)	Std. Dev.
1	Sway	1.654	0.033
2	Lateral – anti-symmetric	1.958	0.018
3	Lateral – symmetric	3.129	0.032
4	Torsional	3.600	0.028
5	Vertical – anti-symmetric	4.275	0.032
6	Vertical – symmetric	4.461	0.044

Table 7.4: Identified natural frequencies: swung open position.

Mode	Description	Nat. Freq. (Hz)	Std. Dev.
1	Lateral – anti-symmetric	0.244	0.001
2	Vertical – anti-symmetric	0.342	0.042
3	Lateral – symmetric	1.050	0.042
4	Sway	1.856	0.024
5	Vertical – symmetric	2.092	0.014
6	Torsional	2.922	0.014

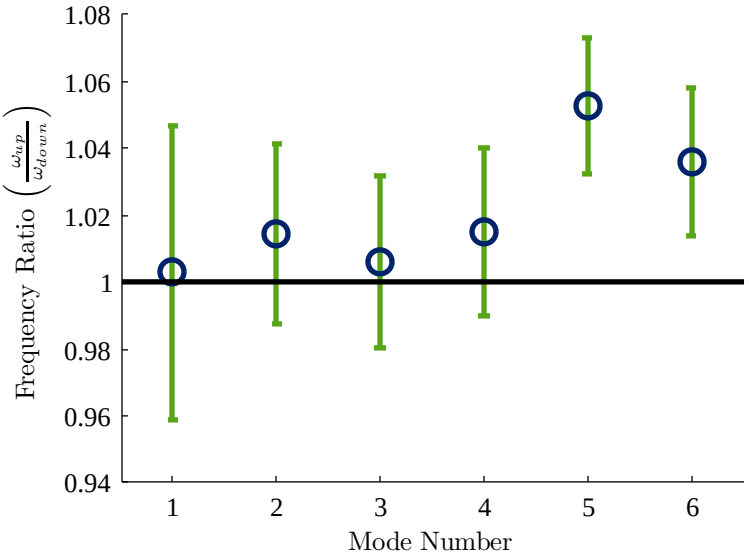

Figure 7.7: Ratio of locked stairs upstream and stairs downstream natural frequencies with 95% confidence limits.

bridge is in the downstream position. The existence of the difference in natural frequencies is not surprising as it confirms the observations of the strain data presented in Section 5.5. The results of the model updating optimization discussed in Section 6.2.3 also confirm this observation. The optimal values for the stiffness of the vertical end springs were indeed determined to be greater in the upstream position.

The descriptions associated with each natural frequency in Tables 7.2, 7.3, and 7.4 are intended to provide a general idea of the dominant behavior of each mode. Figures 7.8–7.25 illustrate the measured mode shapes. The "stick" drawings of the mode shapes in these figures are comparable to the FE mode shapes that have been reduced to show just the measured nodes in Figures 6.12(b)–6.29(b). In looking at the measured mode shapes, a few nodes have zero amplitude. These nodes represent sensor nodes that had temporary communication difficulties during data acquisition.

7.1.4 Conclusions

A wireless smart sensor network has been installed on the Rock Island Bridge. The WSSN consisting of twenty-two Imote2 sensor nodes has been used to successfully collect acceleration data from the bridge in all three of its positions. The data has been processed, including attitude corrections, and the frequency domain decomposition method has been used to determine the natural frequencies and mode shapes for the bridge. It was these modes and natural frequencies that were used to perform the model updating of the finite element model created for the bridge. Observations of the natural frequencies and mode shapes confirm that the bridge has three distinct positions that need to be considered in determining whether any measured value has changed.

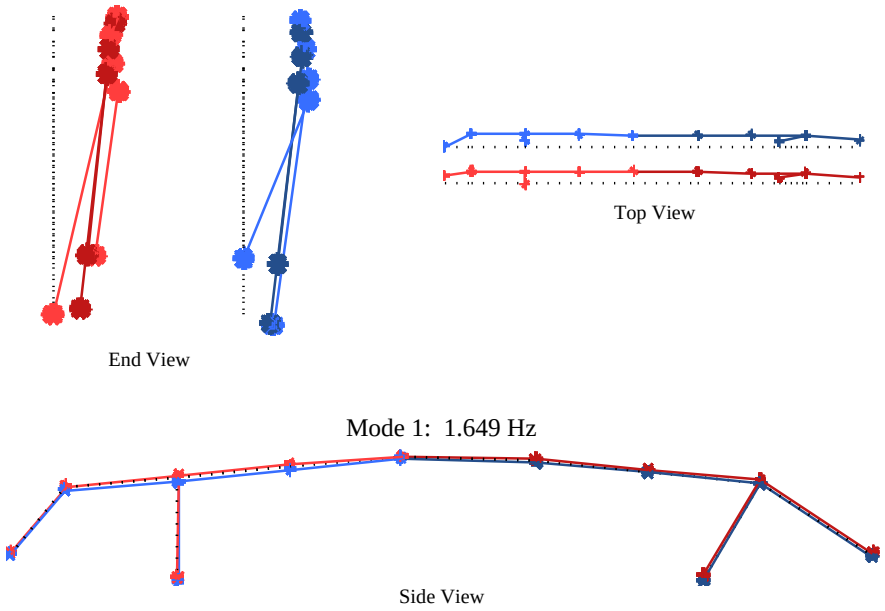

Figure 7.8: Measured mode shape: Locked Downstream position, Mode 1 – Sway.

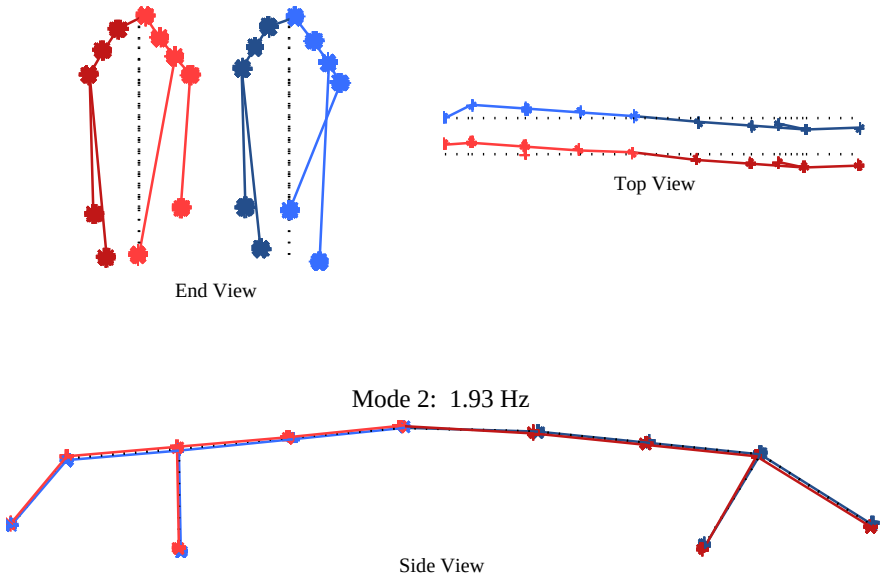

Figure 7.9: Measured mode shape: stairs downstream position, Mode 2 – Lateral Anti-Symmetric.

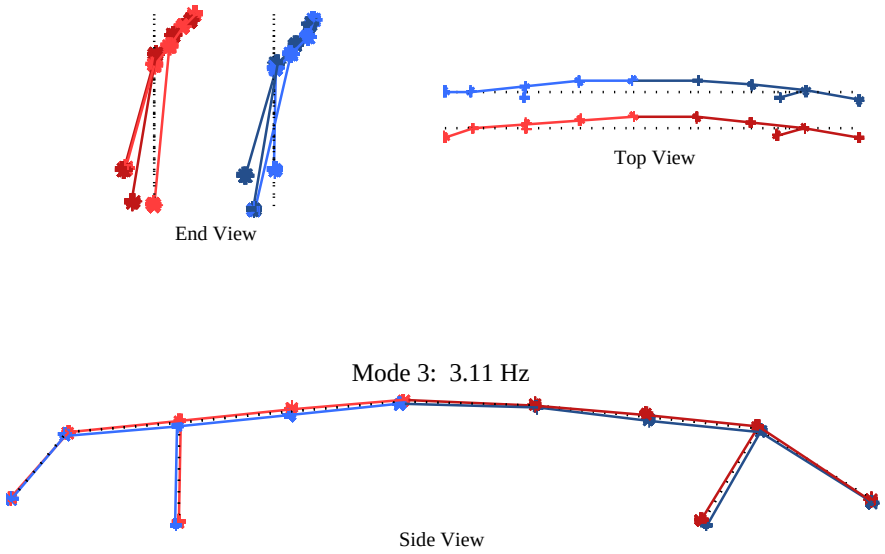

Figure 7.10: Measured mode shape: stairs downstream position, Mode 3 – Lateral Symmetric.

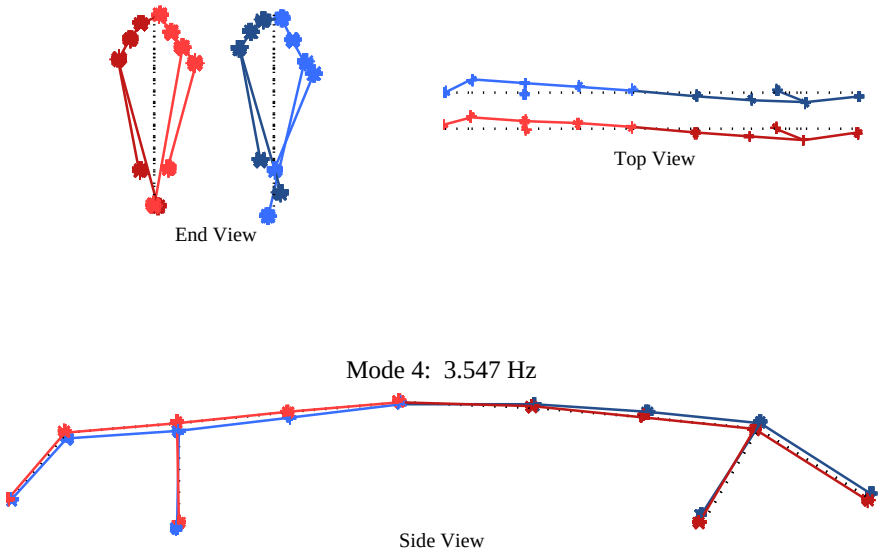

Figure 7.11: Measured mode shape: stairs downstream position, Mode 4 – Torsional.

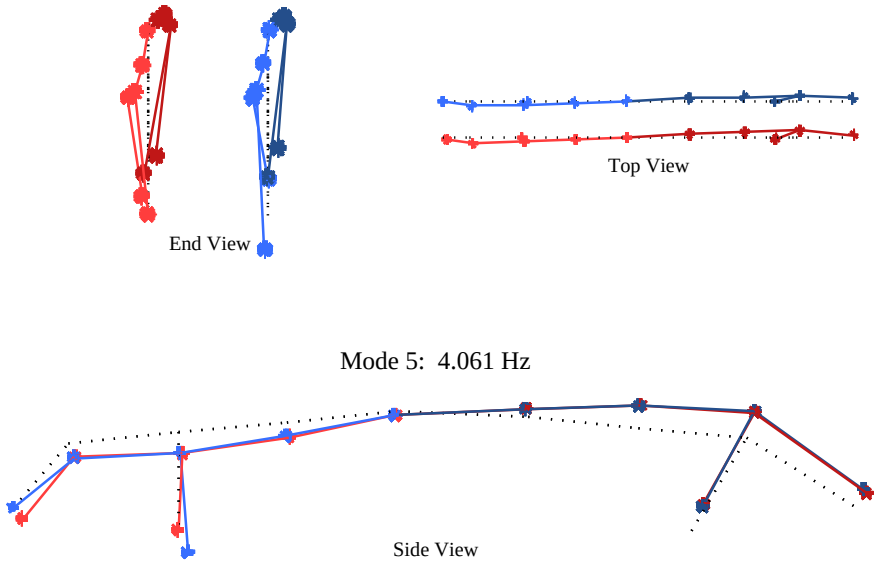

Figure 7.12: Measured mode shape: stairs downstream position, Mode 5 – Vertical Anti-Symmetric.

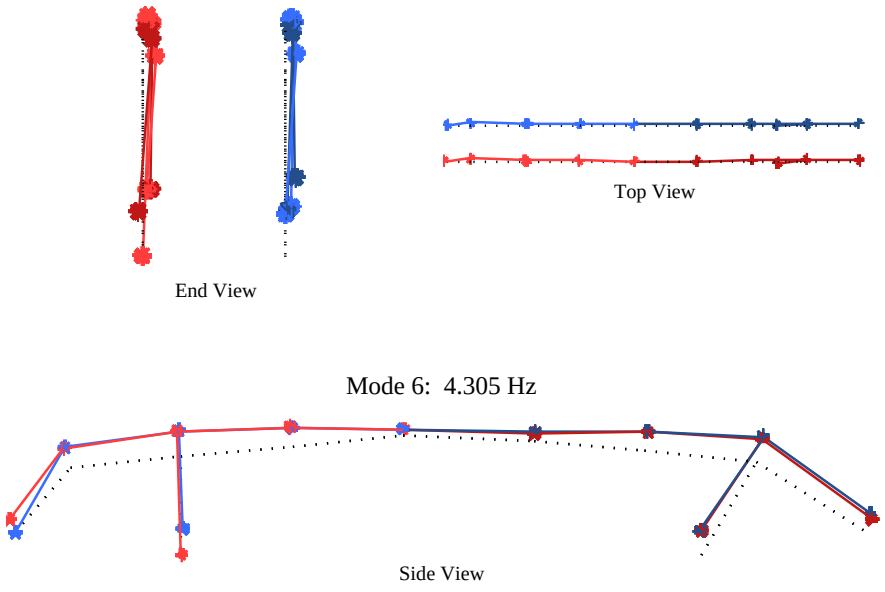

Figure 7.13: Measured mode shape: stairs downstream position, Mode 6 – Vertical Symmetric.

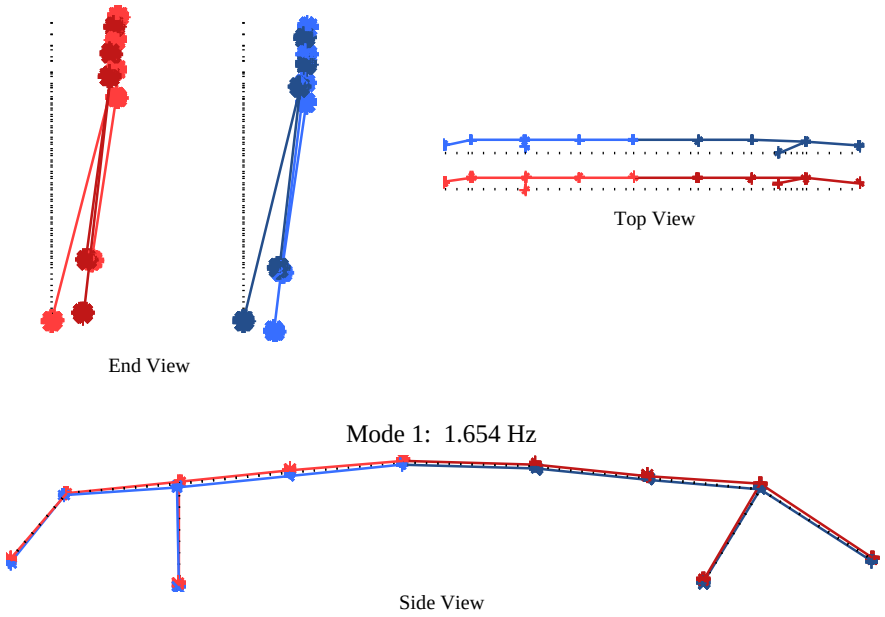

Figure 7.14: Measured mode shape: stairs upstream position, Mode 1 – Sway.

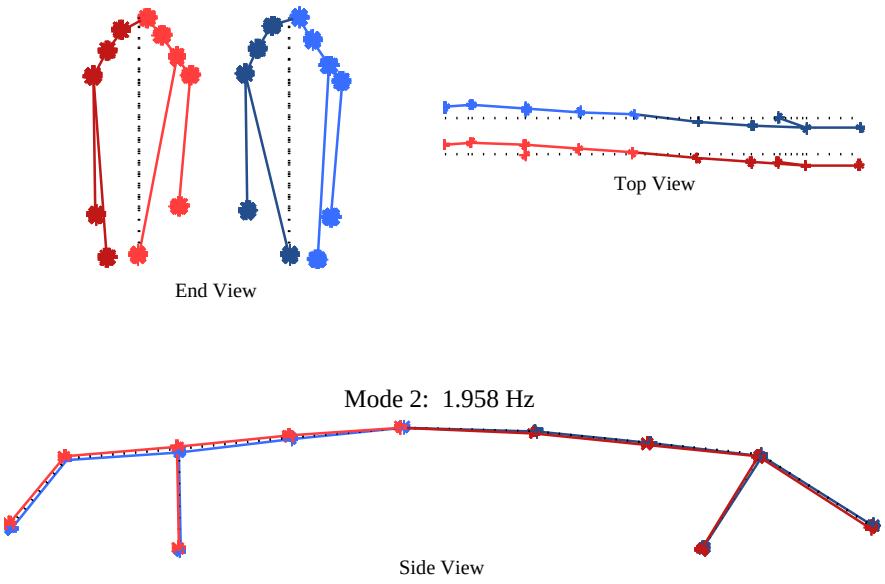

Figure 7.15: Measured mode shape: stairs upstream position, Mode 2 – Lateral Anti-Symmetric.

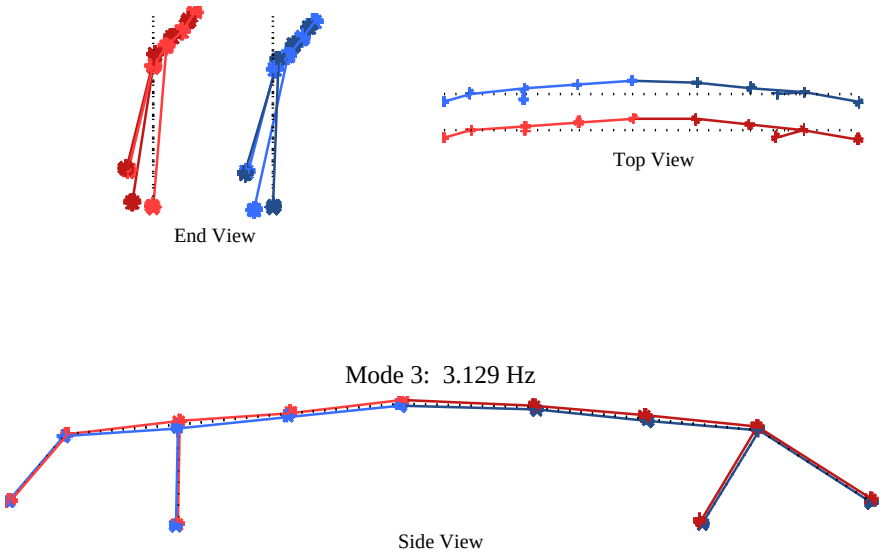

Figure 7.16: Measured mode shape: stairs upstream position, Mode 3 – Lateral Symmetric.

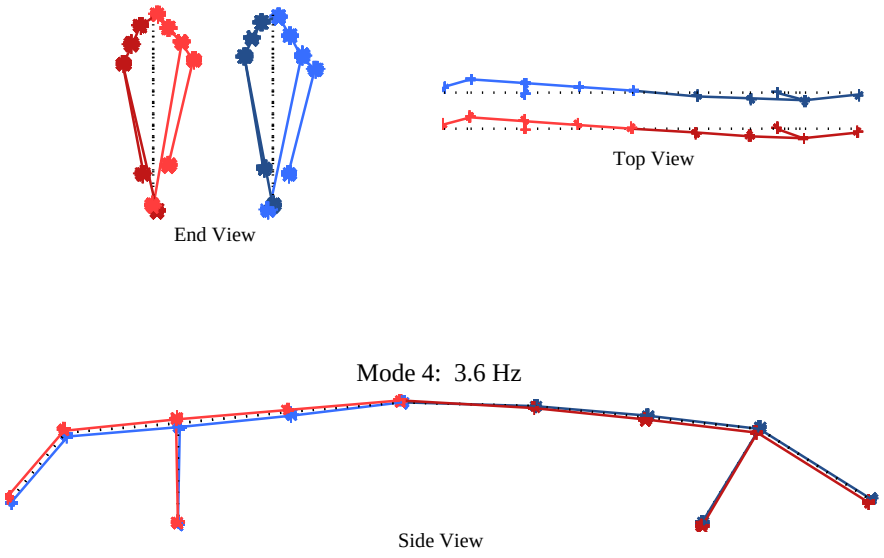

Figure 7.17: Measured mode shape: stairs upstream position, Mode 4 – Torsional.

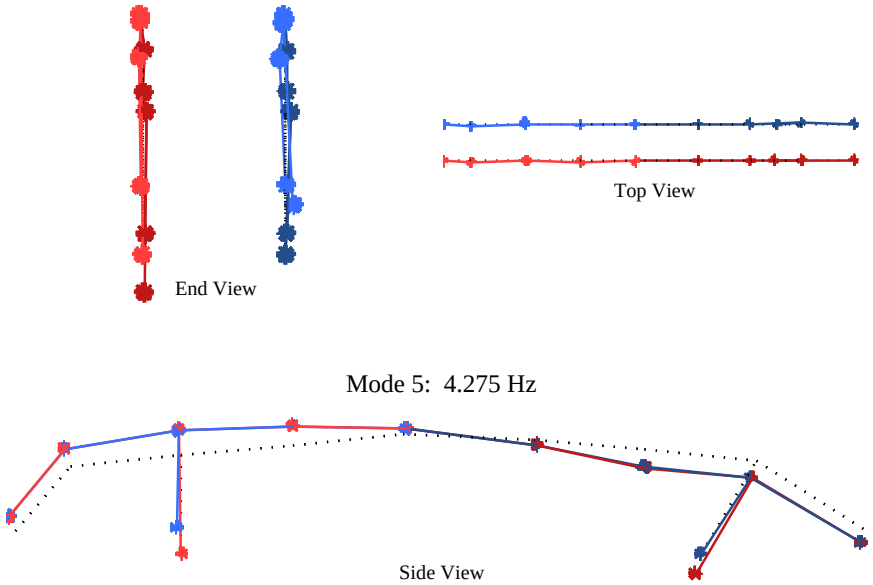

Figure 7.18: Measured mode shape: stairs upstream position, Mode 5 – Vertical Anti-Symmetric.

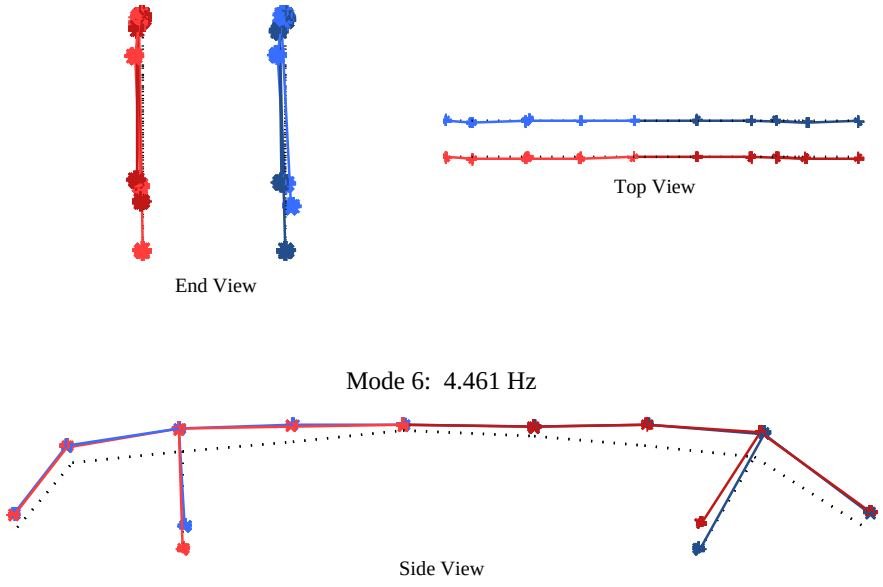

Figure 7.19: Measured mode shape: stairs upstream position, Mode 6 – Vertical Symmetric.

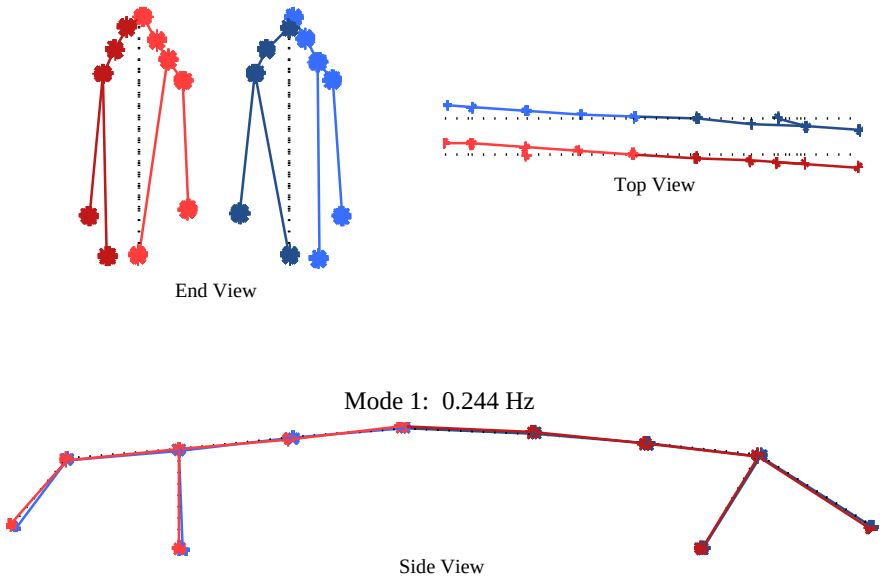

Figure 7.20: Measured mode shape: swung open position, Mode 1 – Lateral Anti-Symmetric.

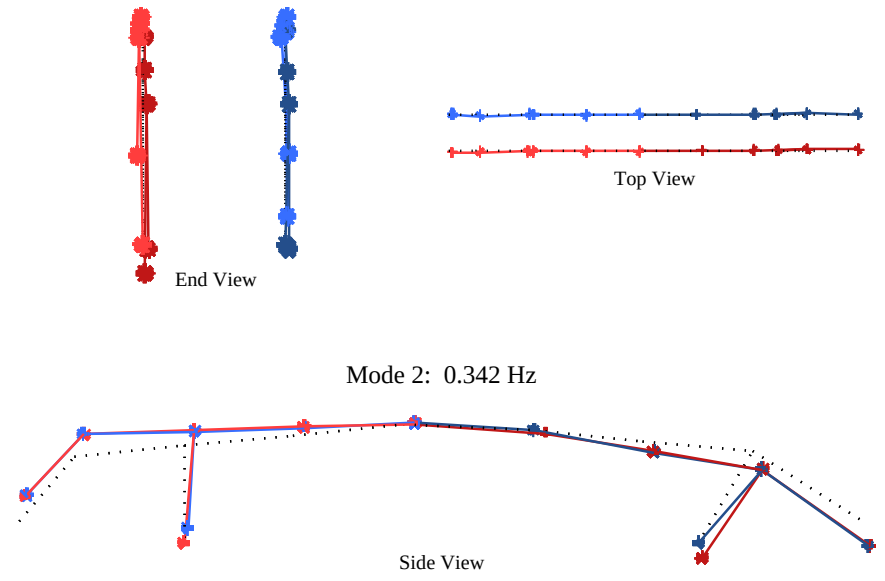

Figure 7.21: Measured mode shape: swung open position, Mode 2 – Vertical Anti-Symmetric.

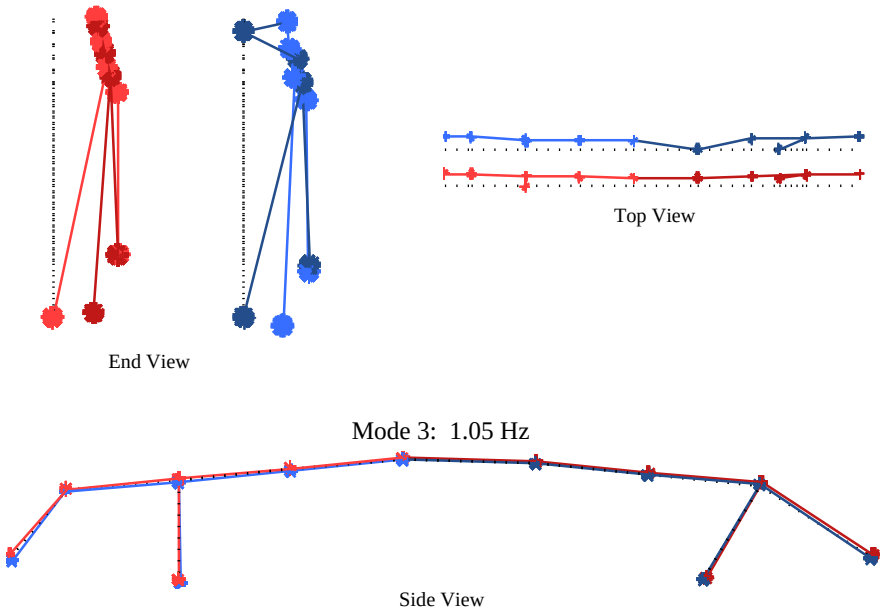

Figure 7.22: Measured mode shape: swung open position, Mode 3 – Lateral Symmetric.

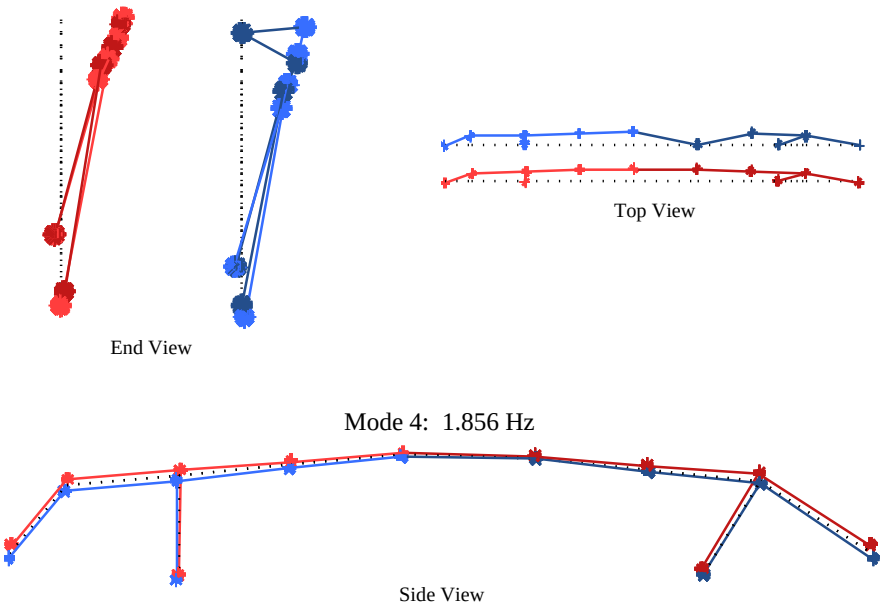

Figure 7.23: Measured mode shape: swung open position, Mode 4 – Sway.

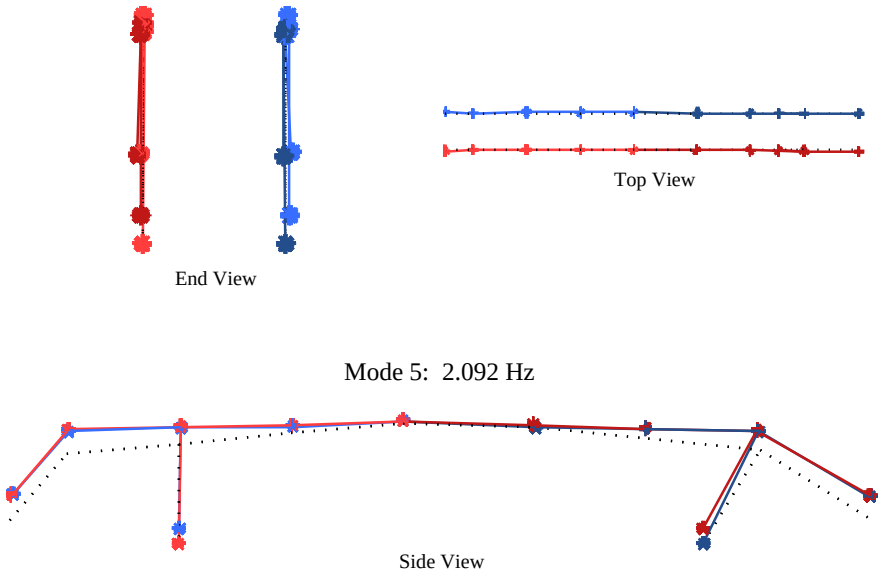

Figure 7.24: Measured mode shape: swung open position, Mode 5 – Vertical Symmetric.

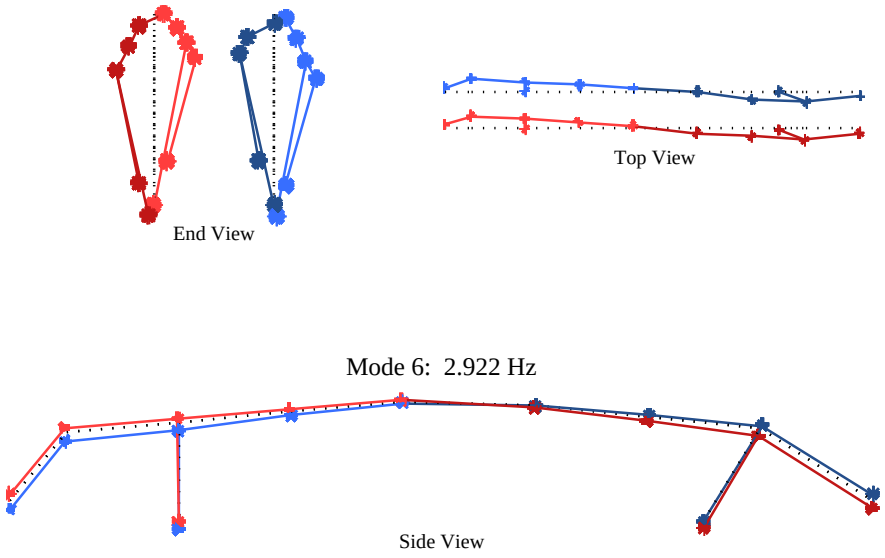

Figure 7.25: Measured mode shape: swung open position, Mode 6 – Torsional.

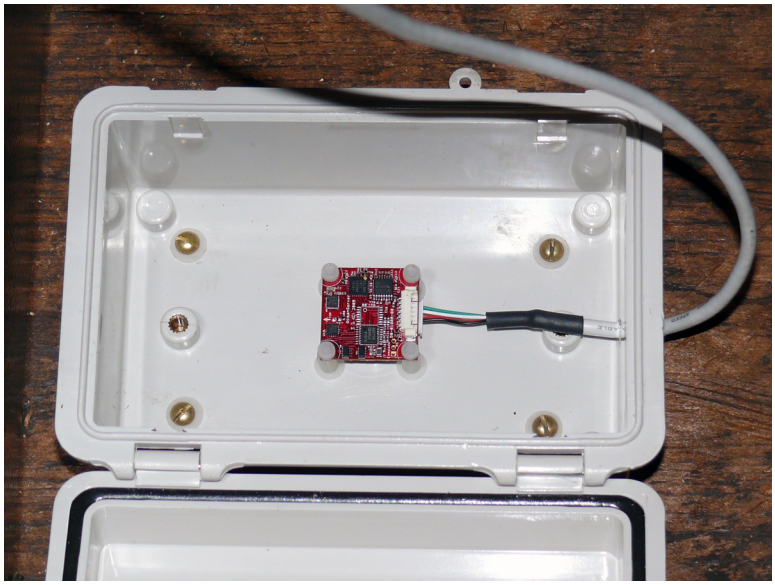

Figure 7.26: OceanServer OS5000 digital compass as installed on the Rock Island Bridge.

7.2 Digital USB Compass

To aid in the determination of the bridge position in real time, an Ocean Server OS5000 digital USB compass was installed in the operator's house near the base station computer that controls all the SHM systems. Shown in Figure 7.26, installed in its environmental enclosure, the OS5000 is a MEMS-based electronically gimbaled compass. The OS5000 contains two Honeywell anisotropic magnetoresistance (AMR) sensors that provide triaxial magnetic plane readings and a STM triaxial accelerometer for onboard gimballing.

The OS5000, like all magnetic sensors, is susceptible to error caused by nearby distortions in the Earth's magnetic field. The distortion causes are generally referred to as hard iron (magnetized) or soft iron (ferrous, un-magnetized materials) sources. Ideally the installation site of the compass is far enough away from these distortion sources so as not to affect the accuracy of the heading. In a steel truss bridge, finding a position far from steel members is difficult. Nevertheless, calibrating the digital compass to minimize the effects of the distortion sources is possible. The OS5000 was installed and calibrated with the stairs in the downstream position. In this position the compass has a heading of 152° which corresponds well with the orientation of the bridge with respect to the north-south axis.

The compass was installed on the bridge to help keep track of the orientation of the bridge so that what closed position the bridge is in and also to help verify when the bridge is swinging. Figure 7.27 shows the measured compass heading and Strain R2 during a swing event and train event. The bridge starts in the upstream locked position and then unlocks to swing just after 19:25. The bridge begins to swing, and the compass heading starts to change shortly after the bridge unlocks. The bridge turns clockwise as can be determined from the increasing heading. The heading itself wraps from 360° to 0° as the bridge continues to turn clockwise and eventually reach the downstream position. After the bridge stops turning the strain record indicates the bridge locks again and then a train passes

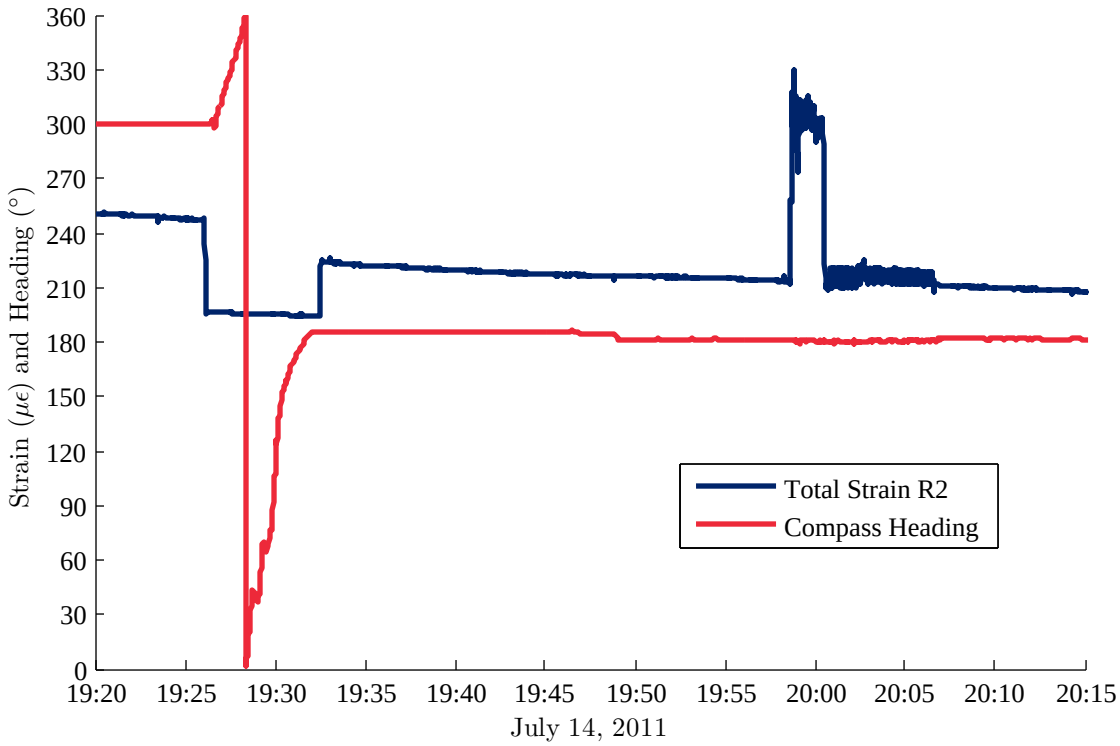

Figure 7.27: Measured compass heading and strain during a swing and train event.

over the bridge at 20:00. The compass heading shows a small degree of change when the train passes due to the accelerometers on the compass trying to continuously gimbal the reading. The compass heading is not affected by the outside temperatures or solar radiation (partly because of its location in the operator's house and partly because the acceleration measurements are corrected onboard) and is therefore a good metric to use to determine orientation and whether the bridge is moving.

However, the equipment in the operator's house can cause some inaccuracies in the absolute heading, despite best effort attempts at calibration. Figure 7.28 shows the compass heading for a time period of approximately fourteen hours during which the bridge swings multiple times. The bridge begins in the downstream position with the heading of approximately 152°[4] before it begins to turn at 22:00. This turn is a complete half turn of the bridge clockwise though the bridge pauses in the quarter turn position to allow the boat to pass before completing the turn. The heading does not change by 180° even though the bridge makes a complete 180° turn. The hiking compass used to calibrate the digital compass, when attached to the top of the digital compass enclosure, shows a similar phenomenon. Nevertheless, the compass headings are consistent enough to determine the orientation of the bridge and the direction of the turn.

[4]The compass was calibrated to this angle while the stairs where in the downstream position. This angle also indicates that the USB compass points toward Rock Island when the bridge is in the downstream position.

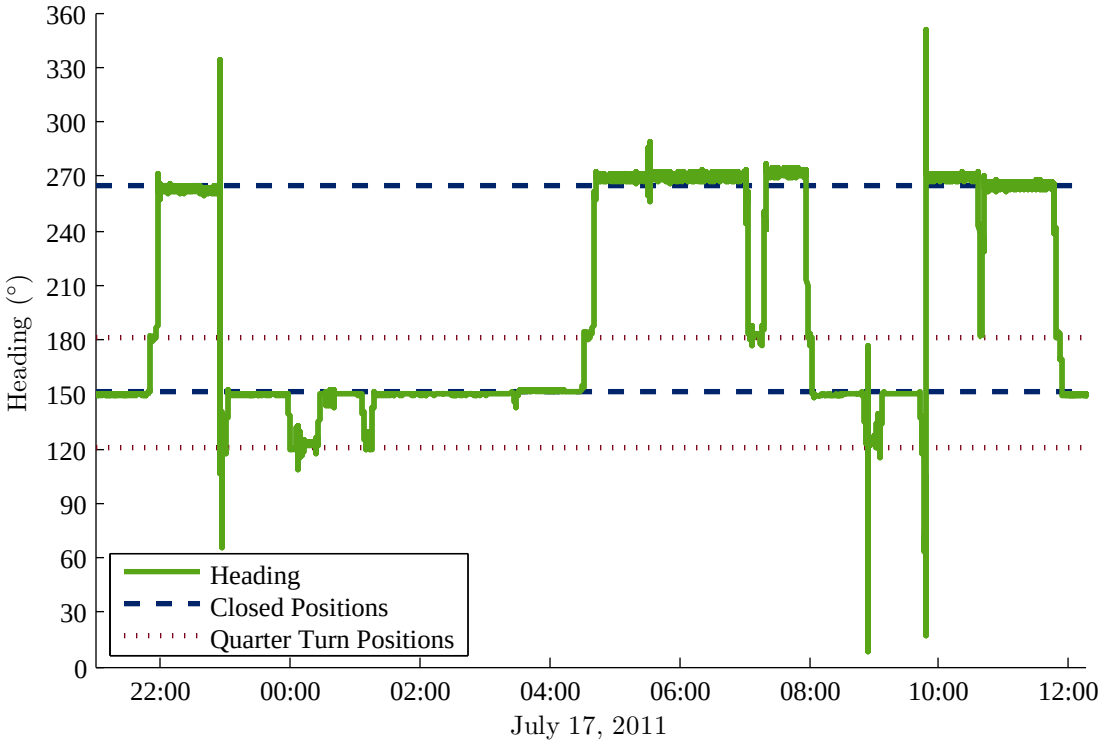

Note: The stairs downstream position is at 152°.

Figure 7.28: Compass heading with the closed and quarter positions marked.

7.3 Summary

Two new sensor systems were installed on the Rock Island Bridge. The wireless smart sensor network was installed to measure accelerations on the bridge. The acceleration measurements enable the application of a wide variety of damage detection algorithms that have been developed based on changes to the dynamic properties of structures to be applied to the Rock Island Bridge. One of these methods will be discussed in Section 10.1.

The installation of the compass allows for confirmation of the bridge's position. Because a delay exists in the time that it takes for the bridge to begin to rotate after unlocking, the compass cannot be relied upon the trigger taking data before and after a swing event. However, it can help confirm the direction of the swing or that the change in strain the bridge experienced was actually a train.

Both the wireless sensor network and the compass were installed and tested on the Rock Island Bridge. Integrating the data collected by both of these supplemental systems with the data provided by the fiber optic system will be the subject of the next chapter.

Chapter 8

INTEGRATED SHM DATA COLLECTION PROGRAM

A multimetric structural health monitoring system requires that the data from the various sensors all be collected in a single program. Sensors of the same general type (fiber optic or electromagnetic), even with different metrics, typically use the same data acquisition system and are therefore easily collected into a single program. However, the Rock Island Bridge SHM system has three distinct data acquisition systems, one for each of the fiber optic, wireless, and compass systems. Data from all three sensor systems needed to be collected and processed together. The Integrated SHM Data Collection Program, created as part of this research, collects data from each of these sensor systems.

The Integrated SHM Data Collection Program constitutes one part of the larger Integrated SHM Analysis Program introduced in Figure 1.3. The constitutive parts of the Integrated SHM Analysis Program, and how they interact with the sensor systems, database, and FEM model are shown in Figure 8.1. The algorithms and methods for the Anomaly Detection and Determination Program and the Damage Localization and Quantification Program will be discussed in Chapter 9 and Chapter 10, respectively.

The Integrated SHM Data Collection Program must perform a number of tasks. It must read in the data from the respective sensor systems, filter and process the data, and then store appropriate data in a database. The key development of the program is the event detection algorithm that is able to determine when the bridge unlocks or locks for a swing. Furthermore, the program is able to detect when trains cross the bridge despite the large variation in the train's loading, speed, length, and car composition. The development of this algorithm will be discussed first followed by the presentation of the integrated SHM program and the creation of the associated database used.

8.1 Event Detection Algorithm

The ability of the bridge to be in three distinct positions requires data collected from these positions to be analyzed separately to ensure "apples" are compared to "apples." The presence of the train loadings in the two closed positions further complicates the situation because the train load is much greater than the vehicular live load. To make sure data is properly labeled with the bridge position and loading, the Integrated SHM Data Collection Program must include an algorithm that can, in real time, perform the following tasks:

- Determine the starting and stopping times of the swing or train event.
- Differentiate a swing event from a train event.
- Record the starting and ending orientations of the bridge and the direction of rotation of the swing

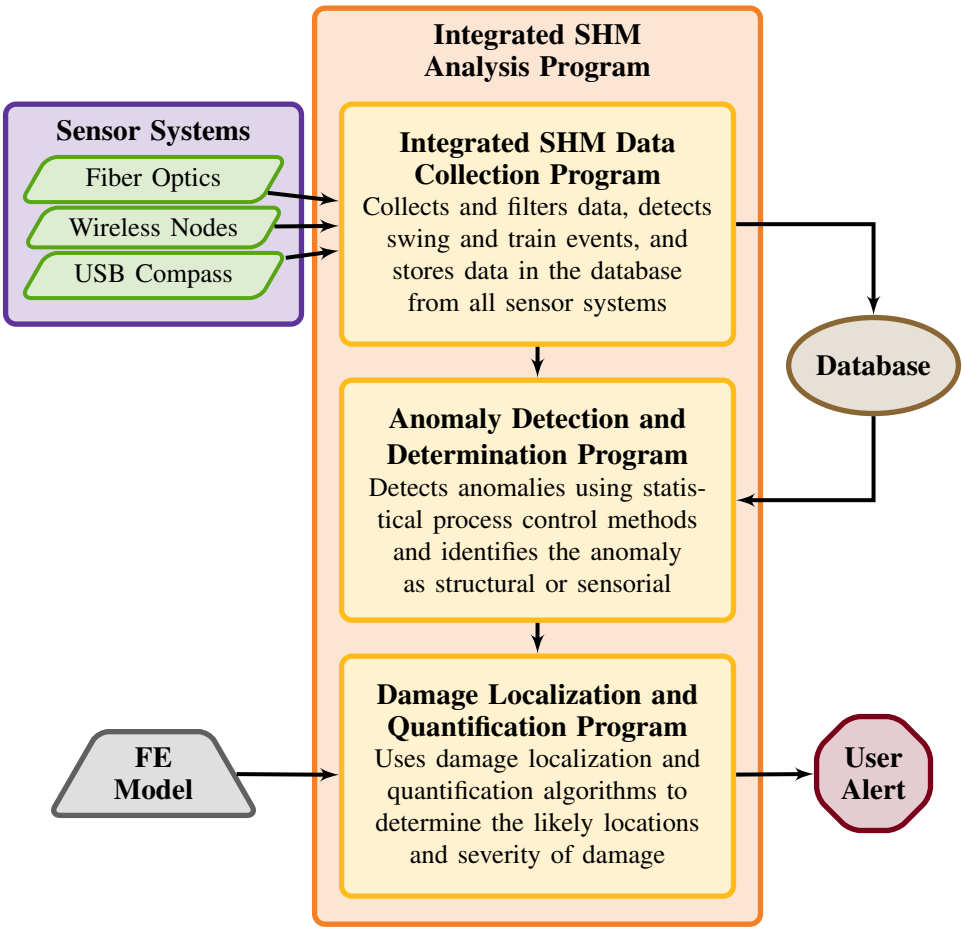

Figure 8.1: Flowchart of the Integrated SHM Analysis Program showing the component programs.

	L2–U2 Sensors	
M5–U6 Sensors	Increase	Decrease
Increase	Train Start	Swing Start
Decrease	Swing Stop	Train Stop

Table 8.1: Strain characteristics that indicate events.

- Record the change in strain caused by the swing events as a health monitoring metric.
- Determine the direction a train is traveling.
- Record the maximum strain difference caused by the train.[1]

The information obtained by the algorithm is also used to tag acceleration records with information about what took place during the recording period. The event detection algorithm effectively sorts through the streaming strain and compass data and records only the relevant information.

The event detection algorithm is essentially an exercise in pattern recognition. Therefore, at the root of the event detection algorithm are the characteristics in the strain records observed in Figures 5.22 and 5.23 in Section 5.5. The strain measured by sensor R2, located on a L2–U2 member, goes down when a swing event starts and comes back up when the swing ends. The strain in sensor R4, located on a M5–U6 member, does the opposite and goes up when the swing starts and goes down when the swing ends. When a train crosses the bridge, both sensor R2 and R4 increase when it the train enters the bridge and decreases when the train leaves the bridge. By monitoring whether these sensors have significant changes at the same time and whether those changes are in the same or opposite directions, whether the bridge is being swung or a train is passing over the bridge can be determined. Table 8.1 shows a summary of what the changes in strain in L2–U2 and M5–U6 members signify. The L2–U2 sensors are the most important sensors for the event detection algorithm, because they were the only ones that were installed that are on members that decrease in strain when the bridge swings or trains pass over the bridge.

The detection of swing events using the principles in Table 8.1 is straightforward, as the swing events are highly repeatable because the change in load is constant. However, the train events need to be handled a little differently, because of the variability that can exist in the length, weight, and speed of the train. Figure 8.2 shows a typical train event for three of the four sensors on L2–U2 members.[2] As noted in Table 8.1, the strain initially goes up at the start of the event at 21:03:30 and comes down at 21:05:30. The largest strains occur at the beginning of the event when the engine passes. The fact that the maximum of L19 is greater than that of Strain R2, which are across the rail deck from each other, leads to the conclusion that the train is passing closest to the left truss, which means the stairs are

[1]The maximum strain difference at the start of the train was collected but has not been used in any analysis so far. The train load (combination of static and dynamic loads) that causes this maximum value is not known. However, during the development of the program, the Army Corps of Engineers felt that this value might provide some insight into possible fatigue issues in the bridge members.

[2]Strain R16 was not functioning at the time the data was collected

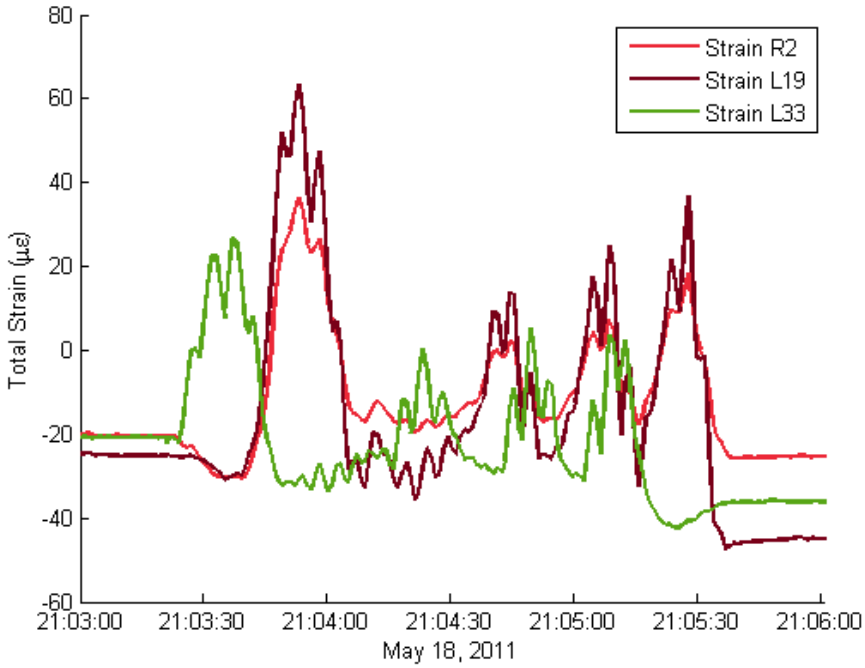

Figure 8.2: Strain record for a typical train.

located in the upstream position. The direction of the train can be determined by noting that Strain L33 reaches its maximum before Strain R2 and Strain L19 which are located on the opposite end of the bridge from L33. At the start of the train crossing, Strain R2 and Strain L19 first have a strain decrease while the engine is on the opposite side of the bridge. The vibrations of the bridge can cause some slippage or settlement in some of the joints in the bridge which is why Strain L19 and Strain L33 do not return to the same strain level after the train has left the bridge. For this reason, the end of train cannot be readily determined by noting when the strain returns to its original levels. Most trains are very similar to this typical train and all the information about position and direction of the train in addition to the maximum strain change due to the passage of the engine are determined by the event detection algorithm.

However, some train events do not conform to the features of the typical train. Figure 8.3 shows the strain record for a "half-train" event and includes an inset photo taken with a cell phone of the actual event. The Iowa Interstate Railroad that runs the railroad that crosses the bridge has a train yard in Rock Island, IL. In the process of making trains, the yard master often moves engines up the track to the bridge, stops them on the bridge for a period of time, and then has the trains backup off the bridge. Because the train does not fully cross the bridge but only goes halfway, these events have been termed "half-trains." The bridge operators report that half-trains are common occurrences. The loads induced by the half-trains are not problematic. However, the half-trains can be mistaken for a swing if only the strain measurements are considered. Figure 8.3 shows that Strain R2 and L19 have a pattern that would normally be indicative of a swing event because they are on the side of the bridge that the train does not cross. The normal train shown in Figure 8.2 also has a

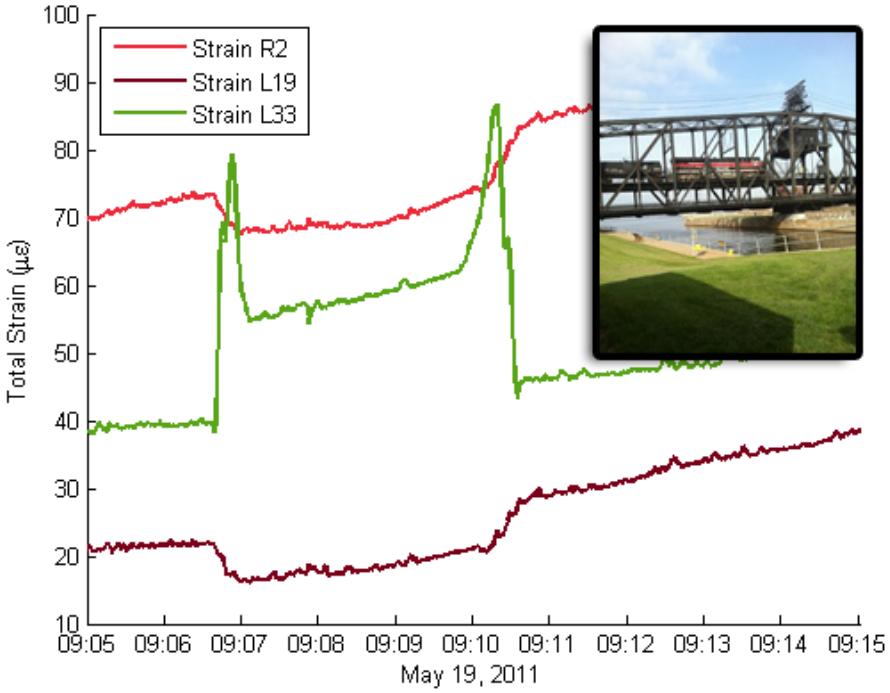

Figure 8.3: Strain record for a 'Half-Train' event with inset picture of actual event.

dip in those two sensors before the train crosses on to their side of the bridge. However, because the half-train does not continue to the other side, the strain levels do not increase as is expected for a train event. The bridge heading from the USB compass helps make sure that the half-trains are not misidentified as swings by confirming that he bridge is not swinging.

Events other than swings and trains have also been observed in the strain records. Figure 8.4 shows two hours of recorded strain from the evening of October 7, 2010. During the two hours, the bridge swung twice to allow barges through with a train passing over the bridge between the two swings. However, Figure 8.4(a) shows that at 17:50 the strain record shifted approximately 10 $\mu\epsilon$. The shift is an isolated incident and is smaller than a typical train or swing event. The swing between 17:20 and 17:30 shows the scale of a typical swing event for the sensor for comparison. Furthermore, Figure 8.4(b) shows that sensor L19 experienced no such shift at 17:50, but that the swing and train events are apparent in both sensors. The likely cause of this shift in strain is that thermal stress that had built up in the member from turning into the sun during the 17:20 swing was released when the joints of the member slipped slightly and caused the strain to increase. The joints in the member slipping is also the likely cause of the strain level before and after a train often being different from each other. Observations have shown that a shift is more likely to occur during a train event because the vibrations can loosen the joints and decrease the friction that prevents the free slippage of the member. Nevertheless, if the thermal stresses are sufficient, the member can experience the shift at any time[3]. The event detection algo-

[3]Anecdotally, the bridge operators have reported hearing an occasional "pop" at times during the day. These noises used to give them quite the fright but they have come to except them as a part of "normal" bridge

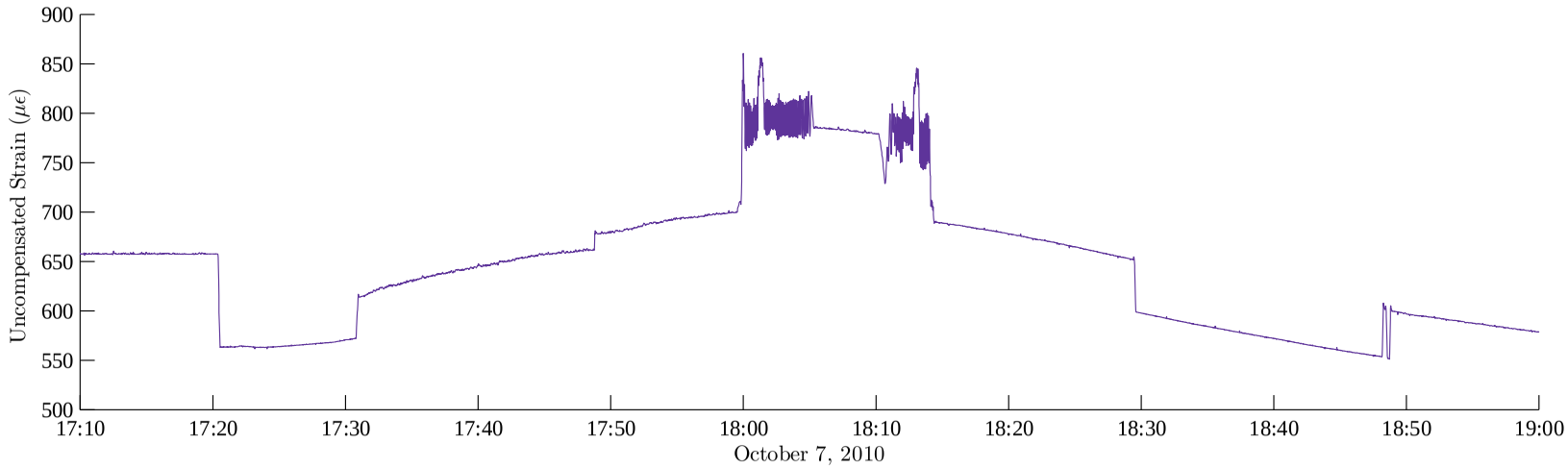

(a) Sensor Strain R2.

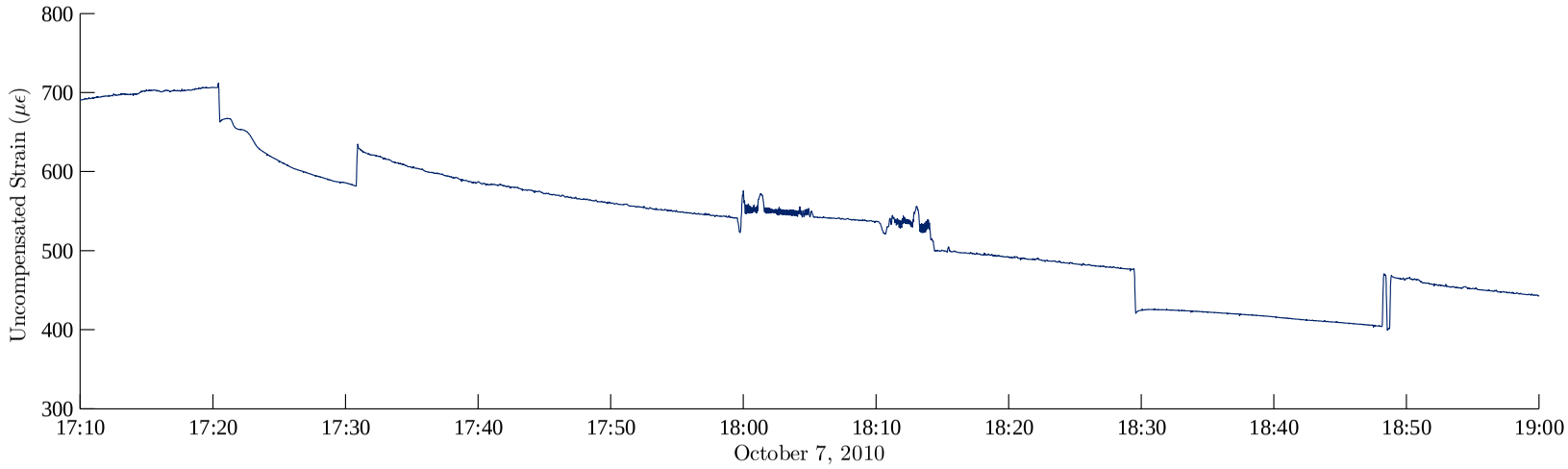

(b) Sensor Strain L19.

Figure 8.4: Strain records demonstrating local strain shifts caused by heat and train induced vibrations.

rithm can falsely identify a small shift as a swing or train event if *a*) the threshold for the event trigger is set too low, or *b*) multiple sensors are not required to detect the event.

Figure 8.4 also illustrates the problem of multiple attempts at locking the bridge in place. A close look at the data for both sensors R2 and L19 show that when the bridge closed at 18:50, the operator made two attempts at locking the bridge. A spike exists in the data where the bridge is briefly locked and then immediately unlocked before being locked in place again. The time scale of the brief locking is on the order of a few seconds. The likely cause of this phenomenon is that when the bridge operator tries to lock the bridge the first time, the bridge is not perfectly aligned. He therefore unlocks the bridge, makes a quick adjustment, and then locks the bridge again with better alignment. Up to three repeated locking attempts have been observed for a single swing event. The event detection algorithm can record the wrong strain value for the bridge in the open position if the operator attempts to lock the bridge multiple times in quick succession. The error can occur because the event detection algorithm records an average strain value of the last forty seconds before the swing takes place. The multiple closing attempts will be present in the averaged data causing the average strain value to be off. Therefore, the event detection algorithm has been programed to recognize the multiple attempts at closing as a single event and record the strain before the first one and after the last one to get a more accurate $\Delta\epsilon$ value. The fact that multiple attempts at locking the bridge occurred is also recorded in the event database and these points are excluded from the statistical analysis of the data.

The event detection algorithm has been programmed into the Integrated SHM Analysis Program. Figure 8.5 demonstrates the effectiveness of the event detection algorithm by comparing the full strain record with the data points recorded by the event detection algorithm. The algorithm successfully detected both swing events and the train event in the figure. The detected event data is very sparse and does not track the strain data exactly between swing and train events. The data shown is very smooth because the data was collected after the sun has set and the bridge temperature has equalized. During the day, the algorithm is still able to detect the events and distinguish trains from swings. However, the large amounts of variation caused by temperature differentials and direct solar heating of the sensors typical in the strain records is not present in the detected events. Neither does the detected event data show all the dynamic variation that takes place during a train event. Nevertheless, the detected event data keeps the important information – the change in strain caused by the opening and closing of the bridge – that is very useful in the monitoring of the structure.

By just keeping the pertinent information, the event detection algorithm also reduces the amount of data that needs to be stored. The strain system can output data at a rate of up to 125 Hz. At that maximum rate, 12 GB of data is produced every day. The event detection algorithm reduces the daily output to just 14 kB, depending on the number of swings and trains that pass the bridge each day. The reduced data load makes analysis quicker and the proper identification of the event and bridge position makes the analysis more meaningful.

operation. All attempts to correlate observed sudden shifts in strain with a "pop" heard by the operators has so far proved unfruitful because they do not record when they hear these noises. However, the speculation is that the release of energy that is likely causing the strain shift is also causing the noises heard by the operators.

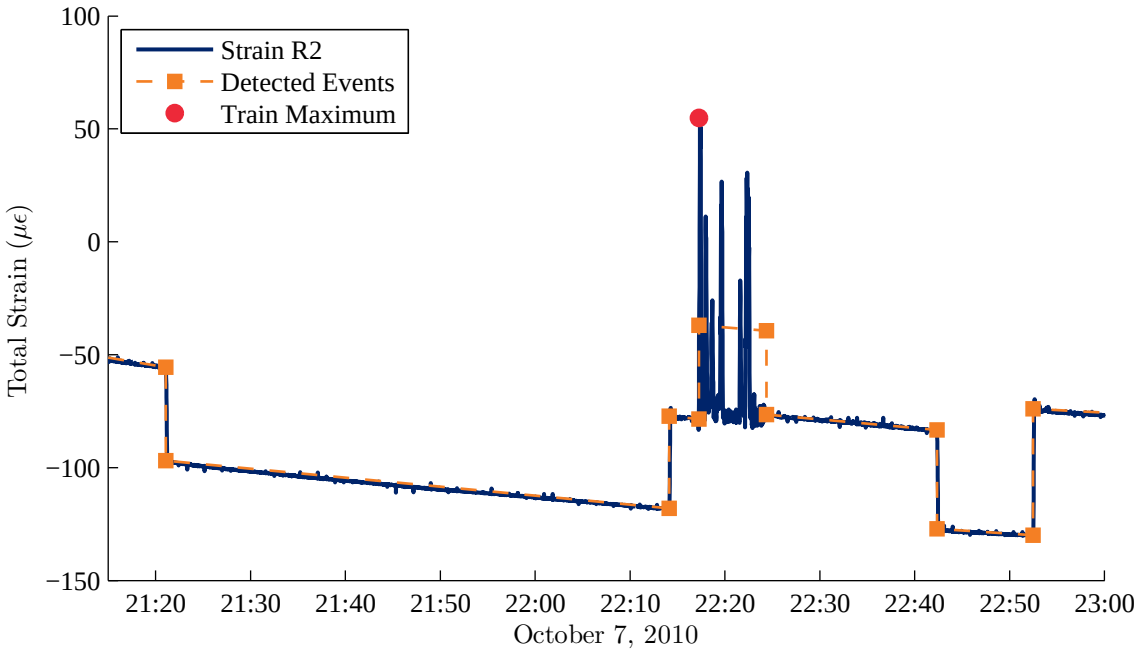

Figure 8.5: Unprocessed strain and the detected events and train maxima from the detection algorithm.

Thus, the robust event detection algorithm that has been developed is a key in producing a functional structural health monitoring system.

8.2 Integrated SHM Data Collection Program

To enable the Event Detection Algorithm to identify the swing events, data from the strain system and the compass system need to be provided to it. Therefore, the Integrated SHM Data Collection Program has been developed to integrate the three sensor systems installed on the bridge and record the appropriate information. The event detection algorithm discussed in the previous section is a fundamental part of the program. The integrated program has a graphical user interface that allows the user to change options, select which sensors to include in analyses, and produce reports. The Army Corps of Engineers operates a web cam that is focused on the bridge and a website about the movement of barges through the locks underneath the bridge. These sources of additional information have been integrated into the program as well.

The program has been written in the C♯ language[4]. C♯ was selected because Chandler Monitoring System used it to develop their IntelOptics software. Using the same language was expected to simplify the initial linking to the fiber optic system and eventual communication back to IntelOptics. The choice of C♯ has not been ideal because library packages

[4]C♯ is pronounced “see sharp.” C♯ is a C-like language developed by Microsoft as part of their .NET framework.

Figure 8.6: Flowchart of filtering and recording process.

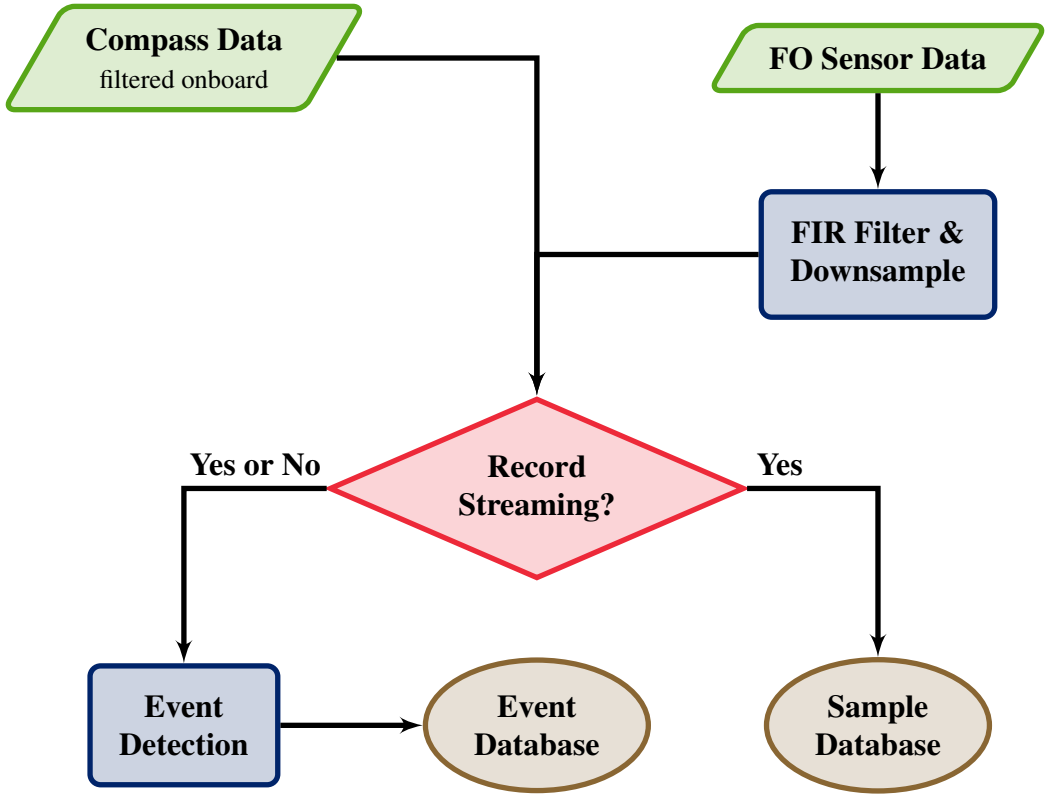

that include the complex mathematical and statistical functions that are required to process and analyze the data are not readily available in C♯. A number of custom functions have been produced, as part of the development of the Integrated SHM Data Collection Program, to perform simple mathematical operations such as calculating the mean of a set of data that handle a `NaN` as dropped data point. Sunrise and sunset is calculated for each day based on formulas provided by NOAA (National Oceanic and Atmospheric Administration). The benefit of C♯ is that it is designed to be used with graphical user interfaces and has its own "garbage collection" procedures which simplifies the declaration of variables and the allocation/deallocation of memory for those variables. Some C++ function libraries that contain the necessary mathematical and statistical formulas needed can be ported to C♯, but care has to be taken to ensure compatibility between the underlying data types.

Figure 8.6 is a flow chart of the part of the Integrated SHM Data Collection Program that deals with the basic functionality of data collection and event detection for the strain system . The Integrated SHM Data Collection Program interfaces with ENLIGHT via a TCP port to receive data from the fiber optic sensors at 125 Hz – the maximum sampling rate of the interrogator. The data collection program then proceeds to filter and downsample the data to a user selectable 25 Hz, 5 Hz, or 1 Hz. A 30 pole FIR digital filter has been hard coded into the program. If desired, all the unprocessed streaming data can be stored in a database. Regardless of whether the data is streamed to the database, the data at 1 Hz is sent to the Event Detection algorithm for processing.

Figure 8.7: Event detection database organization.

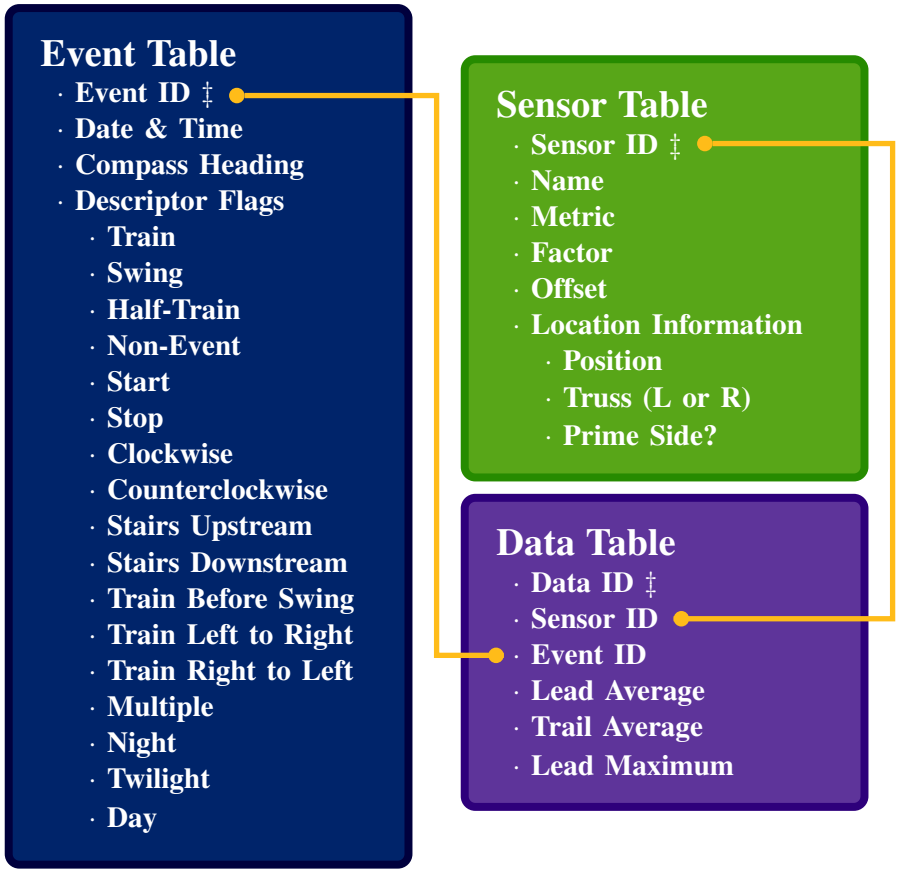

‡ indicates the field is the table's primary key

When an event is detected, the information about the event, including the time, type, position etc., is recorded in the Detected Events database. The databases were built and are managed in Microsoft SQL Server. As shown in Figure 8.7, the Detected Events Database consists of three separate tables, each of which contains an ID field that serves as the primary key for the table and is a unique, self-incrementing, integer for each entry in the table. The Data Table uses the primary key to link the recorded data for one sensor during one event to all the information about that sensor and event. The benefit of this organization is that any number of sensors can be recorded for a given event so sensors can be added or removed as needed without having to recreate the database. Thus, the database organization contributes to the scalability of the SHM system as a whole. The descriptor flags in the Event Table are all Boolean values that describe the event that is taking place.

To control the recording and event detection algorithm, a graphical user interface (GUI) was created to serve as the entry point to the program. Figure8.8 shows the front tab of the GUI after the program has started. The four buttons along the bottom left side start and stop the different functions of program. The buttons, from left to right, control the digital compass (compass needle), the fiber optic strain system ($\mu\epsilon$), recording streaming data to the database (rec), and the event detection algorithm (train and boat). The 'rec' button is

actually just an indicator light that turns green if the streaming data is being recorded. The other three buttons will turn the indicated functions on and off without having to access the tab associated with that function.

The front tab also features a picture, captured from the US Army Corps of Engineers web cam, of the bridge that is updated when an event is detected. The pictures are labeled with information collected during the event detection process. For example in Figure 8.9(a) the event detection algorithm put the label `WS|D|CC|XXX|D` in the bottom right corner. The `WS` stands for "swing start"; the first `D` stands for the stairs being "downstream" at the start of the event; the `CC` indicates the bridge turned "counterclockwise"; the `XXX` is space reserved for train events; the second `D` stands for "day". Table 8.2 lists the code options available. The web cam captures help confirm that the Event Detection Algorithm is correctly identifying the events. The limitations with the web cam captures is that sometimes during swing events (and occasionally when a train is on the bridge), the base station computer loses its internet connection. Because, the refresh rate of the web cam is only every sixty seconds, the exact moment the event occurs cannot be captured. However, as seen in Figure 8.9 the web captures happen soon enough after the event that information contained in the web cam capture label code can be confirmed.

The other tabs control the various options available for each aspect of the sensing systems or the event detection algorithm. The ENLIGHT tab shown in Figure 8.10 controls which

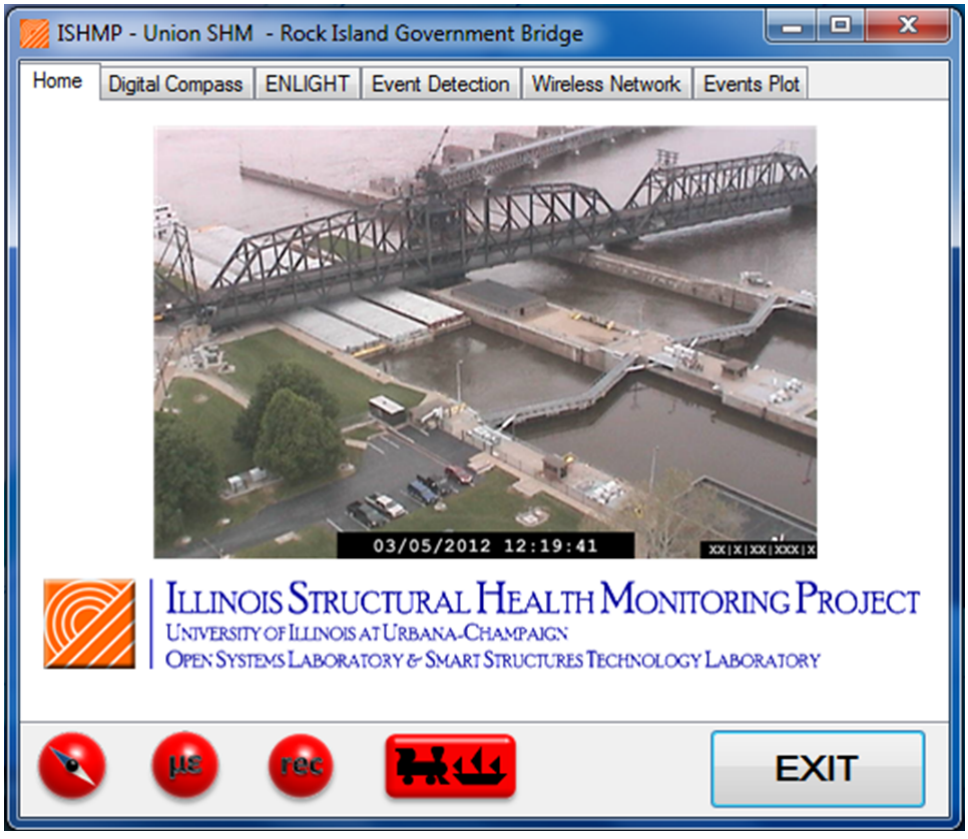

Figure 8.8: Front tab of the graphical user interface for the Integrated SHM Data Collection Program created for the Rock Island Bridge.

(a)

(b)

Figure 8.9: Swing of the Rock Island Bridge as captured and labeled by the event detection algorithm: (a) start of the swing; (b) end of the swing.

Table 8.2: Detected event web cam capture label codes.

Description	Code
Swing Start	WS
Swing Stop	WP
Train Start	TS
Train Stop	TP
Stairs Upstream	U
Stairs Downstream	D
Turn Clockwise	CW
Turn Counterclockwise	CC
Not a Swing Event	XX
Train goes left to right	L2R
Train goes right to left	R2L
Not a Train Start	XXX
Day	D
Twilight	T
Night	N

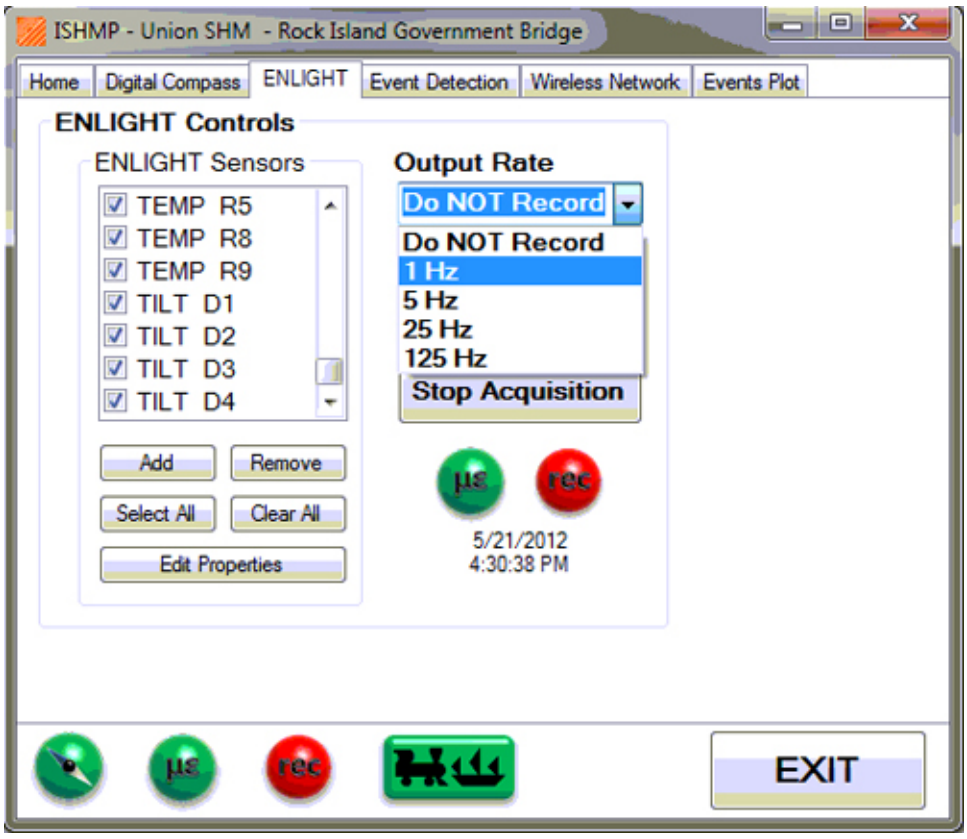

Figure 8.10: ENLIGHT tab of the Integrated SHM Data Collection Program GUI.

sensors are available for processing. Checking a sensor makes it available for streaming to the database. Sensors can be added or removed[5] from the list of available sensors as needed. The properties of the sensors listed in the Sensor Table in Figure 8.7 can be edited using the "Edit Properties" button which brings up a form in a new window.

Figure 8.10 shows the Output Rate menu on the ENLIGHT tab extended so the output rate can be selected. The program starts up with "Do NOT Record" as the default option. Selecting any of the available output rates will turn on the record option and stream the data to the database at that rate.[6] Even when the recording option is off, the fiber optic data will be filtered and downsampled to 1 Hz in preparation for the event detection algorithm. The time of the last streamed datum is displayed under the "$\mu\epsilon$" and "rec" indicator lights in the tab itself.

The Event Detection tab, as seen in Figure 8.11, looks very similar to the ENLIGHT tab. The Event Detection tab also contains a list of available sensors, but sensors can not be added on this tab. Checking a sensor on this causes its data to be recorded when an event

[5]The sensors are actually not removed from the database as doing so would make any previous data recorded for the sensor inaccessible. Instead the sensor is made inactive using an internal Boolean flag. If a sensor of the same name as the original sensor is added again, the original sensor is just reactivated

[6]The base station computer starts to get bogged down at anything greater than the 5Hz output rate as it is constantly having to make the connection to the database, insert the data, and close the connection again. An improved streaming algorithm that maintains a database connection open would resolve this issue.

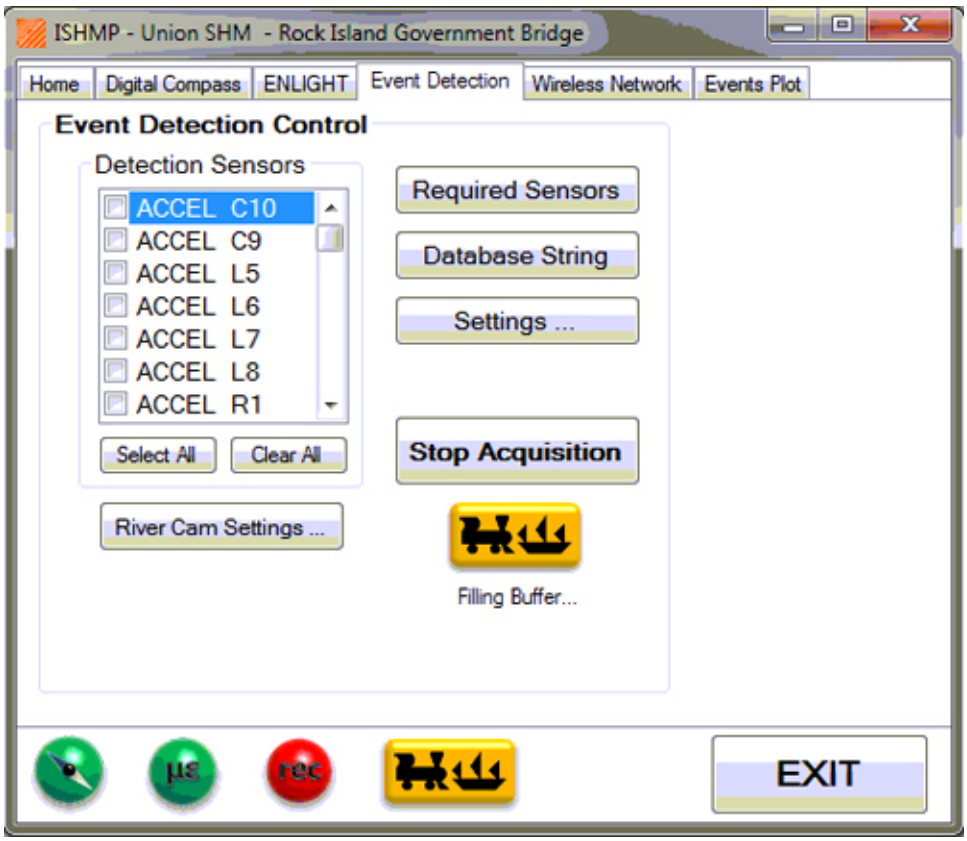

Figure 8.11: Event Detection tab of the Integrated SHM Data Collection Program GUI.

is detected. This list is separate from the list of streaming sensors; therefore, sensors being streamed do not have to be recorded in the data base and vice versa, but they can be if so desired. Figure 8.11 also shows the intermediate condition of the indicator lights. When, the filter or event detection buffers are filling up, the respective lights will be yellow and "Filling Buffer" will be displayed where the last recorded event is displayed. The location where the labeled web cam captures are stored can be set by clicking on the "River Cam Settings ..." button.

The Wireless tab is shown in Figure 8.12. This tab is functionally different from the other two, because the interaction with the wireless sensor system is slightly different. The "Close Connection" button in Figure 8.12 starts out as an "Open Connection" button. When pushed, the Integrated SHM Data Collection Program opens up three programs developed by the Illinois Structural Health Monitoring Project that are used to interface with the wireless sensor. The programs run hidden in the background and can only be shut down by the Integrated SHM Data Collection Program GUI or directly in the list of running processes in the Windows Task Manager. One instance of `autocomm.exe` is used to send commands to the sensors, another instance of `autocomm.exe` is used to receive data from the gateway node, and one instance of `forwarder.exe` is used to synchronize the gateway node and the base station computer. The output for these programs is redirected from displaying in the hidden process command windows to display instead in the large text box on the Wireless tab. Commands can be typed in the small text box and sent by pressing the

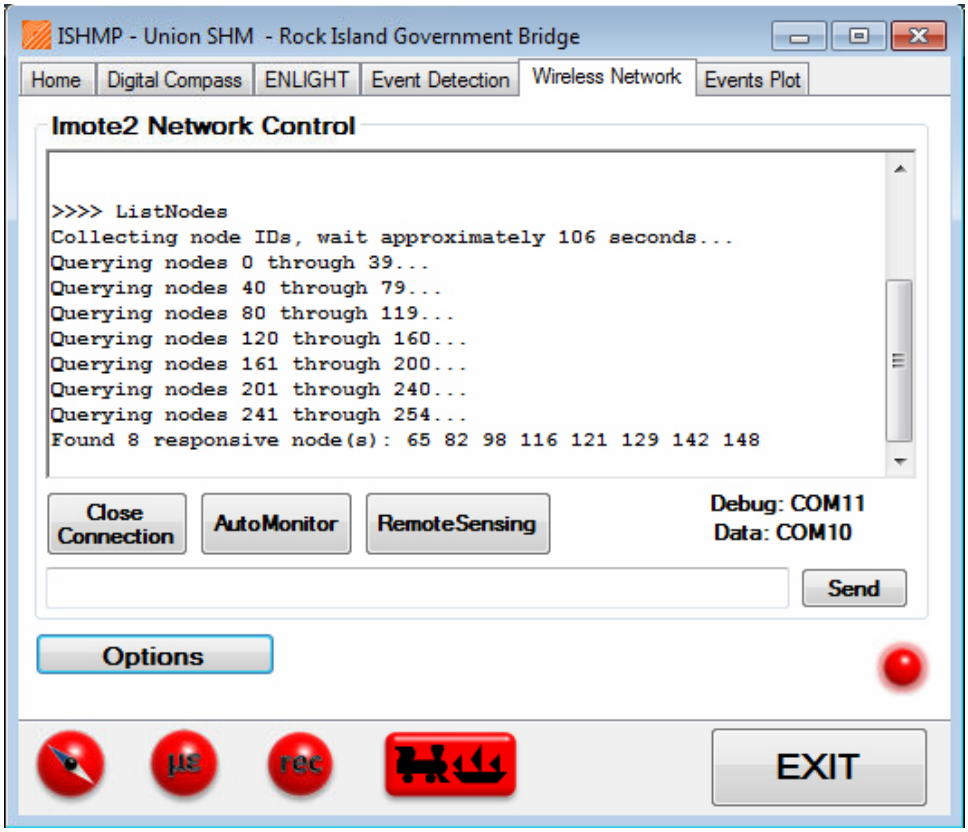

Figure 8.12: Wireless Sensor tab of the Integrated SHM Data Collection Program GUI.

"Send" button or hitting the return key on the keyboard.

To simplify the structural health monitoring process two options are available. The first is that the user can click the "AutoMonitor" button, seen in Figure 8.12, to begin running the `AutoMonitor` service developed by the ISHMP. This service takes acceleration data when a threshold acceleration of a sentry node is reached. It also monitors the power use, charging status, and temperature of the network nodes. Alternatively, the user can click on the "RemoteSensing" button and the wireless system will take a single set of acceleration measurements at that moment from the network. Both these options make the use of the system easier for the end user who does not have to manually enter the commands needed to perform these functions.

The performance of the `AutoMonitor` and `RemoteSensing` functions is controlled by options that can be selected from the menu that appears when the "Options" button is clicked on the Wireless tab. The Wireless Options Window, shown in Figure 8.13, controls all aspects of the interface with the wireless sensor network. The General Settings sections has options for setting the COM ports used by gateway node and the general location and file name seed for the output files.[7] The settings also include a section for setting the parameters of the `RemoteSensing` application and a place to choose the input file for the `AutoMonitor` service.

[7]The output file names consists of the file name seed and a timestamp. Therefore, each output file has a unique file name and data is not overwritten.

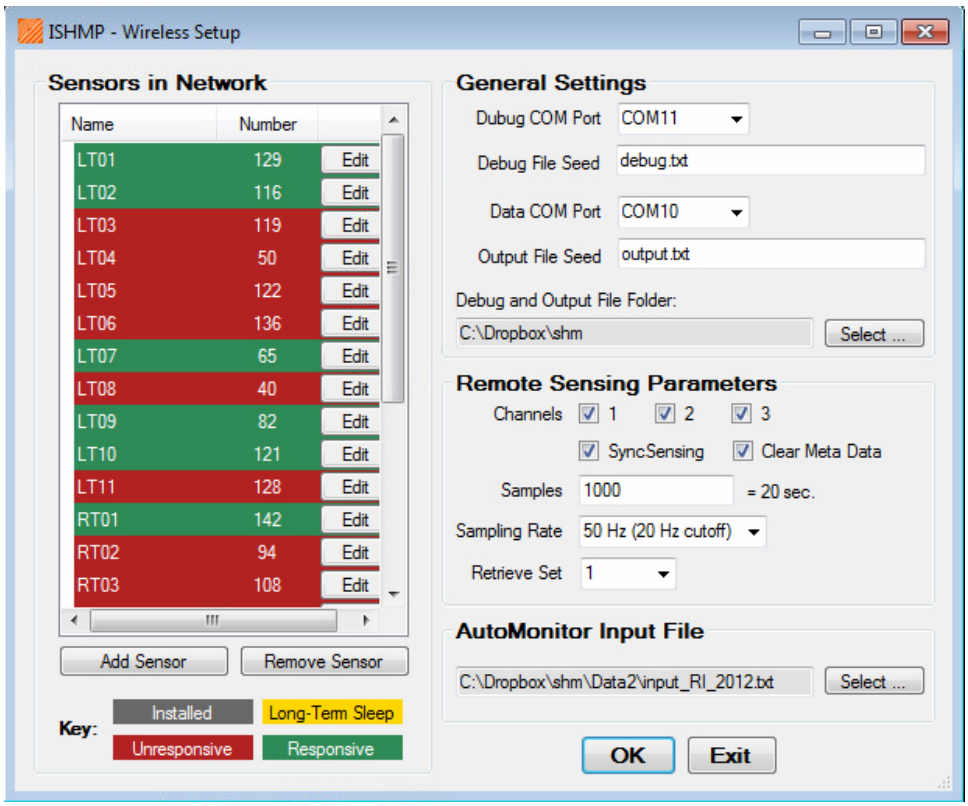

Figure 8.13: Wireless Sensor Menu tab of the Integrated SHM Data Collection Program GUI.

The Wireless Options Window is also where the list of sensors in the wireless smart sensor network is kept. The sensor list has been programmed to reflect the current status of the sensors. The Integrated SHM Data Collection Program reads the output sent to the large text box on the Wireless tab and scans it for known program responses. For example, in Figure 8.12, the `ListNodes` command was issued and the output of the program shown in the window. After executing, the `ListNodes` command responded with a message of the form "Found x responsive node(s):" where x is the number of nodes found in the network. The Integrated SHM Data Collection Program recognizes this response and will change the status of the sensors to reflect any changes. The statuses are stored in a database and marked with a timestamp enabling the user to to track the responsiveness of the sensors overtime.

The end user of the Integrated SHM Data Collection Program has the option of entering commands in the Wireless tab if needed to control the wireless sensor network. However, the Integrated SHM Data Collection Program was programmed to use the detected swing events to trigger the collection of acceleration data. In this way, the output files of the sensor network can be tagged with information regarding the bridge position. Tagging is accomplished by triggering `RemoteSensing` when a swing event (open or close) is detected and noting the most recent event ID at the start of sensing. When sensing is complete, the Integrated SHM Data Collection Program checks the most recent event ID again to make sure the event ID is still the same. If the event ID changes, because a train came along or the bridge closed while the data was being taken, the file is marked as such so as to be excluded from analysis. If the ID is the same, the file is labeled with the bridge position and period of day (day, night, twilight) so that it can be analyzed properly.

The Event Plots tab, shown in Figure 8.14, provides a way to look at the detected event data from within the Integrated SHM Data Collection Program itself. The program can plot any of the available sensors from the drop-down menu for a period of time between any two selectable dates. This tab was designed as just the most basic of ways to observe that data was being collected properly. The analyses that will be presented in the next few chapters have yet to be fully implemented in the Integrated SHM Data Collection Program.

8.3 Summary

The Integrated SHM Data Collection Program was created so that the data fiber optic sensor system, the wireless sensor system, and the MEMS compass could be used together. The program was written in C♯ and features a graphical user interface with tabs that can control the individual sensor systems. The Integrated SHM Data Collection Program also uses a database to store the collected data. Data can be collected from the fiber optic sensors as a stream or only at discrete events as determined by the event detection algorithm included in the program. The event detection algorithm can also trigger the wireless sensor system to collect data and label the output files with information as to the bridge position and train status.

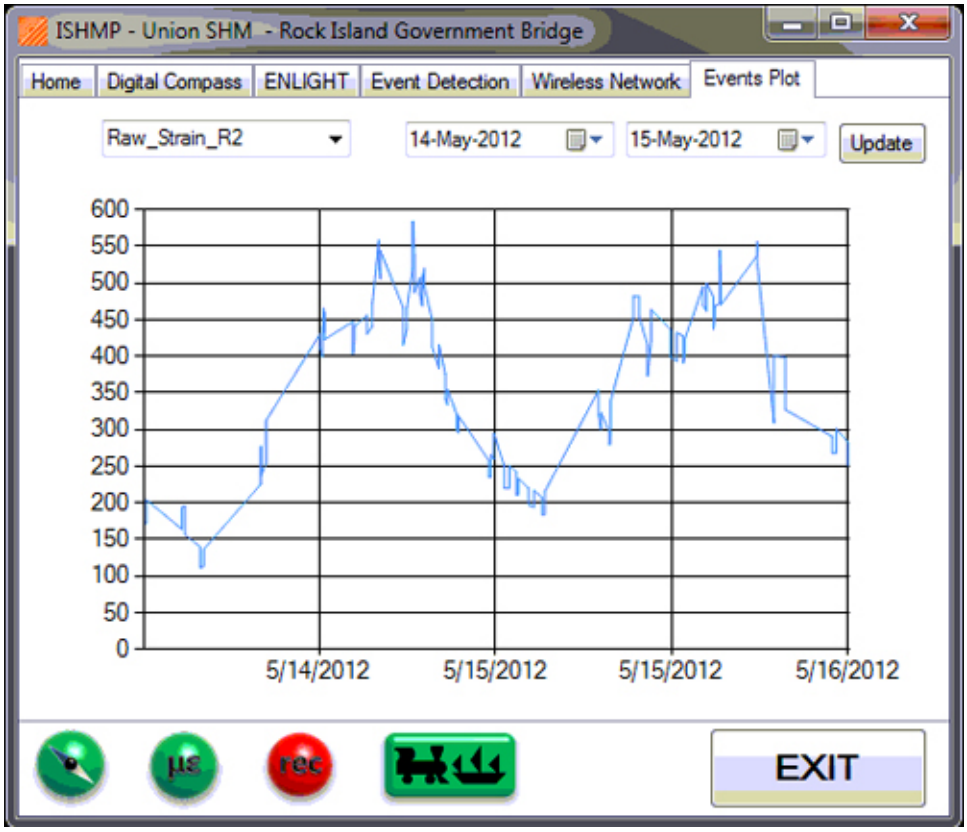

Figure 8.14: Event Plots tab of the Integrated SHM Data Collection Program GUI.

Chapter 9

ANOMALY DETECTION FOR COLLECTED DATA

Once data has been collected and features have been extracted by an SHM system, the question still remains as to what the features reveal about the health of the structure. If the condition of the structure were to never change, the features themselves should also never change. However, as the structure changes with time, the features are expected to also change; the SHM system then needs to be able to determine when the changes take place and what the changes in the data signify. Thus, an algorithm that detects "anomalies", or deviations from the expected behavior of the structure is needed.

Figure 9.1 shows a flowchart of the anomaly detection algorithm developed for the SHM framework for the Rock Island Bridge. Interpreting the data collected by the SHM system occurs in three primary steps. The first step is detection of a change in the data features. Any measurement will have some noise present in the metric. The task of anomaly detection is to determine if the collected data represents a change that is statistically different from the previous observed behavior and to determine the likely source of the change. Statistics computed using the data stored in databases by the Integrated SHM Data Collection Program provide a basis for determining the level of uncertainty in the data. Then, statistical process control methods can be used to determine if a new data point is a statistical anomaly that warrants further investigation.

After the detection step, determination of the likely source of the anomaly is next. The detected anomaly can represent one of the two general types of anomalies that need to be differentiated: sensor anomalies and structural anomalies. Sensor anomalies, without proper identification, could be misconstrued as structural problems. A number of different things can happen to the sensors that might cause problems with the data. The simplest form of a sensor problem is when it fails to return any data to the system. This sensor failure is often preferable to the alternative: sensors that are returning bad data. A sensor can return "bad" data when it has become detached from the structural member it is supposed to be measuring. "Bad" data can also result from long term stability issues with the sensors themselves; sensors can drift or lose mechanical stability. Methods were developed to detect certain sensor anomalies and are presented in this chapter.

The number of changes in the structure and its loadings that can be detected as anomalies is very large. Corrosion damage, loose bolts, debris build-up in pin joints, and permanent deformation are just a few changes that can alter the behavior of the structure. Some of these changes are reversible (e.g., debris in the pin joints can be cleaned out) while others are not (e.g., corrosion damage). The anomaly detection algorithm needs to be robust enough to function in all bridge condition states that can be considered "normal" operating conditions. However, the algorithm must also be sensitive enough to determine when conditions that can affect the safety of the bridge are changing. As an example, this chapter will discuss the elongation of the eye bar holes on the Rock Island Bridge. Visual bridge inspection reports have shown that over the lifespan of the bridge, many of the eye bars

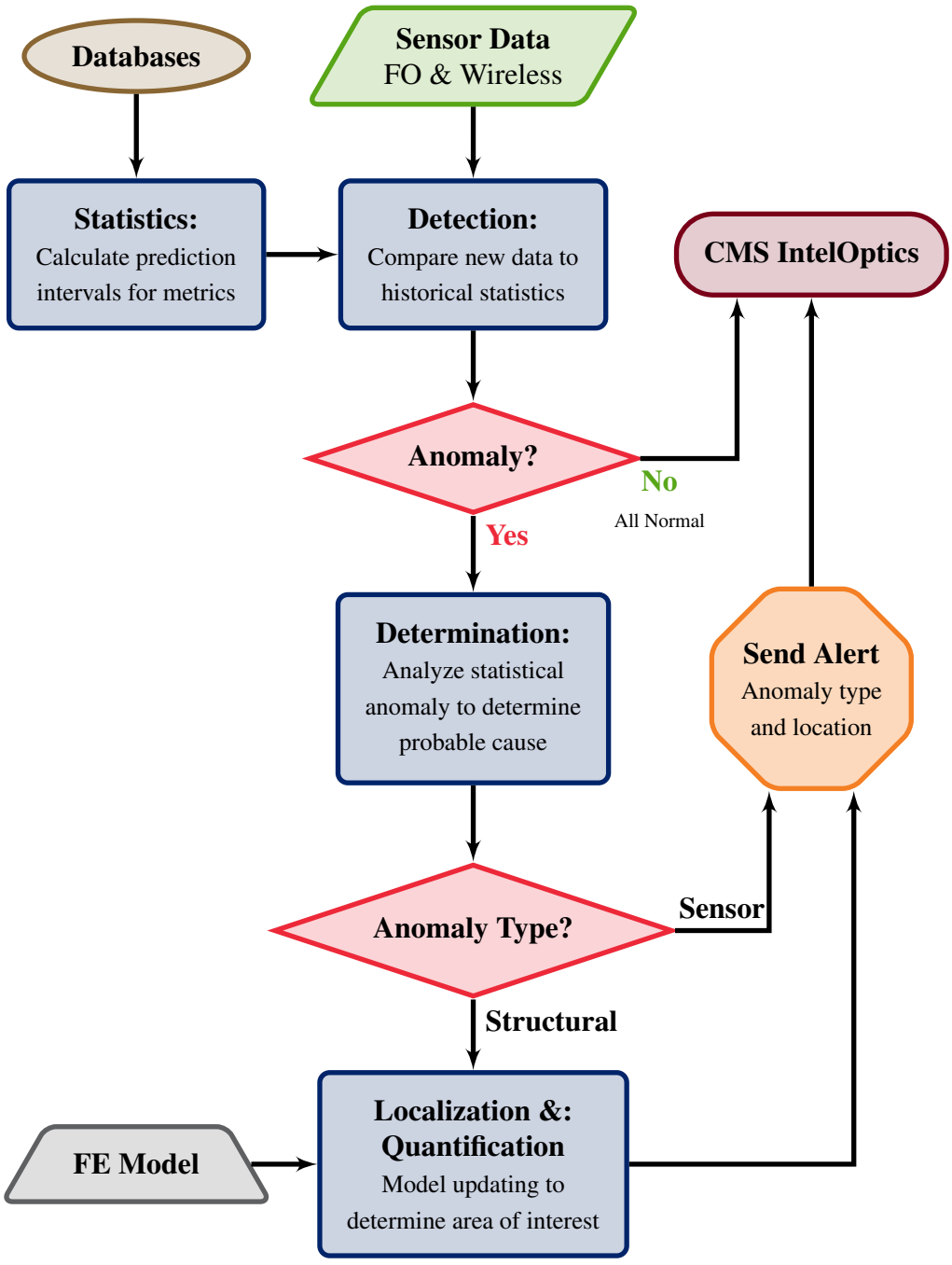

Figure 9.1: Flowchart of anomaly detection and reporting inside the Integrated SHM system.

have developed small elongations in their holes. In their current condition, the bridge is still safe; however, future changes to the hole elongations may be of concern. This chapter shows how the effects of hole elongations can change the data features and how the anomaly detection algorithm can function while accounting for these, and other, variations in the normal behavior of the structure.

9.1 Statistical Process Control

Statistical Process Control (SPC) is a method typically used in manufacturing to statistically analyze production to ensure quality and uniformity in the production of goods. The invention of SPC is attributed to Walter A. Shewhart[1] who was working for Bell Laboratories in the early 1920s. The goal of SPC is to identify sources of variation within a process and then eliminate, or at least minimize, the source of the identified variation.

In statistical process control, variation is normally classified as either common or special. Common variation is a source that is always present in the system and can be described statistically. "Noise" in the sensor measurements are an example of a common variation because it is describable and omnipresent. In SPC, a process is "in control" if the only common variation is present in the system. In contrast to common variation, special variation is something new, or developing, that causes changes to the system that are beyond the expected based on the historical record. These sources of special variation are the signal in the data that SPC is trying to identify.

For manufacturing processes, SPC is looking for changes in the manufacturing process that influence the end product. To make an analogy that describes using SPC for structural health monitoring, the end product is the measured dynamic or strain responses. The process being observed is therefore the structure's response to forces. In the SPC of manufacturing processes, creating a flowchart that describes each of the machines or steps that a product goes through is an essential step. For the SHM analogy, the flowchart is defined by the structural mechanics that transform the forces into measurable strains or detectable vibrations. Changes to the underlying stiffness, geometry, or mass of the structure are the possible sources for the special variation the SPC methods are trying to detect.

9.1.1 Control Charts

Statistical process control, as the name suggests, uses statistical methods and tools to identify sources of special variation in the monitored process. Control charts[2] are a graphical representations of this statistical hypothesis testing. The control charts are testing the null hypothesis (H_0) that the mean and variation of the process have not changed. When the hypothesis is correct, the system is said to be "in control."

[1] Shewhart received his undergraduate degrees from the University of Illinois at Urbana–Champaign before getting his doctorate in physics from the University of California – Berkeley.

[2] Control charts are also referred to as Shewhart Charts.

In manufacturing processes, SPC is usually performed by taking multiple samples of the product at regular intervals and tracking the desired metric. For example, a bolt manufacturer might remove five bolts every hour on the hour and measure the bolt diameter and length. The average and standard deviation of the five sample bolts is then computed and it is this value that is typically plotted in a control chart. Control charts become more powerful as the number of samples in each test batch is increased. [129]

However, not all processes allow for having multiple samples for a given measurement. Structural health monitoring is one situation where multiple samples are not possible. Typically in SHM, the number of sensors are limited and so placing multiple sensors at the same location to get multiple samples of a given value is not very likely[3]. For the Rock Island Bridge, each swing is unique and represents the only sample that is taken in each "batch" of swings. Therefore, for a process like the bridge opening and closing where every event is measured, the best control chart to use is one for individual measurements. To create a control chart, a number of previous measurements of the metric are needed. The control chart values are then calculated as follows. [130] First, the mean, $\bar{x}$, and standard deviation, σ, are calculated for the n number of individual values, x_i, that have been collected.

$$\bar{x} = \frac{1}{n}\sum_{i=1}^{n} x_i \tag{9.1}$$

$$\sigma^2 = \frac{1}{n}\sum_{i=1}^{n} (x_i - \bar{x})^2 \tag{9.2}$$

Once the mean is calculated, it becomes the centerline of the control chart as see in Figure 9.2. The next step in creating the control chart, as in hypothesis testing, is to calculate the unbiased standard deviation, $\hat{\sigma}$ as follows.

$$\hat{\sigma} = \sqrt{n-1}\frac{\Gamma\left(\frac{n-1}{2}\right)}{\Gamma\left(\frac{n}{2}\right)}\frac{1}{\sqrt{2}}\sigma \tag{9.3}$$

Once the unbiased estimation of the standard deviation is calculated, the control limits for the chart can be calculated. Control charts use two types of control limits: the Upper Control Limit (UCL) and the Lower Control Limit (LCL). These limits are calculated as follows:

$$UCL = \bar{x} + 3\hat{\sigma} \tag{9.4}$$

$$LCL = \bar{x} - 3\hat{\sigma} \tag{9.5}$$

The UCL and LCL are plotted in the control chart above and below the centerline respectively. The measured values for new samples can then be plotted on this chart.

The control charts can be tuned to a desired confidence level, as is done in hypothesis testing, because the underlying distribution of a control chart is assumed to be normal.[4]

[3]Even if multiple sensors are used in an SHM application to measure the same value, it is still not equivalent to using the same sensor to take multiple measurements of the same event. The sensors are not exactly identical and have their own noise associated with it.

[4]Some control chart formulations use other probability distributions (e.g., the gamma distribution [129]),

The use of $3\hat{\sigma}$ in Equations 9.4 and 9.5 indicates that 99.73% of all measured values of a process in control are expected to fall between the control limits. Though the control limits can be tuned to other probabilities, $3\hat{\sigma}$ is traditionally used. Intermediate limits at $2\hat{\sigma}$ (94.45%) and $1\hat{\sigma}$ (68.27%) are sometimes plotted in control charts (as seen in Figure 9.2) so that other observations about the data can be made.

With the control limits set at $3\hat{\sigma}$, a 0.27% chance exists for the control chart to exhibit a Type I error (false positive) for each new data point. Put in other words, for a process that is in control, approximately three in every one thousand samples would be expected to be beyond the control limits even if the process, and the mean and standard deviation of the underlying normal distribution, does not change at all. Computing the probability of exhibiting a Type II error (false negative) will depend on any change that takes place in the process. The number of samples that a control chart will take to detect the change that is causing the Type II error is called the Average Run Length (ARL). As an example, the ARL for an individual value control chart that experiences a shift in its mean is calculated as follows. Given the original mean, $\bar{x}_0$ and standard deviation, $\hat{\sigma}$ the shifted mean, $\bar{x}_1$ can be written.

$$\bar{x}_1 = \bar{x}_0 + \delta\hat{\sigma} \tag{9.6}$$

In this example if δ is assumed to be positive, then $\bar{x}_1$ will be closer to the UCL and the probability, γ, that a measured value will exceed the UCL is given as:

$$\begin{aligned}\gamma(\delta) &= 1 - P(\bar{x}_1 \leq UCL) \\ &= 1 - \Phi\left(\frac{UCL - \bar{x}_1}{\hat{\sigma}}\right) \\ &= 1 - \Phi(3 - \delta)\end{aligned} \tag{9.7}$$

From this probability, the ARL can be computed as:

$$ARL = \frac{1}{\gamma} \tag{9.8}$$

As an example, if the mean of a normally distributed process were to shift such that $\delta = 0.5$ then the ARL would be 161.0 meaning that on average it will require 161 samples to detect the given change. As δ increases, the control chart is more likely to detect a change.

The data contained in a control chart can be analyzed in other ways to decrease the ARL and increase the ability of the chart to detect changes in the underlying process. These methods of evaluation are called "run rules." Run rules are ways of analyzing the data in a control chart that identifies when a special variation has arisen in the process. The simplest run rule is that a data point is flagged when a datum exceeds either the upper or lower control limit. It is easy enough to program a monitoring program to check each new datum for exceeding the control limits and then take a specified action (e.g., sound an alarm or send an e-mail). Other run rules exist and some have been compiled into well-known lists. One of the most common sets of run rules is that compiled by Nelson [131]. *Nelson's Run*

but the data observed at the Rock Island Bridge conforms to normal distributions and therefore the other distributions are not presented here.

Rules is a list of eight run rules where each rule is designed to look for specific patterns in the control chart data.

The following rules are all illustrated in Figure 9.2.

Rule 1: *Any point greater than 3σ from the mean.* This rule looks for points that are "grossly out of control." Only this first rule is dependent on a single point. Therefore, this rule is not designed to detect subtle changes in the system but a point that is completely outside the statistically significant range. In the context of a manufacturing process, a point that triggers this rule could be indicative of a machine that has suddenly stopped working. In the context of SHM for bridges, the point may be caused by a vehicle crashing into the bridge or a member that experiences sudden failure.

Rule 2: *Nine or more consecutive points on the same side of the mean.* This rule is designed to detect a shift in the mean of the system or a prolonged bias in the measurements. In the context of SHM of bridges for corrosion effects, this rule is perhaps the most applicable. Corrosion is s slow and gradual process that will change the expected value of the strain measurements. Rule 2 is more sensitive to the change in mean expected from corrosion induced changes.

Rule 3: *Six consecutive points are either all increasing or all decreasing.* This rule identifies if a trend exists in the data. If the system is changing at a rate that approaches the sample rate then this rule can be helpful. For corrosion and most other sources of structural degradation, the rate of change is likely too slow for this rule to be very helpful.

Rule 4: *Fourteen consecutive points that alternate direction.* This rule indicates neither a change in the mean nor a change in the standard deviation of the process. Nevertheless, the alternating changes in direction indicates an oscillation in the system that is likely not attributable to noise.

Rule 5: *Two out of three consecutive points are greater than 2σ from the mean on the same side of the mean.* This rule detects a process that is moderately out of control. The likelihood of one point exceeding 2σ is less than that in Rule 1. However, the additional requirement of having two of three points in a row exceed 2σ reduces the likelihood to a level similar to Rule 1.

Rule 6: *Four out of five consecutive points are greater than 1σ from the mean on the same side of the mean.* This rule, when compared to Rule 1 and Rule 5, is designed to detect a process that is only slightly out of control. Like Rule 5, the additional requirement of having four out of five all greater than 1σ reduces the probability of this rule flagging a point to a level only slightly greater than Rule 5.

Rule 7: *Fourteen consecutive points are all within $\pm 1\sigma$ of the mean.* This rule is designed to detect when the variation of the system has perhaps decreased. For fourteen points, greater variation in the value would be expected.

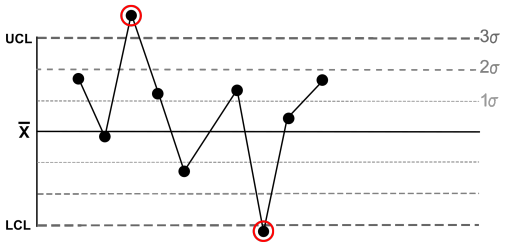

(a) Rule 1: Any point greater than 3σ from the mean.

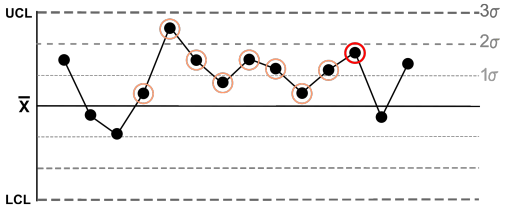

(b) Rule 2: Nine or more consecutive points on the same side of the mean.

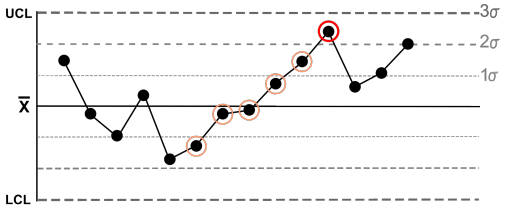

(c) Rule 3: Six consecutive points are either all increasing or all decreasing.

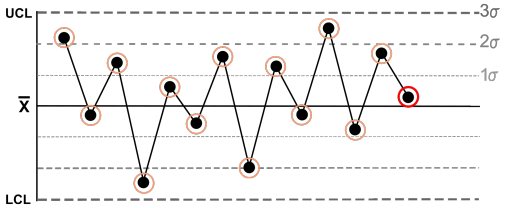

(d) Rule 4: Fourteen consecutive points that alternate direction.

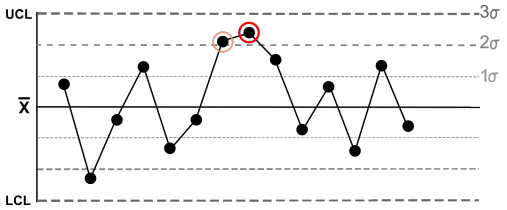

(e) Rule 5: Two out of three consecutive points are greater than 2σ from the mean on the same side of the mean.

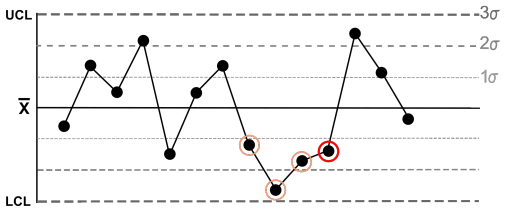

(f) Rule 6: Four out of five consecutive points are greater than 1σ from the mean on the same side of the mean.

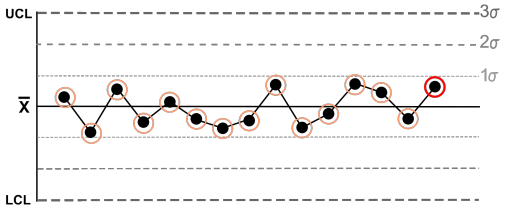

(g) Rule 7: Fourteen consecutive points all within $\pm 1\sigma$ of the mean.

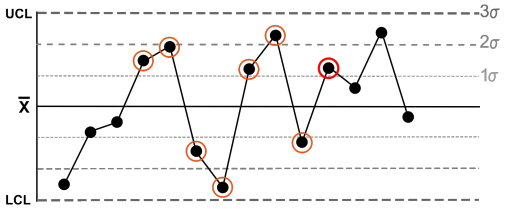

(h) Rule 8: Eight consecutive points that are all greater than 2σ of the mean and some of the eight are on both sides of the mean.

(GMcGlinn / Wikimedia Commons)

Figure 9.2: Nelson Run Rules for control charts.

Rule 8: *Eight consecutive points that are all greater than 2σ of the mean and some of the eight are on both sides of the mean.* This behavior is indicative of a process that, like Rule 4, may not be indicative of a change in the mean or standard deviation of the process. However, it may indicate a duality in the process that is not defined by a normal distribution. In this instance, the true underlying distribution could be the sum of two normal distributions.

The run rules that are to be used in an analysis based on what type of change to the system the control chart is trying to detect. Multiple run rules can be used on the same data and chart simultaneously. When used together, the run rules are designed to reduce the ARL to identify a special variation or change in the normal process that describes the data [132]. As seen in Table 9.1, only approximately three out of every thousand data points would be expected to be identified by Rule 1. Rules 2, 5, and 6 have slightly higher probabilities of indicating a Type I risk.

9.1.2 Cumulative Sum (CUSUM) Charts

Even with the additional run rules, control charts of individual values lack power in detecting small changes to the process. As an alternative, the Cumulative Sum (CUSUM) or other variations of sequential methods are at times more effective [129]. The cumulative sum, S_n, is calculated for each sample taken as follows:

$$S_n = \sum_{i=1}^{n} (x_i - \bar{x}) \tag{9.9}$$

For a normally distributed variable, the cumulative sum should remain around zero in the long term. If the mean of the system shifts, then the CUSUM chart will begin to drift in that direction.

To aid in the identification of when a CUSUM chart is indicating the system has become out of control, a "V-mask" is often superimposed on the CUSUM chart. Figure 9.3 shows a representation of a V-mask. The shape of the V-mask is determined by user selected values for the desired probability of Type I risk α, the desired probability of Type II risk β, and the amount of shift to detect expressed as a multiple δ of the standard deviation. These three values are used to calculate: k, the unit run slope of the V-mask arms; d, the distance from the origin (latest point) to the vertex of the V-mask; and h, the rise in the arm from

Table 9.1: Probability of Type I Risk (false positives) for select Nelson Run Rules.

	1–Sided Test	2–Sided Test
Rule 1	0.00135	0.00270
Rule 2	0.00195	0.00391
Rule 5	0.00153	0.00306
Rule 6	0.00277	0.00554

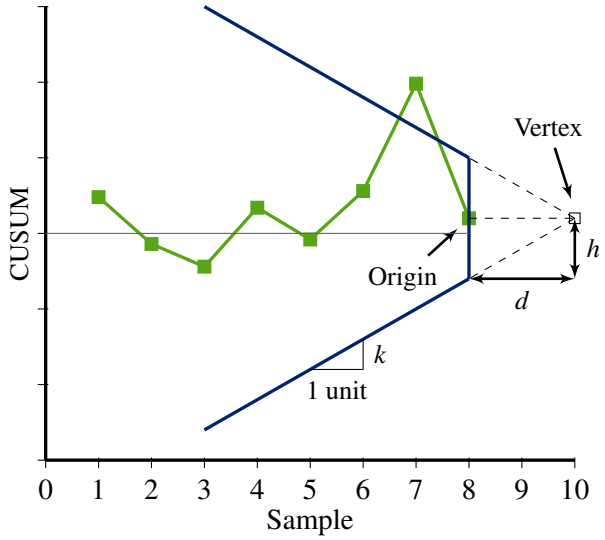

Figure 9.3: Formulation of V-Mask for CUSUM Chart.

the origin to the vertex. These parameters are calculated as follows:

$$k = \frac{\delta\hat{\sigma}}{2} \tag{9.10}$$

$$d = \frac{2}{\delta^2}\ln\left(\frac{1-\beta}{\alpha}\right) \tag{9.11}$$

$$h = dk \tag{9.12}$$

Once the CUSUM chart has been constructed, the V–mask moves with each successive point and all previous points are analyzed with the V-mask placed at the new origin. The ARL for a CUSUM chart is less for small shifts in the mean than for a typical Shewhart control chart.

9.1.3 SPC in SHM

The literature contains a few instances of using statistical process control methods as a tool in structural health monitoring. Sohn et al. [133] and Fugate et al. [134], working at Los Alamos National Laboratories, used SPC to detect damage to a concrete pillar in the laboratory. They extracted features from vibration measurements using an autoregressive model and used SPC control charts to monitor the features as the concrete column was progressively damaged. Sohn et al. focused mainly on shifts in the mean ($\bar{x}$-charts) while Fugate et al. observed changes in the variation (s-charts) of the system. SPC methods proved to be useful in tracking the damage to the structure as it occurred.

Another use of SPC for SHM purposed in the literature was performed by Zapico-Valle et al. [135] on a steel frame in their laboratory. They measured vibration data and extracted features to monitor using statistical process control methods. They varied the mass of the

structure using weights and also loosened bolts in the connections to change the stiffness of the structure and simulate damage. Zapico-Valle et al. were able to detect slight mass increases and the loosening of bolts in the laboratory setting using SPC control charts.

One study by Deraemaekera et al. [136] looked at the effectiveness of SPC methods on a bridge by examining its simulated use on a large finite element model of a bridge. They simulated the monitoring of natural frequencies under different environmental temperatures and conditions to determine if the SPC control charts were sensitive to these changes. They also introduced damage to the structure and analyzed how long it would take a control chart to recognize the damage given the natural noise in the measurements and the environmental changes. They found that without correcting for environmental factors, the natural frequencies are not an ideal metric because they are too influenced by temperature. However, the mode shape is not as affected by environmental factors and therefore a better metric if compensation is not available.

In one instance, SPC has been applied to an actual bridge structure. Kullaa [137] used Shewhart and CUSUM control charts on the Z24 Bridge in Switzerland. The control charts were used to monitor the changes in natural frequencies, mode shapes, and damping ratios of the bridge before and after pier settlements that were measured to be 40 and 95 mm. The control charts proved to be sensitive to the pier settlements and easily detected when they occurred.

9.2 Data Collection and Feature Selection

To implement SPC as part of the anomaly detection algorithm, data needed to be collected and analyzed. From March 13, 2012 to June 7, 2012, the Integrated SHM Data Collection Program, as described in Chapter 8, continuously[5] collected data and implemented the event detection algorithm. During this period, the Integrated SHM Data Collection Program detected and recorded 440 swing events that took place at night, did not immediately follow a train, and did not have multiple attempts at opening or closing. Of these events, 223 of them had the bridge locking/unlocking from the stairs downstream position and 217 of them took place in the stairs upstream position. As expected, the position of bridge had a distinct effect on recorded strain values and so any analysis of the data must needs be done according to the bridge position.

Other metadata about the swings proved to be less significant. For example, 174 of the recorded events were the bridge unlocking at the start of a swing and 266 of them were the bridge re-locking after a swing. The reduced number of unlocking events is due to two primary reasons: *a*) some starts were excluded because they followed the passage of a train; or *b*) some swings began during daylight or twilight hours and ended at night[6].Statistically,

[5]Data collection was interrupted a few times during daylight hours when software upgrades of the program were implemented. However, very few events were missed during the interruptions and data collection was always resumed by sunset to capture all events during the night.

[6]A few swings started at night and ended during twilight or day hours, but these occur less often. The barges usually start to pass through the locks just before or after dawn each day. As seen in Figure 4.6, few barge lockages end at the dawn hours.

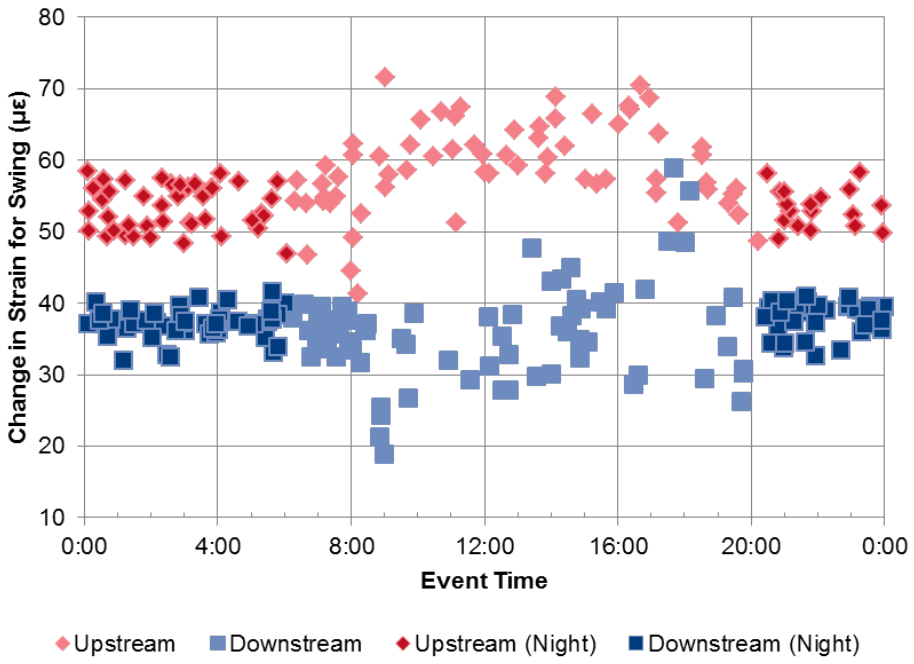

Figure 9.4: Change in strain ($\Delta\epsilon$) of swing events versus time of event.

whether the bridge was locking or unlocking made no difference to the strain changes recorded by the system.

Additionally, the bridge swung clockwise 218 times and counterclockwise 215 times. The seven times the event detection algorithm failed to determine the direction of the swing is likely due to the bridge operator taking longer than one minute to either begin to move the bridge after unlocking it or re-lock the bridge after swinging it back into position. The direction of the swing also had no statistical influence on the measured strain differences.

In selecting which features to analyze, the loads applied to the structure were considered. The primary live loads on the structure are the temperature, trains, swings, and vehicles. In looking for features, consistency is paramount for establishing a sensitive indication of structural health. The train and vehicular loadings are highly variable, because the size, weigh, and speed of one train or vehicle is not the same as another. However, temperature variations and the swings do represent consistent loads that can be the basis for monitoring features.

The analysis of the fiber optic sensors presented in Section 5.6 showed that at night the temperature on the bridge becomes even. At these times the bridge is not affected by temperature differentials and can be assumed to be at a constant temperature. The effects on the structure of changes in temperature at night will serve as one feature.

The analysis of the fiber optic strain sensors discussed in Section 5.5 demonstrated that the change in strain ($\Delta\epsilon$) when the bridge swings open is highly regular. Figure 9.4 shows the change in strain in Sensor R2 for all the swing events that were detected using the event detection algorithm between March 13 and April 30, 2012 plotted against the time of day the event took place. The two colored bands of data points represent events that swung from either the upstream (red) or downstream (blue) position. The swing events

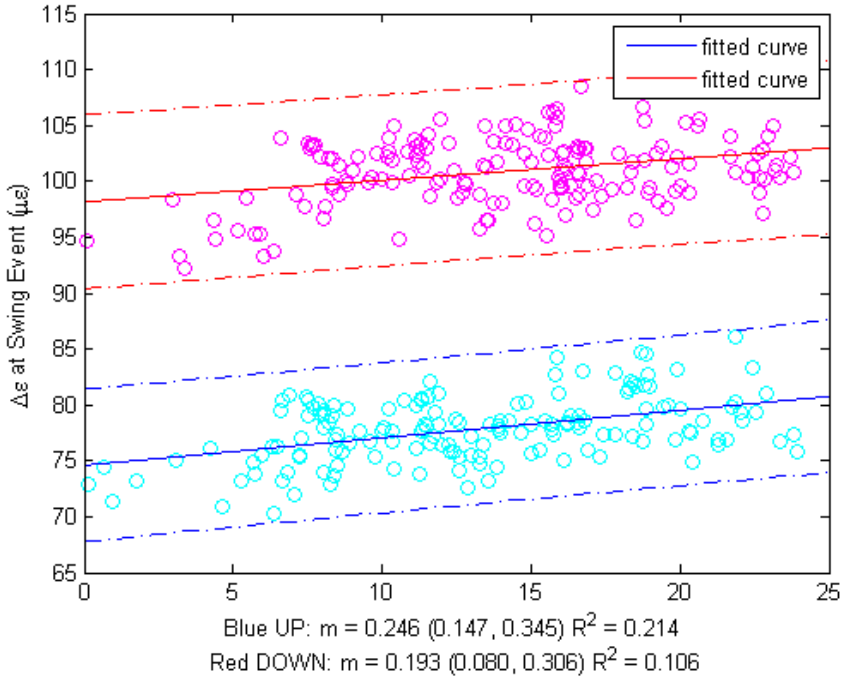

Figure 9.5: Change in strain ($\Delta\epsilon$) of swing events versus temperature with prediction bands.

that took place during the night have been shaded darker. The $\Delta\epsilon$ that result from night swings are highly regular while those during the day have greater variation and slightly different values. During the day, temperature differentials can develop that alter the strain profile of the structure. The greatest variation can be seen in the early morning and late afternoon when the sun is more directional and the temperature differentials can be greater. The regularity of the $\Delta\epsilon$ for the swings during the night indicate that $\Delta\epsilon$ is a good feature for monitoring structural behavior.

The mechanical strain of the system, not the differential at the swing events, can be used as a third feature. The mechanical strain is already used in calculating the observed coefficient of thermal expansion and the $\Delta\epsilon$ for the swings. However, the raw strain readings can also provide insight into the behavior of the sensors themselves.

Each of these three features – observed coefficient of thermal expansion, change in strain at swing events, and mechanical strain – has a role to play in detecting both sensor and structural anomalies. The following sections will discuss each metric in more detail and how it can be used to detect anomalies.

9.3 Coefficient of Thermal Expansion

In calculating the statistics for the $\Delta\epsilon$, a slight temperature dependency on the $\Delta\epsilon$ value was observed. Figure 9.5 shows the $\Delta\epsilon$ for the night swings for Sensor L31 plotted against the average temperature recorded by the fiber optic sensors. Linear regression has been

performed to fit the data to lines that have the form of:

$$\Delta\epsilon = m \cdot T_{avg} + b \tag{9.13}$$

The slope of this line represents the dependency of $\Delta\epsilon$ on the temperature. Prediction bands for the 95% confidence level have also been computed and plotted in the figure using dashed lines. As displayed in Figure 9.5, the slopes for the fitted lines were calculated to be 0.246 $\mu\epsilon/^{\circ}C$ for swings originating or terminating in the upstream position and 0.193 $\mu\epsilon/^{\circ}C$ for downstream swing events. To determine if these values are statistically significant, the linear regression fits were hypothesis tested with a null hypothesis that the slope of the fit line is not statistically different from zero. The hypothesis testing for Strain L33 rejected the null hypotheses for both the upstream and downstream data sets. Therefore, the change in strain is significant and when using this statistic in the anomaly detection algorithm, the temperature of the measurement must be considered. Table 9.2 shows the linear regression and hypothesis tests for all the sensors.

As seen in the Table 9.2, the hypothesis testing rejected the null hypothesis in most cases indicating that the temperature variation is statistically significant. Those sensors where the null hypothesis was accepted in both the upstream and downstream positions were the exception. Sensors R6 and L24 were expected to accept the null hypothesis because both sensors are located on the M7 pins and essentially measure only the thermal strain. The low intercept values for these two sensors (b in the table) indicate that the change in strain is essentially the noise in the system.

To investigate why the $\Delta\epsilon$ exhibited a statistically significant variance with temperature, the values that are used to calculate the $\Delta\epsilon$ (the total strain just before the bridge locks or unlocks and the total strain just after) were analyzed further. Figure 9.6 shows plots of the total strain for the swung position and the two locked positions with linear regression lines calculated for each position. The swung strain values showed a distinct linear trend irrespective of which locked position the bridge was locking to or unlocking from. However, the two locked positions showed distinct difference from each other. At the scale of the plot, the three linear regression lines appear parallel. However, the equations in Figure 9.6 indicates that the slopes of the three linear regression lines are different. Table 9.3 shows the slopes (net CTE) for the three positions for all the fiber optic strain sensors. When these slopes are subtracted (UP -Swung and DOWN-Swung) the results approximate the values presented in Table 9.2. The values do not exactly match up because the $\Delta\epsilon$ reduces some of the variation. For example, the strain value in the downstream position and the strain value in the swung position for the same swing event are correlated. The fact the slopes of the three positions are not equal indicates that the mechanical properties of the individual member being measured within the truss has an effect on the net coefficient of thermal expansion.

To determine what source of the positional influence on the net CTE, the histogram in Figure 9.7 of the swung slopes (net CTE) was prepared. The strain sensors are color coded by the type of member they are mounted on. For example, sensor Strain L31 is on the eye-bar diagonal M5'–U6' and has a slope (see Figure 9.6) of 16.438 $\mu\epsilon/^{\circ}C$. Therefore, in Figure 9.7, sensor Strain L31 is represented by one of the three eye-bar diagonals in the 16–16.5 bin. Figure 9.7 shows that all but one of the plotted slopes falls between the range

Table 9.2: Linear regression and hypothesis testing results for change in strain of for night swings with respect to temperature.

$$\Delta\epsilon = m \cdot T + b$$

	Upstream				Downstream			
Sensor	m	b	R^2	H_o	m	b	R^2	H_o
R1	—	—	—	—	—	—	—	—
R2	-0.122	36.263	0.054	Reject	-0.020	24.532	0.002	Accept
R3	0.030	6.564	0.244	Reject	0.008	4.208	0.022	Accept
R4	0.319	87.561	0.336	Reject	0.261	70.032	0.377	Reject
R5	0.093	44.651	0.112	Reject	0.068	36.866	0.104	Reject
R6	0.000	0.806	0.000	Accept	0.001	0.622	0.000	Accept
R7	-0.015	0.895	0.056	Reject	-0.053	2.355	0.372	Reject
R8	0.150	45.550	0.205	Reject	0.120	37.858	0.181	Reject
R9	0.169	56.799	0.209	Reject	0.126	48.169	0.190	Reject
R10	—	—	—	—	—	—	—	—
R11	—	—	—	—	—	—	—	—
R12	—	—	—	—	—	—	—	—
R13	—	—	—	—	—	—	—	—
R14	—	—	—	—	—	—	—	—
R15	—	—	—	—	—	—	—	—
R16	—	—	—	—	—	—	—	—
R17	-0.216	78.232	0.046	Reject	0.153	14.755	0.028	Reject
L18	—	—	—	—	—	—	—	—
L19	-0.537	39.909	0.733	Reject	-0.816	54.823	0.743	Reject
L20	0.028	8.016	0.131	Reject	0.016	11.811	0.039	Reject
L21	—	—	—	—	—	—	—	—
L22	0.114	36.222	0.206	Reject	0.088	48.770	0.094	Reject
L23	0.022	0.799	0.041	Reject	0.036	6.914	0.004	Accept
L24	0.002	1.141	0.001	Accept	0.009	1.588	0.023	Accept
L25	-0.004	0.706	0.002	Accept	0.001	0.540	0.000	Accept
L26	—	—	—	—	—	—	—	—
L27	—	—	—	—	—	—	—	—
L28	—	—	—	—	—	—	—	—
L29	—	—	—	—	—	—	—	—
L30	—	—	—	—	—	—	—	—
L31	0.246	74.599	0.214	Reject	0.193	98.165	0.106	Reject
L32	0.021	6.524	0.069	Reject	0.026	8.628	0.089	Reject
L33	-0.292	23.866	0.147	Reject	-0.524	34.482	0.291	Reject
L34	-0.069	29.104	0.014	Accept	0.029	33.429	0.002	Accept

Data from 13-Mar-2012 to 08-May-2012

Note: A dashed line (—) indicates that the given strain sensor was not functioning when the data was collected.

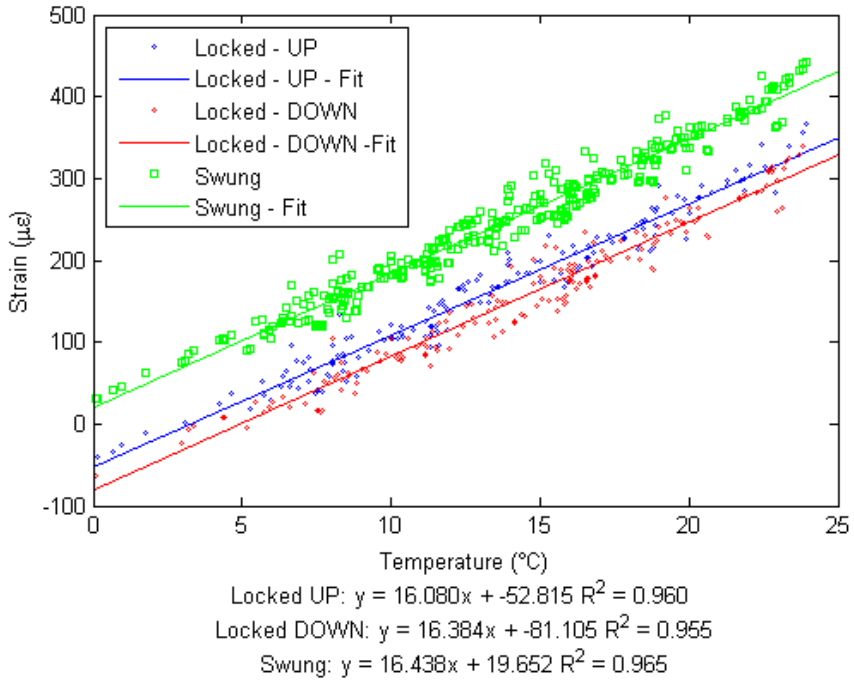

Figure 9.6: Total strain versus temperature with linear regression lines.

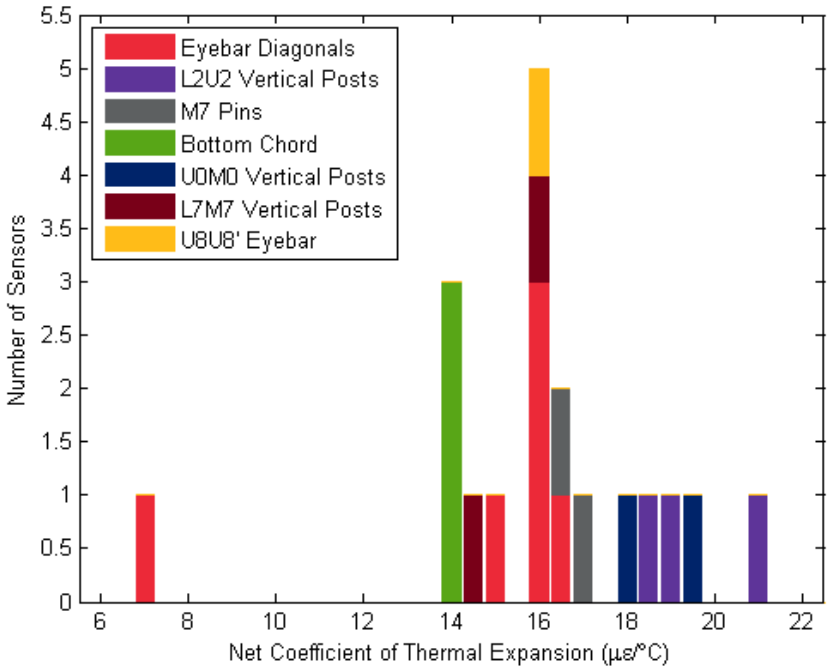

Figure 9.7: Net coefficient of thermal expansion by member type in the swung open position.

Table 9.3: Slope for the linear regression of strain with respect to temperature.

$$\epsilon = m \cdot T + b$$

Strain Sensor	Locked Upstream	Locked Downstream	Swung
Strain R1	—	—	—
Strain R2	18.395	18.501	18.538
Strain R3	14.003	13.974	13.985
Strain R4	15.627	15.818	15.992
Strain R5	16.056	16.147	16.172
Strain R6	16.447	16.767	16.579
Strain R7	19.374	19.393	19.400
Strain R8	15.626	16.562	16.249
Strain R9	15.922	15.983	16.105
Strain R10	—	—	—
Strain R11	—	—	—
Strain R12	—	—	—
Strain R13	—	—	—
Strain R14	—	—	—
Strain R15	—	—	—
Strain R16	—	—	—
Strain R17	14.980	14.524	14.704
Strain L18	—	—	—
Strain L19	18.451	18.440	19.099
Strain L20	14.054	14.136	14.089
Strain L21	—	—	—
Strain L22	14.649	15.279	15.075
Strain L23	18.071	18.247	18.185
Strain L24	17.032	17.197	17.088
Strain L25	7.390	7.141	7.243
Strain L26	—	—	—
Strain L27	—	—	—
Strain L28	—	—	—
Strain L29	—	—	—
Strain L30	—	—	—
Strain L31	16.080	16.384	16.438
Strain L32	14.114	14.374	14.243
Strain L33	20.639	20.421	20.947
Strain L34	15.903	15.900	15.945

Data from 13-Mar-2012 to 08-May-2012

Note: A dashed line (—) indicates that the given strain sensor was not functioning when the data was collected.

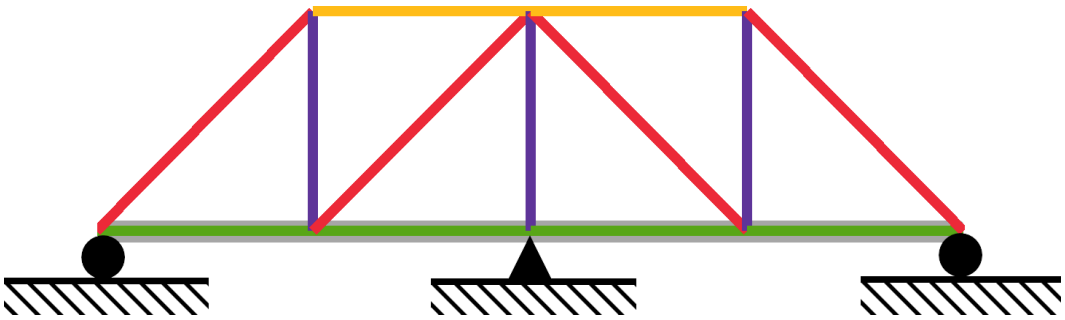

Figure 9.8: Simple truss model with steel members and a concrete deck.

of 14 – 21 $\mu\epsilon/^{\circ}C$. This range of slopes includes 18.3 $\mu\epsilon/^{\circ}C$ that Equation (5.9) predicts the slope of the line should be based on the principles of thermal compensation of the FBG strain gages.

The reason the slopes are not all 18.3 $\mu\epsilon/^{\circ}C$ or normally distributed around this value has to do with the indeterminate nature of the truss and the difference in the CTE of the concrete deck. To demonstrate this theory, a simple truss model was created that had three supports (as shown in Figure 9.8) and the same classes of members present in the Rock Island Bridge: top chord, diagonals, vertical posts, and bottom chord. The bottom chord was modeled using two elements (one of steel and one of concrete) per span. Thermal strains due to a change in temperature were induced in the model where the steel members had a CTE of 12 $\mu\epsilon/^{\circ}C$ and the concrete members had a CTE of 6 $\mu\epsilon/^{\circ}C$. The lower CTE of the concrete means that it will want expand less than the steel under the same thermal change and therefore resist the expansion of the steel and convert some of the thermal strains to mechanical strain inside the member. Thus the lower chord would be expected to have a net CTE of less than the expected value of 12 $\mu\epsilon/^{\circ}C$ for unrestrained steel. Figure 9.9 confirms this supposition and the bottom chord of the simple truss has the lowest net CTE of the four member types. Note that the vertical posts have net CTEs that are greater than the linear CTE of steel. Members of the same type are grouped near each other though there is some additional variation based on other mechanical factors unique to those members.

The histogram of net CTEs of the simple truss in Figure 9.9 and the experimentally obtained net CTEs for the Rock Island Bridge in Figure 9.7 are very similar. In both figures, the bottom chords closest to the concrete decks have the lowest value and the vertical posts have a net CTE that is greater than the gross CTE for the sensor/substrate combination. Therefore, the most likely source of the deviation of the net CTEs of the sensors is the influence of the mismatched CTE of the concrete deck and the steel superstructure. When the boundary conditions change in the locked position, the mechanical properties of the individual members change as does the net CTE. Therefore, a temperature dependency appears in the $\Delta\epsilon$ metric because it is derived from strain readings from positions with different boundary conditions.

The investigation into the temperature dependency of the $\Delta\epsilon$ metric proved useful because it highlighted one method of detecting anomalies in the sensors themselves. In Figure 9.7, one diagonal member is significantly less than the other members that are centered

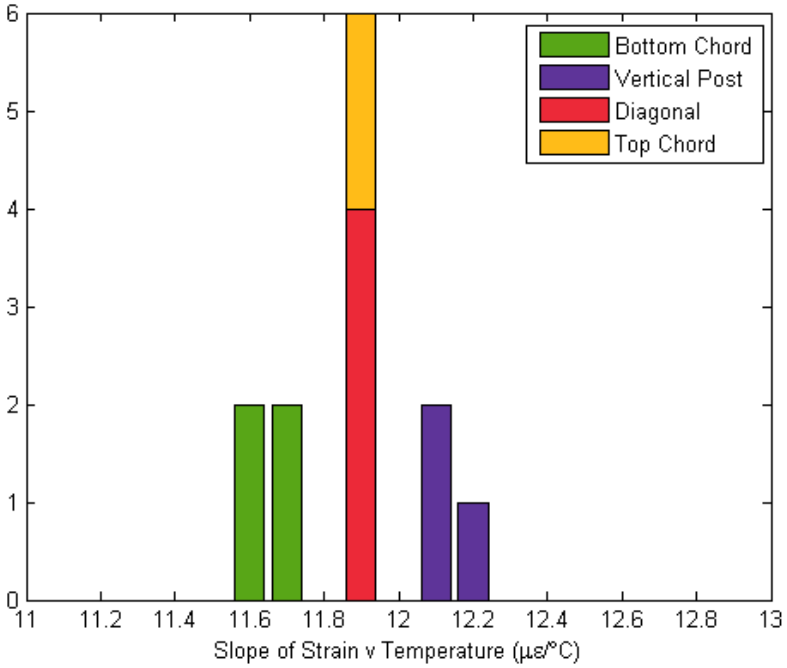

Figure 9.9: Net coefficient of thermal expansion by member type for a simple truss.

on 18.3 $\mu\epsilon/^{\circ}C$ net CTE for the FBG mounted on steel from Equation (5.9). Table9.3 indicates that the outlier is sensor Strain L25 and its net CTE is only 7.243 $\mu\epsilon/^{\circ}C$. This value is nearly equivalent to the α_{δ}/k term in Equation (5.6) that is the change in refraction index due to temperature change ($\alpha_{\delta} = 6.23\ \mu\epsilon/^{\circ}C$) divided by the gage factor ($k = 0.89$) which is equal to 7.0 $\mu\epsilon/^{\circ}C$. Essentially the influence of the CTE is missing from the sensor reading. In addition, Table 9.2 indicates that the mean value for the $\Delta\epsilon$ for Strain L25 is less than one microstrain while the other working sensor on a M7-U8 member – Strain R8 – has $\Delta\epsilon$ values of 45.55 $\mu\epsilon$ and 37.86 $\mu\epsilon$. Together, these results indicate that the sensor has become detached from the structure. Looks for changes in the net CTE of a sensor to indicate whether or not it has become detached from the structure is an integral part of the anomaly detection algorithm.

9.4 Change in Strain at Swing Events ($\Delta\epsilon$)

Monitoring the change in strain, $\Delta\epsilon$, caused by the bridge locking and unlocking has many advantages. Principal among the advantages is that as long as the sensors remain attached to the structure, then other sensor issues should cancel each other out in the subtraction of the strain values. For example, any long-term drift the sensors experience should not affect the strain measurements taken just before and after a swing. The same principle applies even

if the sensors are replaced by additional sensors of the same or different type.[7] Another advantage is that the load of the swings is consistent and therefore any observed changes in the $\Delta\epsilon$ value can be isolated to changes in the stiffness of the structure. Whether that stiffness is a change in the cross-sectional area of the member or changes to the member's connection will still need to be deduced from the data.

The $\Delta\epsilon$ was derived from the recorded strain events. The recorded strains were each individually temperature compensated according to the observed CTE for the corresponding position as found in Table 9.3. The temperature compensation reduced the slopes of the regression lines shown in Figure 9.5 such that statistically, the $\Delta\epsilon$ no longer was temperature dependent. With the temperature compensation complete, control charts were created using all the data with the expectation that the processes would be "in control". The initial control charts for the viable[8] sensors are shown in Figures 9.12(a)–9.35(a). However, in looking at these figures, every one of them shows multiple points that are deemed out of control with respect to just Rule 1. For the 223 samples in the downstream plots, on average only 0.594 of them should be out of control, but Figure 9.14(a) shows that 23 points are out of control. The number of out of control points is 38.7 times greater than expected. In addition, these out of control points occur both above the UCL and below the LCL.

In accordance with the principles of SPC, determining why the points were out of control required further investigation. Figure 9.14(a) shows shifts in the data points that are not typical of noisy data. Points 149 to 179 are all below the centerline. The last twenty-one of these thirty points also trigger Rule 2 indicating a prolonged bias. This run of thirty points in a row should have a probability of occurring of $1{:}2^{30}$ or about $1{:}1$ billion, assuming the underlying statistics were unchanged. What is even more unlikely is that points 30 to 51 also trigger Rule 2, but they are all above the centerline. Similarly, between points 80 and 120, run Rule 2 identifies a point that is out of control both above and below the centerline.

Finding an explanation for this observed behavior requires an understanding of the nature of structural damage and structural response over time. Because run Rule 2 is identifying multiple out of control points on either side of the centerline, corrosion damage to the member itself can be ruled out. Corrosion to the member would cause a permanent loss of material in its cross section and the data would not be expected to return or exceed its previous mean as Figure 9.14(a) shows it does.

The long sets of points that trigger Rule 2 are indicative that the next recorded event is not entirely independent of the previous recorded event. An underlying assumption in SPC is that the collected data follows a normal distribution where observations are independent from one another. Figure 9.14(b) can help further illuminate this trend because the $\Delta\epsilon$ are plotted with respect to time and not sample number. Figure 9.14(b), and its counterparts for the other sensors, shows that typically sensor readings taken on the same night have a very low variation but the change from day to day can be greater. Thus even if the structure has

[7] This principle is also why the verification of the fiber optic sensors with foil strain gages worked. Though the two sets of sensors were installed at different times and recorded different values, the swings could be matched up to determine that the fiber optic and foil gages were measuring the same response to the load change.

[8] The viable sensors were those that *a*) returned data to the system *b*) were not detached from the structure *c*) were not placed on the pin ends.

one swing event just after dusk and another just before dawn, these swings are very likely to exhibit the same $\Delta\epsilon$ than are swing events that are separated by daylight hours.

In addition to the apparent lack of independence in the observed data, the data also appears to not completely conform to the normal distribution. Figure 9.14(c) shows the histogram, fitted normal probability distribution function, and normal probability plot for the data. If the underlying distribution of the data is normal, then the data (purple dots) in the normal probability plot should closely follow the red line. However, the upper and lower tails of the data in the figure move away from the normal line indicating the underlying process demonstrates some non-normality. However, the histogram in Figure 9.14(c) appears almost to be at least two normal bell curves added together indicating that the observed $\Delta\epsilon$ is actually assuming more than one value with natural variation between them.

As will be discussed in Section 9.5, the observations that the $\Delta\epsilon$ appear to be neither independent nor from a single normal distribution cannot be explained by malfunctions in the sensors themselves or the fiber optic interrogator. With the sensors eliminated as a source of variation, the structure itself is the most likely source of the variation. The CUSUM[9] chart in Figure 9.14(a) shows portions that have a definite slope to the sequential progression of the cumulative sum. The first horizontal section indicates that the mean is a good estimate for this portion of the data. However, the slope of CUSUM chart soon changes indicating there has been a shift in the mean. The slope, and therefore the mean, shifts multiple times over the course of the collected data.

In comparing the CUSUM charts for sensor R2 in the downstream (Figure 9.14(a)) and upstream (Figure 9.15(a)) positions, they have very similar shapes. The shapes are not exact duplicates of one another because the data points in those charts are plotted by sample number and not date, but the overall trends' directions are the same. The similarity indicates that whatever is causing the shifts from day to day are consistent for each sensor regardless of whether the bridge is in the upstream or downstream position. If sensor R2's CUSUM charts are compared to the other sensors, the shifts in patterns among the other sensors are neither symmetric nor anti-symmetric to the R2 patterns. Therefore, the large shift is not caused by a global parameter such as the boundary conditions.

Because the large shifts in the strain values are reversible, in that it can return to the same mean value days later, traditional "damage" is not the cause. Damage caused by corrosion or other sources is an irreversible process. For sensor R2, which will switch from a tensile to compressive state and back over the course of the swing, the changes might be considered to be a change in the curvature of the member in the compressive state. A curvature change could cause the reversible nature of the state changes as measured by the surface mounted strain gages. However, the sensors, such as R4 (Figures 9.18(a) and 9.19(a)) and R8 (Figures 9.22(a) and 9.23(a)), that are on the diagonal eye beams that always remain in tension, and therefore have to compressive buckling to cause curvature, also exhibit similar behavior. Sensor R1, in the upstream position as shown in Figure 9.13(a), does exhibit a clear two mean behavior that could be contributed to a change in curvature in a compressive element. The member R1 is mounted on is the end post that only supports the railroad

[9]The V-mask that can indicate a change has been left off the CUSUM charts and just the cumulative sum is plotted.

deck and is not pinned on either end. The primary loads for these members are during train events and is purely compressive.

Recall, from Section 8.1 and Figure 8.4, that some members suddenly shifted by small amounts at apparently random points during the day and that sometimes the strain levels immediately before and after a train event were not always the same. To account for the former issue, the event detection algorithm had to have a difference tolerance and multi-sensor confirmation programmed into it so these shifts were not misconstrued as swing events. The latter issue required that a return to a temperature corrected strain level could not be used as an indicator that the train had finished its transit of the bridge. However, these issues also indicate that the bridge members have nearly discrete states in which they can exist and transitions from these states can be induced by temperature differentials during the day or by the large vibrations caused by a passing train. The likely cause for the out of control signals is that the strains are being measured in these various states and therefore the same "process" is not being measured.

The most likely explanation as to the existence of the various states of the bridge is that the pinned joints have experienced some corrosion and elongation. In the years since Modjeski oversaw the initial construction of the bridge, the pinned joints have experienced years of wear and exposure to the elements. The bridge inspection reports have reported that there has been some elongation of the holes through which the connecting pins have been placed. Corrosion in and around the pinned joint members can create rough surfaces and powdered corrosion material that can cause friction to develop in the joints. This combination of elongation and corrosion allows the joints to slide and stick in various positions. Once the joints slip, the stresses developed by the differential temperatures on the bridge during the day can develop sufficiently to overcome the friction in the joint. Large temperature swings, caused by cold fronts and rain, appear to have some effect on the likelihood that the bridge will shift states. The cold fronts allow large thermal stresses to develop and the rain reduces the friction in the joints. Similarly, the vibrations caused by the trains can overcome the friction in the joints and the member can end up in a more favorable state for the given conditions.

Additional evidence that supports that the pinned members are shifting in their elongated holes comes from those few members that are not pinned on either end. Only a few sensors, e. g. sensor R1 (Figures 9.12(a) and 9.13(a)) or sensor R3 (Figures 9.16(a) and 9.17(a)), are mounted on members that are not pinned at either end, but these sensors exhibited much less out of control behavior. For example, sensor R2, located on a pinned/pinned member, had twenty-three out of control points in the downstream position but sensor R3, located on the lower chord which is continuous and has riveted connections at its joints, had only three points that were out of control in the same position. There still appear to be small mean shifts in R3 but they are smaller in proportion to the standard deviation of the measured response in other sensors. These small shifts can be attributed to the shifts in other members that cause a redistribution of the loads throughout the structure.

The presence of shifts in the mean does not exclude the use of SPC methods and control charts from use a structural health monitoring technique; however, adjustments to the charts are necessary. The chart needs to be adjusted to account for the multiple means that are present in the observed process and the variation about those means. The altered control charts are called acceptance charts [129] and have an "acceptance band" of acceptable

mean values. The UCL and LCL are calculated from the limits of the acceptance band using a standard deviation calculated for data for an individual mean. The probability of having an out of control point are significantly reduced in this case because the process will only trigger the run rules if the system is out of control while in the lowest or highest mean states. Therefore, the largest proportion of points should be located in the acceptance band.

To create acceptance charts for the data, upper and lower mean limits and new UCLs and LCLs were computed. The first step in the computation of the UCL and LCL for the acceptance chart is to determine the mean and standard deviation for the constituent distributions. The underlying mathematical model of the data is a Gaussian mixture of normal distributions and with unknown participation factors. The MATLAB statistical toolbox provides the `gmdistribution.fit` command that can be used to analyze data and fit it to a set number of underlying normal distributions. The `gmdistribution.fit` command uses an expectation maximization algorithm to calculate maximum likelihood estimates of the parameters in a Gaussian mixture model The function outputs the means, standard deviations, and participation factor for each of the underlying distributions.

Unfortunately, the number of means in each set of data is unknown. Therefore, a procedure was developed to determine the parameters of the underlying distributions. First, the `gmdistribution.fit` calculated twenty possible mix components. The variance of the distributions are required to be equal to represent sensor variation for the means. Figures 9.10(a) and 9.11(a) show the means and participation factors for the calculated distributions. As the figures show, multiple computed distributions are close to the same mean. A second step was to average the means that are within 1σ of each other and sum their participation factors together. This step yields a reduced number of distributions in the Gaussian mix model. Figures 9.10(b) and 9.11(b) show the reduced number of component distributions and their participation factors. Some of the distributions contribute less than 5% to the total distribution. These component distributions with less than 5% participation were excluded from computing the upper and lower mean limits. The highest mean with more than 5% participation becomes the upper mean limit and the UCL is $3\hat{\sigma}$ greater than that. Likewise the smallest mean in the Gaussian mix with more than 5% participation becomes the lower mean limit and the LCL is $3\hat{\sigma}$ less than that.

Figures 9.12(b) to 9.35(b) show the acceptance charts that were produced. The data has been plotted on a time scale to allow for easier comparison between the upstream and downstream data. In addition to the UCL and LCL, dotted yellow lines have also been plotted to mark the $2\hat{\sigma}$ level. In creating a Green-Yellow-Red monitoring system similar to that used in the IntelOptics program, the $2\hat{\sigma}$ and $3\hat{\sigma}$ would be appropriate limits for the yellow and red regions respectively. The acceptance control charts show a reduced number of point that are out of control.

The acceptance control charts are still sensitive to changes in the loading of the members. For example, in Figure 9.30(b), the acceptance band represents a change in load of 2.5 kips which is only 1.8% of the original design load. Therefore it could be reasonably expected that the acceptance chart for L22 would be able to detect changes in the expected response of the bridge on the same order of magnitude.

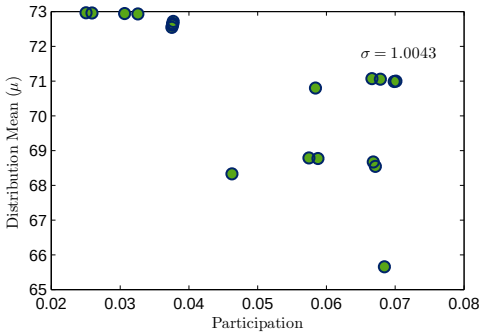

(a) All twenty original distribution parameters.

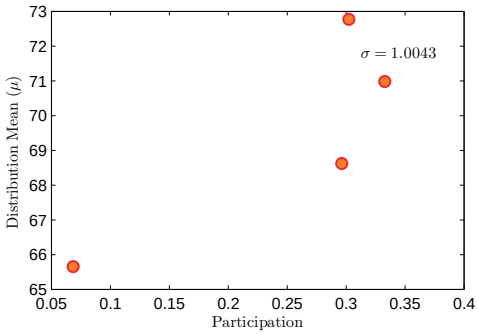

(b) Averaged distribution parameters.

Figure 9.10: Mean and participation for Gaussian mixture model for sensor R4 in the stairs downstream position.

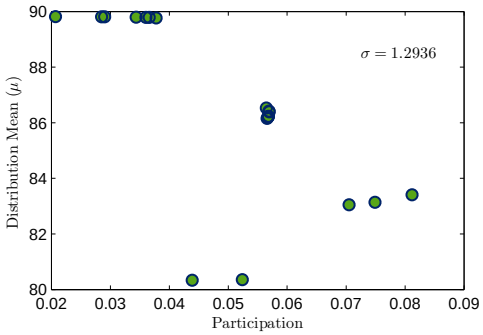

(a) All twenty original distribution parameters.

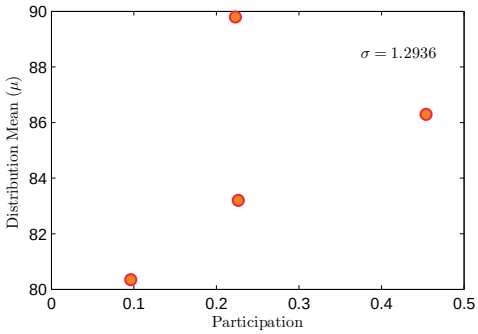

(b) Averaged distribution parameters.

Figure 9.11: Mean and participation for Gaussian mixture model for sensor R4 in the stairs upstream position.

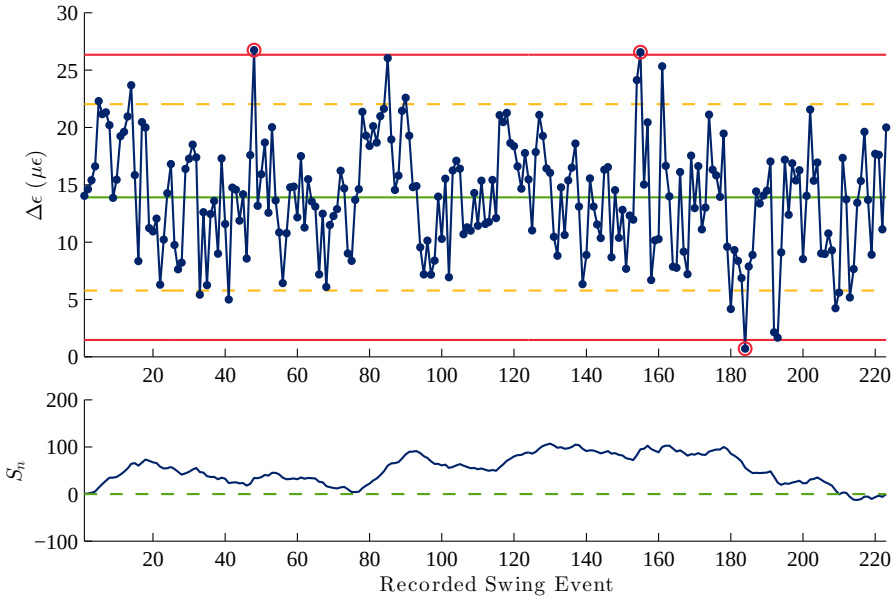

(a) Control and CUSUM chart: All Data.

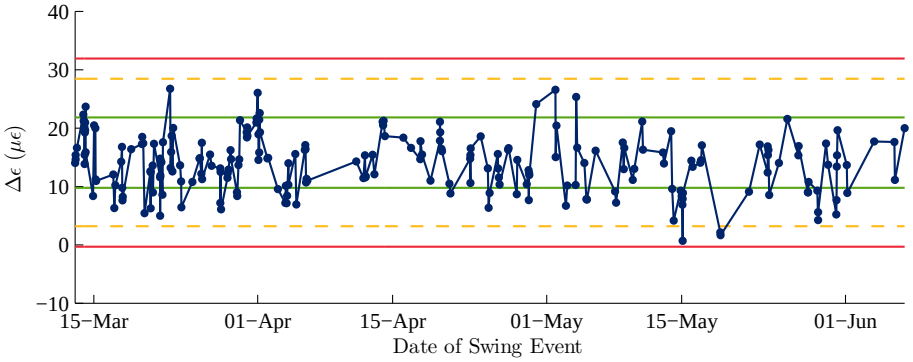

(b) Acceptance Control Chart.

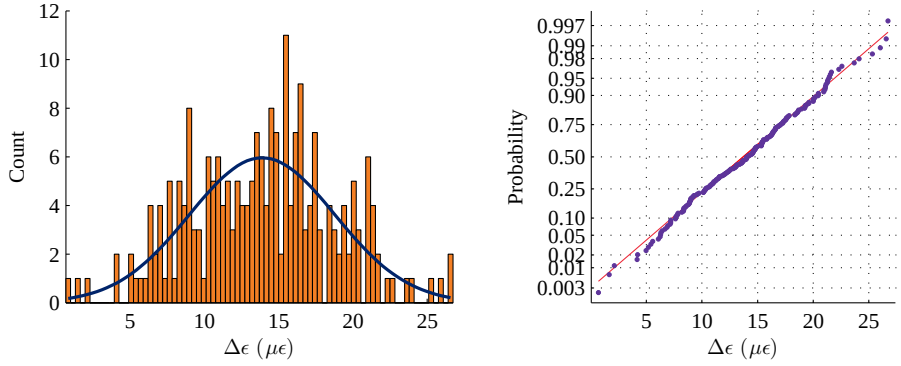

(c) Histogram and Normal Probability Plots of $\Delta\epsilon$ Values.

Figure 9.12: Statistical process control charts for sensor R1 $\Delta\epsilon$ stairs downstream position.

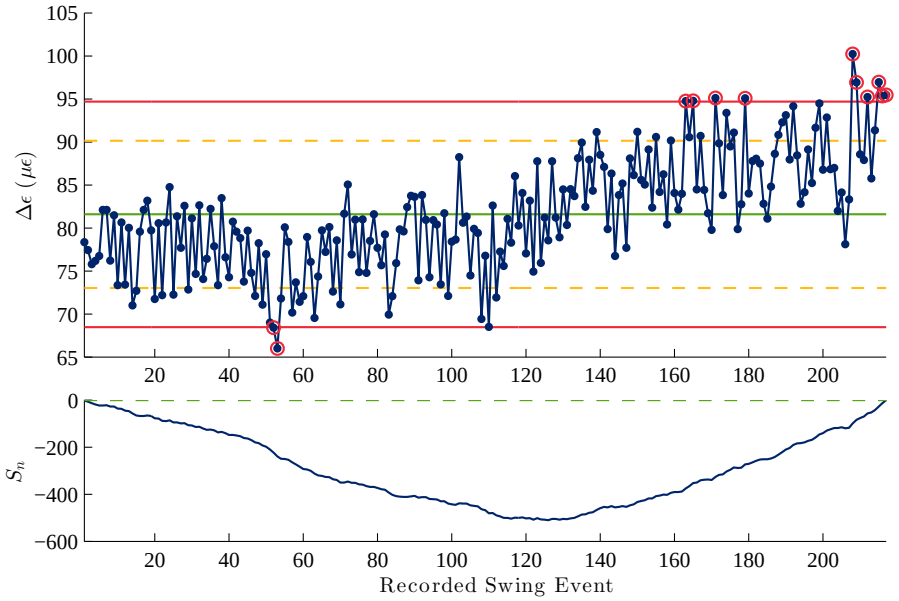

(a) Control and CUSUM chart: All Data.

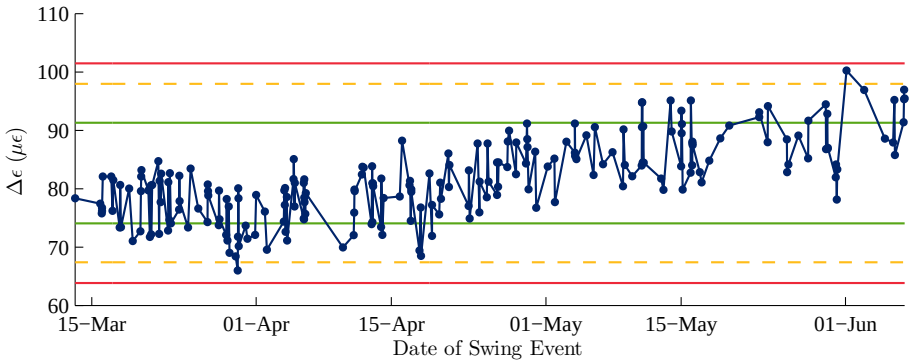

(b) Acceptance Control Chart.

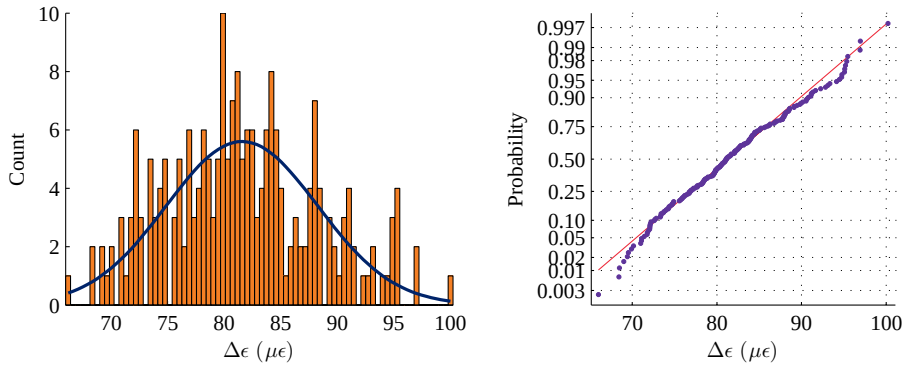

(c) Histogram and Normal Probability Plots of $\Delta\epsilon$ Values.

Figure 9.13: Statistical process control charts for sensor R1 $\Delta\epsilon$ stairs upstream position.

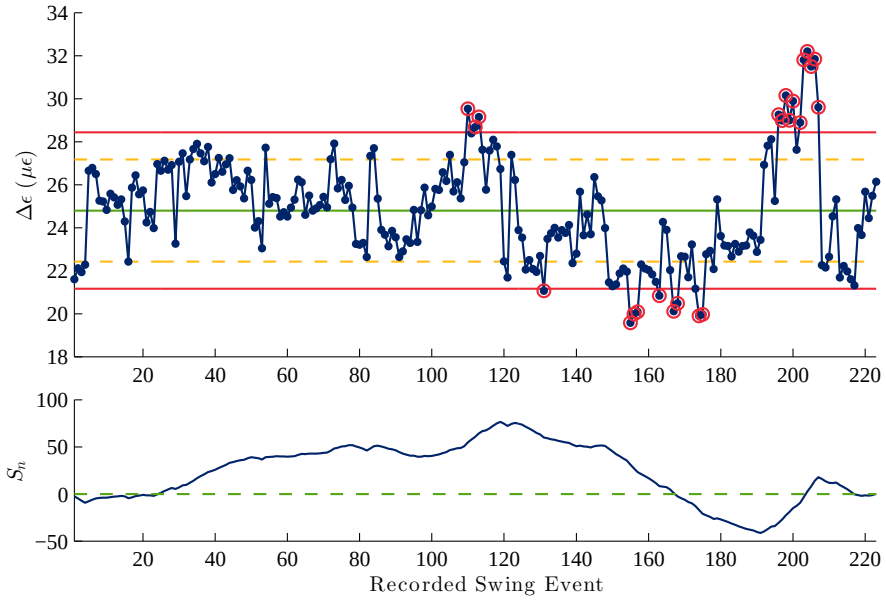

(a) Control and CUSUM chart: All Data.

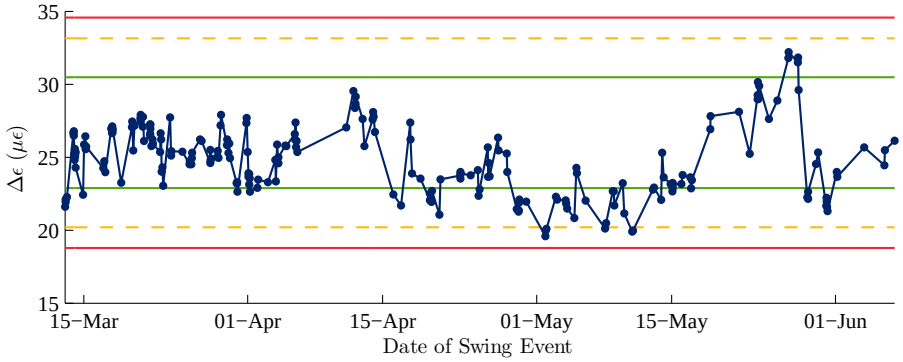

(b) Acceptance Control Chart.

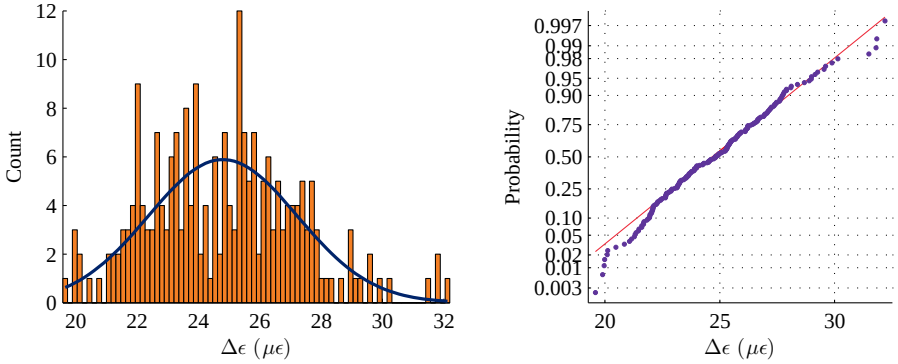

(c) Histogram and Normal Probability Plots of $\Delta\epsilon$ Values.

Figure 9.14: Statistical process control charts for sensor R2 $\Delta\epsilon$ stairs downstream position.

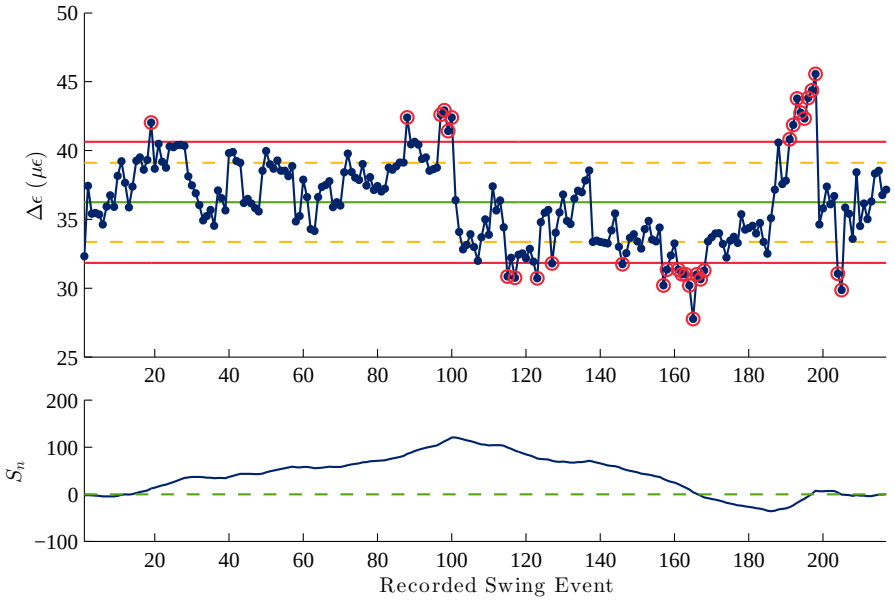

(a) Control and CUSUM chart: All Data.

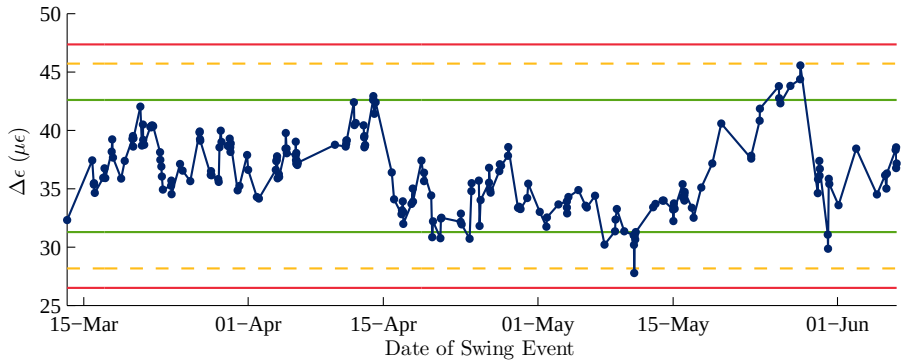

(b) Acceptance Control Chart.

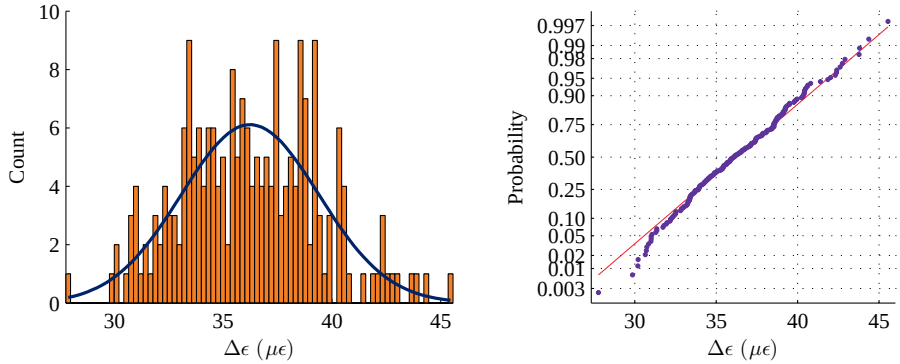

(c) Histogram and Normal Probability Plots of $\Delta\epsilon$ Values.

Figure 9.15: Statistical process control charts for sensor R2 $\Delta\epsilon$ stairs upstream position.

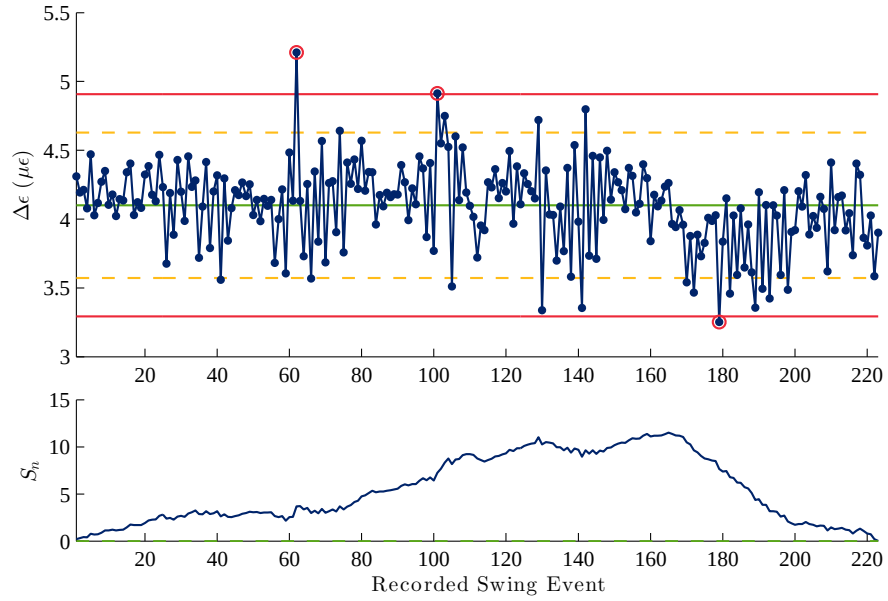

(a) Control and CUSUM chart: All Data.

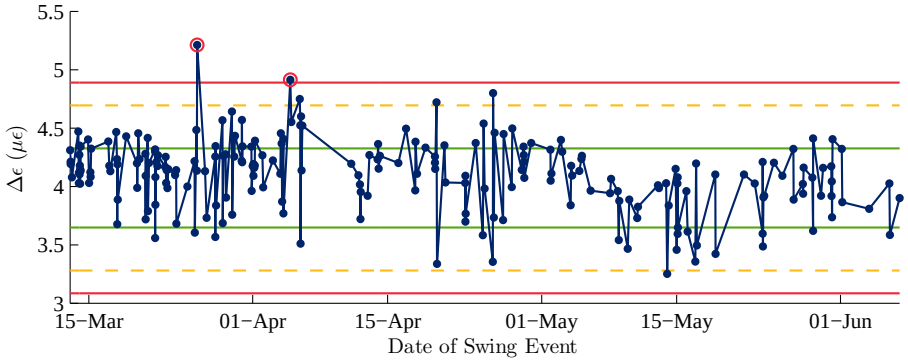

(b) Acceptance Control Chart.

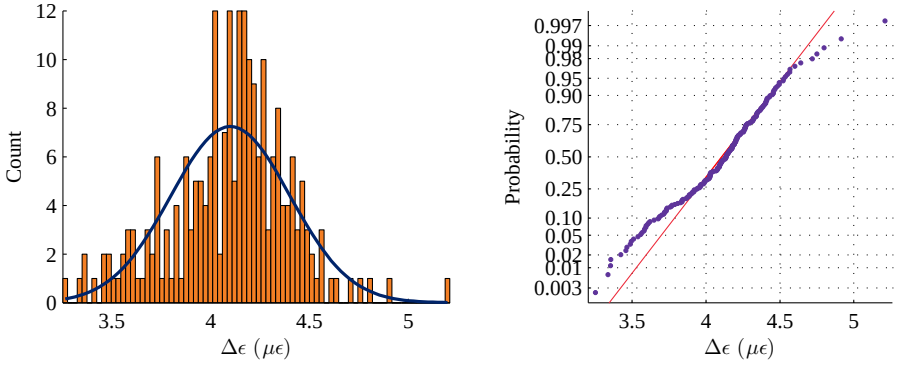

(c) Histogram and Normal Probability Plots of $\Delta\epsilon$ Values.

Figure 9.16: Statistical process control charts for sensor R3 $\Delta\epsilon$ stairs downstream position.

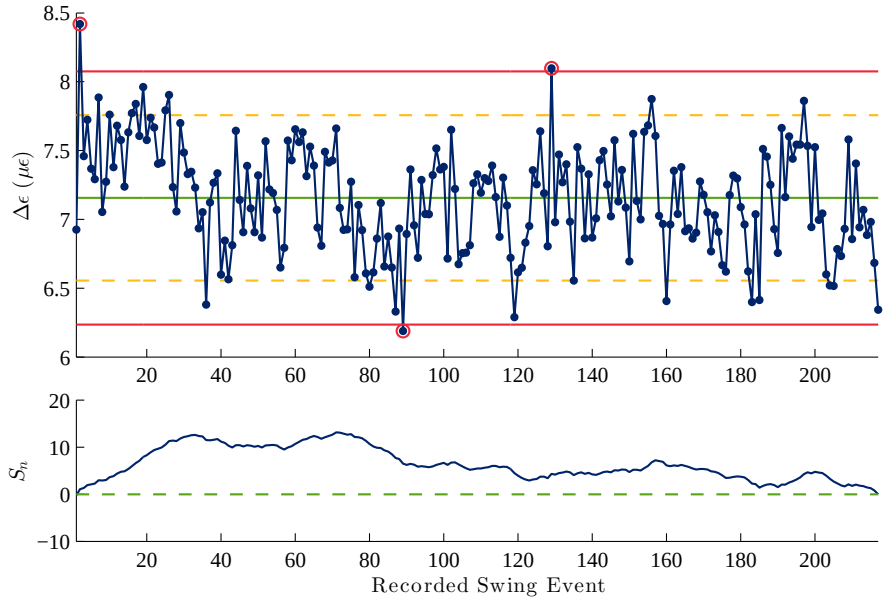

(a) Control and CUSUM chart: All Data.

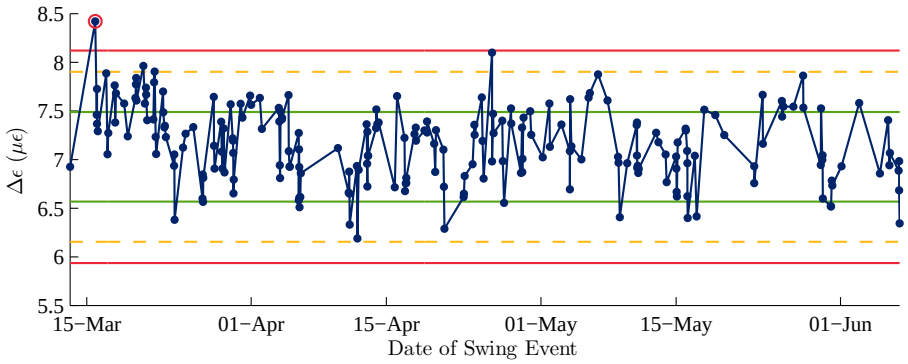

(b) Acceptance Control Chart.

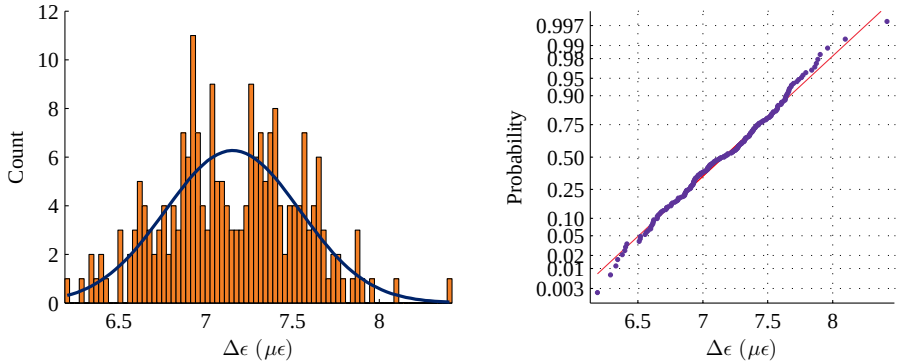

(c) Histogram and Normal Probability Plots of $\Delta\epsilon$ Values.

Figure 9.17: Statistical process control charts for sensor R3 $\Delta\epsilon$ stairs upstream position.

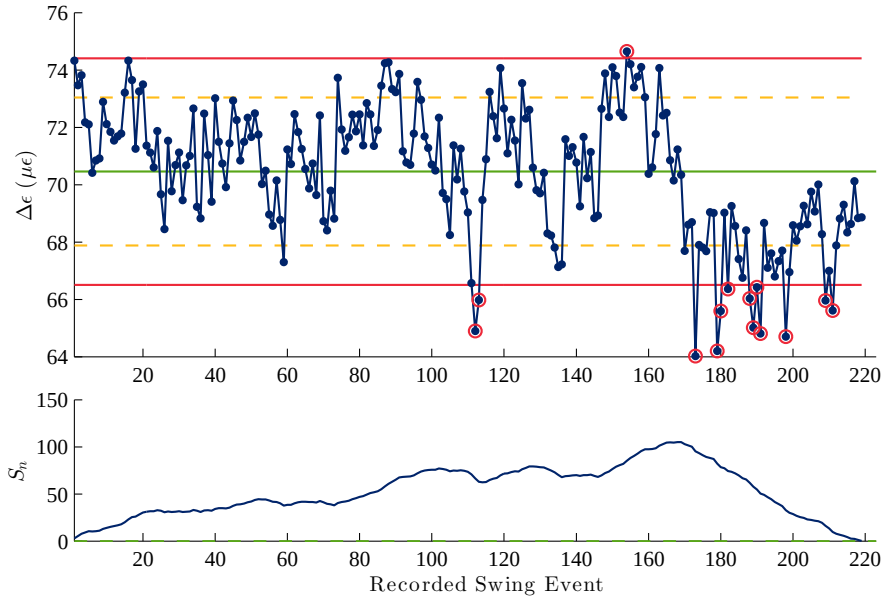

(a) Control and CUSUM chart: All Data.

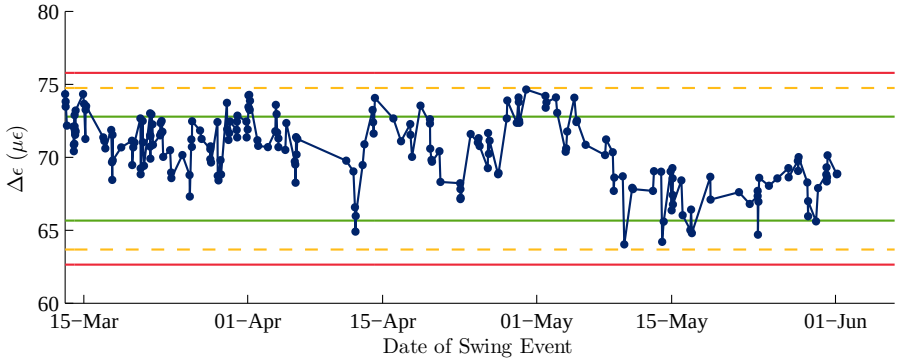

(b) Acceptance Control Chart.

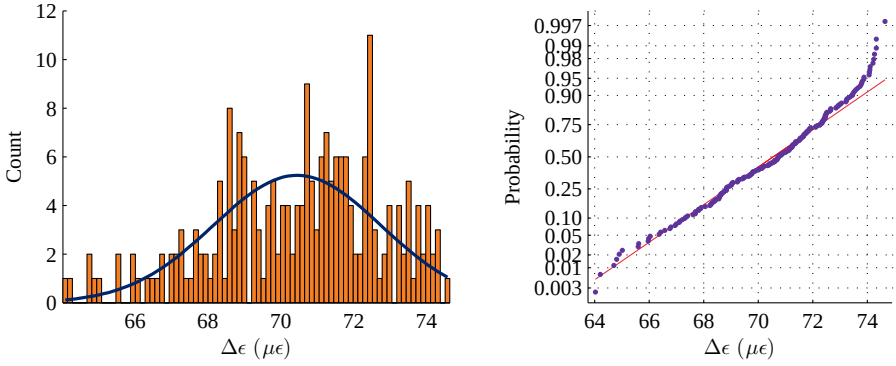

(c) Histogram and Normal Probability Plots of $\Delta\epsilon$ Values.

Figure 9.18: Statistical process control charts for sensor R4 $\Delta\epsilon$ stairs downstream position.

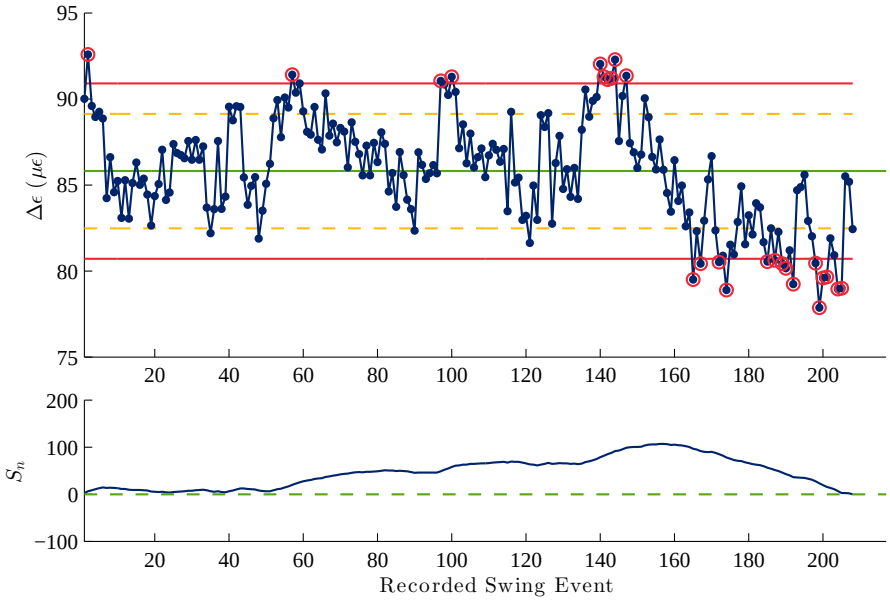

(a) Control and CUSUM chart: All Data.

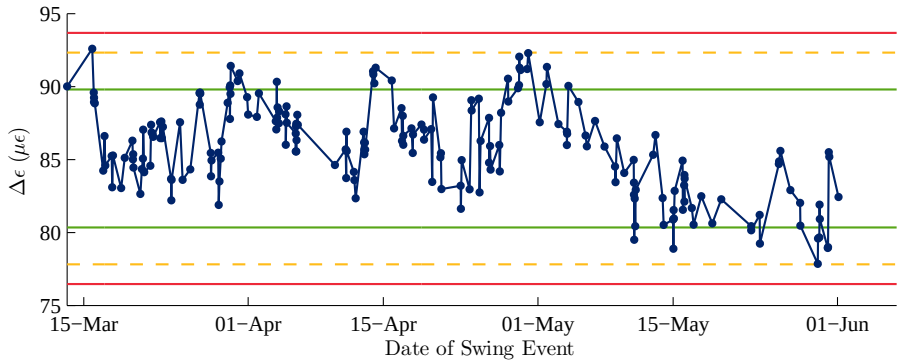

(b) Acceptance Control Chart.

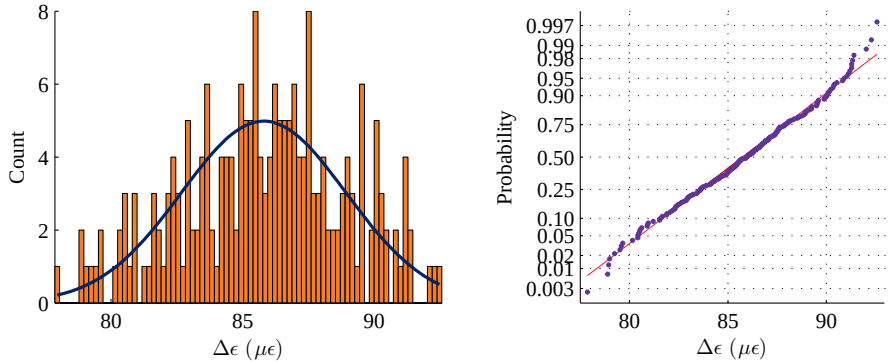

(c) Histogram and Normal Probability Plots of $\Delta\epsilon$ Values.

Figure 9.19: Statistical process control charts for sensor R4 $\Delta\epsilon$ stairs upstream position.

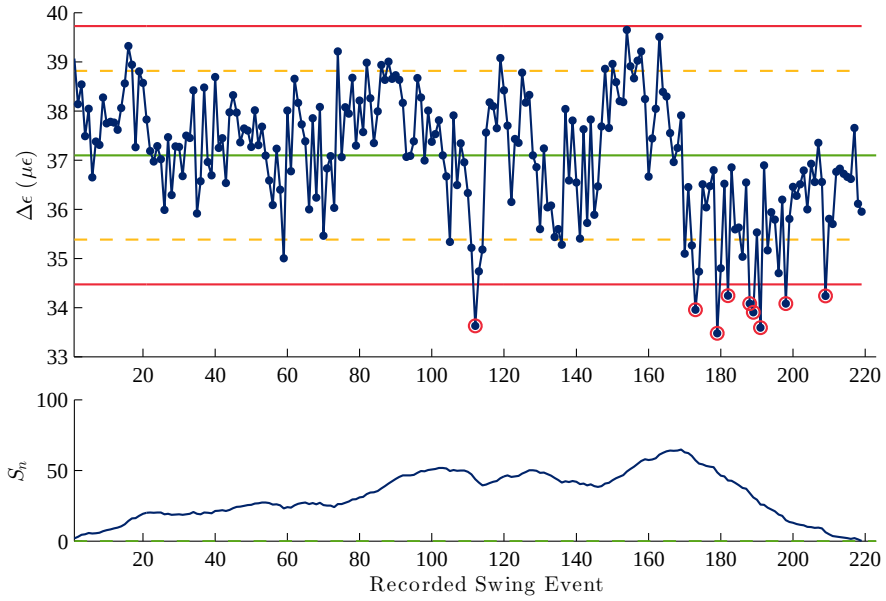

(a) Control and CUSUM chart: All Data.

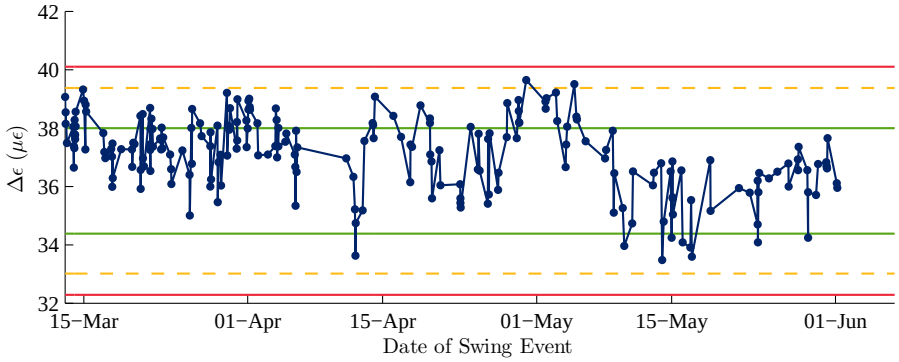

(b) Acceptance Control Chart.

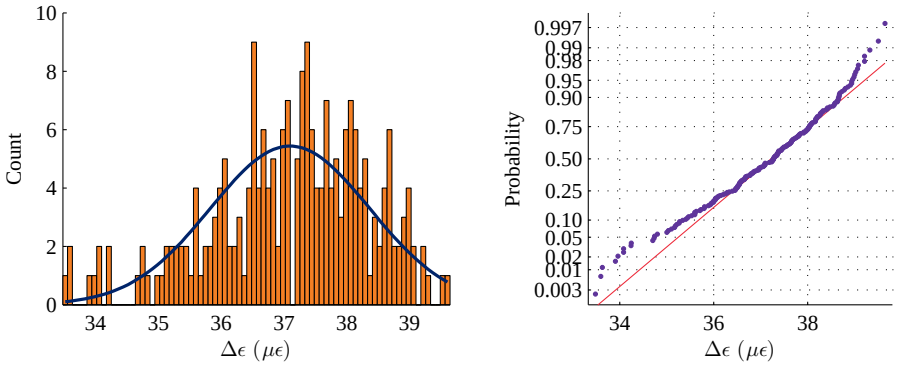

(c) Histogram and Normal Probability Plots of $\Delta\epsilon$ Values.

Figure 9.20: Statistical process control charts for sensor R5 $\Delta\epsilon$ stairs downstream position.

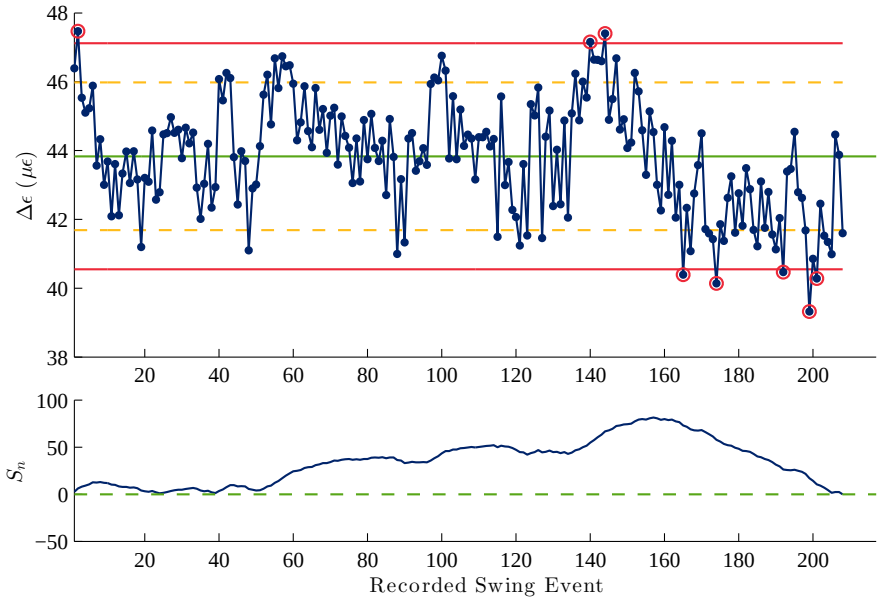

(a) Control and CUSUM chart: All Data.

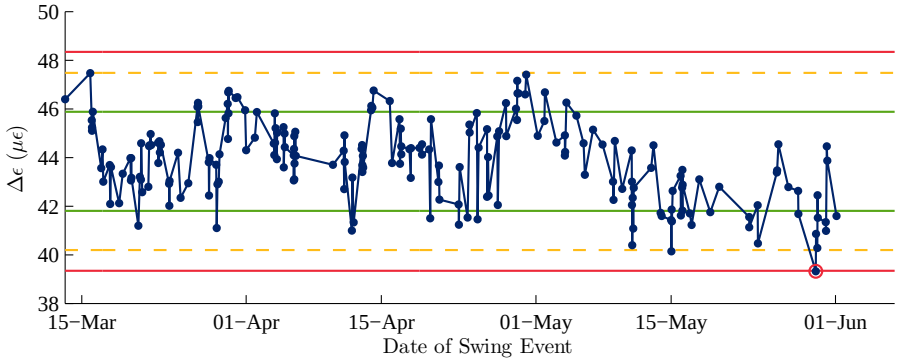

(b) Acceptance Control Chart.

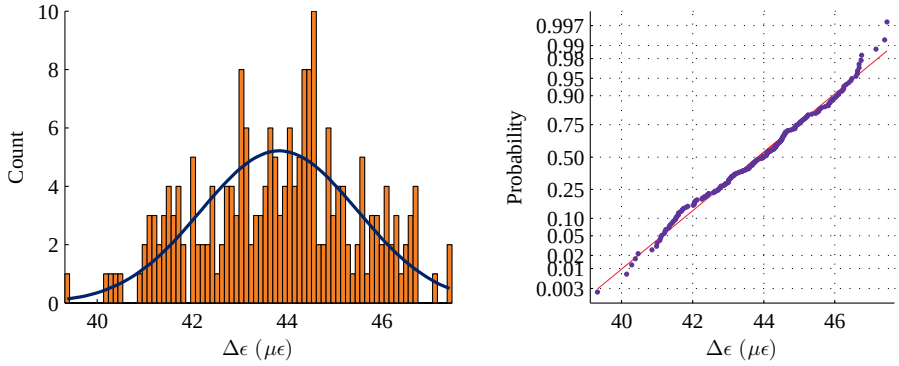

(c) Histogram and Normal Probability Plots of $\Delta\epsilon$ Values.

Figure 9.21: Statistical process control charts for sensor R5 $\Delta\epsilon$ stairs upstream position.

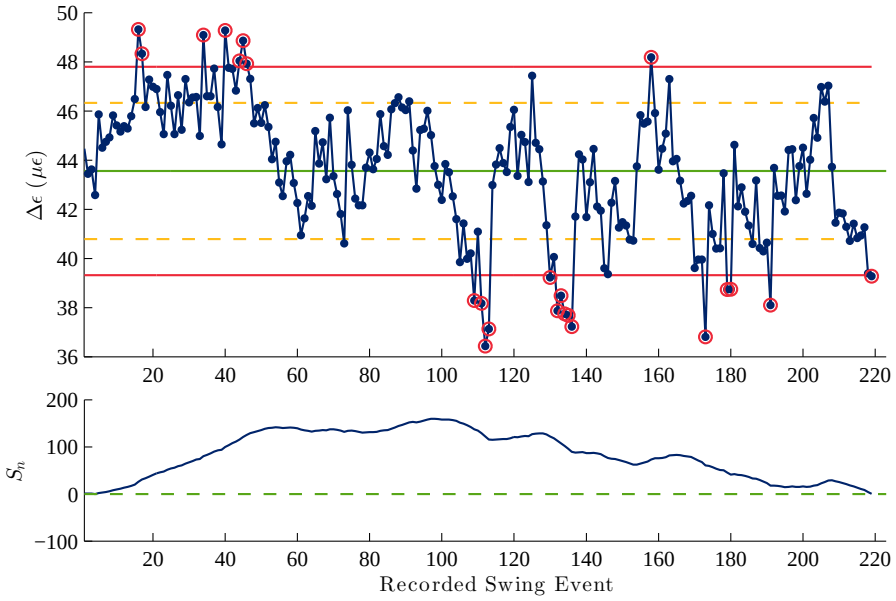

(a) Control and CUSUM chart: All Data.

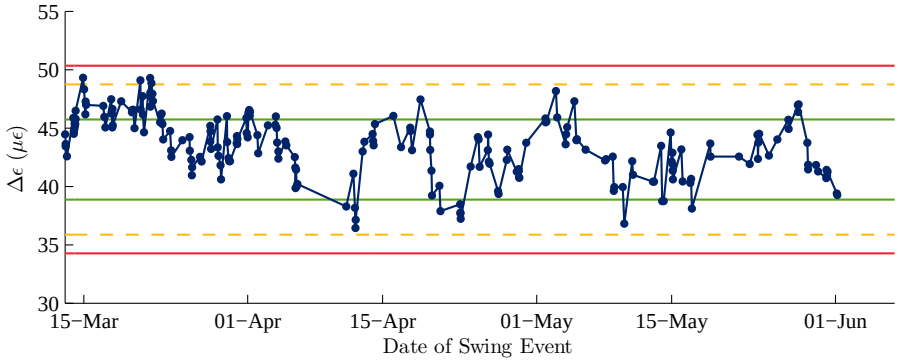

(b) Acceptance Control Chart.

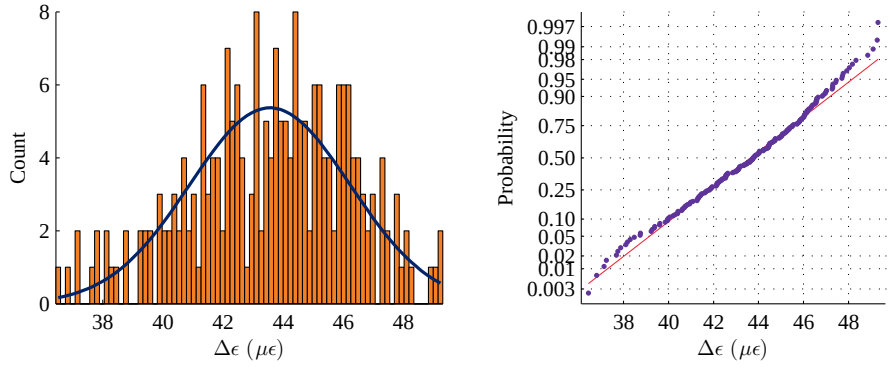

(c) Histogram and Normal Probability Plots of $\Delta\epsilon$ Values.

Figure 9.22: Statistical process control charts for sensor R8 $\Delta\epsilon$ stairs downstream position.

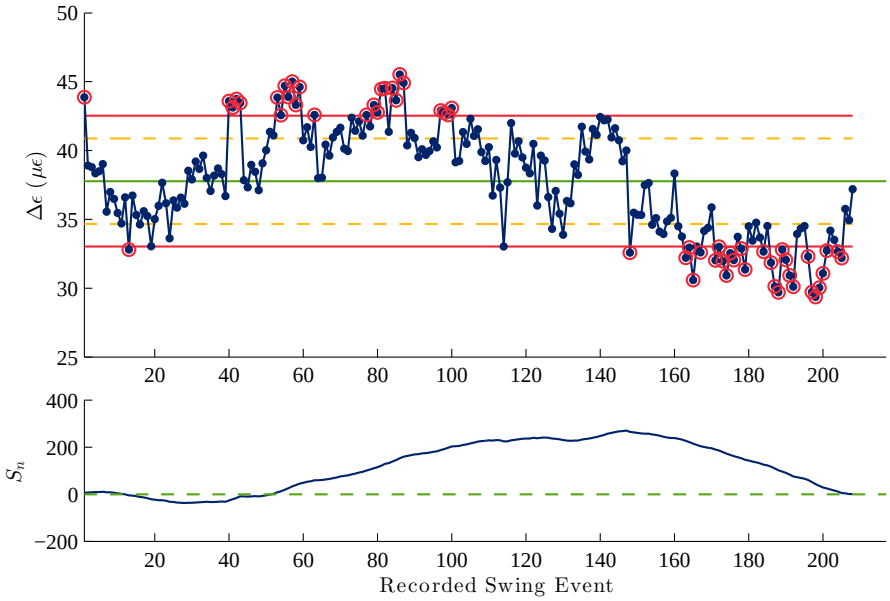

(a) Control and CUSUM chart: All Data.

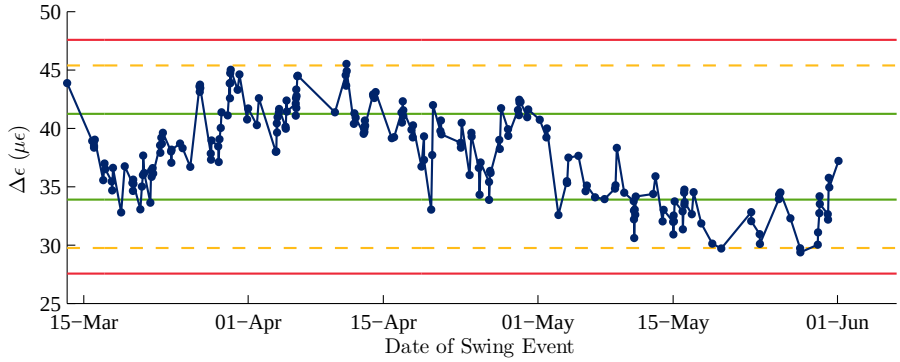

(b) Acceptance Control Chart.

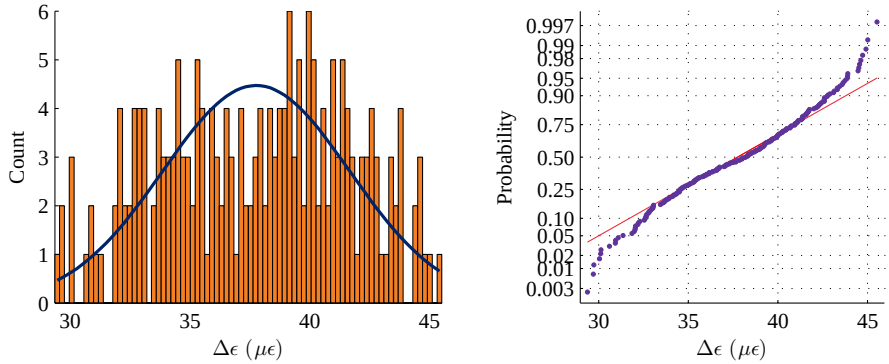

(c) Histogram and Normal Probability Plots of $\Delta\epsilon$ Values.

Figure 9.23: Statistical process control charts for sensor R8 $\Delta\epsilon$ stairs upstream position.

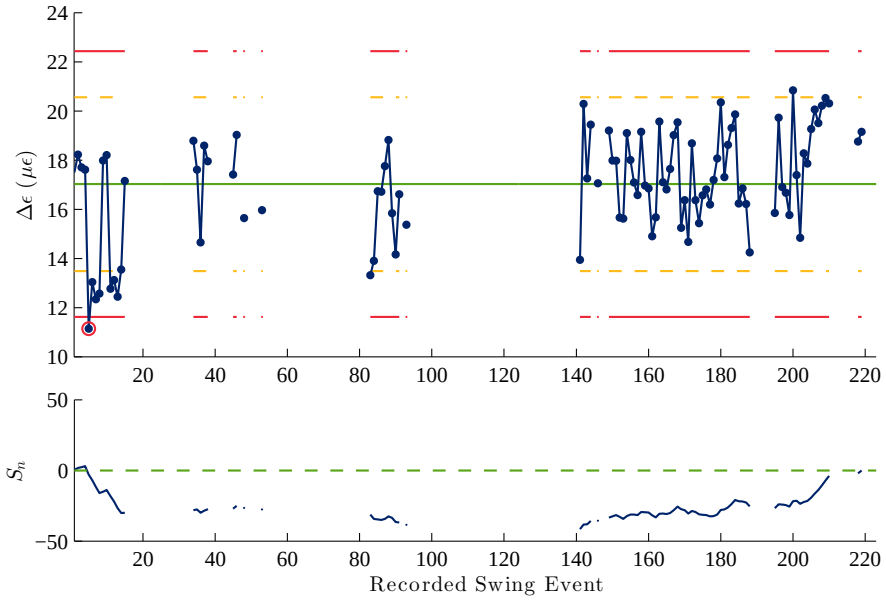

(a) Control and CUSUM chart: All Data.

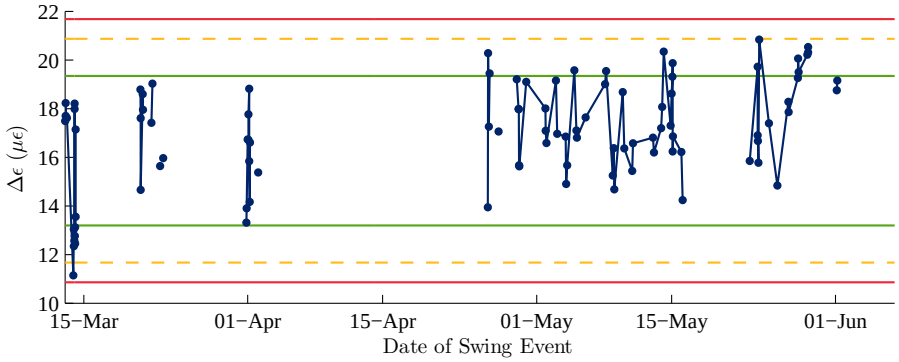

(b) Acceptance Control Chart.

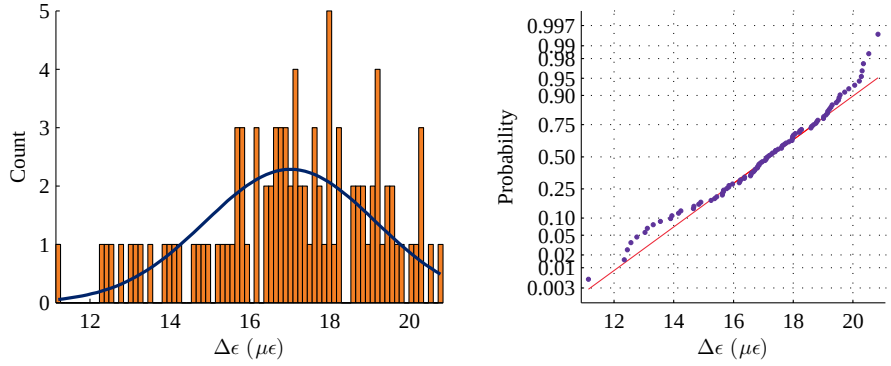

(c) Histogram and Normal Probability Plots of $\Delta\epsilon$ Values.

Figure 9.24: Statistical process control charts for sensor L18 $\Delta\epsilon$ stairs downstream position.

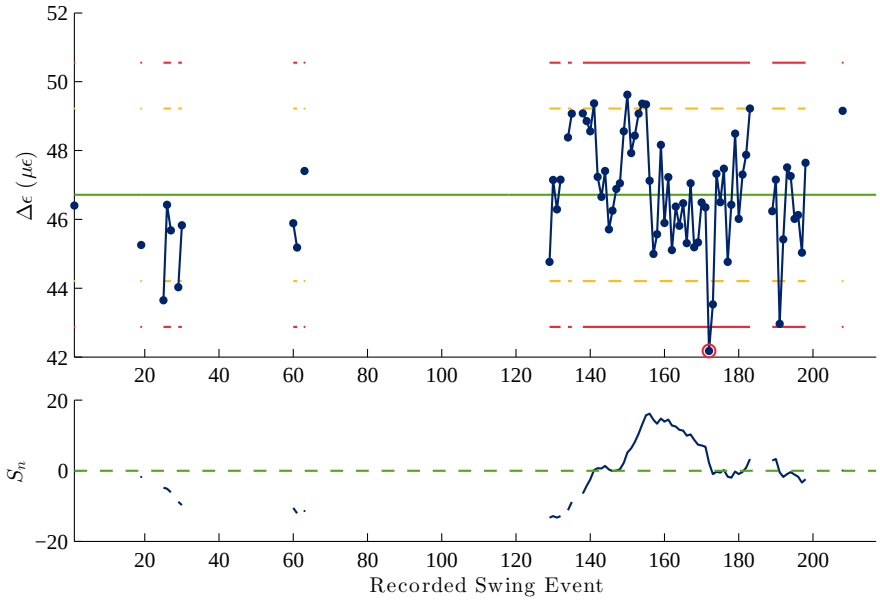

(a) Control and CUSUM chart: All Data.

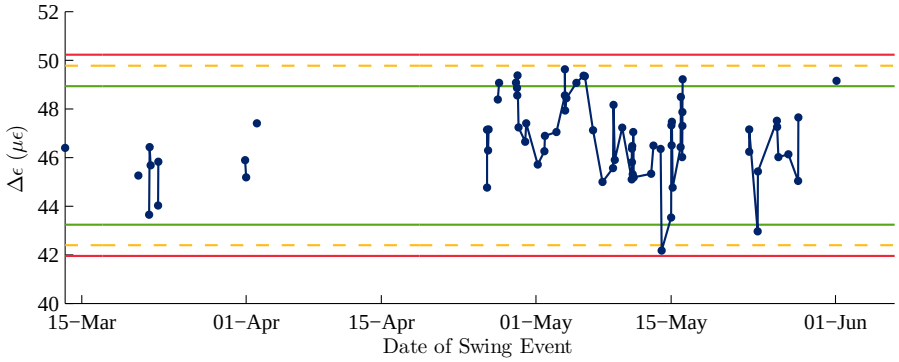

(b) Acceptance Control Chart.

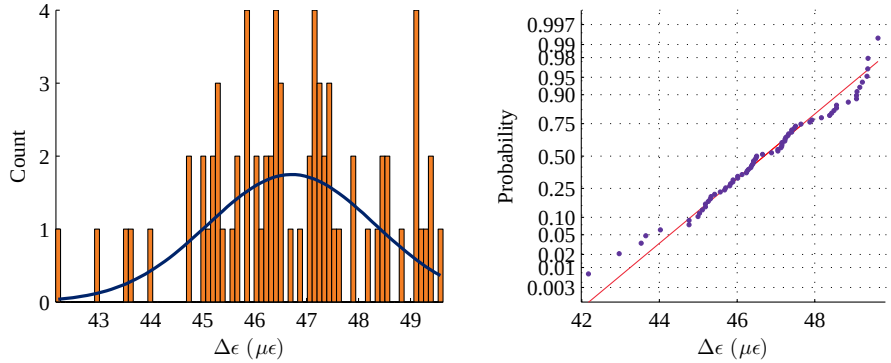

(c) Histogram and Normal Probability Plots of $\Delta\epsilon$ Values.

Figure 9.25: Statistical process control charts for sensor L18 $\Delta\epsilon$ stairs upstream position.

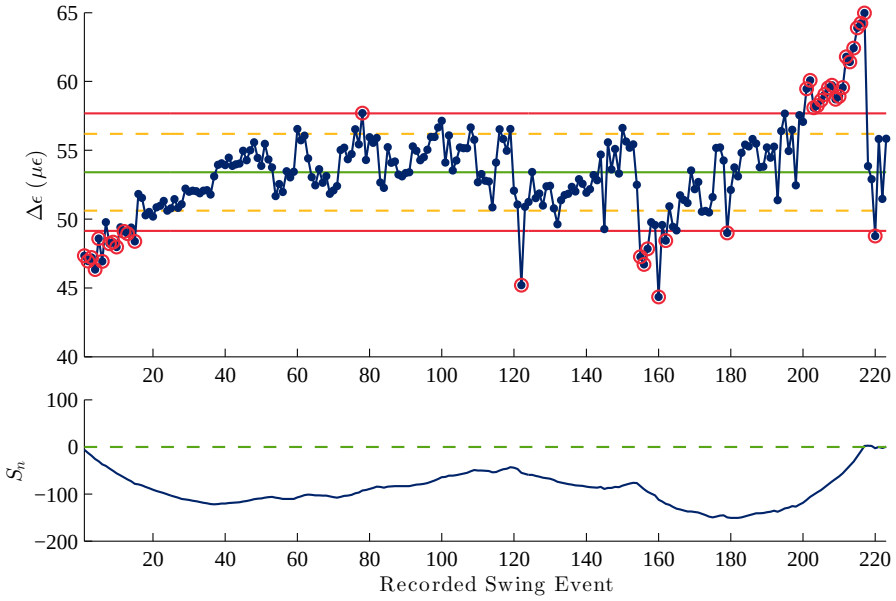

(a) Control and CUSUM chart: All Data.

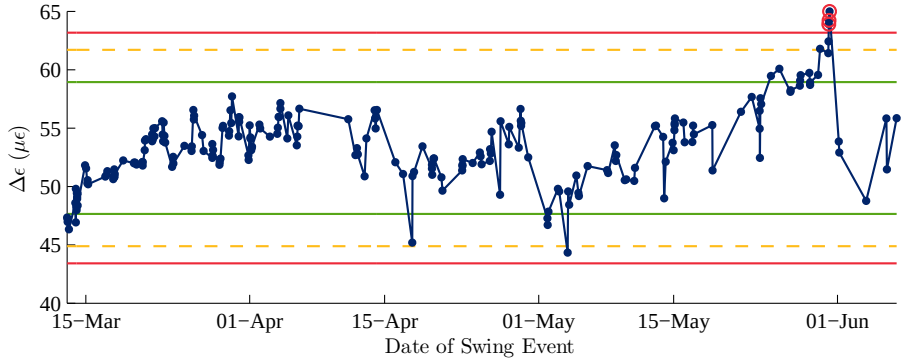

(b) Acceptance Control Chart.

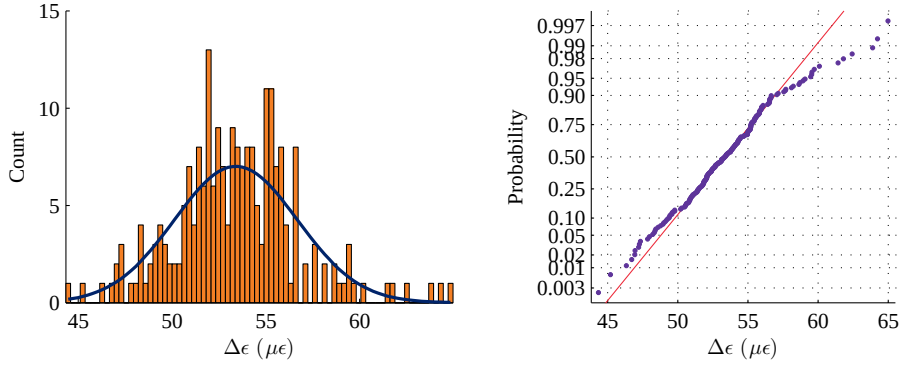

(c) Histogram and Normal Probability Plots of $\Delta\epsilon$ Values.

Figure 9.26: Statistical process control charts for sensor L19 $\Delta\epsilon$ stairs downstream position.

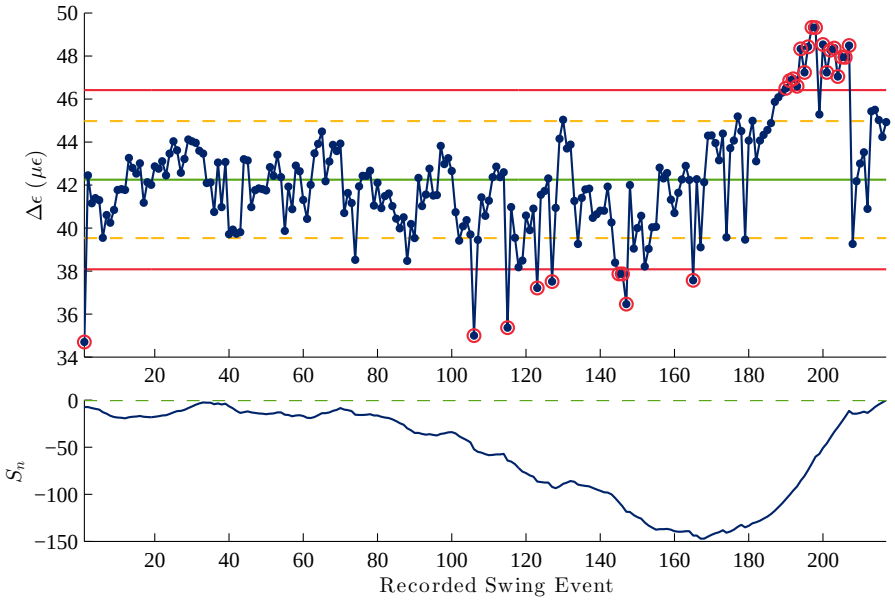

(a) Control and CUSUM chart: All Data.

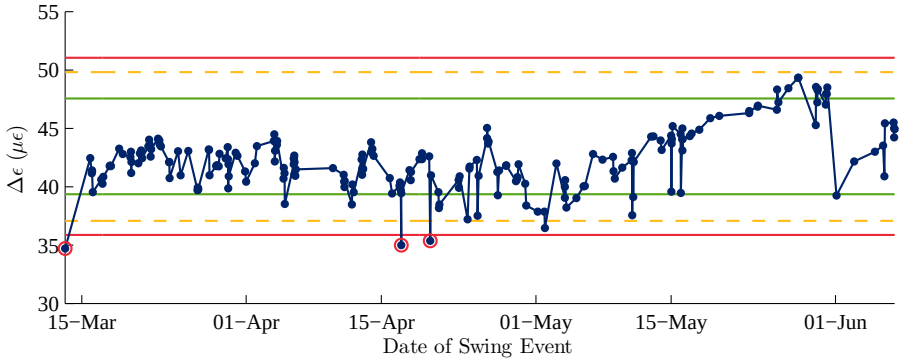

(b) Acceptance Control Chart.

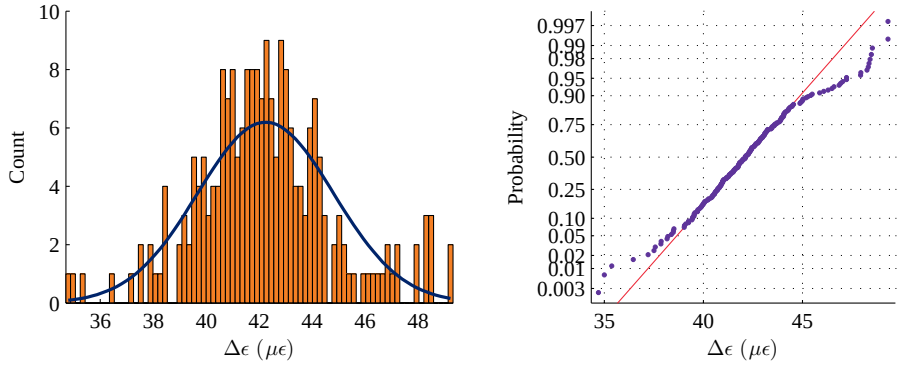

(c) Histogram and Normal Probability Plots of $\Delta\epsilon$ Values.

Figure 9.27: Statistical process control charts for sensor L19 $\Delta\epsilon$ stairs upstream position.

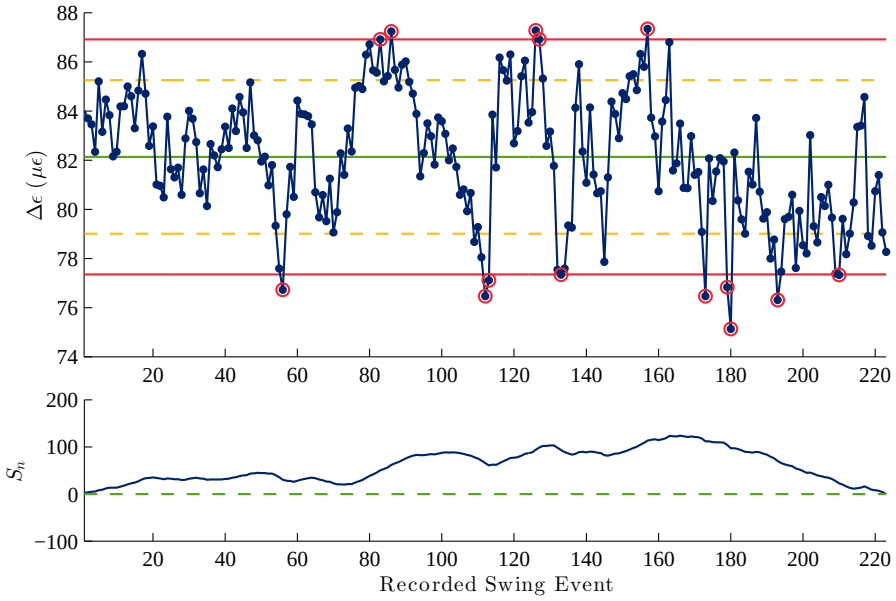

(a) Control and CUSUM chart: All Data.

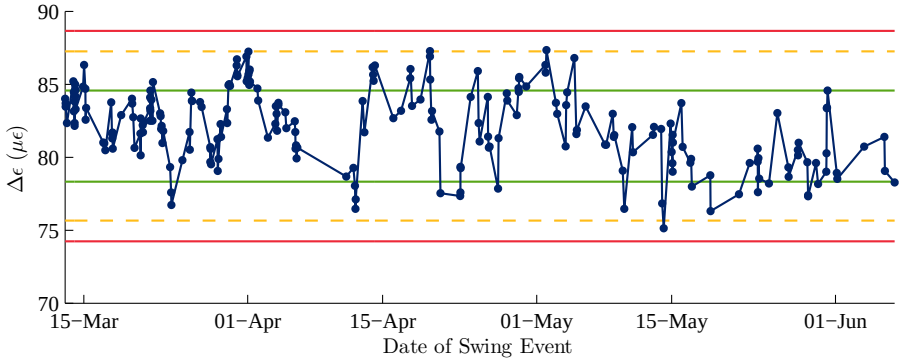

(b) Acceptance Control Chart.

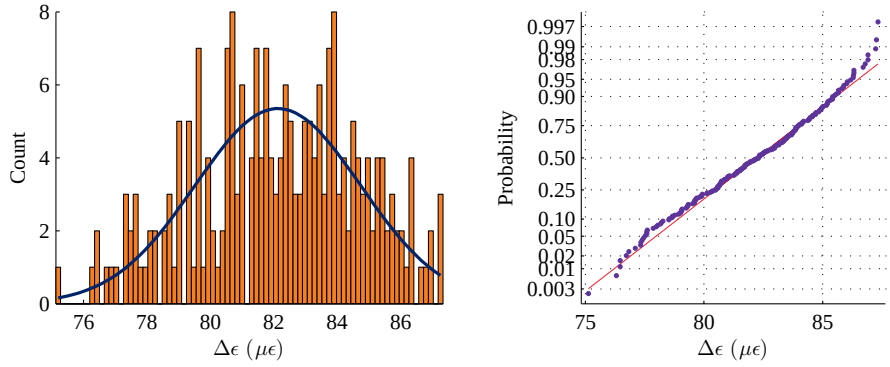

(c) Histogram and Normal Probability Plots of $\Delta\epsilon$ Values.

Figure 9.28: Statistical process control charts for sensor L21 $\Delta\epsilon$ stairs downstream position.

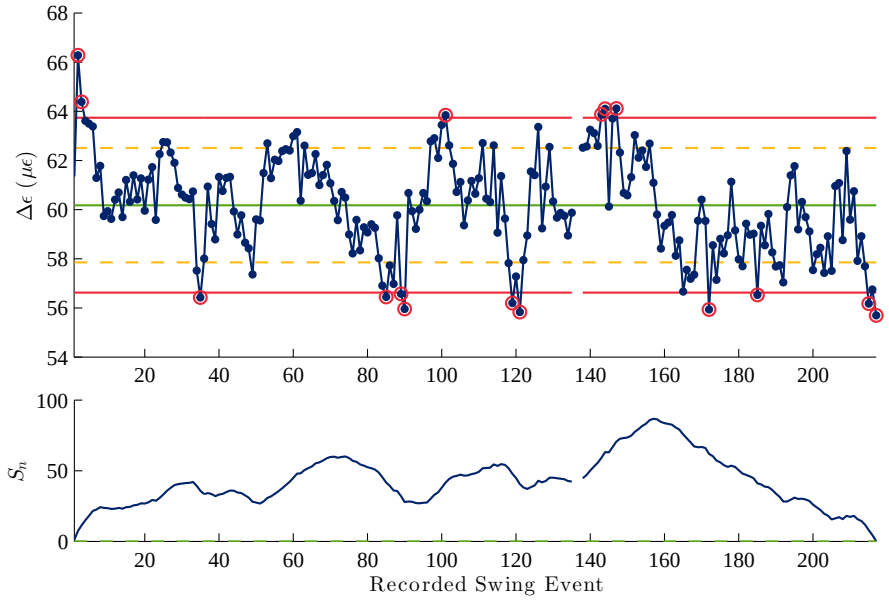

(a) Control and CUSUM chart: All Data.

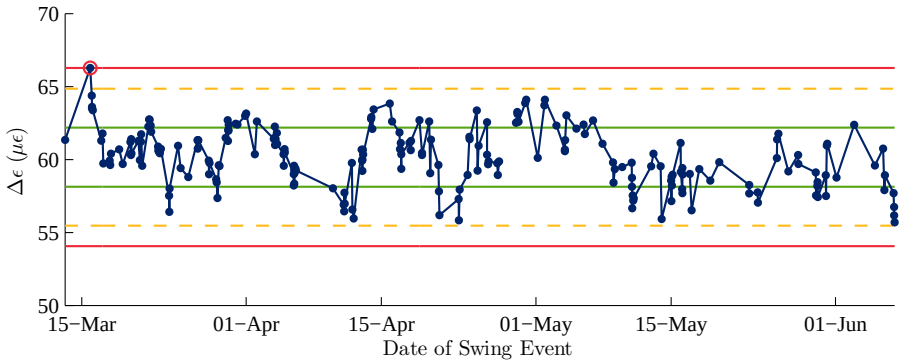

(b) Acceptance Control Chart.

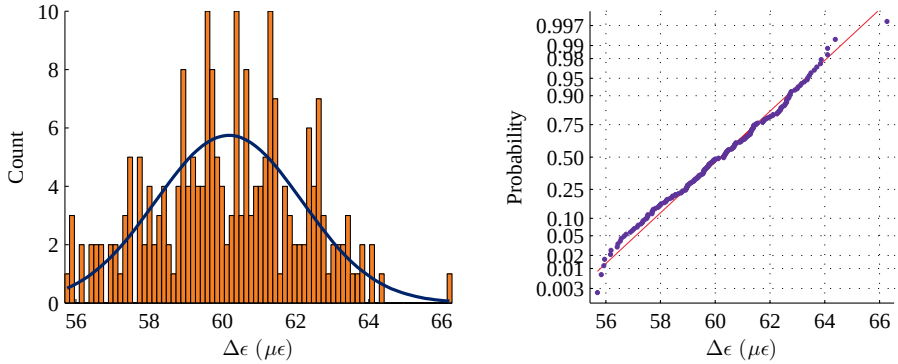

(c) Histogram and Normal Probability Plots of $\Delta\epsilon$ Values.

Figure 9.29: Statistical process control charts for sensor L21 $\Delta\epsilon$ stairs upstream position.

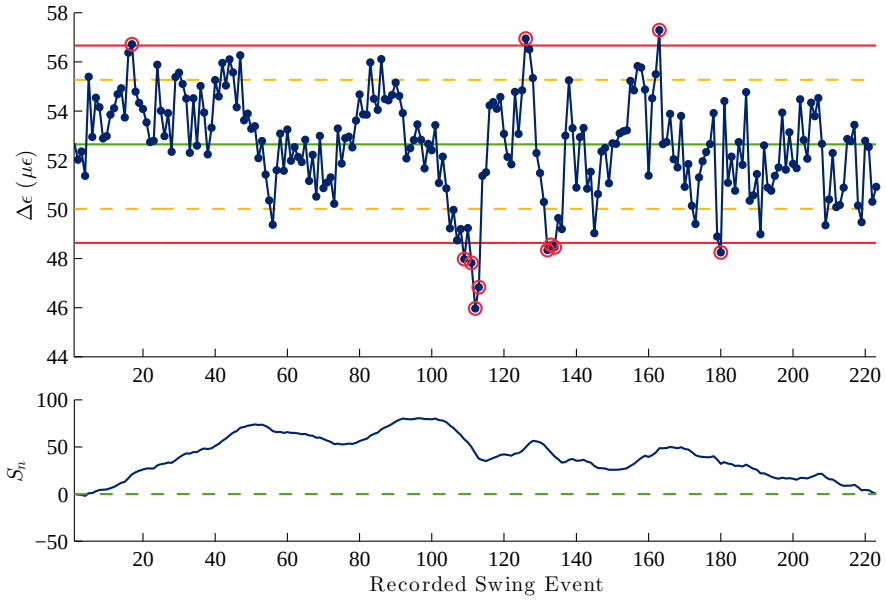

(a) Control and CUSUM chart: All Data.

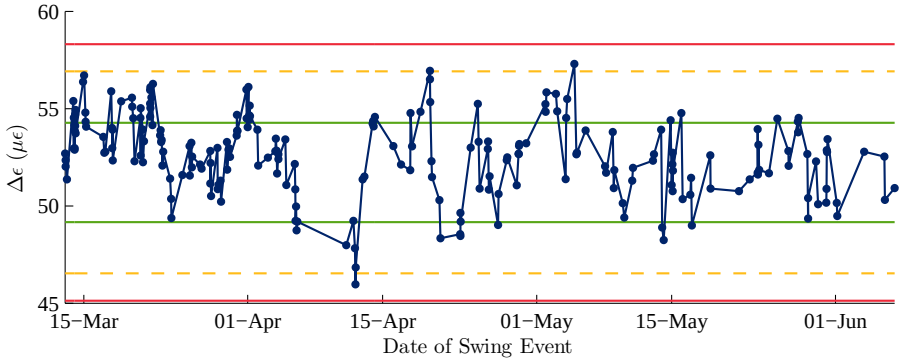

(b) Acceptance Control Chart.

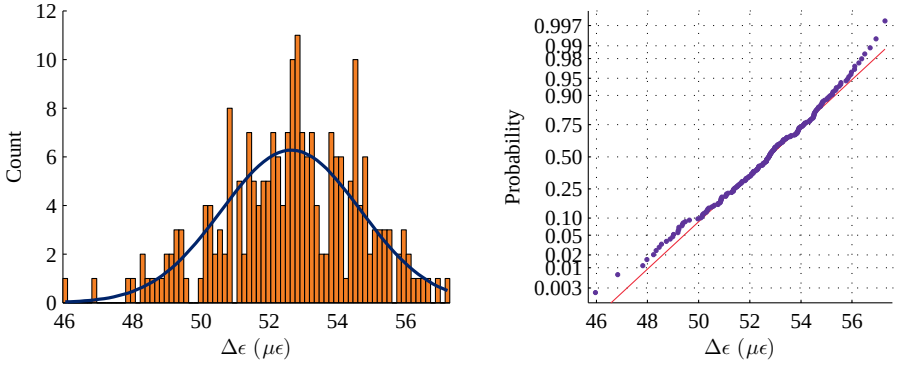

(c) Histogram and Normal Probability Plots of $\Delta\epsilon$ Values.

Figure 9.30: Statistical process control charts for sensor L22 $\Delta\epsilon$ stairs downstream position.

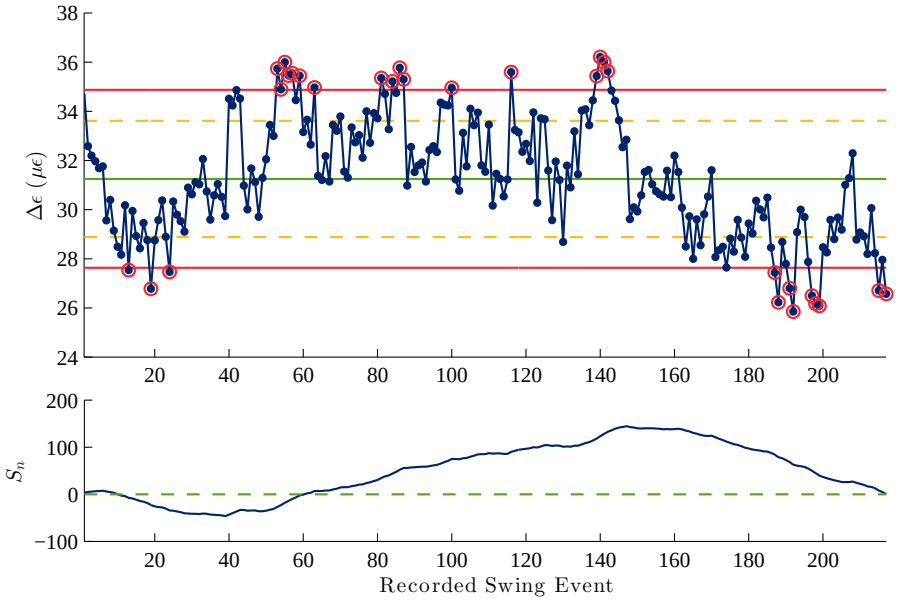

(a) Control and CUSUM chart: All Data.

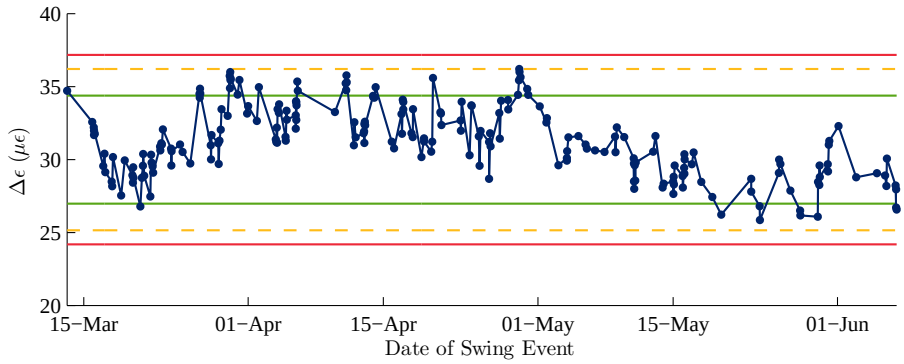

(b) Acceptance Control Chart.

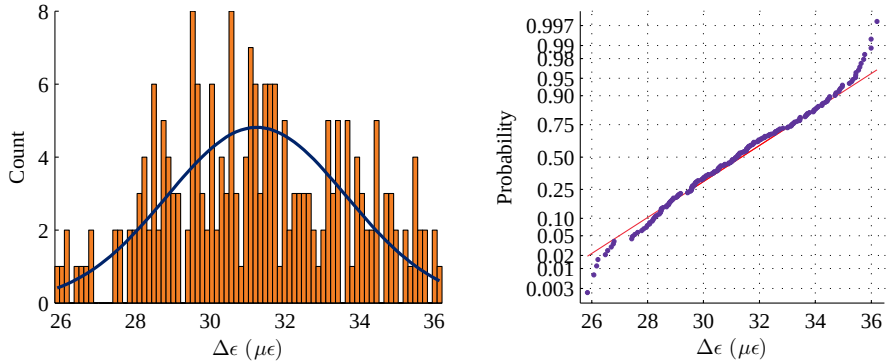

(c) Histogram and Normal Probability Plots of $\Delta\epsilon$ Values.

Figure 9.31: Statistical process control charts for sensor L22 $\Delta\epsilon$ stairs upstream position.

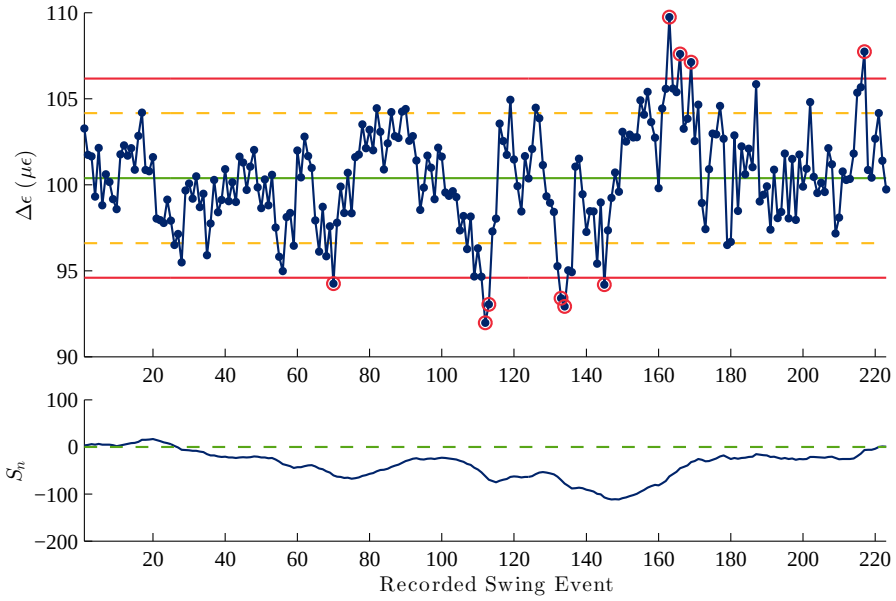

(a) Control and CUSUM chart: All Data.

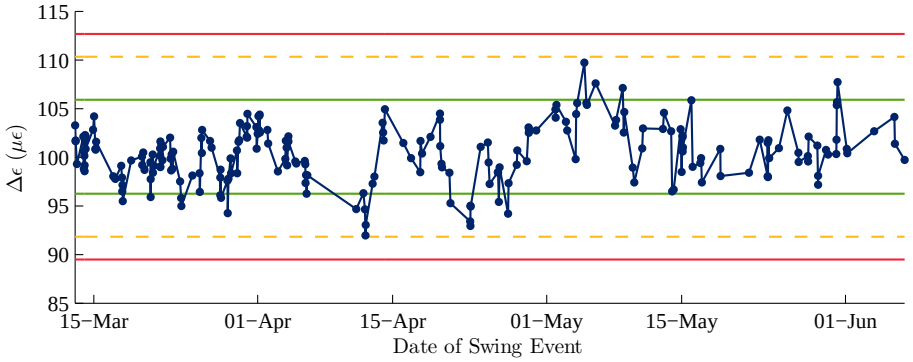

(b) Acceptance Control Chart.

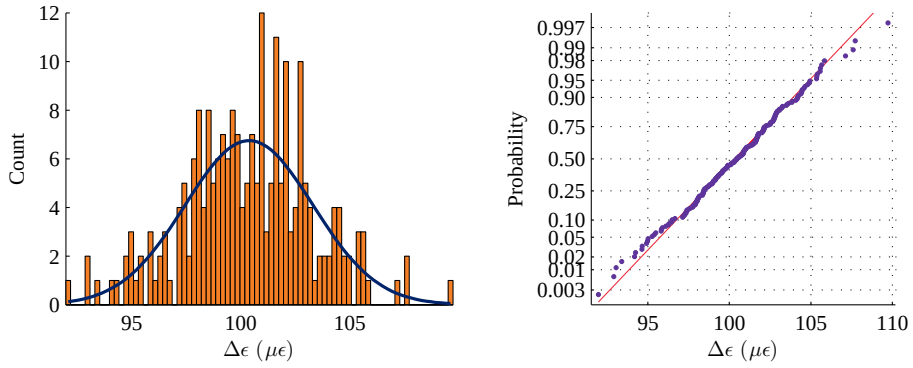

(c) Histogram and Normal Probability Plots of $\Delta\epsilon$ Values.

Figure 9.32: Statistical process control charts for sensor L31 $\Delta\epsilon$ stairs downstream position.

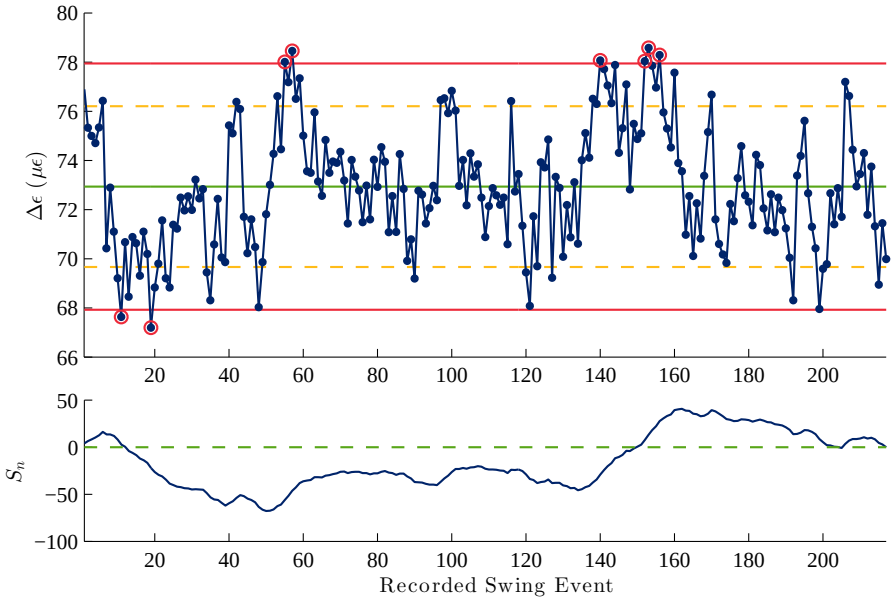

(a) Control and CUSUM chart: All Data.

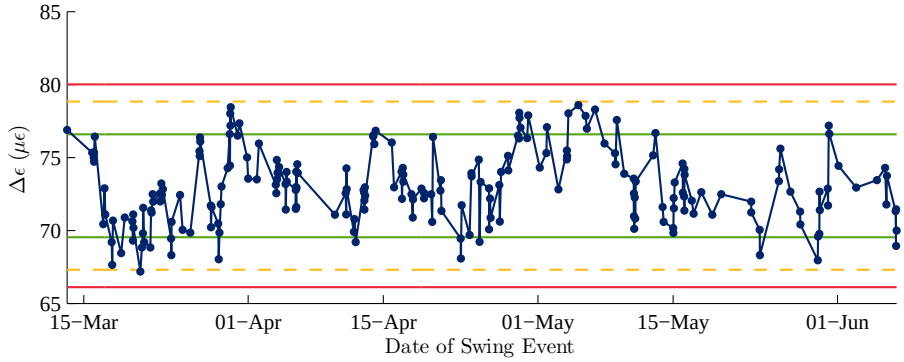

(b) Acceptance Control Chart.

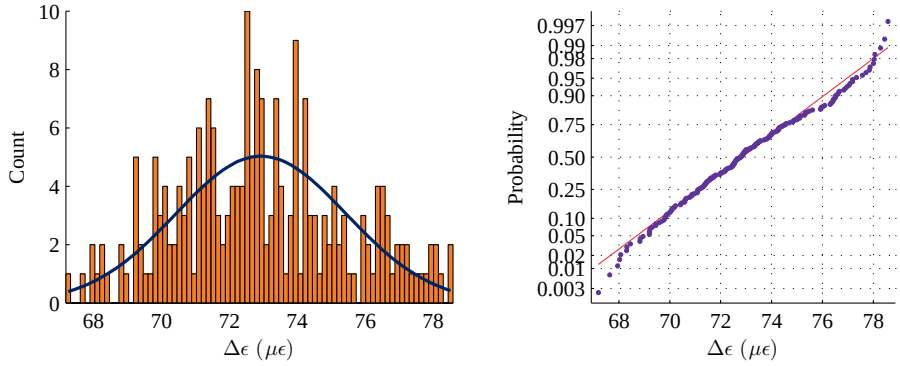

(c) Histogram and Normal Probability Plots of $\Delta\epsilon$ Values.

Figure 9.33: Statistical process control charts for sensor L31 $\Delta\epsilon$ stairs upstream position.

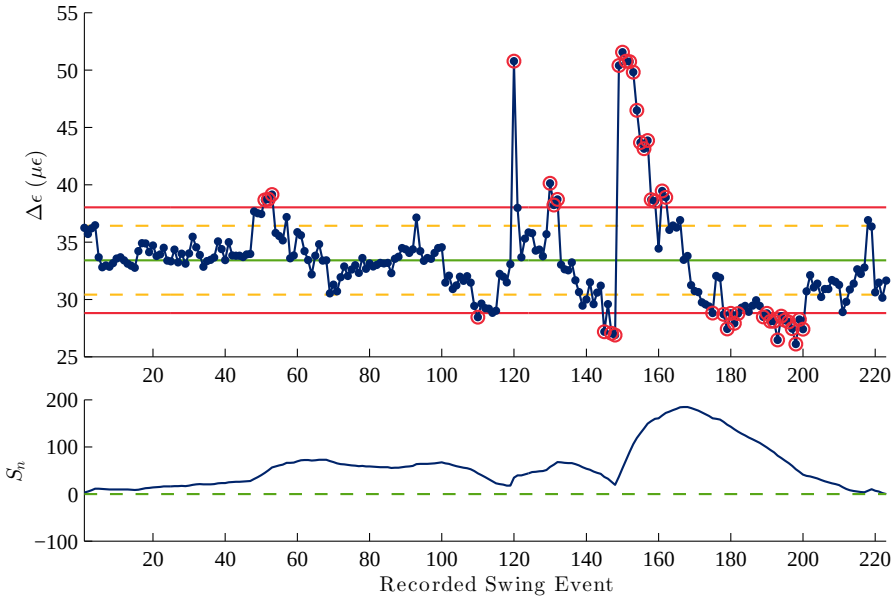

(a) Control and CUSUM chart: All Data.

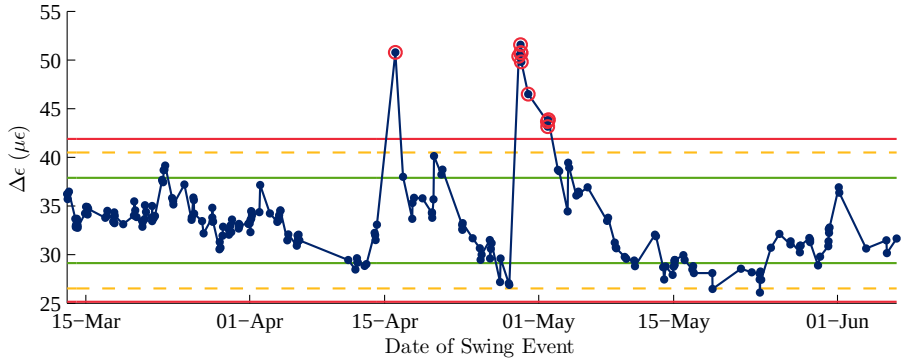

(b) Acceptance Control Chart.

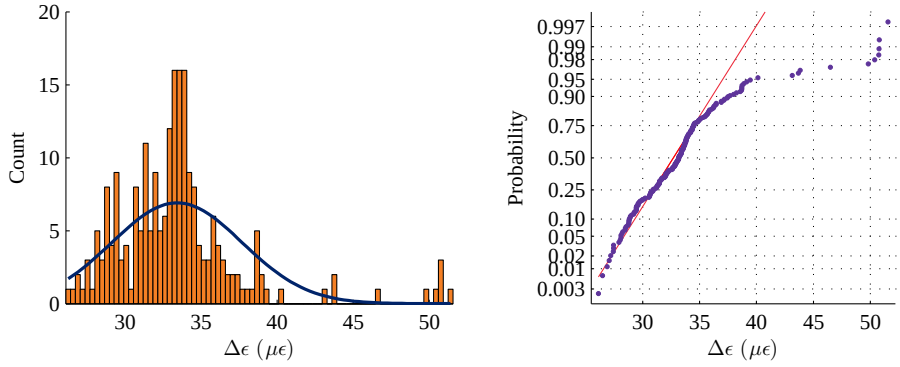

(c) Histogram and Normal Probability Plots of $\Delta\epsilon$ Values.

Figure 9.34: Statistical process control charts for sensor L33 $\Delta\epsilon$ stairs downstream position.

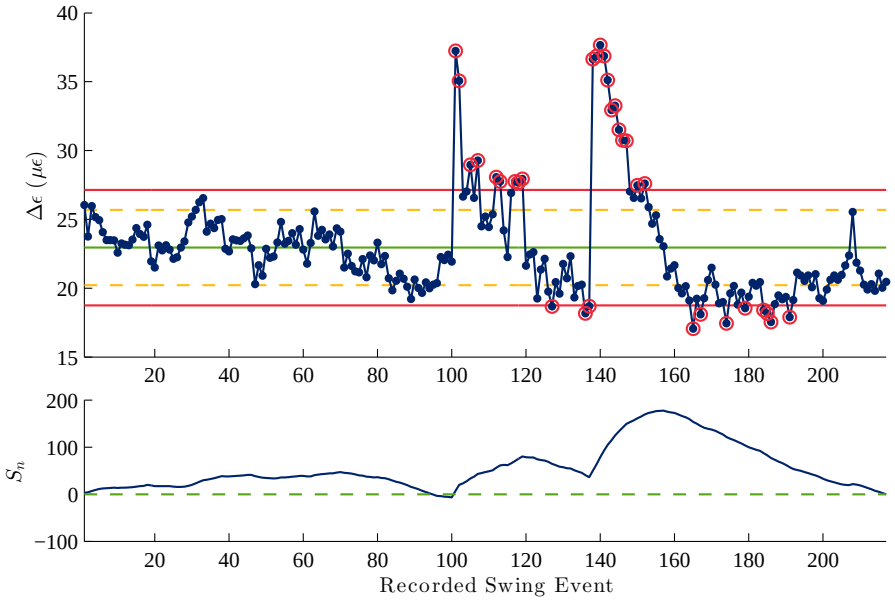

(a) Control and CUSUM chart: All Data.

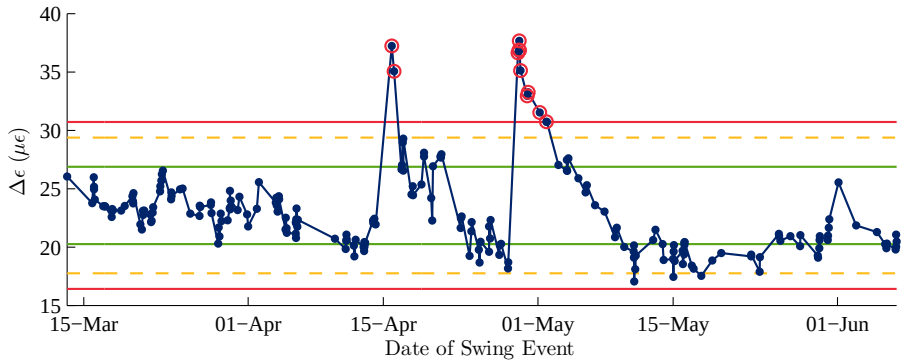

(b) Acceptance Control Chart.

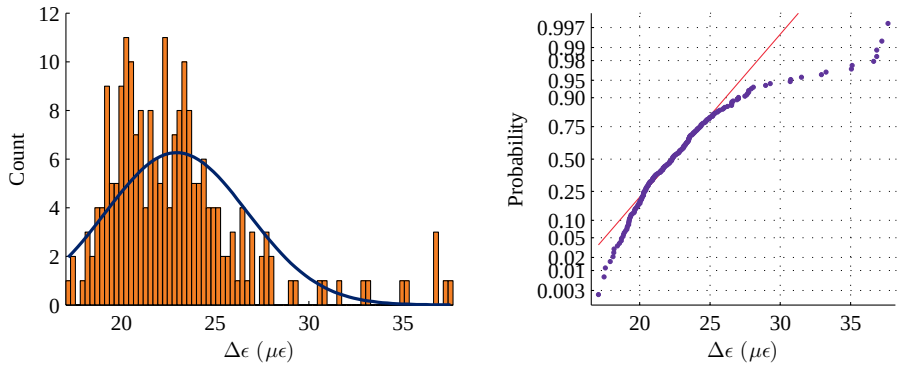

(c) Histogram and Normal Probability Plots of $\Delta\epsilon$ Values.

Figure 9.35: Statistical process control charts for sensor L33 $\Delta\epsilon$ stairs upstream position.

9.4.1 Long-Term Application of SPC Methods

In June of 2013, the FBG strain and temperature sensors were replaced with os3155 sensors, as shown in Figure 9.36. The os3155 model has two FBGs on the same sensor – one to measure strain and one to measure temperature. These sensors were placed in the same locations as the original sensors as shown in Figure 5.5. The strain and temperature sensors were collocated and additional insulation measures taken to resolve some of the temperature issues that had been observed previously in Section 5.6. Using the new sensors, additional data was collected using the Integrated SHM Data Collection Program for the last half of June and the first half of August.[10] The event detection algorithm identified 49 downstream swing events and 34 upstream swing events that took place at night.

The data collected in 2013 was plotted on the acceptance control charts that were developed previously. The upper and lower limits of the acceptance band and the upper and lower control limits were not recalculated. If no significant changes occurred in the structure between June 2012 and June 2013 then the data was expected to fall within the control limits previously established. Figure 9.37 shows three examples of the downstream acceptance control charts that contain the data collected in 2013. The charts show that for the selected sensors, the 2013 data does, in general, fall within the control chart limits established in 2012.

Figure 9.37(a) is a slight exception to this rule. Sensor R4 has a number of points that fall below the lower control limit. The repetitive violation of Nelson Rule 1 could indicate that a change occurred in the structure (e.g., corrosion to the cross-section or further elongation of the eye-bar hole) that affects the member. However, the out of control points could indicate that the structure has not changed but was never in the exact configuration that produced the new data when the old data was collected and the control limits calculated. More data can help distinguish between the two possibilities.

Figure 9.37 also shows that one point was out of control in each of the three sensors at the same time. The out of control point occurred at 01:09:14 on the morning of June 20, 2013. All the sensors indicated that this event did not conform to the expected behavior of the bridge. The bridge operators reported that nothing unusual happened that night and they did not hear any unusually loud noises. All the data collected by the event detection algorithm prior to, and just after, the event in question was examined to determine the cause

[10] The base station computer was inoperative during the month of July. For unknown reasons, the computer had shut down and was not restarted.

(Micron Optics [138])

Figure 9.36: Micron Optics os3155 weldable FBG dual strain gage and temperature sensor.

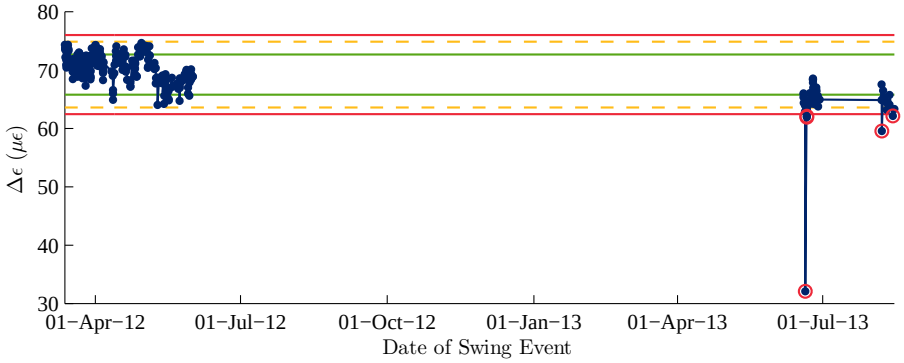

(a) Strain R4 on M5–U6 eye-bar: Downstream.

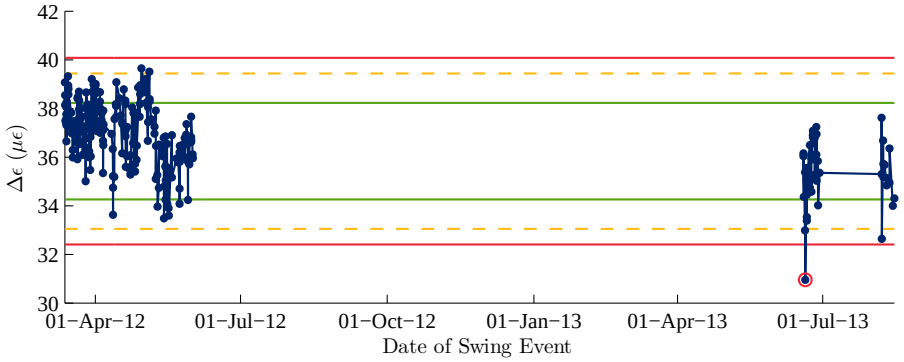

(b) Strain R5 on L6–M7 eye-bar: Downstream.

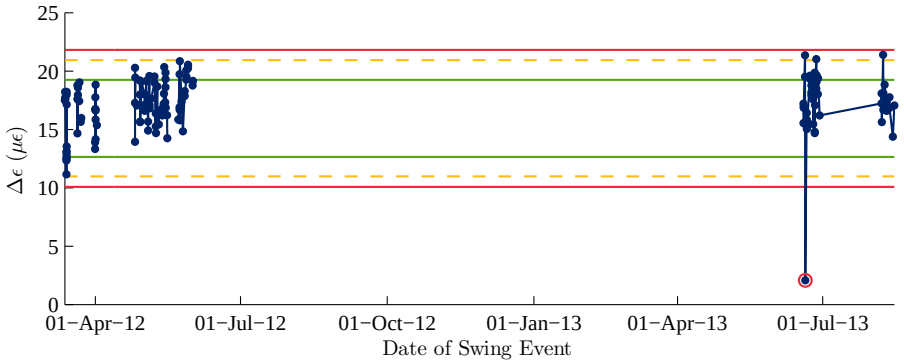

(c) Strain L18 on L0–M0 Vertical Post: Downstream.

Figure 9.37: Statistical process control charts established with 2012 data with the 2013 data plotted.

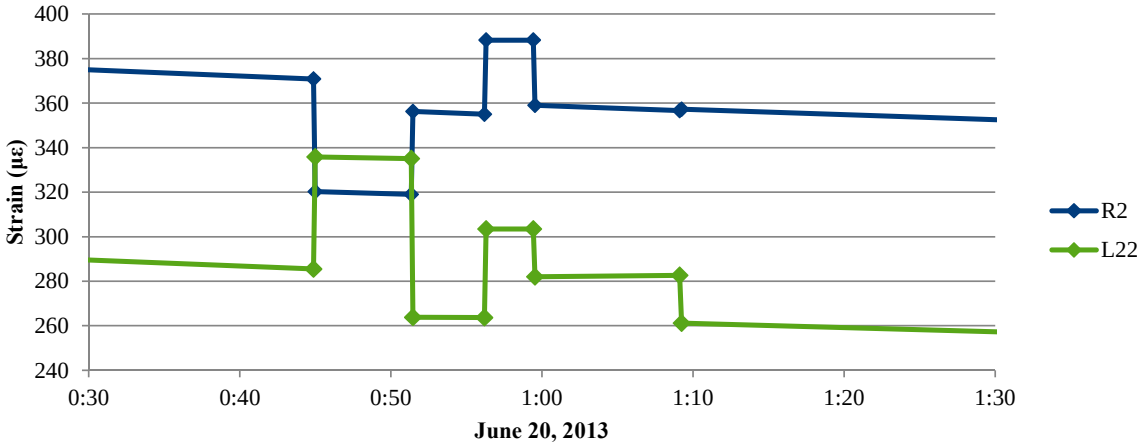

Figure 9.38: Chart showing the events preceding the out of control event in June 2013.

and effects of the out of control event. Figure 9.38 shows the data for sensors R2 and L22 plotted at the time the detected events occurred. These two sensors indicate that the bridge swung open at approximately 00:45 and closed again at 00:51. Then, a train cam by at 00:56 and finished crossing the bridge at 1:00. However, sensor L22 did not return to the same strain level it recorded prior to the train crossing the bridge.[11] Then, the unusual event occurred at 01:09.

According to the event detection algorithm, because L22 is decreasing and R2 is increasing, the detected event was labeled as the bridge closing after a swing event. The other data in the chart clearly indicates that the bridge had not swung open after the train passed and therefore could not be closing. Figure 9.39 is the screen shot taken by the Integrated SHM Data Collection Program at the out of control event. As seen in the photo, no train is crossing, the bridge is closed, and the bridge has not rotated at all. Therefore, the evidence points to a larger than normal shift in the strain level of a member or members near sensor L22[12] caused by the passing train that "corrected" itself after the train had left the bridge. The eye-bar diagonals with the elongated holes are the likely source of the sudden shift. The change in strain level at this shift was larger than typical and exceeded the threshold established in the Event Detection Algorithm of the Integrated SHM Data Collection Program.

Though shifts in strain caused by an eye-bar diagonal settling is not the event that should concern a bridge manager, it has shown the utility of the SPC approach and the process of identifying the source of the observed special variation. The thresholds of the Event Detection Algorithm were not changed as a result of this observation. Until an event such as a vehicular or barge collision occurs and its effect on the bridge strain signature is known, the thresholds should not be changed.

[11] Sensor R2 also did not return to the same strain level, but its difference is much more in line with what had been seen previously in Figure 8.2 and does not exceed the threshold programmed into the Event Detection Algorithm of the Integrated SHM Data Collection Program.

[12] The other sensors near L22 also indicated large changes.

Figure 9.39: Photograph taken by the Integrated SHM Data Collection Program at the June 2013 out of control event.

9.5 Mechanical Strain

As demonstrated in the previous section, the application of structural process control methods to the analysis of the $\Delta\epsilon$ can provide insight into the behavior of the bridge. The advantage of using the $\Delta\epsilon$ is that it eliminates many sensor problems that can arise. However, the assumption in structural health monitoring applications is that the sensors are always returning correct data even though this assumption is not always correct. Sensors can experience drift or other changes that alter the accuracy of the measured response. Understanding and detecting issues with the sensors is therefore a necessary function of a structural health monitoring system. Monitoring the temperature corrected strain itself, appropriately distinguished by whether the bridge is swung open or in one of the two closed positions, can reveal more about the sensors themselves.

The IntelOptics system, as discussed in Section 5.2.2, is designed to monitor temperature corrected strain at regularly scheduled intervals. No distinction is made in the IntelOptics system as to whether the bridge is swung open or closed when the strain measurement is taken. The large strain differences, caused by the bridge being in different positions, can make the IntelOptics data hard to interpret. The data collected that was used to calculate the $\Delta\epsilon$ can also be plotted and monitored for each position of the bridge.

Figure 9.40 shows the temperature compensated data collected in the swung position for all the swing events recorded for strain sensor L22. Though the figure only shows the swung strains, the upstream and downstream measurements taken at the same events shows

a similar pattern. The most obvious feature in the plotted data is the large change in strain that occurs as indicated on May 1, 2012. The change in strain observed over these dates is statistically significant. Both before and after May 1, the data has a mean value, with a statistical variation, that is much less than the observed change. The first reaction is to assume the structure has changed significantly. Sensor L22 is mounted on one of the four eye bars that span L6-M7. It is possible that the four eye bars can share the load unevenly and this could be indicative of larger problems with the structure. However, the most likely cause of this change is strain is not structural.

The main evidence against the change in strain observed in Figure 9.40 is that there is no similar shift present in the plots of $\Delta\epsilon$ shown in the control charts of Figures 9.30 and 9.31. The $\Delta\epsilon$ have been plotted for both the upstream and downstream simultaneously in Figure 9.41 with the points differentiated by color according to the date the event occurred as in Figure 9.40. The $\Delta\epsilon$ removes any sensor issues that can occur. No shift in value of the $\Delta\epsilon$ is present as exists in the plot of just the strain data in the swung position. If the load in the four eye-bars were redistributed, then a corresponding change in the $\Delta\epsilon$ should exist. Small changes in $\Delta\epsilon$, as discussed in Section 9.4, are likely due to shifts in the elongated holes, but those shifts are on the order of a few microstrain and not the 150 microstrain shift in the swung swing strains shown in Figure 9.40.

Further corroboration that the data shows a sensor anomaly and not a structural anomaly comes from the net coefficient of thermal expansion as discussed in Section 9.3. As noted previously, a change in the boundary conditions of the members will result in a change in the net CTE observed in the member. Figure 9.42 shows the swung strains (uncompensated) for L22 plotted against temperature in degrees Celsius. The data before May 1, 2012 experienced some colder temperatures than the data after May 1 as expected. Nevertheless, both before and after May 1, the recorded temperatures between the two sets both had a significant number of data points between $15°$C and $25°$C. Regression lines were fit to the

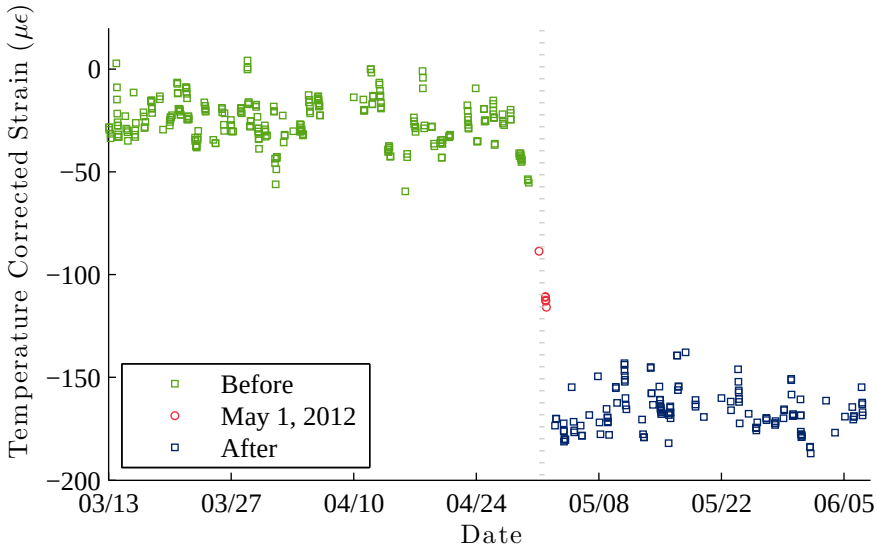

Figure 9.40: Temperature compensated strain for Sensor L22 in the swung open position.

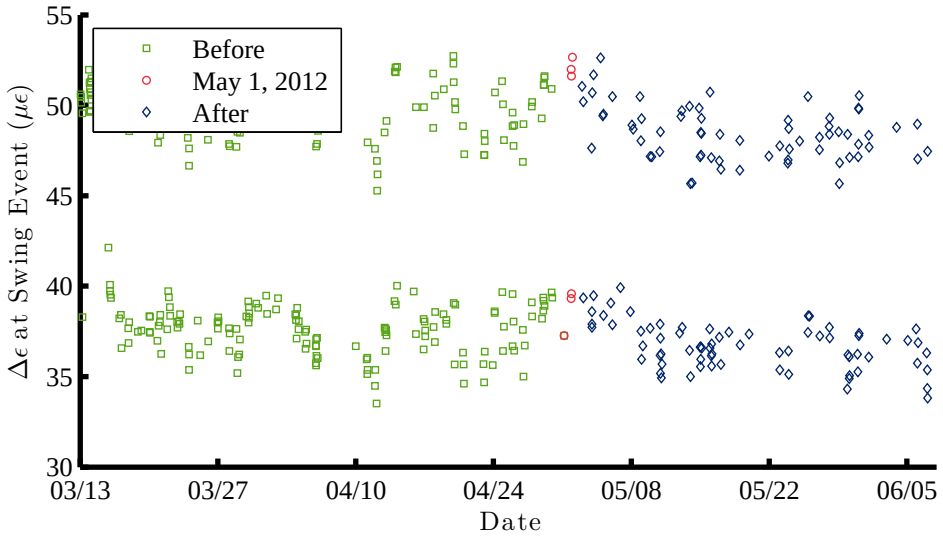

Figure 9.41: $\Delta\epsilon$ for Sensor L22 in the stairs upstream and downstream positions.

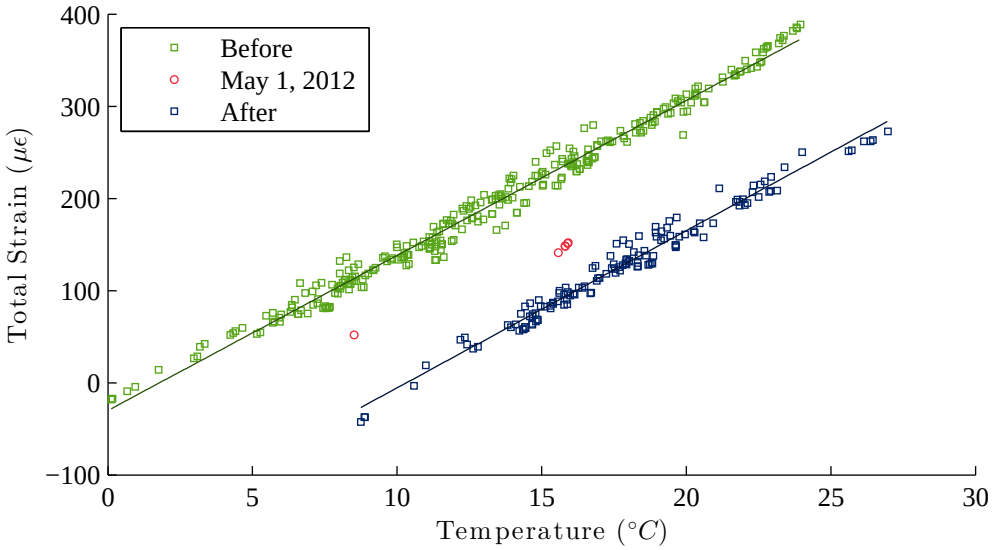

Figure 9.42: Strain vs Temperature for Sensor L22 in the swung open position.

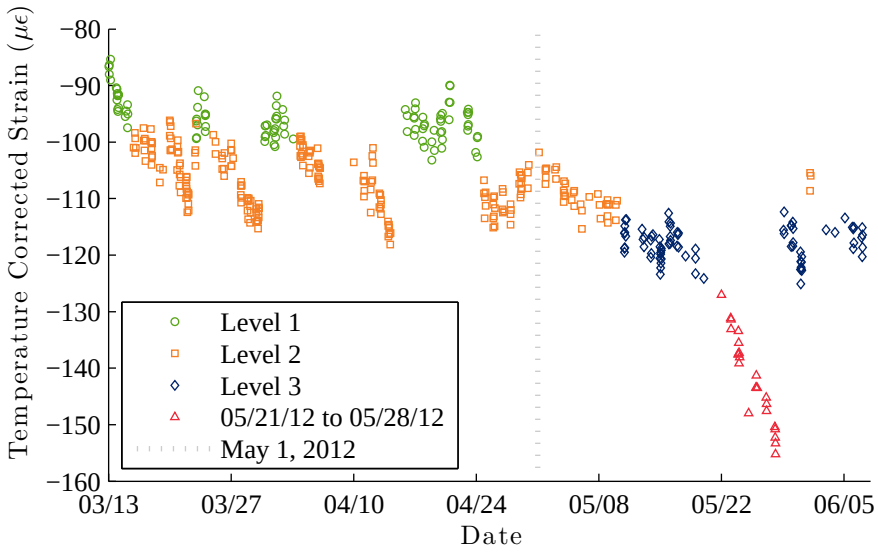

Figure 9.43: Temperature compensated strain for Sensor R2 in the swung open position.

data before and after May 1 to determine the temperature dependence of the strain level. The two fitted lines are shown in Figure 9.42. Before May 1, the fitted line has a slope of 16.82 $\mu\epsilon/°$C whereas after May 1 the slope of the fitted line is 17.05 $\mu\epsilon/°$C. Both these slopes are within the 95% confidence limits of each other and are therefore statistically the same. Therefore, no change has occurred that has affected the determinacy of the structure. These slopes also indicate that the sensor has remained attached to the structure.

The large change in strain of sensor L22 shown in Figure 9.40 does not appear in any other strain record. The large change in strain seen in the sensor record could possibly by caused by one of the eye bars that was previously unloaded to suddenly take on its share of load. If the loading change did occur, strain sensors across the bridge should have detected a shift in their values too. Figure 10.13 shows that as the stiffness in an eye bar decreases toward zero, simulating not carrying any load, the other eye bars and many other members with sensors on them also experience changes in their strain values. The other sensors do not show a pattern that would indicate a structural change (like an eye bar taking on more load) is not a probable cause of the large strain shift.

The uniqueness of the May 1 event in sensor L22 points toward the source being at the sensor itself and not in the interrogator or the ENLIGHT software. For example, Figure 9.43 shows the swung strain values for sensor R2 plotted temporally. Unlike for sensor L22, sensor R2 does not show a single large jump in the strain values. Instead, it has a series of small jumps between what have been called "levels" in the figure. Each level is about 10 $\mu\epsilon$ different from the level on either side. In total, there was an approximately 70 $\mu\epsilon$ difference between the highest and lowest measured temperature compensated strain. The change in load necessary to induce a 70 $\mu\epsilon$ in the member R2 is mounted on is approximately 35,500 lbs. or a change of 26% of the members design load. This dramatic change took place over about two months which is a rate much faster than any typical form of structural damage. To lose that much capacity in two months after over a century of service is very unlikely. In contrast to sensor L22, no other parallel members can share the load

that could possibly account for these sudden and significant changes.

Other than the severity of the changes in strain observed in the swung data, the repeatability of the levels is one of the most striking differences between the L22 and R2 strain data. Returning to a prior value is not indicative of of damage to the structure. Some members that have elongation in their pin holes can experience repeatable shifts in the strain values. However, these shifts are on the order of a few microstrain, not the amount observed in the data. When the $\Delta\epsilon$ for R2 are calculated and plotted with the observed levels in the strain values, as in Figure 9.44, the observed strain levels and the changes in the $\Delta\epsilon$ values are not correlated. In fact the first four weeks of the data show that as the strain data switched from Level 1 to Level 2 and back repeatedly, the $\Delta\epsilon$ values experienced no meaningful change other than normal deviation from a single mean.

However, one section of the two plots seems to have some correlation. The data in Figure 9.40 from May 21–28, 2012 marked with red triangles is slightly different from the other portions of the data. These data points show a significant downward trend before returning the Level 3. While there appear to be local trends in some of the other levels, none span such a large change in strain. These same set of data, when used to calculate the $\Delta\epsilon$ values for the swing events also shows a sustained upward trend as seen in Figure 9.44. Furthermore, these same points were those that were still out of control in the acceptance control charts in Figures 9.32 and 9.33. Therefore, this period likely has some structural cause. The reversal of the trend from downward in the strain plot to upward in the $\Delta\epsilon$ plots indicates that the issue affects the swung position slightly more than the locked ones.

Once again, the strain plots have been temperature corrected based on the net CTE and the changes in "levels" does not significantly change those values. Figure 9.45 plots the uncompensated strain data as a function of the measured temperature with the "levels" distinguished by the color and shape of the marker. As done previously, linear regression was performed on the data in there levels to determine the net CTE. The slope for Levels 1, 2, and 3 were 18.40 $\mu\epsilon/^{\circ}$C, 18.67 $\mu\epsilon/^{\circ}$C, and 18.41 $\mu\epsilon/^{\circ}$C respectively. Statistically, these slope values are all the same indicating that no fundamental changes to the structural member or its boundary conditions has occurred. The slope values also indicate that the sensor is still attached to the structure.

This analysis points to potentially long term stability issues and drifts in the individual sensors. The noise floor of the sensors in the short term is very low (approximately one microstrain). Therefore, the large changes in strain that are neither structural nor from sensor detachment are likely caused by drifts or mechanical issues within the sensors themselves. The fiber optic cable in any sensor has to be attached to its mount in some manner. The metal casing of the sensors used in the Rock Island system has to grip the fiber optic cable to transfer the strain from the welding sites to the cable. It is speculated that the mechanical bond that holds the fiber in place has slipped or shifted back and forth under the environmental conditions on the bridge.

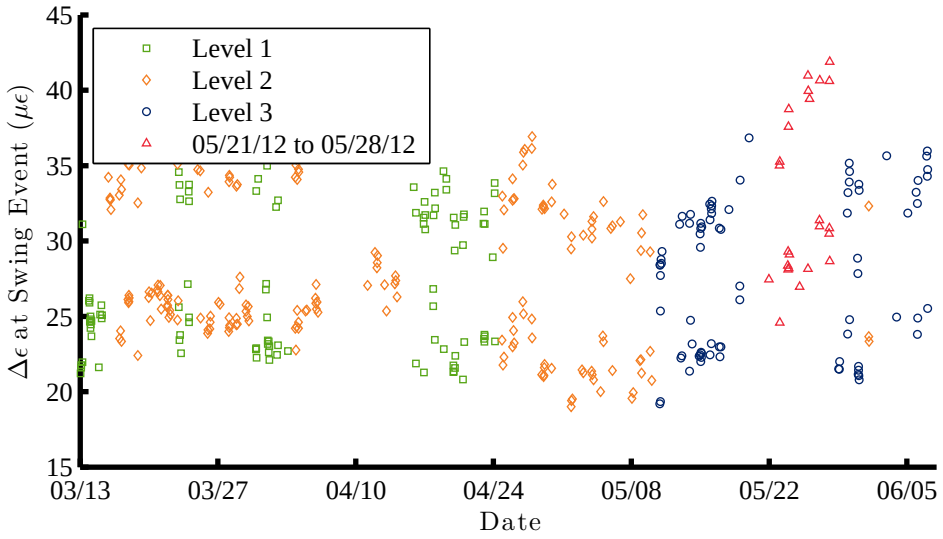

Figure 9.44: $\Delta\epsilon$ for Sensor R2 in the stairs upstream and downstream positions.

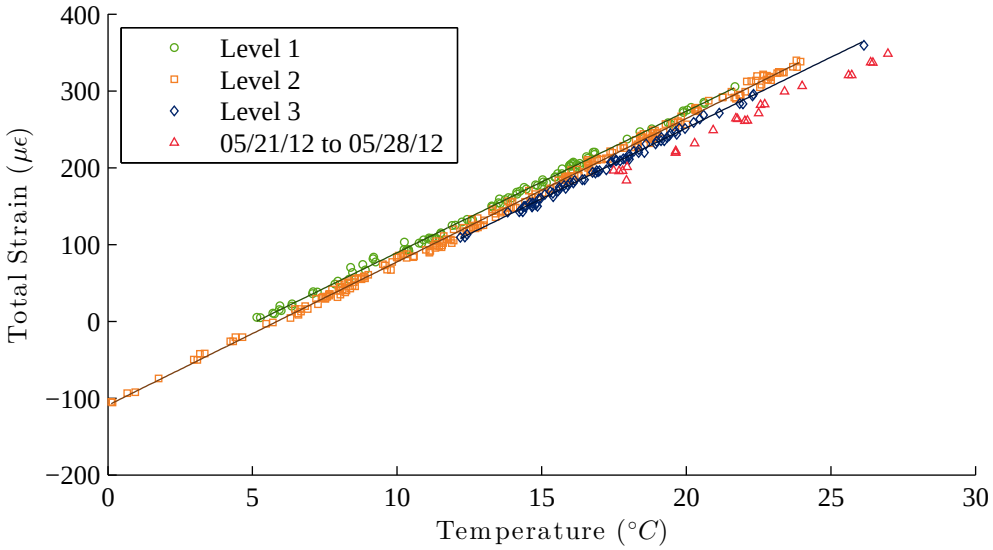

Figure 9.45: Strain vs Temperature for Sensor LR2 in the swung open position.

9.6 Summary

The statistical process control methods that are presented in this chapter for use in anomaly detection can detect both short-term, sudden changes and long-term, gradual changes. A single data point caused by a barge or truck crashing into the bridge may immediately cause one point that is significantly different than the expected value and a violation of Nelson Rule 1 would be detected. A detachment of the sensor will trigger a number of run rules and it can be confirmed by noting the change in the net CTE for that sensor. Corrosion will cause a very gradual shift in the mean value in sensors that are close to the damage location. Given enough time, the control charts will be able to detect these changes as well.

The fact that multiple SPC charts are observing different measurements of the same process improves the reliability of the system as a whole. As stated in Section 9.1.1, a 0.27% chance exists for one sensor to have a measurement that exceeds the 3σ control limits due to the natural noise in the measurement. However, the probability that any two or more sensors exceed the control limits at the same time without a change to the underlying process is different. Assuming the noise in one sensor is independent of the others, when any combination of k sensors of the n total sensors detect values that simultaneously exceed the control limits, a ${}_nC_k \left(0.27^k\right)\%$ probability exists of a Type I error (false positive). Given, as calculated in Section 4.2.6, that only about 556 swing events take place at night annually, a false positive would be expected less than once every 2 years if nine of sixteen sensors [13] are required for an anomaly to be detected. Therefore, requiring multiple sensors to detect an anomaly simultaneously before notification occurs will reduce the occurrence of false positives and thus the reporting rate to the managing engineer. Once an anomaly is detected, and the SHM program determines it to be a structural anomaly, then the last step shown in the flowchart in Figure 9.1 at the beginning of this chapter is to locate and quantify any damage that has occurred. Damage localization and quantification are the subject of Chapter10.

[13] Though the fiber optic system contains 34 strain sensors, only 16 of them are in viable locations. Sensors located on a pin, the flange of the bottom chord, the L7-M7 vertical member, and the 0L-0M vertical post are those that are excluded from this number.

Chapter 10

DATA INTERPRETATION AND DAMAGE DETECTION

Once data has been collected and statistically significant changes in a feature are detected, a successful SHM system needs to be able to interpret the structural significance of the change. The method used to interpret the change in the feature will depend on what the feature is and what information is desired. Damage detection algorithms can be classified by what level of detection they provide. Farrar and Worden [25] described the classifications based on the answer to five questions:

- **Existence**: Is there damage in the system?
- **Location**: Where is the damage in the system?
- **Type**: What kind of damage is present?
- **Extent**: How severe is the damage?
- **Prognosis**: How much useful life remains?

Some of these questions are easier to answer than others.

The task of damage detection is further complicated by the nature of the assumed damage itself. Different structures made of different materials will experience different levels of damage. Concrete bridges will always have cracks in them, but those cracks are not always considered damage, but rather an expected development in the material. However, excessive cracking or spalling caused by corrosion and the subsequent expansion of the internal rebar would be considered damage. For steel bridges, damage typically results, in the most general terms, from either corrosion or from overloads[1] to the structure.

Corrosion damage itself can come in many different forms. Corrosion can be isolated and lead to the development of pitting corrosion, crevice corrosion, or similar corrosion mechanisms. Corrosion can also be more general and cause the member to develop an overall section loss. Isolated crevice corrosion can lead to cracks that can cause local changes to the strain field but will not affect the strain in locations even a few crack lengths away. Therefore, unless a strain gauge is located very near the crack, the crack must reach an advanced stage of development before a change in strain is detected. Similarly, the crack may cause changes in the local modes of the member but have very little effect on the global natural frequencies and mode shapes. A dense array of sensors would be necessary to detect the local effects of crack formation in steel structures. Corrosion damage that is more general and causes an overall loss in the cross section of the member has a more

[1] Overloads can be from near static events such as an overloaded truck crossing the bridge or from dynamic events such as impacts, explosions, or earthquakes. Design and construction flaws can be classified as overloads, because they reduce the capacity of the as-built structure so the bridge is overloaded by loads less than the design load.

global effect on the capacity of the member. The uniform loss of cross section can be both modeled and detected more easily than corrosion induced localized cracking.

The sparsity of strain sensors on the Rock Island Bridge and the location of the installed sensors in the center of the members reduces the likelihood that corrosion induced cracks will be detected by any damage detection algorithm. The members of the bridge are more likely to corrode at the joints where water can pool or remain trapped between members. The lacing in the built up members creates some joints that are more distributed across the members. However, inspection reports still indicate that most corrosion in the Rock Island Bridge has occurred at joints or along horizontal members that allow for pooling along their bottom member. If the crack were to develop in the vicinity of the sensors, they would be detected by the statistical process control methods. However, the likelihood of cracks developing in the vicinity of the sensors is less than the likelihood that cracks will develop at the joints. The sparsity and placement of the acceleration sensors to observe global modes has a similar effect.

Nevertheless, the sensors should be placed such that they are able to detect changes that affect the stiffness of the members in a global sense. The FE model developed for the Rock Island Bridge can be used to simulate a uniform loss of stiffness in a member akin to corrosion of the gross cross section of a member. Methods to detect this type of damage have been developed. For the Rock Island Bridge, two such damage detection methods have been explored: the Damage Locating Vector (DLV) method and the First Order Flexibility (FOrFlex) method. Both methods detect the existence and location of damage in a structure, and the FOrFlex method also can make an estimation of the extent of the damage. The DLV method uses the acceleration data from the wireless sensor network while the FOrFlex method uses the strain data from the fiber optic system. The methods are not in competition with each other but should work together to confirm the results of the other and provide greater confidence in their results.

10.1 Damage Locating Vector Method

Bernal [139] introduced a damage detection and localization method based on changes to the flexibility matrix. The method was designed to be used with experimentally derived flexibility matrices using dynamic data. The idea behind the method is that there exists a set of load vectors – called the damage locating vectors (DLVs) – that when applied to a structure as static forces, no stress develops in both the damaged and undamaged structure at the damaged element. Therefore, once the DLVs have been computed and applied to the analytical model, members with near zero stress become the likely candidates where damage has occurred.

10.1.1 Derivation of the DLV Method

The first step in the DLV algorithm is to determine the change in flexibility matrix. For a linear structure, the flexibility matrix is derived from measured acceleration data using

both the Natural Excitation Technique (NExT) and the Eigensystem Realization Algorithm (ERA) [140]. This process is performed in the initial, undamaged state to derive the undamaged flexibility matrix $\mathbf{F}_u$ and again later in the damaged state to get the damaged flexibility matrix $\mathbf{F}_d$. The first step in the DLV method is to determine all the load vectors $\mathbf{L}$ that satisfy the condition:

$$\mathbf{F}_d\mathbf{L} = \mathbf{F}_u\mathbf{L} \tag{10.1}$$

$$(\mathbf{F}_d - \mathbf{F}_u)\,\mathbf{L} = 0 \tag{10.2}$$

$$\mathbf{F}_\Delta\mathbf{L} = 0 \tag{10.3}$$

These equations dictate the load vectors will produce the same displacement pattern before and after damage has occurred. The desired DLVs will also satisfy the conditions of Equation (10.1), because the zero stress in the damaged element will not affect the displacements in the structure. Therefore the set of load vectors $\mathbf{L}$ are actually the DLVs. Singular Value Decomposition (SVD) is used to calculate the load vectors using the change in flexibility matrix, $\mathbf{F}_\Delta$, as follows:

$$\mathbf{F}_\Delta = \mathbf{U}\mathbf{S}\mathbf{V}^* \tag{10.4}$$

where $\mathbf{U}$ and $\mathbf{V}^*$ are unitary matrices whose columns contain the left and right singular vectors, respectively, and the * indicates the conjugate transpose of the matrix. The diagonal values of the positive, real-valued, rectangular diagonal matrix $\mathbf{S}$ are the singular values of $\mathbf{F}_\Delta$. The matrices from the SVD can be partitioned as follows:

$$\mathbf{F}_\Delta = \begin{bmatrix}\mathbf{U}_1 & \mathbf{U}_0\end{bmatrix}\begin{bmatrix}\mathbf{S}_1 & \mathbf{0} \\ \mathbf{0} & \mathbf{0}\end{bmatrix}\begin{bmatrix}\mathbf{V}_1 & \mathbf{V}_0\end{bmatrix}^* \tag{10.5}$$

Then, because $\mathbf{V}^*$ is unitary such that $\mathbf{V}^*\mathbf{V} = \mathbf{I}$, multiplying both sides by $\begin{bmatrix}\mathbf{V}_1 & \mathbf{V}_0\end{bmatrix}$ yields the following result:

$$\begin{bmatrix}\mathbf{F}_\Delta\mathbf{V}_1 & \mathbf{F}_\Delta\mathbf{V}_0\end{bmatrix} = \begin{bmatrix}\mathbf{U}_1\mathbf{S}_1 & \mathbf{0}\end{bmatrix} \tag{10.6}$$

From Equation (10.6) it can then be seen that:

$$\mathbf{F}_\Delta\mathbf{V}_0 = \mathbf{0} \tag{10.7}$$

Comparing Equation (10.3) and Equation (10.7) leads to the conclusion that that:

$$\mathbf{L} = \mathbf{V}_0 \tag{10.8}$$

Therefore, the DLVs can be obtained by performing SVD on the change in flexibility matrix, $\mathbf{F}_\Delta$.

To then locate the likely location of damage in the structure, the DLVs obtained through SVD are applied to the undamaged finite element model of the structure. The stress in each element of the model is then calculated and used to obtain a normalized cumulative stress from all possible DLVs. The normalized cumulative stress for the j^{th} element, $\bar{\sigma}_j$ is

calculated as follows.

$$\bar{\sigma}_j = \frac{\sigma_j}{\max_k (\sigma_k)} \tag{10.9}$$

where σ_j is the cumulative stress in the j^{th} element and is defined as:

$$\sigma_j = \sum_{i=1}^{n} \left| \frac{\sigma_{ij}}{\max_k (\sigma_{ik})} \right| \tag{10.10}$$

where σ_{ij} is the stress in the j^{th} element induced by application of the i^{th} DLV. Theoretically, if an element has a zero normalized cumulative stress, then it is likely a damaged element. However, in real world applications, errors from measurement or modeling also accumulate in the normalized cumulative stress causing non-zero, but near zero, values. The user of the DLV method needs to set appropriate thresholds for determining when an element should be considered as a damaged element. The normalized cumulative stresses can be considered a damage index for the structural elements.

10.1.2 Simple Example of the DLV Method

The small, simply supported, truss structure shown in Figure 10.1(a) will demonstrate the effectiveness of the DLV method. The small truss consists of six nodes connected by seven members and is statically determinate. The members all share the same stiffness. To simulate damage in the structure, the stiffness of element seven, the diagonal, was reduced by 5% while the rest of the members' stiffness was left unchanged. Using the undamaged and damaged stiffness matrices to calculate the undamaged and damaged flexibility matrices, the DLV method was performed to produce damage indices. The damage indices are plotted in Figure 10.1(b). The graph shows that the normalized cumulative stress and damage index for element seven is exactly zero. The damage indices for the other elements are not all unity due to the influence of the damaged element on the surrounding elements.

This small example assumed that sensors were located at all nodes and that a complete flexibility matrix could therefore be reconstructed. Though the DLV method will compute the normalized cumulative stress for every element in the model once the load vectors have been applied, it has been found that for the damage indices to be meaningful, the element must be located between two sensor nodes [140].

10.1.3 Application of the DLV method to the Rock Island Bridge

The small truss model presented as an example in the previous section is a significantly less complex structure than the Rock Island Bridge. To verify that the DLV method was viable on such large, complicated, real-world structure, the DLV method was performed on the FE model of the Rock Island Bridge. The large number of elements in the Rock Island Bridge FE model makes charts like that in Figure 10.1(b) difficult for the average user to quickly understand and interpret. Therefore, the damage indices that are calculated with the DLV method have been plotted as a color gradient on the elements of the model. In the

figures presented in this section, an element colored red has a normalized cumulative stress damage index close to zero. As the damage index increases from zero to one, the color of the element changes from red to purple to blue. Therefore, the elements that are predicted to be the least damaged by the DLV method will be colored bright blue. Elements that have a lower DI but are still not likely damaged will be dark purple.

The implementation of the DLV on the Rock Island Bridge FE model was altered to simulate the real functionality of an installed sensor system. Limitations on the number of sensors available often limits the placement of sensors.Arranging the sensors to form a hierarchical network composed of small groups of sensors is more efficient and allows for more reliable communication [119, 141]. To simulate realities of SHM systems, the DLV method was performed with a limited number of sensors. As noted in the previous section, meaningful results from the DLV method can only be derived for elements that have a sensor on either side. Therefore, the members that are "unmeasured" by the local group of sensors have been colored gray in the figures presented in this section. To help clarify where the sensors are located, green spheres have been placed where the virtual

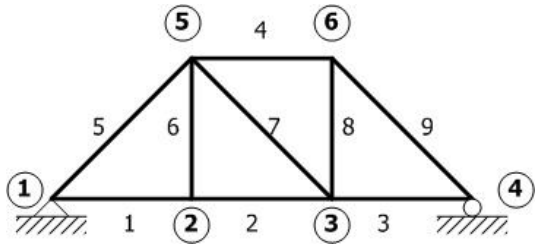

(a) 2D truss model with nodes and elements labeled.

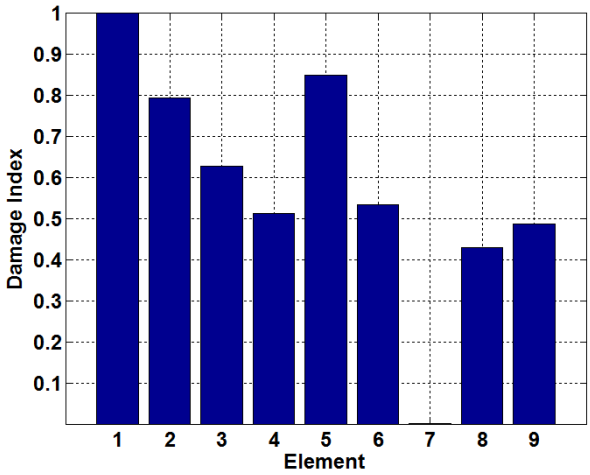

(b) Graph of the damage indices computed using the DLV method for the truss shown where element 7 has been simulated as damaged.

Figure 10.1: Simple two dimensional truss DLV method example.

sensors were placed[2] during these numerical studies. Larger red spheres were place on the damaged elements in the scenario so they can be distinguished more easily.

To simulate damage due to corrosion in the model, the stiffness of the element was reduced by a given percentage. The number of members damaged and the location of the damaged members were varied to determine the effectiveness of the DLV for a wide range of damage possibilities. Ideally, a damage localization algorithm should detect multiple damage locations in all critical members of the structure. A limited number of test cases are presented here to demonstrate the effectiveness of the method and show how the DLV method can be applied to the Rock Island Bridge. The stiffness reduction used for the damaged elements was 5%. Trials were performed for higher stiffness reductions [142], but as will be shown, the method was capable of handling the lower 5% reduction well and so the trials with greater stiffness reductions are not presented here.

One of the most likely damage scenarios is that of corrosion damage to the elements along the bottom chord of the structure. These members are exposed to the deicing salts that are spread along the deck in the winter and are more prone to the pooling of water in the joints. Both these conditions are likely to accelerate corrosion at these locations[3]. Therefore, the first damage scenario presented in Figure 10.2 consisted of one member on the bottom chord experiencing a stiffness loss of 5%. Sensors were placed on one section of the front panel of the bridge including nodes that are located at the end joints of the damaged member. The DLV method properly identifies the damaged member as colored red in the figure. All the other members in the measured panel are various shades of blue indicating that they are undamaged.

In the experimental verification of the DLV on small laboratory scale truss models [140], the DLV can be more sensitive to damage in members in different locations and orientations. Therefore, a number of different elements in the test panel were damaged individually to test the effectiveness of the DLV method. Figure 10.3 displays the results of the DLV method when one member in the top chord has been damaged. The DLV method properly locates the damage location.

With multiple groups of sensors covering the bridge, damage to a member outside a sensor group should not cause a false positive in the sensor group of interest. To simulate this situation, a member in the vertical post in the rear truss but on the same side as the measured panel was damaged by 5%. Figure 10.4 shows the unmeasured damaged member in grey highlighted by the red sphere. The elements that are located between the sensors are all shades of blue indicating no damage in the sensed panel. Thus no damage was falsely reported and the DLV is robust to this scenario.

Damage does not always occur in just one element at a time. Therefore, scenarios were tested that had multiple damaged elements. Figure 10.5 shows the DLV results for damaging two members: one on the bottom chord and one on the top chord. Both damaged elements are identified; the other elements in the measured region are all blue and therefore have damage indices greater than the threshold used to identify damaged elements.

[2]These locations are not related to those chosen for the actual network of wireless smart sensors installed on the bridge. Instead these locations were chosen to simulate an alternate sensor configuration.

[3]The bottom chord and underside of the bridge have recently been repainted to inhibit corrosion. The rest of the bridge was not painted because the corrosion risk and general wear and tear on the paint of the upper members is less than the bottom sections.

Figure 10.6 similarly shows three damaged elements as measured by two sensor groups (one on the front panel and an analogous one on the back panel). In this scenario, all three elements are identified by the proper group of sensors. The three damaged elements in this example are harder to distinguish as they are not as bright red as in the previous figures. The decrease in the level of damage and the increase in the number of damaged elements have made them harder to detect and distinguish from the undamaged elements.

These test scenarios have shown that the DLV method has potential to be used in truss structures as complicated as the Rock Island Bridge. Further research that evaluates the effects of measurement noise and system identification of the actual structure would advance this demonstration of the DLV method. The DLV method can also be further expanded to include the strain measurements in improving the method's effectiveness for the Rock Island Bridge.

10.2 First Order Flexibility Strain Damage Detection

Using strain measurements in damage detection algorithms has received less research attention than using acceleration measurements and their derivatives. Nevertheless, a number

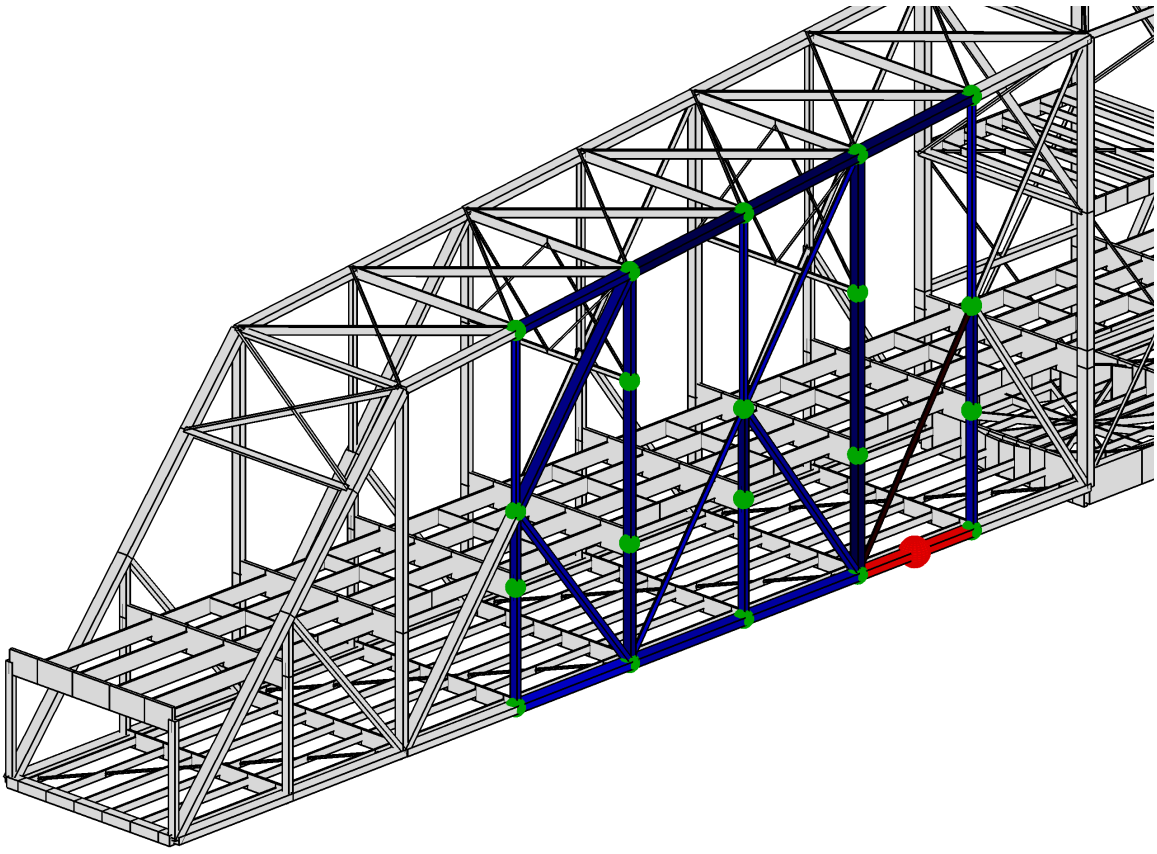

Figure 10.2: DLV results for damaged element in the bottom chord with 5% stiffness reduction and sensors on one panel.

of approaches to damage detection have been developed that have used strain measurements [143]. Since Yao et al. [144] formulated in 1992 the concept of the strain mode shape as derived from the strain frequency response function, strain mode shapes have been used like traditional mode shapes. For example, methods that use changes in the curvature of the strain mode shapes have been developed [145].

Other methods have been developed to determine an approximation of the flexibility matrix from the strain mode shapes. The flexibility matrix can then be used by methods like the DLV as long as symmetry of the flexibility matrix is guaranteed [30, 146]. In these methods, the strain flexibility matrix $\mathbf{F}_s$ is formulated such that:

$$\mathbf{F}_s = \mathbf{\Phi}_s \mathbf{D} \mathbf{\Phi}_s^T \tag{10.11}$$

where $\mathbf{\Phi}_s$ is the strain mode shape matrix and $\mathbf{D}$ is defined as:

$$\mathbf{D} = \text{diag}\left(\left[\left(\frac{d_1}{\omega_1}\right)^2, \quad \left(\frac{d_2}{\omega_2}\right)^2, \quad \cdots, \quad \left(\frac{d_j}{\omega_j}\right)^2, \quad \cdots\right]\right) \tag{10.12}$$

and d_j is a mass normalization constant and ω_j is the j^{th} natural frequency.

These previously developed methods focused primarily on localization of damage and

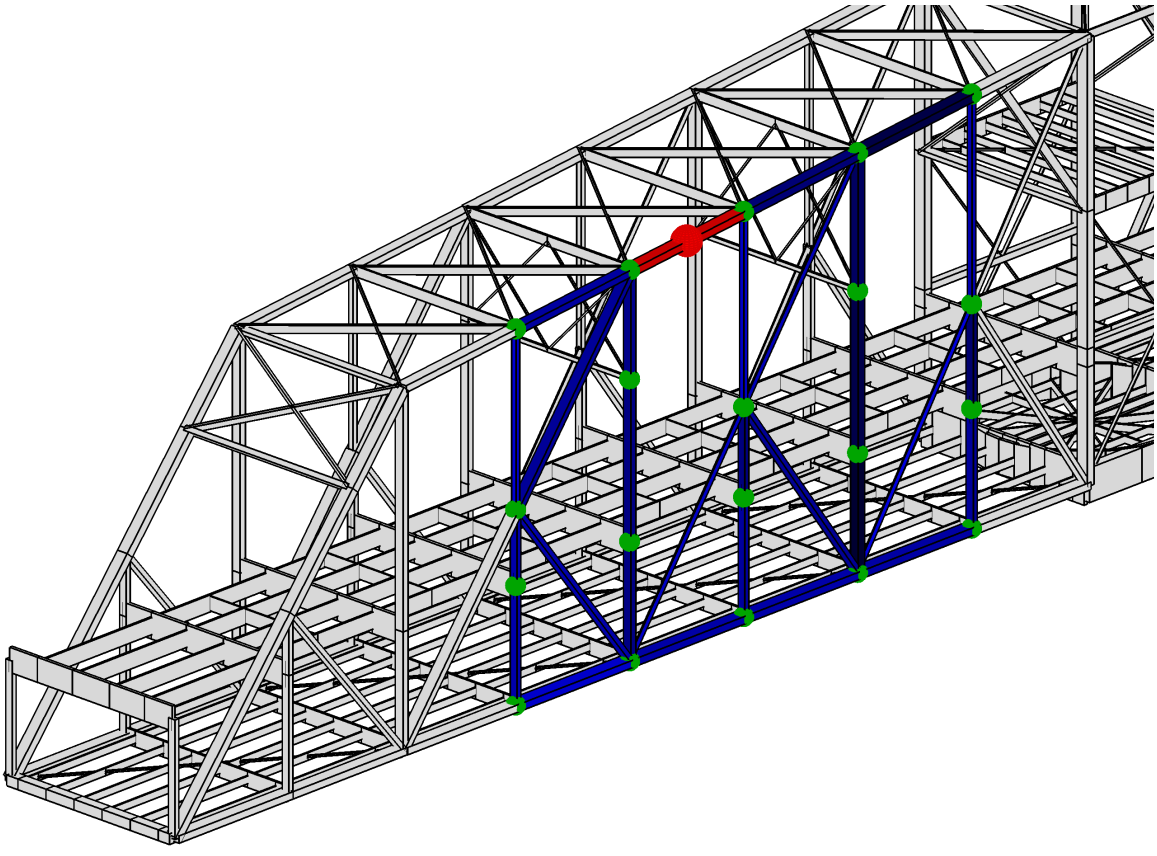

Figure 10.3: DLV results for damaged element in the top chord with 5% stiffness reduction and sensors on one panel.

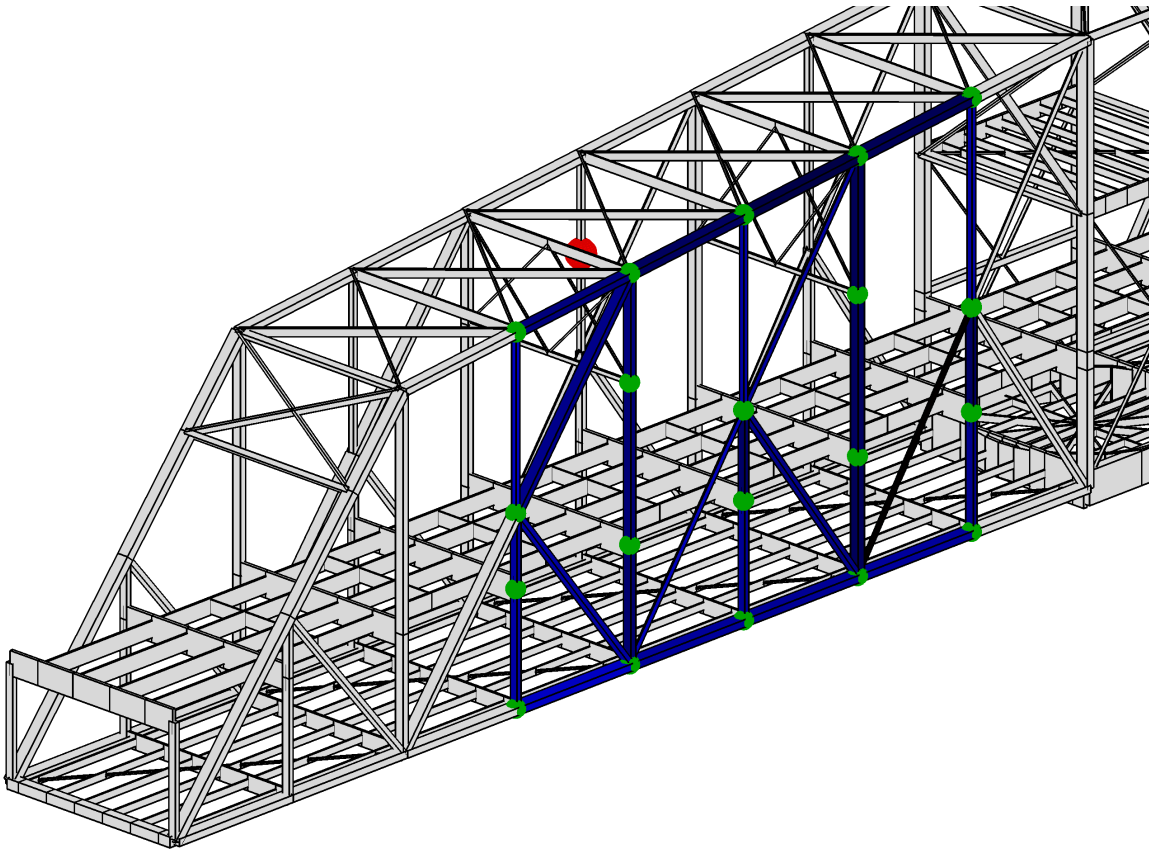

Figure 10.4: DLV results for damaged element with 5% stiffness reduction not included in the sensed elements.

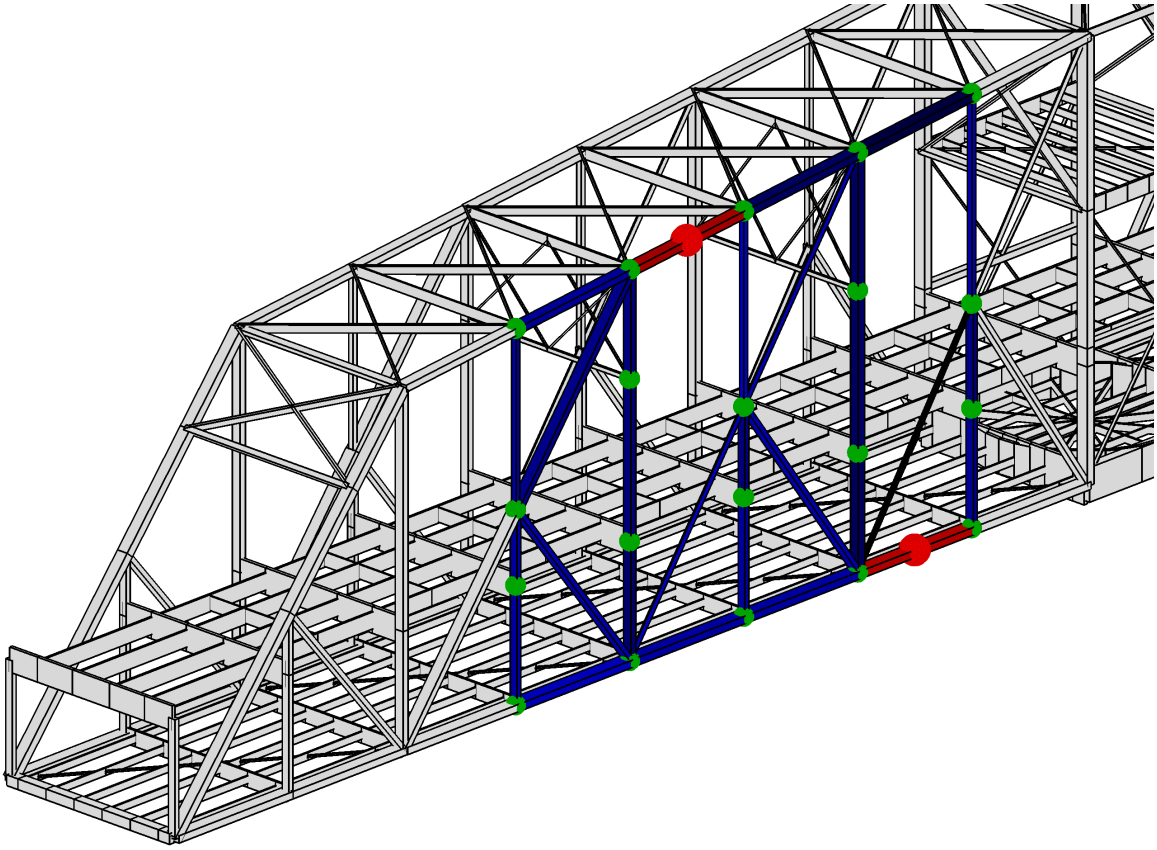

Figure 10.5: DLV results for two damaged elements with 5% stiffness reduction and sensors on one panel.

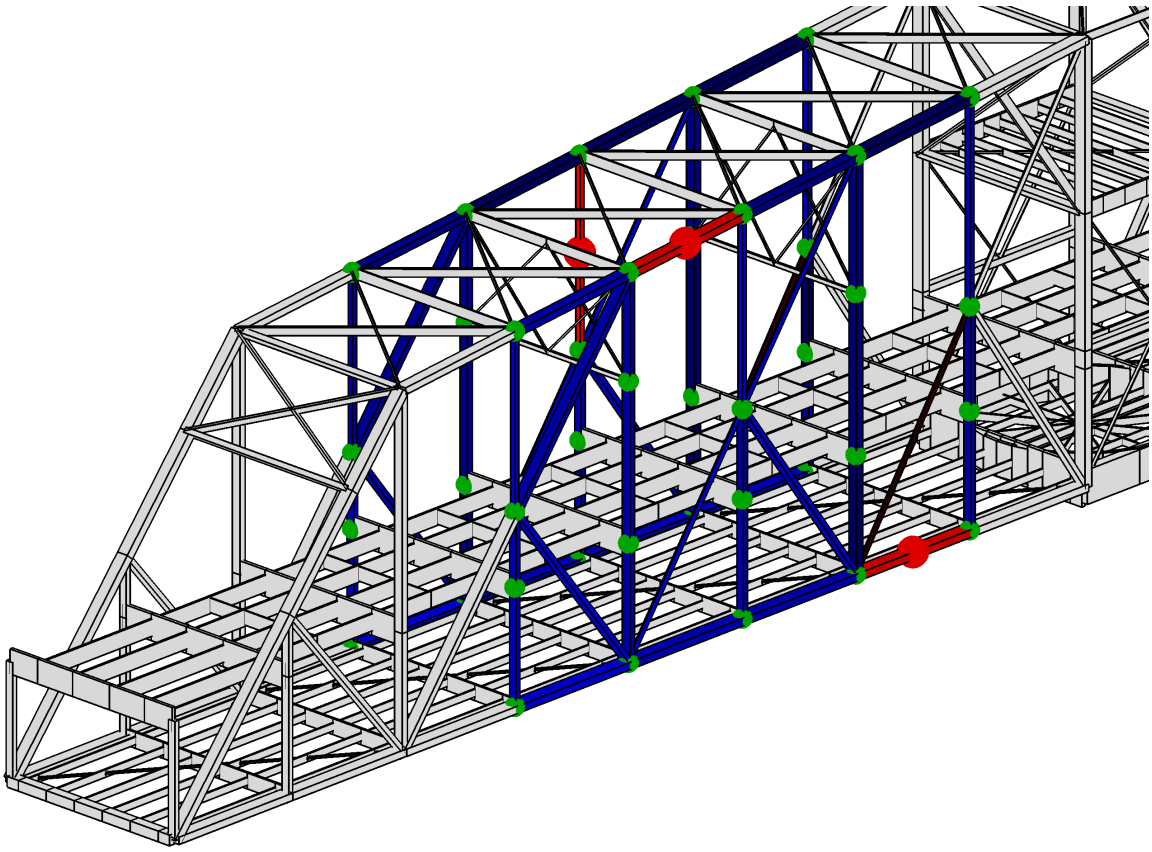

Figure 10.6: DLV results for three damaged elements with 5% stiffness reduction and sensors on two panels.

not necessarily quantification of the damage. With the SHM system that has been developed for Rock Island, the statistical process control methods detect the presence of structural changes and some localization based on the affected sensors. The DLV method using the acceleration data can be used to confirm and further locate structural changes. Before alerting the end user to the probability of structural damage, a quick estimation of the amount of damage needs to be performed. A first-order flexibility (FOrFlex) method has been developed that uses the measured strain data to locate and quantify the changes to the structure.

10.2.1 Basis for the Effects of Damage on Strain Values

The first order flexibility method is based on observing the effects of certain damage scenarios on the strain patterns in the structure. When an element is damaged, it loses stiffness that alters the structure and its typical load path. These changes are what the SPC methods monitoring the strain and $\Delta\epsilon$ are designed to detect. In determining how sensitive and what types of damage the SPC methods could detect, a large number of were considered for various degrees of stiffness loss. Examples for two elements at three different stiffness reduction levels are presented in Figures 10.7–10.12. These figures have colored members that experience more than a 0.5 $\mu\epsilon$ change in strain[4] (or $\Delta\epsilon$). The location of the strain sensors have been marked with green spheres and the location of the damaged element with a red sphere. The threshold of 0.5 $\mu\epsilon$ was chosen based on the shift in mean that can reasonably be expected to be determined by the SPC methods.

Figures 10.7–10.9 show the strain responses to damage in member L5-L6 in the bottom chord of the front panel at 5%, 15%, and 30% reduction in the stiffness of the member. The stiffness change is performed by reducing the Young's modulus of the member prior to calculating the stiffness matrix. The L5-L6 member is one that Figure 6.37 identified as having a large negative change in strain from the closed to open positions as it transitions from tension into compression. Figure 10.7 shows that at the 5% reduction level, only the member itself experiences a significant, measurable change in either the strain or $\Delta\epsilon$. As the amount of stiffness reduction increases, other members begin to experience larger changes in their strain. When the reduction has reached 15%, the neighboring members on the bottom chord now also have measurable changes in their strain as shown in Figure 10.8. Unfortunately, none of the three members with significant strain changes are measured. Continued degradation of the member eventually causes changes in strain that are measurable by the strain gages. Figure 10.9 shows those members with significant changes when the reduction in stiffness of L5-L6 has reached 30%. In this figure, the sensor in the R3[5] should have strain and $\Delta\epsilon$ values that have changed by more than 0.5 $\mu\epsilon$.

Figures 10.10–10.12 show similar results for simulated damage to the third eye-bar of

[4]The figures use the notation $\Delta(\epsilon)$ to denote a change in strain from the undamaged state to the damaged state. Likewise, the notation $\Delta(\Delta\epsilon)$ to denote a change from the undamaged state to the damaged state in the difference between the strain levels in the bridge when it is opened and closed.

[5]This would assume that the R3 sensor was installed on the axis of the member but it was not so the current system would still not likely be able to detect the 30% reduction.

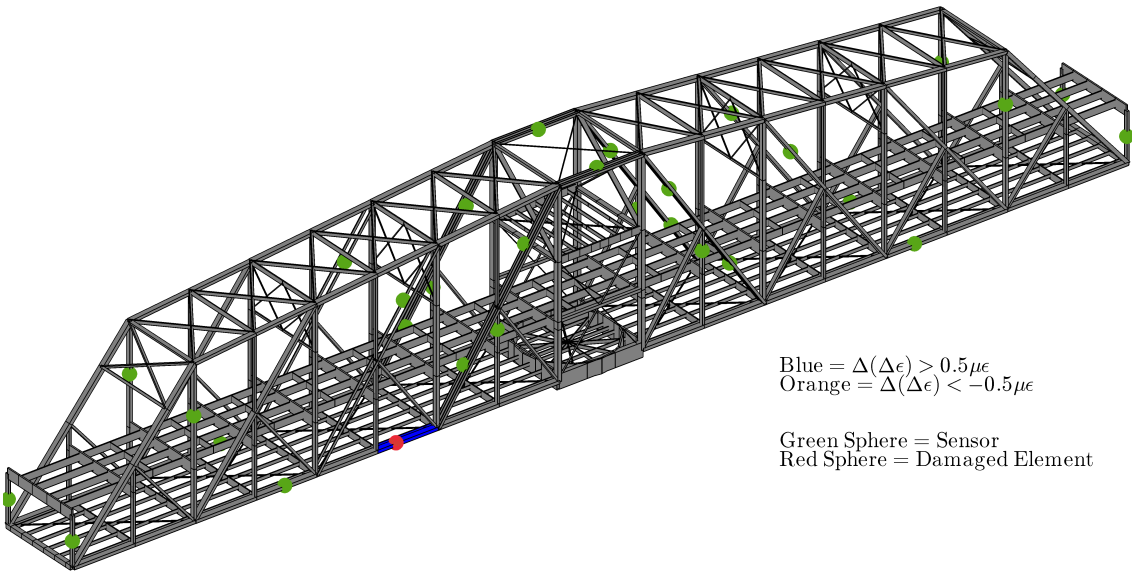

(a) Change in $\Delta\epsilon$.

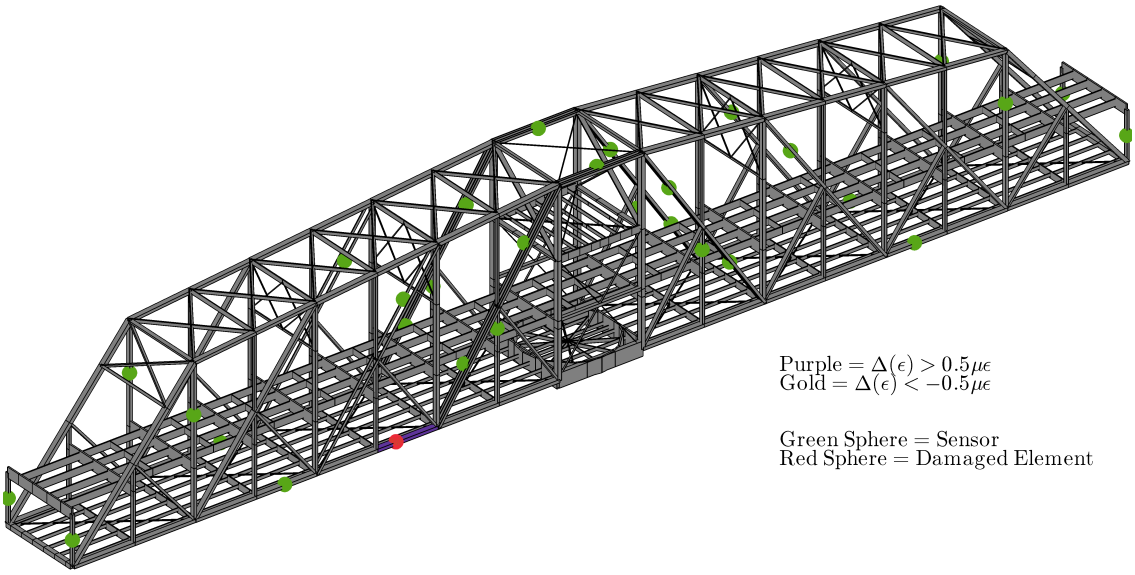

(b) Change in ϵ.

Figure 10.7: Change in $\Delta\epsilon$ and ϵ with a 5% reduction in stiffness in a bottom chord element in the stairs downstream position.

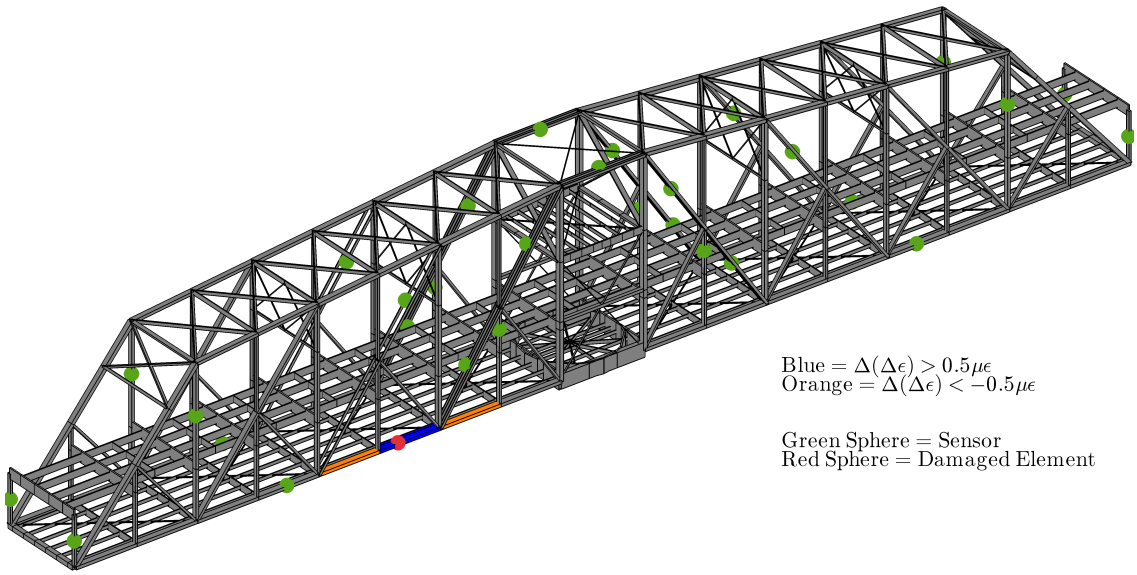

(a) Change in $\Delta\epsilon$.

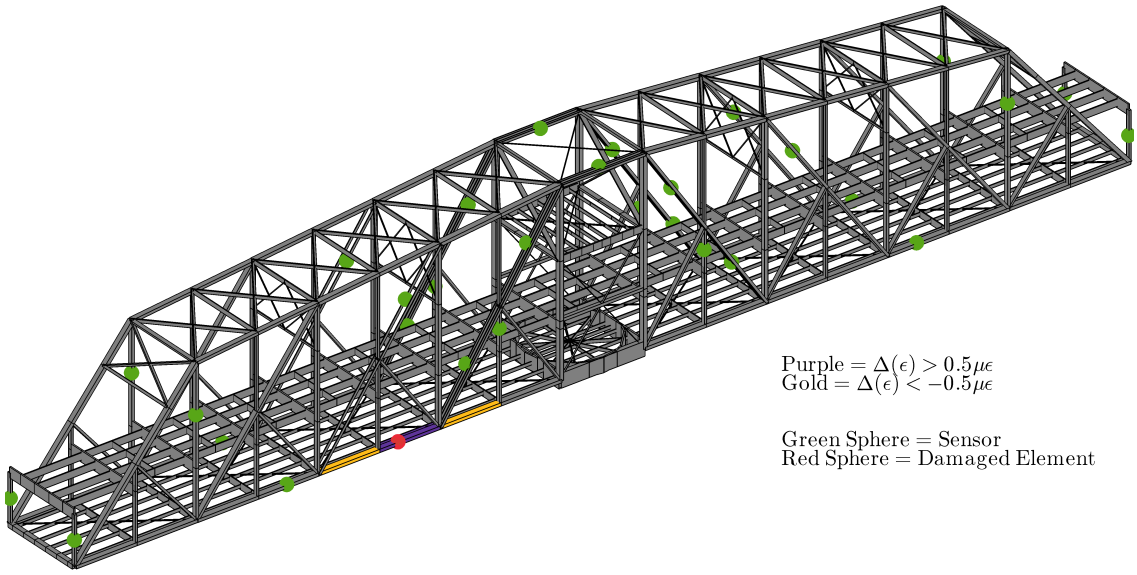

(b) Change in ϵ.

Figure 10.8: Change in $\Delta\epsilon$ and ϵ with a 15% reduction in stiffness in a bottom chord element in the stairs downstream position.

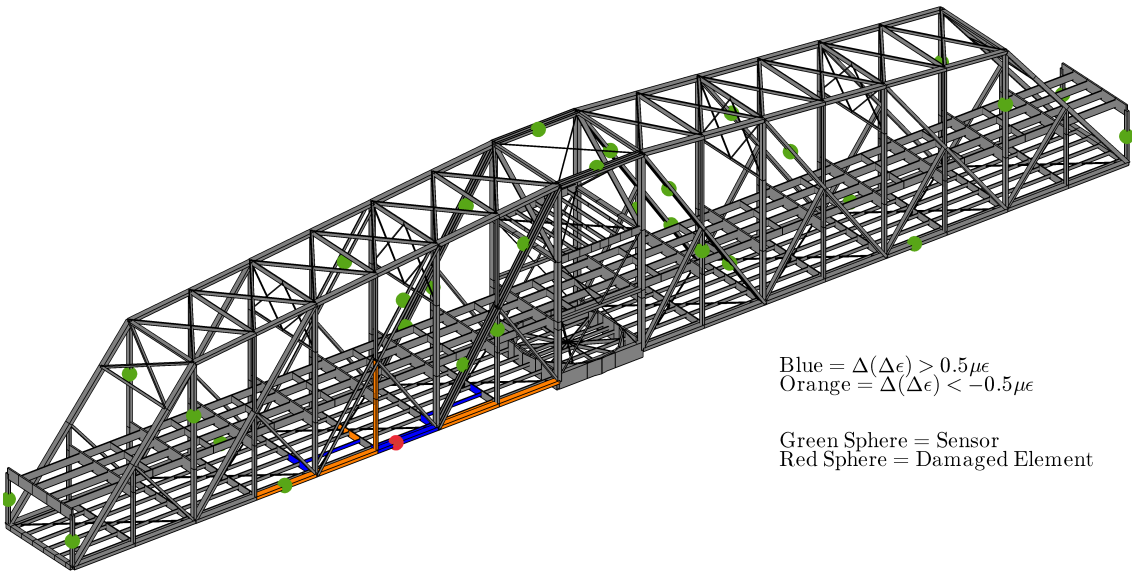

(a) Change in $\Delta\epsilon$.

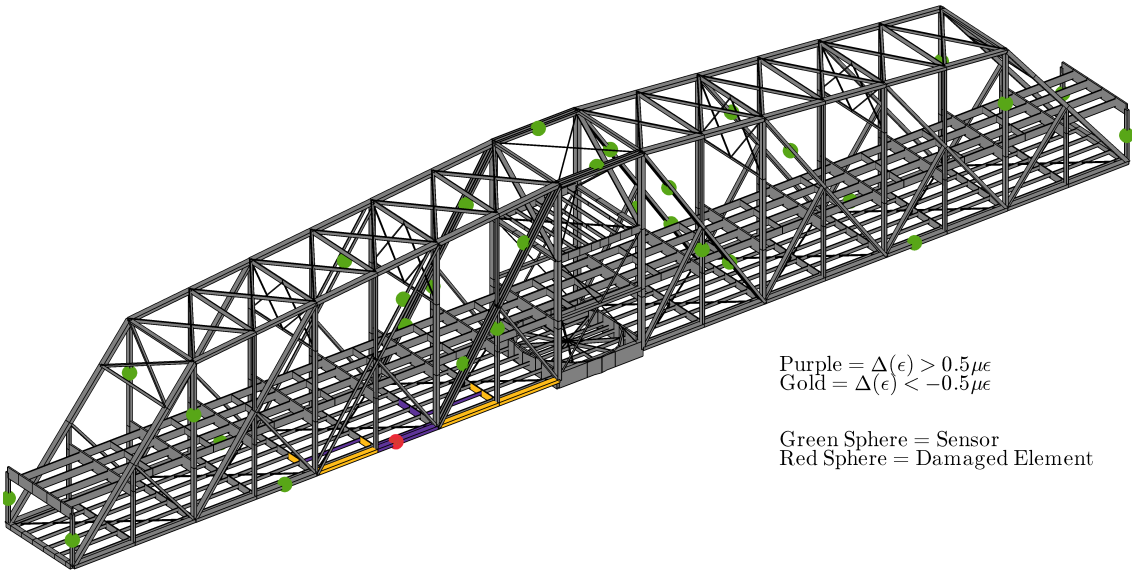

(b) Change in ϵ.

Figure 10.9: Change in $\Delta\epsilon$ and ϵ with a 30% reduction in stiffness in a bottom chord element in the stairs downstream position.

the four eye-bars that span M7–U8. The eye-bars themselves are very sensitive to damage in the other eye-bars, but only larger stiffness reductions induce changes that spread to other sensors. The stiffness changes do not induce changes in other sensors because the eye-bars themselves are redundant or statically indeterminate locally. The load in the M7–U8 members is shared among all the eye-bars and it can be redistributed according to the strength of each member. In a determinate truss, the loads in the members do not change because there exists only one solution for the distribution of the loads. Therefore, in a determinate truss, each member would need to be instrumented for changes in that member to be detected. What Figures 10.7–10.9 show is that the truss, though indeterminate globally, behaves locally as a determinate truss and therefore, ideally, each member would need to be measured to best detect damage.

Figure 10.13 shows the results of a 90% reduction in stiffness to demonstrate how the failure of one of the redundant eye-bars could be detected in multiple strain sensors.

The examples in this section demonstrate that each member in the structure will be affected, if only by a small amount, by a change in stiffness by any other member. Therefore, the measured change in strain of the i^{th} member, $\Delta\left(\epsilon_i\right)_m$, is a result of all the changes in strains induced in the i^{th} member by any changes in the stiffness of all the other members. Mathematically this can be written such that:

$$\Delta\left(\epsilon_i\right)_m = \sum_{j=1}^{n} \Delta\left(\epsilon_i\right)_{\Delta K_j} \tag{10.13}$$

Here $\Delta\left(\epsilon_i\right)_{\Delta K_j}$ is the change in strain induced in the i^{th} member by changes in the stiffness (ΔK) of the the j^{th} element. If a set of induced change in strains for a unit percent change in stiffness can be calculated then a vector formulation for Equation (10.13) can be determined.

$$\Delta\left(\epsilon_i\right)_m = \left\{\Delta\left(\epsilon_i\right)_{\text{unit}\Delta K_1} \quad \cdots \quad \Delta\left(\epsilon_i\right)_{\text{unit}\Delta K_j}\right\} \begin{Bmatrix} \beta_1 \\ \vdots \\ \beta_j \end{Bmatrix} \tag{10.14}$$

In this formulation, β_j represents a scaling factor that represents the degree of damage or stiffness change that has taken place in the j^{th} member. The first order flexibility method was developed to determine what these values are.

10.2.2 FOrFlex Derivation

The formulation of the FOrFlex method is derived from the matrix analysis of structures. In the standard formulation of the stiffness method, the product of the stiffness matrix $\mathbf{K}$ and the vector of displacements $\mathbf{u}$ results in the force vector $\mathbf{P}$:

$$\mathbf{P} = \mathbf{K}\mathbf{u} \tag{10.15}$$

This formulation is typically used because the stiffness matrix is easily formulated. However, the vector of applied forces is typically known or can be estimated and the problem

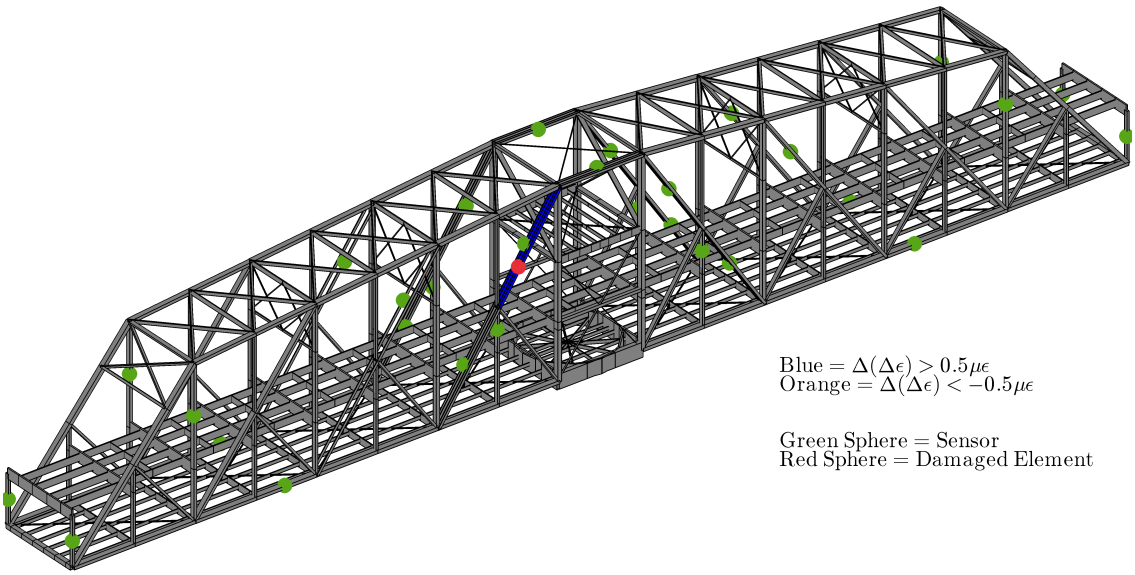

(a) Change in $\Delta\epsilon$.

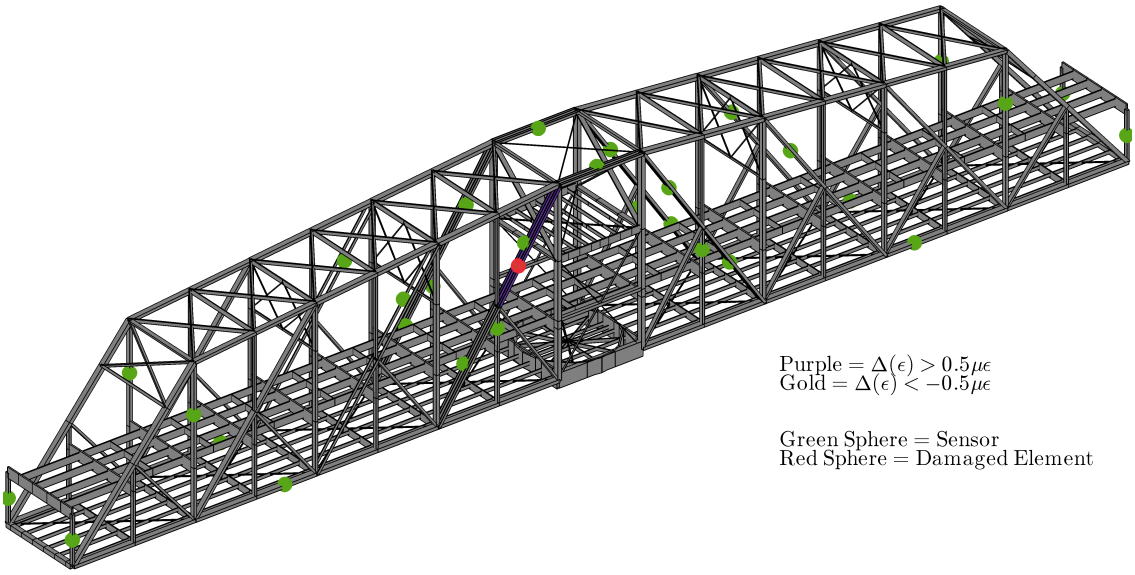

(b) Change in ϵ.

Figure 10.10: Change in $\Delta\epsilon$ and ϵ with a 5% reduction in stiffness in an eye-bar element in the stairs downstream position.

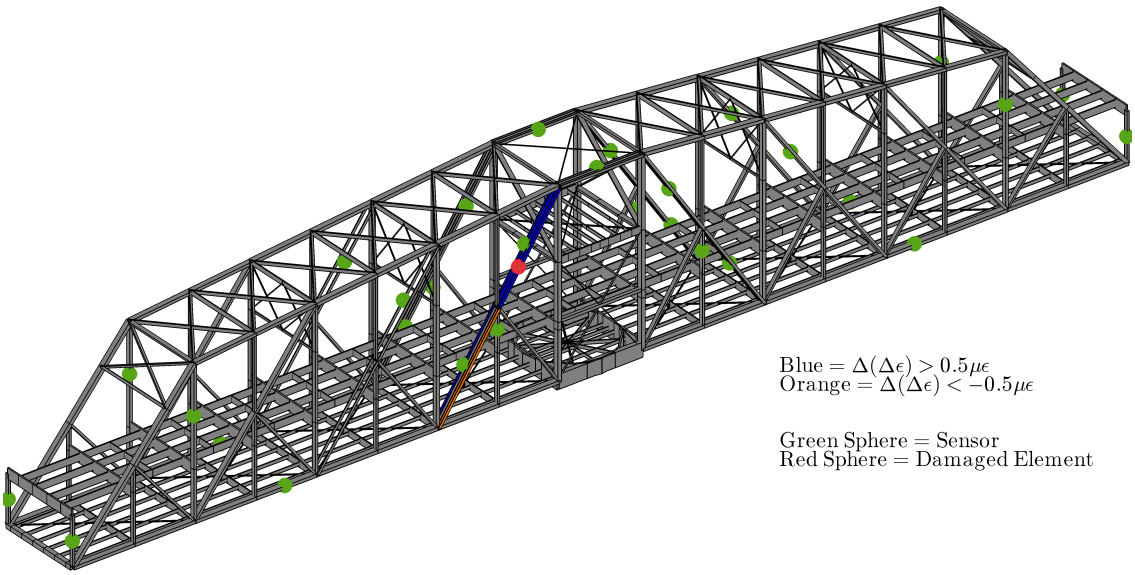

(a) Change in $\Delta\epsilon$.

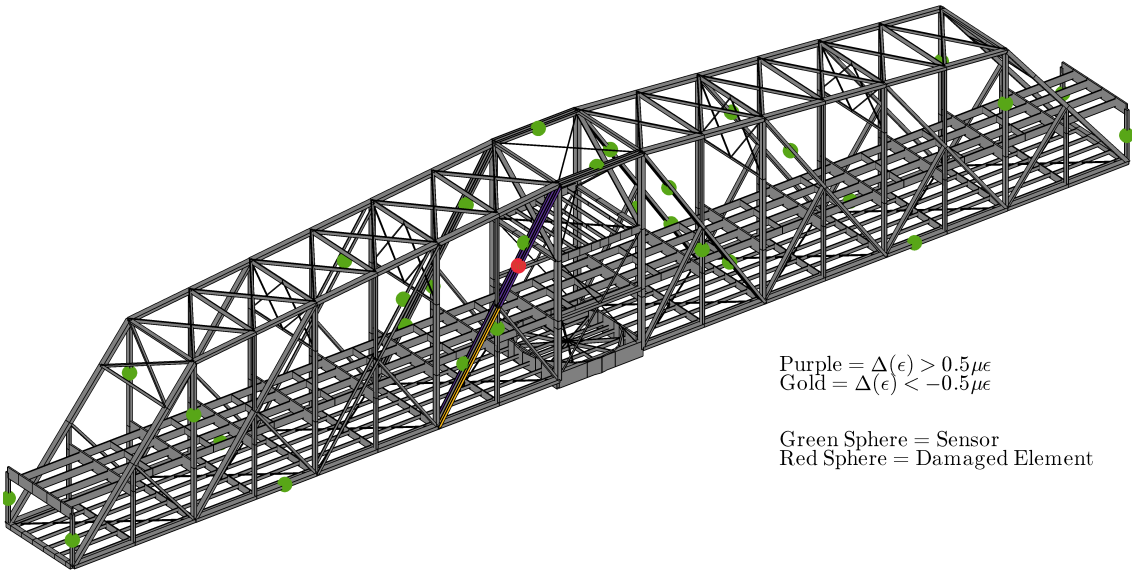

(b) Change in ϵ.

Figure 10.11: Change in $\Delta\epsilon$ and ϵ with a 15% reduction in stiffness in an eye-bar element in the stairs downstream position.

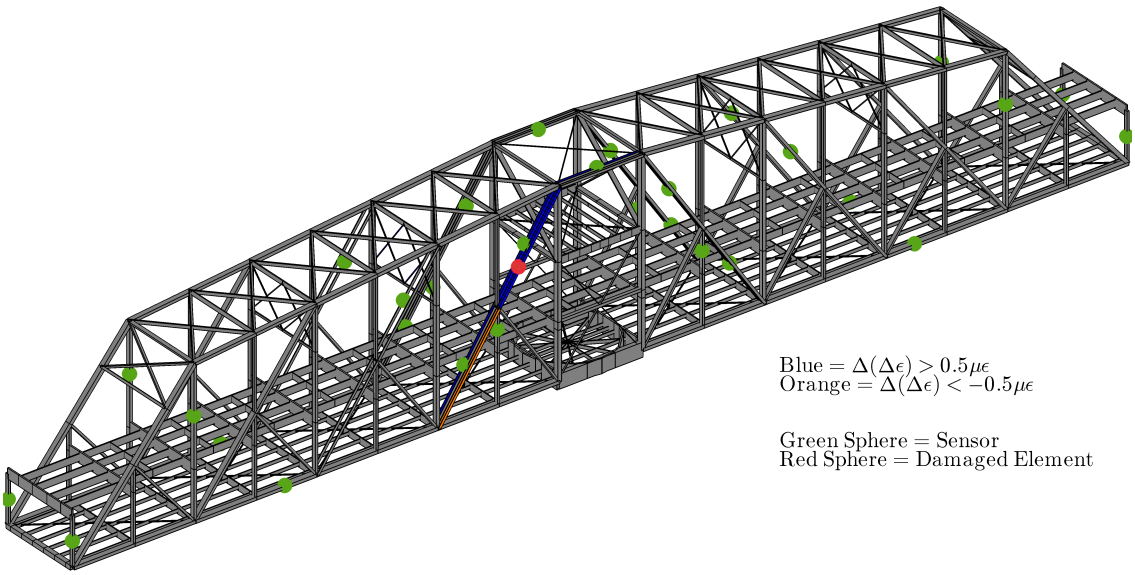

(a) Change in $\Delta\epsilon$.

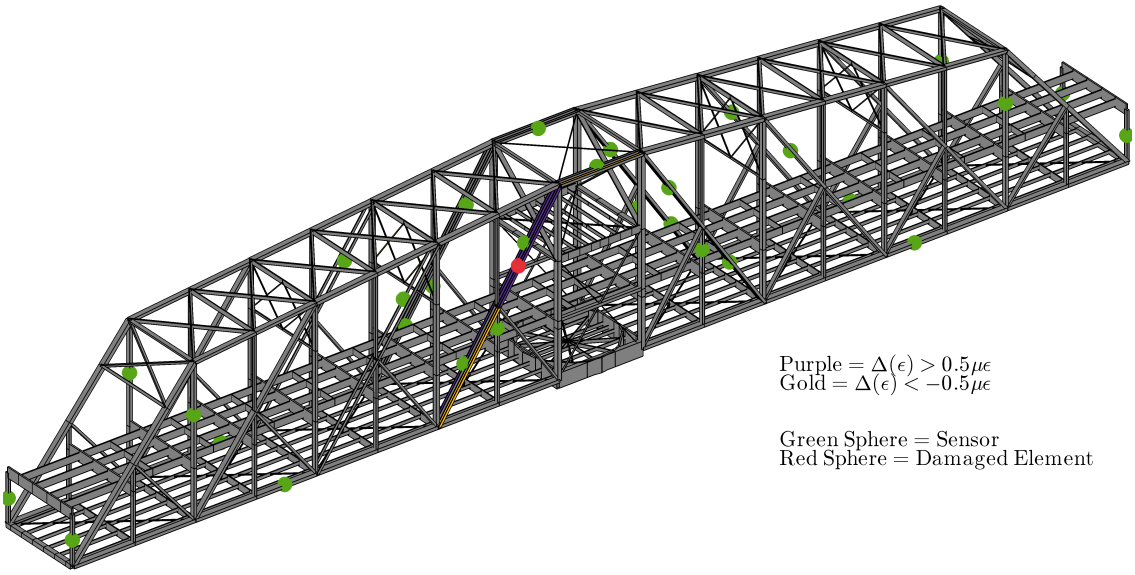

(b) Change in ϵ.

Figure 10.12: Change in $\Delta\epsilon$ and ϵ with a 30% reduction in stiffness in an eye-bar element in the stairs downstream position.

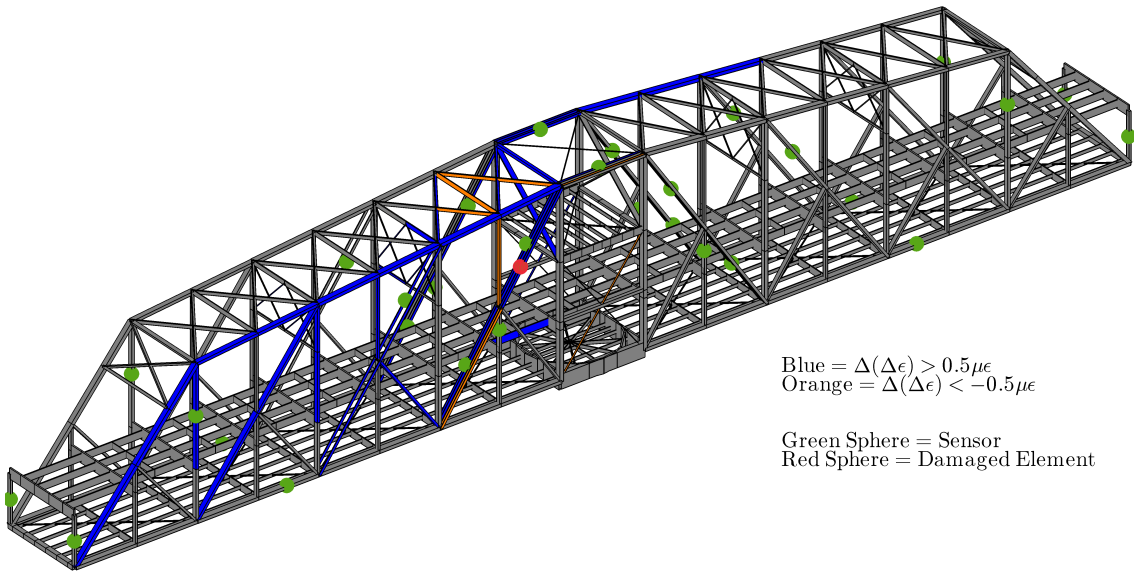

(a) Change in $\Delta\epsilon$.

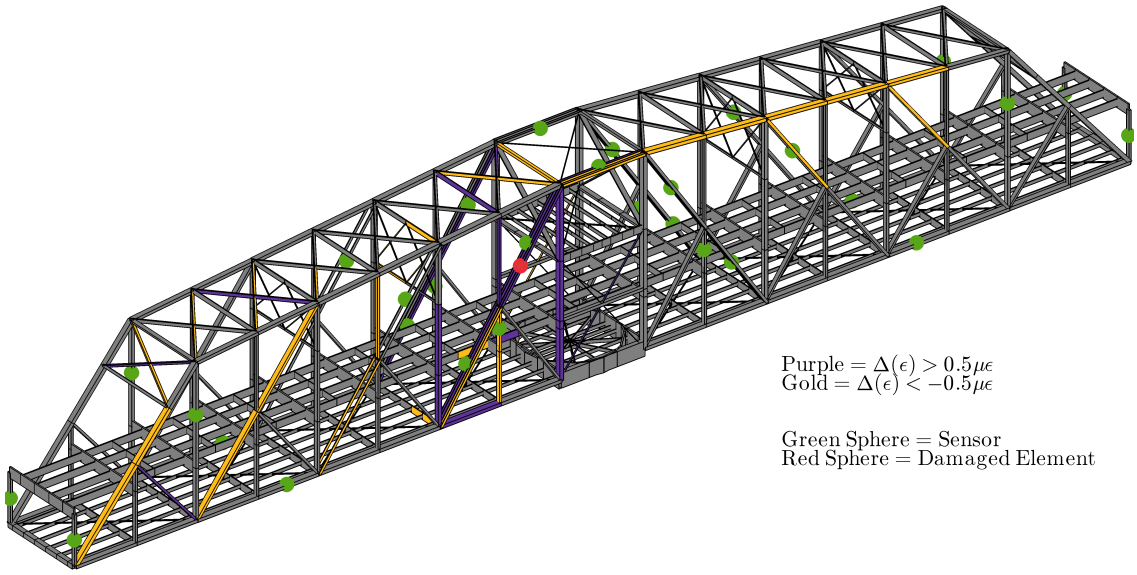

(b) Change in ϵ.

Figure 10.13: Change in $\Delta\epsilon$ and ϵ with a 90% reduction in stiffness in an eye-bar element in the stairs downstream position.

is to solve for the unknown displacement vector. To solve for the unknown displacements, the inverse of the stiffness matrix is calculated and the stiffness formulation is rewritten:

$$\mathbf{K}^{-1}\mathbf{P} = \mathbf{u} \tag{10.16}$$

In this formulation, $\mathbf{K}^{-1}$ could also be called the flexibility matrix, $\mathbf{F}$. For the matrix to be invertible it must, among other conditions, be square and nonsingular (i.e., the determinant of the matrix ($\det \mathbf{A}$) cannot be zero). The stiffness matrix, after applying the boundary conditions, is a square non-singular matrix that can be inverted to solve for the unknown displacements.

Once calculated, the displacement vector can be used to determine the member forces according to the relationship:

$$\mathbf{p}_{ij} = \mathbf{s}\mathbf{u}_{ij} \tag{10.17}$$

where $\mathbf{s}$ is the vector that transforms the displacements into the member forces.

If the stiffness in the structure were never to change, then the above formulations would be sufficient. However, in the real world, the stiffness matrix of the identified structure undergoes changes due to various forms of "damage." Damage in this sense is typically discussed in terms of a decrease in the stiffness (e.g., due to corrosion, etc.) but can also represent an increase in stiffness (e.g., retrofitting that adds capacity to a member, etc.). Thus, a formulation for the damaged/altered stiffness matrix, $\mathbf{K_d}$, can be written in terms of the undamaged stiffness matrix, $\mathbf{K_u}$, and a change in stiffness matrix, $\mathbf{\Delta K}$.

$$\mathbf{K_d} = \mathbf{K_u} + \mathbf{\Delta K} \tag{10.18}$$

The change in stiffness matrix can be written as a summation of changes to the elemental stiffness matrices that are aggregated to formulate the stiffness matrix:

$$\mathbf{\Delta K} = \sum_{j=1}^{n} \alpha_i \mathbf{K_{u}}_i \tag{10.19}$$

where n is the number of elements, α_i is a scalar that represents the degree of change to the original elemental stiffness and can vary between -1 (i.e., a complete loss of stiffness) and +∞ (i.e., the member becomes infinitely stiff), and $\mathbf{K_{u}}_i$ is an $m \times m$ stiffness matrix where m is the size of the full stiffness matrix that is zero except for the local stiffness matrix for the ith undamaged element. An $\alpha_i > 0$ represents an increase in stiffness and an $\alpha_i < 0$ represents a decrease in stiffness.

To determine the displacements in the damaged state, Equation (10.19) is substituted into Equation (10.16) to yield:

$$\left(\mathbf{K_u} + \mathbf{\Delta K}\right)^{-1} \mathbf{P} = \mathbf{u}_d \tag{10.20}$$

In this formulation $\mathbf{\Delta K}$ is not guaranteed to be non-singular and therefore to solve for the vector $\mathbf{u_d}$, a formulation for determining $\left(\mathbf{K_u} + \mathbf{\Delta K}\right)^{-1}$ is necessary. Miller [147] derived the following lemma for calculating the inverse of the sum of two matrices that meet the specified conditions.

Lemma. *Let* $\mathbf{G}$ *and* $(\mathbf{G}+\mathbf{E})$ *be nonsingular matrices where* $\mathbf{E}$ *is a matrix of rank one. Let* $g = \operatorname{tr}\mathbf{E}\mathbf{G}^{-1}$. *Then* $g \neq -1$ *and*

$$\mathbf{G}^{-1} - \frac{1}{1+g}\mathbf{G}^{-1}\mathbf{E}\mathbf{G}^{-1} = (\mathbf{G}+\mathbf{E})^{-1} \tag{10.21}$$

The lemma requires some restrictions to the $\mathbf{\Delta K}$ matrix. The requirement in the lemma that $\mathbf{E}$ be a matrix of rank one limits the problem to allow just one element to be damaged. The rank one requirement also limits the problem to an one dimensional spring problem or a two-dimensional, statically determinate truss problem. For an series of one dimensional springs, the elemental stiffness matrix is

$$\mathbf{K}_i = \begin{bmatrix} k_i & -k_i \\ -k_i & k_i \end{bmatrix} \tag{10.22}$$

The elemental stiffness matrix is a rank one matrix with the basis being the vector $\mathbf{u} = \begin{bmatrix} 1 & -1 \end{bmatrix}^{\mathrm{T}}$ so that $\mathbf{K}_i$ can be decomposed such that

$$\mathbf{K}_i = k_i \begin{bmatrix} 1 \\ -1 \end{bmatrix} \begin{bmatrix} 1 & -1 \end{bmatrix} \tag{10.23}$$

Therefore, if only one spring or truss element is allowed to be damaged, such that $\mathbf{\Delta K} = \alpha_i \mathbf{K}_{\mathbf{u}i}$, then Equation (10.21) from the lemma is applicable. As a result, a formulation for the damaged stiffness matrix can be derived as follows:

$$\mathbf{K_d}^{-1} = (\mathbf{K_u} + \alpha_i \mathbf{K_{ui}})^{-1} = \mathbf{K_u}^{-1} - \frac{1}{1 + \operatorname{tr}\left(\alpha_\mathbf{i}\mathbf{K_{ui}}\mathbf{K_u}^{-1}\right)}\mathbf{K_u}^{-1}\alpha_\mathbf{i}\mathbf{K_{ui}}\mathbf{K_u}^{-1} \tag{10.24}$$

Notice that the formulation does not require the inversion of the non-singular $\mathbf{K}_{\mathbf{u}i}$ matrix.

Equation (10.24) can be further simplified by noting that for the statically determinate truss

$$\operatorname{tr}\left(\alpha_\mathbf{i}\mathbf{K_{ui}}\mathbf{K_u}^{-1}\right) = \alpha_i \tag{10.25}$$

such that

$$(\mathbf{K_u} + \alpha_i \mathbf{K_{ui}})^{-1} = \mathbf{K_u}^{-1} - \frac{\alpha_i}{1+\alpha_i}\mathbf{K_u}^{-1}\mathbf{K_{ui}}\mathbf{K_u}^{-1} \tag{10.26}$$

Therefore, to solve for the damaged deflections $\mathbf{u}_d$ and assuming that the loads, $\mathbf{P}$, have not changed[6], then Equation (10.26) can be substituted into Equation (10.20) to yield:

$$\mathbf{u}_d = \left(\mathbf{K_u}^{-1} - \frac{\alpha_i}{1+\alpha_i}\mathbf{K_u}^{-1}\mathbf{K_{ui}}\mathbf{K_u}^{-1}\right)\mathbf{P} \tag{10.27}$$

By noting that the undamaged displacements, $\mathbf{u}_u$,can be written as,

$$\mathbf{u}_u = \mathbf{K_u}^{-1}\mathbf{P} \tag{10.28}$$

[6]This assumption is valid for the Rock Island bridge where the strains are measured when the bridge is carrying just the dead load. The dead load will not change significantly for small changes to the stiffness

then Equation (10.27) can be simplified after multiplying the load vector into the parenthetical expression:

$$\mathbf{u}_d = \mathbf{u}_\mathbf{u} - \frac{\alpha_i}{1+\alpha_i}\mathbf{K_u}^{-1}\mathbf{K_{ui}}\mathbf{u_u} \tag{10.29}$$

Measuring the displacement vectors in both the undamaged and damaged conditions is not a trivial task. Measuring strains in the member is more easily accomplished so the results of Equation (10.29) need to be transformed into strain values. To do so, Equation (10.17) is used, and the vector $\mathbf{s}$ needs to be determined. For a truss element, the strain in the k^{th} element in terms of the displacement of its end nodes i and j is:

$$\epsilon_k = \frac{1}{L}\begin{bmatrix}1 & 0 & -1 & 0\end{bmatrix}\mathbf{T}\mathbf{u}_{ij} \tag{10.30}$$

where L is the element length and $\mathbf{T}$ is the element transformation matrix to change from global to local coordinates. In this expression $\frac{1}{L}\begin{bmatrix}1 & 0 & -1 & 0\end{bmatrix}$ is the $\mathbf{s}$ vector from Equation (10.17).

Equations 10.30 and 10.29 are then used to calculate the strains in the damaged condition as follows:

$$\epsilon_{dk} = \mathbf{s}\mathbf{u}_{\mathbf{d}ij} \tag{10.31}$$

$$\epsilon_{dk} = \mathbf{s}\left(\mathbf{u}_{\mathbf{u}ij} - \left(\frac{\alpha_i}{1+\alpha_i}\mathbf{K_u}^{-1}\mathbf{K}_{\mathbf{u}i}\mathbf{u_u}\right)_{ij}\right) \tag{10.32}$$

$$\epsilon_{dk} = \mathbf{s}\mathbf{u}_{\mathbf{u}ij} - \frac{\alpha_j}{1+\alpha_j}\mathbf{s}\mathbf{K_u}^{-1}\mathbf{K}_{\mathbf{u}j}\mathbf{u}_{\mathbf{u}ij} \tag{10.33}$$

$$\epsilon_{dk} = \epsilon_{uk} - \frac{\alpha_j}{1+\alpha_j}\mathbf{s}\mathbf{K_u}^{-1}\mathbf{K}_{\mathbf{u}j}\mathbf{u}_{\mathbf{u}ij} \tag{10.34}$$

Note that the damaged strain in the k^{th} element, ϵ_{dk}, can be written in terms of the undamaged strain, ϵ_{uk}, and a term that represents the change in strain due to the change in stiffness of the member. The negative sign indicates that the relationship between a change in stiffness and the change of strain is inversely proportional. This is intuitive because an increase in stiffness, given the load is constant, will yield smaller strains; likewise, a decrease in stiffness, given the load is constant, will yield higher strains. For an α_j value of 0%, representing no damage, ϵ_{dk} and ϵ_{uk} are equivalent as expected.

Further note that for different changes in stiffness only the alpha changes. Thus Equation (10.34) is of a linear form $y = mx + b$ where y is equivalent to ϵ_{dk}, m is equivalent to $\mathbf{s}\mathbf{K_u}^{-1}\mathbf{K}_{\mathbf{u}j}\mathbf{u}_{\mathbf{u}ij}$, and b is equivalent to ϵ_{uk}. Therefore, the variable x is equivalent to $-\alpha_j/(1+\alpha_j)$

Lemma 10.21 needs to be extended to allow for a a matrix with a rank greater than one in order for this derivation to work for multiple damage locations. Miller [147] again derived the following theorem to calculate the inverse of the sum of two matrices with less strict conditions.

Theorem. *Let* $\mathbf{G}$ *and* $(\mathbf{G}+\mathbf{H})$ *be nonsingular matrices and let* $\mathbf{H}$ *have a positive rank* r*. Let* $\mathbf{H} = \mathbf{E}_1 + \mathbf{E}_2 + \cdots + \mathbf{E}_r$ *where each* $\mathbf{E}_k$ *has rank one and* $\mathbf{C}_{k+1} = \mathbf{G} + \mathbf{E}_1 + \cdots + \mathbf{E}_k$

is nonsingular for $k = 1, \ldots, r$. *Then if* $\mathbf{C}_1 = G$,

$$\mathbf{C}_k^{-1} - \nu_k \mathbf{C}_k^{-1} \mathbf{E}_k \mathbf{C}_k^{-1} \quad k = 1, \ldots, r \tag{10.35}$$

where

$$\nu_k = \frac{1}{1 + \operatorname{tr} \mathbf{C}_k^{-1} \mathbf{E}_k} \tag{10.36}$$

In particular

$$(\mathbf{G} + \mathbf{H})^{-1} = \mathbf{C}_r^{-1} - \nu_r \mathbf{C}_r^{-1} \mathbf{E}_r \mathbf{C}_r^{-1} \tag{10.37}$$

The theorem above loosens the restrictions on the singular matrix being added so that it can have a rank r so that the $\mathbf{\Delta K}$ matrix can represent damage to more than one member. As seen in Equation (10.23), the individual elemental stiffness matrices have rank one and they can be combined to form the $\mathbf{\Delta K}$ matrix as follows:

$$\mathbf{\Delta K} = \sum_{i=1}^{n} \alpha_i \mathbf{K}_{\mathbf{u}i} \tag{10.38}$$

Therefore, making the appropriate substitutions into Equations 10.35–10.37 such that $\mathbf{C}_1 = \mathbf{K}_\mathbf{u}$, then:

$$\mathbf{C}_k^{-1} - \nu_k \mathbf{C}_k^{-1} \mathbf{K}_{\mathbf{u}k} \mathbf{C}_k^{-1} \quad k = 1, \ldots, n \tag{10.39}$$

where n is the number of damaged elements $\mathbf{K}_{\mathbf{u}k}$ is the individual stiffness matrix for the k^{th} element and

$$\nu_k = \frac{1}{1 + \operatorname{tr} \mathbf{C}_k^{-1} \mathbf{K}_{\mathbf{u}k}} \tag{10.40}$$

So that after n iterations

$$(\mathbf{K}_\mathbf{u} + \mathbf{\Delta K})^{-1} = \mathbf{C}_n^{-1} - \nu_n \mathbf{C}_n^{-1} \mathbf{K}_{\mathbf{u}n} \mathbf{C}_n^{-1} \tag{10.41}$$

Because Equation (10.41) represents the end of an iterative process, the results are more easily seen in a simple example. Consider a truss structure that has two damaged elements such that:

$$\mathbf{\Delta K} = \alpha_1 \mathbf{K}_{\mathbf{u}1} + \alpha_2 \mathbf{K}_{\mathbf{u}2} \tag{10.42}$$

Then, using the theorem to calculate the inverse of the $\mathbf{K}_\mathbf{d}$ matrix in terms of the α_i yields the expression:

$$\begin{aligned}
(\mathbf{K}_\mathbf{u} + \alpha_1 \mathbf{K}_{\mathbf{u}1} + \alpha_2 \mathbf{K}_{\mathbf{u}2})^{-1} = {} & \mathbf{K_u}^{-1} - \frac{\alpha_1}{1+\alpha_1} \mathbf{K_u}^{-1} \mathbf{K_{u1}} \mathbf{K_u}^{-1} - \frac{\alpha_2}{1+\alpha_2} \mathbf{K_u}^{-1} \mathbf{K_{u2}} \mathbf{K_u}^{-1} \\
& + \frac{\alpha_1 \alpha_2}{(1+\alpha_1)(1+\alpha_2)} \mathbf{K_u}^{-1} \mathbf{K_{u1}} \mathbf{K_u}^{-1} \mathbf{K_{u2}} \mathbf{K_u}^{-1} \\
& + \frac{\alpha_1 \alpha_2}{(1+\alpha_1)(1+\alpha_2)} \mathbf{K_u}^{-1} \mathbf{K_{u2}} \mathbf{K_u}^{-1} \mathbf{K_{u1}} \mathbf{K_u}^{-1} \\
& - \frac{\alpha_1^2 \alpha_2}{(1+\alpha_1)^2 (1+\alpha_2)} \mathbf{K_u}^{-1} \mathbf{K_{u1}} \mathbf{K_u}^{-1} \mathbf{K_{u2}} \mathbf{K_u}^{-1} \mathbf{K_{u1}} \mathbf{K_u}^{-1}
\end{aligned} \tag{10.43}$$

Note that if $\alpha_2 = 0$, then Equation (10.43) simplifies to Equation (10.26) as derived for the case of only one damaged element. Also note that this equation includes higher-order terms that involve both $\mathbf{K_{u1}}$ and $\mathbf{K_{u2}}$. The number of terms needed to calculate the inverse of $\mathbf{K_d}$ will increase with each additional damage element that is considered. In a large structure or model, the number of terms becomes unwieldy.

Remembering that the ultimate goal is to calculate the deflections and forces in the damaged state, the presence of higher-order terms in Equation (10.43) signifies that there is a relationship between the change in stiffness in one element and the change in strain of another. However, for a determinate truss, a change in stiffness does affect the strain in the other elemenrs. Because the loads in a determinate truss are not dependent on the cross-sectional or material properties of the members, changing the properties of one member will not have any effect on the others. Thus, in a determinate truss, the higher-order terms disappear. Therefore, Equation (10.43), in the case of a determinate truss can be simplified so that:

$$(\mathbf{K_u} + \mathbf{\Delta K})^{-1} = \mathbf{K_u}^{-1} - \sum_{j=1}^{n} \frac{\alpha_j}{1+\alpha_j} \mathbf{K_u}^{-1} \mathbf{K_{u}}_j \mathbf{K_u}^{-1} \tag{10.44}$$

where n is the number of elements. This equation is the basis for the first-order flexibility method. The assumption will be that even in indeterminate trusses and frames only the first-order terms are significant. Investigations into the validity of this assumption will be presented in the next section.

Once again, finding the inverse of the $\mathbf{K_d}$ matrix in terms of the α_i is not the ultimate goal. What is needed is an equation to calculate first the damaged displacements, and then, ultimately, the damaged strains. Substituting Equation (10.44) into Equation (10.20) the following expression is derived:

$$\mathbf{u_d} = \left(\mathbf{K_u}^{-1} - \sum_{j=1}^{n} \frac{\alpha_j}{1+\alpha_j} \mathbf{K_u}^{-1} \mathbf{K_{u}}_j \mathbf{K_u}^{-1} \right) \mathbf{P} \tag{10.45}$$

$$\mathbf{u_d} = \mathbf{K_u}^{-1}\mathbf{P} - \sum_{j=1}^{n} \frac{\alpha_j}{1+\alpha_j} \mathbf{K_u}^{-1} \mathbf{K_{u}}_j \mathbf{K_u}^{-1}\mathbf{P} \tag{10.46}$$

$$\mathbf{u_d} = \mathbf{u_u} - \sum_{j=1}^{n} \frac{\alpha_j}{1+\alpha_j} \mathbf{K_u}^{-1} \mathbf{K_{u}}_j \mathbf{K_u}^{-1}\mathbf{P} \tag{10.47}$$

Finally, substituting Equation (10.47) into Equation (10.17) and solving yields:

$$\epsilon_{di} = \mathbf{s}_i \mathbf{u_d}_{ab} \tag{10.48}$$

$$\epsilon_{di} = \mathbf{s}_i \left(\mathbf{u_u}_{ab} - \left(\sum_{j=1}^{n} \frac{\alpha_j}{1+\alpha_j} \mathbf{K_u}^{-1} \mathbf{K_{u}}_j \mathbf{K_u}^{-1}\mathbf{P} \right)_{ab} \right) \tag{10.49}$$

$$\epsilon_{di} = \mathbf{s}_i \mathbf{u_u}_{ab} - \left(\sum_{j=1}^{n} \frac{\alpha_j}{1+\alpha_j} \mathbf{s}_i \mathbf{K_u}^{-1} \mathbf{K_{u}}_j \mathbf{K_u}^{-1}\mathbf{P} \right)_{ab} \tag{10.50}$$

$$\epsilon_{d\,i} = \epsilon_{u\,i} - \sum_{j=1}^{n} \frac{\alpha_j}{1+\alpha_j} \mathbf{s}_i \left({\mathbf{K_u}}^{-1} \mathbf{K_{u}}_j {\mathbf{K_u}}^{-1} \mathbf{P} \right)_{ab} \tag{10.51}$$

$$\epsilon_{d\,i} - \epsilon_{u\,i} = - \sum_{j=1}^{n} \frac{\alpha_j}{1+\alpha_j} \mathbf{s}_i \left({\mathbf{K_u}}^{-1} \mathbf{K_{u}}_j {\mathbf{K_u}}^{-1} \mathbf{P} \right)_{ab} \tag{10.52}$$

$$\Delta\left(\epsilon_i\right) = \left\{ \mathbf{s}_i \left({\mathbf{K_u}}^{-1} \mathbf{K_{u}}_j {\mathbf{K_u}}^{-1} \mathbf{P} \right)_{ab} \right\} \left\{ \frac{-\alpha_j}{1+\alpha_j} \right\}^T \tag{10.53}$$

Equation (10.53) shows the change in strain in the i^{th} element ($\Delta\left(\epsilon_i\right)$) between the undamaged and damaged state as a function of the α terms. Note that the subscript ab indicate the displacements or terms associated with the degrees of freedom at the ends of the i^{th} element. Equation (10.53) is of the same form as Equation (10.14) meaning that the row vector $\left\{ \mathbf{s}_i \left({\mathbf{K_u}}^{-1} \mathbf{K_{u}}_j {\mathbf{K_u}}^{-1} \mathbf{P} \right)_{ab} \right\}$ represents the basis of strains caused by changes in the stiffness of the other elements. Equation (10.53) is not linear in terms of α_j, but can be linearized with respect to $\alpha_j / \left(1+\alpha_j\right)$.

In matrix form for all changes in strain Equation (10.53) becomes:

$$\mathbf{\Delta}\left(\epsilon\right) = \begin{bmatrix} \mathbf{s}_1 \left({\mathbf{K_u}}^{-1} \mathbf{K_{u}}_1 {\mathbf{K_u}}^{-1} \mathbf{P} \right)_{ab} & \cdots & \mathbf{s}_1 \left({\mathbf{K_u}}^{-1} \mathbf{K_{u}}_n {\mathbf{K_u}}^{-1} \mathbf{P} \right)_{ab} \\ \vdots & \ddots & \vdots \\ \mathbf{s}_m \left({\mathbf{K_u}}^{-1} \mathbf{K_{u}}_1 {\mathbf{K_u}}^{-1} \mathbf{P} \right)_{ab} & \cdots & \mathbf{s}_n \left({\mathbf{K_u}}^{-1} \mathbf{K_{u}}_n {\mathbf{K_u}}^{-1} \mathbf{P} \right)_{ab} \end{bmatrix} \begin{Bmatrix} \frac{-\alpha_1}{1+\alpha_1} \\ \vdots \\ \frac{-\alpha_n}{1+\alpha_n} \end{Bmatrix} \tag{10.54}$$

Equation (10.54) is of the form $Ax = b$ and the matrix, which will be referred to as $\mathbf{S}$, has a number of interesting properties. First, for determinate trusses $\mathbf{S}$ is non-singular and square and therefore is invertible. The matrix $\mathbf{S}$ is also computed from only information about the undamaged state. Therefore, it can be calculated once at the beginning from experimentally derived flexibility matrices or a calibrated FE model. The inverse of the $\mathbf{S}$ matrix can be used to determine the damage in the structure given the measured changes in strain experienced from the undamaged to the damaged state.

$$\mathbf{\Delta}\left(\epsilon\right) = \mathbf{S}\boldsymbol{\beta} \tag{10.55}$$

$$\mathbf{S}^{-1}\mathbf{\Delta}\left(\epsilon\right) = \boldsymbol{\beta} \tag{10.56}$$

where

$$\beta_i = \frac{\alpha_i}{1+\alpha_i} \tag{10.57}$$

For indeterminate trusses, $\mathbf{S}$ is not of full rank and is therefore not invertible. However, the pseudo inverse of $\mathbf{S}$ can be used to give the "best fit" estimation of the α values given the measured strains. Because the $\mathbf{S}$ matrix in not full rank, its null space exists and is the size of the number of indeterminacies in the structure. The actual damage scenario is therefore the "best fit" calculated from the pseudo inverse plus a linear combination of the null space of $\mathbf{S}$ as follows.

$$\boldsymbol{\beta} = \mathbf{S}^{+}\mathbf{\Delta}\left(\epsilon\right) + \mathrm{Null}\left(\mathbf{S}\right)\boldsymbol{\gamma} \tag{10.58}$$

where $\boldsymbol{\gamma}$ is a vertical vector the length of the nullity of $\mathbf{S}$ that contains the coefficients for the linear combination of null space vectors. The γ coefficients can be calculated based on

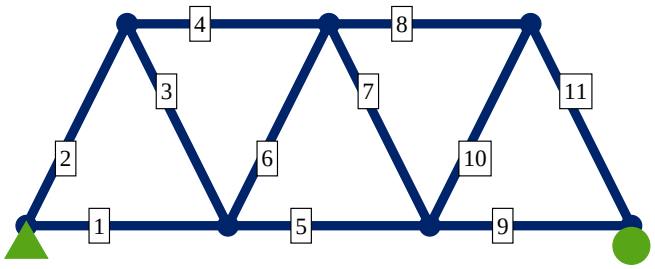

Figure 10.14: Determinate Warren truss.

probabilities or expectations as will be shown in an example in the next section.

10.2.3 Verification of the FOrFlex Method

To verify the validity of the first order flexibility method as an approximate method to simply calculate estimates of the change in stiffness of structural elements, two simple models are used. The first model, is a simply supported, determinate, five-bay Warren truss as shown in Figure 10.14. The members in the figure have been numbered to simplify the discussion of the example. All members have the same initial cross-section and material properties.

The stiffness of member 5 of the determinate truss was varied from a 50% decrease to a 50% increase from the initial stiffness ($-0.5 \leq \alpha \leq 0.5$). The strains in the elements in the undamaged and damaged states were calculated exactly by inverting $\mathbf{K_d}$ to calculate the displacements according to Equation (10.16). The displacements were used to calculate the member forces and the strains using Equation (10.17). The change in strain due to damage was then calculated by simple subtraction for comparison with the estimation provided by the FOrFlex method.

To calculate the FOrFlex estimation, Equation (10.54) was used to calculate the $\mathbf{S}$ matrix which, in the case of one damaged element, is a column vector. The change in strain, $\Delta(\epsilon)$, due to the change in stiffness was then calculated by multiplying $\mathbf{S}$ by the appropriate β value for each α evaluated.

Figure 10.15 shows a graphical representation of the results of the analysis for the "damaged" member, element 5. When the $\Delta(\epsilon)$ of both the exact value and FOrFlex estimate are plotted with α value on the abscissa as in Figure 10.15(a), the two are indistinguishable. The plot of the percent error shown in Figure 10.15(c) confirms the visual evidence. As noted in the derivation, for a determinate truss the FOrFlex method is an exact solution.

Figure 10.15(a) further demonstrates that the relationship between $\Delta(\epsilon)$ and α is not linear. When β, as defined by Equation (10.57), is used on the x-axis instead as in Figure 10.15(b), the linear relationship between $\Delta(\epsilon)$ and β is clear. In physical terms, α is easier to understand because a loss of stiffness has physical meaning whereas β is an abstract, mathematical construction. Nevertheless, the linear relationship that the strains, and therefore the changes in strain, have with β that is employed here.

Only the damaged element in the determinate truss experiences a change in strain, be-

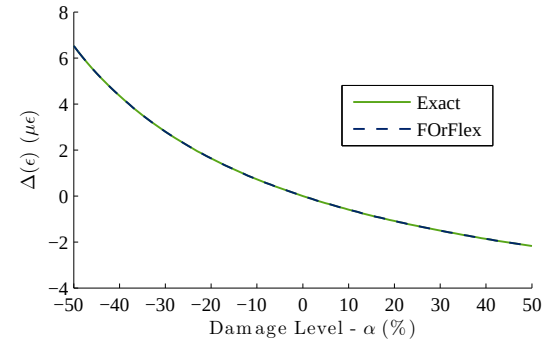

(a) $\Delta(\epsilon)$ v. Damage change percent.

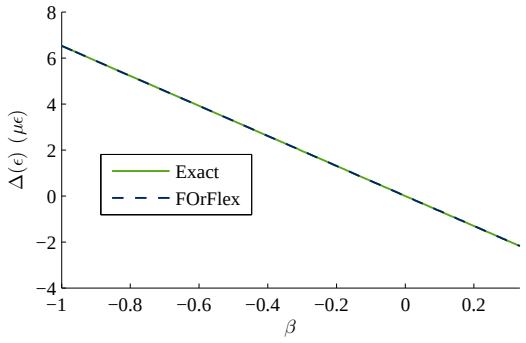

(b) $\Delta(\epsilon)$ v. Linearized β factor.

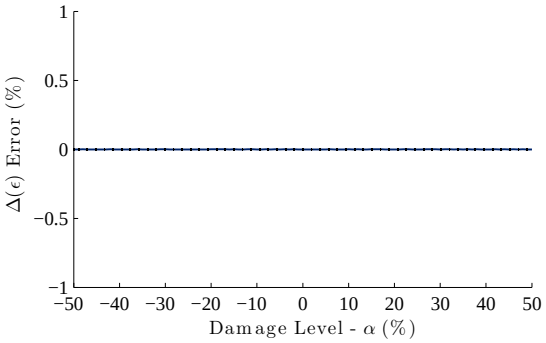

(c) Percent error v. Damage change percent.

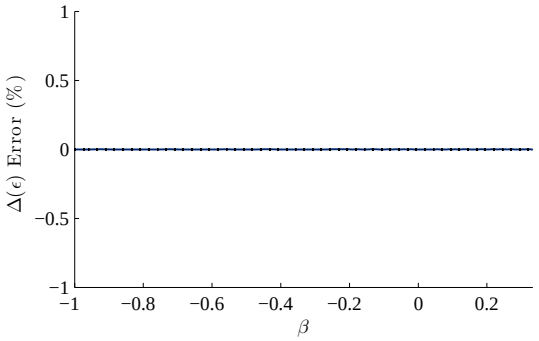

(d) Percent error v. Linearized β factor.

Figure 10.15: Comparison between exact and estimated $\Delta(\epsilon)$ for determinate truss: Element 5.

cause the load and material properties in the other elements do not change. Figure 10.16 shows the results for element 6. Element 6 shares a node with the damaged element 5, however, regardless of the level of damage in element 5, the strain levels in element 6 do not change. The other members in the truss exhibit the same behavior.

The determinate truss proved that a basis for determining the changes in strain of a structure is possible and this basis is linear in terms of β. To demonstrate the effect of indeterminacy on the FOrFlex method, a twelfth member was added to the determinate Warren truss. The new structure, shown in Figure 10.17 has a diagonal that crosses over, but does not intersect, the diagonal element 6. The material properties and dimensions were the same for every member and also the identical to those used in the determinate truss.

A change in stiffness that ranged from a 50% decrease to a 50% increase from the initial stiffness $(-0.5 \leq \alpha \leq 0.5)$ was imposed on element 5. The exact and estimated strains were calculated as described for the determinate truss. Figure 10.18 shows the results of the analysis for the damaged element 5 of the indeterminate truss. For small changes in stiffness, the estimation using the first order flexibility method very closely matches the exact value. The indeterminacy of the structure implies that the strain in other members will be affected by the change in stiffness of the members. Figures 10.19, 10.20, and 10.21, show the results for elements 4, 6, and 12, respectively. The elements all show a different change in strain levels that reflect the element's role in carrying compression or tension in the truss. Elements 3 and 7 are also diagonals and have results identical to element 6. Elements 1, 2, and 8–11 are not influenced by the indeterminacy in the structure and therefore, they behave as if the truss were determinate and are not affected by the change in stiffness in element 5.

Though the change in strain levels in the various members affected by the change in stiffness in element 5 have different numerical values, the percent error of all elements show a similar pattern. The percent error in the estimation is only zero when α equals zero signifying the undamaged sate. As α decreases, representing degradation of the element, the percent error increases. In looking to reduce the error in the estimation seen in the plots for the indeterminate truss, an alternative formulation for $\mathbf{S}$, denoted $\mathbf{S}^*$ will be derived.

The desire is to have $\mathbf{S}^*$ have the same matrix properties as $\mathbf{S}$ but yield zero error at a given level of damage. To formulate $\mathbf{S}^*$, begin by substituting $\mathbf{S}^*$ into Equation (10.55) as follows:

$$\mathbf{S}^*\boldsymbol{\beta} = \boldsymbol{\Delta}(\epsilon) \tag{10.59}$$

Expanding the change in strain to include the undamaged and damaged strain vectors yields.

$$\mathbf{S}^*\boldsymbol{\beta} = \epsilon_d - \epsilon_u \tag{10.60}$$

The implications of Equation (10.60) is that if a calibrated model exists, then $\mathbf{S}^*$ can be computed by determining the strains, ϵ_d, at a given level of damage, β.

$$\mathbf{S}^* = \left[\frac{\epsilon_{d,i} - \epsilon_{u,i}}{\beta_j}\right] \tag{10.61}$$

Here i is the number of elements in the structure and j is the number of damaged elements and therefore also the number of columns in $\mathbf{S}^*$. Equation (10.61) therefore consists of

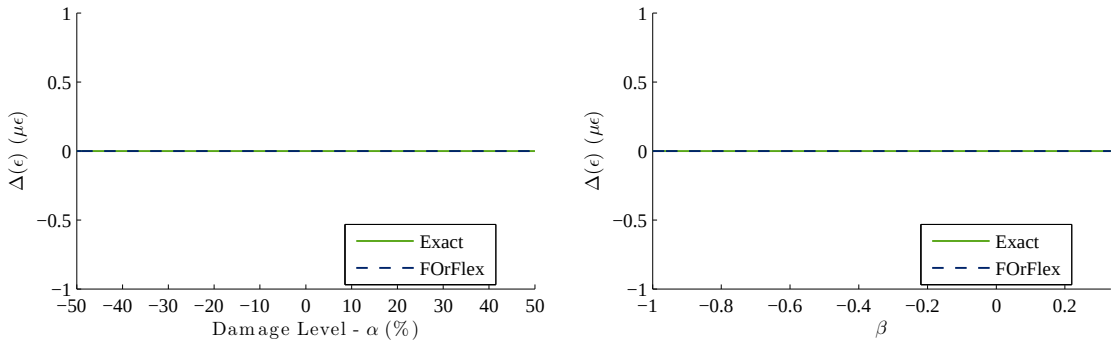

(a) $\Delta(\epsilon)$ v. Damage change percent.

(b) $\Delta(\epsilon)$ v. Linearized β factor.

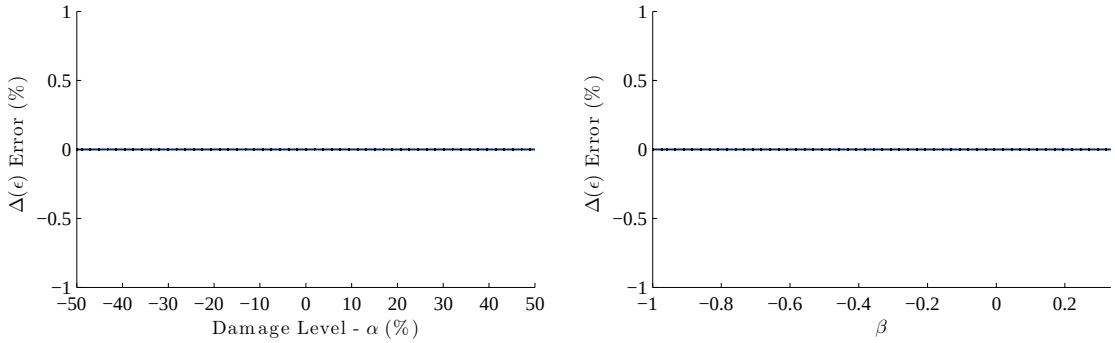

(c) Percent error v. Damage change percent.

(d) Percent error v. Linearized β factor.

Figure 10.16: Comparison between exact and estimated $\Delta(\epsilon)$ for determinate truss: Element 6.

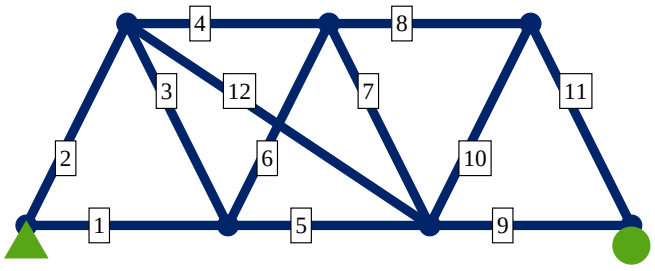

Figure 10.17: Indeterminate truss.

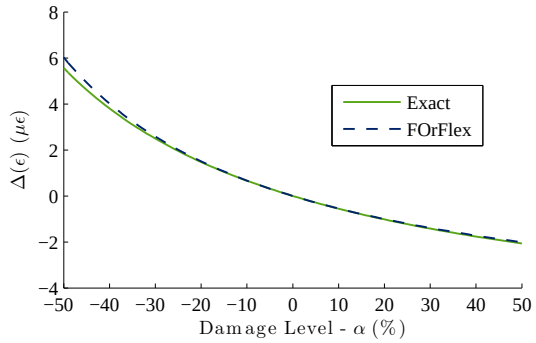

(a) $\Delta(\epsilon)$ v. Damage change percent.

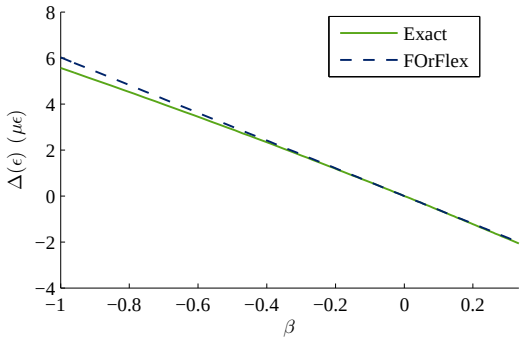

(b) $\Delta(\epsilon)$ v. Linearized β factor.

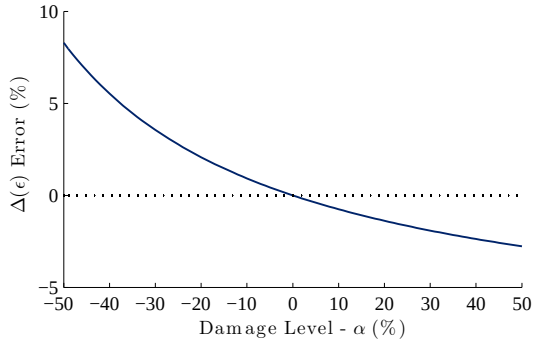

(c) Percent error v. Damage change percent.

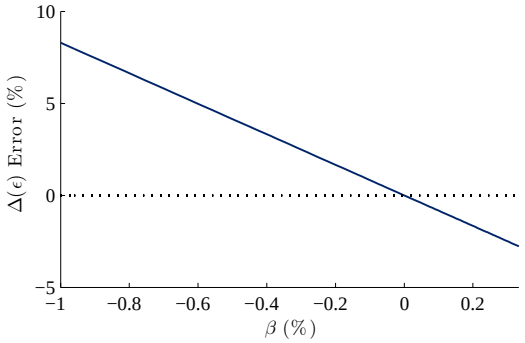

(d) Percent error v. Linearized β factor.

Figure 10.18: Comparison between exact and estimated $\Delta(\epsilon)$ for indeterminate truss: Element 5.

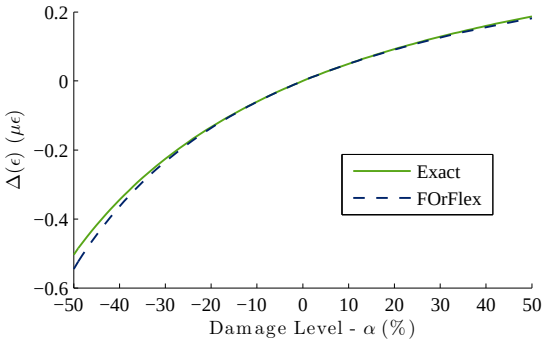

(a) $\Delta(\epsilon)$ v. Damage change percent.

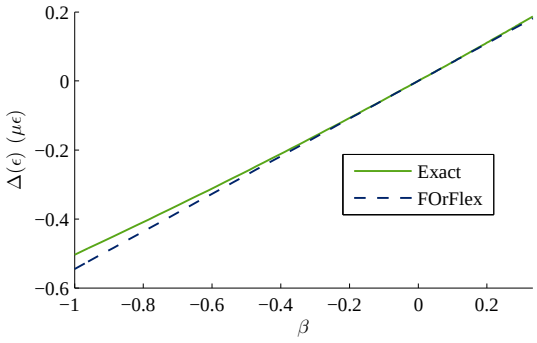

(b) $\Delta(\epsilon)$ v. Linearized β factor.

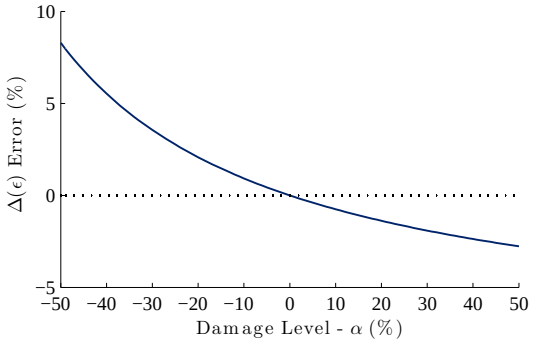

(c) Percent error v. Damage change percent.

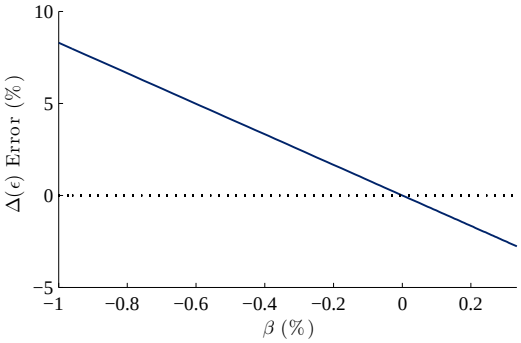

(d) Percent error v. Linearized β factor.

Figure 10.19: Comparison between exact and estimated $\Delta(\epsilon)$ for indeterminate truss: Element 4.

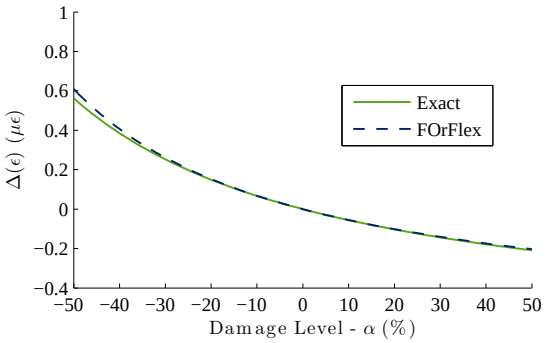

(a) $\Delta(\epsilon)$ v. Damage change percent.

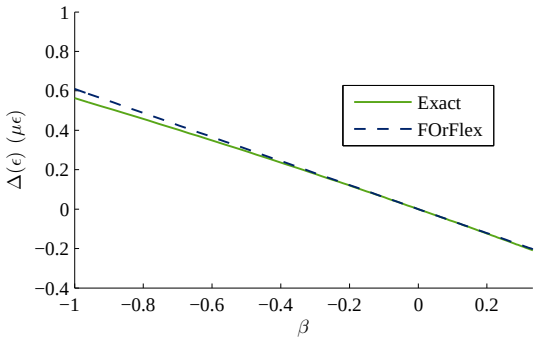

(b) $\Delta(\epsilon)$ v. Linearized β factor.

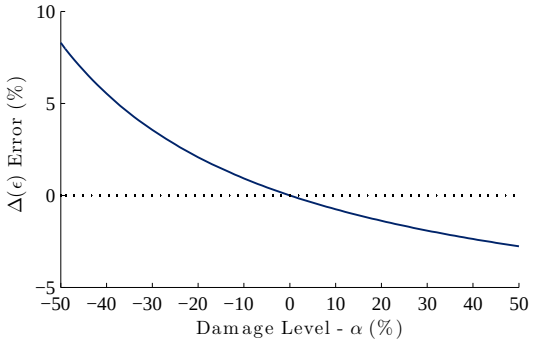

(c) Percent error v. Damage change percent.

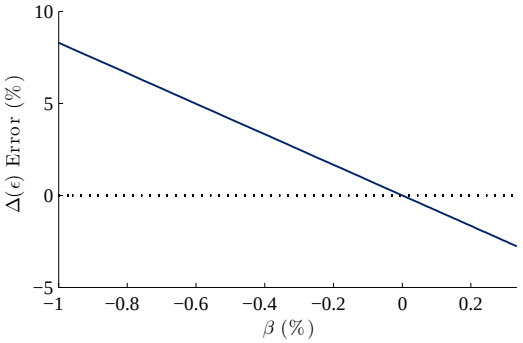

(d) Percent error v. Linearized β factor.

Figure 10.20: Comparison between exact and estimated $\Delta(\epsilon)$ for indeterminate truss: Element 6.

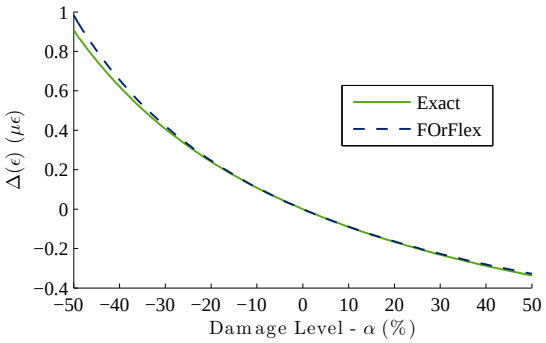

(a) $\Delta(\epsilon)$ v. Damage change percent.

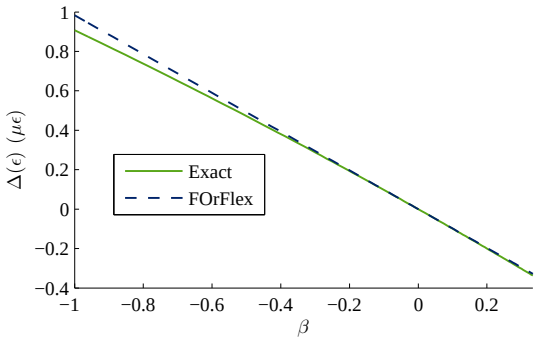

(b) $\Delta(\epsilon)$ v. Linearized β factor.

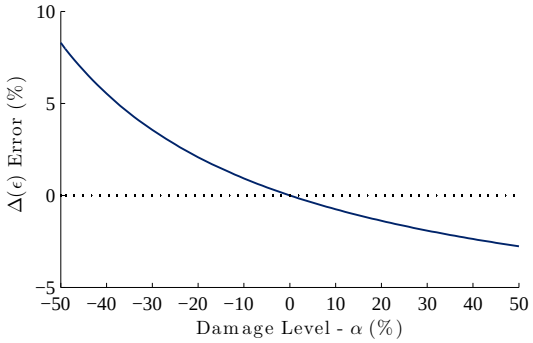

(c) Percent error v. Damage change percent.

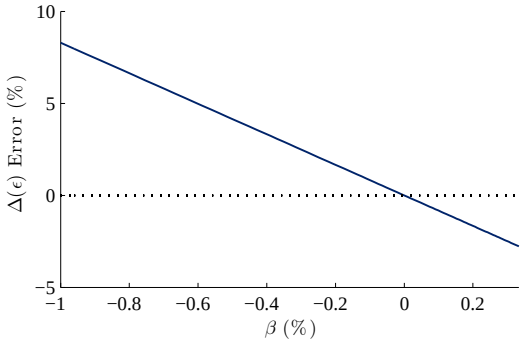

(d) Percent error v. Linearized β factor.

Figure 10.21: Comparison between exact and estimated $\Delta(\epsilon)$ for indeterminate truss: Element 12.

columns that represent the change in strain induced in the structure for a given change in stiffness divided by the beta value associated with that change in stiffness. Essentially this process is defining the slope of a line that passes through the points (0, 0), representing the undamaged structure, and (β^*, $\Delta(\epsilon)$), representing the damaged structure at a given set of β values. Doing so guarantees that the estimate of $\mathbf{\Delta}(\epsilon)$ in Equation (10.59) will be exact for the undamaged case and also for the stiffness changes designated in β. Any value of β can be used for this linearization.

For the case of the indeterminate truss shown in Figure 10.17, $\mathbf{S}^*$ was prepared for the case of damage to element 5 at a 15% reduction in the stiffness. The $\mathbf{S}^*$ matrix was then used to estimate the change in strain in the structure for other values of α. Figure 10.22 shows the results of the estimation for element 5. The difference in the estimation on the $\Delta(\epsilon)$ when compared to the plots in Figure 10.18 are imperceptible. The main difference appears in the plots of the percent error. Whereas in the estimate using just $\mathbf{S}$ there is 0% error at 0% degradation as seen in Figure 10.18(c); with the $\mathbf{S}^*$ estimate, the plot of the percent error (Figure 10.22(c)) crosses the x-axis at 15% degradation (i.e., the level used in preparing $\mathbf{S}^*$). Thus the absolute value of the percent error is less over a longer range of the abscissa. The plot of the simple error, not the percent error, of the estimate shown in Figure 10.22(e) clarifies what the $\mathbf{S}^*$ estimate does. As the figure shows, the simple error has a zero value twice: first with 0% reduction and again with 15% reduction. The scale of Figure 10.22(e) shows that the simple errors are very small.

The above examples of the indeterminate truss both deal only with one "damaged" element in the structure. Nevertheless, because $\mathbf{S}^*$ can be formulated according to Equation (10.61) for any number of damaged elements, the method is scalable. Figure 10.23 shows a plot that evaluates the maximum percent error in the structure when two (or one member on the main diagonal) elements of the indeterminate truss have a 15% reduction in stiffness. The color of the square is scaled so that the highest observed percent error (2.4%) is black and combinations with exact estimations are in white. The most error occurs when elements 5 and 6 are damaged in combination. These elements share a node and serve as a principle path for the internal forces. When both are damaged, the effects of the indeterminacy are essentially doubled causing the larger, but still reasonable error. In a larger structure such as the Rock Island Bridge, where the points of indeterminacy are farther apart, a reasonable expectation is that the error in estimating the change in strain caused by stiffness changes in members would remain small regardless of the number of elements affected.

Up until this point, the examples have been to prove that the first order flexibility approximations can, given a set of stiffness changes, reproduce with acceptable error the change in strain that would be expected to be measured in the structural members. However, in structural health monitoring, the reverse process is what is desired. For SHM, the change in strain is what is measured and the estimate of the change in stiffness is what is desired. As an example, the indeterminate truss used previously and shown in Figure 10.17 will be used again. Given the undamaged stiffness matrix, the $\mathbf{S}$ matrix was calculated assuming damage could occur in every member according to Equation (10.54). Note that $\mathbf{S}$ is not invertible and the pseudo inverse will have to be used.

To simulate corrosion in the structure, two members had their stiffness reduced by the percentages given in the second column of Table 10.1. Element 8 was given an 8% reduc-

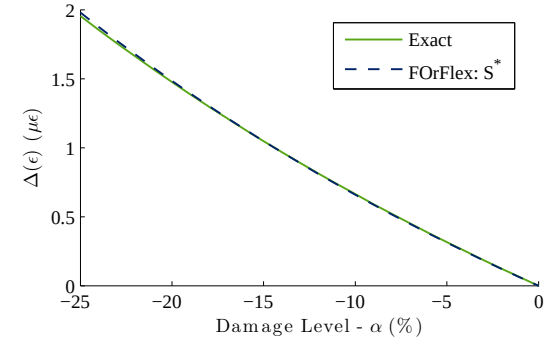

(a) $\Delta(\epsilon)$ v. Damage change percent.

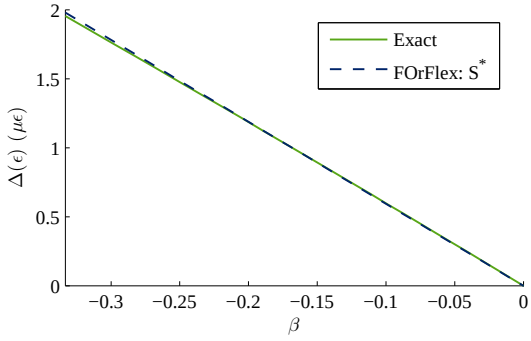

(b) $\Delta(\epsilon)$ v. Linearized β factor.

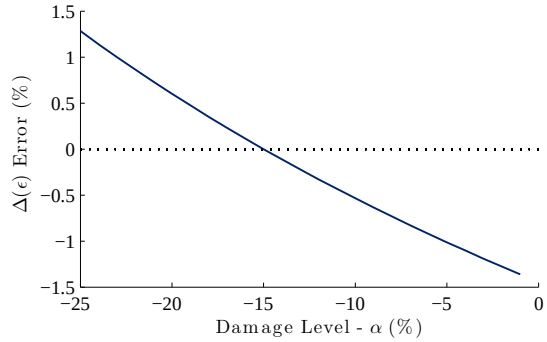

(c) Percent error v. Damage change percent.

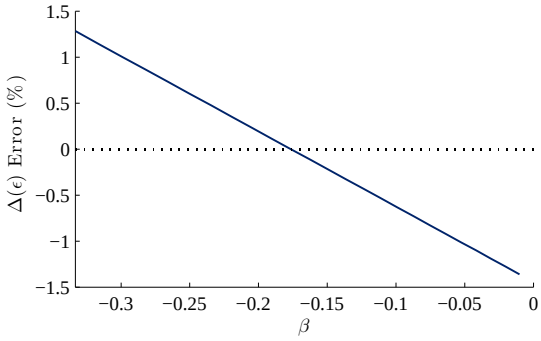

(d) Percent error v. Linearized β factor.

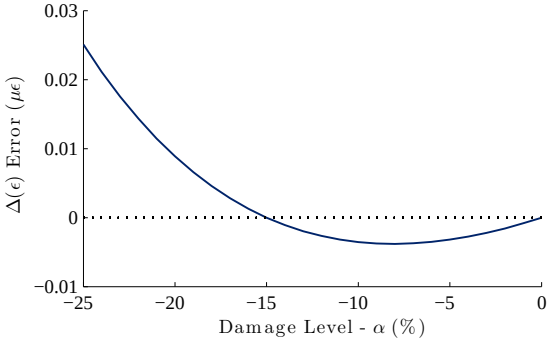

(e) Error v. Damage change percent.

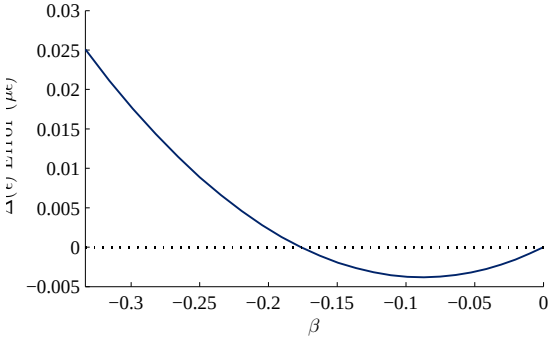

(f) Error v. Linearized β factor.

Figure 10.22: Comparison between exact and estimated $\Delta(\epsilon)$ for indeterminate truss using S^* set at 15% reduction: Element 5.

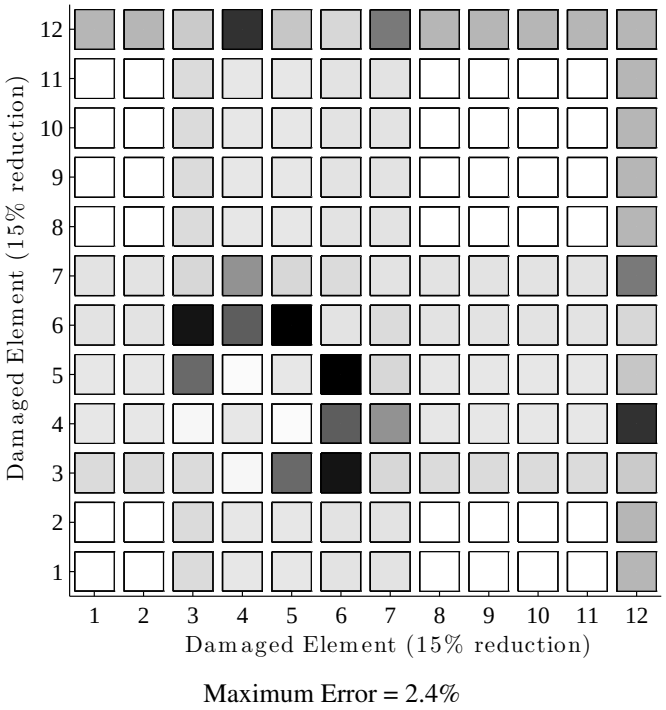

Figure 10.23: Maximum percent error for 15% reduction in stiffness for given member combinations.

Table 10.1: Estimation of damage in 2D indeterminate truss.

Member	Actual (%)	$\mathbf{S}^+$ (%)	$\mathbf{S}^+ + \gamma\text{Null}(\mathbf{S})$ (%)
1	0.00	0.00	0.00
2	0.00	0.00	0.00
3	0.00	-0.66	0.00
4	0.00	0.42	0.00
5	0.00	-0.46	0.00
6	0.00	-4.57	0.00
7	0.00	1.81	0.00
8	-8.00	-8.00	-8.00
9	0.00	0.00	0.00
10	0.00	0.00	0.00
11	0.00	0.00	0.00
12	-10.00	-5.85	-10.05

$\gamma = -0.0655$

tion in stiffness and element 12 was given a 10% reduction. The strains in the damaged and undamaged cases were calculated to simulate measurement of these values in the two states. Subtraction of the undamaged strains from the damaged strains yielded the change in strain.

Therefore, knowing both $\mathbf{S}$ and the measured changes in strain, $\Delta(\epsilon)$, Equation (10.58) can be used to solve for the β values. The third column in Table 10.1 is the result[7] of multiplying the pseudo inverse of $\mathbf{S}$ by the $\Delta(\epsilon)$ vector. The stiffness reduction in element 8 is properly identified without further manipulation because, as noted previously, it is not affected by the indeterminacy in the structure. Elements 1, 2, 9, 10, and 11 are also not affected by the indeterminacy and are therefore properly identified as having no change in stiffness. However, the reduction estimated for element 12 is only half of the actual value and the values in elements 3–7 are not zero as expected.

The use of the pseudo inverse of $\mathbf{S}$ in calculating the β vector means that the solution in the third column of Table 10.1 is a least squares fit of all the infinite number of solutions. To better match the actual imposed stiffness reductions, Equation (10.58) uses the $\mathrm{Null}(\mathbf{S})$ multiplied by a factor, γ. The null space of $\mathbf{S}$ for the indeterminate truss with one degree of indeterminacy is rank one and therefore there is only one γ factor. To solve for γ, a restraint or restriction needs to be imposed. The restriction arises from the fact that corrosion only reduces the stiffness in members. Thus, all estimations for stiffness changes necessarily must be less than zero. Yet, elements 4 and 7 are estimated to have positive changes in stiffness using the pseudo inverse alone. The γ factor can then be determined through an iterative process to eliminate the positive values beginning with the largest. Eventually, the positive values disappear and the estimate of the change in stiffness in the last column of Table 10.1 is the result. At the end of the iterative process, the estimate for the change in stiffness for element 12 is off by only 0.05% and γ was calculated to be -0.0665.

10.2.4 Application to Rock Island Bridge

The examples in the previous section were all for simple trusses with few members and only one cross section. The Rock Island Bridge and its model is much more complicated. Therefore, to be useful, the FOrFlex method has to be scalable.

Using the Rock Island Bridge FE model, the $\mathbf{S}^*$ matrix was calculated for the damage scenario previously presented in Figure 10.9, where one of the bottom chord elements is damaged. The $\mathbf{S}^*$ matrix was calculated using a β value equivalent to a 15% reduction as done in the case of the indeterminate truss in the previous section. The fact that the Rock Island Bridge FE model is a frame model adds another layer of complexity to the method. The rank of the elemental stiffness matrix for a two dimensional truss is one whereas the rank of the elemental stiffness matrix for a frame structure is not. However, the theorem used to derive the FOrFlex method stipulated that the elemental stiffness matrices have a rank of one. Therefore, to compute the $\mathbf{S}$ matrix would require that the number of β factors exceed the number of elements and they would begin to lose some of their physical meaning. However, by using the calibrated model to construct the $\mathbf{S}^*$ matrix, as in

[7] The β values have been transformed to percent reduction values using Equation (10.57).

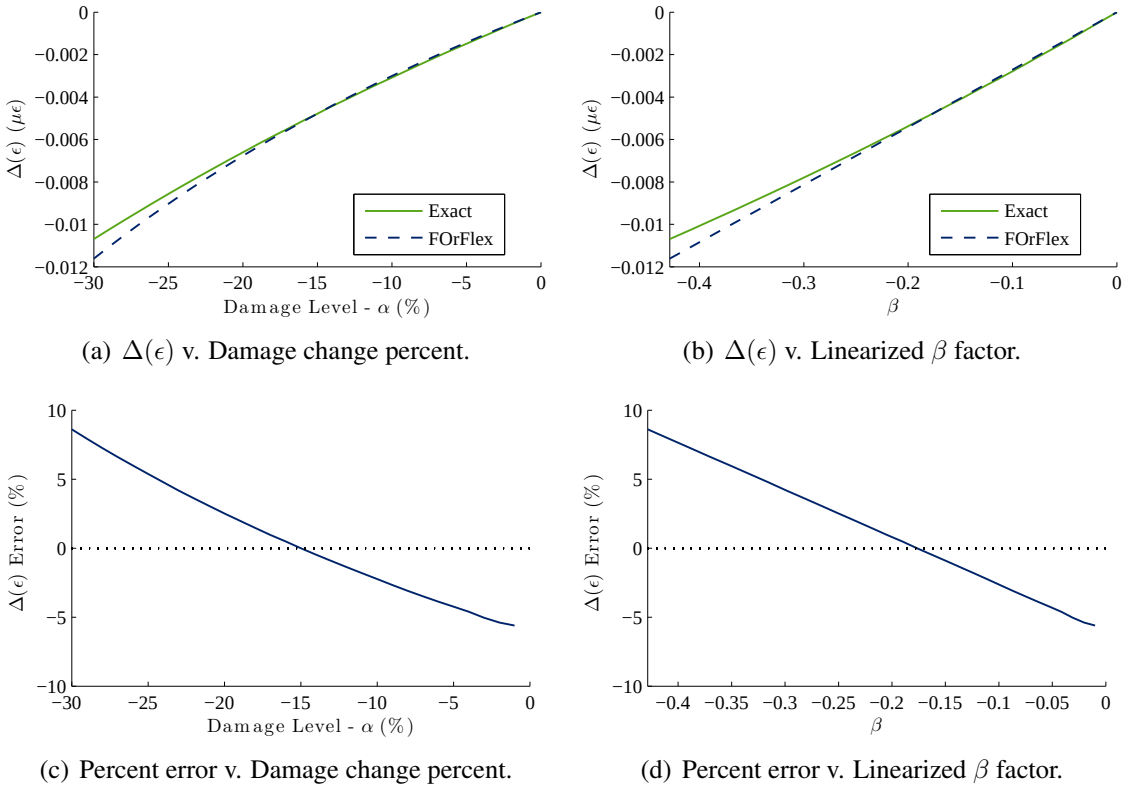

(a) $\Delta(\epsilon)$ v. Damage change percent.

(b) $\Delta(\epsilon)$ v. Linearized β factor.

(c) Percent error v. Damage change percent.

(d) Percent error v. Linearized β factor.

Figure 10.24: Comparison between exact and estimated $\Delta(\epsilon)$ for Rock Island FE model: Strain R02.

Equation (10.61), the method is still viable. After constructing the $\mathbf{S}^*$ matrix for the Rock Island Bridge FE model, the $\Delta(\epsilon)$ for α values ranging from 0% to 30% were calculated.

Figures 10.24–10.28 show the results of the FOrFlex estimation when compared to the expected values for the sensors near the damaged element. The percent errors are also plotted with respect to both α and β. Overall the graphs show that even for stiffness reductions of 30% the estimated values have an acceptable error level.

After confirming that the FOrFlex method could predict the change in strain for a large structure like the Rock Island Bridge, the FOrFlex method was used to simulate the use of the method as part of the SHM system. Four elements, as shown by the red spheres in Figure 10.29, were damaged with the stiffness reductions shown in the second column of Table 10.2. The full $\mathbf{S}^*$ matrix was constructed that allowed for stiffness changes to occur in every element. Thus, every member in the model had a corresponding α. The $\mathbf{S}^*$ was tuned to 15% reduction in stiffness for every element in the model. After computing the pseudo inverse of $\mathbf{S}^*$, Equation (10.58) and the calculated changes in strain for the given damage scenario were used to compute the estimated β values.

The third column of Table 10.2 shows the estimated stiffness reduction percentages for the four damaged elements using just the pseudo inverse term. The estimates in the table are less than 7% off from the actual values. The largest difference is in member L4-L5 that also had the greatest change in stiffness. Not listed in the table were those elements that

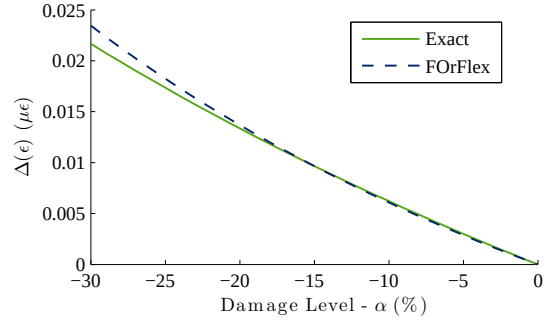

(a) $\Delta(\epsilon)$ v. Damage change percent.

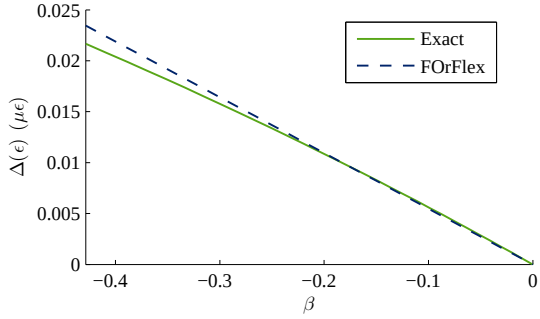

(b) $\Delta(\epsilon)$ v. Linearized β factor.

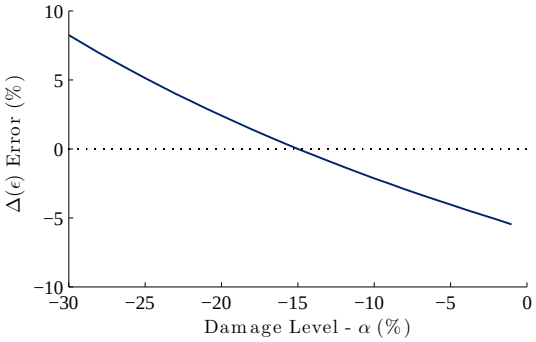

(c) Percent error v. Damage change percent.

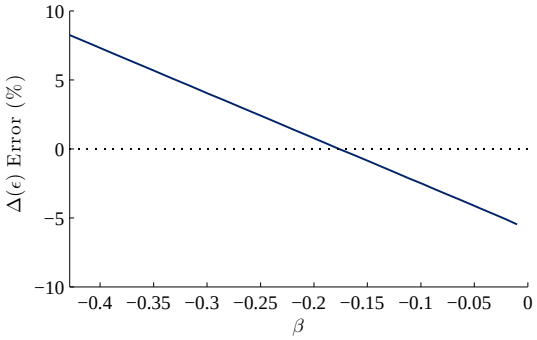

(d) Percent error v. Linearized β factor.

Figure 10.25: Comparison between exact and estimated $\Delta(\epsilon)$ for Rock Island FE model: Strain R03.

Table 10.2: Estimation of damage in Rock Island FE model.

Member	Actual (%)	$\mathbf{S}^+$ (%)	$\mathbf{S}^+ + \gamma\text{Null}(\mathbf{S})$ (%)
L2-L3	-7.00	-7.02	-7.18
L3-L4	-10.00	-9.96	-10.11
L4-L5	-16.00	-14.95	-15.27
L5-L6	-13.00	-12.50	-12.75

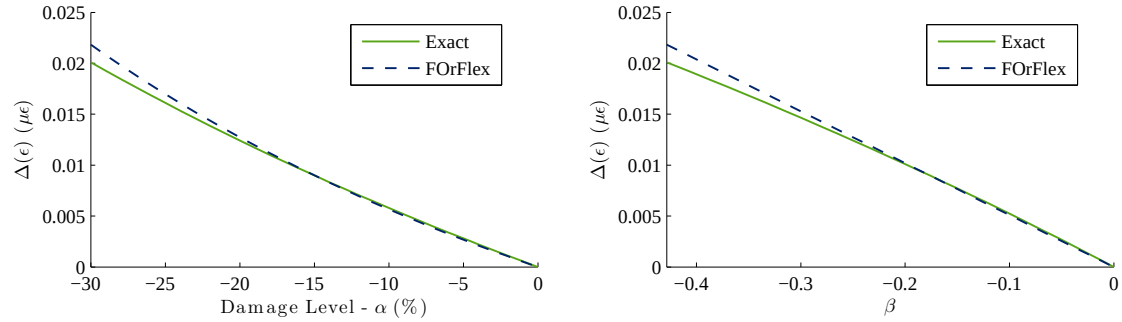

(a) $\Delta(\epsilon)$ v. Damage change percent.

(b) $\Delta(\epsilon)$ v. Linearized β factor.

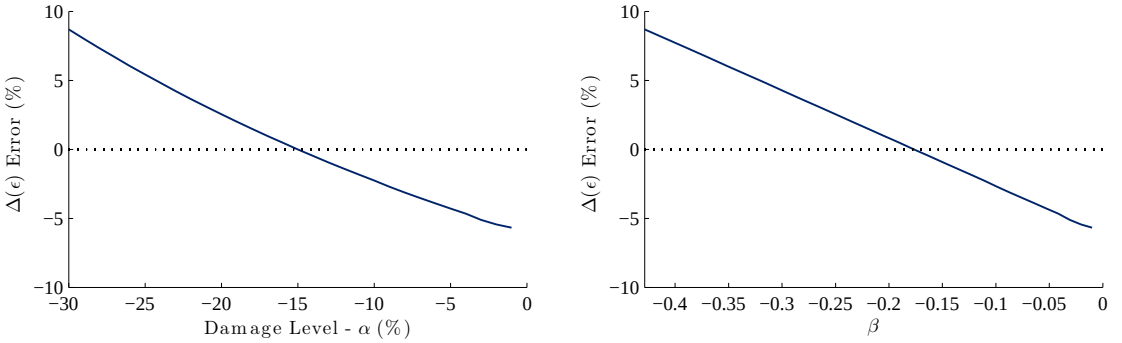

(c) Percent error v. Damage change percent.

(d) Percent error v. Linearized β factor.

Figure 10.26: Comparison between exact and estimated $\Delta(\epsilon)$ for Rock Island FE model: Strain R04.

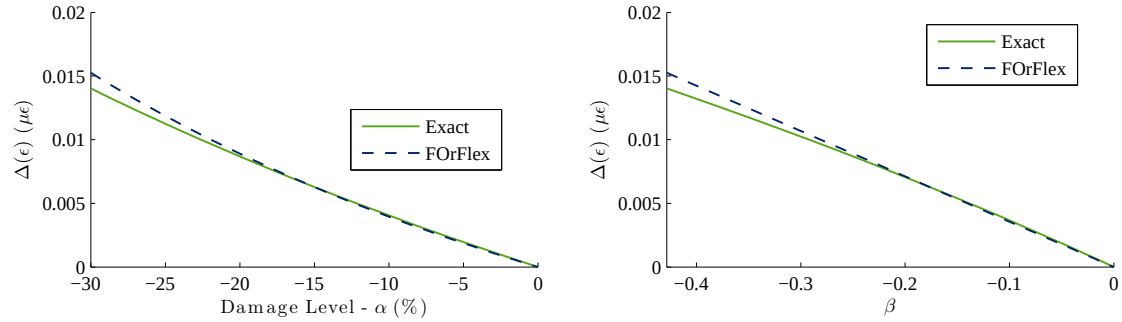

(a) $\Delta(\epsilon)$ v. Damage change percent.

(b) $\Delta(\epsilon)$ v. Linearized β factor.

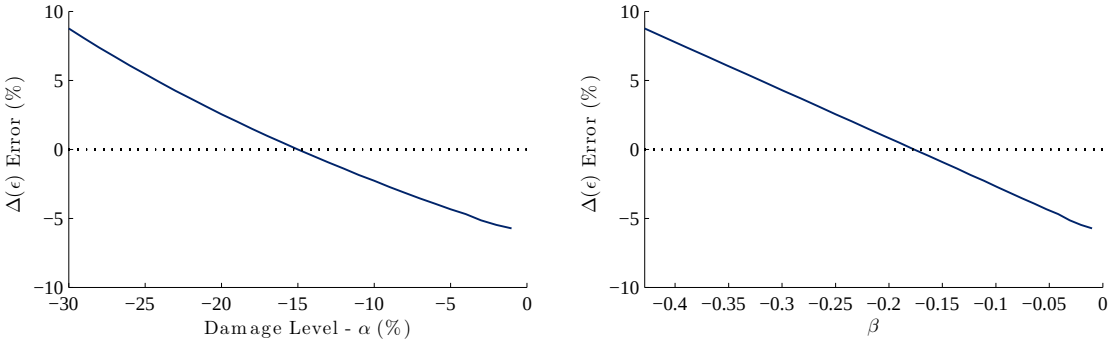

(c) Percent error v. Damage change percent.

(d) Percent error v. Linearized β factor.

Figure 10.27: Comparison between exact and estimated $\Delta(\epsilon)$ for Rock Island FE model: Strain R05.

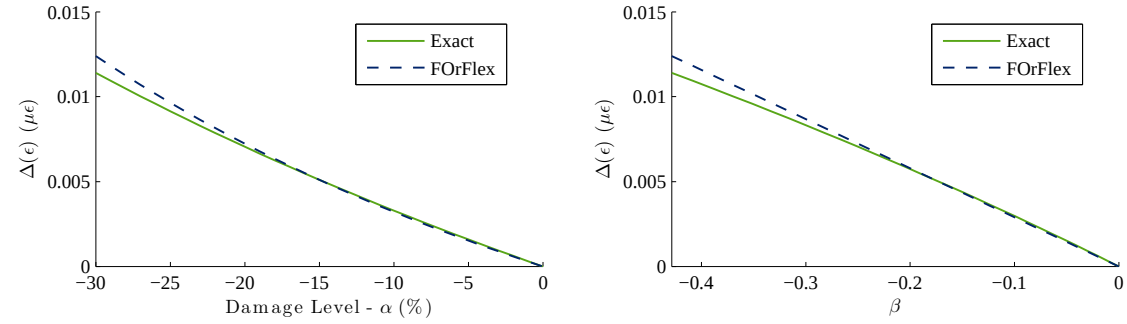

(a) $\Delta(\epsilon)$ v. Damage change percent.

(b) $\Delta(\epsilon)$ v. Linearized β factor.

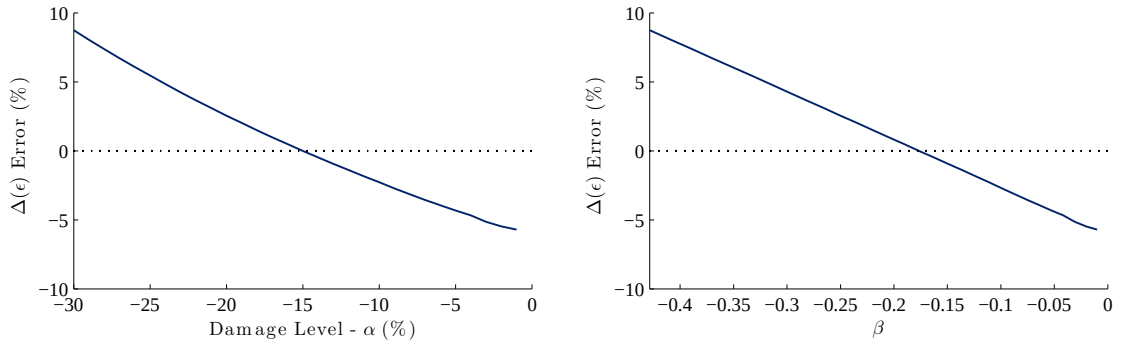

(c) Percent error v. Damage change percent.

(d) Percent error v. Linearized β factor.

Figure 10.28: Comparison between exact and estimated $\Delta(\epsilon)$ for Rock Island FE model: Strain R08.

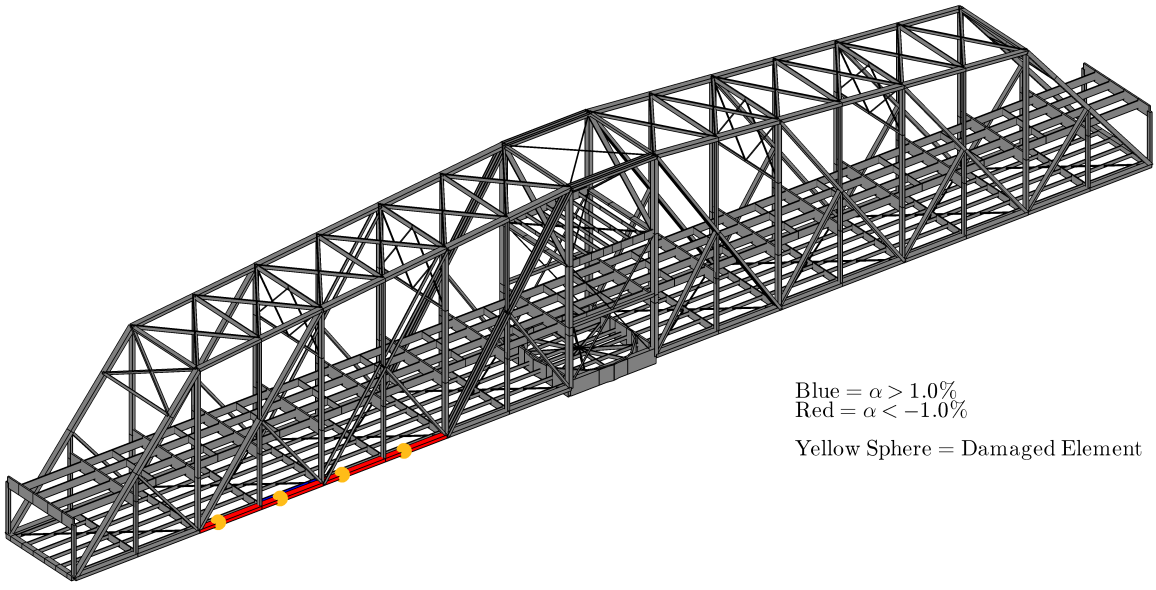

Figure 10.29: Damage scenario and estimated damages using FOrFlex method.

were not damaged in the scenario. Using just the pseudo inverse term, the FOrFlex method estimated that 1,004 of these elements had a stiffness increase of which none had stiffness increases of more than 1.0%. Excluding the four damaged elements, three elements had estimated stiffness decreases of more than 1.0%.

To improve the estimate, the null space term of Equation (10.58) was calculated. The null space of the $\mathbf{S}^*$ matrix contains 496 columns,[8] so 496 γ values need to be determined. To calculate the γ values, an optimization objective function was established. Relying on the assumption that there were no stiffness increases in the structure, the objective function was the sum of all α values greater than zero, as follows:

$$f(\boldsymbol{\gamma}) = \sum_{i=1}^{n} \max\{0, \alpha_i\} \tag{10.62}$$

To minimize the objective function, the `fminsearch` function provided by MATLAB. The `fminsearch` function implements the Lagarias simplex search method and is a form of unconstrained linear optimization. The optimization was seeded with a zero vector starting point and ran until convergence was achieved.

Using both the pseudo inverse and null space terms, final estimates for the change in stiffness of the elements were computed. The last column in Table 10.2 shows the final estimations for the change in stiffness of the four elements in the damage scenario. Though the estimate for elements L2-L3 and L3-L4 have gotten worse due to a move away from the least squars fit provided by the pseudo inverse, the other two estimates have improved significantly. The maximum percent error is now 4.5% and the total error has decreased as well.

The situation with the undamaged elements has also improved, now only 842 elements have stiffness increases though two elements had stiffness changes greater than 1.0%. Figure 10.29 shows the location of the two members with greater than 1.0% stiffness increases were the deck stringer located in the same bay as, and parallel too, the damaged member L3-L4. In addition, only two elements, excluding the four in the damage scenario, experienced stiffness decreases greater than 1.0%. Figure 10.30 shows a histogram of the change in stiffness estimates for the elements not damaged in the scenario. 95% of the undamaged members have an estimated stiffness change of $\pm 0.2\%$ and would fall below a reasonably set threshold.

10.3 Summary

The multimetric SHM system installed on the Rock Island Bridge has been designed to use statistical process control methods to determine when the monitored features indicate that the structure has changed enough to warrant a more in depth investigation. Two damage locating algorithms, the Damage Locating Vector (DLV) method and a First Order Flexibility (FOrFlex) method, which can be used after the control charts indicate structural changes,

[8] Reminder, there are 1,764 elements in the model.

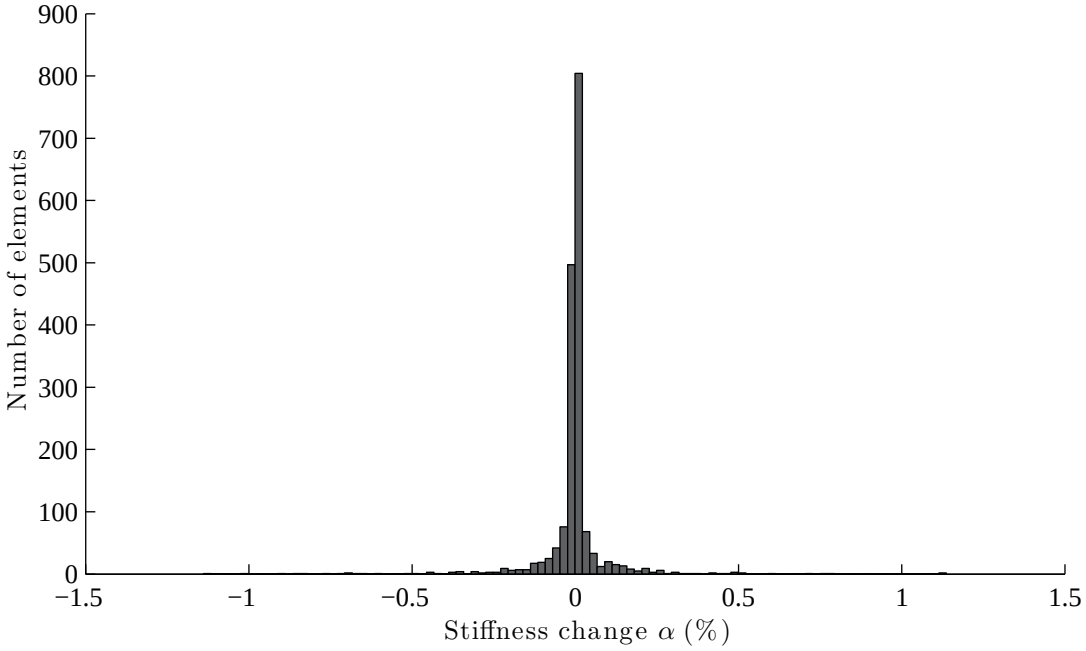

Figure 10.30: Histogram of the estimated stiffness changes in undamaged members of the Rock Island FE model.

were tested numerically for suitability to detect uniform gross cross section loss in members of the Rock Island Bridge. The FOrFlex method has the advantage in that it locates and quantifies damage while the DLV just locates it. The DLV method was primarily designed for using the acceleration measurements and the FOrFlex method is designed exclusively for strain measurements. This chapter has shown, using the Rock Island FE model, the applicability of both to a structure as complex as the Rock Island Bridge. While both the DLV and FOrFlex methods can detect damage as well as locate it, the SPC methods are simpler for real-time detection.

As with any damage detection algorithm, the DLV method and the FOrFlex method have their limitations. Both methods were demonstrated to work for damage that can be best represented as a uniform gross cross section loss in the individual bridge members. Cracks that may form in the members, as discussed in the introduction to this chapter do not affect the overall stiffness of the member but can cause large strains and stresses locally. Therefore, it is unlikely that either method would detect a crack unless it forms near the strain sensor or has grown to such an extent that the overall capacity of the member has been reduced. Likewise, the development of the FOrFlex method has shown that away from the indeterminate locations in the truss, even a complex structure like the Rock Island Bridge will behave as a determinate structure would be expected to behave. A change to the cross section of the member will change the strain observed on the member but will not alter the load carried by the member so the neighboring members will experience no observable changes. Therefore, small changes will only be observable on instrumented members.

While mindful of the limitations of the methods, like all damage detection methods, a level of "art" or "experience" helps the DLV and FOrFlex algorithms work properly. In a real-world setting, selecting a threshold for the DLV method that is too low might mean that a false negative is detected. The FOrFlex method assumes that reliable strain readings can be determined. Averaging of data in both cases would help reduce the noise in the methods and improve the reliability of the methods. Thus, the definition of "real-time" needs not to be confused with the definition of "instantaneous" in the discussion of a structural health monitoring system for a complex structure like the Rock Island Bridge. As long as the expectations of the damage detection algorithms is to confirm the results of one another and provide a bridge inspector with a better idea of where to look, then both the DLV and FOrFlex methods are suitable for the Rock Island Bridge.

Chapter 11

CONCLUSIONS AND FUTURE WORK

The process of creating a structural health monitoring system has four primary steps: *a*) acquire data *b*) identify metrics *c*) evaluate data statistically *d*) interpret data. Each of these steps includes many significant sub-steps that require a broad range of knowledge. Each step is essential in creating a structural health monitoring system that can do more than collect data and display it on a screen. Engineering knowledge and decision making need to be an essential part of any SHM framework so that it can serve as a useful tool in the management of bridge resources.

In this research, a structural health monitoring framework that addresses all four primary SHM steps has been developed for the Rock Island Government Bridge. The framework was developed using a pre-existing fiber optic network of strain and temperature sensors. Observations of the fiber optic system indicated that supplementary sensors were necessary. A network of wireless smart sensors was installed to provide acceleration measurements. System identification was performed using the wireless sensor network to determine the natural frequencies and mode shapes of the bridge. The identified dynamic properties were used to update a finite element model of the bridge.

A digital compass was also installed on the bridge to supplement the fiber optic system. The compass and the fiber optic system were used together to identify in real time the position of the bridge, when the bridge opens and closes, and when trains pass over the bridge. The event detection algorithm was programmed as part of an integrated SHM program that is capable of collecting and storing data from all three sensor systems.

The Integrated SHM Data Collection Program stored the data it collected in databases before it was analyzed manually. The observed net coefficient of thermal expansion could serve as an indicator of both changes in the structure and whether the sensors have remained attached to the bridge. The change in strain when the bridge opens and closes was also shown to be robust to changes in the sensors and sensitive to changes in the structure. The control charts established for the $\Delta\epsilon$ demonstrated the importance of multi-sensor correlation in determining the significance of changes in the metrics. The control charts also showed that the structure changes between certain geometric configurations due to the looseness in the pinned joints. Gaussian mixture models were used to determine the appropriate acceptance band and control limits for each sensor.

This research demonstrated the effectiveness of two damage detection algorithms that utilize the wireless and fiber optic sensors on the bridge that can be implemented in the SHM framework for the Rock Island Bridge. A numerical simulation of the damage locating vector method successfully identify damage locations even in limited sensor groups that are part of a hierarchical sensor arrangement. Likewise, the first order flexibility matrix was able to locate and give severity estimates for simulated corrosion damage introduced to the finite element model.

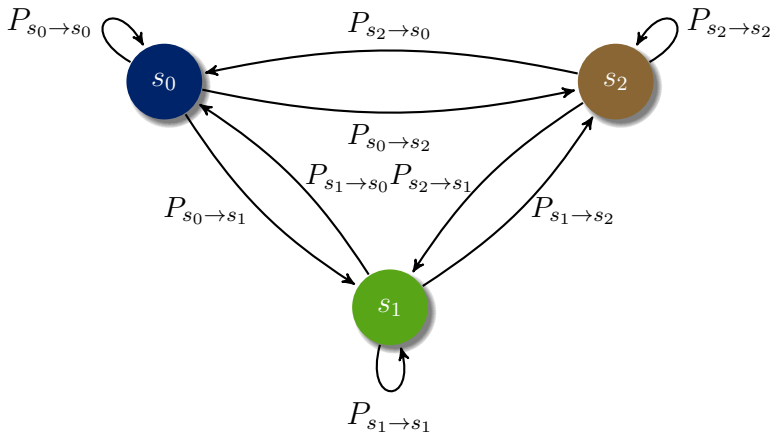

Figure 11.1: Three state Markov Chain.

11.1 Future Work

The continued operation of the Rock Island SHM system will provide plentiful opportunities for continued research. One use is as a test bed for other damage detection algorithms. The two damage detection algorithms developed for this research are not individually multimetric; the DLV method, as presented, uses only acceleration measurements and the FOrFlex method is derived exclusively for strain measurements. However, other researchers [30, 146] have developed damage detection algorithms that utilize both strain and acceleration measurements simultaneously. The multimetric approach has been shown to improve the sensitivity and reliability of the acceleration-only DLV method and decrease both false positives and false negatives. A multimetric DLV method, and other methods that can be developed, can be included in software updates to the Rock Island SHM system.

The data collected from the Rock Island Bridge SHM system has provided valuable insight into the behavior and health of the bridge. Further research will benefit from the data that will continue to be collected. The observations about the behavior the eye bar members that led to the use of acceptance control charts in Section 9.4 has some interesting consequences that warrant future research. The bridge appears to have a few "states" that it can occupy. These states are the combinations that the bridge members that, like the eye-bars, can shift in their joints. The bridge can transition, given the right conditions and forces, from one state to another based on the state that it currently occupies. Observations have shown that every time the bridge swings, a train traverses the bridge, or the bridge experiences differential heating a chance exists that the bridge will change states. However, the change in state does not depend on what state the bridge has been in previously but only on its current state. A Markov Chain can be used to describe the state changing behavior of the bridge.

Figure 11.1 illustrates a simple three state Markov chain. If the system described in Figure 11.1 is in state s_0 then there exists a probability, $P_{s_0 \to s_0}$, that the system will remain in state s_0 and also probabilities, $P_{s_0 \to s_1}$ and $P_{s_0 \to s_2}$, that the state will change to s_1 or s_2 respectively. For the Rock Island Bridge, the number of states, the probabilities for state change, and what factors influence those probabilities are not known. Initial observations

indicate that the bridge is more likely to change its state on sunny afternoons when a train passes over the bridge than at night regardless of any trains or swings. Most $\Delta\epsilon$ recorded on any given night showed small variation. It is the variation of the values from night to night that indicates the presence of the states and that the probability of transition is affected by differential temperature changes. The data collected and used in this research however, is insufficient to calculate the transition probabilities or fully identify the possible states the bridge exhibits. Continued data collection by the Rock Island Bridge SHM system and analysis could potentially better define the Markov chain that describes the bridge system and thus provide greater insight into its normal behavior.

The apparent use of a Markov chain to describe the behavior of the structure could also lead to the creation of a multi-scale finite element model of the bridge. The current FE model was designed to simulate the global dynamic properties and axial strains of the truss members. A multi-scale model can be developed that accounts for the effects of temperature differentials, eye-bar elongations, and friction in pin joints among other behaviors. This model could also then be developed to account for the probabilities of change of state in the observed Markov chain model. Accounting for the changes in states would create a statistical mechanics model that would provide further insight into the bridge behavior under operational conditions. This model could be used to aid in the development of damage detection algorithms or SHM techniques that are suited for the complex behavior of real structures.

11.2 Discussion

Some aspects of the SHM framework devoloped in this reasearch are by necessity custom to the Rock Island Government Bridge. For example, the strain levels that signal an event in the event detection algorithm will need to be adjusted for other movable bridge or even more so for bridges whose primary loads are vehicular. However, the principle of using pattern recognition to detect loadings that can then be used to determine changes in strain that can be fit to a model will be the same for any bridge. The use of statistical process control methods, multiple metrics, and complementary damage detection algorithms can also be used for any bridge. In addition, some of the lessons learned are most applicable to the development of SHM systems for other bridges.

Among the lessons learned is that the Rock Island Bridge SHM system has shown that data quality is important to the success of the system. To ensure data quality it is necessary to understand exactly what is being measured and correct for external factors that can pollute the data. For example, the issues that were discovered with the temperature compensation of the fiber optic strain sensors during the daylight hours are not necessarily unique to the Rock Island Bridge. Other SHM systems on bridges with surface mounted sensors will experience similar behavior if the sensors are not sufficiently insulated from all sources of heat other than conduction from the structural member. Without the swings of the Rock Island Bridge, this issue might have gone unnoticed and the changes in the measured result assumed to due to changes in the forces in the bridge.

Another important lesson is that understanding the limitations of the installed sensors

and how that influences data quality is important. The fiber optic accelerometers proved to be inadequate for SHM applications because the necessary anti-aliasing filtering could not be provided. Other sensors may not be sensitive enough and quantization errors can occur as the fiber optic accelerometers also demonstrate. Therefore it is imperative to install the right sensor, with the right capabilities, at the right location to ensure data quality.

In the long term, measures need to be taken to ensure that the reliability of the sensors exceeds the rate of inspection of the bridge so data from past inspection cycles can be used in tracking the health of the structure. Not only do the sensors need to be able to survive the environmental conditions to which they will be exposed to over years of service, methods need to be implemented that can detect when the sensor is returning erroneous data. The use of the observed coefficient of thermal expansion, developed in this research for use in the Rock Island SHM framework, is one example of detecting when a sensor is not performing as expected. With each layer of complexity that is added to the system, more things can go wrong and the SHM system needs to be able to detect these issues so that false alarms about the failure of members are not common.

The most important part of creating an SHM system is to know what you want to learn from the system at the start of the development process. Doing so requires an understanding of the structural behavior and expected responses to loading conditions. This knowledge will lead to a better understanding of what can be measured and lead to the selection of appropriate sensors. In-depth structural knowledge will also help identify critical members whose failure could lead to catastrophic failure of the bridge. Visual inspections focus on these critical members and an SHM system should as well. Communication between the bridge manager and the parties responsible for the design and installation of the system is essential to creating the most useful SHM system.

Throughout the whole process of monitoring a structure, it is requisite to have reasonable expectations of what the SHM system can do. The scope of any SHM system is limited. More and better sensors can always provide more detailed information but there are costs associated with both “more” and “better”. An SHM system with limited sensors cannot be expected to detect every type of damage that can occur at any location in the bridge. Full disclosure of the limitations associated with any SHM system is important for establishing an appropriate bridge management strategy that integrates the SHM system and traditional bridge inspections. In addition to the limitations on an SHM system imposed by the hardware selection and quantity, the software and algorithms also have their own limitations. No one damage detection method is going to be the perfect solution for every situation; all methods have their strengths and weaknesses. Using a variety of sensors and a variety of methods that can complement each other is the best way to create a system.

Each structural health monitoring system will need to be adapted to the individual bridge. The system created for the Rock Island Bridge did its best to use the resources available to provide the most useful information it could. The distinctive history and function of the Rock Island Government Bridge provided a unique opportunity to create a framework that can help preserve the bridge for many more generations to come.

REFERENCES

[1] ASCE, "Report card for America's infrastructure," American Society of Civil Engineers, Tech. Rep., 2013.

[2] S. Alampalli and M. Ettouney, "Structural health monitoring as a bridge management tool," in *ASCE Structures Congress*, 2006.

[3] C. LeRose, "The collapse of the Silver Bridge," *West Virginia Historical Society Quarterly*, vol. 15, no. 4, October 2001. [Online]. Available: http://www.wvculture.org/history/wvhs1504.html

[4] "National bridge inspection standards," *23 C.F.R §650, subpart C*, 2004.

[5] AREMA, *AREMA Bridge Inspection Handbook*, C. 10, Ed. The American Railway Engineering and Maintenance of Way Association, 2008.

[6] TXDOT, "Bridge inspection manual," Texas Department of Transportation, Tech. Rep., 2002.

[7] M. Moore, B. Phares, B. Graybeal, D. Rolander, and G. Washer, "Reliability of visual inspection for highway bridges," Federal Highway Administration, Tech. Rep. FHWA-RD-01-020, June 2001.

[8] P. D. Thompson and R. W. Shepard, "AASHTO commonly-recognized bridge elements: Successful applications and lessons learned," in *National Workshop on Commonly Recognized Measures for Maintenance*, 2000.

[9] AASHTO, "AASHTOWare - Bridge - Management (formerly Pontis)," October 2013. [Online]. Available: http://www.aashtoware.org/Bridge/Pages/Management.aspx?PID=2

[10] J. Schaffer, "National Bridge Element implementation." Presented at Western Bridge Preservation Partnership Meeting, May 2012. [Online]. Available: http://tsp2bridge.pavementpreservation.org/western-wbpp/annual-meetings/2012-2/?vid=11

[11] AASHTO, *AASHTO Guide for Commonly Recognized (Core) Structural Elements*. American Association of State Highway & Transportation Officials, 1998.

[12] D. D. Oxtoby and N. H. Nachtrieb, *Principles of Modern Chemistry*, 3rd ed. Saunders College Publishing, 1996.

[13] R. Francis, "Bimetallic corrosion," National Physical Laboratory, Tech. Rep., 2008. [Online]. Available: http://www.npl.co.uk/upload/pdf/bimetallic_20071105114556.pdf

[14] G. H. Koch, M. P. Brongers, N. G. Thompson, Y. P. Virmani, and J. H. Payer, "Corrosion cost and preventive strategies in the United States," Federal Highway Administration, Tech. Rep. FHWA-RD-01-156, 2002.

[15] FHWA, "Material type of structure by state," Dec 2011, US Department of Transportation, Federal Highway Administration. [Online]. Available: http://www.fhwa.dot.gov/bridge/material.cfm

[16] FHWA, "Bridges by year built," Dec 2011, US Department of Transportation, Federal Highway Administration. [Online]. Available: http://www.fhwa.dot.gov/bridge/year.cfm

[17] A. Halsey, III, "Decaying infrastructure costs U.S. bilions each year, report says," *The Washington Post*, July 27 2011.

[18] ASCE, "Report card for America's infrastructure," American Society of Civil Engineers, Tech. Rep., 2009.

[19] I. E. Harik, A. Shaaban, H. Gesund, G. Y. S. Valli, and S. T. Wang, "United States bridge failures, 1951-1988," *Journal of Performance of Constructed Facilities*, vol. 4, no. 4, pp. 272–277, November 1990.

[20] C. Storey and N. Delatte, "Lessons from the collapse of the Schoharie Creek Bridge," in *Forensic Engineering*, ser. Proceedings of the Third Forensic Engineering Congress. ASCE, 2003, pp. 158–167.

[21] K. Wardhana and F. C. Hadipriono, "Analysis of recent bridge failures in the United States," *Journal of Performance of Constructed Facilities*, vol. 17, no. 3, pp. 144–150, August 2003.

[22] J.-L. Briaud and B. E. Hunt, "Bridge scour & the structural engineer," *Structure*, pp. 59–61, December 2006.

[23] M. V. Biezma and F. Schanack, "Collapse of steel bridges," *Journal of Performance of Constructed Facilities*, vol. 21, no. 5, pp. 398–405, October 2007.

[24] E. E. Muñoz Diaz, F. Núñez Moreno, and J. Mohammadi, "Investigation of common causes of bridge collapse in colombia," *Practice Periodical on Structural Design and Construction*, vol. 14, no. 4, pp. 194–200, November 2009.

[25] C. R. Farrar and K. Worden, "An introduction to structural health monitoring," *Philosophical Transactions of the Royal Society A*, vol. 365, no. 1851, pp. 303–315, February 2007.

[26] C. R. Farrar and N. A. J. Lieven, "Damage prognosis: the future of structural health monitoring," *Philosophical Transactions of the Royal Society A*, vol. 365, pp. 623–632, 2007.

[27] J. M. W. Brownjohn, "Structural health monitoring of civil infrastructure," *Philosophical Transactions of the Royal Society A*, vol. 365, no. 1851, pp. 589–622, February 2007.

[28] J. M. López-Higuera, L. R. Cobo, A. Q. Incera, and A. Cobo, "Fiber optic sensors in structural health monitoring," *Lightwave Technology, Journal of*, vol. 29, no. 4, pp. 587 –608, Feb.15, 2011.

[29] T. W. Ryan, R. A. Hartle, J. E. Mann, and L. J. Danovich, *Bridge Inspectors Reference Manual*. Federal Highway Administration, 2006, no. FHWA NHI 03-001.

[30] S. Sim, B. Spencer, and T. Nagayama, "Multimetric sensing for structural damage detection," *Journal of Engineering Mechanics*, vol. 137, no. 1, pp. 22–30, 2011.

[31] K.-Y. Wong, "Instrumentation and health monitoring of cable-supported bridges," *Structural Control and Health Monitoring*, vol. 11, no. 2, pp. 91–124, 2004.

[32] T. Chan, L. Yu, H. Tam, Y. Ni, S. Liu, W. Chung, and L. Cheng, "Fiber Bragg grating sensors for structural health monitoring of Tsing Ma Bridge: Background and experimental observation," *Engineering Structures*, vol. 28, no. 9, pp. 648–659, September 2006.

[33] M. Çelebi, "Real-time seismic monitoring of the new Cape Girardeau Bridge and preliminary analyses of recorded data: An overview," *Earthquake Spectra*, vol. 22, no. 3, pp. 609–630, 2006.

[34] Y. Zhang, J. Caicedo, S. Sim, C. Chang, B. F. Spencer, Jr., and X. Guo, "Modal identification of Bill Emerson Bridge," in *14th World Conference on Earthquake Engineering*, 2008.

[35] S. Cho, H. Jo, S. Jang, J. Park, H.-J. Jung, C.-B. Yun, B. F. Spencer, Jr., and J.-W. Seo, "Structural health monitoring of a cable-stayed bridge using wireless smart sensor technology: data analyses," *Smart Structures and Systems*, vol. 6, no. 5-6, pp. 461–480, 2010.

[36] F. Magalhães, A.Cunha, and E.Caetano, "Vibration based structural health monitoring of an arch bridge: From automated OMA to damage detection," *Mechanical Systems and Signal Processing*, vol. 28, pp. 212–228, April 2012.

[37] A. G. Lichtenstein, *Manual for Bridge Rating through Load Testing*, ser. Research Results Digest. National Cooperative Highway Research Program, 1998, no. 234.

[38] M. Sanayei, J. E. Phelps, J. D. Sipple, E. S. Bell, and B. R. Brenner, "Instrumentation, nondestructive testing, and finite-element model updating for bridge evaluation using strain measurements," *Journal of Bridge Engineering*, vol. 17, no. 1, pp. 130–138, January 2012.

[39] F. Matta, F. Bastianini, N. Galati, P. Casadei, and A. Nanni, "Distributed strain measurement in steel bridge with fiber optic sensors: Validation through diagnostic load test," *Journal of Performance of Constructed Facilities*, vol. 22, no. 4, pp. 264–273, August 2008.

[40] D. V. Jáuregui and P. J. Barr, "Nondestructive evaluation of the I-40 bridge over the Rio Grande River," *Journal of Performance of Constructed Facilities*, vol. 18, no. 4, pp. 195–204, November 2004.

[41] S. Su, "Decentralized damage detection in civil infrastructure using multi-scale wireless sensor networks," Doctoral, University of Notre Dame, Notre Dame, Indiana, July 2011. [Online]. Available: www.nd.edu/~crane/PUBLICATIONS/THESES/Su.pdf

[42] G. Yannis and C. Antoniou, "Integration of weigh-in-motion technologies in road infrastructure management," *ITE Journal*, vol. 75, no. 1, pp. 39–43, January 2005.

[43] M. J. Whelan, M. V. Gangone, and K. D. Janoyan, "Highway bridge assessment using an adaptive real-time wireless sensor network," *Sensors Journal*, vol. 9, no. 11, pp. 1405–1413, November 2009.

[44] M. Frövel, J. M. Pintado, A. Güemes, E. del Olmo, and A. Obst, "Multiplexable fiber Bragg grating temperature sensors embedded in CFRP structures for cryogenic applications," in *Proceedings of the Third European Workshop on Structural Health Monitoring*, A. Güemes, Ed. DEStech Publications, Inc., 2006, pp. 938–953.

[45] M. Fuchs and C. B. Tanner, "Radiation shields for air temperature thermometers," *Journal of Applied Meteorology*, vol. 4, pp. 544–547, August 1965.

[46] Honeywell, "1- and 2-axis magnetic sensors HMC1001/1002/1021/1022," Honeywell, Data Sheet, 2008.

[47] V. I. Yudin, A. V. Taichenachev, Y. O. Dudin, V. L. Velichansky, A. S. Zibrov, and S. A. Zibrov, "Vector magnetometry based on electromagnetically induced transparency in linearly polarized light," *Physical Review A*, vol. 82, no. 3, pp. 033 807.1–7, Sep 2010.

[48] B. Åkesson, *Understanding Bridge Collapses*. Taylor & Francis, 2008.

[49] J. F. Unsworth, *Design of Modern Steel Railway Bridges*. CRC Press, 2010.

[50] R. Modjeski, "Bridges old and new," *Journal of the Franklin Institute*, vol. 194, no. 3, pp. 291–327, September 1922.

[51] J. G. Waite, *The Maintenance and Repair of Architectural Cast Iron*, ser. Preservation Briefs. U.S. Dept. of the Interior, National Park Service, Cultural Resources, Preservation Assistance, October 1991, no. 27.

[52] H. Petroski, "The civil engineer: On the occasion of a sesquicentennial," *American Scientist*, vol. 90, no. 2, pp. 118–122, March-April 2002.

[53] R. Modjeski, "Erection of the draw span of the new Rock Island Bridge," *Journal of the Western Society of Engineers*, vol. 2, no. 2, pp. 135–168, April 1897.

[54] T. T. Johnston, I. Randolph, J. H. Peck, P. C. Ricketts, H. W. Rogers, M. U. Ricker, T. C. Roney, G. N. Carman, H. Judson, I. O. Baker, T. A. Sniveley, and R. W. Hunt, "Technical education," *Journal of the Western Society of Engineers*, vol. 2, no. 2, pp. 230–252, April 1897.

[55] F. R. Rutz and K. L. Rens, "Wind loads for 19th century bridges: Design evolution, historic failures, and modern preservation," *Journal of Performance of Constructed Facilities*, vol. 21, no. 2, pp. 157–165, March/April 2007.

[56] S. Whipple, *A work on bridge building: consisting of two essays, the one elementary and general, the other giving original plans and practical details for iron and wooden bridges*. H. H. Curtiss, 1847.

[57] W. Fairbairn, "Experiments to determine the effect of impact, vibratory action, and long-continued changes of load on wrought-iron girders," *Philosophical Transactions of the Royal Society of London*, vol. 154, pp. 311–325, 1864. [Online]. Available: http://www.jstor.org/stable/108871

[58] L. P. Pook, *Metal Fatigue: What It Is, Why It Matters*, ser. Solid Mechanics and Its Applications. Springer, 2007, vol. 145.

[59] R. Tweet, *A History of Navigation Improvements on the Rock Island Rapids: the Background of Locks and Dam 15*. Rock Island, IL: U.S. Army Corps of Engineers, Rock Island District, 1980.

[60] W. H. Clark, *Railroads and Rivers: the Story of Inland Transportation*, ser. The American Cavalcade Series. Boston: L.C. Page & Company, April 1939.

[61] D. A. Pfeiffer, "Bridging the Mississippi: The railroads and steamboats clash at the Rock Island Bridge," *Prologue*, vol. 36, no. 2, pp. 40–47, Summer 2004. [Online]. Available: http://www.archives.gov/publications/prologue/2004/summer/bridge.html

[62] B. Babcock, "Lincoln and the first Mississippi river bridge," *Railroad Man's Magazine*, vol. 4, no. 3, pp. 328–334, February 1931.

[63] A. Lincoln, *The Collected Works of Abraham Lincoln*, R. P. Basler, Ed. Rutgers University Press, 1953, vol. II.

[64] *Mississippi and Missouri Railroad Company vs. Ward*, 67 U.S. 485, 17 L. Ed. 311, 2 Black 485.

[65] *The Galena, Dubuque, Dunleith, and Minnesota Packet Co. v. The Rock Island Bridge*, 73 U.S 213, 18 L. Ed 753, 6 Wall. 213.

[66] R. Modjeski, "The new United States Rock Island Bridge: Part i," *The Engineering Record*, vol. 35, no. 9, pp. 181–182, January, 30 1897.

[67] J. S. Plachta, "One hundred years of the Rock Island Government Bridge," *Journal of Bridge Engineering*, vol. 2, no. 4, pp. 168–175, November 1997.

[68] R. Modjeski, "'Under no consideration would I give up music': An interview with the distinguished engineer, Ralph Modjeski, builder of fifteen world-famous bridges," *Etude*, vol. 44, no. 3, pp. 173–174, March 1926.

[69] J. Glomb, *A Man Who Spanned Two Eras*, H. Chronic, Ed. The Philadelphia Chapter of the Kosciuszko Foundation, 2002.

[70] A. Buffington, "Col. Buffington to the Phoenix Bridge Company," Letter, December, 16 1895, folder 2069, Rock Island Arsenal Archives.

[71] T. Cooper, *General Specifications for Iron and Steel Railroad Bridges and Viaducts*. Engineering News Publishing Company, 1890.

[72] R. Modjeski, "Double deck highway and railway bridge Rock Island, Ill." *Engineering News*, vol. 36, no. 25, pp. 406–408 & insert, December 17 1896.

[73] M. Scheinman, "Altgeld Hall, the original library building at the University of Illinois: Its history, architectrue and art," M.S. thesis, University of Illinois, 1969. [Online]. Available: http://www.math.illinois.edu/History/scheinman_thesis.pdf

[74] C. R. Hsiao, "Baseline finite element modeling of Government Bridge," Master's Thesis, University of Illinois at Urbana-Champaign, 2009.

[75] F. W. Frailey, "The Iowa Interstate story," *Trains*, pp. 30–37, June 2001.

[76] J. Schultz, "A tow truck operator lets the air out of the back tires of a truck stuck under the Government Bridge, Friday, Aug. 19, 2011. The truck is listed at 13 feet 6 inches tall, and the bridge opening is only 11 feet high." in *Quad-City Times*, ser. Historic photos: Q-C's truck-eating bridges. Quad-City Times, 2011. [Online]. Available: http://qctimes.com/gallery/traffic/historic-photos-q-c-s-truck-eating-bridges/collection_0b1b72cc-4fd7-11e0-b650-001cc4c03286.html#37

[77] USACE, "RiverGages.com," June 2013, US Army Corps of Engineers. [Online]. Available: http://rivergages.mvr.usace.army.mil

[78] USACE, "Corps Locks," June 2013, US Army Corps of Engineers. [Online]. Available: http://corpslocks.usace.army.mil

[79] M. Kreuzer, "Strain measurement with fiber Bragg grating sensors," HBM GmbH, Darmstadt, Germany, Tech. Rep., 2007. [Online]. Available: http://www.hbm.com/fileadmin/mediapool/techarticles/2007/FBGS_StrainMeasurement_en.pdf

[80] B. Glisic and D. Inaudi, *Fibre Optic Methods for Structural Health Monitoring*. John Wiley & Sones, Ltd., 2007.

[81] M. Iodice, V. Striano, G. Cappuccino, A. Palumbo, and G. Cocorullo, "Fiber bragg grating sensors based system for strain measurements," in *Proceedings of 2005 IEEE/LEOS Workshop on Fibres and Optical Passive Components*. IEEE, 2005, pp. 307–312.

[82] P. Moyo, J. Brownjohn, R. Suresh, and S. Tjin, "Development of fiber Bragg grating sensors for monitoring civil infrastructure," *Engineering Structures*, vol. 27, pp. 1828–1834, 2005.

[83] C. Barbosa, N. Costa, L. A. Ferreira, F. M. Araújo, H. Varum, A. Costa, C. Fernandes, and H. Rodrigues, "Weldable fibre Bragg grating sensors for steel bridge monitoring," *Measurement Science and Technology*, vol. 19, pp. 125 305.1–10, 2008.

[84] S. Van Damme, B. Boons, J. Vlekken, J. Bentell, and J. Vermeiren, "Dynamic fiber optic strain measurements and aliasing suppression with a pds-based spectrometer," *Measurement Science and Technology*, vol. 18, no. 10, pp. 3263–3266, October 2007. [Online]. Available: http://stacks.iop.org/MST/18/3263

[85] J. Bentell, D. Uwaerts, J. Cloots, T. Bocquet, J. Neys, J. Vlekken, B. Boons, J. V. Roosbroeck, and P. Hong, "250 khz sampling rate fbg interrogator with strong anti-aliasing signal processing," in *20th International Conference on Optical Fibre Sensors*, J. D. C. Jones, Ed., vol. 7503, no. 1. SPIE, 2009, p. 75034S.

[86] T. Buck, M. Mller, A. P. Grassi, and A. Koch, "Detection of aliasing in sampled dynamic fiber bragg grating signals recorded by spectrometers," *Measurement*, vol. 44, no. 6, pp. 1053 – 1058, 2011.

[87] H.-N. Li, D.-S. Li, and G.-B. Song, "Recent applications of fiber optic sensors to health monitoring in civil engineering," *Engineering Structures*, vol. 26, no. 11, pp. 1647–1657, September 2004.

[88] P. L. Fuhr and D. Huston, "Embedded sensors for improved maintenance and assessment of roadways and bridges," *Journal of Smart Materials and Structures*, vol. 7, no. 1, pp. 151–158, 1998.

[89] P. L. Fuhr, D. R. Huston, M. Nelson, O. Nelson, J. Hu, E. Mowat, S. Spammer, and W. Tamm, "Fiber optic sensing of a bridge in Waterbury, Vermont," *Journal of Intelligent Material Systems and Structures*, vol. 10, pp. 293–303, April 1999.

[90] W. Lee, J. Lee, C. Henderson, H. F. Taylor, R. James, C. E. Lee, V. Swenson, R. A. Atkins, and W. G. Gemeiner, "Railroad bridge instrumentation with fiber-optic sensors," *Applied Optics*, vol. 38, no. 7, pp. 1110–1114, March 1999.

[91] S. T. Vohra, G. A. Johnson, M. D. Todd, B. Danver, and B. Althouse, "Strain monitoring during construction of a steel box-girder bridge with arrays of fiber

Bragg grating sensors," Naval Research Laboratory, Washington, DC, Tech. Rep. NRL/MR/5670–99-8390, July 1999.

[92] H. Y. Tam, T. Lee, S. L. Ho, T. Haber, T. Graver, and A. Méndez, "Utilizatization of fiber optic Bragg grating sensing system for health monitoring of railway applications," in *Structural Health Monitoring: Quantification, Validation, Implementation*, F.-K. Chang, Ed., vol. 1, 2007, pp. 1824–1831.

[93] M. L. Filograno, P. C. Guillén, A. Rodríguez-Barrios, S. Martín-López, M. Rodríguez-Plaza, A. Andrés-Alguacil, and M. González-Herráez, "Real-time monitoring of railway traffic using fiber Bragg grating sensors," *IEEE Sensors Journal*, vol. 12, no. 1, pp. 85–92, January 2012.

[94] Micron Optics, "Optical strain gage: os3100," Micron Optics, Data Sheet, 2010. [Online]. Available: http://www.micronoptics.com/uploads/library/documents/Datasheets/MicronOptics-os3100.pdf

[95] Micron Optics, "Non-metallic temperature sensor: os4300," Micron Optics, Data Sheet, 2009. [Online]. Available: http://www.micronoptics.com/uploads/library/documents/Datasheets/MicronOptics-os4300.pdf

[96] Micron Optics, "Accelerometer: os7100," Micron Optics, Data Sheet, 2009. [Online]. Available: http://www.micronoptics.com/uploads/library/documents/Datasheets/MicronOpticsos7100.pdf

[97] Smartec, "12.1030 MUST mono-axial tiltmeter," Smartec, Data Sheet, 2009. [Online]. Available: http://smartec.ch/PDF/SDS12.1030MuSTMono-AxialTiltmeter.pdf

[98] J. A. Hedderman and J. J. Himes, "Structural analysis of the I-20 Bridge in Vicksburg, MS and the Government Bridge at Rock Island, IL," ODonnell Consulting Engineers, Inc. for Concurrent Technologies Corporation, Tech. Rep. OCE 08-677, 2009.

[99] J. A. Hedderman and J. J. Himes, "Sensor thresholds for the I-20 Bridge in Vicksburg, MS and the Government Bridge at Rock Island, IL," ODonnell Consulting Engineers, Inc. for Concurrent Technologies Corporation, Tech. Rep. OCE 08-677, 2009.

[100] Lichtenstein Consulting Engineers, Inc., "Manual for condition evaluation and load rating of highway bridges using load and resistance factor philosophy," National Cooperative Highway Research Program, Paramus, NJ, Tech. Rep. Web Document 28, May 2001. [Online]. Available: http://onlinepubs.trb.org/onlinepubs/nchrp/nchrp_w28.pdf

[101] B. T. Neilson, C. E. Hatch, H. Ban, and S. W. Tyler, "Solar radiative heating of fiber-optic cables used to monitor temperatures in water," *Water Resources Research*, vol. 46, no. W08540, pp. 1–17, 2010.

[102] R. Nakamura and L. Mahrt, "Air temperature measurement errors in naturally ventillated radiation shields," *Journal of Atmospheric and Oceanic Technology*, vol. 22, pp. 1046–1058, 2005.

[103] S.-H. Jeong and A. S. Elnashai, "Analytic assessment of an irregular RC frame for full-scale 3D pseudo-dynamic testing part I: Analytical model verification," *Journal of Eartquake Engineering*, vol. 9, no. 1, pp. 95–128, 2005.

[104] J. Mottershead and M. Friswell, "Model updating in structural dynamics: A survey," *Journal of Sound and Vibration*, vol. 167, no. 2, pp. 347–375, 1993.

[105] R. J. Allemang, "The modal assurance criterion – twenty years of use and abuse," *Sound and Vibration*, vol. 37, no. 8, pp. 14–23, August 2003.

[106] R. J. Allemang and D. L. Brown, "A correlation coefficient for modal vector analysis," in *Proceedings of the 1st international modal analysis conference*, vol. 1. Orlando: SEM, 1982, pp. 110–116.

[107] P. W. Möller and O. Friberg, "Updating large finite element models in structural dynamics," *AIAA Journal*, vol. 36, no. 10, pp. 1861–1868, October 1998.

[108] S. Jang, J. Li, and B. F. Spencer, Jr., "Corrosion estimation of a historic truss bridge using model updating," *Journal of Bridge Engineering*, posted ahead of print April 20, 2012.

[109] R. J. Askew, R. K. Giles, S. Cho, B. F. Spencer, Jr., S. Sweeney, and C. Shield, "Finite element model updating of a historic truss bridge," in *Proceedings of ANCRiSST 2012*. Bangalore, India: ANCRiSST, 2012.

[110] D. E. Goldberg, *Genetic Algorithms in Search, Optimization, and Machine Learning*. Addison-Wesley Professional, 1989.

[111] L. Deng and C. Cai, "Bridge model updating using response surface method and genetic algorithm," *Journal of Bridge Engineering*, vol. 15, no. 5, pp. 553–564, 2009.

[112] N. M. M. Maia and J. M. Montalvão e Silva, Eds., *Theoretical and Experimental Modal Analysis*, ser. Mechanical Engineering Research Studies. Engineering Dynamics Series. Taunton, Somerset, England: Research Studies Press, 1997, no. 9.

[113] A. Preumont, A. Franois, P. D. Man, and V. Piefort, "Spatial filters in structural control," *Journal of Sound and Vibration*, vol. 265, no. 1, pp. 61 – 79, 2003.

[114] J. P. Lynch, A. Sundararajan, K. H. Law, A. S. Kiremidjian, E. Carryer, H. Sohn, and C. R. Farrar, "Field validation of a wireless structural monitoring system on the Alamosa Canyon Bridge," in *Proceedings of SPIE Smart Structures and Materials*. San Diego, CA: SPIE, 2003.

[115] S. W. Arms, J. H. Galbreath, A. T. Newhard, and C. P. Townsend, "Remotely reprogrammable sensors for structural health monitoring," in *Proceedings of NDE/NDT for Highways and Bridges, Structural Materials Technology IV*, Buffalo, NY, 2004, pp. 331–338.

[116] M. Ceriotti, L. Mottola, G. P. Picco, A. L. Murphy, S. Guna, M. Corrá, M. Pozzi, D. Zonta, and P. Zanon, "Monitoring heritage buildings with wireless sensor networks: the Torre Aquila deployment," in *Proceedings of the Eighth ACM/ IEEE International Conference on Information Processing in Sensor Networks*, San Francisco, CA, 2009.

[117] S. Jang, H. Jo, S. Cho, K. A. Mechitov, J. A. Rice, S.-H. Sim, H.-J. Jung, C.-B. Yun, B. F. Spencer, Jr., and G. A. Agha, "Structural health monitoring of a cable stayed bridge using smart sensor technology: deployment and evaluation," *Smart Structures and Systems*, vol. 6, no. 5-6, pp. 439–459, 2010.

[118] M. Healy, T. Newe, and E. Lewis, "Wireless sensor node hardware: A review," in *Sensors, 2008 IEEE*, 2008, pp. 621–624.

[119] T. Nagayama, S.-H. Sim, Y. Miyamori, and B. F. Spencer, Jr., "Issues in structural health monitoring employing smart sensors," *Smart Structures and Systems*, vol. 3, no. 3, pp. 299–320, 2007. [Online]. Available: http://sstl.cee.illinois.edu/papers/SSS_nagayama.pdf

[120] J. Rice and B. F. Spencer, Jr., "Flexible smart sensor framework for autonomous full-scale structural health monitoring," University of Illinois at Urbana-Champaign, NSEL Report 18, 2009. [Online]. Available: http://hdl.handle.net/2142/13635

[121] P. Reynolds and A. Pavic, "Quality assurance procedures for the modal testing of building floor structures," *Experimental Techniques*, vol. 24, no. 4, pp. 36–41, 2000.

[122] S. Živanović, A. Pavic, and P. Reynolds, "Modal testing and FE model tuning of a lively footbridge structure," *Engineering Structures*, vol. 28, no. 6, pp. 857 – 868, 2006.

[123] K. A. Grimmelsman, Q. Pan, and A. E. Aktan, "Analysis of data quality for ambient vibration testing of the henry hudson bridge," *Journal of Intelligent Material Systems and Structures*, vol. 18, no. 8, pp. 765–775, 2007.

[124] M. Setareh, "Vibration serviceability of a building floor structure. i: Dynamic testing and computer modeling," *Journal of Performance of Constructed Facilities*, vol. 24, no. 6, pp. 497–507, 2010.

[125] M. Whelan, M. Gangone, K. Janoyan, and R. Jha, "Operational modal analysis of a multi-span skew bridge using real-time wireless sensor networks," *Journal of Vibration and Control*, vol. 17, no. 13, pp. 1952–1963, 2011.

[126] S. Cho, R. K. Giles, and B. F. Spencer, Jr., "System identification of a historic swing truss bridge using a wireless sensor network employing orientation correction," *Structural Control and Health Monitoring*, 2013, submitted.

[127] D. Gebre-Egziabher, R. Hayward, and J. Powell, "Design of multi-sensor attitude determination systems," *Aerospace and Electronic Systems, IEEE Transactions on*, vol. 40, no. 2, pp. 627–649, 2004.

[128] R. Brincker, L. Zhang, and P. Andersen, "Modal identification of output-only systems using frequency domain decomposition," *Smart Materials and Structures*, vol. 10, no. 3, p. 441, 2001. [Online]. Available: http://stacks.iop.org/0964-1726/10/i=3/a=303

[129] W. A. Levinson, *Statistical Process Control for Real–World Applications*. Boca Raton, FL: CRC Press, 2011.

[130] J. R. Thompson and J. Koronacki, *Statistical Process Control: The Deming Paradigm and Beyond*, 2nd ed. Chapman & Hall/CRC, 2002.

[131] L. S. Nelson, "The Shewhart control chart – tests for special causes," *Journal of Quality Technology*, vol. 16, no. 4, pp. 237–239, October 1984.

[132] C. W. Champ and W. H. Woodall, "Exact results for Shewhart control charts with supplementary runs rules," *Technometrics*, vol. 29, no. 4, pp. 393–399, November 1987.

[133] H. Sohn, J. A. Czarnecki, and C. R. Farrar, "Structural health monitoring using statistical process control," *Journal of Structural Engineering*, vol. 126, no. 11, pp. 1356–1363, November 2000.

[134] M. L. Fugate, H. Sohn, and C. R. Farrar, "Vibration–based damage detection using statistical process control," *Mechanical Systems and Signal Processing*, vol. 15, no. 4, pp. 707 – 721, 2001.

[135] J. Zapico-Valle, M. García-Diéguez, M. González-Martínez, and K. Worden, "Experimental validation of a new statistical process control feature for damage detection," *Mechanical Systems and Signal Processing*, vol. 25, no. 7, pp. 2513–2525, 2011.

[136] A. Deraemaekera, E. Reynders, G. D. Roeck, and J. Kullaac, "Vibration-based structural health monitoring using output-only measurements under changing environment," *Mechanical Systems and Signal Processing*, vol. 22, no. 1, pp. 34–56, January 2008.

[137] J. Kullaa, "Damage detection of the Z24 Bridge using control charts," *Mechanical Systems and Signal Processing*, vol. 17, no. 1, pp. 163–170, January 2003.

[138] Micron Optics, "Optical strain gage: os3155," Micron Optics, Data Sheet, 2011. [Online]. Available: http://www.micronoptics.com/uploads/library/documents/Datasheets/MicronOpticsos3155.pdf

[139] D. Bernal, "Load vectors for damage localization," *Journal of Engineering Mechanics*, vol. 128, no. 1, pp. 7–14, January 2002.

[140] Y. Gao, B. F. Spencer, Jr., and D. Bernal, "Experimental verification of the flexibility-based damage locating vector method," *Journal of Engineering Mechanics*, vol. 133, no. 10, pp. 1043–1049, 2007.

[141] Y. Gao and B. F. Spencer, Jr., "Structural health monitoring strategies for smart sensor networks," Newmark Structural Engineering Laboratory, Tech. Rep. 011, May 2008. [Online]. Available: http://hdl.handle.net/2142/8802

[142] R. K. Giles, R. Kim, B. F. Spencer, Jr., L. A. Bergman, C. K. Shield, and S. C. Sweeney, "Structural health indices for steel truss bridges," in *Proceedings of IMAC XXIX*. Society for Experimental Mechanics, 2011.

[143] D. Zonta and D. Bernal, "Strain-based approaches to damage localization in civil structures," in *Proceedings of IMAC XXIV*. Society for Experimental Mechanics, 2006.

[144] G. Yao, K. Chang, and G. Lee, "Damage diagnosis of steel frames using vibrational signature analysis," *Journal of Engineering Mechanics*, vol. 118, no. 9, pp. 1949–1961, 1992.

[145] J. Maeck and G. de Roeck, "Dynamic bending and torsion stiffness derivation from modal curvatures and torsion rates," *Journal of Sound and Vibration*, vol. 225, 1999.

[146] S. Jang and B. F. Spencer, Jr., "Structural damage detection using static strain data," in *Proceedings of SMSST'07*, 2007.

[147] K. S. Miller, "On the inverse of the sum of matrices," *Mathematics Magazine*, vol. 54, no. 2, pp. 67–72, March 1981. [Online]. Available: http://www.jstor.org/stable/2690437

List of Recent NSEL Reports

No.	*Authors*	*Title*	*Date*
023	Denavit, M.D. and Hajjar, J.F.	Nonlinear Seismic Analysis of Circular Concrete-Filled Steel Tube Members and Frames	March 2010
024	Spencer, B.F. and Yun, C.-B. (Eds.)	Wireless Sensor Advances and Applications for Civil Infrastructure Monitoring	June 2010
025	Eatherton, M.R.. and Hajjar, J.F.	Large-Scale Cyclic and Hybrid Simulation Testing and Development of a Controlled-Rocking Steel Building System with Replaceable Fuses	Sept. 2010
026	Hall, K., Eatherton, M.R., and Hajjar, J.F.	Nonlinear Behavior of Controlled Rocking Steel-Framed Building Systems with Replaceable Energy Dissipating Fuses	Oct. 2010
027	Yeo, D. and Jones, N.P.	Computational Study on 3-D Aerodynamic Characteristics of Flow around a Yawed, Inclined, Circular Cylinder	Mar. 2011
028	Phillips, B.M. and Spencer, B.F.	Model-Based Servo-Hydraulic Control for Real-Time Hybrid Simulation	June 2011
029	Linderman, L.E., Mechitov, K.A., and Spencer, B.F.	Real-Time Wireless Data Acquisition for Structural Health Monitoring and Control	June 2011
030	Chang, C.-M. and Spencer, B.F.	Multi-axial Active Isolation for Seismic Protection of Buildings	May 2012
031	Phillips, B.M. and Spencer, B.F.	Model-Based Framework for Real-Time Dynamic Structural Performance Evaluation	August 2012
032	Moreu, F. and LaFave, J.M.	Current Research Topics: Railroad Bridges and Structural Engineering	October 2012
033	Linderman, L.E., Spencer, B.F.	Smart Wireless Control of Civil Structures	January 2014
034	Denavit, M.D. and Hajjar, J.F.	Characterization of Behavior of Steel-Concrete Composite Members and Frames with Applications for Design	July 2014
035	Jang, S. and Spencer, B.F.	Structural Health Monitoring for Bridge Structures using Wireless Smart Sensors	May 2015
036	Jo, H. and Spencer, B.F.	Multi-scale Structural Health Monitoring using Wireless Smart Sensors	May 2015
037	Li, J. and Spencer, B.F.	Monitoring, Modeling, and Hybrid Simulation: An Integrated Bayesian-based Approach to High-fidelity Fragility Analysis	May 2015
038	Sim, S-H. and Spencer, B.F.	Decentralized Identification and Multimetric Monitoring of Civil Infrastructure using Smart Sensors	June 2015
039	Giles, R.K. and Spencer, B.F.	Development of a Long-term, Multimetric Structural Health Monitoring System for a Historic Steel Truss Swing Bridge	June 2015